LEABHARLANN CHOLÁISTE NA TRÍONÓIDE, BAILE ÁTHA CLIATH | TRINITY COLLEGE LIBRARY DUBLIN
Ollscoil Átha Cliath | The University of Dublin

Terms and Conditions of Use of Digitised Theses from Trinity College Library Dublin

Copyright statement

All material supplied by Trinity College Library is protected by copyright (under the Copyright and Related Rights Act, 2000 as amended) and other relevant Intellectual Property Rights. By accessing and using a Digitised Thesis from Trinity College Library you acknowledge that all Intellectual Property Rights in any Works supplied are the sole and exclusive property of the copyright and/or other IPR holder. Specific copyright holders may not be explicitly identified. Use of materials from other sources within a thesis should not be construed as a claim over them.

A non-exclusive, non-transferable licence is hereby granted to those using or reproducing, in whole or in part, the material for valid purposes, providing the copyright owners are acknowledged using the normal conventions. Where specific permission to use material is required, this is identified and such permission must be sought from the copyright holder or agency cited.

Liability statement

By using a Digitised Thesis, I accept that Trinity College Dublin bears no legal responsibility for the accuracy, legality or comprehensiveness of materials contained within the thesis, and that Trinity College Dublin accepts no liability for indirect, consequential, or incidental, damages or losses arising from use of the thesis for whatever reason. Information located in a thesis may be subject to specific use constraints, details of which may not be explicitly described. It is the responsibility of potential and actual users to be aware of such constraints and to abide by them. By making use of material from a digitised thesis, you accept these copyright and disclaimer provisions. Where it is brought to the attention of Trinity College Library that there may be a breach of copyright or other restraint, it is the policy to withdraw or take down access to a thesis while the issue is being resolved.

Access Agreement

By using a Digitised Thesis from Trinity College Library you are bound by the following Terms & Conditions. Please read them carefully.

I have read and I understand the following statement: All material supplied via a Digitised Thesis from Trinity College Library is protected by copyright and other intellectual property rights, and duplication or sale of all or part of any of a thesis is not permitted, except that material may be duplicated by you for your research use or for educational purposes in electronic or print form providing the copyright owners are acknowledged using the normal conventions. You must obtain permission for any other use. Electronic or print copies may not be offered, whether for sale or otherwise to anyone. This copy has been supplied on the understanding that it is copyright material and that no quotation from the thesis may be published without proper acknowledgement.

Experimental and Numerical Investigation of a Photovoltaic/Thermal/Phase Change Material System

By

Maria Browne B.A., B.A.I., P.G.Dip.

A Thesis submitted to the University of Dublin for the degree of Doctor of Philosophy

February 2016

Department of Civil, Structural and Environmental Engineering

University of Dublin

Trinity College

Dublin

TRINITY LIBRARY
27 JUL 2016
DUBLIN

Thesis 10938

Declaration

I hereby declare that the work contained in this thesis is my own work, and has not been submitted as an exercise for a degree at this or any other university.

I also give the library permission to lend or copy this thesis, upon request, for academic purposes. This permission covers only single copies made for study purposes, subject to normal conditions of acknowledgement.

February 2016

Executive Summary

Hybrid Photovoltaic/Thermal (PV/T) systems generate both electricity and heat simultaneously. Typically 15 – 18 % of solar radiation incident on a PV module is converted to electricity and 82 – 85 % is converted to heat. This heat generated at the PV in a PV/T system is removed using a confined water or air flow. Phase change materials have been used extensively for thermal energy storage. At initial heating, a phase change material (PCM) heats sensibly and when the PCM reaches melting/solidification temperature the material absorbs latent heat, progressively melting. A novel Photovoltaic/Thermal/Phase Change Material (PV/T/PCM) system that generates electricity, stores heat and pre-heats water is presented.

The primary step involved in the design of the PV/T/PCM system was to select a PCM and containment material. An investigation into the characterisation of potential PCM using Differential Scanning Calorimetry and Temperature-History Method was carried out. Capric:palmitic acid was found to be most suited to integration in a PV/T/PCM system in Ireland. A long term corrosion study showed stainless steel to be intrinsically resistant to corrosion by PCM and for this reason it was a suitable PCM containment material.

A large-scale, outdoor PV/T/PCM system was designed, installed, and characterised experimentally in Dublin, Ireland (53.33 N, 6.24W). The system operated for approximately a year, the objective being to achieve an optimal simultaneous combination of useful electrical and heat output as well as an ability to store heat and peak shifting heat availability. The thermal, electrical and economic performance of the system was evaluated. It was shown that the temperature attained by the water was by approximately 5.5 °C higher when compared to a PV/T system with no PCM during summer months. PCM was shown to be an effective means of storing heat in a PV/T system and of extending the amount of time for which heat is available in comparison to that of three reference experimental systems.

The experimental results were used to validate a PV/T/PCM system model which was developed using TRNSYS and COMSOL. TRNSYS, an energy simulation software package, was used to simulate the PV panel and thermal aspects of the system. COMSOL, a finite element based software, modelled the phase change and energy storage of the PCM. The model was used to optimise the system design and improve system performance. Finally, the simulation was used to predict the performance of a PV/T/PCM system in countries with higher

solar radiation levels than that of Ireland. It was shown that the cumulative thermal efficiency of the system in Saudi Arabia (46.2 %) increased to over three times that of the system simulated in Irish conditions (15.8 %).

An economic assessment based on the performance of a PV/T/PCM system in Ireland, UK, Saudi Arabia and Spain was completed, two of which (UK and Spain) implemented incentives to encourage the generation of green energy which had a positive impact on the simple payback period. The calculated simple payback period (SPP) of a PV/T/PCM system in a household depending solely on electricity was 5.1 years in Ireland and 5.0 years in the UK. For the two countries with a high solar resource, Spain had an SPP of 3.1 years compared to Saudi Arabia which was calculated to be 10.8 years. These differences can be attributed to financial incentives for the generation of green energy in Spain and the low non-renewable energy cost in Saudi Arabia.

Dedication

This thesis is dedicated to my Mam,

Who instilled in me the importance of hard work and imparted the value of education.

For this I am ever grateful.

Acknowledgements

Firstly, I would like to thank my project supervisor Dr. Sarah McCormack for her constant support and guidance throughout the research. Her tireless work ethic, invaluable advice and patience throughout the project were greatly appreciated.

I would also like to extend my appreciation to Prof. Brian Norton (Dublin Institute of Technology) for his advice and support for the duration of the project.

Thank you to the EU Structural Funds, ERDF, the Department of Jobs, Enterprise and Innovation and Higher Education Authority through GREP Funding, Science Foundation Ireland through their Research Frontiers Program Code 07/RFP/ENEF719, the Research Support Unit at Dublin Institute of Technology, COST Action TU0802 Next generation cost effective phase change materials for increased energy efficiency in renewable energy systems in buildings (NeCoEPCM) and COST Action TU1205 Building integration of solar thermal systems (BISTS).

Thanks to everyone in Trinity College who helped out along the way, particularly to Kevin Ryan and Gordon O'Brien whose help was greatly appreciated. Also to all in Dublin Institute of Technology for providing me with excellent research facilities, in particular I would like to mention Kevin O'Farrell, Colm Gillen, Thomas Kiely, Eamonn Murphy and Ayda Esfandyari.

A big thanks to Adam, who gave me a platform to discuss problems of a PhD student and perhaps complain a little! I would like to thank all of my Pearse Street office colleagues and friends from the past few years. Hisham, Saniul, Bea, Darragh, Maria, Yasmin, Salah and Joanne. I would like to thank all 'The Girls', Alice, Anne, Claire, Fiona, Kate, Karen, Michelle, Niamh and Rebecca for being so supportive, it's hard to get a chance to thank you between the laughs and chatter so thank you!! Thank you to the "College Crew" for the daily group discussions providing me with many laughs.

A special mention to Seán for being so supportive in the last few years. Your proof reading skills and patience were examined and I'm delighted to say they have passed a very rigorous test!!

Finally, I wish to thank my family for all their support along the way. A special thanks to my Dad, Mick, for all his encouragement and (financial!) backing throughout my years of education. I like to think all those lifts to and from the train station have paid off. I'm also grateful to my sisters and brother, Helen, Karen and Mark, for their patience and all the favours, from making me dinner to lending me laptops!

Table of Contents

Declaration i
Executive Summary iii
Dedication v
Acknowledgements vii
Table of Contents ix
List of Figures xv
List of Tables xxv
Nomenclature xxvii
Subscript xxxi
Abbreviations xxxii
Chapter 1. Introduction 3
1.1 Background 3
1.2 Scope of Research 4
1.2.1 Research Aims and Proposed Methodology 5
1.3 Thesis Outline 6
Chapter 2. Literature Review 11
2.1 Introduction 11
2.2 Photovoltaic (PV) and Solar Thermal Technology 11
2.2.1 Photovoltaic Technologies 12
2.2.1.1 Issues with Photovoltaic Technologies 13
2.2.2 Solar Thermal Collectors 17
2.2.3 Hybrid Solar Systems 20
2.2.3.1 Photovoltaic/Thermal Systems 20
2.2.3.2 Incorporation of PV and Thermal Systems in Buildings 23
2.2.4 Complexities Involved in Solar Energy System Technology 24
2.3 Phase Change Material (PCM) 25
2.3.1 Classification of Phase Change Material 25
2.3.2 Corrosion Properties of Phase Change Material 28
2.4 Application of Phase Change Material in Photovoltaic/Thermal Systems 32
2.4.1 Phase Change Material as Thermal Management Technique 32
2.4.1.1 Thermal Management of PV using PCM 32
2.4.1.2 Thermal Management of Concentrating PV (CPV) using PCM 43
2.4.2 Solar Thermal Collectors with Integrated PCM 47
2.4.3 Hybrid Photovoltaic/Thermal/Phase Change Material Systems 52

2.4.4 Modelling Tools for Solar Systems and PCM 56
2.4.4.1 TRNSYS 56
2.4.4.2 Solar Collector Systems 56
2.4.4.3 Modelling Phase Change Materials in TRNSYS 59
2.5 Conclusion 63
Chapter 3. Materials and Experimental Methods 67
3.1 Introduction 67
3.2 Characterisation Techniques of Phase Change Material 67
3.2.1 Phase Change Material Selection 68
3.2.2 Differential Scanning Calorimetry Methodology 70
3.2.3 Temperature-History Method Methodology 72
3.2.4 Immersion Corrosion Investigation Methodology 77
3.2.5 Scanning Electron Microscope (SEM) 79
3.3 Experimental Design, Fabrication and Installation of a PV/T/PCM System 79
3.3.1 Photovoltaic Panel – System 1 81
3.3.2 Heat Sink (Container) – System 2 86
3.3.3 Thermal Collector – System 3 88
3.3.4 Energy Storage Material – System 4 90
3.3.5 Data Acquisition System 91
3.3.6 Sensor Locations 94
3.3.6.1 System 1 Sensors (Photovoltaic –Reference) 94
3.3.6.2 System 2 Sensors (Photovoltaic with Container –Reference) 95
3.3.6.3 System 3 Sensors (Photovoltaic/Thermal) 97
3.3.6.4 System 4 Sensors (Photovoltaic/Thermal/Phase Change Material) 99
3.3.7 System Installation 100
3.3.8 System Comparison 100
3.4 Modelling Software 102
3.4.1 TRNSYS – Transient System Simulation Tool 102
3.4.2 COMSOL Multiphysics 102
3.5 Conclusion 103
Chapter 4. Characterisation and Corrosion Testing of Phase Change Material 107
4.1 Introduction 107
4.2 Phase Change Material Characterisation 108
4.3 Phase Change Material Characterisation using Differential Scanning Calorimetry . 108
4.3.1 Capric Acid 109
4.3.2 Capric:palmitic Acid 110
4.3.3 Capric:lauric Acid 111

4.3.4 Salt Hydrate SP22 112
4.3.5 Micronal® 112
4.4 Phase Change Material Characterisation using Temperature-History Method 113
4.4.1 Capric Acid 114
4.4.2 Capric:palmitic Acid 114
4.4.3 Capric:lauric Acid 115
4.4.4 Salt Hydrate SP22 116
4.4.5 Micronal® 118
4.5 Comparison of Results of Thermophysical Properties of PCM with Reviewed Literature 119
4.5.1 Conclusion of Characterisation Tests 121
4.6 Long Term Immersion Corrosion Testing 122
4.6.1 Phase Change Material and Material Samples 124
4.6.2 Results and Discussion of Immersion Corrosion Tests 125
4.6.3 Metallographic Investigation 134
4.6.3.1 Capric Acid 134
4.6.3.2 Capric:palmitic Acid 136
4.6.3.3 Capric:lauric Acid 138
4.6.3.4 Salt Hydrate SP22 140
4.6.3.5 Micronal® 142
4.6.4 Evaluation and Recommendation 143
4.6.5 Preventative Measures 147
4.7 Conclusion 149
Chapter 5. Performance Evaluation of a Photovoltaic/Thermal/ Phase Change Material System 153
5.1 Introduction 153
5.2 Overview of Experimental Systems 153
5.3 Thermal Analysis Methodology of PV/T/PCM System 154
5.4 Heat Retention of a Photovoltaic/Thermal Collector with Phase Change Material .. 159
5.4.1 Environmental Conditions 159
5.4.2 Results and Discussion 160
5.5 Analysis of the Performance of Electrical and Thermal Efficiency in a Photovoltaic/Thermal/Phase Change Material System 173
5.5.1 Thermal Performance of the Systems 173
5.5.1.1 Environmental Conditions 173
5.5.1.2 Results and Discussion 174
5.5.2 Electrical Efficiency 178
5.5.2.1 Characterising PV Panels 179

5.5.2.2 Environmental Conditions 179
5.5.2.3 Results and Discussion 179
5.6 Evaluation of Photovoltaic/Thermal/Phase Change Material System Under Increased Simulated Temperatures 183
5.6.1 Methodology of Forced Heating Conditions on a PV/T/PCM System 183
5.6.2 Environmental Conditions 184
5.6.3 Results and Discussion 186
5.6.3.1 Charging and Discharging Phase Change Material 186
5.6.3.2 Available Heat Stored 188
5.6.3.3 Water Temperature 189
5.6.3.4 Thermal Efficiency 190
5.7 Conclusion 193
Chapter 6. Modelling a Photovoltaic/ Thermal/ Phase Change Material System 197
6.1 Introduction 197
6.2 Model Structure 197
6.2.1 TRNSYS 199
6.2.1.1 Photovoltaic (PV) System Model (System 1) 199
6.2.1.2 Photovoltaic/ Thermal (PV/T) System Model (System 3) 203
6.2.2 COMSOL 210
6.2.2.1 Thermal Collector Model 210
6.2.2.2 Thermal Collector with Phase Change Material Model 217
6.2.3 Combining TRNSYS and COMSOL 219
6.3 Validation of Model – Results and Discussion 219
6.3.1 Weather data 220
6.3.2 Photovoltaic (PV) System Model (System 1) – TRNSYS 221
6.3.3 Photovoltaic/Thermal (PV/T) System Model (System 3) – TRNSYS 225
6.3.4 Photovoltaic/Thermal (PV/T) System Model (System 3) – TRNSYS and COMSOL 229
6.3.5 Photovoltaic/Thermal/Phase Change Material (PV/T/PCM) System Model (System 4) – TRNSYS and COMSOL 231
6.4 Conclusion 238
Chapter 7. Optimisation and Up-scale of a Photovoltaic/Thermal/Phase Change Material System 243
7.1 Introduction 243
7.2 Optimisation 243
7.2.1 Phase Change Material Thermal Conductivity 244
7.2.2 Phase Change Material Heat of Fusion 247
7.2.3 Phase Change Material Heat Capacity 249

7.2.4 Mass Flow Rate 250
7.2.5 Thermal Conductivity of Container 253
7.2.6 Discussion of Thermal Efficiency of the Parametric Models 256
7.3 Optimised PV/T/PCM System Performance 260
7.3.1 Optimised PV/T/PCM System in Ireland 260
7.3.2 Optimised PV/T/PCM System in Saudi Arabia 264
7.4 Up-scaling Optimised Domestic Scale PV/T/PCM System 269
7.4.1 Up-scaled Optimised System in Ireland 270
7.4.2 Up-scaled Optimised System in Saudi Arabia 272
7.5 Applications 275
7.6 Pathogenic Bacteria 276
7.7 Conclusion 276
Chapter 8. Economic Assessment of a Photovoltaic/Thermal/Phase Change Material System 281
8.1 Cost Analysis of a PV/T/PCM System 281
8.1.1 Cost of Photovoltaic Panels 282
8.1.2 Cost and Commercial Availability of Phase Change Material 283
8.1.3 Economics of Incorporating PCM with PV 285
8.1.4 Cost of a PV/T/PCM System 285
8.2 Economic Assessment of a PV/T/PCM System 287
8.2.1 Thermal and Electrical Energy Analysis of a PV/T/PCM System 287
8.2.2 Simple Payback Period 289
8.3 Conclusion 295
Chapter 9. Conclusions 299
9.1 Contributions to Knowledge 299
9.1.1 Summary of the Contributions to Knowledge 301
9.2 Recommendations for Further Research 302
References 307
Publications 331
Appendix 1 333
Appendix 2 334
Appendix 3 335

List of Figures

Figure 1.1: Solar energy applications (Ayompe, 2011) 4
Figure 2.1: Confirmed efficiencies for research cells (NREL, 2015) 13
Figure 2.2: (a) Variation of power with voltage of a silicon solar cell (Radziemska, 2003) (b) Variation of power with voltage of a silicon panel temperature (Hadj Arab et al., 2004; Villalva et al., 2009; Lo Brano et al., 2010; Lo Brano et al., 2012; Ciulla et al., 2014) 14
Figure 2.3: Temperature dependence of V_{oc} in DSSC (Usami et al., 2009) 14
Figure 2.4: Current –voltage characteristics of Au/CdTe Schottky diode (Pattabi et al., 2007). 16
Figure 2.5:Temperature dependence of the maximum power of a multi-junction cell (Fernández et al., 2013) 16
Figure 2.6: Schematic diagram of a flat plate collector (Kalogirou, 2004) 17
Figure 2.7: Schematic of (a) evacuated tube (b) evacuated tube collector 18
Figure 2.8: (a) Single-sided coated absorber (b) Double-sided coated absorber (Nkwetta and Smyth, 2012) 19
Figure 2.9: Cross section of PV/T experimental models: (a) PV/Water (b) PV/Water + Glazing (c) PV/Air (d) PV/Air + Glazing (Tripanagnostopoulos et al., 2002) 21
Figure 2.10: (a) Sheet-and-tube PVT collectors, (b) Channel PV/T collectors (c) Free flow PV/T collectors and (d) two absorber PV/T-collectors (Zondag et al., 2003) 22
Figure 2.11: Efficiency Vs Temperature of dye sensitised solar cells (DSSC), polycrystalline silicon (poly-Si) and Cadmium Telluride (CdTe) solar cells (Raga and Fabregat-Santiago, 2012) 24
Figure 2.12: Graphical representation of the variation of stored heat of a PCM with increasing temperature (Günther et al., 2009) 26
Figure 2.13: PCM classification based on melting temperatures and melting enthalpy (Cabeza et al., 2011) 27
Figure 2.14: Phase change material integrated with a photovoltaic model (Stultz and Wren, 1978) 33
Figure 2.15: Configuration of electrochemical cell incorporated with PCM (Al-Hallaj and Selman, 2005) 34
Figure 2.16: Photographic image of melting front of PV/PCM system (Huang et al., 2004) 35
Figure 2.17: PV/PCM system with fins (Huang et al., 2011) 35
Figure 2.18: System A, B, C and D (Hasan, 2010b) 36
Figure 2.19: Results from experiments at (a) 750 W/m^2 and (b) 1000W/m^2(Hasan, 2010b) 36

Figure 2.20: Heat exchange in a PV/PCM system modelled using COMSOL (Cellura et al., 2008) 37
Figure 2.21: Schematic of heat transfer through BIPV PV/PCM system (Ho et al., 2012) 37
Figure 2.22: Schematic of heat transfer in a PV/MEPCM module (Ho et al., 2013) 38
Figure 2.23: Optics, electrical conversion and heat transfer mechanism in PV/PCM systems (Sarwar et al., 2014) 39
Figure 2.24: (a) Aluminium honey comb (b) Experimental set up where (1) PV/PCM T_{melt} 45°C (2) PV/PCM T_{melt} 27°C (3) PV insulated and (4) PV standalone (Jay et al., 2010) 40
Figure 2.25: Experimental set-up of PV-PCM systems, location of thermocouples and attachment of PV to PCM container (Hasan et al., 2014a) 41
Figure 2.26: Surface temperatures of reference PV and PV-PCM systems measured in (a) Dublin and (b) Vehari (Hasan et al., 2014a) 41
Figure 2.27: Encapsulation of PCM and experimental installation (Lo Brano et al., 2013) 42
Figure 2.28: Experimental equipment (1) PCM, (2) heat exchangers, (3) PCM intake valve, (4) structure system, (5) flowmeter, (6) air intake valve, (7) metal stand and (8) insulation material (Biwole et al., 2013) 43
Figure 2.29: ACPPVC integrated with PCM (a) schematic and (b) photo (Wu, 2009) 44
Figure 2.30: V-trough PV system with integrated metal-wax composite PCM (Maiti et al., 2011) 45
Figure 2.31: Schematic of PV-thermoelectric power system with the use of PCM as TES (Li et al., 2013) 46
Figure 2.32: Concentrating PV system with PCM and fins for cooling (Sarwar, 2012) 46
Figure 2.33: Solar collector storage system with integrated PCM (Rabin et al., 1995) 48
Figure 2.34: (a) Solar water heater (b) Solar water heater with integrated PCM (Chaabane et al., 2014) 48
Figure 2.35: Solar domestic hot water system with PCM (Haillot et al., 2013) 49
Figure 2.36: Cross-section of solar collector with absorber-container unit (Mettawee and Assassa, 2006) 50
Figure 2.37: Combined single unit solar collector and energy storage (Koca et al., 2008) 51
Figure 2.38: Solar collector with PCM filled cavity (Bouadila et al., 2014) 51
Figure 2.39: Cross section of residential PV/T system (Yin et al., 2013) 53
Figure 2.40: Schematic of simulated system (Malvi et al., 2011) 54
Figure 2.41: Simulated BIPV/T system with integrated PCM wallboard (Aelenei et al., 2013) 54

Figure 2.42: Thermal processes and diurnal periodicities that distinguish between PV/T and PV/PCM solar collectors and associated storage systems 55
Figure 2.43: TRNSYS flow diagram for a combined PV/T system (Kalogirou, 2001) 57
Figure 2.44: Representation of Type 240 developed by Schranzhofer (2006) 59
Figure 2.45: Phase change room combining Type 272 with Type 56 61
Figure 2.46: PCM enhanced ceiling ventilation system with PVT collectors (Lin et al., 2014). 62
Figure 3.1: Schematic of (a) power compensation DSC (b) Heat-flux DSC (Klančnik et al., 2010) 71
Figure 3.2: Power compensation DSC (PerkinElmer Diamond machine) 72
Figure 3.3: Schematic of the THM (Sarwar, 2013) 73
Figure 3.4: THM experimental set-up (a) melting PCM in a water bath for three hours (b) cooling PCM in the fridge (c) Data logger and recording equipment 74
Figure 3.5: T-history curve of (a) PCM with subcooling (b) PCM without subcooling (c) water during cooling process (Yinping et al., 1999) 76
Figure 3.6: (a) Schematic of each system (b) experimental set-up of all systems 80
Figure 3.7: Solar Technology PV panel used in the experiment 82
Figure 3.8: Schematic of solar electrical circuit 83
Figure 3.9: Photograph of elements of the solar electrical circuit 84
Figure 3.10: Schematic of final electrical load circuit connected to PV 85
Figure 3.11: Resistances of each PV circuit 86
Figure 3.12: A sealed stainless steel heat sink i.e. container 87
Figure 3.13: Dimensions of the stainless steel container, back view, and two side views in mm 87
Figure 3.14: (a) Photograph of heat exchanger (b) schematic of heat exchanger with dimensions 88
Figure 3.15: Closed loop water flow system of System 3 and System 4 89
Figure 3.16: (a) Solid capric acid (b) melting PCM eutectic (c) fully liquid fatty acid eutectic. 90
Figure 3.17: (a) Davis weather station, Vantage Pro2 (b) Kipp and Zonen pyranometer, Sp Lite2 91
Figure 3.18: (a) Agilent 34972A LXI front and back (b) Delta-t DL2e and channel connections 92
Figure 3.19: IFM ultrasonic flowmeter SU 7000 93
Figure 3.20: (a) Wire thermocouple (b) probe thermocouple 93
Figure 3.21: Thermocouple locations on the back of PV panel, all dimensions are in mm 95

Figure 3.22: (a) Container positioned on the back of PV with thermocouple positions as indicated (b) side elevation view of the PV attached to the container 96
Figure 3.23: System 2 (PV with container) dimensions 96
Figure 3.24 (a) Heat exchanger inside the container prior to sealing (b) schematic of the heat exchanger inside the container 97
Figure 3.25: (a) Stainless steel gland and probe in the back of the container (b) copper gland welded to the copper pipe (probe not yet inserted) 98
Figure 3.26: Dimensions of System 3 illustrating the locations of the thermocouple probes 98
Figure 3.27: Heat exchanger immersed in liquid PCM in the container of System 1 99
Figure 3.28: Location of the experiment on the roof top solar laboratory 100
Figure 3.29: (a) Photograph of completed experimental set-up (b) cross–section drawing of experimental set-up 101
Figure 4.1: DSC results of capric acid during melting and solidification 109
Figure 4.2: DSC results of capric:palmitic acid during melting and solidification 110
Figure 4.3: DSC results of the eutectic mixture, capric: lauric acid 111
Figure 4.4: DSC results of SP22 during melting and solidification 112
Figure 4.5: DSC results of Micronal® during melting and solidification 113
Figure 4.6: Temperature history curve of capric acid 114
Figure 4.7: Temperature history curve for capric:palmitic acid 115
Figure 4.8: Temperature history curve for capric:lauric acid 116
Figure 4.9: Temperature history curve of SP22 116
Figure 4.10: SP22 (a) before first melt (b) after melting (c) first solidification 117
Figure 4.11: SP22 in (a) liquid form and (b) solid state after an a series of thermal cycles 118
Figure 4.12: Temperature history curve of Micronal® 119
Figure 4.13: Sample aluminium containers sealed using (a) CT 1 and (b) MS 5000 123
Figure 4.14: Effects of PCM on adhesive (a) CT 1 and (b) MS 5000 123
Figure 4.15: Material mass loss due to immersion in capric acid 126
Figure 4.16: Corrosion rate during immersion tests of material samples with capric acid 127
Figure 4.17: Material mass loss due to immersion in capric:palmitic acid 128
Figure 4.18: Corrosion rate during immersion tests of material samples with capric:palmitic acid. 128
Figure 4.19: Material mass loss due to immersion in capric:lauric acid 129
Figure 4.20: Corrosion rate during immersion tests of material samples with capric: lauric acid 130

Figure 4.21: Copper and brass samples in (a) capric acid (b) capric:palmitic acid (c) capric:lauric acid 131
Figure 4.22: Material mass loss due to immersion in SP22 131
Figure 4.23: Corrosion rate during immersion tests of material samples with SP22 132
Figure 4.24: Material mass loss due to immersion in Micronal® 133
Figure 4.25: Corrosion rate during immersion tests of material samples with Micronal® 133
Figure 4.26: Copper immersed in capric acid on (a) Day 1 6000x magnification (b) Day 25 6000x magnification (c) Day 540 6000x magnification 134
Figure 4.27: Brass immersed in capric acid on (a) Day 1 6000x magnification (b) Day 200 6000x magnification (c) Day 540 6000x magnification 135
Figure 4.28: Aluminium immersed in capric acid on (a) Day 25 6000x magnification (b) Day 200 6000x magnification (c) Day 540 3000x magnification 135
Figure 4.29: Mild steel immersed in capric acid on (a) Day 1 6000x magnification (b) Day 25 6000x magnification (c) Day 540 6000x magnification 136
Figure 4.30: Copper immersed in capric:palmitic acid on (a) Day 1 6000x magnification (b) Day 200 3000x magnification (c) Day 540 3000x magnification 136
Figure 4.31: Brass immersed in capric:palmitic acid on (a) Day 1 6000x magnification (b) Day 200 3000x magnification (c) Day 540 200x magnification 137
Figure 4.32: Aluminium immersed in capric:palmitic acid on (a) Day 1 3000x magnification (b) Day 200 3000x magnification (c) Day 540 3000x magnification 138
Figure 4.33: Mild steel immersed in capric:palmitic acid on (a) Day 1 3000x magnification (b) Day 25 3000x magnification (c) Day 540 3000x magnification 138
Figure 4.34: Copper immersed in capric:lauric acid on (a) Day 1 3000x magnification (b) Day 25 3000x magnification (c) Day 540 3000x magnification 139
Figure 4.35: Brass immersed in capric:lauric acid on (a) Day 1 6000x magnification (b) Day 25 6000x magnification (c) Day 540 3000x magnification 139
Figure 4.36: Aluminium immersed in capric:lauric acid on (a) Day 1 6000x magnification (b) Day 200 6000x magnification (c) Day 540 3000x magnification 140
Figure 4.37: Mild steel immersed in capric:lauric acid on (a) Day 1 6000x magnification (b) Day 200 6000x magnification (c) Day 540 3000x magnification 140
Figure 4.38: Copper immersed in SP22 on (a) Day 1 6000x magnification (b) Day 200 6000x magnification (c) Day 540 6000x magnification 141
Figure 4.39: Aluminium immersed in SP22 on (a) Day 1 3000x magnification (b) Day 25 3000x magnification (c) Day 540 200x magnification 141

Figure 4.40: Copper immersed in Micronal® on (a) Day 1 3000x magnification (b) Day 200 3000x magnification (c) Day 540 6000x magnification 142
Figure 4.41: Brass immersed in Micronal® on (a) Day 25 3000x magnification (b) Day 200 3000x magnification (c) Day 540 3000x magnification 143
Figure 4.42: Aluminium immersed in Micronal® acid on (a) Day 1 3000x magnification (b) Day 200 3000x magnification (c) Day 540 3000x magnification 143
Figure 4.43: Summary of mass loss experienced by each material due to PCM 145
Figure 4.44: Summary of corrosion rates experienced by each material due to PCM 145
Figure 5.1: Ambient temperature, wind speed and solar irradiance measured in Dublin (53.33 N, 6.25 W) on the 4th - 6th of July 2013 160
Figure 5.2: Temperature on the back of the PV panel in System 1 (PV), System 2 (PV/container), System 3 (PV /T), and System 4 (PV/T/PCM) 161
Figure 5.3: Effect of the addition of (a) container (b) water (c) PCM on the temperature of the back of the PV panel 162
Figure 5.4: Temperature regulation of PV due to addition of PCM and the power gained due to the temperature regulation 163
Figure 5.5: Internal container temperature in (a) System drivers – solar irradiance and ambient temperature, (b) System 2 (PV with container) and (c) System 3 (PV/T) and (d) System 4 (PV/T/PCM) 164
Figure 5.6: The effect of (a) the water and (b) the PCM on the internal container temperature 165
Figure 5.7: Temperature of the back of container in (a) System drivers (b) System 2 (PV/container), (c) System 3 (PV/T) and (d) System 4 (PV/T/PCM) 167
Figure 5.8: The effect of (a) water and (b) the PCM on the temperature of the back of the container 168
Figure 5.9: Temperature at the inlet and outlet pipes in System 4 (PV/T/PCM) and System 3 (PV/T) 169
Figure 5.10: (a) Solar irradiance and ambient temperature. Temperature differential of water at the inlet and outlet of (b) System 3 (PV/ T) and (c) System 4 (PV/T/PCM) 170
Figure 5.11: Time for which heat can be transferred from PCM to water on each day 171
Figure 5.12: Temperature comparison of the back of panel in System 4 and ambient temperature 172
Figure 5.13: Flow of the water in the pipe network and solar irradiance for the experimental period 172
Figure 5.14: Useful heat efficiency, Q_u, of each system on Day 1, Day 2 and Day 3 174

Figure 5.15: Stored heat efficiency of System 4 on Day 1, Day 2 and Day 3 175
Figure 5.16: Efficiency of System 4 on Day 1, Day 2 and Day 3 of the time for which the PCM extended heat availability 176
Figure 5.17: Total thermal efficiency of each system 177
Figure 5.18: Daily average value of outlet water temperature of System 4 (PV/T/PCM) over (a) entire experimental period (b) October 2013 – September 2014 178
Figure 5.19: Meteorological conditions on the 30th of June 2014 179
Figure 5.20: Power generated by PV in each system 180
Figure 5.21: Temperature of the back of the PV panel in each system 181
Figure 5.22: Power generated over (a) entire experimental period (b) October 2013 – September 2014 182
Figure 5.23: Heat mat with temperature controls used to generate forced heat 184
Figure 5.24: Environmental conditions for duration of experiment 185
Figure 5.25: Temperature at the back of the panel 185
Figure 5.26: Inlet and outlet water temperatures of (a) System 3 (b) System 4 186
Figure 5.27: Temperature difference between inside of container and outlet temperature in PV/T/PCM and PV/T systems 187
Figure 5.28: Available heat stored (y-axis) and preheat water potential with and without heating mats 188
Figure 5.29: Temperature differential of the water inlet and outlet in PV/T-PCM and PV/T .. 189
Figure 5.30: Useful heat gain, Q_u, by each system 190
Figure 5.31: Heat stored, Q_s, by System 4 191
Figure 5.32: Heat storage potential of each system 192
Figure 5.33: Total efficiency of the PV/T/PCM systems 192
Figure 5.34: Stage process diagram of a PV/T/PCM system 193
Figure 6.1: Schematic indicating the software used for various components of (a) System 1 (PV panel) (b) System 3 (PV/T) (c) System 3 (PV/T) (d) System 4 (PV/T/PCM) 198
Figure 6.2: Model of PV system (a) information flow diagram (b) TRNSYS schematic 200
Figure 6.3: Model of PV/T system (a) information flow diagram (b) TRNSYS schematic 203
Figure 6.4: PV/T system as modelled in TRNSYS (Type 560) (TRNSYS Manual, 2014) 205
Figure 6.5: Assumptions based on Type 560 209
Figure 6.6: Geometry of the thermal collector built using COMSOL (a) container (b) pipe network 211
Figure 6.7: Mesh of PV/T system generated in COMSOL 216

Figure 6.8: Variation in outlet temperature at 12 and 6 minute time steps 216
Figure 6.9: Schematic illustration of heat transfer mechanism in PVTPCM system as modelled in COMSOL 217
Figure 6.10: Solar irradiance experimental with simulated results 220
Figure 6.11: Characterisation of System 1 at a resistance of 5 ohms 221
Figure 6.12: Experimental and simulated results of PV (a) current (b) voltage and (c) power simulated for 30th of June 2014 222
Figure 6.13: Corrected experimental and simulated values of PV (a) current (b) voltage (c) power 224
Figure 6.14: Experimental and simulated PV/T power generated 226
Figure 6.15: Maximised voltage when using a MPPT 227
Figure 6.16: Experimental and simulated maximum power generated In PV/T simulated in TRNSYS 227
Figure 6.17: Experimental and simulated temperature at the inlet of the PV/T system 228
Figure 6.18: Experimental and simulated temperature at the outlet of the PV/T system in TRNSYS 228
Figure 6.19: Experimental and simulated temperature at the inlet of the PV/T system in COMSOL 230
Figure 6.20: Experimental and simulated temperature of the air inside the container of PV/T system in COMSOL 230
Figure 6.21: Experimental and simulated temperature at the outlet of the PV/T system in COMSOL 231
Figure 6.22: Experimental and simulated power generated in a PV/T/PCM system simulated in TRNSYS 232
Figure 6.23: Solar irradiance on the 23rd of December and 5th of July 2013 233
Figure 6.24: Experimental and simulated inlet water temperature in a PV/T/PCM system simulated in COMSOL (23rd December 2013) 233
Figure 6.25: Experimental and simulated temperature of PCM in a PV/T/PCM system modelled in COMSOL (23rd December 2013) 234
Figure 6.26: Experimental and simulated outlet water temperature in a PV/T/PCM system simulated in COMSOL (23rd December 2013) 235
Figure 6.27: Experimental and simulated inlet water temperature in a PV/T/PCM system simulated in COMSOL (5th July 2013) 236

Figure 6.28: Experimental and simulated temperature of PCM in a PV/T/PCM system modelled in COMSOL (5th of July 2013) 237
Figure 6.29: Experimental and simulated outlet water temperature in a PV/T/PCM system simulated in COMSOL (5th of July 2013) 237
Figure 7.1: Effect of varying the PCM thermal conductivity (W/m.K) on the PCM temperature over the course of (a) one day (b) three hours 245
Figure 7.2: Effect of varying the PCM's thermal conductivity (W/m.K) on the outlet water temperature 246
Figure 7.3: Effect of varying the PCM's heat of fusion (kJ/ kg) on the PCM 248
Figure 7.4: Effect of varying the PCM's heat of fusion (kJ/ kg) on the water outlet temperature 248
Figure 7.5: Effect of varying the PCM heat capacity (kJ/kgK) on the (a) PCM (b) water outlet temperature 249
Figure 7.6: Effect of varying the PCM heat capacity (kJ/ kg K) on the outlet water temperature 250
Figure 7.7: Effect of varying the PV/T/PCM system mass flow rate (kg/ sec) on the PCM 251
Figure 7.8: Effect of varying the PV/T/PCM system mass flow rate on the outlet water temperature 252
Figure 7.9: Temperature of inlet and outlet flow at 0.05 kg/ sec 252
Figure 7.10: Effect of varying the thermal conductivity of the PCM encasement material (W/mK) on the PCM temperature 254
Figure 7.11: Effect of varying the thermal conductivity (W/mK) of the water outlet temperature 255
Figure 7.12: Change in thermal energy utilisation for different models as presented in Table 7.3 258
Figure 7.13: Ambient temperature and solar irradiance of Ireland 260
Figure 7.14: PCM temperature of the optimised and validated models 261
Figure 7.15: Outlet water temperature of the optimised and validated models 262
Figure 7.16: Images of the temperature of the PCM at (a) 06:00 hours (b) 12:00 hours (c) 18:00hours (d) 00:00 hours 263
Figure 7.17: Ambient temperature and solar radiation of Saudi Arabia 265
Figure 7.18: Results of the optimised model under environmental conditions of Saudi Arabia266
Figure 7.19: Images of the temperature of the PCM at (a) 00:00 hours (b) 06:00 hours (c) 12:00 hours (d) 18:00hours (e) 24:00 hours 267

Figure 7.20: The design of an up-scaled PV/T/PCM system 270
Figure 7.21: PCM temperature of an up-scaled optimised model of a PV/T/PCM system under Irish weather conditions 271
Figure 7.22: Outlet temperature of an up-scaled optimised model of a PV/T/PCM system under Irish weather conditions 271
Figure 7.23: PCM temperature of the up-scaled optimised and optimised model of a PV/T/PCM system under Saudi Arabian weather conditions 272
Figure 7.24: Water outlet temperature of the up-scaled optimised and optimised model of a PV/T/PCM system under Saudi Arabian weather conditions 273
Figure 7.25: Venn diagram of the advantages of a PV/T/PCM system 275
Figure 8.1: Illustrative ranges for thermal management and heat removal in a PV system (Browne et al., 2015b) 282
Figure 8.2: Average U.S PV installation prices over time (Feldman, 2014) 283
Figure 8.3: SPP of a PV/T/PCM system of a household depending solely on electricity 292
Figure 8.4: SPP of a PV/T/PCM system of a household depending solely on gas 293
Figure 8.5: SPP of a PV/T/PCM system of a household depending solely on oil 294
Figure 9.1: Schematic of PV/T/PCM system with varying PCM melting temperatures 304

List of Tables

Table 2.1: Advantages and disadvantages of organic and inorganic PCM for thermal storage (Zalba et al., 2003) 27
Table 2.2: Suitability of the metal-PCM pairs (Cabeza et al., 2001b) 29
Table 2.3: Corrosion rate after 500 days of metal-PCM pairs studied without (left) and with (right) graphite (Cabeza et al., 2005) 30
Table 2.4: Properties of Eicosane, the first PCM integrated with PV (Stultz and Wren, 1978) . 33
Table 2.5: Annual performance figures of a PV/T system (Axaopoulos and Fylladitakis, 2013) 58
Table 2.6: Comparison of PCM as a thermal management technique with other available methods 63
Table 3.1: Guide for corrosion weight loss used in the industry 78
Table 3.2: PV panel specifications (Solar Technology International, 2013) 81
Table 3.3: Thermophysical properties of capric:palmitic acid 91
Table 3.4: System attributes 94
Table 4.1: Comparison of thermophysical properties reported in literature and in this study .. 120
Table 4.2: List of materials and PCM used in corrosion experiments 124
Table 4.3: Composition of metals and plastic samples 125
Table 4.4: Corrosion results obtained by gravimetric analysis after 722 days 144
Table 4.5: Suitability of material – PCM pairs studied 147
Table 5.1: Table indicating the form of thermal energy in each system 158
Table 6.1: Experimental input parameters of photovoltaic panel 202
Table 6.2: List of experimental parameters of the PV/T collector 208
Table 6.3: List of experimental parameters of the water tank 209
Table 6.4: Material and phase change properties as defined in model 218
Table 7.1: Material parameters of the experimental system (used in the validated model) 243
Table 7.2: Range of thermal conductivities modelled in a PV/T/PCM system 253
Table 7.3: The results of the thermal analysis of the parametric study 257
Table 7.4: Efficiencies of the optimised PV/T/PCM system under Irish environmental conditions 264
Table 7.5: Efficiencies of the optimised PV/T/PCM system under environmental conditions of Saudi Arabia 268

Table 7.6: Efficiencies of the up-scaled optimised systems in Ireland and Saudi Arabia compared to a conventional PV/T system 274
Table 8.1: Commercial PCM manufacturers (Agyenim et al., 2010) 284
Table 8.2: Summary of manufacturing and material costs of a PV/T/PCM system 287
Table 8.3: Total energy yield of a PV/T/PCM system in Ireland and Saudi Arabia 288
Table 8.4: PV/T/PCM energy generation, annual household energy consumption and energy cost in Ireland and the UK 290
Table 8.5: PV/T/PCM energy generation, annual household energy consumption and energy cost in Saudi Arabia and Spain 291

Nomenclature

A = Cross sectional area (m^2)

A_{PV} = Surface area of PV (m^2)

C = Number of covers

CR = Corrosion rate (mg/cm^2 year)

C_p = Specific heat capacity (J/ kg K)

C_L = Latent heat capacity (J/ kg K)

$C_{p,s}$ = Specific heat capacity of a solid (J/ kg K)

$C_{p,l}$ = Specific heat capacity of a liquid (J/ kg K)

$C_{p,w}$ = Specific heat capacity of water (J/ kg K)

$C_{p,t}$ = Specific heat capacity of test tube material (J/ kg K)

C_c = Cloudiness factor of the sky [0…1]

C_B = Conductance between absorber plate and bond tube (kJ/ hr K)

C_0 = Initial system cost (€)

C_x = Constant

C_y = Constant

D_t = Diameter of the tube (m)

d_h = Hydraulic diameter (m)

Eff_T = Modifier for PV efficiency as a function of cell temperature

Eff_G = Modifier for PV efficiency as a function of incident solar irradiance

F_R = Collector heat removal factor

f_D = Darcy friction factor

$\mathbf{F}$ = Volume force term (N)

g = gravitational acceleration (m/s^2)

$G_{dif,h}$ = Diffuse solar irradiance on the horizontal (W/m^2)

G_{bh} = Beam solar irradiance on the horizontal (W/m^2)

G_{gh} = Total solar irradiance on the horizontal (W/m^2)

G_{Tilt} = Tilt solar irradiance on the horizontal (W/m^2)

G_{Tot} = Total solar irradiance (beam and diffuse) incident upon the collector surface ($kJ/hr\ m^2$)

G_{ref} = Solar irradiance at reference conditions (W/m^2)

h = Elevation above sea level (m)

h_{air} = Natural convective heat transfer coefficient of air

h_p = Peak sunshine hours (hours)

h_{outer} = Heat transfer coefficient from the top of the collector (PV surface) to the ambient air ($kJ/hr.m^2.K$)

h_{rad} = Radiative heat transfer coefficient from the top of the collector (PV surface) to the sky ($kJ/hr.m^2.K$)

h_f = Internal fluid heat transfer coefficient ($kJ/hr\ m^2\ K$)

h_w = Heat transfer coefficient of wind ($kJ/hr\ m^2\ K$)

h_{p-c} = Heat transfer coefficient between the plate and the cover plate of the absorber ($kJ/hr\ m^2\ K$)

H_m = Heat of fusion (kJ/ kg)

h = Heat transfer coefficient ($kJ/hr.m^2.K$)

h_{cn} = Natural convection heat transfer coefficient ($kJ/hr.m^2.K$)

h_{int} = Internal heat transfer coefficient of the pipe ($kJ/hr\ m^2\ K$)

h_{ext} = External heat transfer coefficient of the pipe ($kJ/hr\ m^2\ K$)

i = Plate spacing (cm)

I = Current (A)

I_T = Total current passing (A)

I_{PV} = PV current (A)

I_{Bat} = Battery current (A)

$I_{L,\ ref}$ = Module photocurrent at reference conditions (A)

$I_{o,\ ref}$ = Diode reverse saturation current at reference conditions (A)

K = Extinction coefficient (cm^{-1})

k = Thermal conductivity (W/mK)

k_B = Boltzmann constant (J/K)

L = Thickness of the glass cover (m)

m = Mass (kg)

m_w = Mass of water (kg)

m_p = Mass of phase change material (kg)

m_t = Mass of test tube (kg)

n = Refractive index

P_{atm} = Atmospheric pressure (atm)

P_0 = Atmospheric pressure at height h_0 (atm)

p = Pressure (Pa)

P = Power (W)

P_m = Maximum power (W)

q = Electron charge constant

q'_f = Heat transfer to the fluid stream per unit length of the collector (kJ/hr m)

Q_u =Useful heat gain by thermal collector (J)

Q_s = Heat stored by thermal collector (J)

Q_u = Useful energy gain (J)

Q = General heat source (J)

Q_{wall} = Heat exchange through pipe wall (J)

Q_y = Energy yield per peak sunshine hour (kW h/ year)

R_{Tot} = Total resistance (Ω)

R_p = Resistance of resistors in parallel (Ω)

R_s = Module resistance in series (Ω)

R = Radius of a tube (m)

R_T = Resistance of heat transfer provided by the material between the PV cells and the absorber (°C)

Re = Reynolds number

r_0 = Outer pipe radius (m)

r_n = Inner pipe diameter (m)

S = Savings (€)

S = Net absorbed solar irradiance (W/m^2)

t = Time (hours)

t_{ext} = Time for which PCM extended availability of heat (hours)

t_{pp} = Period of time for which there is potential for heat to transfer from inside the container to the water (hours)

T = Temperature (°C)

T_{amb} = Ambient temperature (°C)

T_{sat} = Dew point temperature at ambient temperature (°C)

T_{sky} = Sky temperature (°C)

T_{abs} = Absorber plate temperature (°C)

T_{PV} = PV cell temperature (°C)

T_b = Temperature of the base area of the absorber plate (°C)

T_f = Temperature of the fluid (°C)

T_p = Temperature of the plate (°C)

T_{cp} = Temperature of the cover plate (°C)

T_m = Melting temperature of PCM (°C)

T_s = Solidification temperature of PCM (°C)

T_{ext} = External temperature (°C)

Tref =Reference temperature (°C)

U_T = Top loss coefficient (W/m K)

U_L = Overall heat loss coefficient (W/m^2)

u = Cross sectional average velocity (m/s)

V_{PV} = PV voltage (V)

$V_{Battery}$ = Battery voltage (V)

V_w = Wind velocity (m/s)

V_{Load} = Load voltage (V)

X_{ct}= Multiplier for the PV cell efficiency as a function of the cell temperature (1/°C)

X_{rad} = Multiplier for the PV cell efficiency as a function of the incident irradiation ($h.m^2/kJ$)

Z = Wetted perimeter (m)

η = Efficiency (%)

η_{PV} = Efficiency of the PV (%)

η_{TH} = Thermal efficiency of the system (%)

η_{nom} = Efficiency at reference conditions (%)

μ = Viscous forces (Ns/m^2)

ρ = Density (kg/m^3)

ε_0 = Emittance of clear sky [0…1]

γ = Empirical PV curve fitting parameter

ρ = Monochromatic hemispherical reflectance

α = Absorptivity

τ_r = Transmisivity due to reflection

τ_a = Transmisivity due to absorption

τ = Transmisivity of PV glass

η_{TH} = Thermal efficiency (%)

α = Absorptivity of plate (m^{-1})

Subscript

c = Cell

Preheat potential = preheat = Potential for water to be pre-heated

Eff = Effective value

Sol = Solid

Liq= Liquid

θ = Fraction representing material phase

pc = Phase change

i = Inlet

o = Outlet

amb = Ambient

w = Water

IC = Inside container

Con = Container

Stc = Standard test condition

Abbreviations

AHS = Available Heat Stored

BIPV = Building Integrated Photovoltaic

CPV = Concentrated Photovoltaic

DSC = Differential Scanning Calorimetry

FPC = Flat Plate Collector

HSP = Heat Storage Potential (hours)

PCM = Phase Change Material

PV = Photovoltaic

PV/T = Photovoltaic/Thermal

PV/T/PCM = Photovoltaic/Thermal/Phase change material

STC = Standard Test Conditions

SPP = Simple Payback Period

TRNSYS = Transient System Simulation Tool

TES = Thermal Energy Storage

THM = Temperature History Method

Chapter 1

Introduction

Chapter 1. Introduction

1.1 Background

Projected growth of global energy consumption is 1.5 % per annum from 2010 to 2040 which corresponds to 820 quadrillion British Thermal Unit (where 1 Btu = 1.055 kJ) compared to 524 quadrillion Btu in 2010 (IEA, 2013). Fossil fuels dominate global energy usage, accounting for 80 % in 2010, a figure which is not predicted change through to 2040 (IEA, 2013). It is difficult to predict when fossil fuel reserves will be depleted, although it has been suggested oil (tar sands and oil shales), coal and gas will be depleted in 35, 107 and 37 years respectively (Shafiee and Topal, 2009). Rapid deployment of renewable sources of energy must be made if global dependence on fossil fuels is to be reduced.

Carbon dioxide emissions from burning fossil fuels have increased exponentially since the industrial revolution (Boden et al., 2010) currently estimated to be 74 % of all CO_2 emissions (Moriarty and Honnery, 2012). As one of the primary greenhouse gases, carbon dioxide has a detrimental effect on the global climate by accelerating the greenhouse effect which causes the atmosphere to retain heat increasing the global temperature (IPCC, 2014). This effect has seen an increase of 0.85°C in the last 132 years which has a knock on effect of increasing sea levels and weather extremities (IPCC, 2014). Increasing the move toward renewable energies could lead to a reduction of global CO_2 levels and mitigating these effects.

Energy security is a primary concern for countries who import the majority of their demand. Ireland is one such country whose import dependency has remained at approximately 90% for the last decade (Sustainable Energy Ireland, 2011). Political instability can further highlight vulnerable energy supplies. In 2014, Europe imposed sanctions on Russia, their main supplier of crude oil, natural gas and solid fuels (EUROSTAT, 2014) due to events in Ukraine causing widespread fear for Europe's gas supply. Renewable sources of energy can provide alternative, indigenous, sources of power which will not destabilise a country's security of energy supply but contribute to the flexibility of the system and its resistance to political and financial uncertainties outside of its control (Ölz et al., 2007).

The EU's renewable energy directive sets a binding target of 20% final energy consumption from renewable sources by 2020 (EU Directive 2009/28/EC, 2009), an equivalent saving of 250 million toe (tonnes of oil equivalent) per year. Solar energy, wind power, hydropower and

biomass are expected to play a major role in meeting these targets and are the main renewable sources of energy available. The International Energy Agency (IEA) estimates approximately 885 million Terawatt hours (Philibert, 2011) of energy reach the earth's surface from the Sun annually. Considerably larger than the global energy demand, predicted as 16,500 Mtoe (million tonnes of oil equivalent) for 2030 (Solangi et al., 2011). Solar energy is environmentally advantageous relative to any other energy source which does not compromise or add to global warming. Further benefits are an increase in national energy independence and security of energy supply due to consistent and abundant supply. However, the issue lies with how best to exploit solar energy and the most efficient and cost effective way to do so.

1.2 Scope of Research

In order to decrease the global dependence on fossil fuels and also to play its part in global warming mitigation, renewable energy technologies must be developed further to become sustainable in the long term. Solar energy based technologies have enormous potential in delivering clean and reliable energy compared to other forms of energy. Energy from the sun can be used in three major ways to provide usable forms of passive energy, photovoltaic energy and solar thermal energy as shown in Figure 1.1.

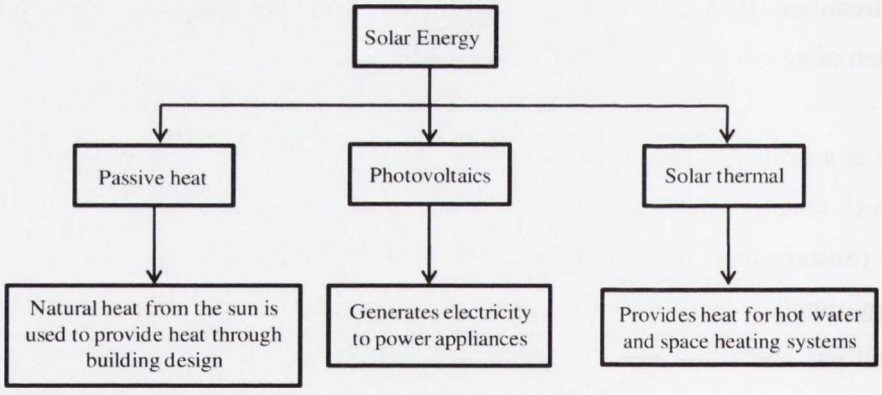

Figure 1.1: Solar energy applications (Ayompe, 2011)

The scope behind this research is to design a Photovoltaic (PV) system which integrates a thermal collector to take full advantage of solar radiation, to generate electricity and to provide heat for water or space heating. The main focus of the research was on the area of heat recovery from the PV and storing the thermal energy as latent heat at a constant phase change

temperature. The research assesses the thermal efficiency of the collector to store heat during the day and discharge it at night thereby shifting availability.

An issue with solar energy and most other forms of renewable energy is matching the energy generation with the energy profile of domestic and commercial dwellings. There exists a mismatch in peaks whereby the generation of energy occurs during the day in the case of solar energy at midday when most domestic dwellings are empty as people are at work.

1.2.1 Research Aims and Proposed Methodology

The primary aim of this thesis is to design, install and optimise a Photovoltaic/Thermal/ Phase Change Material (PV/T/PCM) system that can generate electrical and thermal energy for use in a domestic dwelling. However, in order to do this a series of investigations into the PCM properties and the corrosive nature of PCM had to be undertaken.

The objectives of the thesis are:

- to characterise selected PCM which could potentially be used in a PV/T/PCM system in Ireland
- to assess the thermophysical properties of PCM (i) Differential Scanning Calorimetry and (ii) Temperature-History Method
- to identify PCM that would be most suited to integration with a PV/T/PCM system in Ireland.
- to assess the most suitable PCM and containment material, immersion corrosion tests are required whereby a material sample is immersed in a PCM for a prolonged period of time
- to calculate the effect of the PCM on the material based on the corrosion rate of the material and the material mass loss
- to design, fabricate and install a PV/T/PCM system in Dublin

- assess the electrical and thermal performance of the PV/T/PCM system and its ability to take advantage of the solar resource through the production of electrical and thermal energy and draw comparisons with reference systems
- to numerically analyse the thermal and electrical behaviour of a PV/T/PCM system and validate the results using the experimental data
- to investigate significance of specific values of PCM thermophysical properties and container properties on the system outputs using parametric studies
- to numerically optimise the PV/T/PCM system design based on the results of the parametric study
- to numerically calculate the variation in a PV/T/PCM system performance under an increased solar resource than that of Ireland
- to numerically investigate the performance of an up-scaled PV/T/PCM system to draw comparisons between the efficiencies of the system under a low and high solar resource
- to determine the economic viability of a PV/T/PCM system based on the payback period under different climates
- to determine the effect of various financial incentives on the payback period of a PV/T/PCM system

1.3 Thesis Outline

Chapter 2 contains an extensive literature review focussing on three key areas of the research (i) an overview of photovoltaic, thermal collectors and hybrid solar systems which integrate both technologies; (ii) phase change material classification and thermal and corrosion properties; (iii) integration of PCM with solar technology.

Chapter 3 describes the methodology used to characterise the thermophysical properties of PCM and the process involved in the immersion corrosion tests of material and PCM pairs. The description of the PV/T/PCM system design, as well as three reference systems, is also

presented. Chapter 4 presents the process of building and installing the PV/T/PCM system and reference systems. Chapter 5 presents analysis of the electrical and thermal results from the performance of a PV/T/PCM system and draws a comparison between them and the reference systems.

The process of generating a numerical model which simulates the performance of a PV/T/PCM system is presented in Chapter 6. Chapter 7 presents an optimised numerical model of the PV/T/PCM system based on a parametric study. The optimised model is up-scaled and the performances of the system under a low and high solar resource are presented.

In Chapter 8, an economic assessment is carried out which calculates the simple payback period of the PV/T/PCM system in different climatic regions and with different incentive programs and feed in tariffs. Finally, Chapter 9 details the conclusions drawn from the research and the recommendations for future research.

Chapter 2

Literature Review

Chapter 2. Literature Review

2.1 Introduction

This chapter presents a review of the research which has been published in the area of solar technology and phase change material. The chapter is arranged into the following subsections:

- Photovoltaic (PV) and Solar Thermal Technology
- Phase Change Material (PCM)
- Application of Phase Change Material in Photovoltaic and Solar Thermal Technology

The findings of the review identified knowledge gaps which paved the way for the development of a system which integrates phase change material with a photovoltaic/thermal system. PCM was used as a method of temperature regulation of PV initially however it was identified that the thermal energy storage properties could be applied to shift the time at which heat was available.

2.2 Photovoltaic (PV) and Solar Thermal Technology

Photovoltaic panels and solar thermal collectors are the most common devices used to trap the sun's energy to convert it to electrical or thermal energy. Solar technology is emerging as a major power source in the renewable energy sector as it is increasingly becoming more affordable as technology improves (IRENA, 2014). As this work concentrates on combining a PV module and a solar thermal system a review of the current state of the technologies is presented.

The main types of PVs are presented; crystalline silicon, organic PV, dye sensitised solar cells, thin film PV and multi-junction PV, with a brief discussion on operational advancements which is generally associated with an increase in electrical efficiency.

Solar thermal collectors collect heat by absorbing thermal energy and transferring it to liquid passing through pipes attached to the absorber plate. A series of different solar collector designs have been presented, concentrating on the more efficient methods of absorbing solar radiation.

2.2.1 Photovoltaic Technologies

Photovoltaic (PV) technologies produce electricity directly using solar radiation. When energy of the absorbed radiation is greater than the band gap energy in the region of the p-n junction, it creates an electron-hole pair. These electrons escape from their positions in the atoms of the semiconductor PV material becoming part of the current in an electrical circuit (Radziemska, 2003).

PV devices are classified according to the light absorbing materials used in the technology. Crystalline silicon solar cells constituted approximately 86 % of the current global market PV in 2012 (Fraunhofer Institute, 2013). This is because silicon is widely available, non-toxic, can be doped easily and production dominance economies of scale arise from its use in PV being a facet of the much larger microelectronics industry (Bruton, 2002). Mono-crystalline and poly-crystalline are the main silicon crystalline solar cells. Mono-crystalline modules are manufactured from single crystalline silicon and have a higher efficiency than poly-crystalline PV but their low cost makes them an attractive option.

Organic solar cells have efficiencies of between 8.6 % (National Renewable Energy Laboratory, 2012) and 12 % (Peach, 2013). Poly-fullerene solar cells have been found to have maximum conversion efficiency in the 47 °C – 60 °C temperature range (Katz et al., 2001), at temperatures both above and below this range the efficiency is lower (Bagienski and Gupta, 2011).

Dye sensitised solar cells (DSSC), which have achieved efficiencies exceeding 10 % (Gao et al., 2008), are thin film solar cells with a layer of organic dye molecules to allow for extended absorption across the solar spectrum into the visible light region.

Thin-film PV entail low material cost as they consist of a series of thin layers of semi-conducting materials, generally amorphous silicon (a-Si), placed on a backing material (Hoffmann and Pellkofer, 2012). Current crystalline silicon thin film technologies available on the market have efficiencies of around 12 % (Guha et al., 2013). Thin film PV cells have been fabricated from gallium arsenide (GaAs), copper and copper ternaries such as copper indium diselenide ($CuInSe_2$) and copper indium gallium diselende ($CuIn_xGa_{(1-x)}Se_2$); as well as cadmium telluride (CdTe) and cadmium sulphide (CdS).

Multi-junction (MJ) cells, theoretically, have a limiting efficiency of about 86 % but currently reach efficiencies of 46 % which use multiple materials to match the solar spectrum (Kurtz, 2006). However, the high efficiency comes at a high cost and it was found using MJ cells maybe cost effective with flat module PV when operated at high concentration ratio of 1000 suns (Swanson, 2000).

The evolution of the conversion efficiencies of different types of PV is presented from 1976 to 2015 in Figure 2.1 (NREL, 2015) where multi-junction are proving to be the most efficient under controlled labatory conditions where the highest efficiency is 46 %. However, this is not enough of an advantage over less expensive and more versatile traditional silicon due to the cost and complexity of manufacture of MJ cells (Lu, 2014).

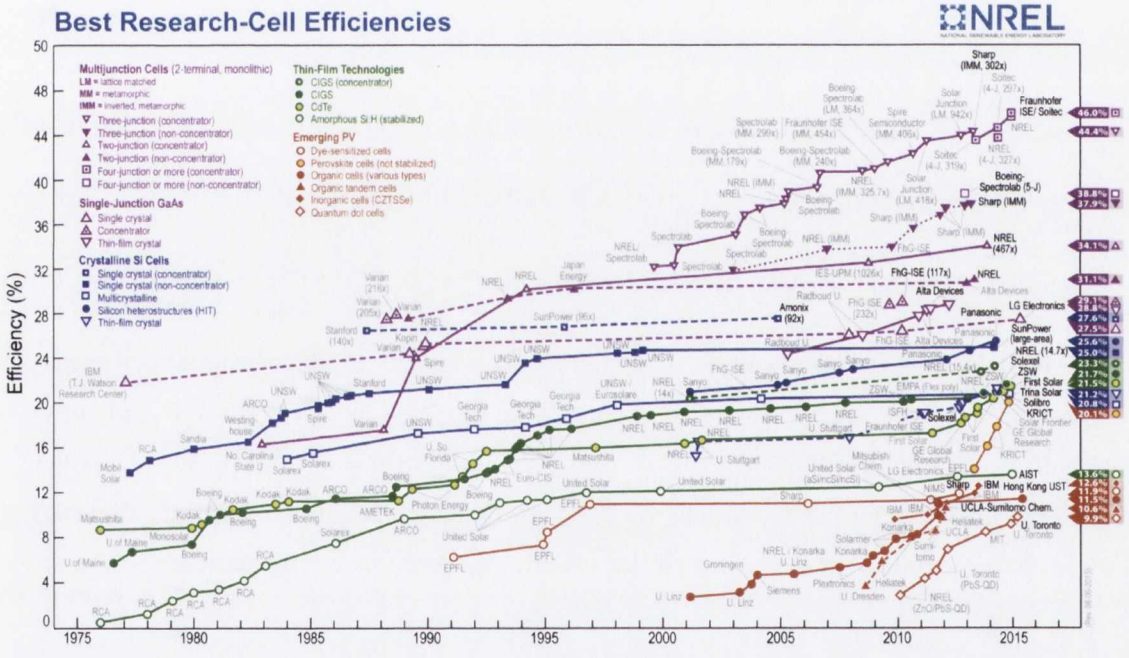

Figure 2.1: Confirmed efficiencies for research cells (NREL, 2015)

2.2.1.1 Issues with Photovoltaic Technologies

There are issues which adversely affect the performance of PV cells, namely parasitic resistance (the cell efficiency is reduced by the dissipation of power across the internal resistance) and PV temperature (when exposed to higher temperatures the open circuit voltage decreases).

Figure 2.2(a) shows the variation of output power, P_L and voltage, U_L of a solar cell at four different temperatures at constant solar radiation (Radziemska, 2003). The graph shows an

initial increase in power with voltage before declining. Temperature dependence of the maximum output power $P_m(T)$ reflects the reduction of power as the temperature increases. A similar graph of output power and voltage of a PV panel can be seen in Figure 2.2(b) emphasising the effect of temperature elevation on the power reduction of a silicon PV panel.

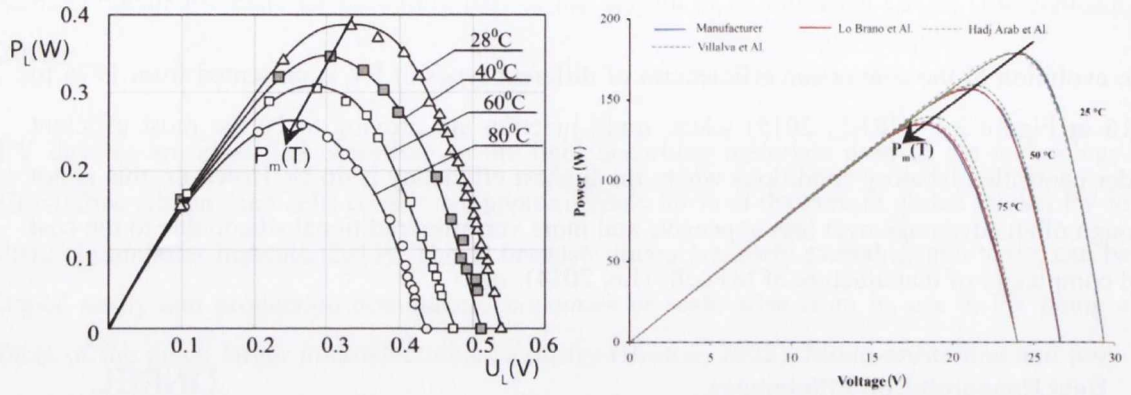

(a) (b)

Figure 2.2: (a) Variation of power with voltage of a silicon solar cell (Radziemska, 2003) (b) Variation of power with voltage of a silicon panel temperature (Hadj Arab et al., 2004; Villalva et al., 2009; Lo Brano et al., 2010; Lo Brano et al., 2012; Ciulla et al., 2014)

The transfer of electric charge is temperature independent for organic solar cells (Christ et al., 2013). Maintaining organic cells at an optimal specific temperature that maximises efficiency could be technically feasible. However, as the efficiency of organic cells is low and, more specifically, only small efficiency improvements would arise from operation at an optimal temperature. The current cost margin available is thus too small for optimal efficiency maintenance of organic PV cells by temperature control to be commercially feasible at present.

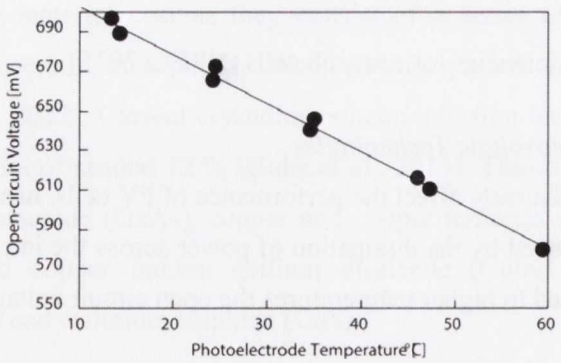

Figure 2.3: Temperature dependence of V_{oc} in DSSC (Usami et al., 2009)

DSSC have attracted intense research attention owing to their ease of fabrication and cost-effectiveness (Hou et al., 2013). Temperature was found to affect the open circuit voltage (V_{oc}) of DSSC by approximately -2.5 mV for every 1 °C increase in the cell. This effect originates from a shift in the titanium dioxide conduction band, as shown in Figure 2.3.

Successive temperature rampings of aging DSSC have been shown to slow down the reduction in cell efficiencies as the short circuit current degraded (Toivola et al., 2007). Following temperature treatment, cells were found to regenerate resulting in overall lower degradation rate of the cell performance. Successive temperature rampings of the aged cells did re-establish cell function, it was seen that the total efficiency drop over the experiment was on average 18% per cell less for the temperature treated cell than for the reference cell aged at constant temperature.

The effect of elevated temperatures on a thin film solar cell depends on the properties of the materials involved. Amorphous silicon thin film modules have minimum variation in conversion efficiency due to initial light induced degradation over the first month of solar exposure however, after this period the rising temperatures during summer can cause regeneration of the material characteristics increasing charge carrier lifetime and decreasing band gap making them suited to tropical climates (Akhmad et al., 1997). For a high efficiency thin film silicon solar cell fabricated using amorphous silicon oxide/ microcrystalline silicon double junction cells, the temperature coefficient was found to be -0.32 %/ °C (Sriprapha et al., 2011). Thin film PV manufactured from copper ternaries have generally shown small increases in characteristic energy of up to 15 meV in the -173 °C to 27 °C temperature range (Wasim et al., 2001). CdTe was found to have increasing current and decreasing voltage with an increase in temperature in the range of -63 °C – 37 °C as in Figure 2.4 (Pattabi et al., 2007). Although, there was no change in characteristic energy with temperature for $Cu(In,Ga)Se_2$ (Troviano and Taretto, 2011).

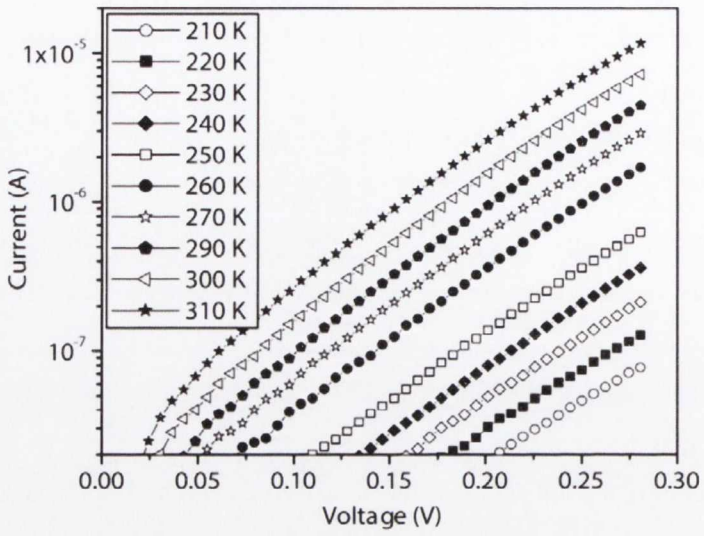

Figure 2.4: Current –voltage characteristics of Au/CdTe Schottky diode (Pattabi et al., 2007)

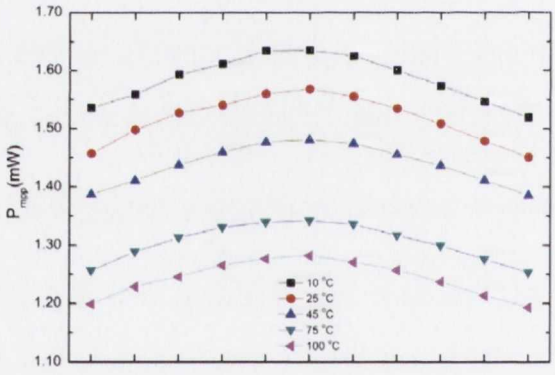

Figure 2.5:Temperature dependence of the maximum power of a multi-junction cell (Fernández et al., 2013)

Although, this cannot be said for all types of multi-junction cells, a study of triple junction cells found a decrease of around 5% in cell efficiency with increase in temperature from 5 °C to 170 °C. Although, the short circuit current did increase, the open circuit voltage decreases with increasing temperature resulting in an overall decrease in efficiency (Helmers et al., 2013).

2.2.2 Solar Thermal Collectors

Solar thermal collectors convert energy from a solar resource to thermal energy which is transferred to its working fluid in solar thermal applications. The heat carried by the working fluid, generally air or water or water/glycol mix, can be used to provide domestic hot water or heating. Solar thermal collectors are divided into two categories non-concentrating and concentrating (Kalogirou, 2004). Non-concentrating systems include flat plate collectors and evacuated tube collectors which are the most common forms of solar thermal collectors.

Flat plate collectors, as shown in Figure 2.6, are robust, cost efficient, of simple geometry and effective even with diffuse solar radiation which make them very suited to countries who receive high levels of diffuse radiation (Kalogirou, 2004).

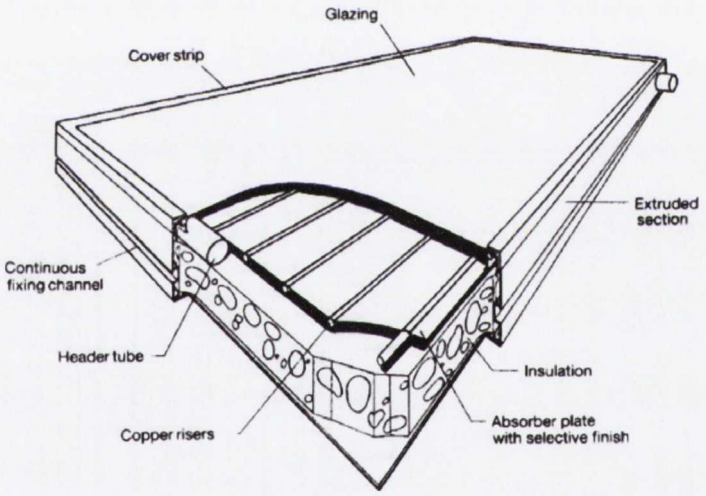

Figure 2.6: Schematic diagram of a flat plate collector (Kalogirou, 2004)

They usually consist of glazing covers, absorbing plates, insulation layers and a heat exchanger, the content of the literature review focuses on these components to improve system performance.

Glass is the most commonly used material to glaze solar collectors as they can transmit as much as 90% of the incoming shortwave solar radiation while transmitting very little of the long wave radiation emitted outward by the absorber plates (Kalogirou, 2004). Double glazing glass with a coating on the inner pane was tested to improve the insulation of the transparent cover to increase the temperatures of flat plate collectors above 100 °C (Ehrmann and Reineke-Koch,

2012; Ehrmann et al., 2013). The layer was found to increase solar transmission but not emissivity. The air gap between single and double glazing was analysed using the CFD software ANSYS FLUENT. It was found if the air gap spacing for both single and double glazing are such that the corresponding Rayleigh number is in the vicinity of the critical value 1708, then there exists a minimum heat loss coefficient which when optimised, the water temperature increase is higher by about 14% compared to reference systems (Subiantoro and Ooi, 2013).

The function of the absorbing plates is to absorb as much irradiation as possible through the glazing, while minimising the heat loss upward to the atmosphere and downward through the back of the casing (Kalogirou, 2004). Various colours have been suggested for absorbing plates; however this has generally been for aesthetic reasons (Tripanagnostopoulos et al., 2000; Wazwaz et al., 2002; Kalogirou et al., 2005). Using electrolytic or chemical treatments, plate materials can be coated in a selective absorbing layer to increase solar radiation absorptance and decrease longwave emittance (Cheng et al., 2013; Li and Zhao, 2013; Gong et al., 2015).

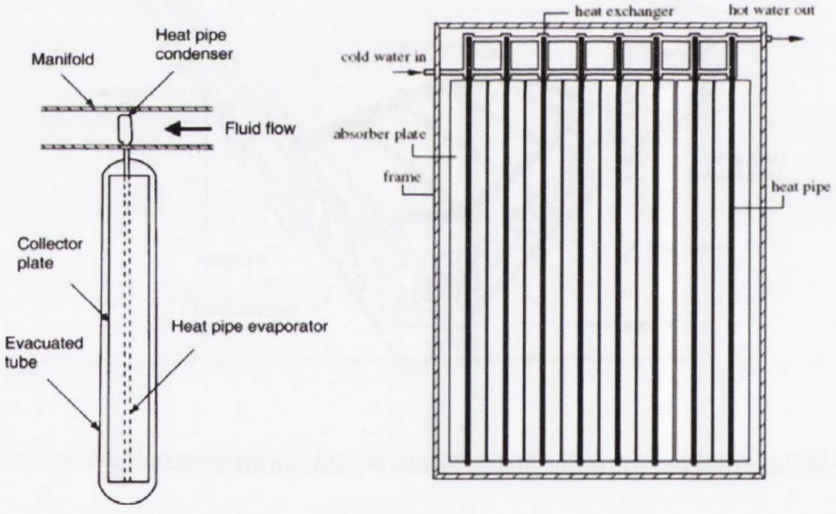

Figure 2.7: Schematic of (a) evacuated tube (b) evacuated tube collector

Evacuated tube collectors contain vacuum sealed tubes containing heat pipes, as illustrated in Figure 2.7. The vacuum reduces convection and conduction losses so the collectors can operate at higher temperatures than flat plate collectors. Their efficiency is also higher at low incidence angles due to their geometry which give the evacuated tube collectors an advantage over flat plate collectors in day-long performance (Kalogirou, 2004).

Heat pipes are very efficient conductors which permit the transport of heat with a temperature differential. The pipe is attached to an absorber plate and contains a liquid vapour phase change material which undergoes an evaporating condensing cycle. Solar heat evaporates the liquid which moves to the heat sink region where it condenses and releases the latent heat. Water, or glycol, collects the heat from the tubes where it is used to indirectly heat a solar storage tank of water (Kalogirou, 2004).

The behaviour of evacuated tube collectors has been investigated by many researchers (Nkwetta et al., 2012b; Nkwetta et al., 2012a; Redpath, 2012; Ayompe and Duffy, 2013a). Azad (2012) has presented an assessment of three types of evacuated tube solar collectors, two with shell and tube condensers and one with a double pipe condenser. It was found that the shell and tube collectors, though easier and cheaper to manufacturer, have the disadvantage that damage to one heat pipe can cause the entire system to stop operating. The performance of two concentrated evacuated tube solar collectors were analysed and compared using indoor solar simulated conditions (Nkwetta and Smyth, 2012). The systems differed as one had a single-sided coated absorber (SSACPC) as shown in Figure 2.8(a) and the other consisted of a double-sided coated absorber (DSACPC), illustrated in Figure 2.8(b).

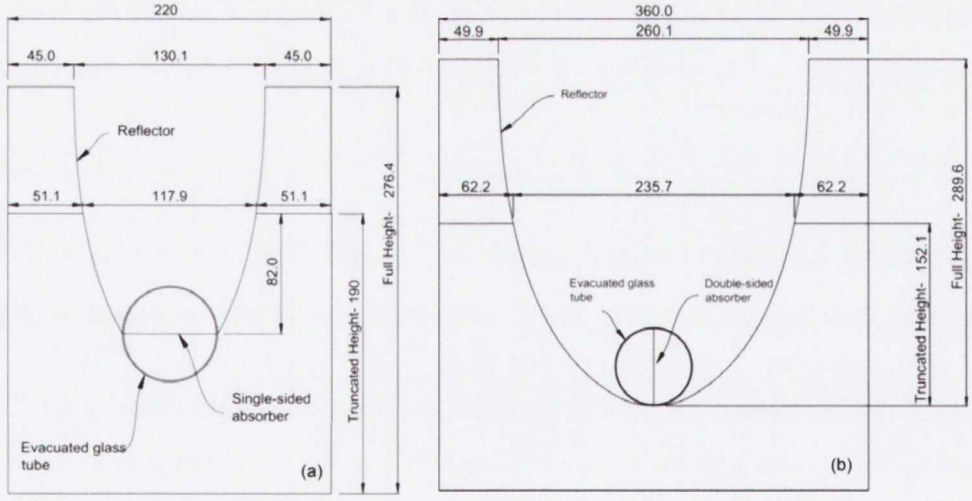

Figure 2.8: (a) Single-sided coated absorber (b) Double-sided coated absorber (Nkwetta and Smyth, 2012)

Over a 6 hour experimental period, the energy collection was 82.11 W and 150.67 W for the SSACPC and DSACPC respectively. The overall improvement was 42.4% in average inlet and outlet fluid temperature differential by the truncated DSACPC compared to the SSACPC.

Evacuated tube collectors have efficiencies of about 50 % - 80% where as flat plate collectors have typical efficiencies of 50 % or less, the difference mainly due to the heat loss via the cover surface as a result of conduction and convection. Although on the other hand flat plate solar collectors are a simpler structure and easier to manufacture (Riffat et al., 2005).

2.2.3 Hybrid Solar Systems

Hybrid PV/T systems can generate electricity and heat simultaneously. Solar radiation incident on the PV module is converted to electricity, depending on the conversion efficiency, typically 15 % - 18 %; the rest (82 % – 85 %) is lost to heat. This heat generated by the PV cell in a PV/T system is captured using water or air. There are two options for disposal of the excess thermal energy; heat transfer to air or water or heat storage for later use. Passive removal of heat is a naturally induced temperature difference and the use of an external mechanical system is known as active or forced removal.

Combining a PV module and thermal collector in a single system is a challenging task due to the required input of each system. Solar thermal systems work best under high radiation levels and high ambient temperatures due to the requirement to heat the working fluid. However, high temperatures reduce PV efficiency as discussed in Section 2.2.1. So the location of the absorber surface is important in a PV/T system to remove the heat from the PV most efficiently and transfer to the thermal collector.

2.2.3.1 Photovoltaic/Thermal Systems

Research into integrated PV and thermal systems was initiated in the mid 70's by Wolf (1976) who simulated a combined heat and power system of a residential building in Boston. Investigations at this time were primarily flat plate PV/T systems (Kern and Russell, 1978; Florschuetz, 1979). In the years following, research concentrated on collector designs (Cox and Raghuraman, 1985; Lalović et al., 1986) which followed on to concentrating systems (Hamdy et al., 1988). PV/T systems became a major area of interest in the 90's and research focused on PV/T system design, simulation, modelling and testing (Garg et al., 1990; Hayakashi et al., 1990; Agarwal and Garg, 1994; Hammad, 1994; Prakash, 1994) and many of the studies have been reported in numerous literature reviews (Charalambous et al., 2007; Zondag, 2008; Chow, 2010; Chow et al., 2012; Zhang et al., 2012b; Kumar et al., 2015).

The assessment of a natural air circulation PV system comparing air and water as a heat transfer fluid with and without glazing was investigated, as seen in Figure 2.9 (Tripanagnostopoulos et al., 2002).

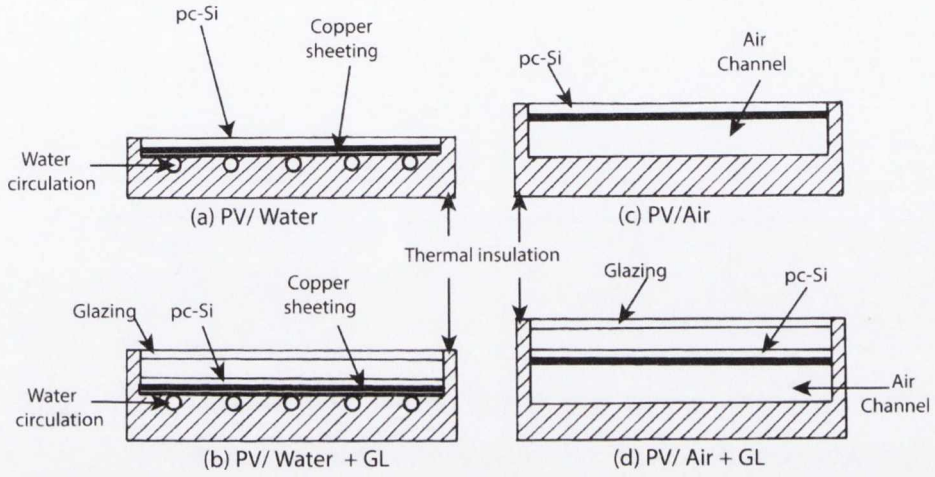

Figure 2.9: Cross section of PV/T experimental models: (a) PV/Water (b) PV/Water + Glazing (c) PV/Air (d) PV/Air + Glazing (Tripanagnostopoulos et al., 2002)

The basic hybrid system with water as the working fluid which flowed through the heat exchanger beneath the polycrystalline panel is shown in (a). Glazing is added to trap daylight and heat transfer as presented in system (b). Air is the working fluid in the PV/T system (c) with additional glazing as shown in (d). Heat extraction by water circulation proved more efficient than using air. Increased values of electrical efficiency were achieved by the hybrid PV/T with water as the transfer fluid due to more effective heat removal. Using glazing provided up to a 30% increase in thermal efficiency compared to basic PV/T systems due to the suppression of thermal losses.

Zondag et al. (2003) investigated the performance of four groups of PV/T systems of nine different designs; (a) sheet-and-tube PVT collector takes a standard PV panel and integrates it with a collector without any modification, (b) channel PV/T collector shows a channel on top of the PV with water as the working fluid (c) free flow PV/T collectors have unrestrained fluid flow over the absorber which eliminates a glass layer and (d) two absorber PV/T-collectors uses a PV laminate as a primary absorber and a black metal plate as a secondary absorber as in Figure 2.10.

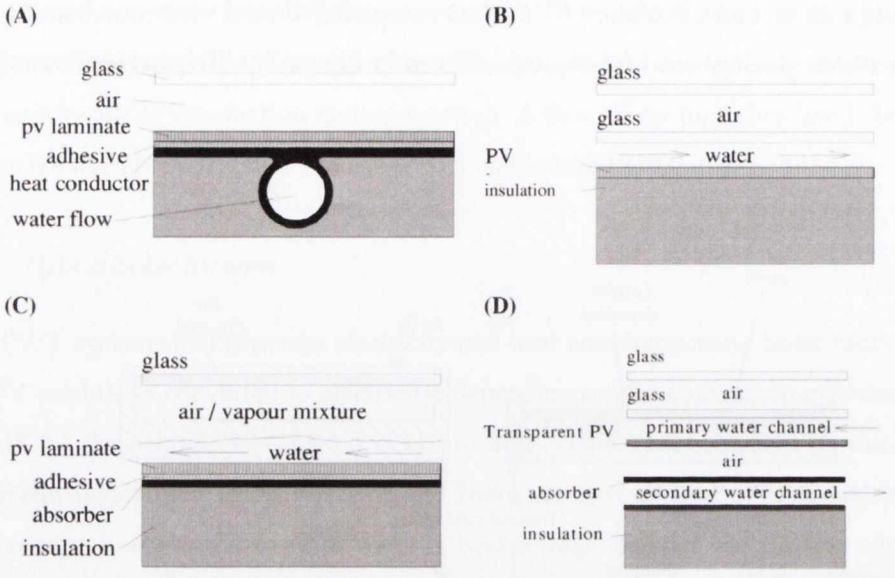

Figure 2.10: (a) Sheet-and-tube PVT collectors, (b) Channel PV/T collectors (c) Free flow PV/T collectors and (d) two absorber PV/T-collectors (Zondag et al., 2003)

Their thermal and electrical efficiencies were compared in addition to the yearly yield of hot water. It was found that (a) (sheet-and-tube PV/T collectors) was the leading design, though it was not the most efficient when compared to the other systems, it was the ease of manufacturing that made it the best option. Wu et al. (2011), modelling a PV/T system using water as the transfer fluid, found that the thermal and electrical efficiencies could reach 63.65 % and 8.45 % respectively. As seen here and in many other PV/T systems the electrical efficiency is lower than a PV module alone which can be attributed to the compromise of generating electrical and thermal energy from a single system. The thermal collector has a minor effect on the PV efficiency. Modelling of a PV/T system with air as the coolant in a duct behind the panel and was simulated under the climatic conditions of Alabama, USA, found 7.3% more energy can be generated with cooling compared to a system without cooling (Najafi, 2012).

PV cooling has been accomplished using versions of the trickle-flow collector (Beard, 1978). In one such PV/T system, water was pumped through a series of nozzles and flowed down the front of the panel cooling it by approximately 22 °C to achieve a net electrical gain of 8 % - 9 % after accounting for the pump's energy requirements (Krauter, 2004). In a similar active PV/T system (Kordzadeh, 2010), the power produced by the PV was used to pump water over the front of the PV array giving an average 3.66 % and 0.69 % increase in nominal power for 90W

and 135W arrays, respectively. The large variation in efficiency was due to the increase in PV area of the 135 W array.

An analytical comparison of (i) a combined PV/thermal collector, (ii) thermal collector and (iii) PV, found that under the same conditions thermal and electrical efficiencies were 33 % and 6.7 % for the combined system, thermal efficiency 54 % for the thermal collector and electrical efficiency of 7.2 % for the PV. The decreased efficiency can be attributed to the integration of a thermal collector with a PV module affecting the temperature of the PV. Although the combined system showed lower efficiencies, the hybrid system harvested both electrical and thermal energy in one device (Zondag et al., 2002; Zondag, 2008; Ullah et al., 2013).

2.2.3.2 Incorporation of PV and Thermal Systems in Buildings

PV and thermal systems can be incorporated in buildings to create additional functionality for the PV as wall and roofing elements, canopies and/or shading devices that replace "conventional" building materials; this is referred to as building integrated PV (BIPV). Building-applied Photovoltaics (BAPV) are integrated into a building following its construction.

Elevated operating temperatures arise as buildings can thermally insulate incorporated PV. Maturi et al. (2014) conducted a full-scale assessment of BIPV modular temperature for different types of PV. Under the same environmental conditions of 1000 W/m^2, copper indium gallium selenide (CIGS) PV operate at a temperature 8 °C higher than the operating temperature of mono crystalline potentially affecting the efficiency by 3 %. A full-scale experiment showed that the thermal-insulating building facade increased PV cell temperature by 20.7 K causing a 9.3 % loss of electrical yield compared to an actively cooled PV cell (Krauter et al., 1999). Simulations using data for Mâcon, France, showed a BIPV system to operate a cell efficiency of 6.8 %, which is equivalent to a 28 % lower efficiency than to a non-integrated PV system, (Fraisse et al., 2007).

In BIPV/thermal (BIPV/T) systems heat is usually removed from behind the PV panel through a convective air or water flow that can be forced or natural. The effects of forced air circulation and natural convection were numerically modelled for a BIPV installation on a hotel building in southern China (Chow et al., 2003), it was shown that the difference in electricity output between using forced or natural convection was less than 1% annually. However, it was found that in subtropical climates natural convection proved marginally better due to the effectiveness in space heat gain reduction compared to BIPV systems. The application of fins and a thin

metallic sheet midway between the PV and wall can improve heat transfer from the PV to the air circulating in a photovoltaic/thermal (PV/T) solar collector (Tonui and Tripanagnostopoulos, 2007). Hydronic cooling of a PV is flowing water on to the front or back surface in order to absorb heat from the system. A 23 % reduction was found in the temperature of the PV when water was sprayed over the front surface of the PV giving an increase in the mean PV cell efficiency of 3.26% (Abdolzadeh and Ameri, 2009).

The incorporation of active and passive solar energy systems will enable a decrease in the energy consumption of buildings (Chwieduk, 2014). The initial observation is the orientation and shape of a building with respect to the Sun where devices for solar energy utilisation can be designed/sized for the specific building.

2.2.4 Complexities Involved in Solar Energy System Technology

The effect of temperature on photovoltaic technology varies according to the type of cell as shown in Figure 2.11 and discussed in Section 2.2.1.1. The idea of cell cooling was discussed in detail and in economic terms the cost of the additional electricity gained by temperature regulation should be less than the option of installing a larger PV array. Conversely, where only a small PV area is available for deployment, as, for example, in solar powered consumer devices a higher cost of PV cooling may be acceptable in the content of the overall device design.

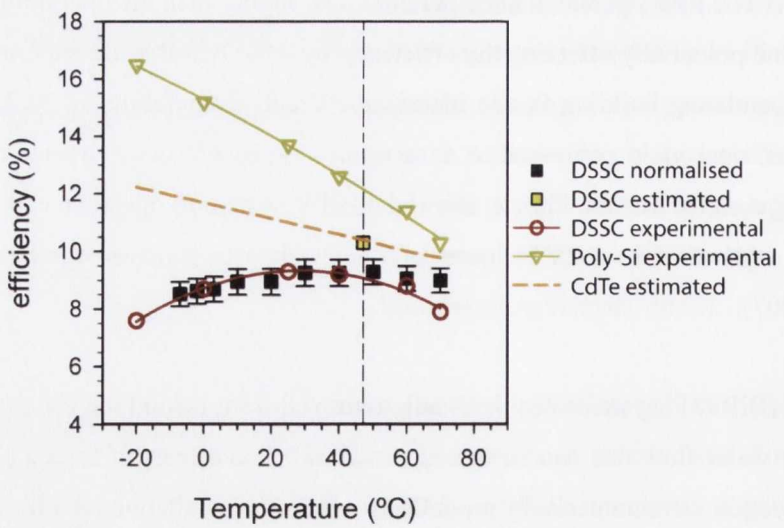

Figure 2.11: Efficiency Vs Temperature of dye sensitised solar cells (DSSC), polycrystalline silicon (poly-Si) and Cadmium Telluride (CdTe) solar cells (Raga and Fabregat-Santiago, 2012)

The thermal management of both organic and thin film silicon solar cells is unlikely to be a feasible option without improvements in underlying cell efficiencies. Integrating a cooling system can be economically viable for crystalline silicon cells in appropriate climatic and generating conditions (Raga and Fabregat-Santiago, 2012) particularly for large or concentrating PV systems. However, the gain by PV cooling is dependent on the solar resource and the temperature coefficient of the module; if the resource is high enough the percentage loss is higher and therefore cooling may be a more viable option.

Another option to increase the efficiency of a solar energy system would be to integrate the PV module with a thermal collector as discussed in Section 2.2.3 whereby there is both electrical and thermal energy generated by a single system with a higher combined efficiency. Ideally the need for heat in the solar thermal system would be cause for removal from the PV module, making a compatible system. Again the difficulty arises in removing the heat to negate the adverse effect of increased temperature on the PV. However, if the option included storage of heat whereby the stored heat could potentially be used for water or space heating applications, then the economic feasibility of cooling would be more apparent.

2.3 Phase Change Material (PCM)

2.3.1 Classification of Phase Change Material

PCM absorb thermal energy as latent heat at a constant phase change temperature. PCM with a suitable phase transition temperature can be used to regulate the temperature of PV cells (Huang et al., 2006a; Hasan, 2010b; Hasan et al., 2014a) thus maintaining high efficiency for an extended period of time. Compared to other methods of temperature regulation, the use of PCM has the added advantage of storing heat energy that can be used asynchronously.

At initial heating, a PCM heats sensibly and when the PCM reaches the melting/solidification temperature, the material absorbs latent heat, progressively melting. Melted PCM continues to warm further as it melts. The duration and temperature range over which the phase change takes place depends on the mass of PCM and the thermal conductivity of PCM and any enhanced heat transfer elements therein. Once PCM has completely changed phase the material will begin to heat sensibly again. This process is illustrated in Figure 2.12 (Günther et al., 2009).

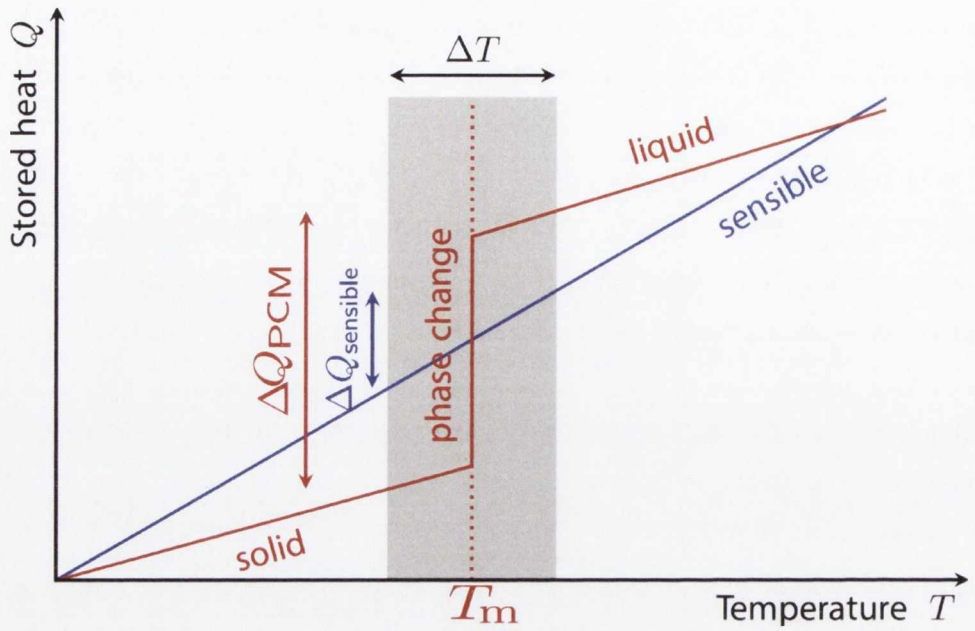

Figure 2.12: Graphical representation of the variation of stored heat of a PCM with increasing temperature (Günther et al., 2009)

A classification of PCM in terms of melting temperature and melting enthalpy is shown in Figure 2.13 (Cabeza et al., 2011). PCMs are divided into organic (paraffin, fatty acid), inorganic (hydrated salts) and eutectic (mixture of organic or inorganic PCM) within the required melting temperature of 20 °C to 100 °C. Cabeza el al. (Cabeza et al., 2011) divided PCM into groups;

- Cooling applications up to 21°C
- 22 °C - 28 °C for comfort in building applications
- 29 °C - 60 °C for hot water applications
- High temperature applications requiring PCM of between 61 °C - 120 °C

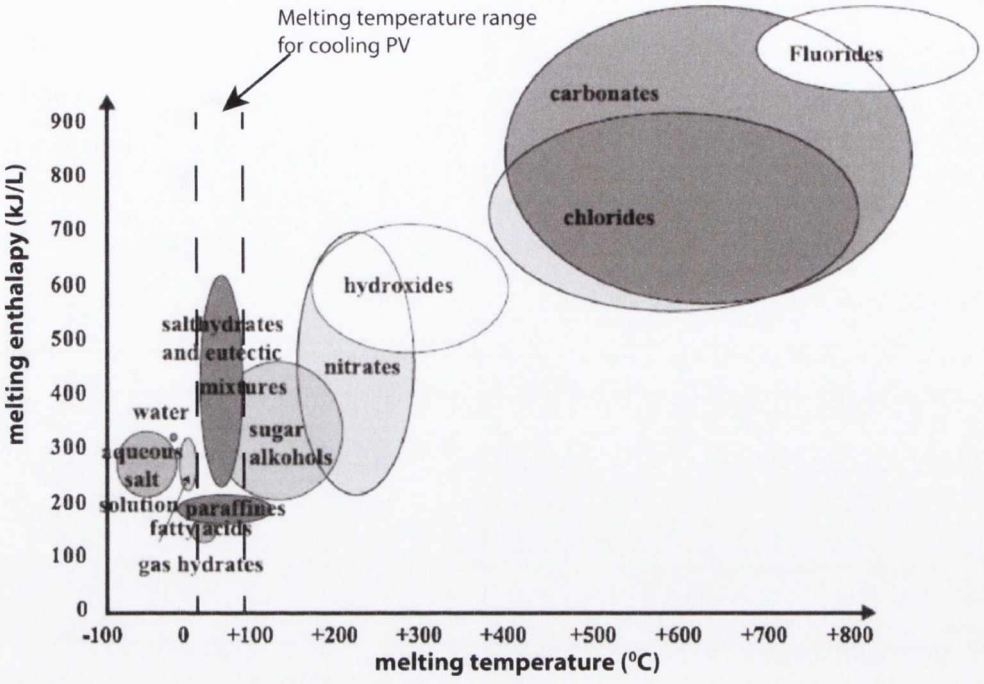

Figure 2.13: PCM classification based on melting temperatures and melting enthalpy (Cabeza et al., 2011)

There has been considerable research on types of PCM, their applications and thermophysical properties (Zalba et al., 2003; Sari et al., 2004; Sharma et al., 2009; Kousksou et al., 2014; Yuan et al., 2014a). The advantages and disadvantages of PCM types for heat storage are summarised in Table 2.1 (Zalba et al., 2003).

Table 2.1: Advantages and disadvantages of organic and inorganic PCM for thermal storage (Zalba et al., 2003)

	Organics	Inorganics
Advantages	Non corrosive Low or no undercooling Chemical and thermal stability	Greater phase change enthalapy
Disadvantages	Lower phase change enthalapy Low thermal conductivity Inflammability	Undercooling Corrosive Phase segregation Lack of thermal stability

The desired characteristics of a material are dependent on the application. However, PCM with a high phase change enthalpy, being non-corrosive, with no subcooling and with chemical and thermal stability would be an ideal choice but where this is unavailable material properties have to be prioritised with regard to the application.

PCM melting temperatures vary considerably due to material type, thermal properties and chemical structure (Cabeza et al., 2011; Oró et al., 2013). PCM with specific melting temperatures are available and their thermophysical properties known (Zalba et al., 2003; Agyenim et al., 2010; Cabeza et al., 2011; Liu et al., 2012). Paraffin waxes are suited to lower temperature applications (<100°C) and molten salts can be used for high temperature requirements.

2.3.2 Corrosion Properties of Phase Change Material

PCM is used as a means of storing thermal energy. The method of containment is important as it is in direct contact with metal piping, plates and housing units which can be damaged if the material is corrosive. The compatibility of PCM with various materials has been investigated and methods to minimise their corrosive behaviour or to mitigate it by using an alternative PCM have been suggested and are described in the following section.

The availability of data on the corrosive nature of PCM was very limited until an investigation into the corrosion resistance of metallic alloys to hydrated salts was carried out (Porisini, 1988). Metal samples were immersed in a PCM sample and contained in airtight capsules which underwent up to 5650 thermal cycles. Stainless steel appeared to be the most corrosion resistant and aluminium the least (Porisini, 1988). Further investigation into the compatibility of high phase change temperature (160 °C - 420 °C) salt eutectics with mild, boiler and austentic steels and the influence of water and other impurities was carried out (Groll et al., 1990). It found LiCl-$LiNo_3$-$NaNO_3$ salt mixtures lead to surface corrosion in all steels, NaCl-$NaNO_3$ is compatible with all steels and KCl-LiCl are much more aggressive (Groll et al., 1990). The corrosion rate of the steel increased when 2 % water was added to the salt. The materials were tested following 42, 84, 168, 336 and 672 thermal cycles of each PCM sample.

Table 2.2: Suitability of the metal-PCM pairs (Cabeza et al., 2001b)

Metal/PCM	$Zn(NO_3)_2 \cdot 6H_2O$	$NaHPO_4 \cdot 12H_2O$	$CaCl_2 \cdot 6H_2O$
Brass	Not recommended	0.5 to 5 mg/cm^{2}yr Recommended	0.4 to 2.5 mg/cm^{2}yr Recommended
Copper	100 to 300 mg/cm^{2}yr Not recommended	5 to 12 mg/cm^{2}yr Caution recommended	0.4 to 5 mg/cm^{2}yr Recommended
Stainless steel	< 0.2 mg/cm^{2}yr Recommended	< 0.2 mg/cm^{2}yr Recommended	0 to 0.4 mg/cm^{2}yr Recommended
Steel	Not recommended	0 to 50 mg/cm^{2}yr Caution recommended	26 to 37 mg/cm^{2}yr Caution recommended
Aluminum	35 to 100 mg/cm^{2}yr Not recommended	Not recommended	4 to 11 mg/cm^{2}yr Caution recommended (gas production)

Cabeza et al. carried out a series of short- (2001a), medium- (2001b) and long- (2005) term corrosion tests. The process involved immersing the metal sample in melted PCM in a test tube which remained in a water bath for the duration of the experiment to ensure the PCM remained in a liquid state. The metals tested were aluminium, brass, copper, stainless steel and steel. The short-term investigation involved leaving the samples immersed in the following salt hydrates; zinc nitrate hexahydrate, sodium hydrogen phosphate dodecahydrate and calcium chloride hexahydrate with melting temperatures of 36 °C, 35 °C and 32 °C respectively for a period of two weeks (Cabeza et al., 2001a). The zinc nitrate hexahydrate emerged as a very corrosive material as aluminium and steel were highly corroded. Calcium chloride hexahydrate produced a pitting effect in aluminium and stainless steel. The samples continued to be immersed for 75 days (Cabeza et al., 2001b) and the final suitability of the metal-PCM pairs is presented in Table 2.2 which indicates the recommended combinations of PCM and metal for use in heat storage applications. The recommendations were based on a guide for corrosion in industry.

The metals previously mentioned were immersed in two PCMs TH29 and a chemical composition of $MgCl_2 \cdot 6H_20$ for a period of 500 days in the long term corrosion tests (Cabeza et al., 2005). As graphite can be used as a method to increase the thermal conductivity of PCM, the study immersed both the graphite and metal pieces in PCM. Aluminium and steel with either PCM are not recommended, brass and copper are recommended with both PCM and stainless steel is recommended for containment of PCM with caution. The corrosion rate after 500 days of the metal-PCM pairs studied in mg/cm^{2}yr is shown Table 2.3 without (left) and with (right) graphite.

Table 2.3: Corrosion rate after 500 days of metal-PCM pairs studied without (left) and with (right) graphite (Cabeza et al., 2005)

Metal/PCM	TH29	Mixture
Aluminum	0.04 / 0.23	0.27 / 0.20
Brass	0.01 / 0.02	0.01 / 0.09
Copper	0.02 / 0.06	0.02 / 0.06
Steel	0.18 / 0.17	0.31 / 0.24
Stainless steel	0.00 / 0.00	0.02 / 0.01

Investigations into the compatibility of commercially available PlusICE E17 and Climsel C18, two salt hydrates with melting temperatures of 17 °C and 18 °C respectively, with an aluminium alloy and copper separately and aluminium in the presence of copper while immersed in an electrolyte (Farrell et al., 2006). The samples were immersed in liquid PCM for 17 hours. It was found copper samples experienced greatest mass loss varying between 0.8 and 0.145g /(m^2h) for ClimSel C18 and PlusICE E17, respectively. Aluminium showed pitting corrosion at a mass loss of 7 x10^{-5} g/(m^2h) while in contact with ClimSel C18 with negligible mass loss when immersed in PlusICE E17. For combined samples of aluminium and copper, no mass occurred on the copper due to the cathodic protection but the corrosion rate increased by a factor of 8 in Climsel 18 compared to aluminium alone (Farrell et al., 2006). García-Romero et al. (2009) presented the corrosion behaviour of four aluminium alloys (EN AW 2024, 3003, 6063 and 1050) in the commercial salt hydrate Glaubers salt ($Na_2SO_4 \cdot 10\ H_20$) which has a melting point of 32 °C. Samples were fully and partially immersed in the PCM and experiments were conducted for a period of up to 90 days. It was found the aluminium alloy 2024 was not compatible with this specific salt hydrate, however, 3003, 6063 and 1050 were shown to be fully compatible.

An investigation into the corrosion resistance of metal samples, stainless steel, carbon steel, aluminium and copper to fatty acids stearic, palmitic, myristic and lauric acid with melting temperatures between 40 °C - 63 °C (Sarı and Kaygusuz, 2003). Following 910 thermal cycles of being fully immersed in each PCM, the metal samples were removed and a gravimetric analysis carried out. The highest corrosion rates calculated were 3.4x10^{-2} and 4.9x10^{-2} mg/cm^2 for carbon steel in contact with myristic acid and copper in contact with stearic acid. Stainless

steel with a chromium oxide layer and aluminium with an aluminium oxide layer were found to be compatible with fatty acids.

An investigation into the compatibility of four organic and one salt hydrate PCM (namely a molecular alloy C_{16}-C_{18}, RT20, RT26, RT25 and TH24) and plastics (high density polyethylene, low density polyethylene, polyethylene terephthalate and polypropylene) was carried out (Lázaro et al., 2006). A furnace was used to cycle the plastic bottles to increase the rate of phase change. LSPE was discarded as an encapsulation material due to the mass variations and large deformations caused by the PCM. Polyethylene terephthalate and polypropylene were shown to be the best encapsulation material of the organic PCM and high density polyethylene for inorganic PCM. Polypropylene, polyethylene terephthalate and low density polyethylene are not recommended for using with TH24.

Further immersion corrosion tests have been carried out for a period of 84 days on aluminium, stainless steel, carbon steel and with salt hydrates, salt hydrate eutectics and fatty acid eutectics (Moreno et al., 2014; Ferrer et al., 2015; Solé et al., 2015). The results suggest that stainless is recommended for use with any of the PCM studied and all other metals would either be recommended with caution or not be recommended at all. Fatty acid eutectic of capric:palmitic (75.2:24.8%) show that copper is the only material tested which is not suitable for containment of the PCM. However, these tests were carried out for a short period of time and further analysis should be carried out to draw accurate conclusions. Oró et al. (2013) has also investigated the compatibility of metal and polymers with PCM with lower phase change temperatures (-22 °C to -16 °C)

There has been no research carried out on eutectic fatty acids, particularly capric, palmitic and lauric acid which have often been used in thermal energy storage systems. The phase change process has been accelerated using furnaces and thermal cycling however, due to the reduced time immersed in PCM may potentially affect the corrosion rate. Real time investigations may be an improved reflection of the corrosion process of material samples immersed in PCM. Finally, there has been no investigation into the effect of PCM on Perspex a commonly used material which can be easily manipulated.

2.4 Application of Phase Change Material in Photovoltaic/Thermal Systems

2.4.1 Phase Change Material as Thermal Management Technique

Phase change materials (PCM) have been used quite extensively in the thermal management of electronic devices (Kandasamy et al., 2007; Kandasamy et al., 2008; El Omari et al., 2011; Jaworski, 2012; Yang and Wang, 2012), Li-ion and fuel cell batteries (Sasmito et al., 2013; Ling et al., 2014), vehicle components (Jankowski and McCluskey, 2014) and cooling systems (Gin et al., 2010; Oró et al., 2012a; Oró et al., 2012b; Walsh et al., 2013). PCM have been used for energy storage in residential and commercial buildings (Pedersen, 2007; Pasupathy et al., 2008; Stritih and Butala, 2010; Evola, 2011; Caliskan et al., 2012; Kośny et al., 2012; Osterman et al., 2012; Rodriguez-Ubinas et al., 2012; Al-Saadi and Zhai, 2013; Royon et al., 2013) as combined PCM with construction materials provides compact thermal mass (Schossig et al., 2005; Pasupathy et al., 2008; Oliver, 2012; Zhang et al., 2012a; Chou et al., 2013; Chwieduk, 2013; Marchi et al., 2013; Toppi and Mazzarella, 2013; Lai and Hokoi, 2014). PCM have been used in hot water tanks (Ibáñez et al., 2006; Nallusamy et al., 2007; Padovan and Manzan, 2014) and with transpired air solar collectors (Rabin et al., 1995; Çakmak and Yıldız, 2011; Summers et al., 2012), (Tyagi et al., 2012; Nkwetta and Haghighat, 2014).

2.4.1.1 Thermal Management of PV using PCM

In 1978, it was suggested PCM could act as a potential thermal storage if integrated with a PV. This concept was patented in 1983 (Ames, 1983). However after this, PCM was not investigated as a means of cooling PV until the mid-1990s. There have been many experimental and computational investigations into the use of PCM to regulate the temperature of PV (Ling et al., 2014). The first study of PCM as a potential method to regulate the temperature of PV is illustrated in Figure 2.14 (Stultz and Wren, 1978).

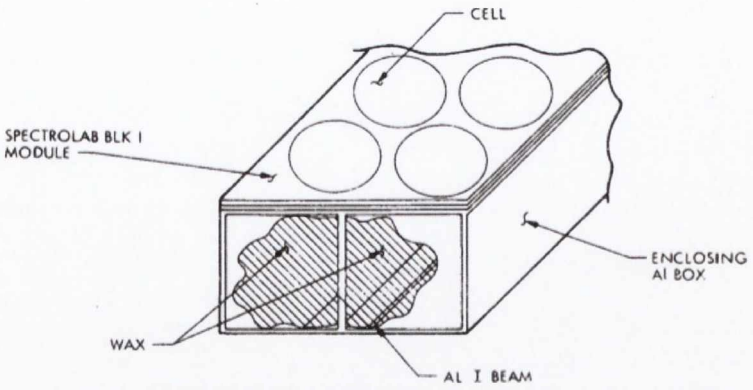

Figure 2.14: Phase change material integrated with a photovoltaic model (Stultz and Wren, 1978)

Stultz (Stultz and Wren, 1978) used Eicosane with a melting point of 36.7 °C, with a Spectrolab PV module used. The properties of Eicosane are detailed in Table 2.4. The high thermal expansion is an undesirable property when integrated into a PV/PCM system.

Table 2.4: Properties of Eicosane, the first PCM integrated with PV (Stultz and Wren, 1978)

Melting temperature (°C)	36.7
Density: Solid (kg/m^3)	855.4
Liquid (kg/m^3)	778.5
Latent heat (kJ/kg)	246.5
Specific heat: Solid (J/kg.K)	2.21
Liquid (J/kg.K)	2.00
Expansion in phase change	15%
Thermal conductivity W/(m^2/K)	0.491

The experiment showed an increase of 1.4 % in the electrical efficiency of the PV. However, it was noted this could be improved with enhanced thermal conductivity of PCM and thus heat transfer from the PV to PCM. Stultz claimed if the PCM were successful in absorbing the excess thermal energy, an improvement in power of 2 % to 3.5 % could be expected. A PV/PCM system was not considered financially viable, however a PV combined with a thermal storage system was seen to have the potential to be cost effective. This work was discussed in a patent in 1983 but was not developed commercially (Ames, 1983).

In a patent published in 2005 (Al-Hallaj and Selman, 2005) PCM was incorporated in a battery module system, including a fuel cell battery system. The invention refers to an arrangement whereby the PCM absorbs a percentage of the heat generated upon a charge or discharge of electrical energy as shown in Figure 2.15. The objective of the system was to improve the power supply of the system by regulating undesired temperature increases, minimise non-uniformity of temperature and act as a heat sink.

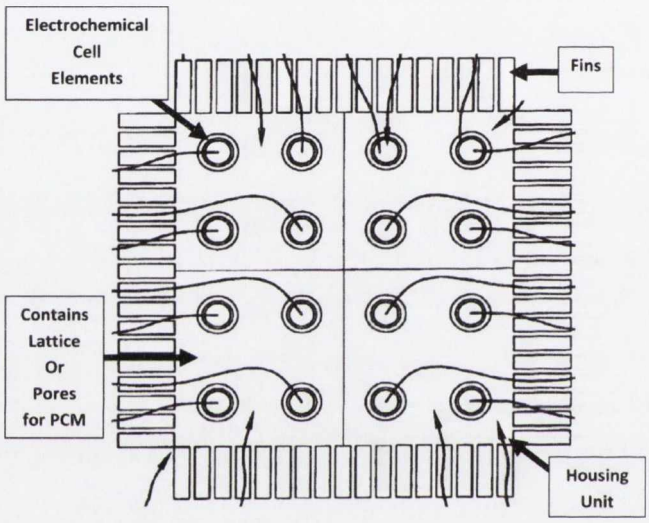

Figure 2.15: Configuration of electrochemical cell incorporated with PCM (Al-Hallaj and Selman, 2005)

Huang et al. (2000) progressed the concept independently with extensive experimental and simulation studies. The first numerical PV/PCM model was validated successfully by comparison with small scale experiments. Three systems were analysed under varying environmental conditions; (i) an aluminium plate to simulate a PV cell; (ii) an aluminium plate with a container filled with PCM to simulate a PV/PCM system; an aluminium plate with a container filled with PCM with integrated fins, as in Figure 2.16.

Temperature variation through the PCM and the solid–liquid transition of the PCM compared well with predictions. Integrated PCM system with fins demonstrated effective temperature regulation of the plate (Huang et al., 2004).

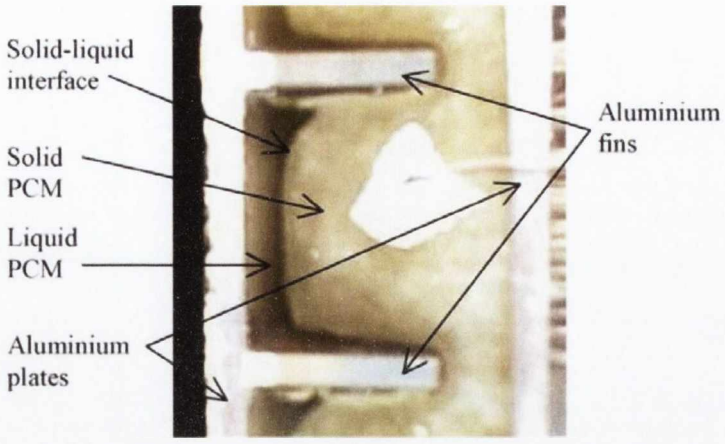

Figure 2.16: Photographic image of melting front of PV/PCM system (Huang et al., 2004)

A 3D thermophysical model for a PV/PCM system based on the Navier-Stokes equation was developed for predicting the convective velocities of melted PCM and temperatures inside the PV/PCM system, this model was compared with a previously published 2D model. The 2D model can be used to predict temperature of a simple linear PV/PCM system however the 3D model allows the prediction of a line-axis system to be resolved (Huang et al., 2006b; Huang, 2007). The application of fins in a PV/PCM system in BIPV to improve low heat transfer rates of PCM was found to moderate the increase in temperature of PV (Huang et al., 2006c). Aluminium fins, shown in Figure 2.17, integrated in a PV/PCM system, (Huang et al., 2011) were used to investigate the melting process of PCM and the effect of differently spaced fins both theoretically and experimentally using PCM RT27. Additional fins were shown to improve the temperature control of the PV.

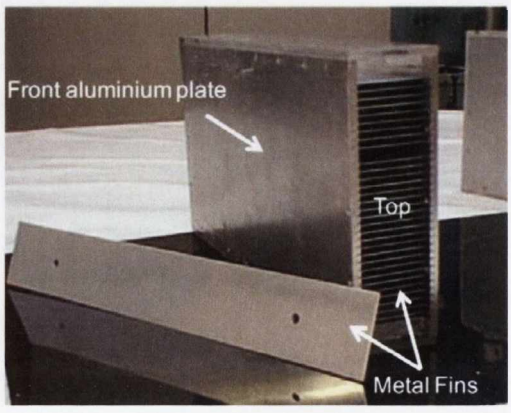

Figure 2.17: PV/PCM system with fins (Huang et al., 2011)

Hasan et al. (2010b) investigated experimentally the use of different PCM types to enhance the thermal regulation of BIPV in a series of small scale indoor experiments. Five PCMs (RT20, capric:palmitic acid, capric:lauric acid, calcium chloride and SP22) and four different systems System A (Aluminium, internal width 5 cm), System B (Perspex, internal width 5 cm), System C (Aluminium, internal width 3 cm) and System D (Perspex, Internal width 3 cm)) as in Figure 2.18 were tested under three insolation values (500 W/m^2, 750 W/m^2 and 1000 W/m^2) in a small scale indoor experiment using a solar simulator to imitate solar conditions at an ambient temperature of ± 1°C.

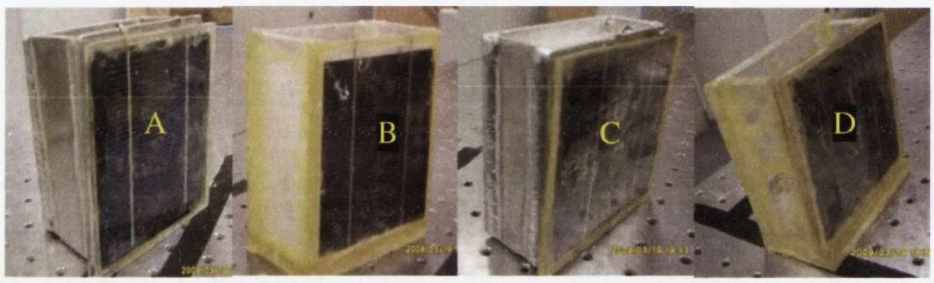

Figure 2.18: System A, B, C and D (Hasan, 2010b)

For insolation of 500 W/m^2, System A with capric: lauric and capric: palmitic was shown to maintain a lower PV temperature for the longest period, (up to 2.5 hours at 10 °C lower than the reference system). At 750W/m^2 and 1000W/m^2 (Figure 2.19) System A with calcium chloride was shown to maintain PV front surface temperatures 10 °C below the reference for a prolonged period of time compared to the other systems.

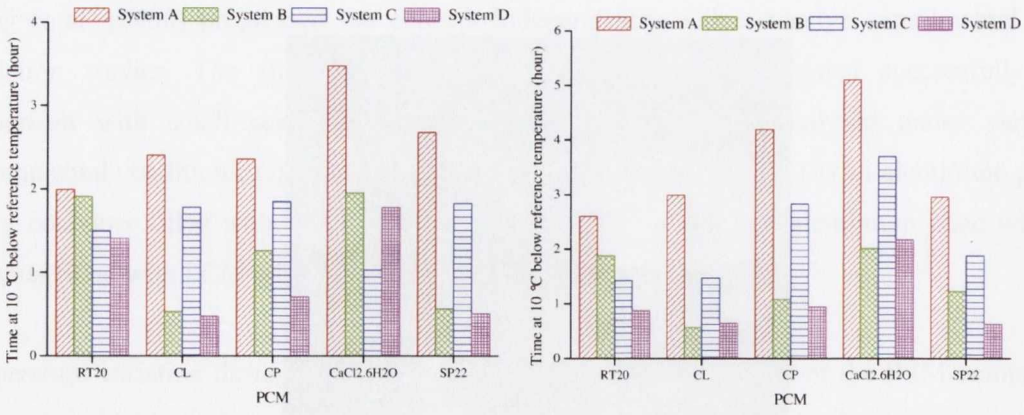

Figure 2.19: Results from experiments at (a) 750 W/m^2 and (b) 1000W/m^2(Hasan, 2010b)

The thermal behaviour of the PV/PCM system presented in Figure 2.20 was simulated for hot climatic conditions (Cellura et al., 2008) with three paraffin waxes, that melted at 26 °C - 28 °C, 31 °C, 28 °C - 32°C for PCM_1, PCM_2 and PCM_3, respectively.

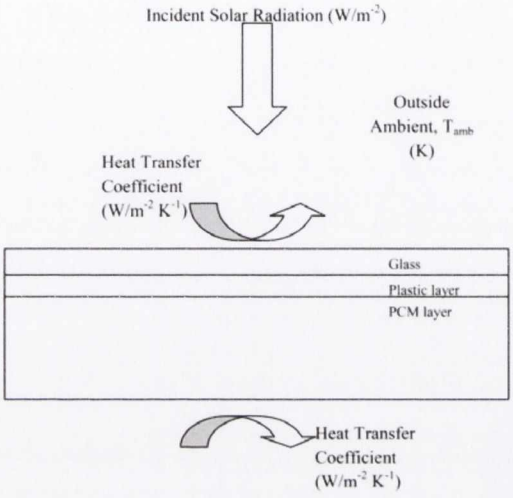

Figure 2.20: Heat exchange in a PV/PCM system modelled using COMSOL (Cellura et al., 2008)

A proposed BIPV PV/PCM system using microencapsulated PCM (MEPCM) as shown in Figure 2.21 (Ho et al., 2012), where navy is glass layer in PV, yellow is plastic layer in PV and grey is PCM and each number represents a surface of the calculation model, each having its own boundary conditions. The model showed an increase of 14 % in the PV/PCM system when compared to a system without PCM, although this model had yet to be validated experimentally.

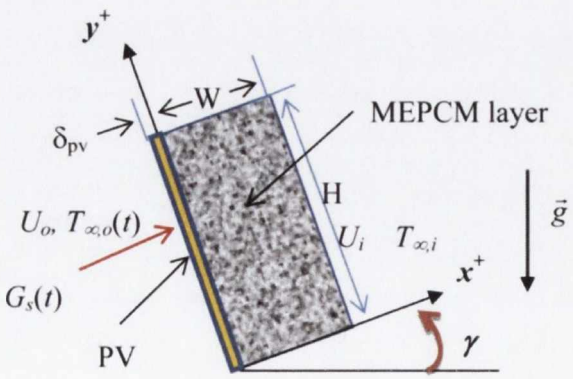

Figure 2.21: Schematic of heat transfer through BIPV PV/PCM system (Ho et al., 2012)

A MEPCM with melting temperature of 26 °C was simulated, during summer an increase of 0.13 % of electrical efficiency was shown with MEPCM compared to without MEPCM, winter time confirmed an increase in efficiency of 0.42 %. The optimum aspect ratio (width/height) of MEPCM incorporated in the system was recommended to be between 0.277 and 1. The melting temperature of the PCM was above ambient and close to standard test conditions of the PV, this was a small phase transition temperature which allowed for maximum transfer of latent heat to PCM. At an ambient temperature of 26 °C and solar irradiance of 600 W/m^2 PCM with melting temperatures of 26 °C and 34°C increase the efficiency of a PV module by 0.09 % and 0.12 %, respectively (Ho et al., 2012). Corresponding results have been reported (Tanuwijava et al., 2013). A similar study was undertaken to assess the performance of water-saturated MEPCM/PV system, as in Figure 2.22, using a CFD numerical simulation (Ho et al., 2013).

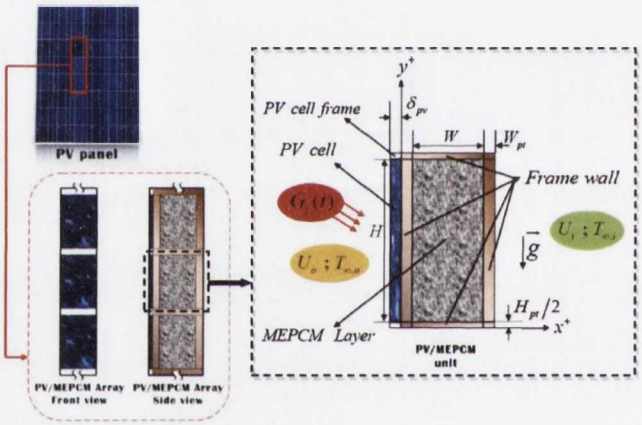

Figure 2.22: Schematic of heat transfer in a PV/MEPCM module (Ho et al., 2013)

The model recommended that under summer conditions corresponding to an ambient temperature of 30 °C and solar irradiance of 650 W/m^2 a melting point of 30 °C and 30 cm layer of MEPCM be incorporated with the PV system. This melting temperature allows for phase change to occur during peak sunshine hours and during night time the MEPCM could discharge fully. Under these conditions an increase of 2 % in efficiency would be expected in the system compared to a PV only. A numerical study of a water-surface floating PV/MEPCM system showed a 1.8 °C reduction in the temperature of the PV surface and 2.1 % increase in the electrical output relative to a PV system without a MEPCM layer (Ho et al., 2015).

Sarwar et al. (2014) simulated the temperature regulation of the PV/PCM system illustrated in Figure 2.23. A finite element numerical heat transfer simulation model was used which took

into account the electrical conversion of incident light and real-time heat loss boundary coefficients. It used a higher order mixed formulation and an iterative solver.

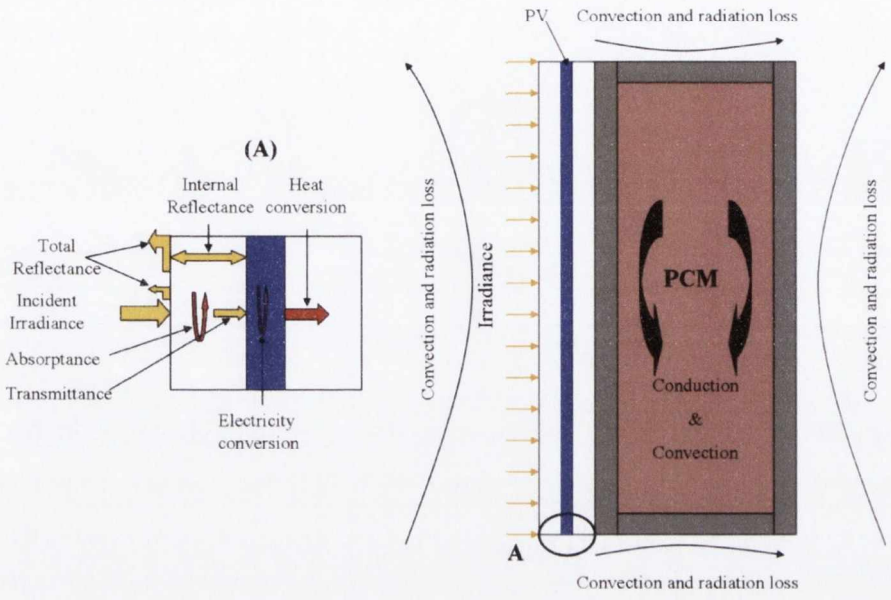

Figure 2.23: Optics, electrical conversion and heat transfer mechanism in PV/PCM systems (Sarwar et al., 2014)

The model was validated by comparing the simulated and experimental temperature evolution of PV at an incident irradiance of 1000 W/m^2. The small-scale indoor experiment was carried out on three inorganic PCM, capric-palmitic, capric-lauric and RT20. A 10 x 10 x 0.05 cm^3 PV cell was encapsulated in 3 mm thick Perspex and attached to an aluminium container which held the PCM. The model investigated the temperature evolution, velocities and phase change fraction of the PCM and found ~1 °C temperature difference between the modelled and experimental results.

Jay et al. (2010) furthered investigations through an indoor analysis and computational investigation. The experimental set-up is shown is Figure 2.24 and consisted of 4 panels, panel 1 and 2 with PCM of melting points 45 °C and 27 °C, respectively, panel 3 is insulated from the rear and a panel 4 is a standalone PV. PCM was encapsulated into a honeycomb made of aluminium to promote heat conduction. Three solar irradiance intensities of 600, 800 and 1000 W/m^2 were simulated using a solar simulator and each system characterised.

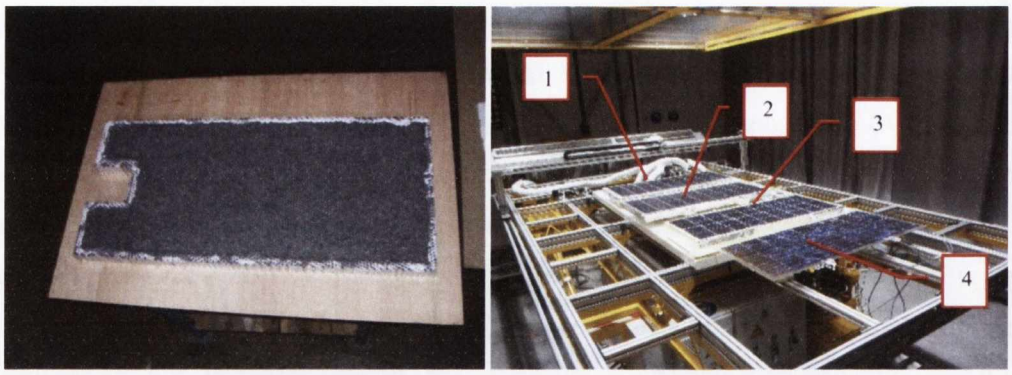

Figure 2.24: (a) Aluminium honey comb (b) Experimental set up where (1) PV/PCM T_{melt} 45°C (2) PV/PCM T_{melt} 27°C (3) PV insulated and (4) PV standalone (Jay et al., 2010)

Under an irradiance of 800 W/m^2, the temperature of the panels coupled with the PCM remained below that of the reference panels for over 5.5 hours. The increase of instantaneous electrical production due to the temperature regulation of the PV by the PCM is estimated to be about 15 % – 23 % compared to a PV system alone. Simulations carried out using GAMBIT 2.4 and FLUENT 12.0.16. CFD codes followed the same trends as the experimental investigations. Differences in the predicted PV temperatures arose due to the approximation of material properties, heat transfer coefficients, surface emissivity and air gap depth.

Japs et al. (2013) undertook an experimental analysis of a PV module integrated with a paraffin based PCM. The PCM was incorporated with an aluminium-polymer compound to improve its thermal properties. The PCM was shown to have a higher thermal conductivity but decreased storage capacity when compared to its non-improved counterpart. Macro-encapsulated PCM bags were attached to the back of a PV and were installed in Paderborn, Germany. Temperature, current, voltage and MPP were recorded and it was found over a 25 day period the PCM minimised daily temperature fluctuation of the surface of the PV compared to a system without PCM. Also, the non-improved PCM provided lower operating temperatures of a PV module initially although when melting occurs the improved PCM regulated the temperature for 5.5 hours compared to non-improved PCM.

Full scale outdoor experiments of the use of PCM to regulate the temperature of a PV system were undertaken in Dublin, Ireland and Vehara, Pakistan (Hasan et al., 2014a). Three 65W PV, as in Figure 2.25, were used in the experiment where one served as a reference and the other

two were PV-PCM systems with a eutectic mixture of capric-palmitic and salt hydrate, respectively.

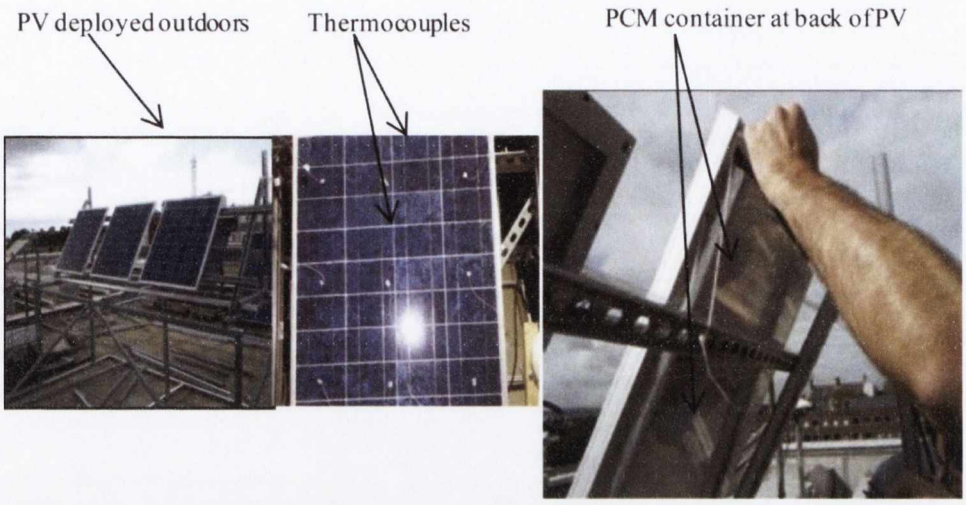

Figure 2.25: Experimental set-up of PV-PCM systems, location of thermocouples and attachment of PV to PCM container (Hasan et al., 2014a)

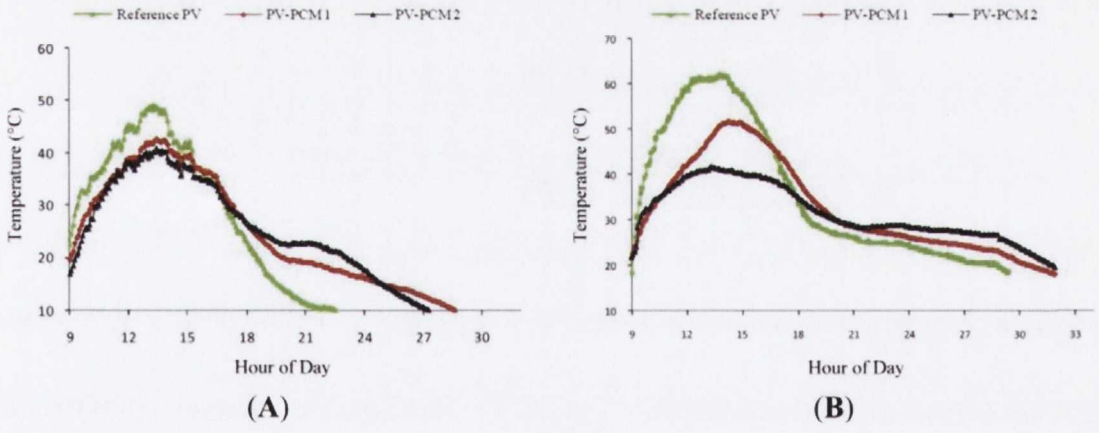

Figure 2.26: Surface temperatures of reference PV and PV-PCM systems measured in (a) Dublin and (b) Vehari (Hasan et al., 2014a)

The results were compared at peak instantaneous temperature of the reference PV. Capric:palmitic PV-PCM system regulated the PV by 7 °C and the PV-PCM system with salt hydrate maintained a temperature reduction of 10 °C compared to the reference PV as illustrated in Figure 2.26(a). This trend was also shown in Vehari, where capric:palmitic maintained a

temperature reduction of 10 °C and salt hydrate 21 °C when compared to the reference PV as shown in Figure 2.26(b).

Lo Brano et al. (2013; Lo Brano et al., 2014) developed a one-dimensional finite difference model which simulated the variable temperature profile of PV, the temperature change in the PCM and melting fraction of the PCM. In the model first the temperature at each node was calculated then the liquid fraction of the PCM. The simulation was validated using data derived from a full scale experiment in Palermo, Italy illustrated in Figure 2.27.

Figure 2.27: Encapsulation of PCM and experimental installation (Lo Brano et al., 2013)

The phase change temperature of the PCM was 26 °C – 28 °C and experimental results were in agreement with simulations. The investigation demonstrated that discharging at night is essential to PCM performance. At night, it was found the PCM would not discharge fully as the temperature of the PCM is higher than the solidification temperature therefore it was unable to solidify so no latent heat storage capacity was available for the next day.

Using computational fluid dynamics (CFD) a 2D model was developed assessing the heat and mass transfer of PCM located in the back of a PV panel (Biwole et al., 2013). The simulation developed used the transient heat transfer diffusion equation along with Navier Stokes

momentum conservation equation to simulate conduction and convection in the PCM. An indoor validation experiment was conducted. The experimental set-up is shown in Figure 2.28.

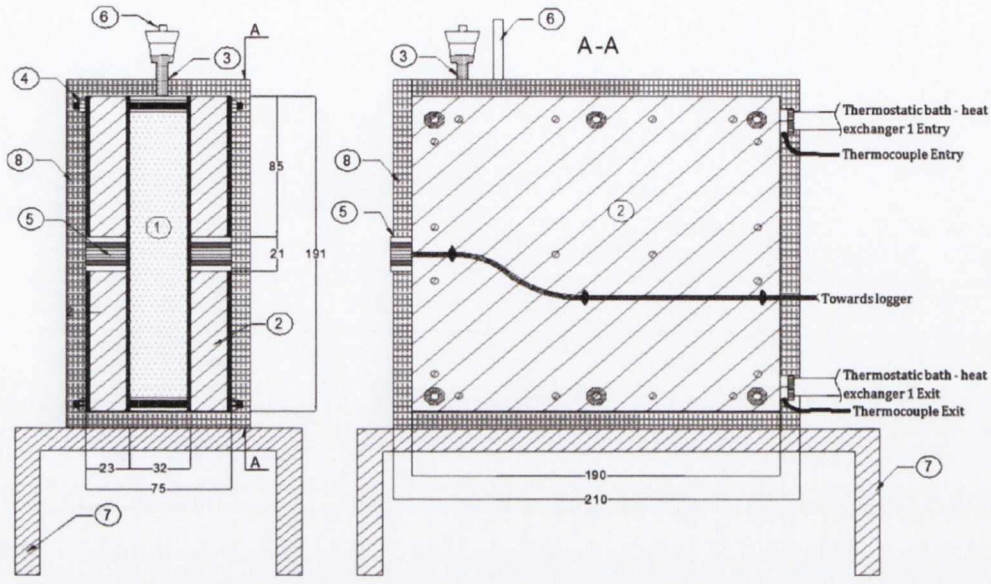

Figure 2.28: Experimental equipment (1) PCM, (2) heat exchangers, (3) PCM intake valve, (4) structure system, (5) flowmeter, (6) air intake valve, (7) metal stand and (8) insulation material (Biwole et al., 2013)

The dimensions of the cavity containing the PCM was 167mm x 167mm x 30mm. Heat plates were positioned on each side of the tank to simulate the heating from a solar panel. The PCM used was RT25. The PCM was shown to maintain the PV temperature under 40 °C for 80 minutes of constant exposure at 1000W/m^2, compared to 5 minutes without PCM.

2.4.1.2 Thermal Management of Concentrating PV (CPV) using PCM

PCM was first used in CPV in a patent in 1993, (Horne, 1993) where the concept of PCM to protect PV cells in a solar concentrator from excessive temperatures was included. The selected PCM melted at a temperature higher than the normal operating temperature range of the PV cells, but less than the temperature at which the PV cells suffer thermal damage.

Further to their work on asymmetric compound parabolic photovoltaic concentrators (ACPPVC) (Wu, 2009; Wu and Eames, 2011) which concentrate significant diffuse solar radiation, Wu et al. designed and constructed an ACPPVC integrating PCM RT27 to the back, as in Figure 2.29, to regulate the temperature. The system had a concentration ratio of 2 (Wu, 2009).

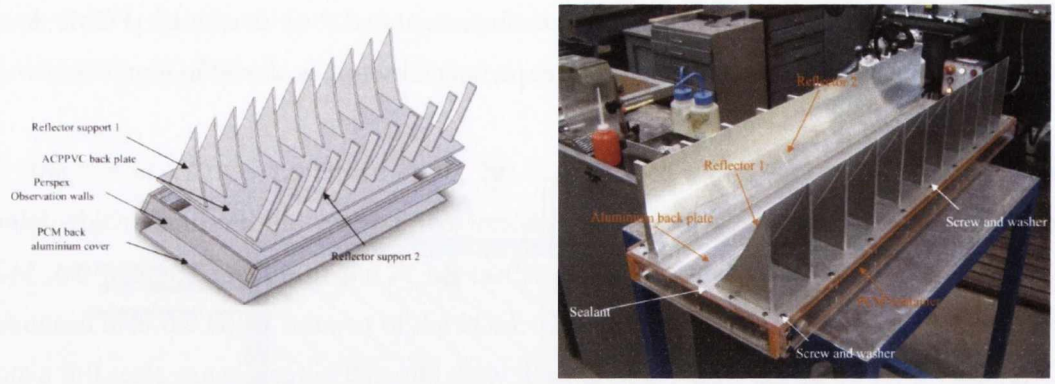

(a) (b)

Figure 2.29: ACPPVC integrated with PCM (a) schematic and (b) photo (Wu, 2009)

At an incident solar irradiance of 672 W/m^2 and incident angle of 0 ° the temperature of the solar cells of the ACPPVC-55/ PCM was reduced by 18 °C during the phase change compared to ACPPVC-55 system. The predicted electrical conversion efficiency of the ACPPVC-55/PCM is 10 %. Further tests under various incident angles and solar irradiance intensities found that at solar irradiance intensities of 280 W/m^2 the PV temperature was reduced by 7°C for approximately 10 hours when using RT27 with an increase of 5 % in the electrical conversion compared to ACPPVC-55.

A V-trough CPV system was investigated where a metal-wax composite PCM was used to regulate PV temperature (Maiti et al., 2011), illustrated in Figure 2.30. Paraffin wax with a phase change range of 56 °C - 58 °C was located on the rear of the module. To enhance low thermal conduction in the PCM, aluminium lathe turnings were embedded. Indoor experiments maintained the temperature between 65 °C - 68°C for 3 hours at 2300 W/m^2 generated using a solar simulator. The temperature of the PV rose to 90°C in absence of the PCM. Outdoor experiments showed maximum temperatures of between 78 °C – 80 °C in the absence of PCM and 64 °C - 65 °C with the PCM as a temperature regulation mechanism though this was at a lower solar irradiance intensity of 1982 W/m^2 generated by the initial radiation being concentrated in the V-trough.

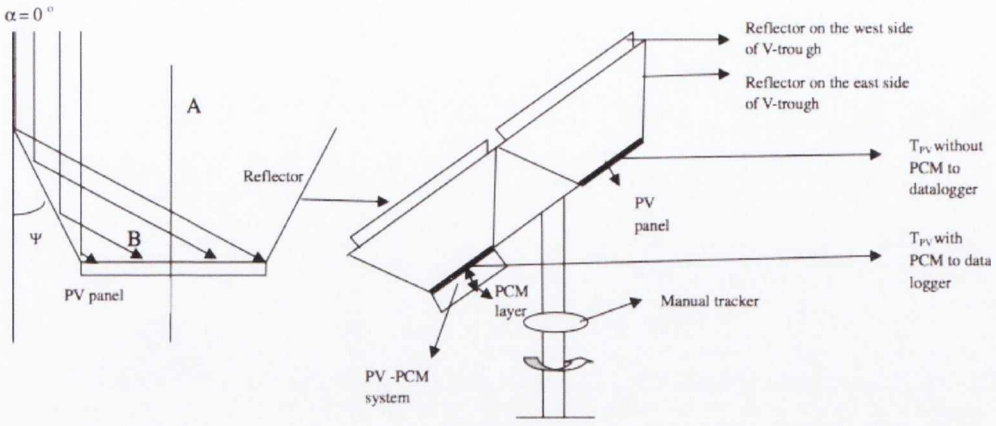

Figure 2.30: V-trough PV system with integrated metal-wax composite PCM (Maiti et al., 2011)

PCM was further investigated theoretically in a CPV system with concentration of 2 suns and was found to be a technically feasible option for suitable sites with high solar concentration (Lillo-Bravo et al., 2011). Twelve sites were chosen for which a CPV/PCM model was simulated under the environmental conditions of each site. Four phase change temperatures were tested, 25 °C, 35 °C, 45 °C, and 55 °C. It was found that a concentrated system located in Cairo generated 37.2 % more electrical power than a system without PCM, followed closely by Cairo and London produced the least increase in energy of 18 %. The improvement in efficiency has been closely linked with the location of installation and the possibility of solar concentration. It should be noted that this model has not yet been validated.

A hybrid CPV-thermoelectric concept integrated PCM as a store of heat generated by a concentrator as in Figure 2.31 (Li et al., 2013). A series of calculations based on conversion efficiencies of the PV cell and thermoelectric generator suggest system efficiency improved by 30 % when a high-grade cold energy storage system was added.

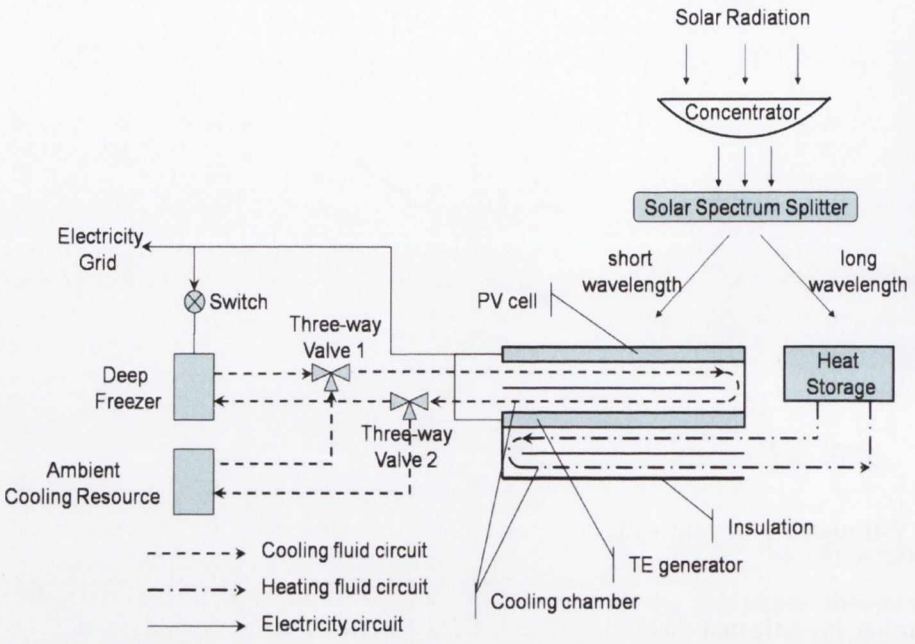

Figure 2.31: Schematic of PV-thermoelectric power system with the use of PCM as TES (Li et al., 2013)

A two-axis concentrating photovoltaic system thermally regulated by PCM was fabricated and tested outdoors in Pakistan as in Figure 2.32 (Sarwar, 2012).

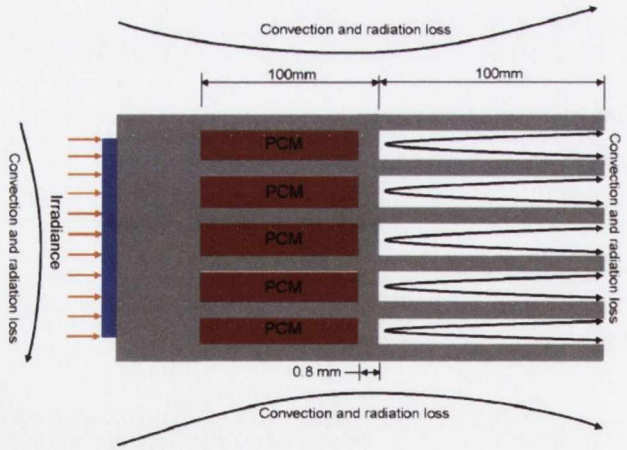

Figure 2.32: Concentrating PV system with PCM and fins for cooling (Sarwar, 2012)

Numerous PCM were tested and it was found that selection of the optimum PCM depends on application. Lauric acid was found to reduce the peak PV temperature by 22 °C and palmitic

found a maximum temperature difference of 19.5 °C. However, palmitic has a higher heat of fusion and temperature regulation capabilities.

2.4.2 Solar Thermal Collectors with Integrated PCM

PCMs have been widely used as an effective latent heat thermal-storage system for solar thermal collectors as they have the added advantage of high-energy storage density. The application of PCM has evolved from its use as a thermal management technique to an energy store. PCM integrated with solar collectors work on the basis that the PCM is charged during sunshine hours indirectly through heat transfer from the sun to a transfer fluid such as water or directly from the sun. At night the PCM discharges releasing heat energy for space heating or water heating. Murali and Mayilsamy (2015) give an overview of notable PCM for this application, the use of PCM and the parameters to characterise stratification and improvement methods. The majority of studies conducted have used thermal energy stored by PCM for water heating as will be shown in the following section.

One of the earliest studies involving solar collectors and PCM was done by Prakash et al. (1985). A built in water storage heater contained a layer of PCM-filled capsules at the bottom was simulated. A computational comparison between different sized latent heat storage and sensible storage vessels in a water tank with varying degrees of stratification was investigated (Ghoneim, 1989). Cylindrical PCM pipes were positioned vertical in a cylindrical tank were surrounded by a heat transfer fluid. A theoretical model has been developed for cylindrical latent heat storage as part of a domestic hot water system. The PCM capsule, both paraffin wax and stearic acid were studied, was located in a closed loop with a solar water heater and during discharging the energy is extracted by a liquid flowing through a water storage unit (Bansal and Buddhi, 1992). Rabin et al. (1995) presents a solar thermal collector storage system based on a salt hydrate material as illustrated in Figure 2.33. The model was solved numerically by an enthalpy-based finite differences method which was validated against experimental data. The experimental study showed in winter in Beer-Sheva, Israel, two thirds of daily solar radiation falling on the collector surface could be collected and stored. The system was investigated for greenhouse applications; the optimum thickness of PCM was 30-65 mm when using a PCM with a melting temperature of 20 °C.

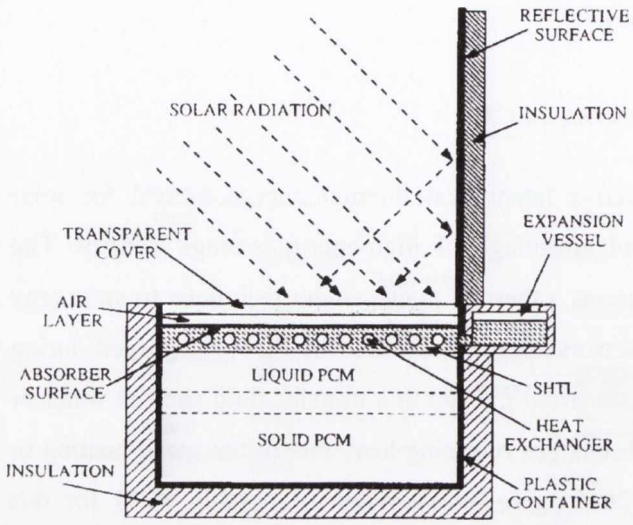

Figure 2.33: Solar collector storage system with integrated PCM (Rabin et al., 1995)

More recently studies have concentrated considerably on solar collector with PCM in the water storage tank. The thermal performance of an integrated collector storage solar water heater (ICSSWH) with PCM was investigated using a 3D CFD numerical model (Chaabane et al., 2014). The design looked at two PCM, myristic and RT42-graphite, and three varying radii of the PCM layer, R=0.2 m, R=0.25m and R=0.3m which is located in the collector storage solar water heater, as illustrated in Figure 2.34.

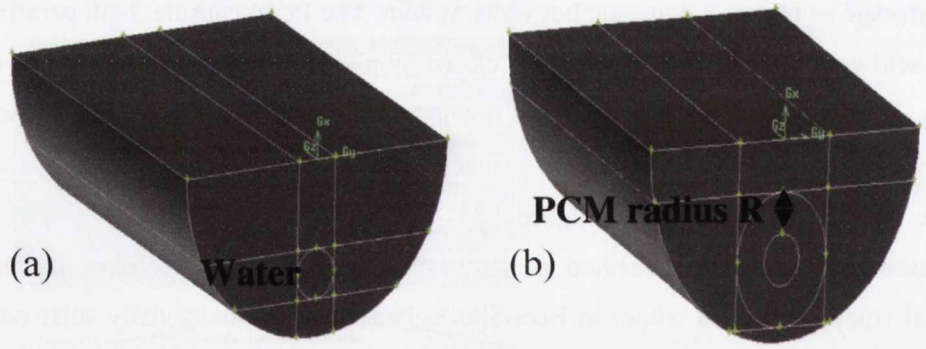

Figure 2.34: (a) Solar water heater (b) Solar water heater with integrated PCM (Chaabane et al., 2014)

The results showed the addition of PCM did improve the thermal performance of the solar water heater compared to a system without PCM. Myristic acid allowed the same maximum water

temperature as that of a sensible heating storage unit to be reached during the day and higher values during the discharge of PCM. The lowest night losses also corresponded to the highest PCM radius suggesting the larger thermal store reduces the loss of heat from the system. An experimental approach was taken to enhancing a solar water heater by integrating a paraffin wax with melting temperature of 55 °C (Fazilati and Alemrajabi, 2013). The PCM was encapsulated in HDPE and embedded inside the tank. It was found the implementation of PCM in the solar collector tank extended the time for which it could supply hot water by up to 25 % in 80 °C charging mode.

Another approach is to separate the heat storage tank from the solar collecting system and position it in the heat transfer fluid loop. Haillot et al. (2013) presents a numerical evaluation of a solar domestic hot water system coupled with flat plate collectors and integrated thermal storage as shown in Figure 2.35. Thermal energy from the solar collector is conveyed to the water tank through the heat transfer fluid circulation in a closed loop using an electrically driven pump.

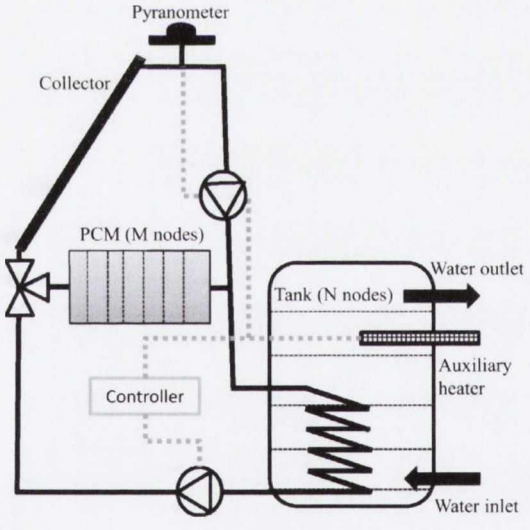

Figure 2.35: Solar domestic hot water system with PCM (Haillot et al., 2013)

Different system parameters and working conditions were investigated; volume of the PCM unit, PCM melting temperature, volume of water tank and meteorological conditions. The optimum system in summer conditions has been reported to have an efficiency of 85 % with system configuration of water tank volume 0.2 m^3, PCM volume 0.037 m^3 and PCM temperature 60.32 °C. However, the auxiliary heat input was 37.3 kWh. As the basis of this

study was to reduce the size of the required storage system and increase system efficiency, the favoured system configuration would be to integrate 0.1 m^3 storage tank with a 0.045 m^3 PCM unit. A system which considers single PCM and multi-PCM thermal storage positions the storage tank on the heat transfer fluid circulation loop (Aldoss and Rahman, 2014). The study reported multi-PCM thermal energy storage system attains higher performance over the conventional single-PCM design, as both charging and discharging cycles are sustained for a longer period of time. Three PCM stages were found to be the optimal design.

A further method of integration of PCM with a solar collector system is to use an absorbing surface with embedded PCM directly in the collector than in a separate tank. This design attempts to minimise thermal losses at night and during cold season; and overheating during the hot season. Mettawee and Assassa (2006) propose an absorber plate-container unit to function as both a method to absorb thermal energy and store a paraffin wax PCM as illustrated in Figure 2.36. A series of thermocouples were used to assess the transfer of heat through the system. The performance of each system is analysed using a finite difference method and a numerical solution is developed using a one-dimensional approach.

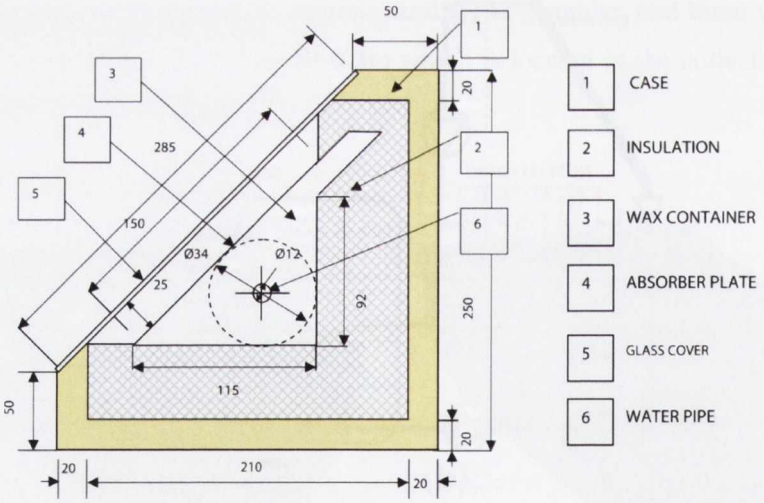

Figure 2.36: Cross-section of solar collector with absorber-container unit (Mettawee and Assassa, 2006)

It was found that as the water mass flow rate increases the useful heat gained also increases. However, the useful heat gained decreases with time due to the low conductivity of the solid paraffin wax. An energy and exergy analysis was carried out on a compact solar collector which

combines a collector surface with a rectangular PCM storage tank beneath the surface as shown in Figure 2.37 (Koca et al., 2008). The experimental set-up was located in Turkey. A total of 30 kg of Glaubers salt was used in the analysis.

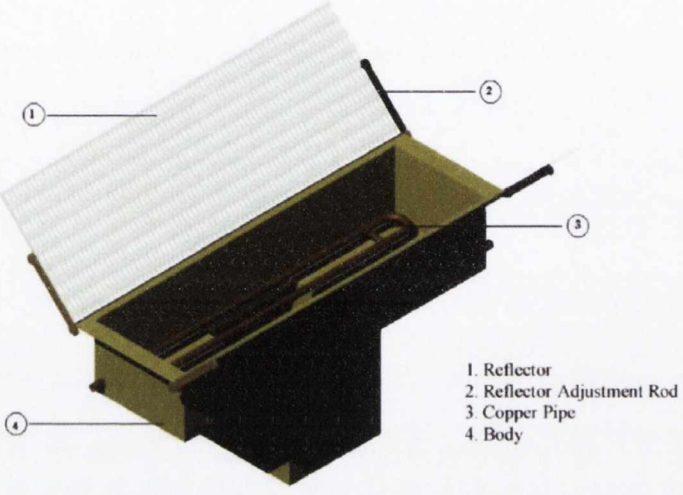

Figure 2.37: Combined single unit solar collector and energy storage (Koca et al., 2008)

The exergy efficiencies of latent heat storage systems with PCM are found to be low, between 1.5 % and 3.3 %, this could be due to the low thermal conductivity of the PCM. The daily energy efficiencies were found to be between 45 % – 42 % for the month of October.

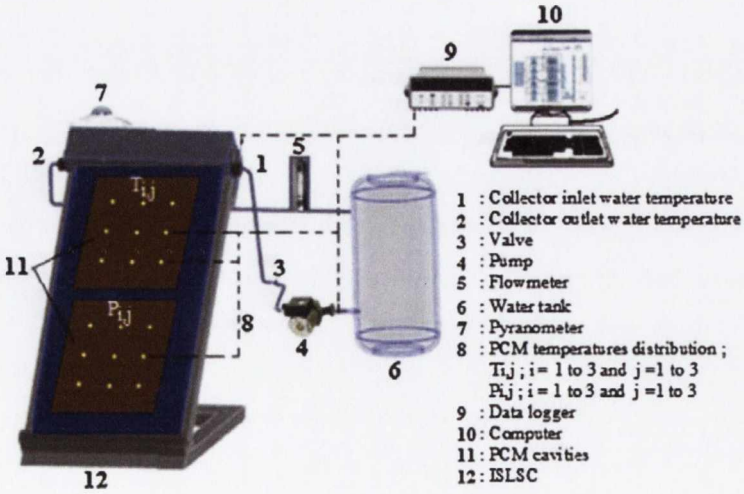

Figure 2.38: Solar collector with PCM filled cavity (Bouadila et al., 2014)

An outdoor experimental investigation was carried out on a solar collector with two PCM filled cavities, as shown in Figure 2.38, and a numerical analysis of the temperature stratification inside the PCM-filled cavities was also studied (Bouadila et al., 2014). A paraffin wax with a melting temperature of 56.3 °C was used.

It was found the PCM integrated solar collector extends the time of availability by 5 hours after sunset with a consistent useful heat of around 400 W. The energy efficiency varied between 25 % and 35 % for the period of a day. It would be interesting to assess the performance of the system without PCM in order to gauge the effect of the PCM.

2.4.3 Hybrid Photovoltaic/Thermal/Phase Change Material Systems

A photovoltaic/thermal (PV/T) system converts solar radiation into electrical and thermal energy. The incorporation of thermal collectors with PV technology can increase the overall efficiency of a PV system as thermal energy is produced as a by-product of the production of electrical energy. Passive cooling is a naturally induced temperature difference and the use of an external mechanical system is known as active or forced cooling. The removal of heat from the PV occurs immediately once a temperature differential develops between the PV and the transfer fluid. There are two options for disposal of excess thermal energy collected from the PV; transfer of heat to air or water. The pre-heated fluid is diverted directly to an end application such as warm water or air which can be used for purposes such a space heating or domestic hot water requirements.

Several review papers have been published in the use of PCM as a thermal management technique of PV, emphasising the growing body of literature in the area (Browne et al., 2015a; Ma et al., 2015). Yin et al. (2013) have presented a PV/T system with integrated heat storage using PCM as shown in Figure 2.39. Water is directly heated by thermal energy from the PV; it flows via a thermosyphon through the PCM which will store the heat from the water for later applications.

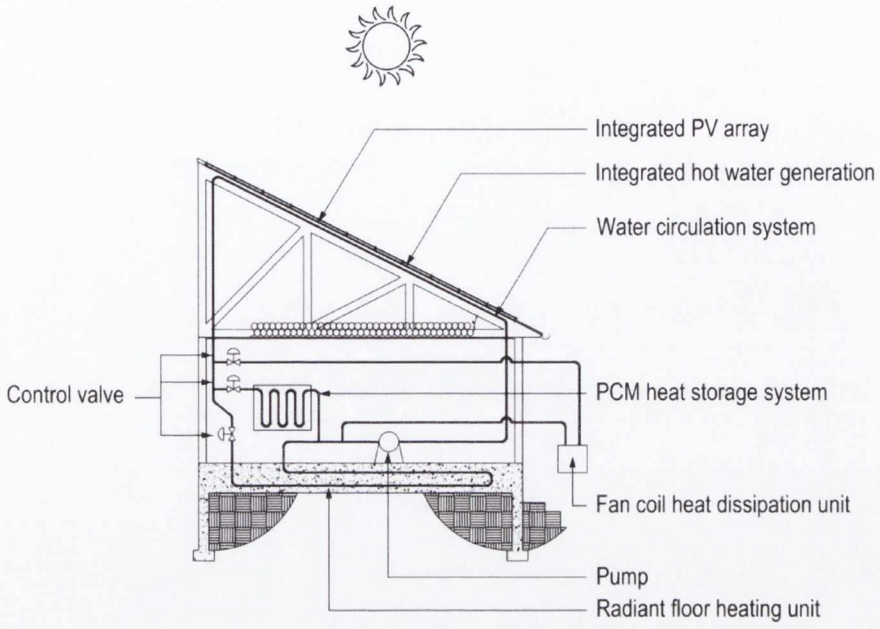

Figure 2.39: Cross section of residential PV/T system (Yin et al., 2013)

The water reached a temperature which was found to be useful in domestic applications. In ambient temperatures heat captured by the PCM prevented it entering the domestic dwelling and significantly reducing the cooling load.

A one-dimensional energy balance model of a PV/T/PCM (PV/Thermal/PCM) system was simulated as shown in Figure 2.40 (Malvi et al., 2011). The model is divided up into a series of nodes; at each of which a temperature is calculated. Investigations into water flow rate, PCM thickness, PCM melting point and PCM conductance were carried out using the model. The most effective flow rate for PV cooling is approximately 10 l/h; however, this is undesired for water heating applications as the water outlet temperature is reduced. The optimum thickness of PCM was found to be 0.03 m which increases the PV efficiency by approximately 6.5 %. The temperature range changes throughout the year which emphasises the issue of having to change the melting temperature of the PCM throughout the year. The PV output increases by 3 % if the conductance of the PCM is increased by a factor of 10. New PCM with improved thermal conductivities would be required. The electrical output of the PV/T/PCM system was shown to increase by 9 % when compared to a PV system only (Malvi et al., 2011).

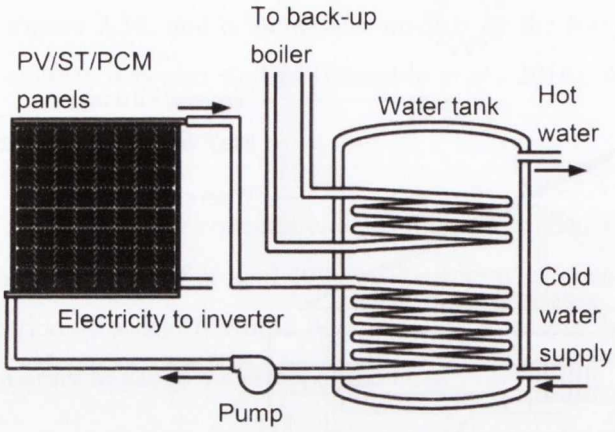

Figure 2.40: Schematic of simulated system (Malvi et al., 2011)

The addition of PCM in PV/PCM systems has been shown to lower the operating temperature of PV by removing excess heat (Malvi et al., 2011).

A numerical simulation of BIPV/T-PCM vented and un-vented Trombe-Michel walls, illustrated in Figure 2.41, was validated via comparison with the experimental results from a BIPV/T system in this case ventilation wall is part of PV/T collector system (Aelenei et al., 2013). The air cavity allows for ventilation and each system has been investigated with and without it. The results of non-ventilation showed the PCM caused a decrease of 7 °C when comparing the temperature of the air cavity this is due to the latent heat storage of the PCM. However, ventilation of the systems showed a much lower difference of 2 °C (BIPV/T-PCM 28 °C and BIPV/T 30 °C) when looking at the maximum air temperature, suggesting that heat is being removed by ventilation rather than the PCM.

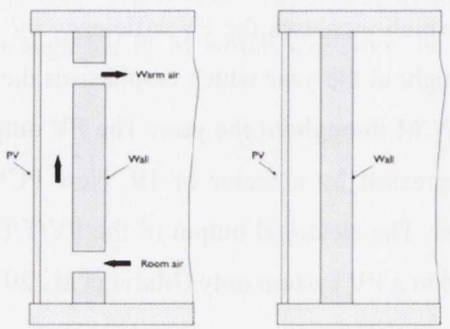

Figure 2.41: Simulated BIPV/T system with integrated PCM wallboard (Aelenei et al., 2013)

The investigations show that the effect of the storage in the PCM reduces the PV temperature and thus raises the PV efficiency. However, during winter conditions the storage of heat causes adverse effects as the heat transfer from air cavity to the interior of the room is reduced (Aelenei et al., 2013). In a numerical and experimental study of this system the maximum electrical and thermal efficiencies reached were 10 % and 12 %, respectively (Aelenei et al., 2014).

Figure 2.42 summarises the main differences between PV/T and PV/PCM systems. The collection of heat in the PV/T is completed using a transfer fluid; however, PV/PCM uses a PCM substrate. The distribution of heat is immediate as the pre-heated supply of fluid is diverted directly to the end application. However, this is not the case with PCM as the heat can be stored and used in an end application at a later time due to the latent heat storage abilities of the PCM. Heat removal from the PV/PCM solar collectors is asynchronous due to the reliance of charging and discharging of the PCM on ambient temperature and the method through which heat is removed from the PCM. Whereas in PV/T system the heat is diverted to the transfer fluid and used immediately as a result the peak amount of thermal energy available will be when the solar insolation is at its peak.

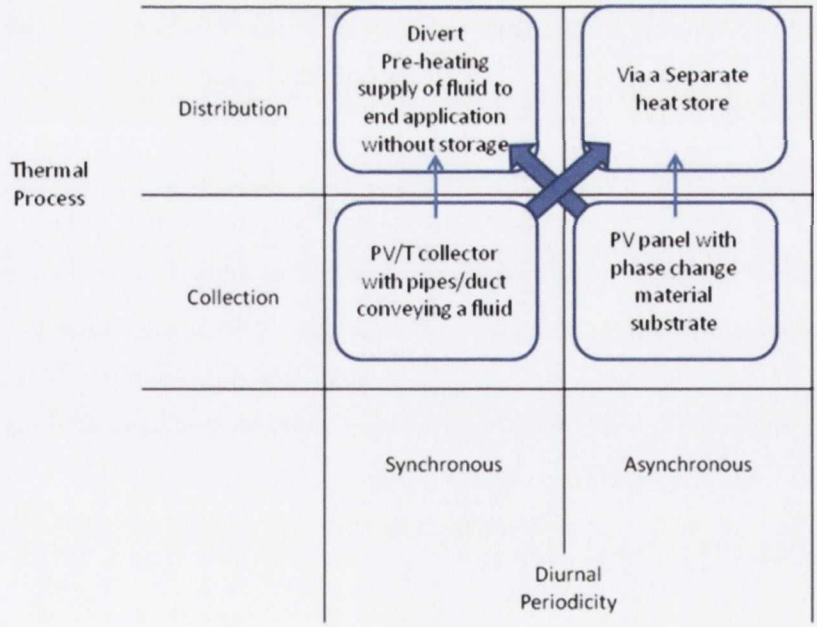

Figure 2.42: Thermal processes and diurnal periodicities that distinguish between PV/T and PV/PCM solar collectors and associated storage systems

2.4.4 Modelling Tools for Solar Systems and PCM

2.4.4.1 TRNSYS

TRNSYS, transient simulation program, is a quasi-steady simulation model. The model was developed by the University of Wisconsin by the members of the Solar Energy Laboratory (Klein, 1976). The program is made up of a modular structure which consists of many subroutines that model subsystem components. The mathematical subsystem components are given in terms of their ordinary differential or algebraic equations. Components, referred to as types, can be developed by the user or they can be chosen from a library within TRNSYS.

TRNSYS has the capability of interconnecting system components in any desired manner, solving differential equations and facilitating information output, the entire problem of system simulation reduces to a problem of identifying all the components that comprise the particular system and formulating a general mathematical description of each (Kalogirou, 2001).

Following the identification and mathematical description of all components is available; an information flow diagram is constructed for the system. The function of the flow diagram is to facilitate the flow of information between components in the system. Each component requires a series of constant parameters and time dependent inputs which will produce a time dependent output. A given output can be an input for any number of other components (Kalogirou, 2001).

2.4.4.2 Solar Collector Systems

TNSYS has been widely used to simulate both thermal and photovoltaic solar systems. The advantage of TRNSYS is many system configurations can be studied as Ulleberg and Mørner (1997) showed when simulating thirteen variations of a solar-hydrogen system for a low energy domestic dwelling. The system included a PV and solar collector. Kalogirou (2001) simulated a combined PV/T system in TRNSYS and optimised its performance under conditions in Cyprus; the flow diagram for the simulation is presented in Figure 2.43.

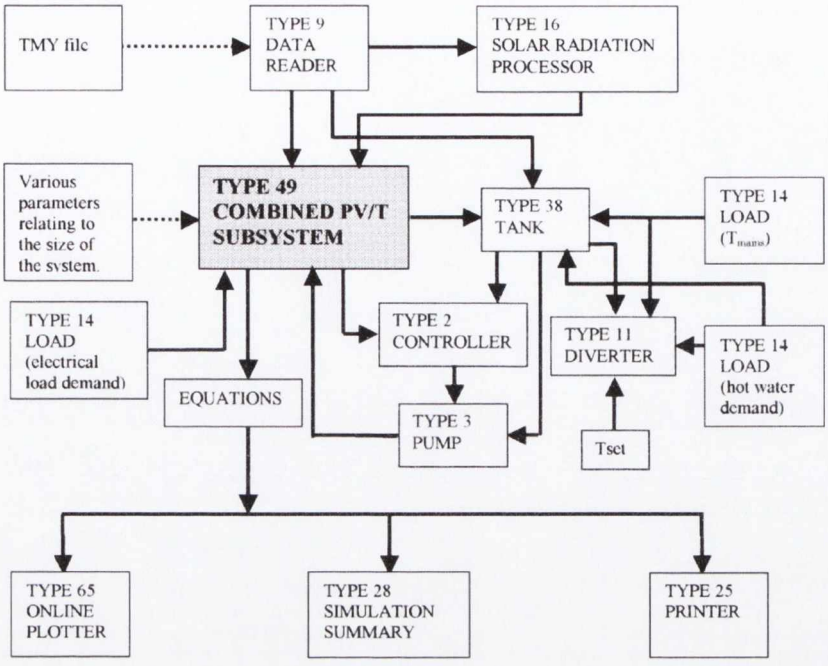

Figure 2.43: TRNSYS flow diagram for a combined PV/T system (Kalogirou, 2001)

The most favourable value of water flow for this system was 25 l/hr. A standard PV system was found to have an average efficiency of 2.8 %, this value increased to 7.7 % for the hybrid system when taking only electricity generation into account. It is worth noting that these results have not been validated by an experimental investigation. An additional investigation looks at the annual performance of a small thermosyphonic type (passive) PV/T solar water heating system 4 m^2aperture area and 160 l storage tank and a large PV/T roof installation of 40 m^2 aperture area with 1500 l water storage located inside the building and a pump for circulation (active) under Nicosia (Cyprus), Athens (Greece) and Madison (US) weather conditions. The results show that the electrical production of the system employing polycrystalline solar cells is more than that employing the amorphous ones, but the thermal contribution is slightly less. A standard PV produces 38 % more electrical energy depending on the location; however, the presented systems contribute a large percentage of hot water needs of the building.

A forced circulation system with flow loop between a PV/T solar collector and a tank was simulated under the environmental conditions of Milan, Rome and Palermo(Italy) using TRNSYS (Aste et al., 2012a). The system includes a PV/T collector, a pump, a differential controller, a tank and an auxiliary heater. For lower values of solar thermal fraction, the heat

required by the auxiliary system is considerable. Subsequently, the total energy savings and payback period were calculated for the system at each location.

A 1.44 kW PV/T hybrid system was simulated in different locations in Taiwan (Huang and Huang, 2013). A TRNSYS type 563 PV/T collector was used in the simulation. It was recommended to locate such a system in Tainan, Taiwan as a system electrical efficiency and a thermal efficiency of 11.7 % - 12.4 % and 26.78 % - 28.41 % respectively was reported. Axaopoulos and Fylladitakis (2013) have added to the development of PV/T systems using TRNSYS simulation software as a PV/T configuration with an auxiliary heating unit was analysed under the environmental conditions of Athens (Greece), Munich (Germany) and Dundee (Scotland) as presented in Table 2.5.

Table 2.5: Annual performance figures of a PV/T system (Axaopoulos and Fylladitakis, 2013)

Location	Athens	Munich	Dundee
Solar irradiation per m^2 (kW h/m^2)	1725.2	1314.1	1065
Thermal load (kW h)	2905.8	3203.8	3389.3
Useful solar heat output per m^2 (kW h/m^2)	304.9	127.6	69.5
Solar thermal system efficiency (%)	17.7	9.7	6.5
Electricity produced (kW h)	940.4	1618	2633.4
Annual yield kW h/kW_p	1390.3	1063.1	916.1
PV conversion efficiency (%)	9.6	9.6	10.2

It is worth noting the PV system yield is the electrical energy generated divided by the installed power. This value indicates the energy generated with respect to the system size. Although, Athens had the highest yield due to the high solar radiation and small installed power, Dundee had the lowest annual yield but it generates more energy per annum compared to the other two systems because of the large surface area of PV panels. An investigation was undertaken to compare two solar roof systems, the first system consisted of a thermal collector and PV panel separately and the second system consisted of PV/T collector and PV panels (Dupeyrat et al., 2014). It was found that the integration of the two systems to create a PV/T system allowed for higher total PV and exergy output and increased primary energy saving. The increase in

electrical output for equivalent roof area for the combination PV/T and PV system is approximately 12.7 % in Paris, 12.6 % in Lyon and 10.7 % in Nice.

There have been a vast number of studies applying TRNSYS to solar collector systems although it is important that the simulation is validated using experimental results to further verify reliability.

2.4.4.3 Modelling Phase Change Materials in TRNSYS

TRNSYS has been used to model PCM in a variety of systems. For the majority of studies a component or Type which simulates PCM behaviour has been combined with a building model component. A numerical simulation of a solar wall made of PCM based on a finite difference model calculated the annual energy falling on the solar wall and the amount of which is transferred to air for ventilation (Stritih and Novak, 1996). The solar wall was found to be 45 % efficient and the model was validated using experimental results.

Components can be developed in TRNSYS for specific applications. Schranzhofer (2006) developed Type 240 capable of treating microencapsulated PCM-slurries as storage medium. The storage volume is divided up into N horizontal segments or nodes; each node is characterised by the enthalpy and mass of the storage fluid in the node. The energy balance equation for each storage node leads to the time evolution of the enthalpy and via an enthalpy/ temperature relationship to the temperature of the given node, the schematic of Type 240 is shown in Figure 2.44.

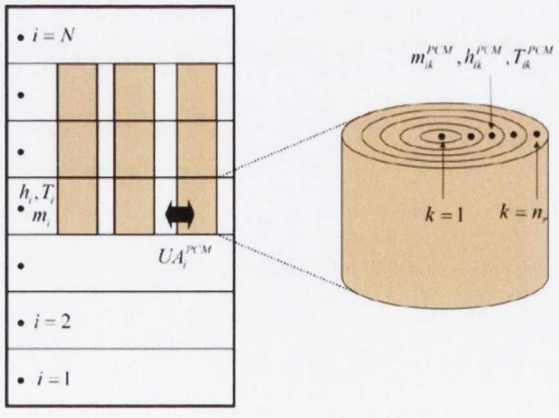

Figure 2.44: Representation of Type 240 developed by Schranzhofer (2006)

The component was validated based on an experiment with water and a PCM slurry storage tank and again with PCM modules in a cylindrical tank. A component based on a PCM was also developed, Type 241, however it has not been validated (Schranzhofer, 2006).

Bony and Citherlet (2007) developed an existing component, Type 60, for stratified fluid tanks based on sensible storage to take into account the PCM calculation. The calculation of heat transfer through the PCM uses the enthalpy method similar to Schranzhofer (2006) where for a given node of specific volume and material, a continuous and reversible function can be calculated which will return the temperature depending on the calculated enthalpy. The model takes into account hysteresis, a delay in the change of phase, and sub cooling, when crystallisation begins at a temperature lower than the solidification temperature. The simulation was compared to experimental results; phase change was complete after 8 hours in the simulation and 3.5 hours for the measurements. A convective heat transfer coefficient was added to the model and the results were in good agreement with the experiment.

Ibáñez et al. (2005) present a study on the approach to simulation of PCMs in building applications using TRNSYS. The idea is to develop a model which evaluated the influence of walls/ ceilings/ floor with PCM in the whole energy balance of the building and not to develop a strict model of the wall to explain its thermal behaviour. Type 56, a multi-zoned building, can be controlled using active wall temperature functions. The simulation was validated based on a small scale experiment. The environmental temperature under which the testing was carried out was 25 °C and 30 °C. The required storage capacity of the panels for the maximum temperature to be reduced enough to be measured is around 15,000 kJ/m^{-3} and 37,500 kJ/m^{-3}. It is recommended a phase change temperature between 25 °C and 27.5 °C; with these considerations an average ambient temperature decrease of up to 3 °C is expected.

A new TRNSYS type was developed and validated for the simulation of external building walls containing PCM (Kuznik et al., 2010). The new type, Type 260, was linked to the multi-zone building, Type 56, to demonstrate its implementation. Type 260 uses the effective heat capacity method to model the heat transfer due to the phase change. The heat capacity method presents additional capacity of the material by the function of temperature during change of phases (Heim, 2005). The model was experimentally validated based on an experiment carried out previously (Kuznik and Virgone, 2009). However, the model was not capable of predicting the phase change in microcapsules.

The effective heat capacity method was used to develop Type 272, a heat transfer model, which was combined with Type 56 and other components to simulate a PCM room, as shown in Figure 2.45 (Lu et al., 2014). It is claimed this is simplified simulation of PCM compared to Type 260 as the PCM's heat capacity as a function of temperature is divided into step functions.

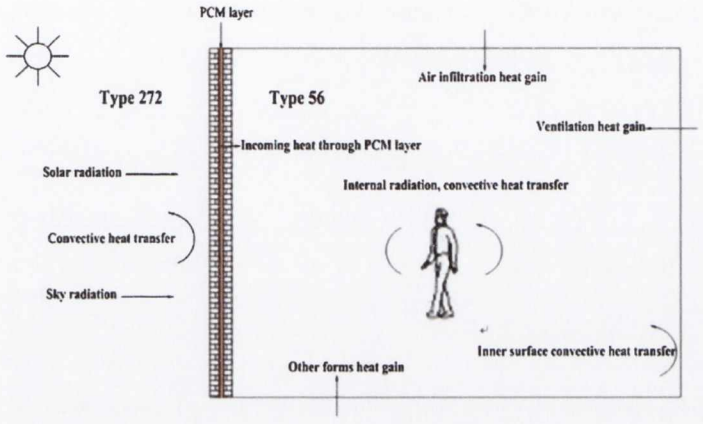

Figure 2.45: Phase change room combining Type 272 with Type 56

The model has been validated under two different conditions, active and passive cool storage, the mean relative error was less than 3 % and 7.59 %, the consistent match degree is between 90.10 % and 98.81 %. Limitations of this model are similar to those previously mentioned, as it does not support a situation that needs to consider internal convective heat transfer of the liquid state PCM, PCM with multiple peaks and troughs and micro heat transfer such as microencapsulated PCM.

TRNSYS was used in conjunction with ANSYS FLUENT, a CFD analysis tool, to evaluate the performance of PCM heat exchangers in an airport terminal building displacement conditioning system (Gowreesunker et al., 2013). TRNSYS controls the weather data, heat gains and ventilation supply air temperature and FLUENT simulates a 2-D transient model of the airport and the PCM- heat exchanger. TRNSYS has also be coupled with Matlab, where TRNSYS simulated a retrofitted domestic dwelling and Matlab was used to simulate the PCM/air system model (Borderon et al., 2015).

A refrigeration system incorporating phase change material for mobile transport, Type 300, was developed in FORTRAN and linked to TRNSYS (Liu et al., 2014). The model has been validated with experimental results (Liu et al., 2011). The system modelled is capable of

predicting temperature in the refrigerated space for various climatic datasets, phase change materials and take account of infiltration through the door opening. The results show that in order to maintain a temperature of the space temperature at -18 °C a total of 250 kg and 3902 kg of PCM are required for no door openings and 20 door openings respectively.

The majority of systems modelled have included solar water heating systems with integrated PCM and the incorporation of PCM in walls and ceilings of buildings. Little has been done with regards to PCM and its application in PV and thermal solar systems in TRNSYS. However, Lin et al. (2014) has presented a PV/T/PCM system modelled in Matlab but linked in TRNSYS, where the PV/T collector is installed on the roof and PCM positioned directly behind it between the ceiling and roof tiling, as in Figure 2.46. The PCM was installed to act as insulation for the ceiling as well as storage of low grade heat from the PV/T collectors. The PCM was modelled based on the enthalpy of the PCM as a function of the temperature. The model was validated using data collected from a laboratory experimental air-conditioning test rig.

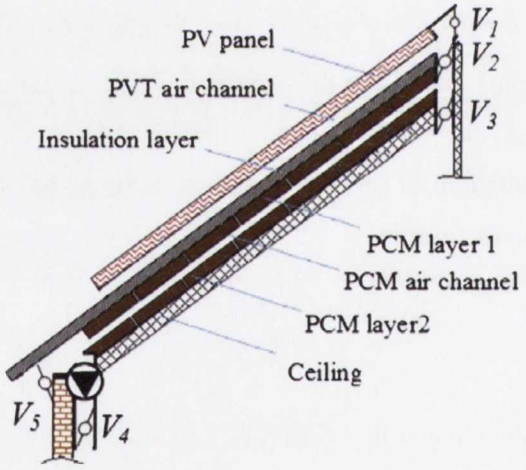

Figure 2.46: PCM enhanced ceiling ventilation system with PVT collectors (Lin et al., 2014)

In winter conditions in Sydney Australia, it was found the PCM layers by ventilation with PV/T system varied between 17.3 % and 62.3 % whilst the PCM storage remained at 0 % using natural ventilation without PV/T collectors. This indicates the PCM increased the thermal mass of the ceiling rather than storing the thermal energy through phase change due to a lower ambient than PCM melting temperature. In summer, the system can improve day time thermal comfort through night time sky radiative cooling.

However, there are constraints when modelling PCM in TRNSYS as described before it is not possible to consider internal convective heat transfer of the liquid state PCM or the phase change inside a microencapsulated PCM. These limitations would reduce the versatility of the model and the investigation of different PCM in a system. The literature presented has developed the heat transfer of PCM with varied success.

2.5 Conclusion

Up to now PCM has been shown to maintain and regulate the temperature of PV for an extended period of time as shown in Table 2.6.

Table 2.6: Comparison of PCM as a thermal management technique with other available methods

Thermal management technique	**Cooling PV**	**PV temperature regulation**	**Passive/ active**	**Thermal storage**	**Heat availability**
Natural air/ water convection	✓		Passive		
Forced air/ water convection	✓		Active		
Heat sink/ spreader	✓		Passive		
Fins	✓		Passive		
Water circulation (PV/T)	✓	✓	Passive/ active	✓ (sensible)	Immediate
Air circulation (PV/T)	✓	✓	Passive/ active	✓ (sensible)	Immediate
Heat pipe cooling	✓		Passive		
Jet impingement	✓		Active		
PCM	✓	✓	Passive	✓ (latent)	Extended

The advantages of PCM compared to other thermal management techniques for PV with thermal storage lie in the versatility of the choice of melting temperature and the extended

period of time for which the temperature of the PV can be regulated. However to further build on such a system, PCM has the potential to store heat that can be used at a later time during the discharging process unlike PV/T systems where the thermal energy must be used immediately or it will be lost to the surroundings. The current research focuses on the application of PCM as a method of storing heat and shifting the time of availability, advancing further the integration of PCM with PV technologies.

The review of PV and solar collector technologies identified the most efficient methods with which to capture solar radiation. Specific attention was applied to PV/T and thermal solar collector system designs to apply more advanced techniques to the design of a PV/T/PCM system.

The literature presented in this chapter shows the evolution of the application of PCM with regard to PV and thermal collectors. Initially, PCM has been shown to regulate the temperature of PV however, the integration of PCM with PV and the manufacturability of systems need to be explored further to ensure successful adoption of the technology is adopted by the building sector. Research into the application of PCM as a store for excess heat generated by PV and thermal collectors has been presented.

It was recognised by studying the presented literature, a long term evaluation of the systems would assist in assessing the discharging of the PCM in both the experimental and simulated analysis. It was shown that a PV/T system could greatly benefit from the integration of PCM due to the potential to store the heat for an extended period of time and only when the heat is required it is sent to an end application such as that of preheating water or space heating.

Chapter 3

Materials and Experimental Method

Chapter 3. Materials and Experimental Methods

3.1 Introduction

The chapter is divided into two sections; (i) 'Characterisation techniques of phase change material (PCM)' and (ii) 'Experimental design, fabrication and installation'. The first section describes the methods that were applied to investigate the thermophysical properties of a range of PCM. This aspect of material investigation allows for a better understanding of the material and its ability to perform as a thermal energy storage material. The results of the characterisation tests were the basis for choosing the specific PCM to be used in the full-scale experiments which are in the second section 'Experimental design, fabrication and installation'. The design of a prototype PV/T system that incorporates a phase change material will be presented in this section along with the fabrication and installation for outdoor testing.

3.2 Characterisation Techniques of Phase Change Material

It is important to determine the thermal and chemical properties of PCM reported by manufacturers by thermophysical characterisation which has been carried out on numerous PCM and summarised in a review paper by Zalba et al. (2003). Thermophysical properties also indicate the level of feasible applications of a material. The main laboratory scale analysis techniques used to study phase change include calorimetry, Differential Scanning Calorimetry (DSC) and Differential Thermal Analysis (DTA) (Zalba et al., 2003) and for larger sample sizes Temperature -History Method (THM) (Yinping et al., 1999).

Although DSC is a standard laboratory method for determining the thermophysical properties of PCM it has limitations with regard to sample size. It accommodates sample sizes in the range of 3-20 mg which is not representative of sizes in practical applications which can be in the range of kilograms, as is the case in this project. For example, DSC does not provide information on whether melting is congruent (whether PCM melts and freezes repeatedly without phase segregation (Sharma et al., 2009)) or incongruent (with phase segregation). In order to determine the properties of PCM with a reasonable sample size THM was introduced (Yinping et al., 1999). THM records the temperature against time of the PCM whilst it is cooling from a temperature at liquid state to lower temperatures at solid state.

For these reasons it was necessary to use both DSC results as a standard measurement method for thermal analysis of materials and THM, a custom built method, as an alternative to DSC for larger sample sizes. The methodology of both characterisation techniques used in this research are presented in Section 3.2.2 and 3.2.3.

3.2.1 Phase Change Material Selection

The properties of the PCM will determine their suitability for integration in a PV/T/PCM system. Ideally the selected PCM properties would include:

- Melting temperature at approximately operating temperature of system, in this case it is 15 °C – 20 °C
- High latent heat of fusion for a given mass of PCM, as latent heat of fusion increases duration of absorbed heat and quantity of energy stored
- Good thermal conductivity for efficient heat transfer through the PCM
- Low or no subcooling, this occurs when the PCM needs to be cooled below it's freezing point to initiate solidification
- Low or no corrosion of the containment material
- Chemical stability ensuring longer life of PCM with minimal material degradation
- No toxicity which assures compatible integration of PCM with buildings and the environment
- No combustibility reduces the risk associated with the PCM particularly with regard to fire safety
- Low cost to achieve economic viability of a PV/T/PCM system

Particular PCM may not possess all the desired characteristics as a result a compromise has to be attained when selecting a PCM. Based on the extensive PCM literature review presented in Section 2.3, it was decided to investigate the following three PCM classes, fatty acids, salt hydrate and paraffin.

Fatty acids are an organic PCM and have many superior properties including high heat capacity, congruent melting, little or no supercooling, non-toxic, good thermal and chemical stability, low cost, non-flammable and small volume change (Feldman et al., 1989; Hasan and Sayigh, 1994; Rozanna et al., 2005). Fatty acids consist of a single type of organic compound that have a high material purity such as capric acid which is commercially available with purity levels of 98 %

(Sigma-Aldrich, 2015). Fatty acids are known to have high melting temperatures which are outside the range of thermal energy storage applications (He et al., 2013). To overcome this, a eutectic mixture of fatty acids is two or more fatty acids combined to form a binary fatty acid with a lower phase change temperature and features the same stability of a single component. The advantage of fatty acid eutectics is the ability to gain a lower melting temperature with all the material advantages of a fatty acid by varying the mass ratio of the mixed fatty acids (He et al., 2013; Yuan et al., 2014b). Capric acid and two fatty acid eutectics, capric:palmitic and capric:lauric acid have been investigated. Capric:palmitic acid is a mixture of 75 % capric and 25 % palmitic by weight and capric:lauric acid is a mixture of 45 % capric and 55 % lauric acid.

Inorganic salt hydrates consist of salt and water which combine in a crystalline matrix when the material solidifies. Different salts are used in combination with water to alter the phase change temperature. As the crystal is heated it melts, releasing the water of crystallisation and allowing the salt to dissolve in the water (Rubiterm, 2015). They are attractive materials for TES due to their high thermal conductivity (Wu and Wang, 2015) and as a result the commercially available salt hydrate SP22 has been investigated as part of the characterisation study for consideration for integration in a PV/T/PCM.

Micronal® is a material designed for temperature regulation applications and its performance has been investigated within buildings (Cabeza et al., 2007). The PCM wax mixture, classified as an organic paraffin, is contained in small vessels (particle diameter 5μm) with the core PCM and a hard covering material. (BASF, 2012).

These PCM were chosen because their melting temperatures are reported to be in the range of 20 °C – 30 °C which is the required temperature range in a PV/T/PCM system. The PCM has the advantage of stabilising the operating temperature as the PCM absorbs latent heat at a constant phase change temperature as explained in Section 2.3.1. If the ambient temperatures are higher than the PCM melting point melting ensues due to the additional heat gain from the environment which may lead to a shorter melt time and period of heat absorption. For this reason the primary reason for choosing these PCM was based on the melt temperature. Further investigation will be carried out on their thermophysical properties and corrosive nature in Chapter 4.

3.2.2 Differential Scanning Calorimetry Methodology

Differential Scanning Calorimetry (DSC) is a thermo analytical technique in which the difference in the amount of heat required to increase the temperature of a sample and a reference are measured as a function of temperature (Höhne et al., 2003). The relationship determined in a DSC test is the enthalpy-temperature relationship h(T), found using a scanning mode consisting of heating and cooling segments which forces the sample to undergo a phase transition where more or less heat will need to flow to it than the reference to maintain both at the same temperature (Klančnik et al., 2010; Cabeza et al., 2015). For example, during melting more heat will flow to the sample to increase its temperature at the same rate as the reference. This is due to the absorption of heat by the sample as it undergoes an endothermic reaction from solid to liquid. Furthermore, when the sample undergoes an exothermic reaction less heat is required to raise the sample temperature (Sarwar, 2013).

There are two types of DSC systems, power compensation DSC and heat-flux DSC. The power compensation DSC has an independent heater for each sample chamber, as in Figure 3.1(a). The temperatures of the sample and reference are controlled individually using identical furnaces. The temperature of the sample and the reference are made identical by compensating the heat flow of the sample furnace (Höhne et al., 2003). The compensating heating power required to maintain identical temperatures is a measure of the enthalpy or heat capacity change in the sample compared to the reference (Czichos et al., 2006).

In heat flux DSC, the sample and reference are enclosed in a single furnace as illustrated in Figure 3.1(b). Under a heating/cooling process, the temperature development of the sample is compared with the temperature of the reference and the temperature differential is used to calculate the heat flux. This value is related to the enthalpy change in the sample compared to the reference (Castellón et al., 2008). The method of DSC is one of the more widely used techniques to investigate the characteristics of PCM (Sari et al., 2004; Sarı, 2006; Barreneche et al., 2013; Gil et al., 2013; Jin et al., 2014).

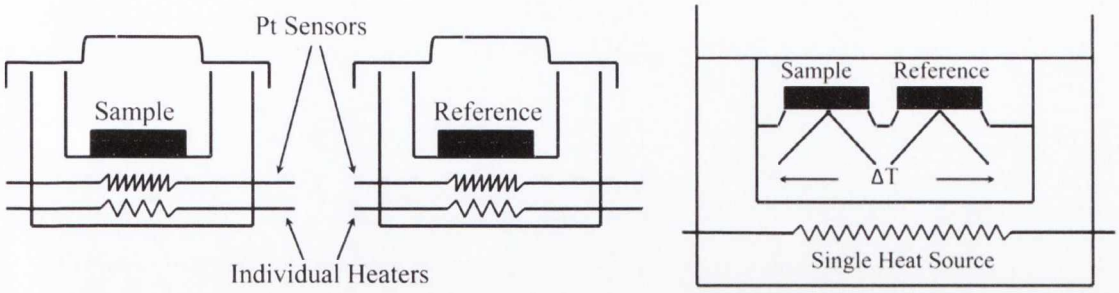

Figure 3.1: Schematic of (a) power compensation DSC (b) Heat-flux DSC (Klančnik et al., 2010)

The procedure of characterising PCM using DSC involved weighing a PCM sample of weight 2 mg to 5 mg along with a reference sample which were placed in separate, self-contained calorimeters. The amount of heat absorbed or released by a sample as it was heated, cooled or held at a constant temperature was measured. The machine was programmed to heat or cool the sample at a rate of 5 °C per minute, as shown in the top left hand corner of the DSC graphs along with the sample mass in Figure 4.1 – Figure 4.5. The DSC was programmed to set the temperature of the sample as follows:

- set the temperature to -10 °C
- hold the sample at -10 °C for one minute
- heat the sample from -10 to 80 °C (at 5 °C per minute)
- hold the sample at 80 °C for one minute
- cool from 80 to -10 °C (at 5 °C per minute)
- hold the sample at -10 °C for one minute
- heat the sample from -10 to 80 °C at (5 °C per minute)

The device used to complete DSC was shown in Figure 3.2. The repeated heating and cooling was to ensure the consistency of the test results.

Figure 3.2: Power compensation DSC (PerkinElmer Diamond machine)

Yinping et al. (1999) identified shortcomings in the DSC method of characterising PCM; including small sample sizes (1-10mg), thermophysical properties of some PCM depends on the quantity used, analysis instrumentation is complex and expensive, and the phase change cannot be visually observed. A round robin characterisation was undertaken involving various partners which required each lab to complete a DSC characterisation on the same PCM sample (from the same bulk material sample) using different types of DSC equipment with a melting temperature of 28.15 °C and enthalpy of 241.65 kg/kJ (COST Action TU0802, 2013). The results found that despite all material samples were coming from the same bulk sample there was high deviation in both enthalpy and melting temperature range, varying within 195 kJ/kg – 265 kJ/kg and 26 °C – 29.5°C, respectively.

3.2.3 Temperature-History Method Methodology

Yinping et al. (1999) proposed the Temperature-History Method (THM) of determining the heat of fusion, specific heat and thermal conductivity of phase change materials. Unlike that of the DSC test, the sample size of the material is much larger, the experimental technique is simpler and the phase change can be visually observed.

The test involves heating test tubes, containing the PCM sample and the reference, in a water bath well above the PCM melting temperature as shown in Figure 3.3. They are removed from the water bath simultaneously and exposed to a temperature below the solidification temperature, generally the ambient temperature. PCM and reference temperatures are recorded

when cooling and the temperature versus time curve of the PCM is obtained (Yinping et al., 1999).

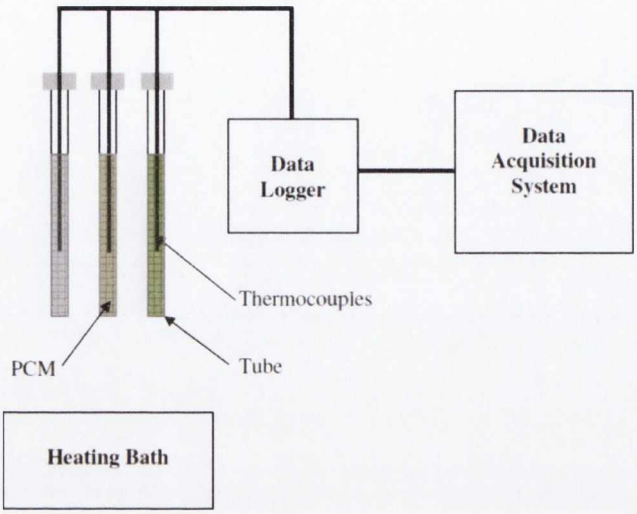

Figure 3.3: Schematic of the THM (Sarwar, 2013)

To characterise the PCM using the Temperature History Method (THM) a 15 cm long test tube with an internal diameter of 1 cm was used. Biot number assesses the 1D heat transfer condition by applying:

$$Bi = \frac{h_{cn}R}{2k}, \tag{3.1}$$

Where r is the radius of the test tube is 1.4 cm, h_{cn} is the natural convection heat transfer coefficient of air outside the tube and k is the thermal conductivity of the PCM. The Biot number of all the selected PCM samples was found to be less than 0.1, thereby satisfying the condition of uniform lumped capacitance method considering the tube to be the lumped system in the temperature below solidification (Incropera and Dewitt, 1985). The curve is used to calculate thermophysical properties of the PCM such as melting temperature, heat of fusion and heat capacity (Solé et al., 2013). The experimental set-up is shown in Figure 3.4.

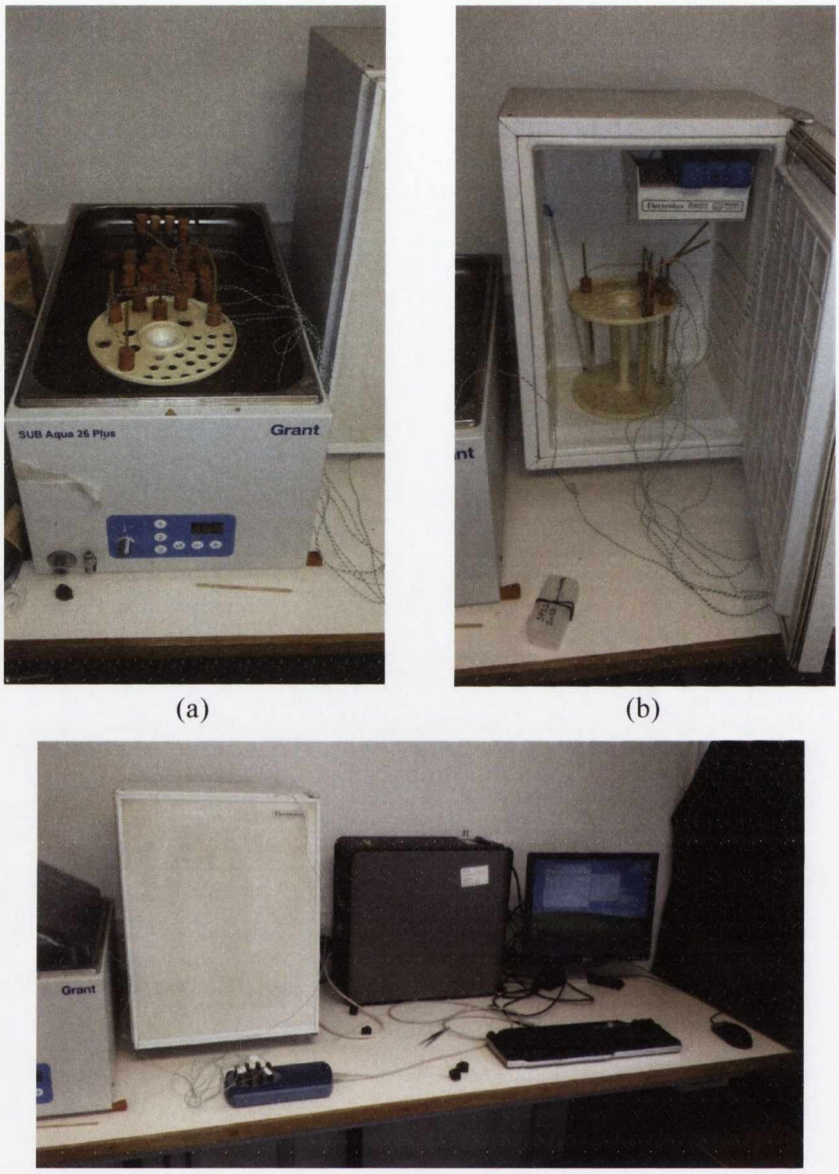

(a) (b)

(c)

Figure 3.4: THM experimental set-up (a) melting PCM in a water bath for three hours (b) cooling PCM in the fridge (c) Data logger and recording equipment

A sample of each PCM was placed in a test tube and heated for approximately three hours in a water bath at 40 °C to ensure all samples were completely melted. All samples were tested using THM simultaneously as the melting temperatures of the samples were reported to be within ± 10 °C of each other. As the PCM phase change temperature ranges were relatively close to ambient temperature, a fridge had to be used to ensure PCM temperatures were below the solidification temperature of each material. The heating tubes were then removed from the hot water bath and placed in the fridge to monitor the rate at which the temperature of the PCM

decreases. Thermocouples remained upright and centred in the test tube with the use of bamboo sticks.

The process used to determine the melting point, heat of fusion and specific heat capacities of PCM are based on a method presented by Yinping et al. (1999). The method allows the calculation of the thermophysical properties of the studied substance (PCM) from the known properties of the reference substance (water) by using the areas under the cooling curves (see Figure 3.5) generated by the THM and applying the results of the test to Equations 3.2 – 3.5 below:

$$C_{p,s} = \frac{m_w\ C_{p,w} + m_p C_{p,t}}{m_p} \cdot \frac{A_3}{A'_2} - \frac{m_t}{m_p} C_{p,t} \tag{3.2}$$

$$C_{p,l} = \frac{m_w\ C_{p,w} + m_p C_{p,t}}{m_p} \cdot \frac{A_1}{A'_1} - \frac{m_t}{m_p} C_{p,t} \tag{3.3}$$

$$H_m = \frac{m_w\ C_{p,w} + m_p C_{p,t}}{m_t} \cdot \frac{A_2}{A'_1} (T_0 - T_s) \text{ (with supercooling)} \tag{3.4}$$

$$H_m = \frac{m_w\ C_{p,w} + m_p C_{p,t}}{m_t} \cdot \frac{A_2}{A'_1} (T_0 - T_{m,1}) - \frac{m_t\ C_{p,t} (T_{m,1} - T_{m,2})}{m_p} \tag{3.5}$$

(without supercooling)

Where,

H_m = Heat of fusion of PCM (kJ/kg)

m_w = Mass of water (kg)

m_p = Mass of PCM (kg)

m_t = Mass of tube (kg)

$C_{p,w}$ = Mean specific heat of water (kJ/kg.K)

$C_{p,t}$ = Mean specific heat of tube (kJ/kg.K)

$C_{p,l}$ = Mean specific heat of liquid PCM (kJ/kg.K)

$C_{p,s}$ = Mean specific heat of solid PCM (kJ/kg.K)

A = Area under curve as indicated by Figure 3.5

T_m = Melting temperature of PCM (°C)

T_s = Solidification temperature of PCM (°C)

T_r =Reference temperature (°C)

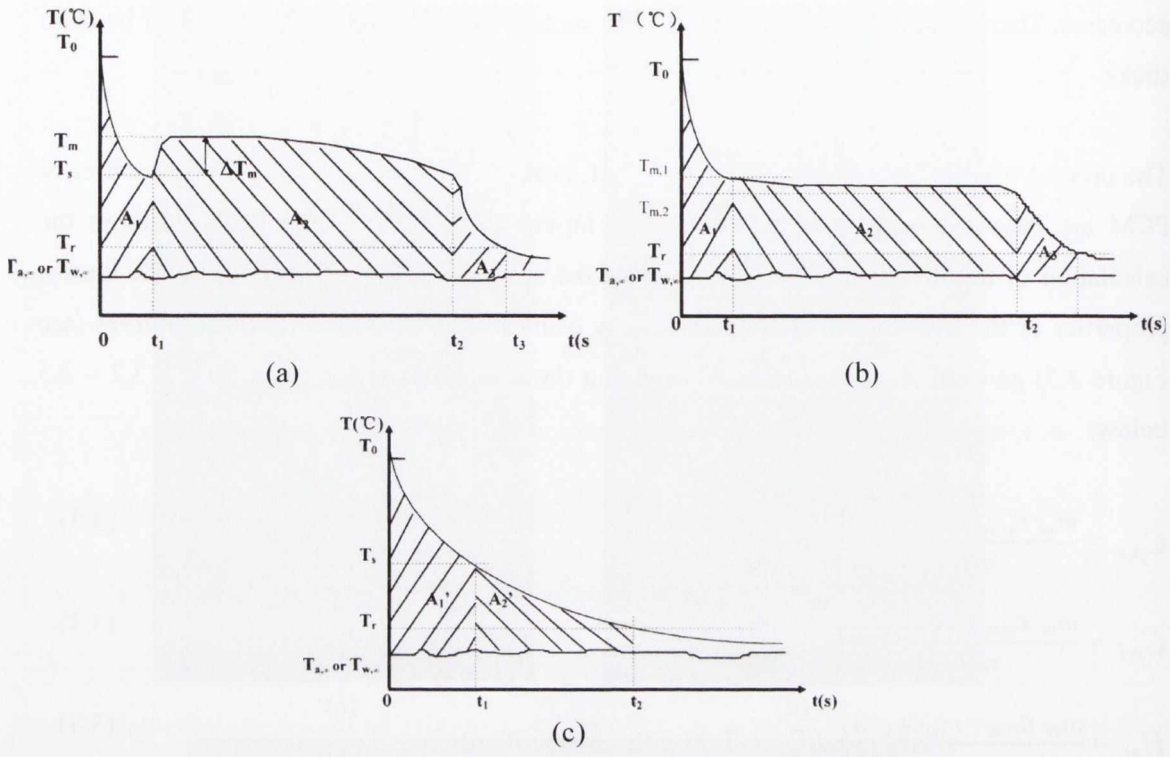

Figure 3.5: T-history curve of (a) PCM with subcooling (b) PCM without subcooling (c) water during cooling process (Yinping et al., 1999)

It is recommended to calculate the end of phase change point by using the point of inflection of the gradient of the cooling curve as this is the boundary between the phase change and solid state periods where the first derivative of the T-history curve becomes minimum (Hong et al., 2004). Using the Equations 3.2 – 3.5, the specific heat capacity of each of the PCM in solid and liquid phases and heat of fusion are calculated and presented in the following sections.

This method assumes a level of supercooling at the end of the latent heat period and neglects sensible heating during phase change which can cause errors when calculating the thermophysical properties (Hong et al., 2004). A modified THM was presented which defines the end of melting as the lowest point of the first derivative of the T-history curve. The improved method also takes into account the heat transfer area of the tube contacting with the PCM. This varies during the process of solidification when the volume of PCM changes when changing phase as a result the mean value for areas before and after phase change is applied in the modified method (Hong et al., 2004). THM is suited to materials with a clear phase transition zone, such as a eutectic, however for materials which are not pure it is recommended to use the enthalpy – time relationship rather than the concept of variation of temperature with

time (Marín et al., 2003). THM has been used to determine the thermophysical properties of organic and inorganic PCM (Peck et al., 2006; Stanković and Kyriacou, 2013; Hasan et al., 2014b).

3.2.4 Immersion Corrosion Investigation Methodology

The methodology used in this study was based on the Standard Practice, Cleaning, and Evaluating Corrosion Test Specimens (ASTM G1-01) and has been applied to corrosion investigations of PCM and metals (Cabeza et al., 2001a; Cabeza et al., 2001b; Cabeza et al., 2005; Moreno et al., 2014). The process was divided into four steps:

1. Preparation of the sample

   The preparations of the samples required cutting them from larger pieces of materials to approximately 1 cm x 1 cm x 0.2 cm. The samples were then cleaned with acetone to remove any impurities from the material surface. Prior to the experiment the samples were weighed using a weighing scales (Kern scales accuracy of ±0.01g) and the values were recorded.

2. Corrosion test of metal and plastic materials

   Following sample preparation, each material sample was placed in a test tube and immersed in PCM. The samples were completely covered in PCM and the test tube was sealed to avoid ingress of moisture and water from the water bath. There was no attempt made to avoid contact with oxygen in the air so as to match as closely as possible the expected on-site conditions within a thermal storage unit. The test tubes were then placed in a water bath at a constant temperature of 45 °C to ensure all PCMs remained in a liquid phase and was not stirred.

3. Sample weighing

   The samples were then cleaned with acetone to remove any impurities from the material surface. Each material sample was removed from the PCM every 7 days, cleaned with tap water to remove any excess PCM and then weighed using a Kerns PCB to the nearest 0.01g. This process was repeated every 7 days for 722 days in total. In addition to this the samples were visually evaluated for bubbles, precipitates, surface changes and pitting.

4. Corrosion assessment

The evaluation of the corrosion results involved completing a gravimetric analysis which consisted of the mass loss of the sample with respect to the initial mass as in Eq. (3.6).

$$\Delta m = m_{t_0} - m_t \tag{3.6}$$

The corrosion rate (mg/cm^2 year) of the samples was then determined by taking into account the mass loss (Δm), the area of the material (A) and the experimental time (t_0 - t) and applying them in Eq. (3.7).

$$\mathrm{CR} = \frac{\Delta m}{A \cdot (t_0 - t)} \tag{3.7}$$

Another method to calculate corrosion loss on an hourly basis determined by the American Society for Testing Materials (ASTM, 1994) has been applied (Farrell et al., 2006). However, as the presented investigation is conducted over a period of time beyond a year, Equation 3.7 is used to calculate the corrosion rate.

Recommendations were made based on the results of the corrosion tests and suggested which materials are most compatible as a containment method for specific PCM. The corrosion weight loss guide used in industry practice was used as a reference, in Table 3.1.

Table 3.1: Guide for corrosion weight loss used in the industry

mg/cm^2 yr	mm/yr	Recommendation
>1000	2	Completely destroyed within days
100 to 999	0.1 - 1.99	Not recommended for service greater than one month
50 to 99	0.1 - 0.19	Not recommended for service greater than one year
10 to 49	0.02 - 0.09	Caution recommended, depending on the specific application
0.3 to 9.9	-	Recommended for long term service
<0.2	-	Recommended for long term service; no corrosion, other than as a result of surface cleaning was evidenced

3.2.5 Scanning Electron Microscope (SEM)

SEM is a scanning electron microscope that produces images by scanning it with a focused beam of electrons. The electrons interact with atoms in the sample material, producing various signals that can be detected and that contain information about the sample's surface topography. To ensure the samples were fully visually examined a Tescan MIRA scanning electron microscope (SEM) was used to take images on Day 1, Day 35, Day 200 and Day 500. SEM allowed for images to be taken at magnifications of 200X, 3000X and 6000X which allowed for the inspection of initial signs of corrosion not visible to the naked eye.

Sample preparation involved removing the material from the test tubes filled with PCM and removing all remnants of the PCM, using a dry cloth. Once the PCM had been removed the sample was blasted with a high velocity air gun to remove all dust particles. The sample was then positioned onto the imaging platform in the SEM.

3.3 Experimental Design, Fabrication and Installation of a PV/T/PCM System

As shown in Figure 3.6, the full scale experiment comprises of four systems. The aim of these experiments is to analyse the thermal behaviour of a PV/T/PCM system in concomitant comparison with that of three reference systems. A stepped approach was taken when designing the experiment, starting from the reference, System 1 (PV panel only), and building on System 1 to produce System 2 with an added heat sink (PV with container) to building on this to produce System 3 which included a PV with a integrated pipe network (PV/T system) and finally System 4 which included all previous components along with PCM energy storage (PV/T/PCM system). The systems are illustrated in Figure 3.6(a). System 1 is a PV panel only and System 2 builds on this with an attached container referred to act as a heat sink. System 3 and System 4 have their PV panel removed to differentiate between each system for illustration purposes. System 3 includes a pipe network within an empty container (air filled) and a tank and System 4 includes the pipe network within a PCM filled container.

The idea of the experimental setup was to assess the PCM as a heat store and its ability to heat water. The stepped approach allows for clear comparisons between the PV/T/PCM system and the reference collector devices.

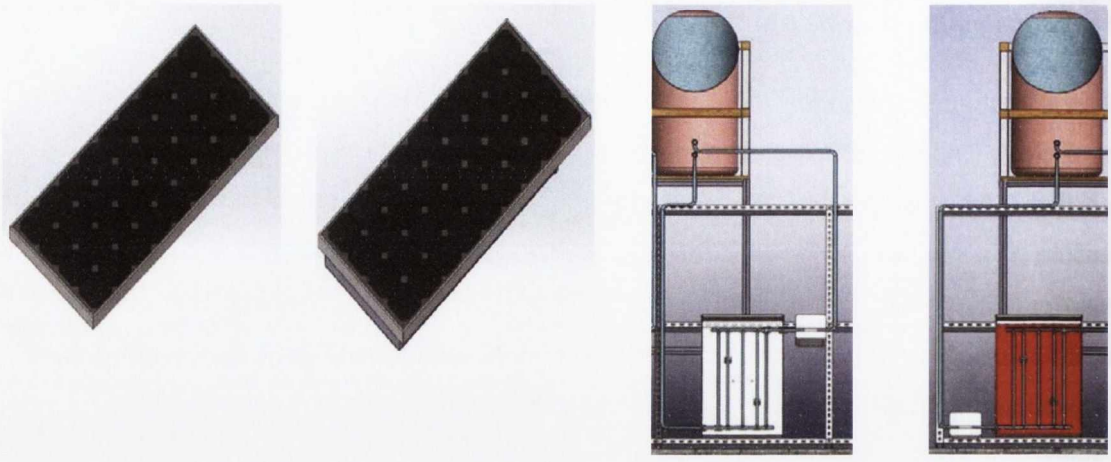

System 1 System 2 System 3 System 4

(a)

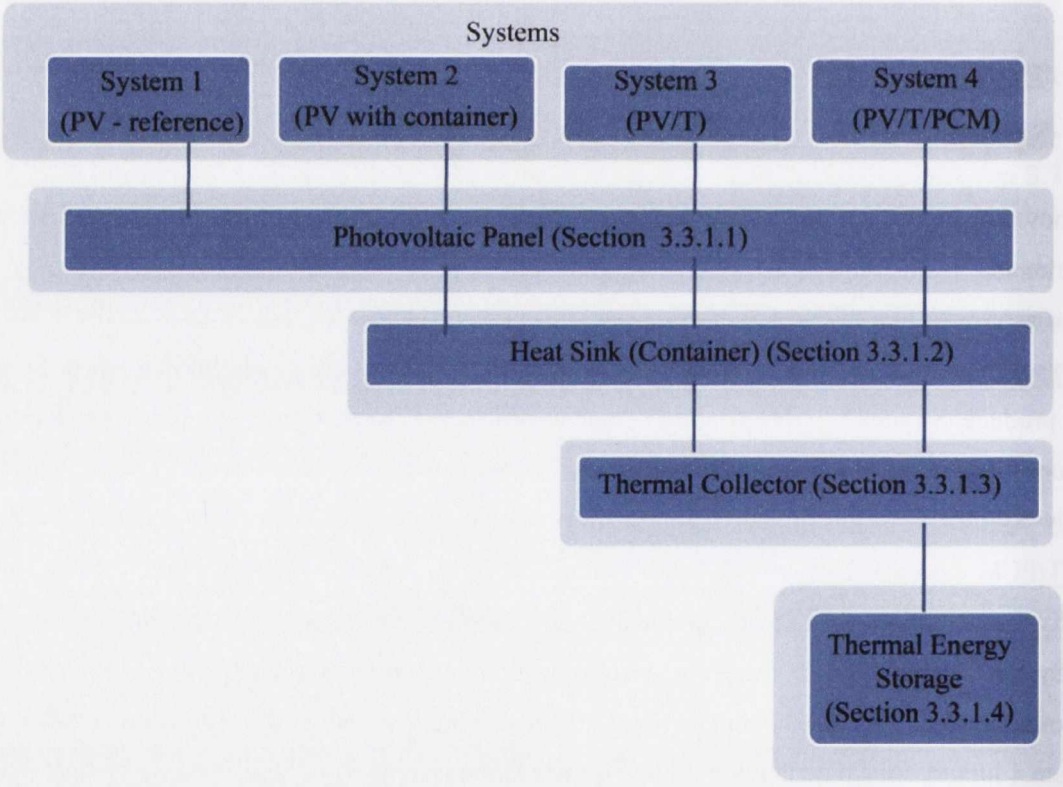

(b)

Figure 3.6: (a) Schematic of each system (b) experimental set-up of all systems

It must be noted that there is no heat load draw-off by the user in the experimental investigation as the water flows, in a closed circuit, from the direct tank to the collector and returning to the tank. The daily draw-off occurs in the morning when each tank is emptied and refilled to ensure both the temperature in both tanks is the same. Each panel can be referred to as a collector device as the incoming heat flux is being stored within the collector. However, each collector device will be referred to as a system in the remainder of the thesis to clearly identify each device.

In addition to an explanation of the components within the systems in following sections, as referenced in Figure 3.6, the data acquisition equipment is also presented.

3.3.1 Photovoltaic Panel – System 1

80 W Solar Technology International monocrystalline silicon PV panels of area 0.648 m^2 were used in the experiment (Solar Technology International, 2013) as shown in Figure 3.7. The module, whose specifications are shown in Table 3.2 with all technical data acquired at standard test conditions of AM 1.5, 1000 W/m^2 and ambient conditions of 25 °C, is composed of 36 monocrystalline solar cells connected in series.

Table 3.2: PV panel specifications (Solar Technology International, 2013)

Model type	STP080
Rated max power (P_{max})	80W
Current at P_{max} (I_{mp})	4.58A
Voltage at P_{max} (V_{mp})	17.5V
Short-circuit curent (I_{sc})	5.04A
Open-circuit voltage (V_{oc})	21.5V
Normal operating cell temperature	50 °C

The module consists of tempered white glass, EVA plastic and a weather protection film. Each panel was characterised using an ISM 490 Solar Module Analyser (Iso-Tech, 2009) which measured the voltage and power output over a specified current range.

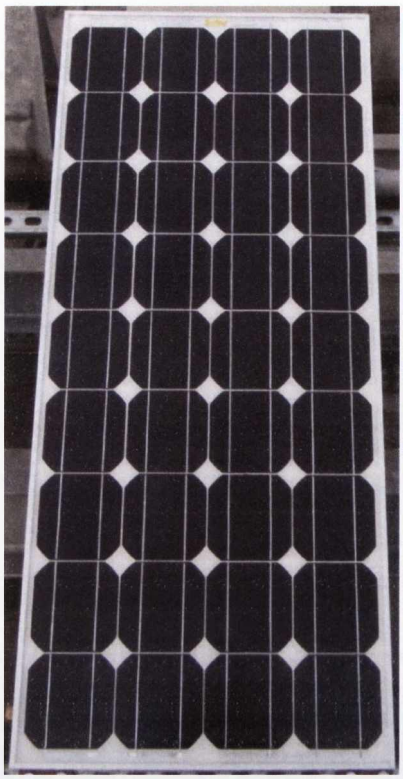

Figure 3.7: Solar Technology PV panel used in the experiment

The PV panel in the particular systems were originally connected to an electrical storage system as in Figure 3.8. A Solar Technology International solar charge controller connected the PV, a 12V battery and an electrical load. The charge controller regulates the current and voltage from the PV into the battery to ensure it is not over-charged at any point. If the battery is full, the solar controller switches the electricity generated to the resistor load which dissipates the energy as heat. The PV were connected originally to batteries and then to resistors to dissipate the power. It was found that the power generated by the PV was not sufficient to warrant connecting them to the grid due to administrative issues with grid connection at the installation site.

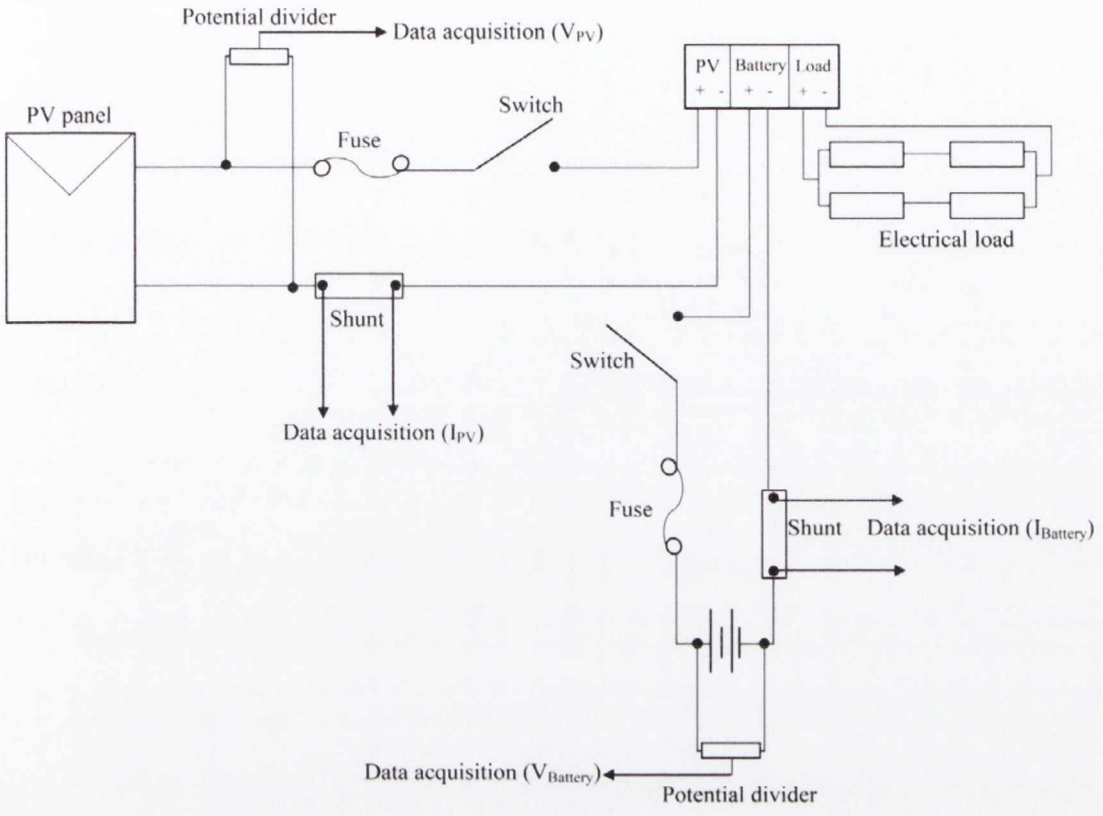

Figure 3.8: Schematic of solar electrical circuit

The electrical loads connected to the solar charge controller are wire wound electrical resistors from ARCOL (ARCOL, 2011). The model HS100 had a resistance of 4.7Ω and an associated rating of 100 W when the resistors were mounted to a heat sink, if this is not the case a maximum of 50 W power dissipation is to be assumed. The resistors were connected as two in parallel and two in series, as shown in the circuit diagram in Figure 3.9 to ensure that the maximum power consumed in each resistor does not exceed the 50 W limit.

$$R_s = 4.7\Omega + 4.7\Omega = 9.4\Omega \tag{3.8}$$

$$\frac{1}{R_{Tot}} = \frac{1}{9.4\Omega} + \frac{1}{9.4\Omega} = \frac{1}{4.7} \tag{3.9}$$

$$R_{Tot} = 4.7\Omega \tag{3.10}$$

Considering the case of the maximum voltage to the batteries (17.5V), the total drained current is:

$$I_T = \frac{17.5V}{4.7\Omega} = 3.72A \tag{3.11}$$

By, Ohms law the current passing through each branch will be 1.86A, where each 4.7Ω will consume a power of:

$$P = (1.86A * 4.7\Omega) * 1.86A = 16.26W \tag{3.12}$$

The 4 resistors will consume a power of 65 W when the voltage drawn off is at 17.5 V, although this is lower than the maximum rated power of the panel the inclusion of losses through the electrical wire had to be allowed for and taken into account.

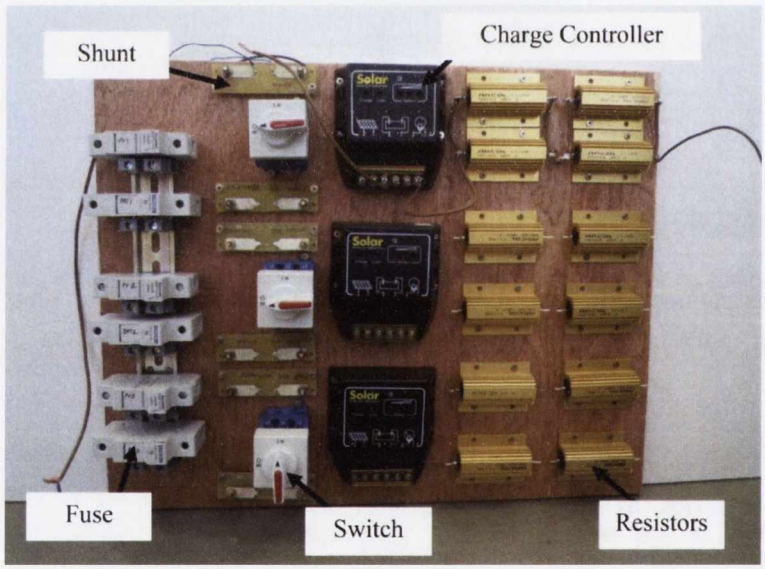

Figure 3.9: Photograph of elements of the solar electrical circuit

Dry cell 12Ah batteries, 12 V, from Yuasa (Yuasa, 2015), were connected to the solar charge controller. The current of the PV and battery in each system was measured using a 20A/60mV shunt. Prior to component implementation all elements of the circuit were characterised. For safety reasons a mechanical switch and 8 A fuses were installed in the circuit.

Following the initial experimental runs, it was noted that failures in the electrical system had occurred. The charge controllers were causing the current and the voltage of the PV to behave

erratically due the restriction of the current as a result of the maximum allowable current. As a result of these, the solar charge controller was removed from the circuit and the PV was connected directly to the resistors, through which the electrical power would be dissipated as heat, the reassembled circuit is shown in Figure 3.10.

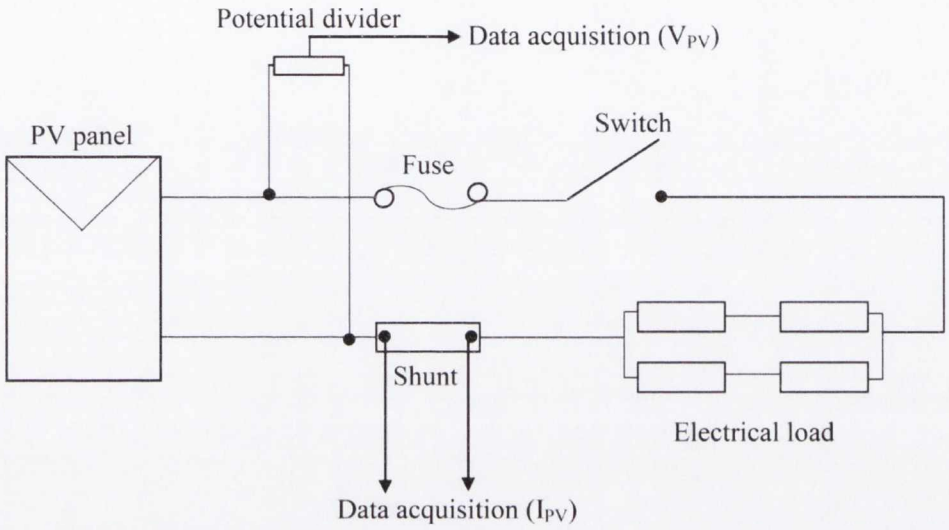

Figure 3.10: Schematic of final electrical load circuit connected to PV

The PV circuit without the charge controllers comprised of the same resistors, shunts, and switch as before and was designed to maintain a resistance of 4.65 Ω as shown. However, the resistances of the systems altered due to the variation in soldering of the wires connecting the shunts, fuse and resistors. The resistance varied from 4.65 Ω for two of the four systems as shown in Figure 3.11. System 3(PV/T) and System 4 (PV/T/PCM) have shown to have resistances of 4.65 Ω, however System 1 (PV panel) and System 2 (PV with container) have resistances of 5.0 Ω and 4.20 Ω, respectively.

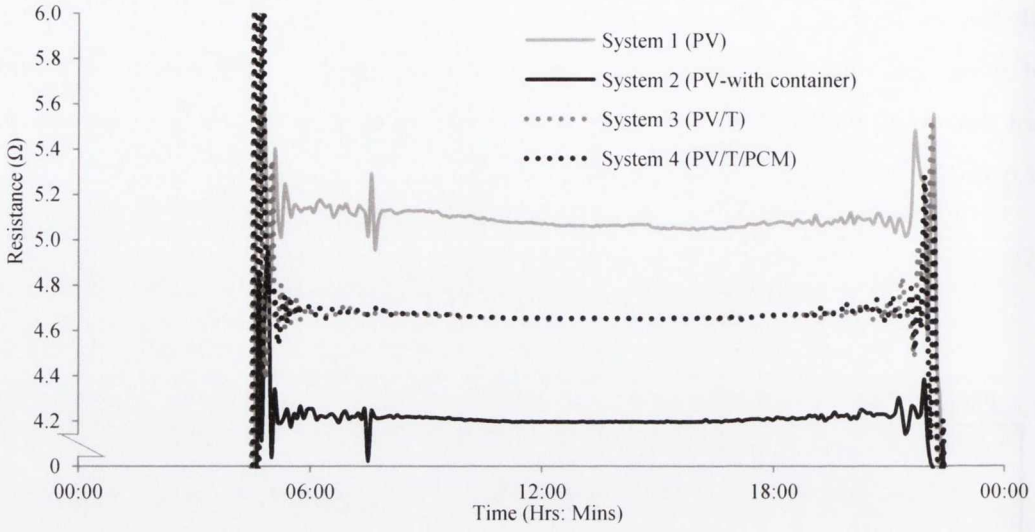

Figure 3.11: Resistances of each PV circuit

The variation in resistances was taken into account when analysing the results of the field data tests.

3.3.2 Heat Sink (Container) – System 2

System 2 is a PV with an added container which acts as a heat sink. In Systems 3 and 4, the container acts as a housing unit to the thermal energy generation system. However in System 2 (a reference system) the container acts purely as a heat sink and allows for meaningful comparisons and assessments to be made between the different thermal energy units.

The heat exchanger is housed in a stainless steel container. The containers were custom made from 2 mm (grade 316) stainless steel as presented in Figure 3.12. This material was chosen as it does not readily corrode or stain which was a very important consideration in the temperate maritime climate of Ireland. It has a thermal conductivity of 19 W/m^2. The container is welded on all sides.

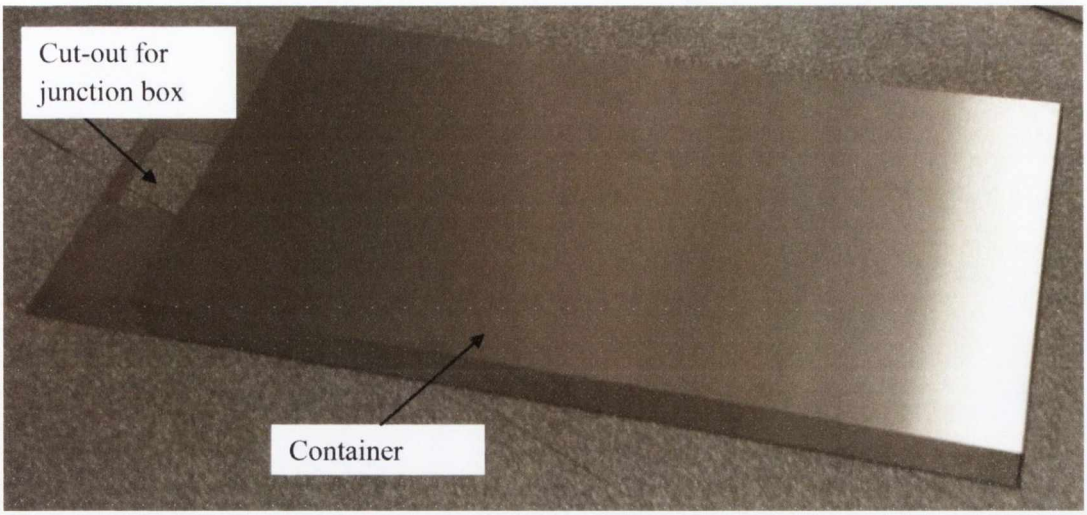

Figure 3.12: A sealed stainless steel heat sink i.e. container

The dimensions of the container are shown in Figure 3.13. The rectangular cut-out is to facilitate the PV junction box as the container will sit behind the PV panel and house the heat exchanger. The excess stainless steel acts as a secondary absorber.

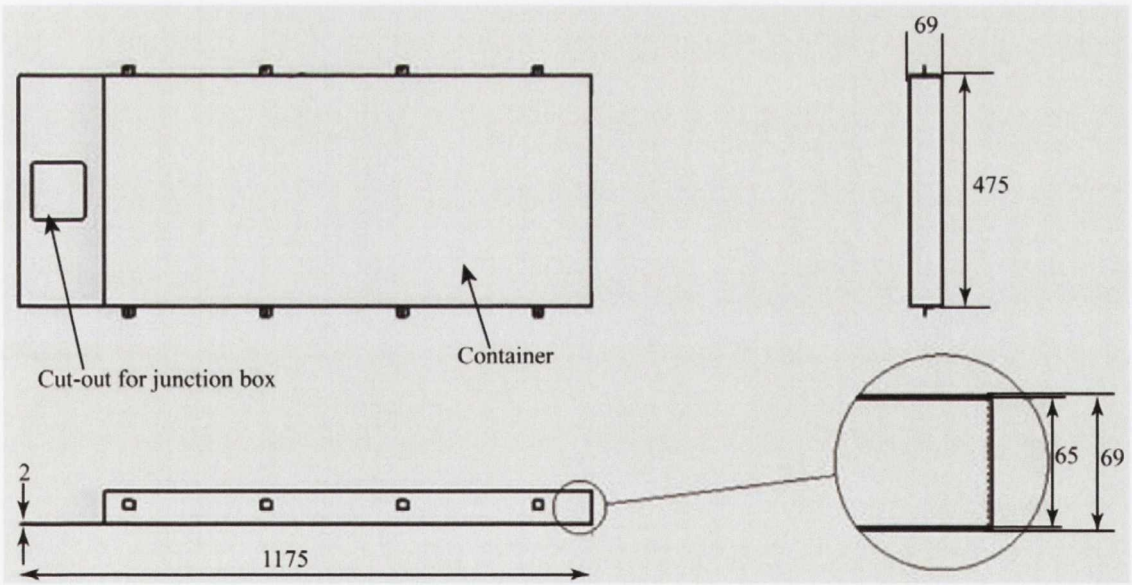

Figure 3.13: Dimensions of the stainless steel container, back view, and two side views in mm

3.3.3 Thermal Collector – System 3

System 3 builds on System 2 as the container is now used to encase the pipe network; together the pipe network and container are referred to as the thermal collector. The purpose of the thermal energy generation factor is to supply heated water to the system. The experiment uses water as the heat transfer fluid for the thermal part of the solar energy system. An insulated direct tank which stores the water supply is elevated above the thermal system to increase the gravitational water flow through the system. A pump is not used as this requires a power input that would have to come from the PV thereby negating the electrical energy generated by the system. The tank dimensions are 0.45 m (diameter) and 1.05 m (height) which give a capacity of 140 Litres of water. As it is a direct supply tank the water flows from the tank to the heat exchanger and then returns back to the tank.

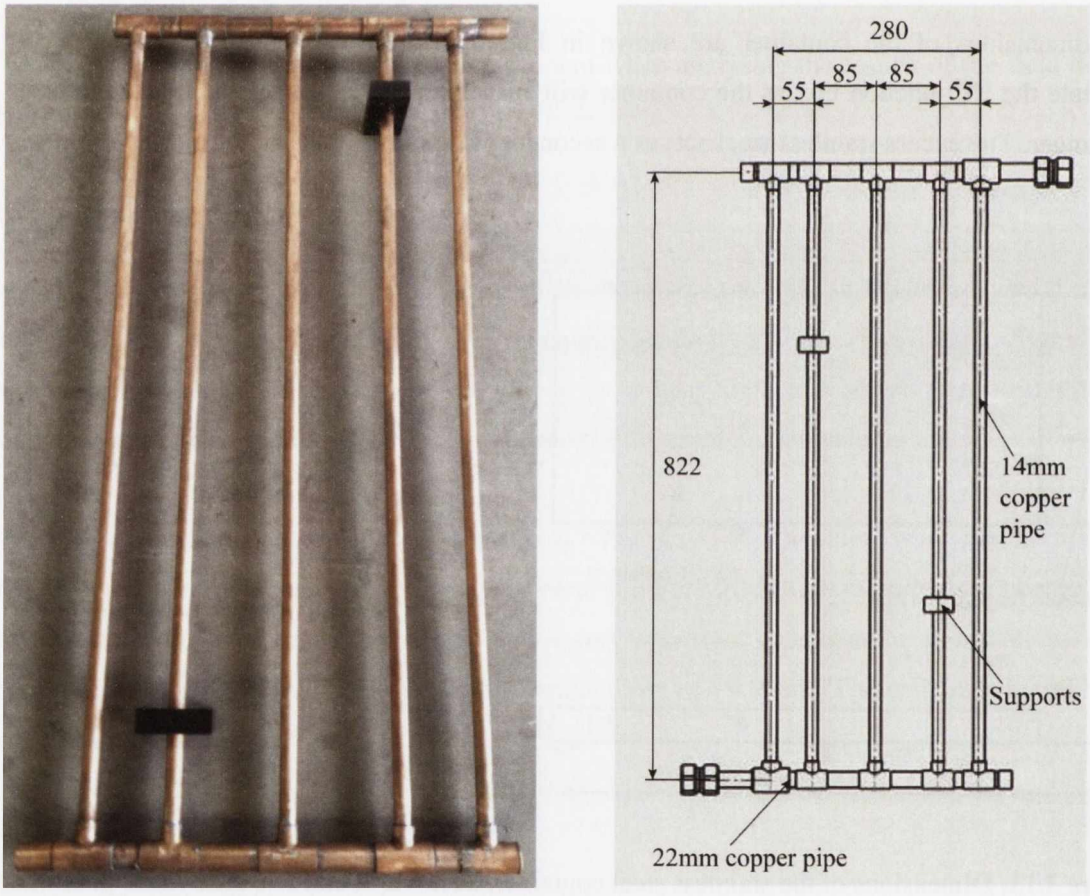

(a) (b)

Figure 3.14: (a) Photograph of heat exchanger (b) schematic of heat exchanger with dimensions

A copper piping of length 3.5 m connects the tank to the heat exchanger and a further 2.5 m of piping attaches the heat exchanger to the tank. The pipe is 22 mm in diameter and is covered

with cellulose thermal insulation to minimise heat loss to the environment. A series of water pipe on/off valves are used to allow for convenient emptying of the water tank. The water tank was emptied daily to ensure all systems had a relatively similar inlet water temperature for comparisons to be carried out. During winter a glycol was mixed with the water to produce a water: glycol mixture (ratio 85:15 volume) to minimise the risk of water freezing and damaged pipes.

The heat exchanger, as shown in Figure 3.14(a) and (b), has two header pipes which have an aperture of 22 mm, larger than that of the five vertical pipes connecting them which have an aperture of 14 mm. The water enters from the tank to the lower header and travels up the risers, collecting heat from the solar collector and then exits out through the top header and returns to the tank. The heat exchanger is housed in the container.

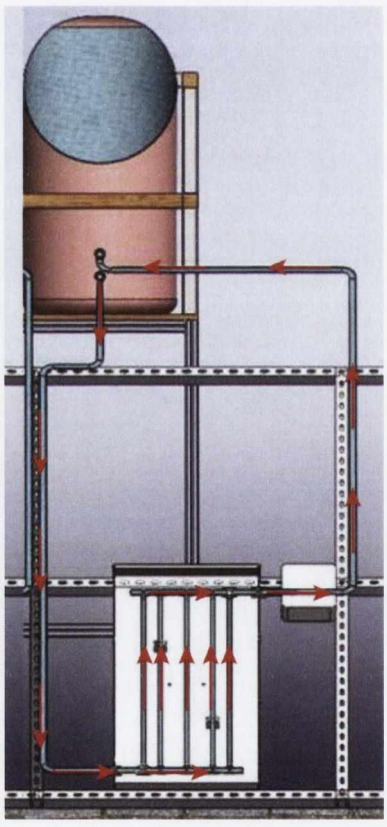

Figure 3.15: Closed loop water flow system of System 3 and System 4

The water was stored in a closed loop, as shown in Figure 3.15, which shows the flow from the tank through the thermosyphon and back to the tank. The water was stored and changed each morning to ensure that the initial water temperature was the same in each system.

3.3.4 Energy Storage Material – System 4

System 4 builds on System 3 as the thermal collector contains a thermal energy storage material (PCM). The PCM is a eutectic mixture of two fatty acids. The mixture was prepared from individual chemicals in the form of capric and palmitic acid which were then combined to form the eutectic capric:palmitic acid (by weight 75%:25%). The material's thermophysical characteristics are found using DSC and THM as described in Chapter 4 and the results are presented in Table 3.3.

The fatty acids were mixed as solids by weight 75%:25% capric:palmitic acid. Each solid mixture was melted at 60°C for three hours using a series of hot plates to obtain a homogenous solution that then cooled to solidify as a eutectic solid. Prior to cooling the liquid, the liquid was put into one of the experimental system containers in one pour to ensure there was no segregation of PCM within the container. There is approximately 24 litres of PCM in the container with a maximum latent heat storage capacity of 4590 kJ when fully charged. The process can be seen in Figure 3.16. The thermophysical properties of capric:palmitic acid are presented in Table 3.3.

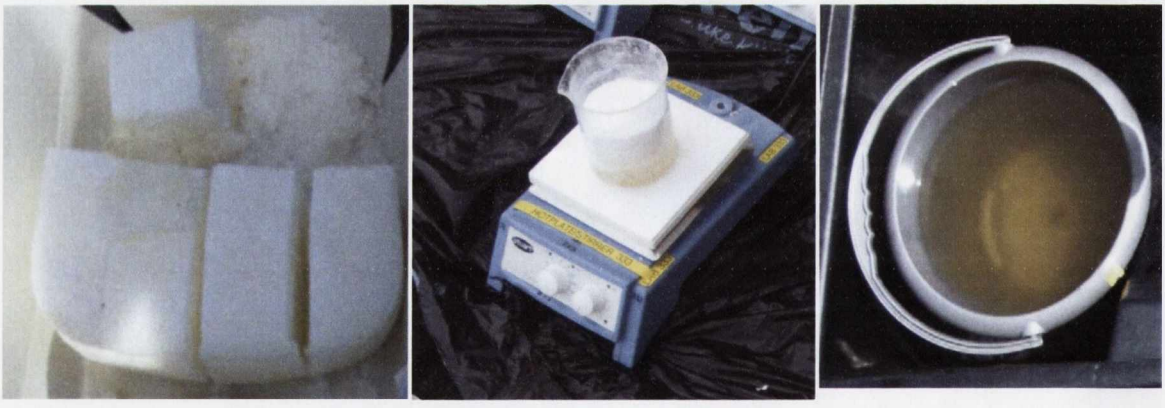

(a) (b) (c)

Figure 3.16: (a) Solid capric acid (b) melting PCM eutectic (c) fully liquid fatty acid eutectic

Table 3.3: Thermophysical properties of capric:palmitic acid

		Capric acid: palmitic acid
Properties	Melting range (°C)	17.72-22.76
	Solidification range (°C)	12.33-15.55
	Heat of fusion ($kJkg^{-1}$)	191.24
	Thermal conductivity ($Wm^{-1}K^{-1}$)	0.143
	Specific heat capacity ($kJkg^{-1}K^{-1}$)	2.3

3.3.5 Data Acquisition System

The objective of the data acquisition system is to monitor and record the changes in each system. Various data acquisition devices were used to monitor changing conditions in the experiment. The weather data was monitored using a Davis weather station, Vantage Pro 2, as shown in Figure 3.17(a). The weather station was located beside the experimental set-up and was connected to a computer in the controls room via a wireless connection.

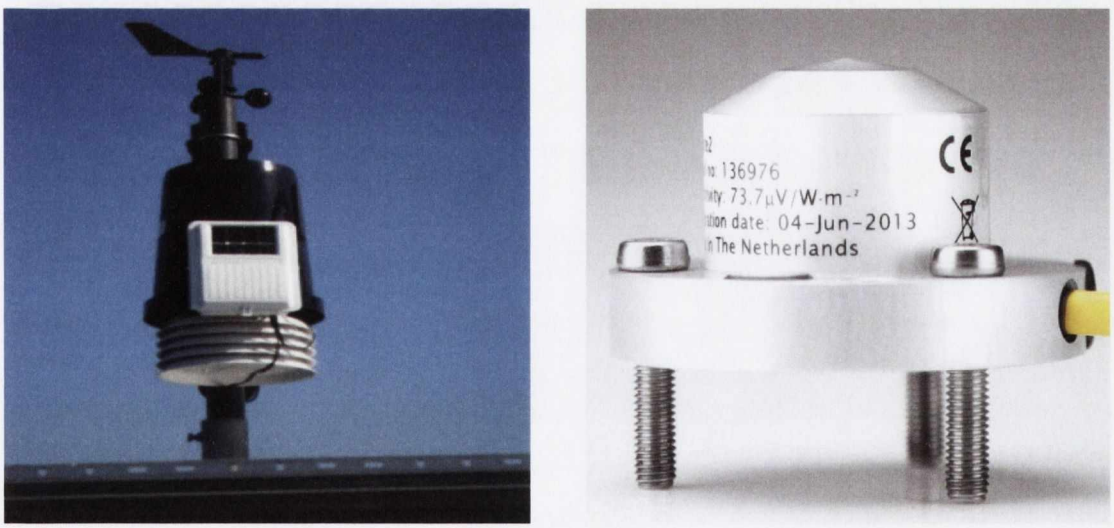

(a) (b)

Figure 3.17: (a) Davis weather station, Vantage Pro2 (b) Kipp and Zonen pyranometer, Sp Lite2

Solar radiation was recorded using a Kipp and Zonen Sp Lite2 pyranometer (see Figure 3.17(b)); it has a directional error of less than 10 W/m^2 and resolution of 1 W/m^2. This was then connected to a datalogger which recorded and stored readings. The diffuse solar radiation were collected using Kipp and Zonen CMP3 Pyranometer integrated with a shading ring.

Two dataloggers were used in the experiment, an Agilent 34972A LXI and Delta-t DL2e, as presented in Figure 3.18 (a) and (b). The Agilent datalogger has three cards which are inserted into the back of the datalogger and each card has 22 slots which can record a thermocouple, voltage or current reading. The first 20 are reserved for thermocouple signals and voltage differentials and the last 2 are for current readings. The data was recorded directly to a memory stick. The Delta-t datalogger has 60 channels which can measure thermocouple signals and voltage differentials. The delta-t has a memory capacity for over 131,000 readings. Both loggers were connected to the mains and stored in weatherproof containers.

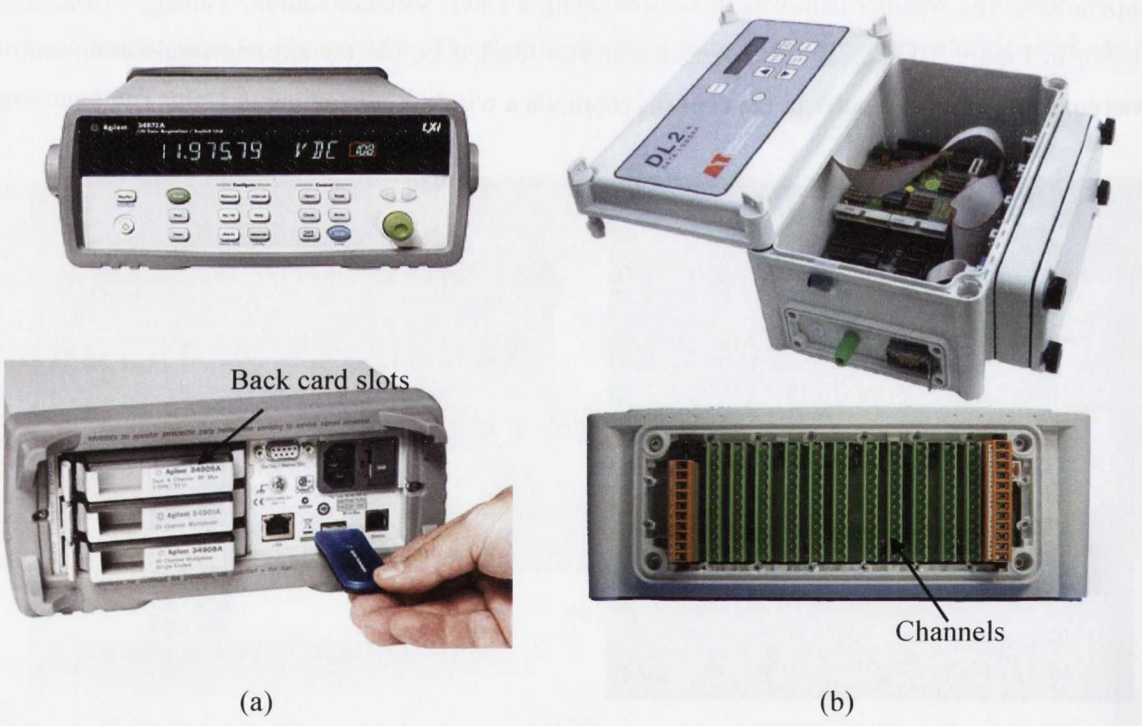

Figure 3.18: (a) Agilent 34972A LXI front and back (b) Delta-t DL2e and channel connections

An inline ultrasonic flowmeter SU 7000, as shown in Figure 3.19, from IFM electronics was used to measure the flowrate of the water in the thermal component of the systems. The

flowmeter is capable of measuring water and glycol solutions. The low pressure drop across the device was critical in ensuring that the flow rate would not be affected by the measuring device. The flowmeters were stored in weatherproof containers in the experiment.

Figure 3.19: IFM ultrasonic flowmeter SU 7000

The temperature across each system was measured using a series of T (copper-constantan) and K (chromel-alumel) type temperature sensors. All thermocouples were calibrated and found to have a maximum measured deviation of ± 0.2°C. Wire thermocouples were used to measure surface temperatures and probe thermocouples were used to measure temperatures inside the container and heat exchanger, as shown in Figure 3.20 (a) and (b). The temperatures of the front and back of the PV, inside and at the back of the container, inside the water tank, and at the inlet and outlet of the heat exchanger were monitored. The exact position of the thermocouples will be described in Section 3.3.6.

(a) (b)

Figure 3.20: (a) Wire thermocouple (b) probe thermocouple

3.3.6 Sensor Locations

This section discusses the location of the sensors which are positioned to assess the temperature variation through the system. There are 4 systems assessed in the experiment, two references (Systems 1 and 2) and two PV/T systems (Systems 3 and 4), as shown in Table 3.4 and illustrated in Figure 3.6.

Table 3.4: System attributes

		PCM (Energy Storage)	**Heat exchanger (Thermal)**	**Container**	**PV panel (Electrical)**
System	1	No	No	No	Yes
	2	No	No	Yes	Yes
	3	No	Yes	Yes	Yes
	4	Yes	Yes	Yes	Yes

3.3.6.1 System 1 Sensors (Photovoltaic –Reference)

System 1 is a PV connected to an electrical load, as previously described in the sub section electrical components. System 1 is the first of two reference systems. The temperature variation of the PV, both front and back, and the power generated are recorded for comparison with the other systems.

One thermocouple was positioned on the front of the PV, in the top left hand corner, to minimise the shading effect and thus, the power generation. A further six thermocouples were positioned on the back of the PV panel in the locations specified in Figure 3.21 to assess the variation in heat distribution on the back of the panel. These locations were chosen as they measured the spread of heat from the centre out towards the edge of the PV.

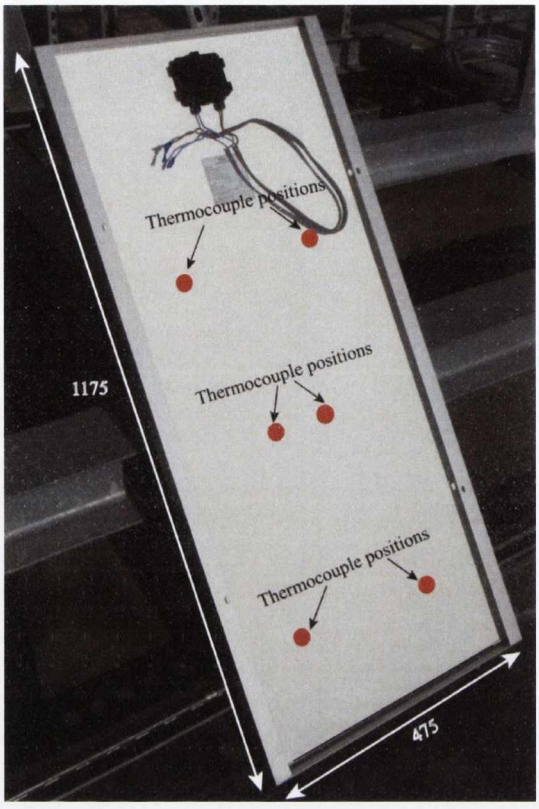

Figure 3.21: Thermocouple locations on the back of PV panel, all dimensions are in mm

3.3.6.2 System 2 Sensors (Photovoltaic with Container –Reference)

System 2 (PV with container) is the second reference system and comprises of a stainless steel container PV attached to a PV panel, both of which have been described in the components sub section 3.3.1. The container is attached to the back of the PV panel frame (see Figure 3.22).

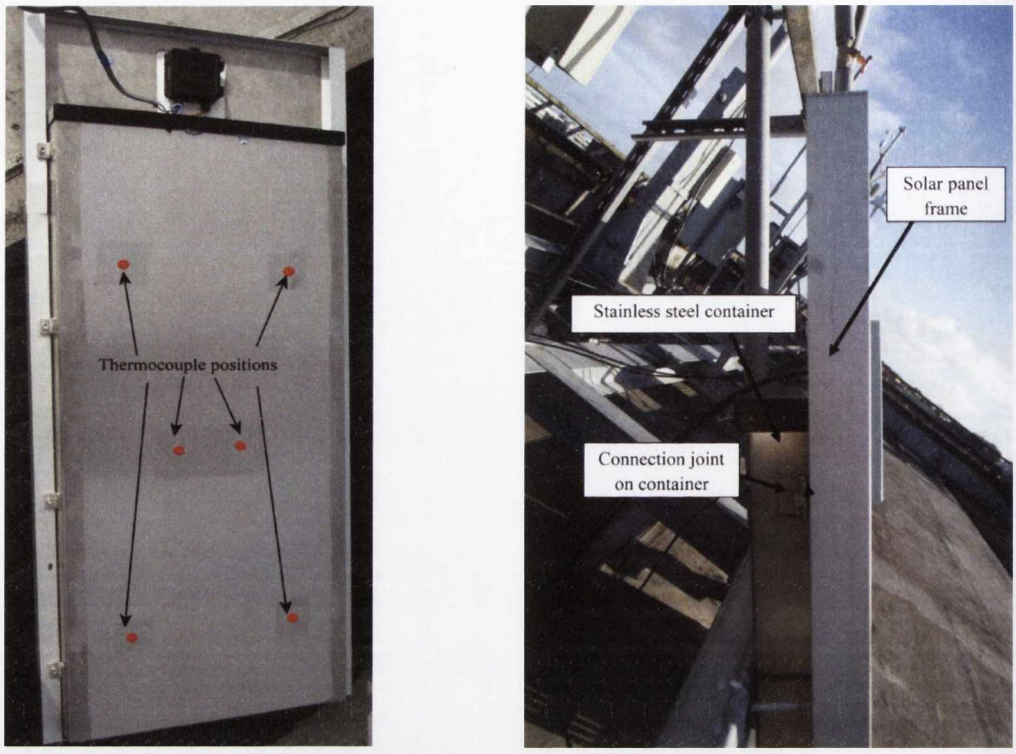

(a) (b)

Figure 3.22: (a) Container positioned on the back of PV with thermocouple positions as indicated (b) side elevation view of the PV attached to the container

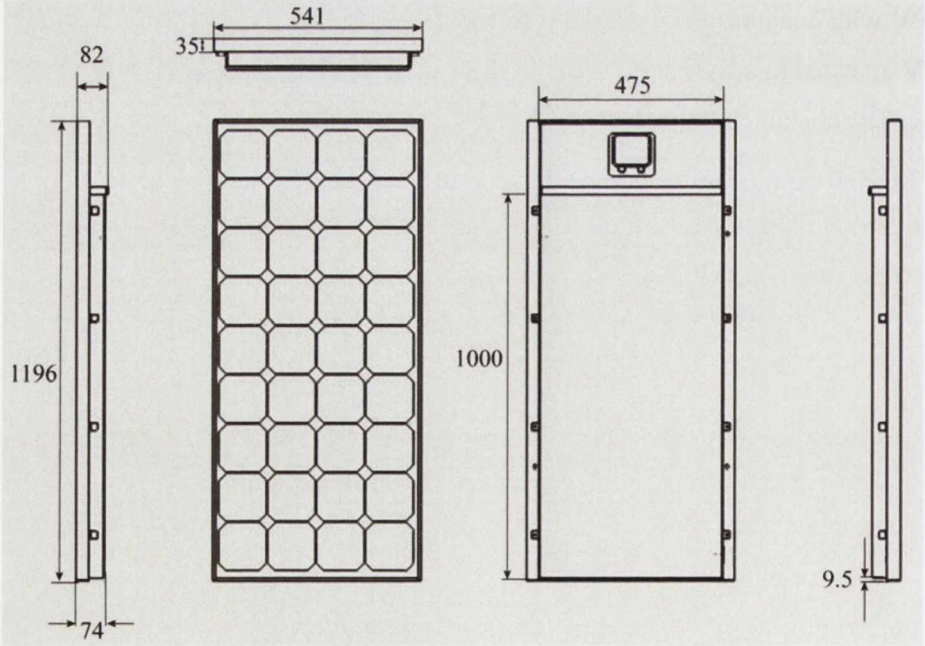

Figure 3.23: System 2 (PV with container) dimensions

The layout of the thermocouples on the back of the container is shown by the red points in Figure 3.22(a). These thermocouples, along with those on the back of the PV, allow the heat transfer through the system to be monitored. The dimensions of the container are shown in Figure 3.23, which also gives a side elevation view of the system.

3.3.6.3 System 3 Sensors (Photovoltaic/Thermal)

System 3 is a PV/T system which encompasses all components of System 2 and in addition to a heat exchanger, tank and flow meter with additional thermocouples. The objective is to achieve an optimal combination of useful electrical and heat output simultaneously. By comparing the performance of System 2 with System 3 the effect of thermal energy utilisation from the PV can be quantified

The heat exchanger, as detailed in section 3.3.1.2, is positioned in the container as shown in Figure 3.24 (a) and (b). The container was welded shut to stop the ingress of moisture.

(a)

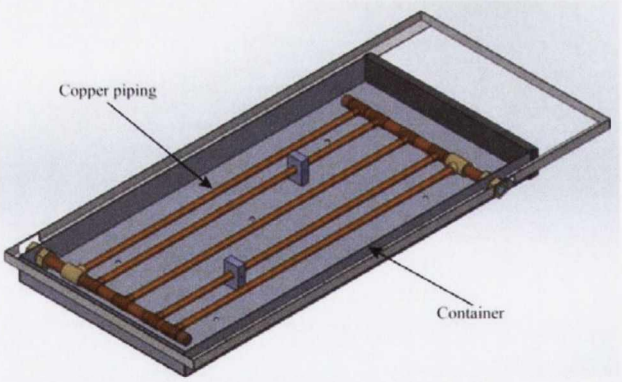

(b)

Figure 3.24 (a) Heat exchanger inside the container prior to sealing (b) schematic of the heat exchanger inside the container

Thermocouples are located on the front and back of the PV (as described in System 1) and on the back of the container (as described in System 2). There is an additional series of thermocouple probes inserted inside the container through a thermocouple gland as shown in Figure 3.25(a). Similar probes were inserted at the inlet and outlet pipes as shown in Figure 3.25(b).

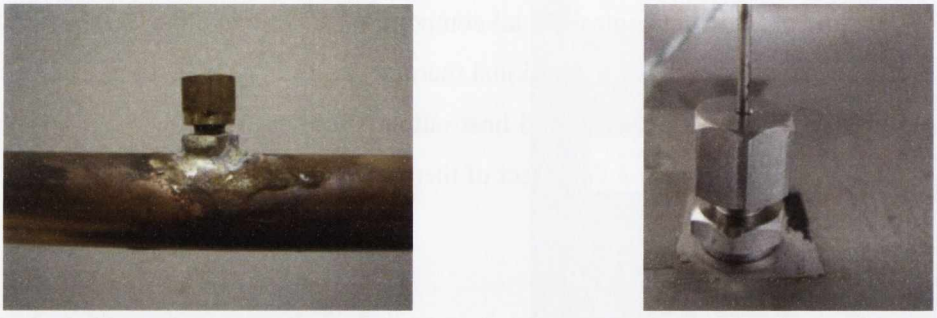

(a) (b)

Figure 3.25: (a) Stainless steel gland and probe in the back of the container (b) copper gland welded to the copper pipe (probe not yet inserted)

The probes are located inside the container at the same position as the thermocouples on the back of the container and the thermocouples on the back of the PV, as shown by indicated dimensions. This layout, along with the dimensions of System 3, is shown in Figure 3.26.

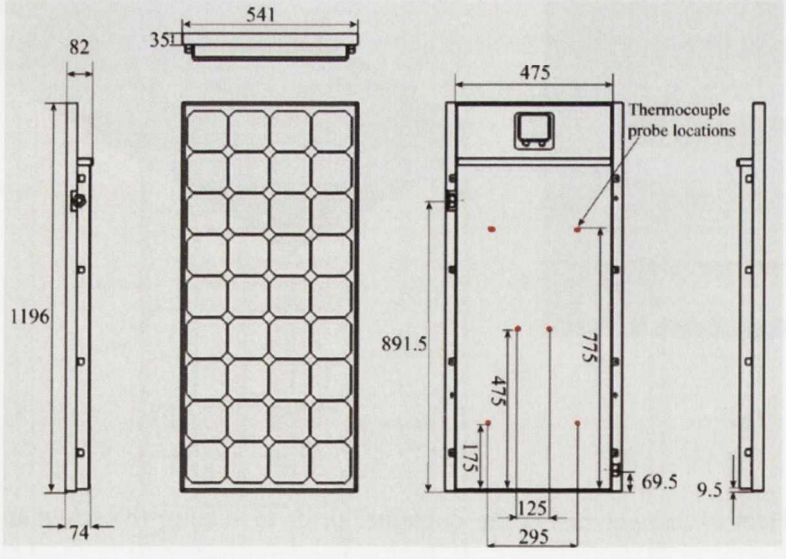

Figure 3.26: Dimensions of System 3 illustrating the locations of the thermocouple probes

3.3.6.4 System 4 Sensors (Photovoltaic/Thermal/Phase Change Material)

System 4, the photovoltaic/thermal/phase change material (PV/T/PCM) system, comprises of all the components of System 3 along with the addition of a thermal energy storage material (TES). The TES material used was the eutectic PCM capric:palmitic fatty acid and has been described in section 3.3.4. The material was poured into the container whilst liquid to avoid segregation, as shown in Figure 3.27. The container was sized to take into account expansion of PCM which has been reported to be 0.00078 %/K (Hasan, 2010a) which did not require significant additional volume.

The thermocouple layout is the same as that in System 3, with thermocouples located on the back and front of the panel, inside and on the back of the container and, at the inlet and outlet of the heat exchanger. However, in this system, System 4, the thermocouple probes inside the container are submerged in PCM, whereas in System 3 the container is filled with air.

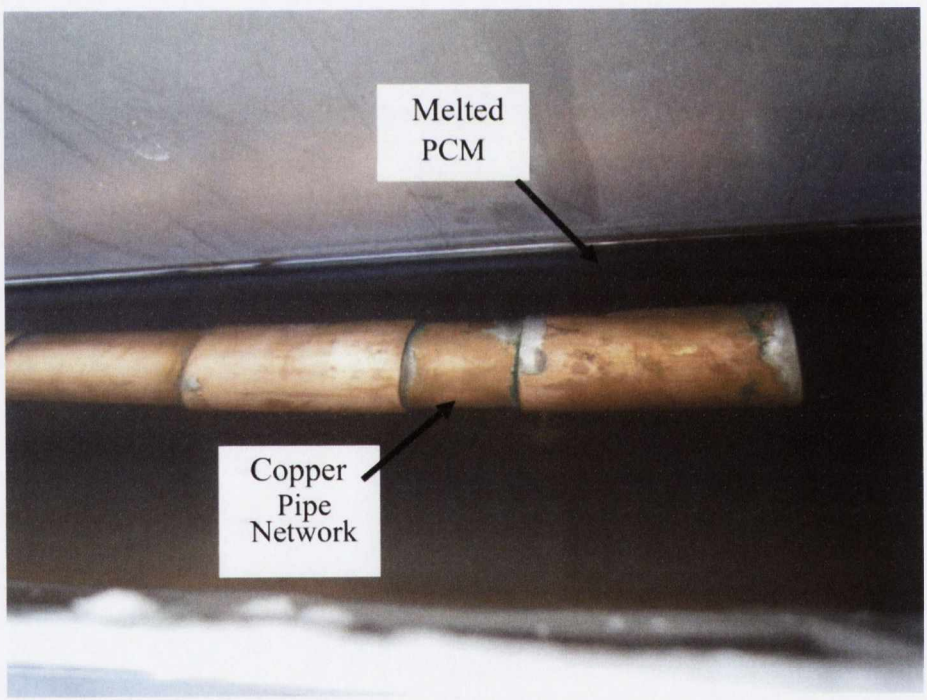

Figure 3.27: Heat exchanger immersed in liquid PCM in the container of System 1

The objective of System 4 is to use the PCM as a method of storing heat during the day. As the temperature of the PV rises due to the increased solar radiation and ambient temperature during daylight hours, the PCM will charge using the heat transferred from the PV. At night when

ambient temperatures decrease, the PCM discharges the stored heat to the water, pre-heating the water.

3.3.7 System Installation

The experiment was conducted on the roof of Dublin Institute of Technology, Kevin Street, Dublin 2, Ireland (53.33 N, 6.24 W) from May 2013 to June 2015, as illustrated in Figure 3.28. The experimental set-up was south face and positioned at an angle of 53 degrees. Each testing period lasted for three consecutive days. The tanks were emptied and refilled daily to ensure the systems were starting from the same base temperatures.

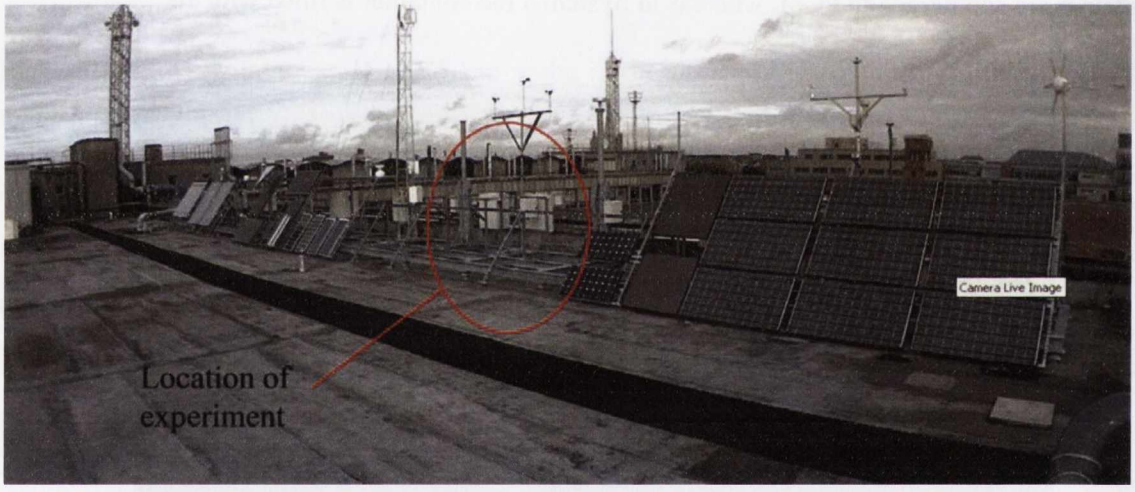

Figure 3.28: Location of the experiment on the roof top solar laboratory

3.3.8 System Comparison

The completed experimental set-up can be seen in Figure 3.29(a). The experiment is designed so that each system builds on the previous system starting from the basic PV (System 1) to the more elaborate PV/T/PCM system (System 4). This stepped experimental concept can be seen in the cross sectional drawing of the experiment Figure 3.29(b). The idea of stepping the design of the experiment allows for comprehensive comparisons to be made, allowing the assessment of the container, heat exchanger and the PCM separately.

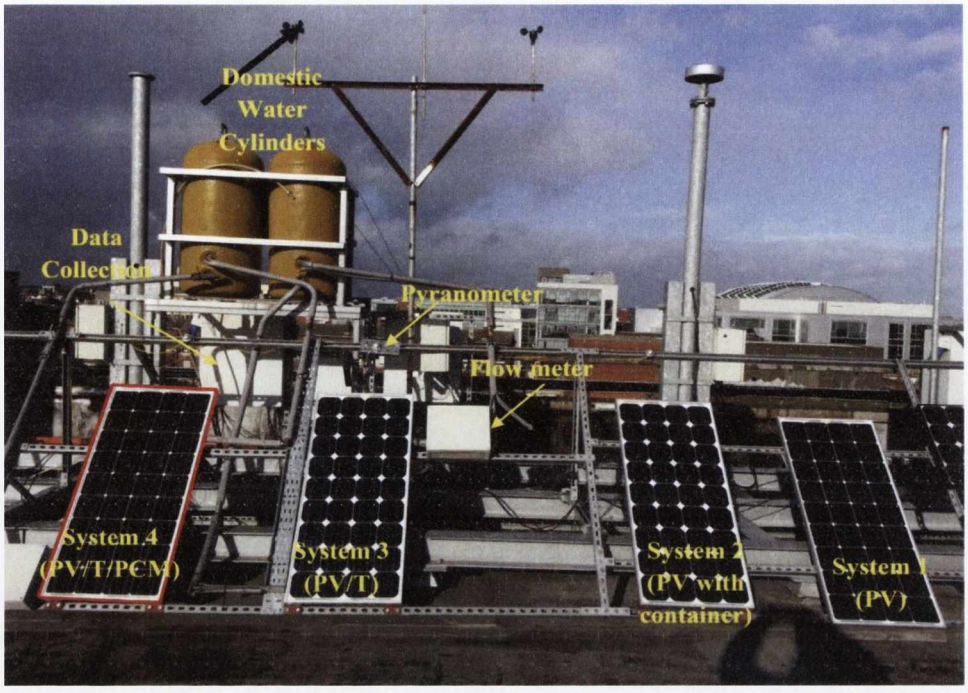

(a)

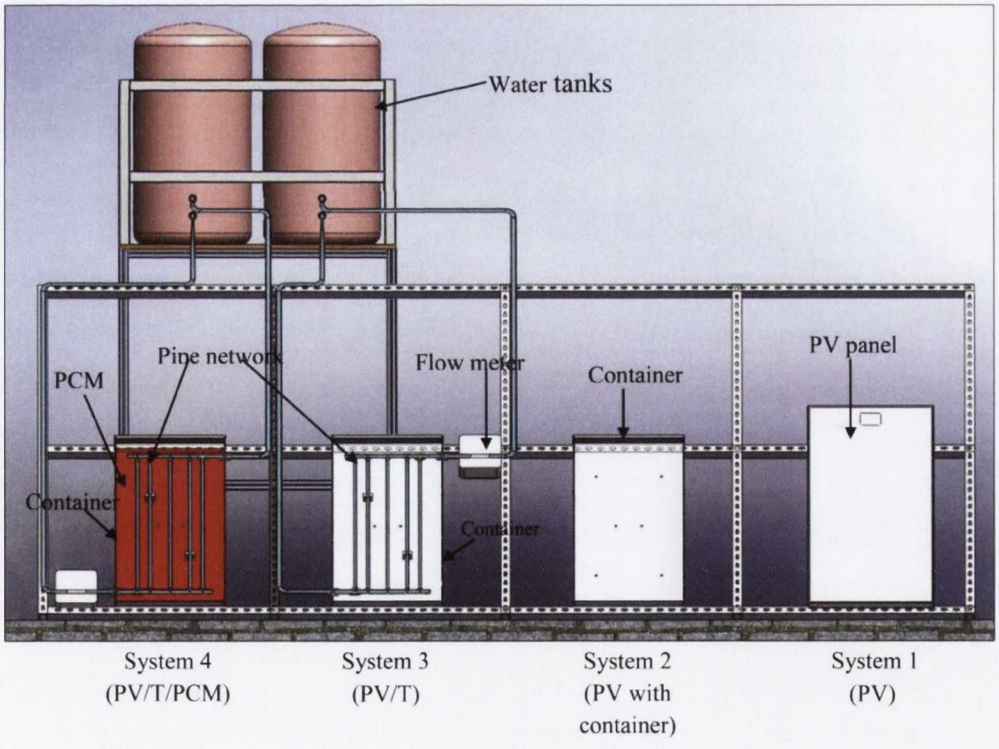

(b)

Figure 3.29: (a) Photograph of completed experimental set-up (b) cross–section drawing of experimental set-up

3.4 Modelling Software

A model of the PV/T/PCM system was developed using a combination of TRNSYS and COMSOL, both commercially available software. In order to simulate the output of the experimental PV/T/PCM system the incorporation of the major components, the PV, the thermal collector and the latent heat storage material, is required. TRNSYS was employed to model the PV and thermal collector elements of the system and COMSOL was introduced to simulate the behaviour of the latent heat storage material, PCM.

3.4.1 TRNSYS – Transient System Simulation Tool

TRNSYS is visual based software used to model and simulate the behaviour of transient energy systems for applications such as solar systems (Kalogirou, 2001; Aste et al., 2012b; Kamel and Fung, 2014), HVAC systems with advanced design features (Chargui et al., 2013; Massaguer et al., 2014; Safa et al., 2015) and assessing the energy performance of buildings (Asadi et al., 2012; Ciobanu et al., 2014; Gallo et al., 2014). Models in TRNSYS consist of a series of components which are connected together to represent an entire system. Components, known as Types, are programmed in FORTRAN which can then be modified. Types have a series of parameters and inputs associated with them which are used in the context of the system to calculate the Type outputs.

TRNSYS has a specifically designed set of components for use in energy systems, referred to as the 'Thermal Energy System Specialist' (TESS) library. The PV and thermal collector of the PV/T/PCM system are modelled in TRNSYS using components which are referred to as Types and can be found in the library of the software package. Other components are also employed to connect the main components together such as pipes and water tanks. TRNSYS has been designed as a tool to simulate the performance of systems and buildings which would reduce the level of detail which can be achieved with regard to simulating the melting of PCM.

3.4.2 COMSOL Multiphysics

COMSOL is a commercially available finite element analysis, solver and simulation software package. It allows the integration of various physical phenomena on one graphical user interface platform, for example electrical, mechanical, chemical and fluid physical process (Salvi et al., 2011; Yoon et al., 2013; Dickinson et al., 2014). The required processes generally originate from traditionally separate fields of engineering and applied physics.

The software allows the geometry of a system to be built within the software. The next step is the allocation of materials to the geometry. The option to appoint a user-defined material is available. Following this the physical processes required for the model are chosen and various boundary conditions are applied. These are packages of physical equations and associated boundary conditions. The software was used to simulate the PCM and the pipe network which will be presented in Chapter 6.

Predicting the behaviour of PCM is difficult due to the need to account for the large amount of energy needed to melt the PCM from solid and the melting interface position. Simulating the PCM with the integrated pipe network all encased in a stainless steel container requires combining the characteristics of the physical processes of heat transfer and pipe flow.

3.5 Conclusion

The characterisation techniques employed to investigate the thermophysical properties have been presented and explained. It was important to use both DSC and THM when characterising the PCM to assess both small and bulk quantities. The results of the test proved advantageous when choosing which PCM to use in the large-scale experiment.

The methodology of corrosion tests has been presented which involve immersing the material sample in PCM for a prolonged period of time. The rates of corrosion and mass loss over the period of the experiment are calculated. SEM imaging technique produced images of the materials over the course of the experiment which indicates the effect of corrosion on the sample's surface due to the microscopic images at magnifications of 200X, 3000X and 6000X.

The experimental design, fabrication and installation have also been presented. The systems were fabricated based on a stepped method, starting with System 1 (PV only) building up to System 4 (PV/T/PCM). Each system has the components of the previous system plus an additional factor. This method was employed to allow for clear comparisons to be made between the systems and to assess the effect of each individual factor on the system.

COMSOL and TRNSYS simulation software and their capabilities have been introduced. They are used in combination with each other to simulate the PV/T/PVM system, the simulation of which is presented in Chapter 6.

This chapter gives an overview of the processes undertaken to investigate the elements of the components in the PV/T/PCM system. The process of characterisation of PCM to assess the most applicable material for the system, the building of the system with respect to a comparative study of each system and finally the modelling of the system to optimise and improve its design were presented.

Chapter 4

Characterisation and Corrosion Testing of Phase Change Material

Chapter 4. Characterisation and Corrosion Testing of Phase Change Material

4.1 Introduction

This chapter includes a study to find the thermophysical properties which relate specifically to the heating, cooling and heat storage of PCM. The idea of this aspect of the project is to identify and specify PCM properties which relate specifically to the potential of the PCM to regulate PV temperature and particularly to the storing of heat for an extended period of time. Further to this, the corrosion resistance of six materials in contact with fully charged PCM for 722 days will be presented.

Two main experimental studies are presented, the first of which presents the results of the thermophysical characterisation of the PCM which include; fatty acids, salt hydrate and paraffin:

- capric acid (fatty acid)
- capric: palmitic acid (fatty acid)
- capric: lauric acid (fatty acid)
- SP22 (salt hydrate)
- Micornal® (Paraffin)

The characterisation was carried out using Differential Scanning Calorimetry (DSC) and Temperature-History Method (THM), both of which were described in Chapter 3. The results were then compared to results from studies in published literature.

The second study investigates the corrosion resistance of six materials in contact with fully charged PCM for 722 days. The PCM melting temperatures all remain within approximately 20 °C - 40 °C range as this is the temperature range the materials would be exposed to in a PV/T/PCM system in Ireland. The primary purpose of this investigation is to give an indication of the potential lifetime of a PV/T/PCM system, by assessing the life span of the PCM container material (one of the main components in a PV/T/PCM system). A series of images of the materials are presented to highlight clearly the process of corrosion on the material samples, which at times may not have been visible to the naked eye. Finally, recommendations are made as to which materials should be used and those that should be avoided.

4.2 Phase Change Material Characterisation

Hasan (2010a) characterised the properties of a number of PCM to investigate the suitability of PCM to regulate the PV temperature at the standard test condition temperature of 25 °C for an extended period of time. PV temperature regulation using PCM was also assessed with respect to concentrated photovoltaic (CPV) systems in regions where ambient temperatures can exceed 50 °C (Sarwar, 2013). However, neither study took into account the application of PCM as an efficient energy store which needs to be considered when using the material in a PV/T/PCM system.

PCM are primarily selected for specific applications based on their melting temperature (Farid et al., 2004). To be considered a viable option in a PV/T/PCM system, PCM must have a melting temperature that is higher than the average peak ambient air temperature so as to ensure that the PCM melts based on the heat generated from the PV and not due to ambient loading. Conversely, at night solidification must be achieved by ensuring the solidification temperature is greater than the night-time ambient air temperature. As the system is assessing the potential of PCM to pre-heat water, it is also important to note the heat of fusion and the thermal conductivity of the PCM in order to preserve efficient heat transfer to and from the PCM. It is also important to assess the level of subcooling of the sample which occurs when a temperature significantly below the melting temperature has to be reached, until the material begins to solidify and release heat. This can affect the latent heat storage performance of the material. Subcooling is to be avoided as it was suggested a small drop in the temperature of the PCM below the phase change temperature resulted in a part of the latent heat being absorbed during the process which can reduce the latent heat capacity of PCM (Solomon et al., 2013)

4.3 Phase Change Material Characterisation using Differential Scanning Calorimetry

The reasoning for using Differential Scanning Calorimetry was described in detail in section 3.2.2 and as such this section will focus the results. A power-compensation PerkinElmer Diamond machine was used to analyse the following characteristics of the PCM samples:

- phase change range
- melting onset
- solidification onset

- heat of fusion
- specific heat capacity

The output thermograms were displayed using Pyris software. The process involved in characterising the materials has been described in Section 3.2.2. The materials analysed using DSC were:

- capric acid
- capric: palmitic acid (75:25 by weight)
- capric: lauric acid (45:55 by weight)
- SP22
- Micronal®

4.3.1 Capric Acid

A capric acid sample with mass of 4.66 mg was used to analyse the thermophysical properties of the fatty acid. The results, presented in Figure 4.1 show the variation of heat flow, measured in mW, against temperature of the sample.

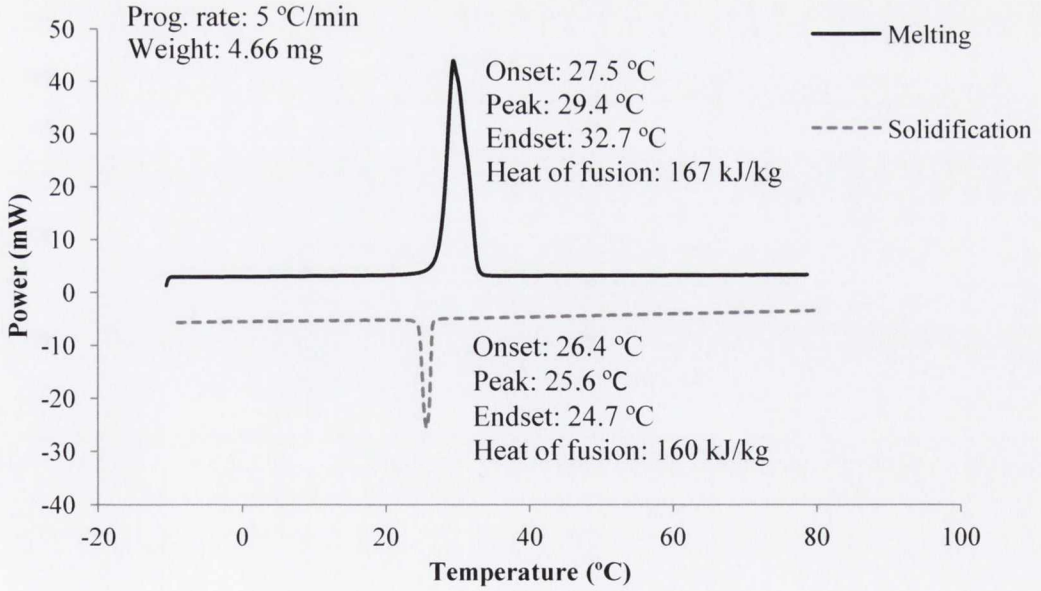

Figure 4.1: DSC results of capric acid during melting and solidification

The melting heat of fusion is 167 kJ/kg during melting and the melting range is 27 °C – 32.7 °C. The DSC peak is observed at 29.4 °C. This result is in agreement with previously conducted investigations (Zalba et al., 2003; Sharma et al., 2005; Sarwar, 2013). There was also subcooling of 1.1 °C observed in the sample, this is due to the material purity which has been reported to be approximately 98% (Rubiterm, 2015).

4.3.2 Capric:palmitic Acid

The capric:palmitic acid sample was prepared in the laboratory from capric acid and palmitic acid at a concentration ratio of 75% capric acid and 25% palmitic acid as discussed in Section 3.2.1. Each solid mixture was melted for three hours at 60 °C to obtain a homogenous solution that would solidify as a eutectic fatty acid.

The thermophysical properties of the eutectic fatty acid, capric:palmitic acid was analysed using power compensation DSC during melting and solidification cycles. A sample with mass of 4.08 mg produced a variation of power against temperature as shown in Figure 4.2.

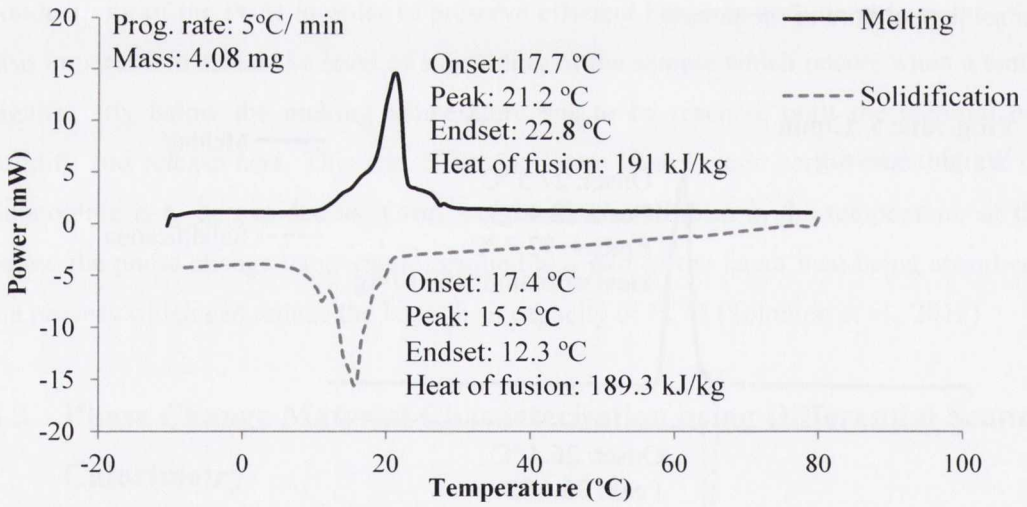

Figure 4.2: DSC results of capric:palmitic acid during melting and solidification

The latent heat of fusion was found to be 191 kJ/kg. Melting begins at 17.7 °C, peaks at 21.2 °C and ends at 22.8 °C. Subcooling for this sample was 0.3 °C.

4.3.3 Capric:lauric Acid

The material capric:lauric acid was prepared in the laboratory by mixing capric acid and lauric acid by a weight ratio of 45% capric acid and 55% lauric acid. Each solid mixture was melted for three hours at 60 °C to obtain a homogenous solution that would solidify as a eutectic fatty acid.

Following this, DSC testing was carried out on the sample of mass 3.10 mg. The variation of heat flow into and out of the sample was measured against the sample temperature and the results are shown in Figure 4.3.

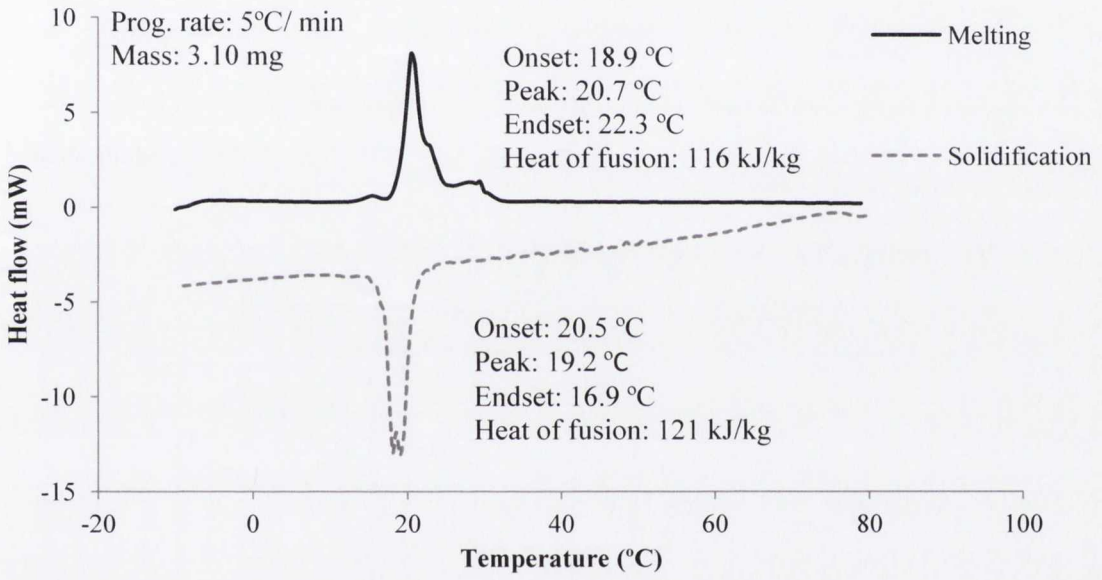

Figure 4.3: DSC results of the eutectic mixture, capric: lauric acid

The latent heat of fusion is 116 kJ/ kg, which is between 20 kJ/kg and 50 kJ/kg less than values previously reported (Hawes et al., 1993; Hasan, 2010b). The onset of melting occurred at 18.9 °C where the slope of the thermograph is highest. The DSC peak is 20.7 °C and the melting process ends at 22.3 °C. It must also be noted that the sample was made in the lab and although a specific process was followed experimental inconsistencies can still exist. DSC sample size is very small.

4.3.4 Salt Hydrate SP22

The DSC results of the salt hydrate SP22 are presented in Figure 4.4. The melting process of the material shows a melt onset temperature of 16.9 °C, melt peak of 18.8 °C and melt end of 25.3 °C. A heat of fusion value of 146 kJ/kg was calculated during the melting phase. These values are in agreement with the values specified by the manufacturing company Rubiterm (2015). However, the heat of fusion value has decreased significantly during the solidification phase reporting a value of 79 kJ/ kg, this would suggest segregation has taken place over the phase change of the material. However, further investigation into this material will be carried out using the T-History method later in this chapter.

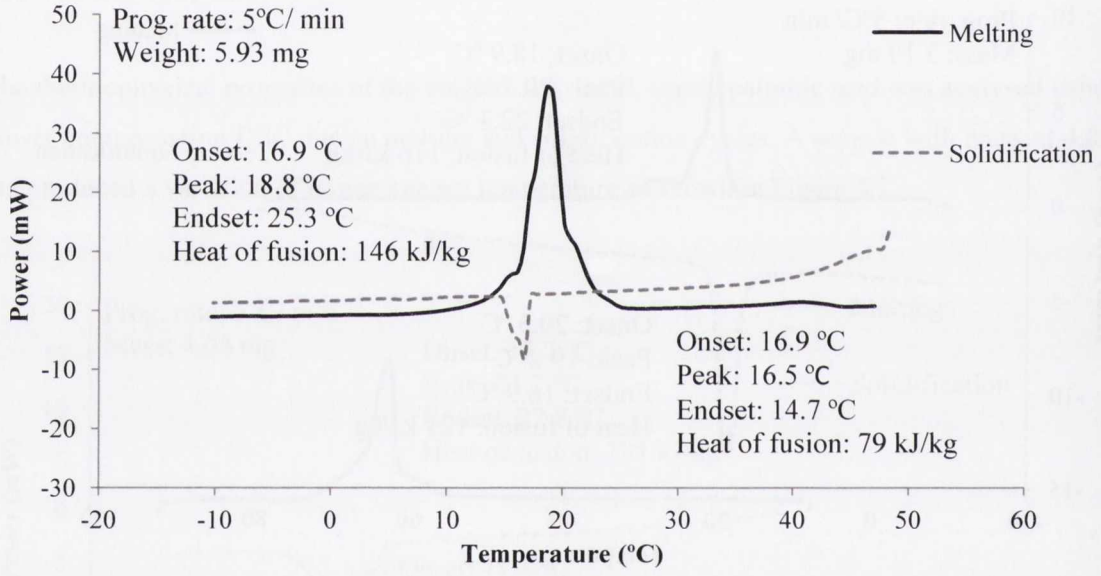

Figure 4.4: DSC results of SP22 during melting and solidification

4.3.5 Micronal®

The PCM Micronal® was analysed using the heat flux DSC during the melting and solidification cycles, as with the previous samples. The variation of power against temperature of the sample is shown in Figure 4.5.

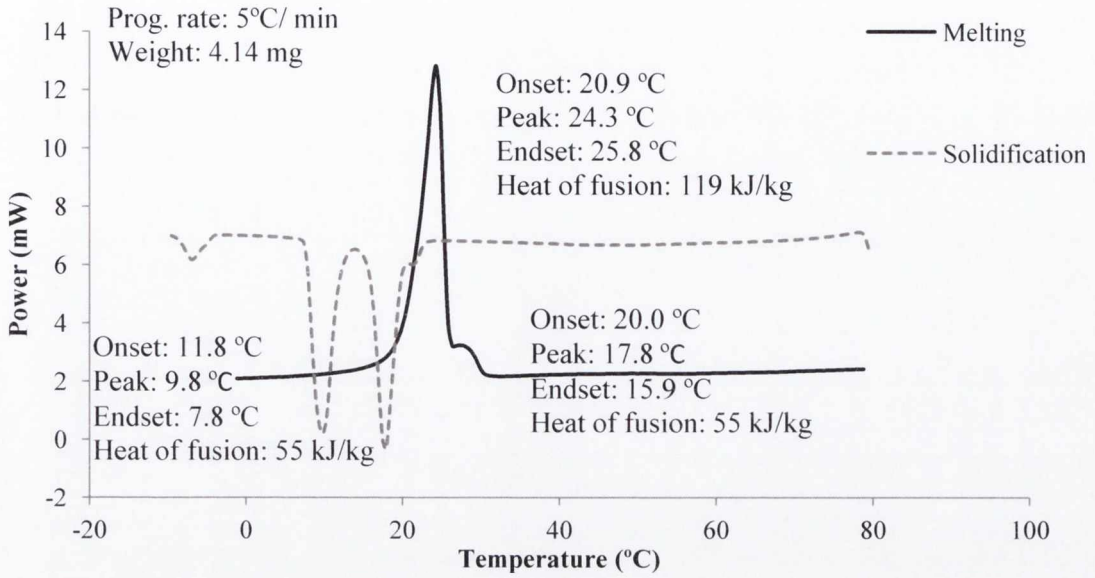

Figure 4.5: DSC results of Micronal® during melting and solidification

The material can be seen to be very unstable; initially the material melts as expected, with a melting onset temperature of 20.9 °C, melting peak of 24.3 °C and heat of fusion of 119 kJ/kg. Solidification occurs over two peaks, each occurring at at 17.8 and 9.8 °C, by adding the heats of fusion of each peak the total gives a value of 110 kJ/kgK. The material is clearly a mixture and as a result not a homogenous. The double peak suggests the material has separated, possible as a result of storage and deterioration over time this would suggest the lifetime of the PCM is shorter than that of any of the others making it an unsuitable option for integration into a PV/T/PCM system. There is subcooling of 0.9 °C.

4.4 Phase Change Material Characterisation using Temperature-History Method

The Temperature-History Method (THM) was the second method which involved characterising larger material samples (25 g) than the DSC. The steps taken and processes involved have been presented in Section 3.2.3.

4.4.1 Capric Acid

The temperature history curve of capric acid found using THM is presented in Figure 4.6. The sample was heated to 40 °C and maintained at that temperature for a period of one hour to ensure it was at a uniform temperature.

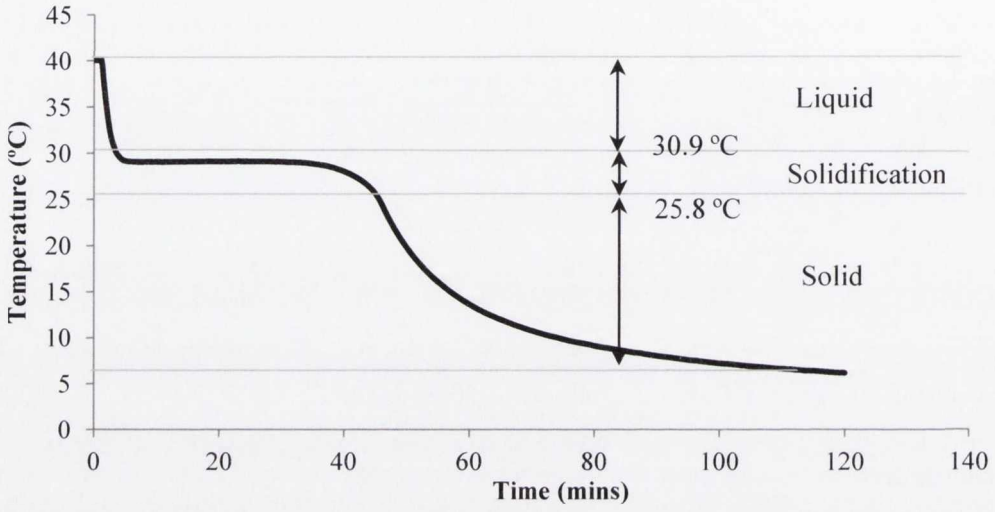

Figure 4.6: Temperature history curve of capric acid

The onset of solidification started at 30.99 °C and the completion of the solidification process occurred at 25.76 °C. This was confirmed by the minimum point of the first derivative of the curve which indicates completion of phase change (Hong et al., 2004). Capric acid shows negligible sensible heat presence during phase change as evident from the temperature history curve. There is no subcooling and it was calculated that the latent heat of fusion is 184 kJ/kg. The specific heat capacity of the solid phase is 2.6 kJ/kgK and the specific heat capacity of liquid phase is 1.4 kJ/kgK. From these results, capric acid has potential to be used in a PV/T/PCM system. However, the melting temperature is too high for that of an Irish climate.

4.4.2 Capric:palmitic Acid

Capric:palmitic characterisation was carried out using THM and the results are presented in Figure 4.7. The onset of solidification was at 25.39 °C and subcooling of ~1 °C was observed. The completion of solidification is at 16.03 °C according to basis presented by Hong et al. (2004) which states the completion of solidification is the minimum point of the value of the gradient at simultaneous points. However it is clear that the transition from latent heat storage to

sensible cooling is not very distinct as can be seen from graph. Latent heat of fusion was found to be 209 kJ/kgK which is a value similar to that found using the DSC material characterisation methods. Heat capacity of the solid phase and liquid phase are 1.46 kJ/kgK and 1.65 kJ/kgK, respectively.

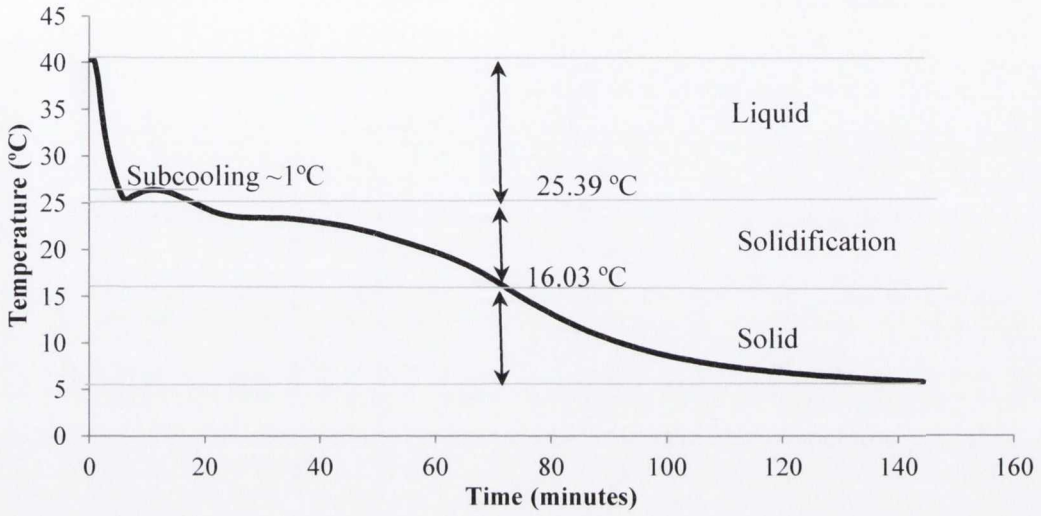

Figure 4.7: Temperature history curve for capric:palmitic acid

4.4.3 Capric:lauric Acid

The thermophysical properties of capric:lauric acid found using THM along with the cooling graph is presented in Figure 4.8. The onset of solidification was 21.75 °C and there was subcooling of 0.6 °C observed during the cooling process. Melting is completed at 12.79 °C as found by calculating the minimum point of the slope. However, it is clear that the transition from latent heat storage to sensible cooling is not very distinct, as can be seen from the gradient of the graph. The phase change range of capric:lauric is 21.75 °C to 12.79 °C. The latent heat of fusion was found to be 169 kJ/kg with the heat capacity of solid and liquid being 1.9 kJ/kgK and 1.8 kJ/kgK, respectively.

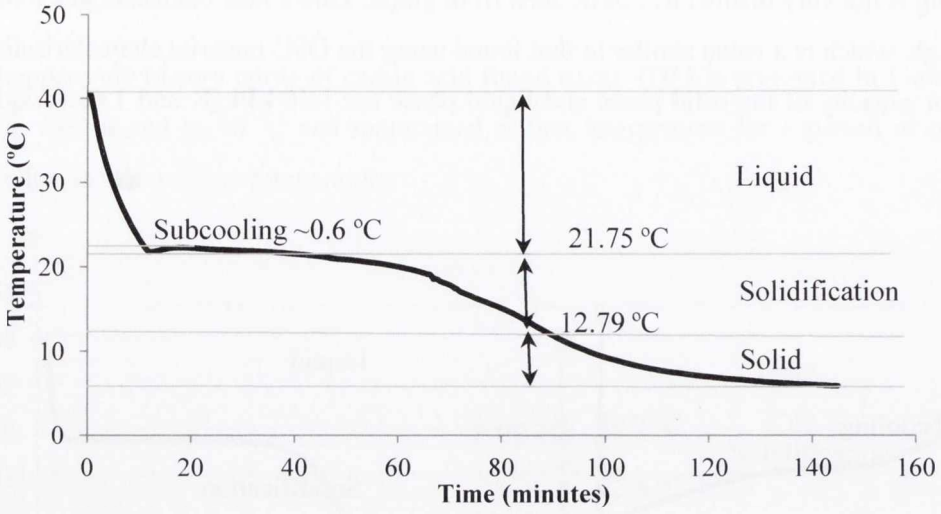

Figure 4.8: Temperature history curve for capric:lauric acid

4.4.4 Salt Hydrate SP22

THM results of the commercially available salt hydrate SP22 are presented in Figure 4.9. Based on repeated experiments, it is clear that there is no evidence of phase change taking place and as a result the thermophysical properties could not be calculated using this method.

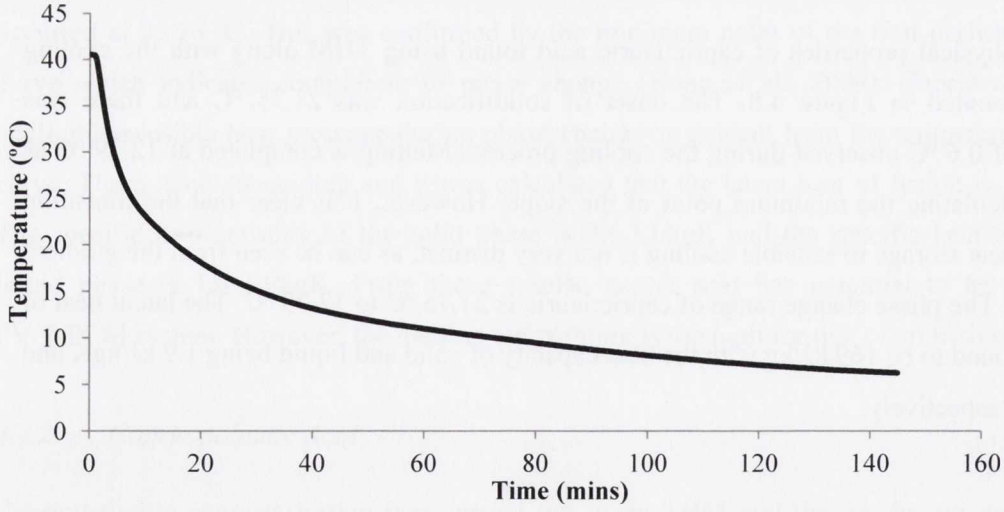

Figure 4.9: Temperature history curve of SP22

It is worth noting that this material was a mixture of a salt hydrates and organic compounds. It was seen over the time period of the experiment that the material segregates in liquid form and

is unable to return to a solid crystallised state as shown in Figure 4.10. The image in Figure 4.10(b) clearly shows the material segregating following the initial melting process. The material segregates progressively with time. Figure 4.11(a) shows the material after being in a liquid for an extended period of time. Even after this has solidified the segregation is still clear to see (Figure 4.11b).

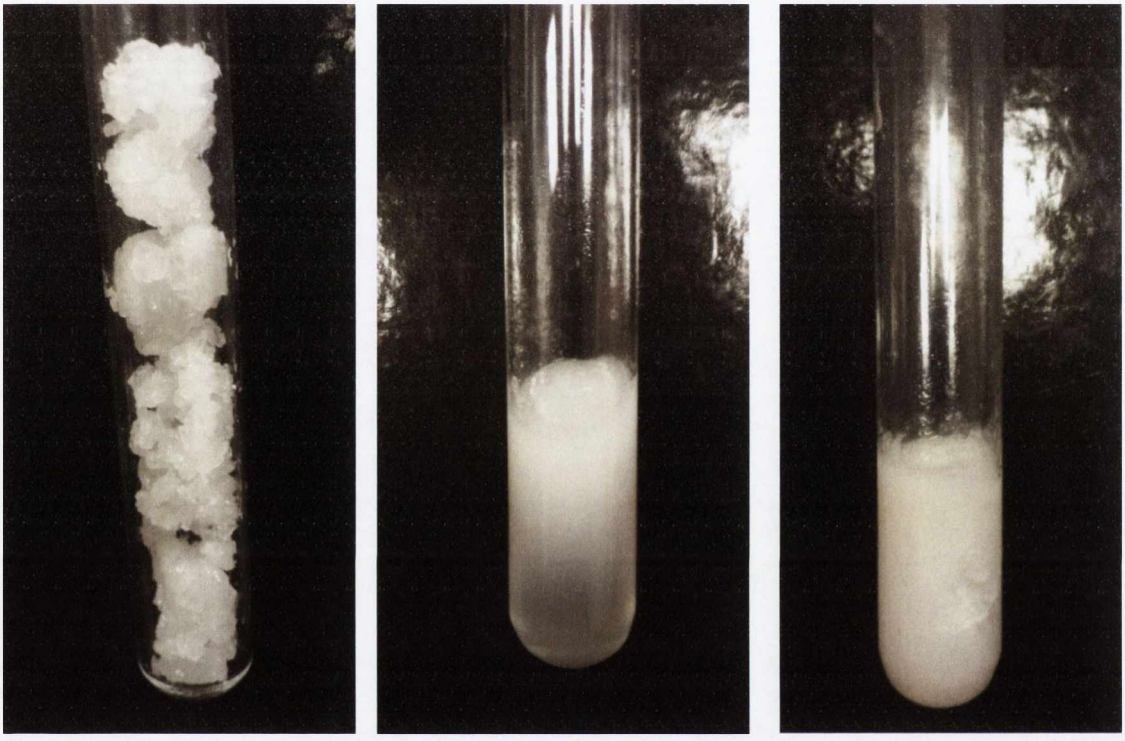

(a) (b) (c)

Figure 4.10: SP22 (a) before first melt (b) after melting (c) first solidification

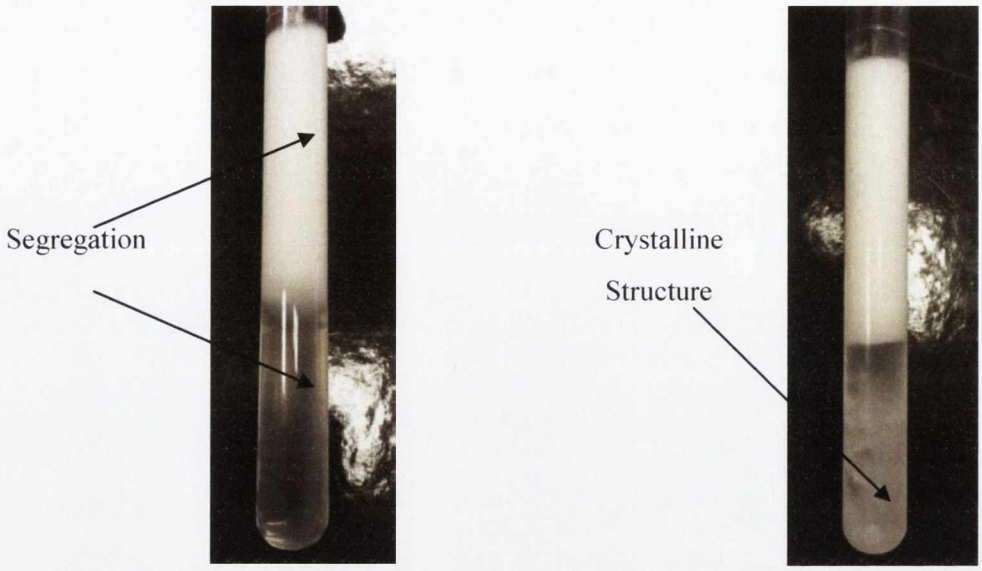

Figure 4.11: SP22 in (a) liquid form and (b) solid state after an a series of thermal cycles

Salt hydrate is prone to segregation (Gutiérrez et al., 2014; Wu and Wang, 2015) making it an unsuitable candidate material for a PV/T/PCM system. However, there are methods which can be applied in order to overcome this issue such as encapsulation of the PCM, mechanical stirring, and the addition of a thickening agent (Sharma et al., 2009).

4.4.5 Micronal®

The results of a THM investigation of Micronal® are presented in Figure 4.12. Phase change occurs during from 26 minutes to 55 minutes as shown by the flat lining of the temperature curve. However, it has been found that the heat of fusion is 60 kJ/ kg, which is similar to the value found in one peak in the DSC results. This suggests the material is presenting one of the peaks of those shown in the DSC. It can be concluded that the chemical stability of the material has been damaged due to prolonged thermal cycling causing it to segregate. The degradation of the material over time is evident suggesting it is unsuitable for integration into a PV/T/PCM system.

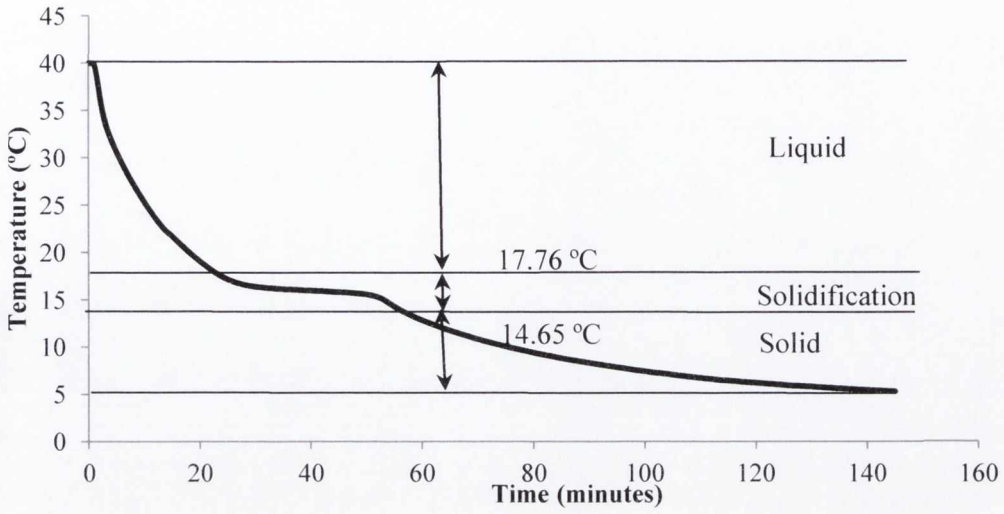

Figure 4.12: Temperature history curve of Micronal®

The specific heat capacity in solid and liquid state is 2.7 kJ/kgK and 3.8 kJ/kgK, respectively.

4.5 Comparison of Results of Thermophysical Properties of PCM with Reviewed Literature

The thermophysical properties of capric acid, capric: palmitic acid. Capric: lauric acid, SP22 and Micronal® are presented in Table 4.1. It is evident there are slight variations in the values reported by manufacturers (Rubiterm, 2015; Sigma-Aldrich, 2015) and published literature (Hawes et al., 1993; Yinping et al., 1999; Zalba et al., 2003; Sharma et al., 2005; Kenisarin and Mahkamov, 2007; Sarı and Karaipekli, 2008; Hasan, 2010b; Hasan, 2010a; Bajare et al., 2011; Sarwar, 2013).

The melting range of capric, capric:palmitic and capric:lauric acid are spread over a range of 5.1 °C, 9.3 °C and 9 °C, respectively in the THM characterisation tests. The wide range associated with capric:palmitic and capric:lauric could be attributed to being a eutectic compared to capric acid which is a purer material. These values differ slightly to the temperature ranges of the fatty acids presented by the DSC results, which are all less than 5.2 °C. The sample sizes evidently have an effect on the results as smaller sample sizes appear to melt over a shorter range.

Table 4.1: Comparison of thermophysical properties reported in literature and in this study

PCM	Material classification	DSC or THM	Melting temperature/ range (°C)	Heat of fusion (kJ/kg)	Thermal conductivity (W/mK)	Heat capacity (solid/ liquid) (kJ/kgK)	Density (solid/ liquid) (kg/m^3)	References
Capric acid	Fatty acid		27-32				893	(Sigma-Aldrich, 2015)
		DSC	32	152.7	0.153	2.1	878/ 1004	(Zalba et al., 2003; Sharma et al., 2005)
		DSC	30.27-32.35	137.92				(Sarwar, 2013)
		DSC	**27.5-32.7**	**167**				**This study**
		THM	30.1	150	0.16	1.95/ 1.72		(Yinping et al., 1999)
		THM	27-30.3	153.38		1.93/ 1.38		(Sarwar, 2013)
		THM	**25.8-30.9**	**184**		**2.6/1.4**		**This study**
Capric: palmitic acid	Eutectic fatty acid	DSC	21.85-22.28	171.22				(Sarı and Karaipekli, 2008)
		DSC	22.33	196	0.143	1.9/ 2.2	883/840	(Hasan, 2010a; Hasan, 2010b)
		DSC	22.1	153				(Kenisarin and Mahkamov, 2007)
		DSC	**17.7-22.8**	**191**				**This study**
		THM	22.4	190		2.4/ 2.2		(Hasan, 2010a)
		THM	**16.03-25.39**	**209**		**1.5/1.7**		**This study**
Capric: lauric acid	Eutectic fatty acid	DSC	21	143				(Hawes et al., 1993)
		DSC	20.78	171.78	0.139	1.9/ 2.3	880	(Hasan, 2010b)
		DSC	**18.9-22.3**	**116**				**This study**
		THM	20.6	179	0.143	1.8/2.12		(Hasan, 2010a)
		THM	**12.8-21.8**	**169**		**1.9/1.8**		**This study**
SP22	Eutectic of fatty acid/ paraffin wax		22-23	160	0.6		1500/1400	(Rubiterm, 2015)
		DSC	24.6	182	0.6	2.5/-	1490/ 1430	(Hasan, 2010b)
		DSC	20.7	109				(Bajare et al., 2011)
		DSC	**16.9-25.3**	**146**				**This study**
		THM	21.6	135	0.6	1.7/ 1.8	1490/1440	(Hasan, 2010a)
		THM	**-**	**-**	**-**	**-**	**-**	**This study**
Micronal®	Paraffin		21	51			980	(BASF, 2012)
		DSC	**20.9-25.8**	**119**				**This study**
		THM	**14.7-17.8**	**60**	**-**	**2.7/3.8**	**-**	**This study**

The heat of fusion values found for all the fatty acids using DSC are smaller than that found using THM again suggesting the sample size has an impact on the results. It would be recommended to assess the material based on the sample size in the system application, for example if a large sample is required THM would give a better indication of material properties due to characterisation of a larger material sample. This method would be more useful for testing the applicability of PCM in a collector device such as that of a PV/T/PCM system due to the large mass of material required.

Melting temperature and heat of fusion affects the thermal energy storage of PCM therefore it was necessary to characterise the PCM to ensure the most suitable PCM was used in the PV/T/PCM experiment and that the correct values were used as inputs for system modelling.

4.5.1 Conclusion of Characterisation Tests

From the results of these tests, it can be seen that in the correct conditions, capric acid could be considered a viable option for use in PV temperature regulation. However, considering air temperatures during summer and winter reach 18°C - 20°C and 8°C (Met Eireann, 2015b), respectively, it is unsuitable in a climate such as Ireland as the melting temperature is too high and it is unlikely that these conditions would be met in order for the PCM to charge.

SP22 has been shown to be an unreliable PCM with problems arising due to segregation. Micronal® is a liquid PCM which has been designed for integration with wet construction processes such as plaster or concrete and would not be suitable for integration in a PV/T/PCM system due to the risk of leakage. There is also uncertainty surrounding its chemical stability after time (as seen from the double peaks in the DSC result).

From the results of these tests it can be seen that capric:palmitic and capric:lauric are potential candidates for integration into a PV/T/PCM system. They have high heats of fusion, are chemically stable and do not undergo segregation. However, considering the climate of Ireland the melting temperature range of capric: palmitic would be more suitable than that of capric: lauric acid as it has a melting point of 21.2 °C approximately, higher than that of capric:lauric at 20.7 °C.

4.6 Long Term Immersion Corrosion Testing

The application of phase change materials as a thermal energy store, particularly in solar energy systems, has been described in detail in Chapter 2. For all of the systems studied in literature, the integration of PCM requires a method of containment. Containment configurations come in the form of microencapsulation and macro-encapsulation. Microencapsulation involves coating individual particles of PCM with a continuous film or coating to produce capsules in a micrometer to millimetre in size (Jamekhorshid et al., 2014). The materials employed in creating the film or coatings are generally synthetic materials such as LDPE, EVA, polystyrene or formaldehyde. Microencapsulation involve capsule sizes above 1000 μm and uses materials such as steel, stainless steel, chromium nickel, aluminium, and plastics (Alam et al., 2015). When a PCM is used as a storage medium corrosion of the container becomes an important factor to be considered when designing a system.

The initial stages of the project involved assessing a means to contain PCM in a PV/T/PCM system in order to minimise cost and thus maximise the economic feasibility of the system, the suitability of two adhesives (CT manufactured by C-TEC and MS 5000 supplied by Action Adhesives) to seal a sample stainless steel container was investigated. The watertight containers are shown in Figure 4.13(a) and (b) sealed with CT1 and MS 5000, respectively.

The containers were tested for approximately five days with liquid phase PCM. The PCM had penetrated the sealant by the end of the test period. The bonding properties of the adhesives were broken down by the acid in the PCM resulting in failure of the sealant, as shown in Figure 4.14 (a) and (b). It can be clearly seen that both adhesives detached completely from the wall of the container allowing the leakage of the PCM from the container. As these materials were deemed unfit for use with PCM, the following experiments were set up to test the suitability of the use of PCM with other commonly used materials.

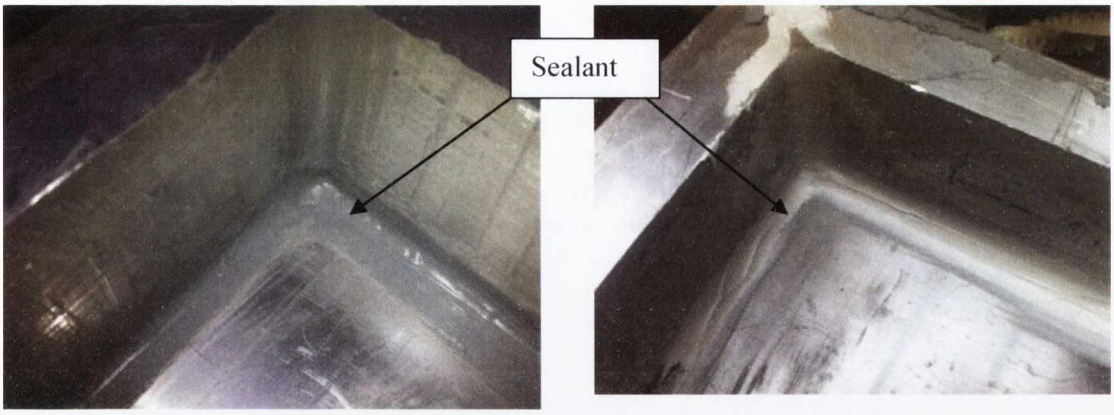

(a) (b)

Figure 4.13: Sample aluminium containers sealed using (a) CT 1 and (b) MS 5000

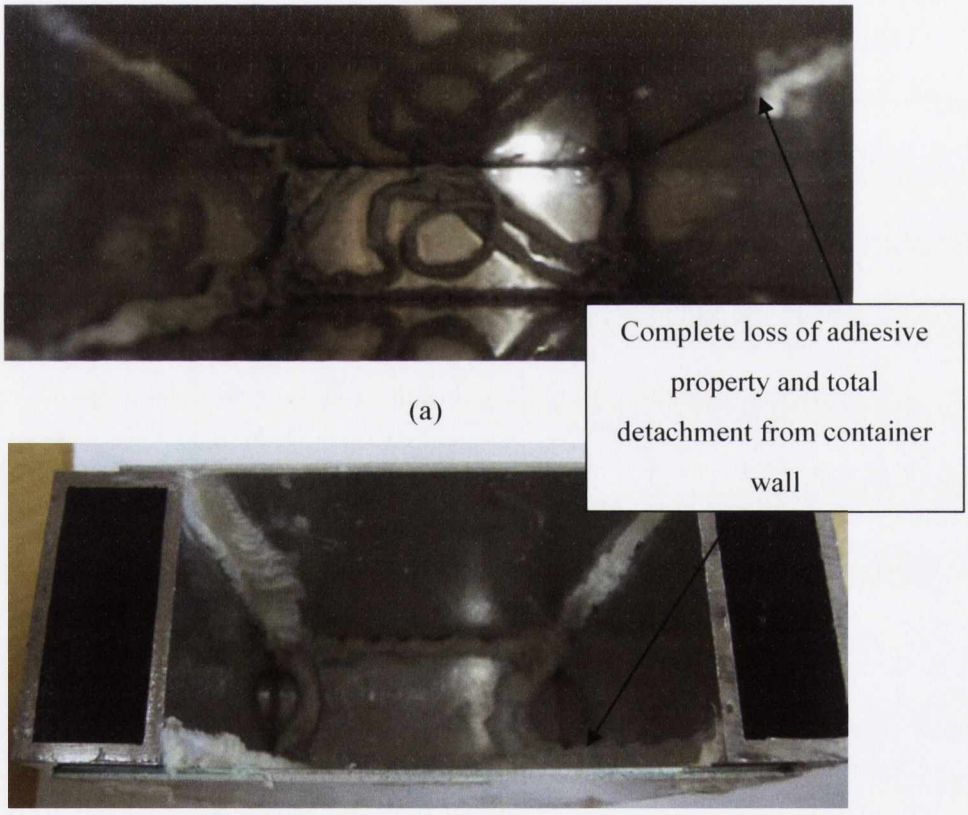

(a)

(b)

Figure 4.14: Effects of PCM on adhesive (a) CT 1 and (b) MS 5000

The corrosive nature of certain PCM with respect to containment materials has been previously investigated, although those tests were performed under programmed cyclic testing of PCM (Porisini, 1988; Sarı and Kaygusuz, 2003; Farrell et al., 2006) or for time periods of less than 500 days (Cabeza et al., 2001a; Cabeza et al., 2001b; Cabeza et al., 2005; Moreno et al.,

2014). Salt hydrates and fatty acids have been investigated; however, the corrosive nature of fatty acid eutectics has yet to be explored. This study assesses the corrosion rate of materials by PCM over a real-time and an extended time period compared to previous studies to ensure long operational life of the system. As such the following subsections describe experiments which examine the corrosion of six different materials with five PCM.

4.6.1 Phase Change Material and Material Samples

The materials being tested for corrosion resistance and the PCMs they were in contact with as part of the test are shown in Table 4.2.

Table 4.2: List of materials and PCM used in corrosion experiments

Material	**PCM**
Copper	Capric acid
Brass	Capric:palmitic acid
Aluminium	Capric:lauric acid
Stainless steel	SP22
Mild steel	Micronal®
Perspex	

Melting temperatures of the PCM ranged from approximately 20 °C to 30 °C (as described in 4.5). These PCM were selected for further investigation as their transition temperatures correspond to the operating temperature of the cooling/heating in a PV/T/PCM system which make them a potential candidate for use in the full-scale experiment.

Five materials that are commonly used in industrial and domestic applications were used in the experiment. The metals were aluminium, brass, copper, stainless steel, steel and the plastic used was Perspex. The chemical compositions of the materials are presented in Table 4.3. The samples were cut from larger pieces of materials and each had dimensions of 50 mm x14 mm and a depth of 2 mm. The depth of the material is the same as that used in the full scale PV/T/PCM experiment.

Table 4.3: Composition of metals and plastic samples

		Material					
		Aluminium	**Brass**	**Copper**	**Stainless Steel**	**Steel**	**Perspex**
Chemical Composition (%)	**Aluminium (Al)**	>99.08	<0.05				
	Titanium (Ti)	<0.05					
	Zinc (Zn)	<0.4	>35.2				
	Silicon (Si)	<0.05			<0.75		
	Magnesium (Mg)	<0.05					
	Copper (Cu)	<0.25	<64	>99.95			
	Iron (Fe)	<0.07	<0.01		>69.9	>99.26	
	Manganese (Mn)	<0.05			<2.0	<0.9	
	Nickel (Ni)		<0.3		<14		
	Lead (Pb)		<0.1	0.005			
	Phosphorous (P)				<0.045	<0.04	
	Bismuth (Bi)			0.001			
	Carbon (C)				<0.08	<0.2	
	Chromium (Cr)				<18		
	Sulfur (S)				<0.03	<0.05	
	Molybdenum (Mo)						
	Nitrogen (N)				<0.1		
	Other		<0.2				Synthetic polymers

4.6.2 Results and Discussion of Immersion Corrosion Tests

The results of the corrosion tests are presented based on the effect of each individual PCM on the different material samples. As a result each graph shows the time dependent effects of one PCM type on the material samples.

The results of the experiment with capric acid are shown in Figure 4.15 and Figure 4.16 for mass loss and corrosion rate, respectively.

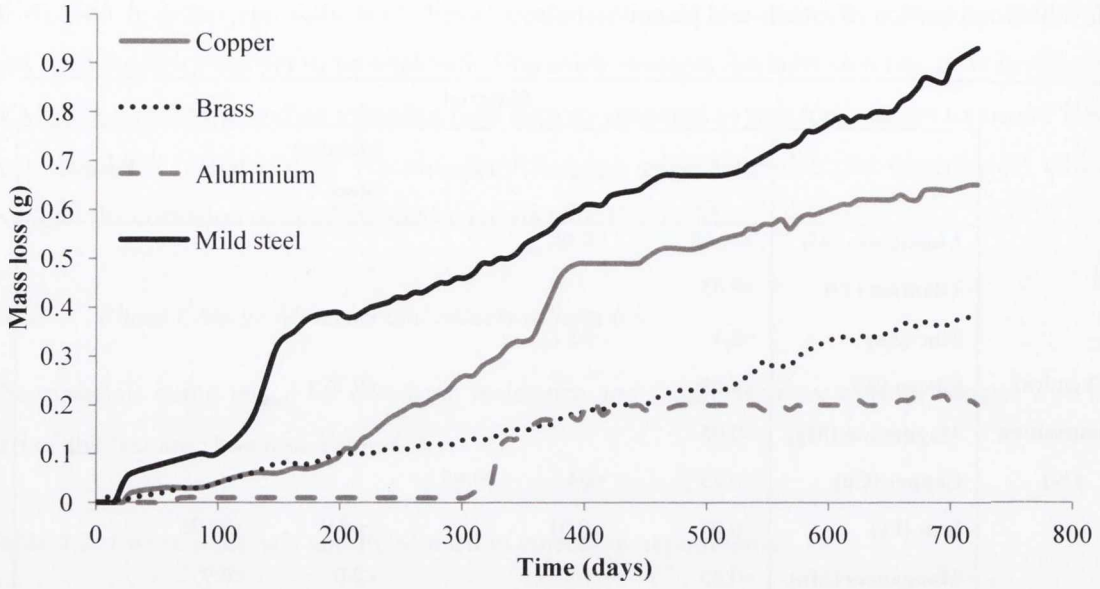

Figure 4.15: Material mass loss due to immersion in capric acid

The mass loss of mild steel and copper can be seen to increase relatively constantly throughout the duration of the experiment, with mild steel having the highest mass loss of all the material samples losing 0.93 g by Day 722 and copper the second highest with a mass loss of 0.65 g. Brass has one of the higher mass losses in the first 200 days reaching 0.08 g, however the rate of mass loss decreases due to the presence of zinc as an alloy element and results in mass loss of 0.37 g following 722 days. There is negligible mass loss (less than 0.01 g) recorded from stainless steel or Perspex due to capric acid

Aluminium shows minimal mass loss of approximately 0.01 g in the first 300 days of the experiment; however following this period the mass loss increases to 0.19 g for a short period before reaching steady state for the remainder of the experiment. Over the initial 300 days, aluminium forms a thin oxide layer which minimises. However, following this period there is a sudden loss in mass, this is caused by pitting corrosion. The pits are caused by local ruptures in the metal. Following the pitting corrosion, the propagation stage is reached. This occurs when the formation of aluminium ions at the bottom of the pit which, under certain conditions, will form a film of aluminium chloride or aluminium oxychloride in the pit and stabilise it. After a while the aluminium chloride will hydrolyse into aluminium hydroxide which precipitates at the rim of the pit and covers the opening, which eventually hinders exchange of ions and slows down the corrosion process (Gustafsson, 2011).

The corrosion rate of each material due to being in contact with capric acid over the course of the experiment is presented in Figure 4.16. Stainless steel and Perspex remain unaffected by the PCM of less than 0.01 g/cm^{2}year. The corrosion rate of all other material samples vary for the first 400 days before stabilising and maintaining a constant corrosion rate for the remainder of the experiment which were found to be 0.022 g/cm^{2}year, 0.013 g/cm^{2}year, 0.01 g/cm^{2}year and 0.03 g/cm^{2}year for copper, brass, aluminium and mild steel, respectively.

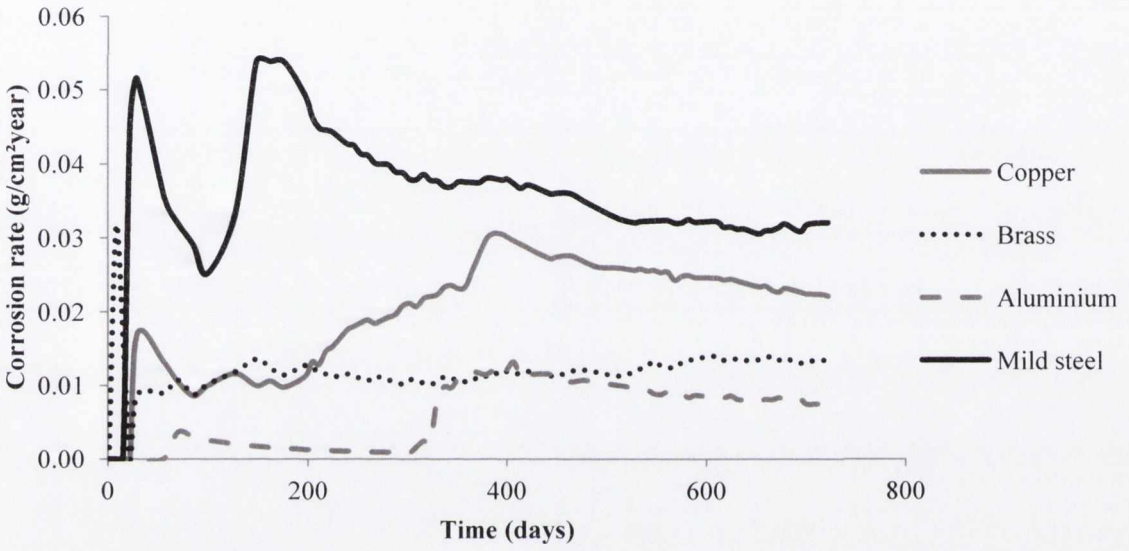

Figure 4.16: Corrosion rate during immersion tests of material samples with capric acid

The mass loss of material samples due to the immersion in the eutectic fatty acid capric:palmitic is presented in Figure 4.17. Stainless steel and Perspex have been unaffected by the fatty acid eutectic with mass loss values of less than 0.05 g. Mass loss of mild steel is high, 1.09 g, compared to copper, brass and aluminium materials which have losses of 0.48 g, 0.27 g and 0.34 g at the end of the experiment.

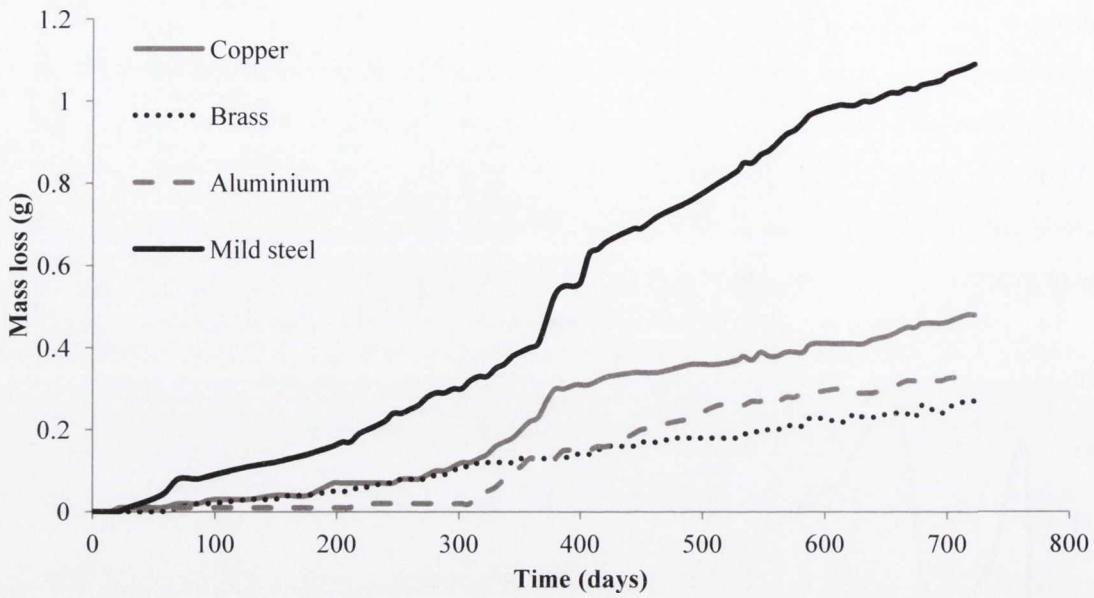

Figure 4.17: Material mass loss due to immersion in capric:palmitic acid

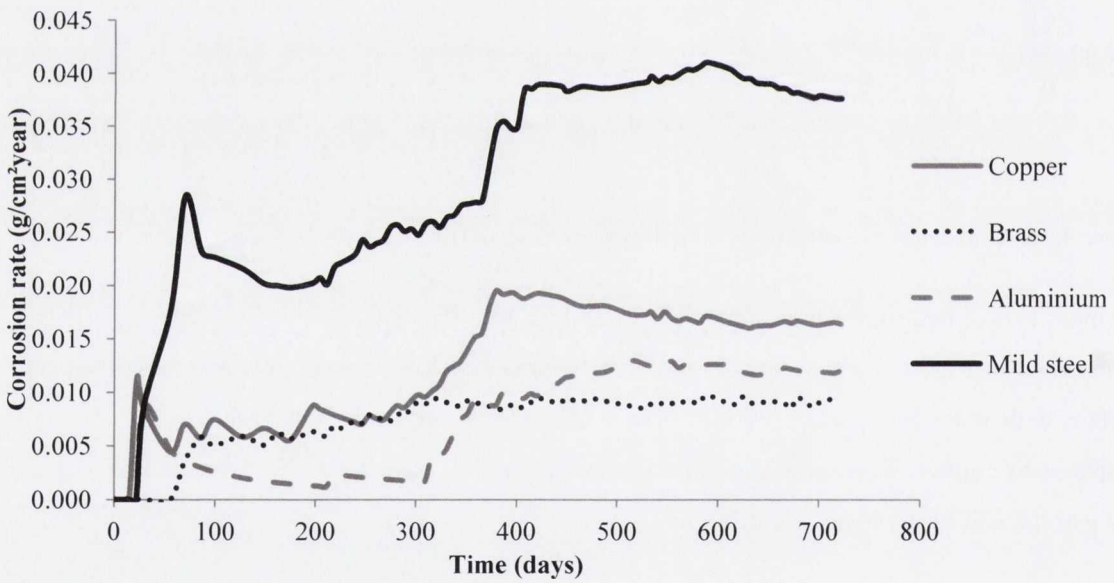

Figure 4.18: Corrosion rate during immersion tests of material samples with capric:palmitic acid.

The corrosion rate of the samples immersed in capric:palmitic acid (Figure 4.18) showed the corrosion rate of stainless steel and Perspex was negligible (less than 0.05 g/cm^{2}year). However, the remaining sample materials show that the corrosion rate is consistently increasing for the duration of the experiment up until Day 400 where upon the graphs reach steady state after reaching at 0.45 g/cm^{2}year, 0.24 g/cm^{2}year, 0.31 g/cm^{2}year and 1.02 g/cm^{2}year for copper,

brass, aluminium and mild steel, respectively. Capric acid is more corrosive than capric:palmitic acid when considering copper and brass as the corrosion rate is higher for capric acid by approximately 0.006 g and 0.004 g, respectively. However, capric:palmitic acid presented corrosion rates higher by approximately 0.01 g and 0.005 g for aluminium and mild steel than that of capric acid.

The aggressive nature of capric:lauric acid can be seen in Figure 4.19 which shows the mass loss of each material sample due to immersion in the fatty acid eutectic. Perspex and stainless steel have negligible corrosion rates of less than 0.001 g. Similar to the material reaction to immersion in previous fatty acids, aluminium is initially unaffected by the PCM, however following Day 300 the material showed an initial mass loss of 0.01 g which increases to 0.15g on Day 400 which continues to increase to 0.27 g on Day 500 which remains at approximately that value for the remainder of the experiment. As can be seen from the graph in Figure 4.19 the mass loss of mild steel, copper and brass samples was relatively constant over the test period which showed corrosion rates of 0.037 g/cm^{2}year, 0.016 g/cm^{2}year and 0.008 g/cm^{2}year.

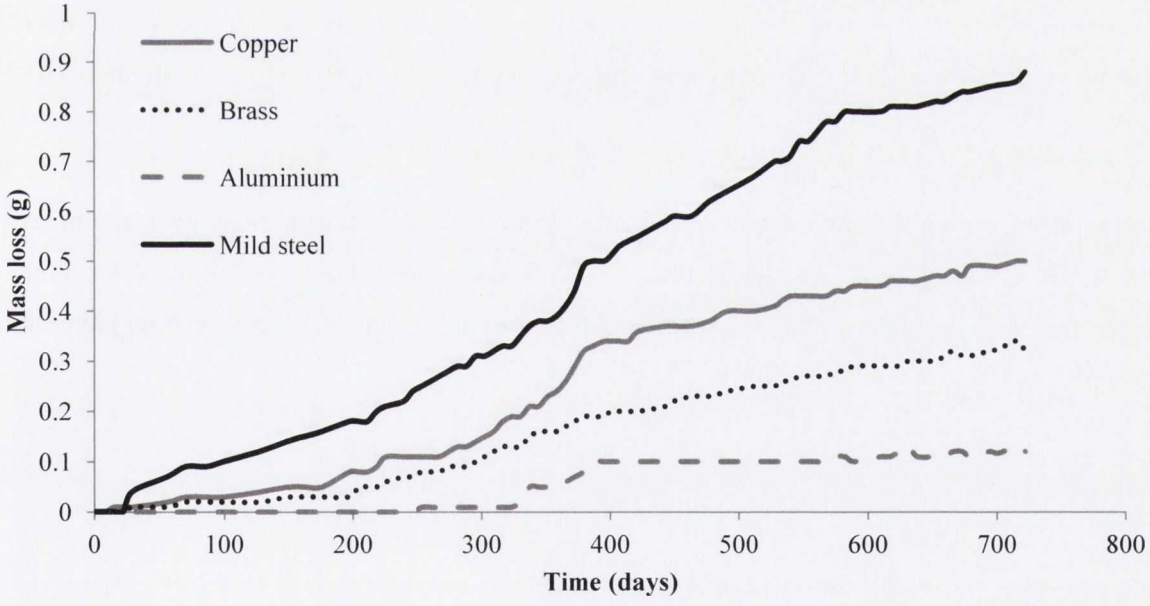

Figure 4.19: Material mass loss due to immersion in capric:lauric acid

The corrosion rate of capric:lauric acid (Figure 4.20) on all of the material samples is similar to that of the other fatty acid materials presented above. Stainless steel and Perspex remain unaffected by the PCM as the mass loss is approximately 0 g.

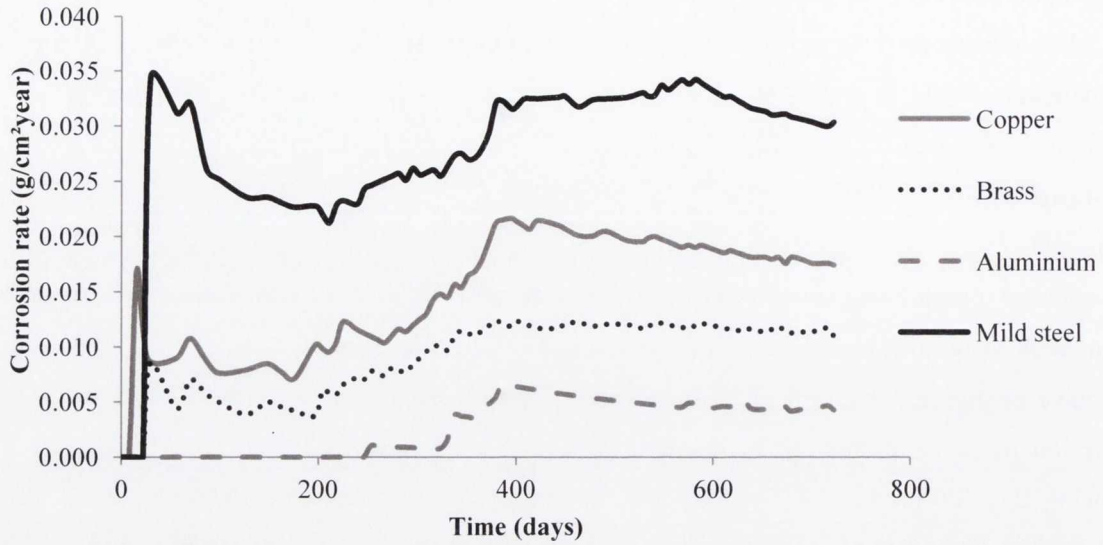

Figure 4.20: Corrosion rate during immersion tests of material samples with capric: lauric acid

The corrosion rate for aluminium was initially relatively low for the first 300 days at 0.001 g/cm^{2}year before increasing to approximately 0.004 g/cm^{2}year for the remainder of the experiment. Mild steel has the highest corrosion rate, stabilising at approximately 0.03 g/cm^{2}year followed by copper and brass with corrosion rates of 0.017 g/cm^{2}year and 0.01 g/cm^{2}year, respectively.

It was noted during the early stages of the experiment, test tubes containing copper and brass immersed in a fatty acid presented a blue colour of the copper and brass salts (sulphates or chlorides) in the test tubes. This was seen in all three fatty acid samples (capric, capric: palmitic acid and capric: lauric acid) as shown in Figure 4.21.

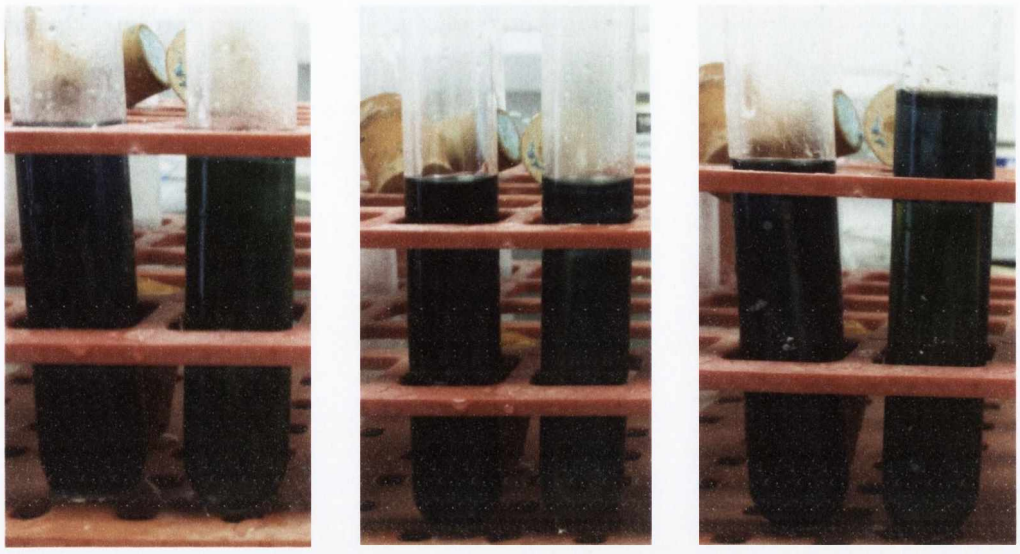

(a) (b) (c)

Figure 4.21: Copper and brass samples in (a) capric acid (b) capric:palmitic acid (c) capric:lauric acid

SP22 was found to be less aggressive than the fatty acid PCM (Figure 4.22). Aluminium was found to be most affected by the salt hydrate having one of the largest mass losses at the end of the experiment at 1.18 g. The mass loss of mild steel increased after 400 days to approximately 0.08 g. The remaining material samples have been unaffected by the salt hydrate immersion tests.

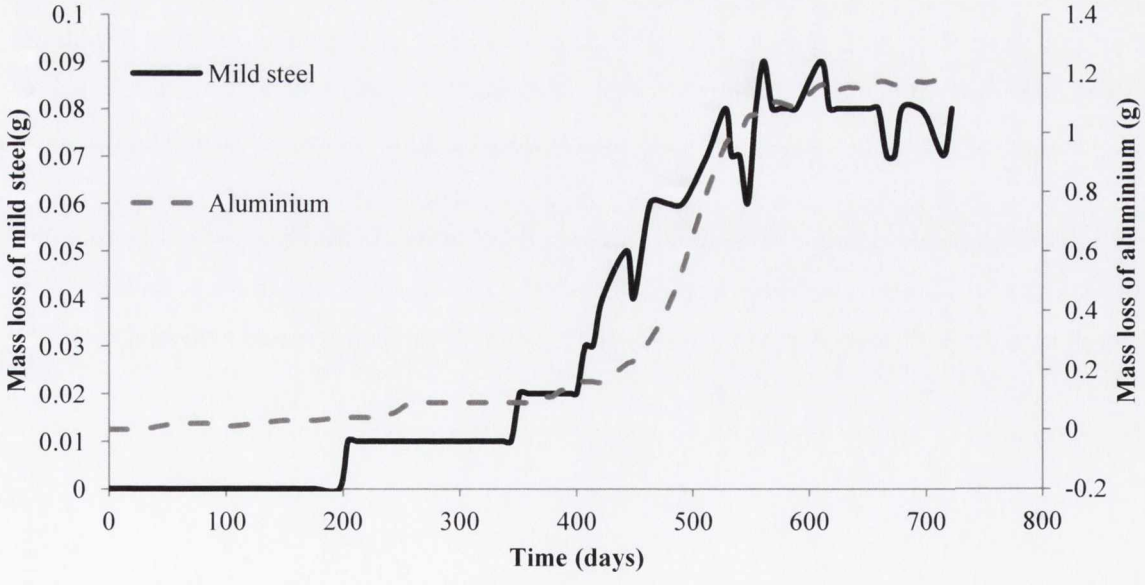

Figure 4.22: Material mass loss due to immersion in SP22

The corrosion rate of aluminium (0.041 g/cm^{2}year) was much higher than any of the other material samples (Figure 4.23). Nearly all had negligible corrosion rates except mild steel which recorded a corrosion rate of 0.002 g/cm^{2}year.

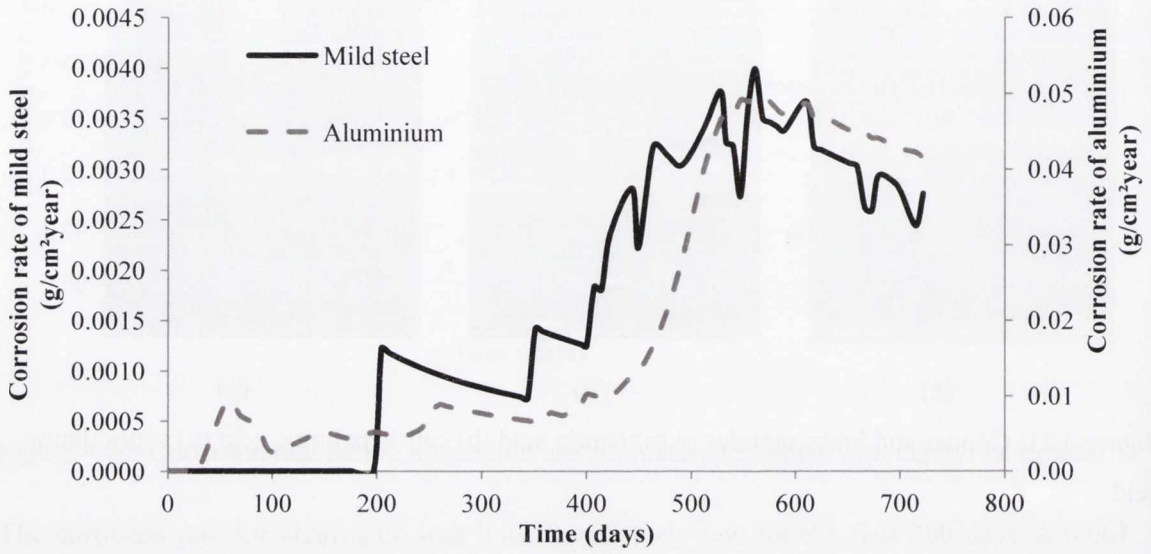

Figure 4.23: Corrosion rate during immersion tests of material samples with SP22

It was observed that the salt hydrate in the test tube with aluminium expelled a gas to cause the PCM to create air voids. This was caused by a chemical reaction between the aluminium and salt which emits hydrogen (Porciúncula et al., 2012).

Mild steel with Micronal® presented much higher mass loss than any other material tested, as shown in Figure 4.24. The mass loss of mild steel reached a value of approximately 0.4 g compared to the corrosion weight loss of all other material samples being less than 0.04 g.

The evolution of corrosion rate of materials immersed in Micronal® is presented in Figure 4.25. Initially, the mild steel corrosion rate is high however following 150 days it stabilises at approximately 0.015 g/cm^{2}year. Mild steel is most susceptible to corrosion by Micronal®.

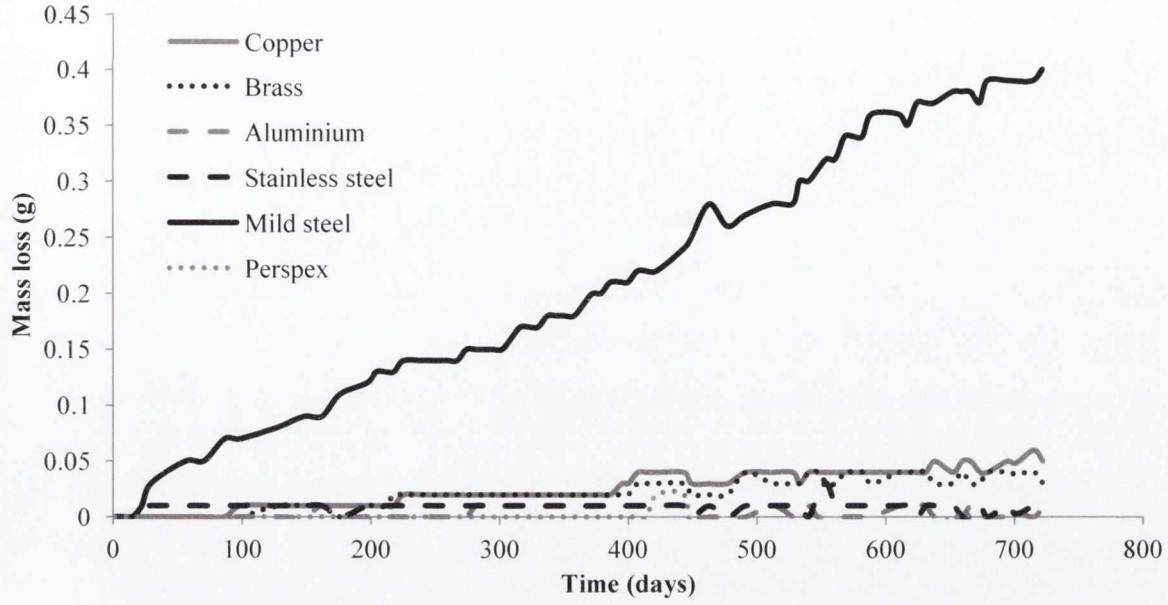

Figure 4.24: Material mass loss due to immersion in Micronal®

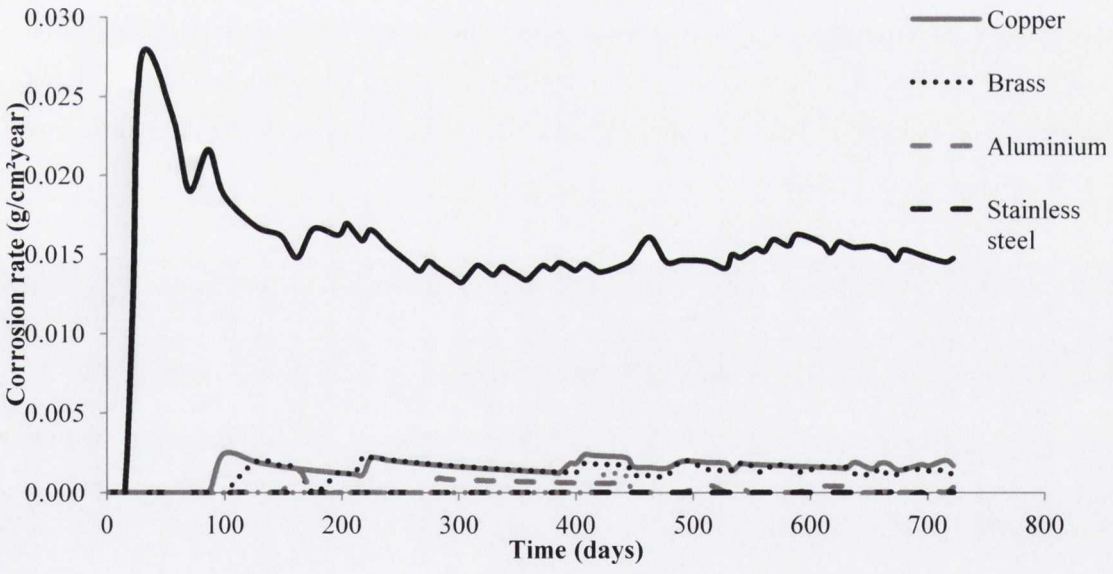

Figure 4.25: Corrosion rate during immersion tests of material samples with Micronal®

On comparing the corrosion results of the fatty acids, capric acid appears to be the most aggressive overall. SP22 has been shown to undergo aggressive corrosion when paired with aluminium. However, when combined with other sample materials the corrosive effect was minimal which is in contrast with the findings of Moreno et al. (2014). However, it must be

noted that SP22 is a mixture of salt hydrate and organic compounds which would likely reduce the corrosive nature.

4.6.3 Metallographic Investigation

The samples were investigated under a microscope for signs of corrosion on Days 1, 25, 200 and 540 using magnifications of 200X, 3000X and 6000X. However, due to the transparent nature of Perspex this material could not be used in the SEM imaging. Stainless steel has not been affected by the PCM in any immersion tests and as a result there is no presentation of images of stainless steel. From photographic images, the rate of corrosion can be visually observed as the size of the pitting in some samples increases with the length of time it was immersed in the PCM.

4.6.3.1 Capric Acid

As shown in Figure 4.26 - Figure 4.29, capric acid is one of the more aggressive PCMs tested. Pitting can be seen in the copper (Figure 4.26) following 25 days of immersion in capric acid which reflected the mass loss of 0.02 g at this stage of the experiments considering the initial mass was 10.51 g. The entire surface layer on the copper has been removed by Day 540 along with a mass loss of 0.57 g (Figure 4.26c) as there are no vertical indents as seen in Figure 4.26(a) which was taken on Day 1.

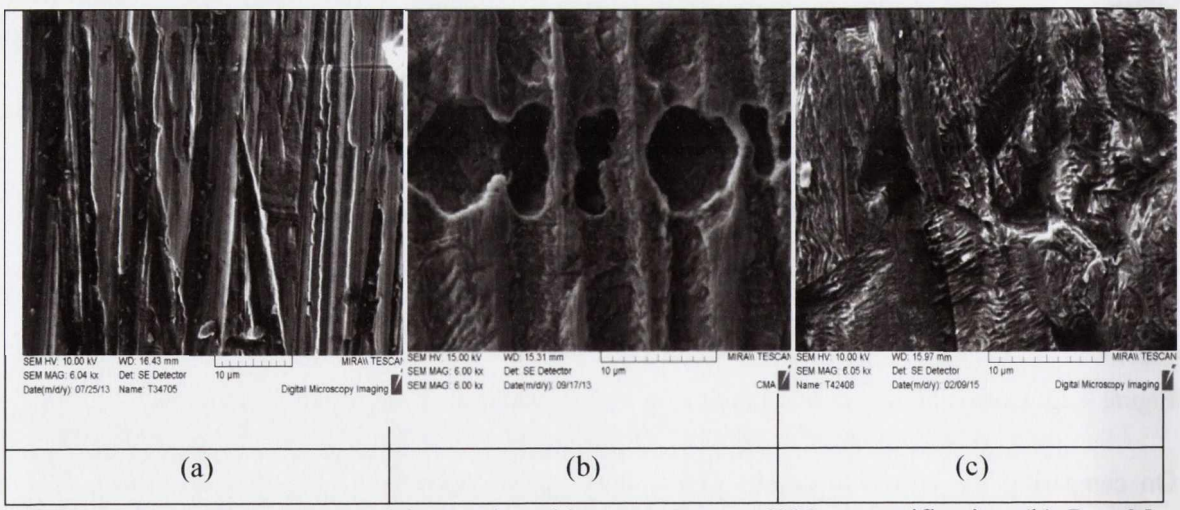

Figure 4.26: Copper immersed in capric acid on (a) Day 1 6000x magnification (b) Day 25 6000x magnification (c) Day 540 6000x magnification

Similarly, brass had an initial mass of 10.12 g and was corroded in the same manner as copper. However, this occurred at a slower rate as on Day 540 the material sample has evidence of

severe pitting (as seen in Figure 4.27) although there still some evidence of the surface layer being intact due to the vertical indents which is expected as the mass loss of 0.29 g is less than that of copper and capric acid.

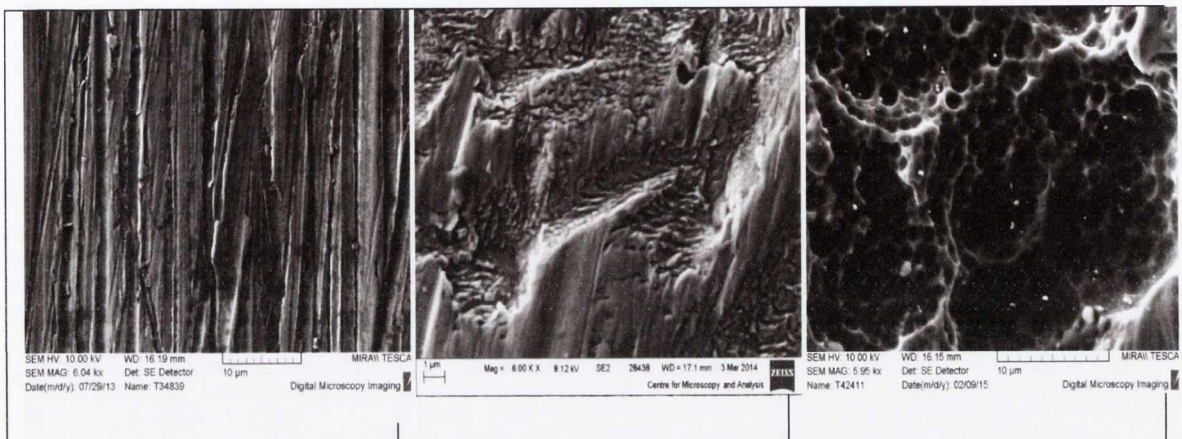

(a) (b) (c)

Figure 4.27: Brass immersed in capric acid on (a) Day 1 6000x magnification (b) Day 200 6000x magnification (c) Day 540 6000x magnification

Aluminium had an initial mass of 3.13g and can be seen to avoid excessive corrosion up to Day 200 as the horizontal textured lines are evident this is also shown in the mass loss of 0.01 g (Figure 4.28b). The pitting is clearly seen in the images taken on Day 540 Figure 4.28(c) when the corrosion got progressively worse as the mass loss was 0.2 g.

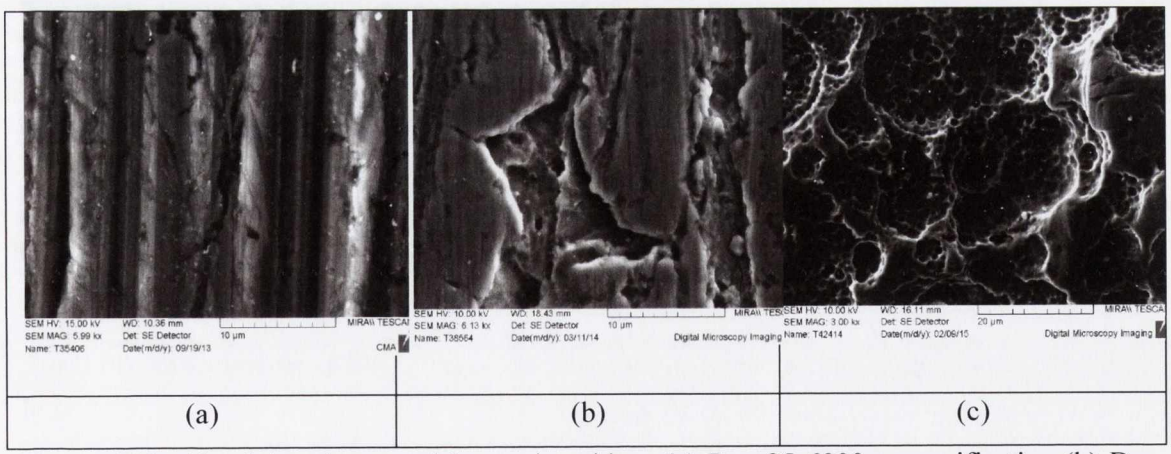

(a) (b) (c)

Figure 4.28: Aluminium immersed in capric acid on (a) Day 25 6000x magnification (b) Day 200 6000x magnification (c) Day 540 3000x magnification

The mass loss and corrosion rate of mild steel in capric acid which was 0.83 g and 0.031 g/cm^{2}year on Day 722 showed that the material was adversely affected by the PCM. The images

shown in Figure 4.29 reflect this and although there is no deep pitting, the layer on the surface of the material can be seen to change over time as it is being worn away by the corrosive PCM.

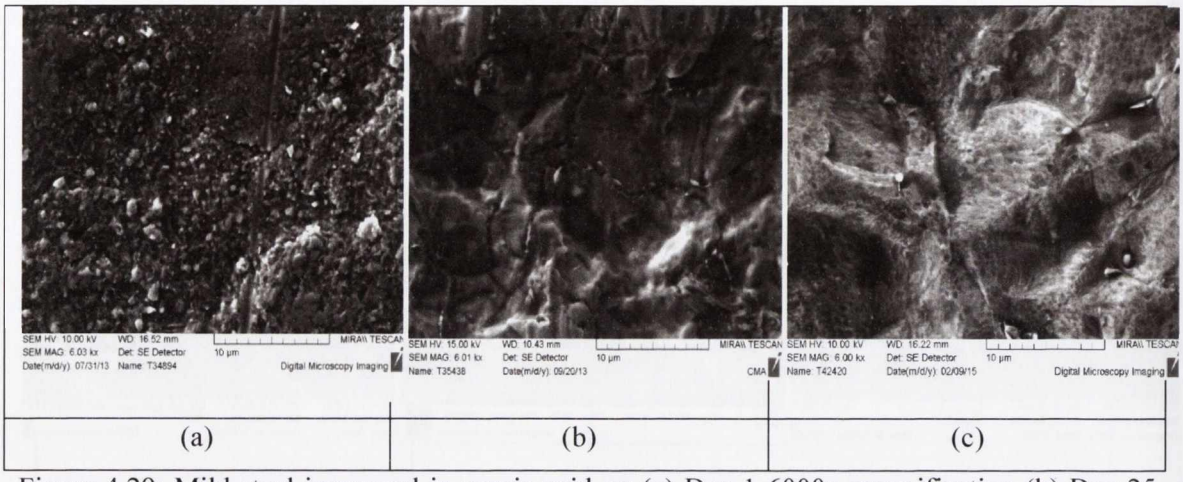

Figure 4.29: Mild steel immersed in capric acid on (a) Day 1 6000x magnification (b) Day 25 6000x magnification (c) Day 540 6000x magnification

4.6.3.2 Capric:palmitic Acid

Capric:palmitic has been shown to be a corrode metals when considering the mass loss and corrosion rate results of the gravimetric study.

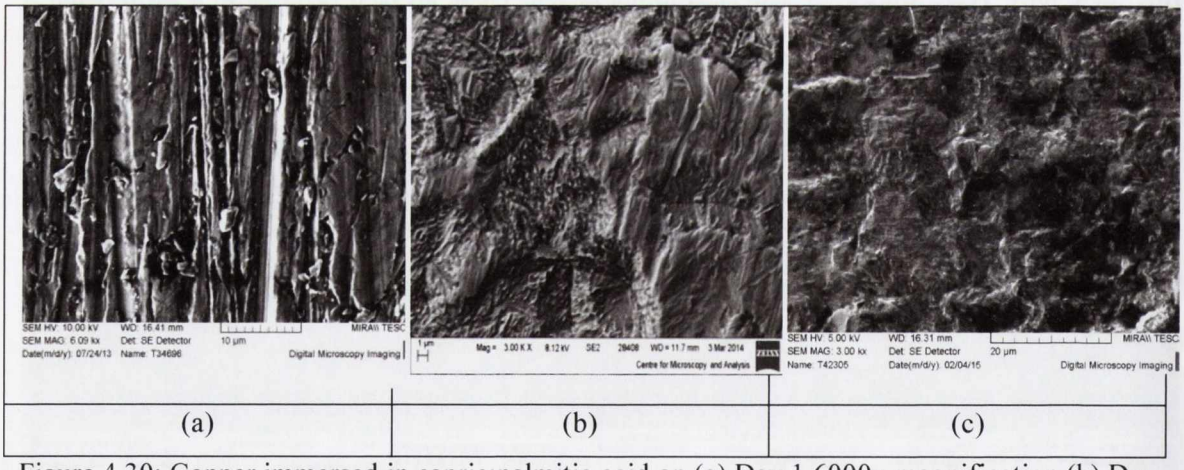

Figure 4.30: Copper immersed in capric:palmitic acid on (a) Day 1 6000x magnification (b) Day 200 3000x magnification (c) Day 540 3000x magnification

Copper had an initial mass of 10.65 g and can be seen to be affected by the corrosive nature of capric:palmitic acid by Day 200 the mass had reduced by 0.07 g. The vertical lines are barely visible and vast areas of pitting can be seen to be forming Figure 4.30(b). Day 540 shows the

surface of the sample has been corroded by the PCM Figure 4.30(c) which was a result from the corrosion of the surface and a mass loss of 0.37 g.

Similar to the copper results, brass immersed in capric:palmitic acid shows areas of pitting after Day 200 (Figure 4.31b) and the entire surface can be seen to be full of large areas of pitting (Figure 4.31c) by Day 540. The corrosion shown the images reflect the mass loss found over the course of the immersion corrosion tests. The initial mass of 10.19 g was reduced by 0.05 g by Day 200 and by 0.19 g on Day 540.

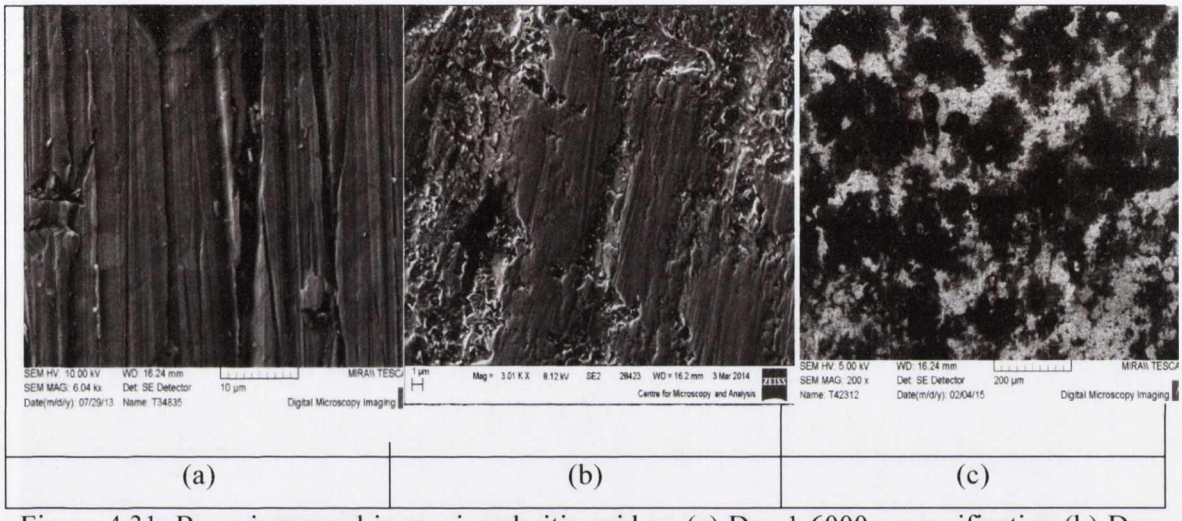

Figure 4.31: Brass immersed in capric:palmitic acid on (a) Day 1 6000x magnification (b) Day 200 3000x magnification (c) Day 540 200x magnification

The aluminium sample immersed in capric: palmitic acid can be seen in Figure 4.32. The sample withstands the corrosive effect of the material until approximately 200 days when pitting can be seen in image (b) along with some of the intact surface material of the sample which would reflect a mass loss of 0.01 g. By Day 540 the surface has been badly corroded as no vertical lines can be seen and this is shown in mass loss of 0.27 g, an 8.6 % loss on the initial mass.

Mild steel can be seen to be corroded from early on in the experiment, as on Day 25 small areas of pitting are obvious which was also seen in the mass loss of 0.1 g (Figure 4.33b) and the surface of the sample can be seen to have vast areas of pitting (Figure 4.33c) by Day 540 which showed a mass loss of 0.85 g, 9.1 % of the total initial mass.

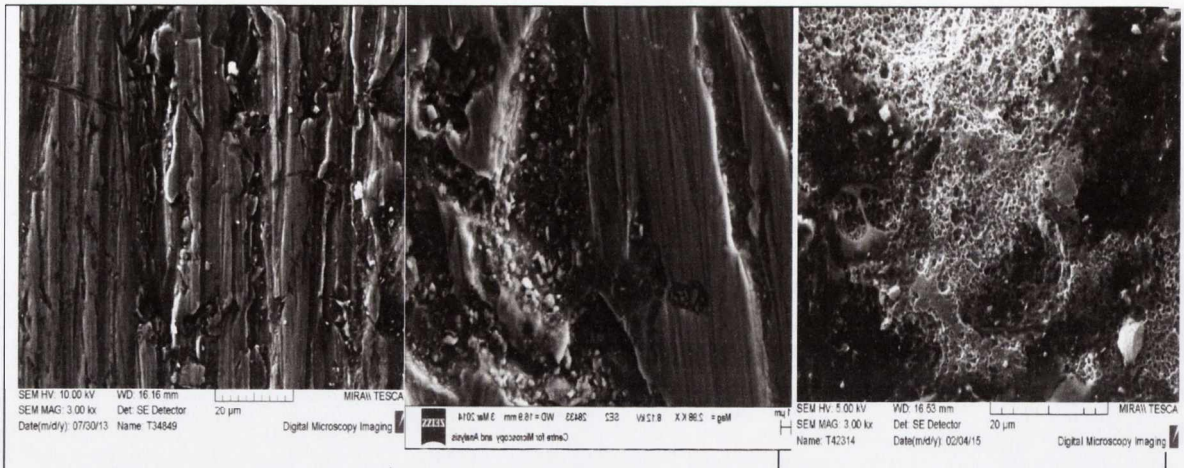

Figure 4.32: Aluminium immersed in capric:palmitic acid on (a) Day 1 3000x magnification (b) Day 200 3000x magnification (c) Day 540 3000x magnification

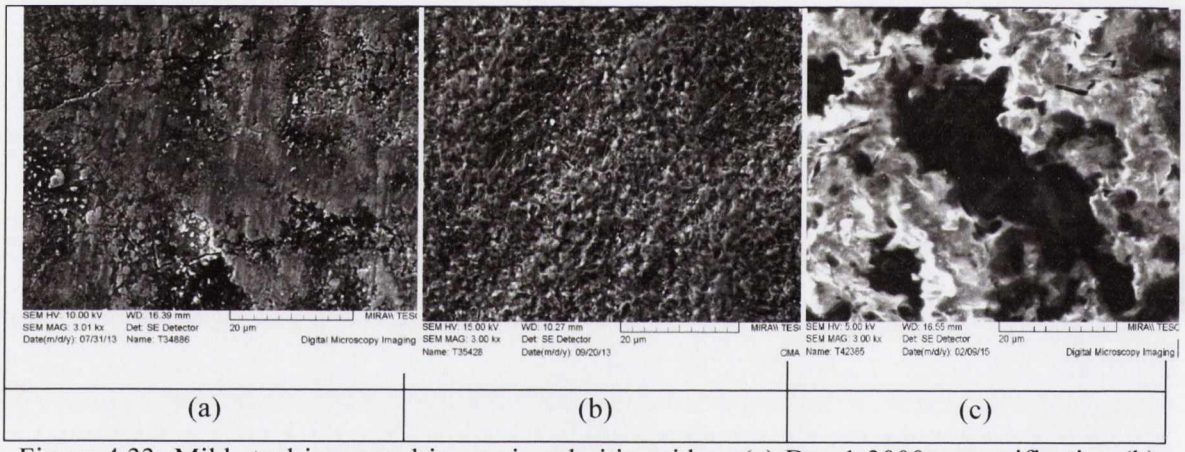

Figure 4.33: Mild steel immersed in capric:palmitic acid on (a) Day 1 3000x magnification (b) Day 25 3000x magnification (c) Day 540 3000x magnification

4.6.3.3 Capric:lauric Acid

Capric:lauric acid showed the same corrosion patterns to that of the previous two fatty acid PCM. Copper and brass samples, as presented in Figure 4.34 and Figure 4.35; appear to have signs of pitting by Day 25 which get progressively worse as the experiment progresses.

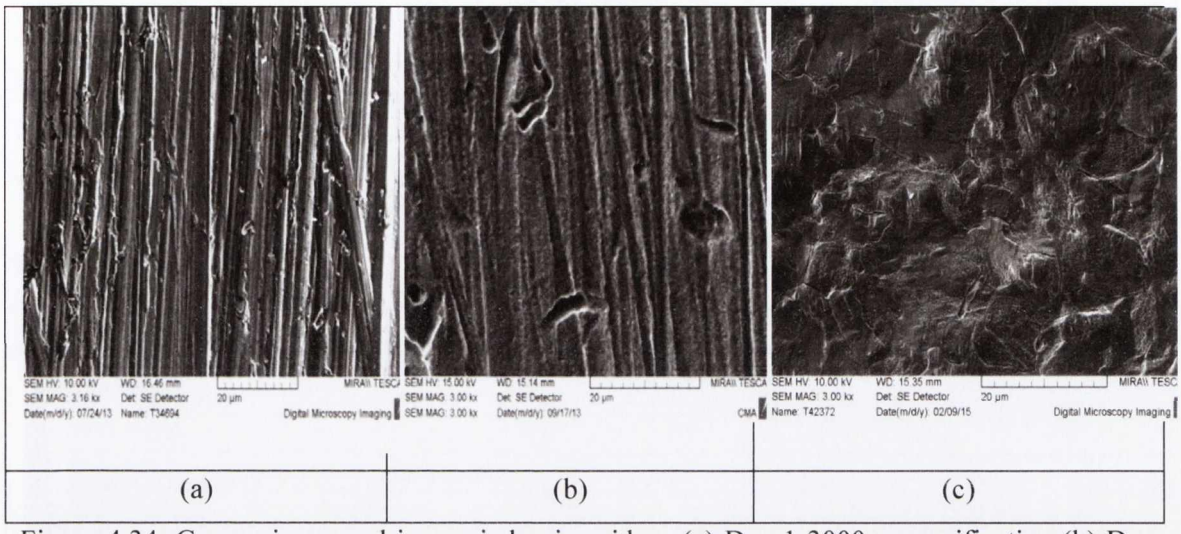

Figure 4.34: Copper immersed in capric:lauric acid on (a) Day 1 3000x magnification (b) Day 25 3000x magnification (c) Day 540 3000x magnification

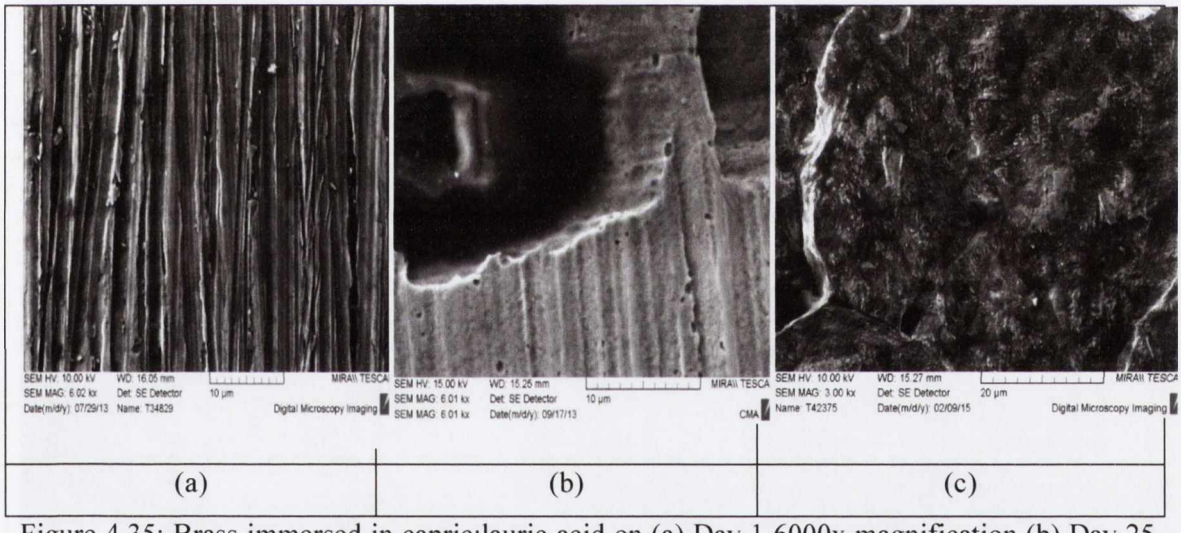

Figure 4.35: Brass immersed in capric:lauric acid on (a) Day 1 6000x magnification (b) Day 25 6000x magnification (c) Day 540 3000x magnification

By Day 540 it can be seen the surface of the samples are completely corroded. The images showed the corrosion process whereby there was a mass loss of 0.01 g on Day 25 by both materials. Copper has shown to be more susceptible to corrosion by capric:lauric acid than that of brass as the mass loss was shown to be 0.43 g by Day 540 for copper and 0.26 g for brass which is reflected in the images taken using SEM.

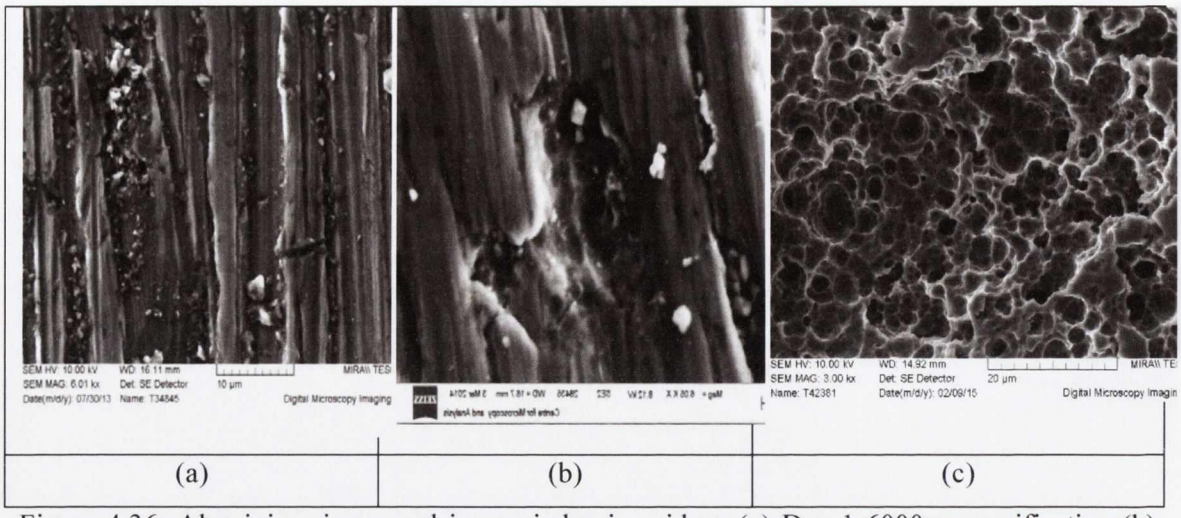

Figure 4.36: Aluminium immersed in capric:lauric acid on (a) Day 1 6000x magnification (b) Day 200 6000x magnification (c) Day 540 3000x magnification

The microscopic evaluation of mild steel immersed in capric:lauric acid is presented in Figure 4.37. The grain boundaries of mild steel can be seen in (b) which indicates the weak points of the material that are most susceptible to corrosion by the fatty acid eutectic and have reported a mass loss of 0.18 g by Day 200. The material is seen to be further corroded by Day 540 with the surface of the material almost entirely corroded where the mass loss was found to be 0.71 g.

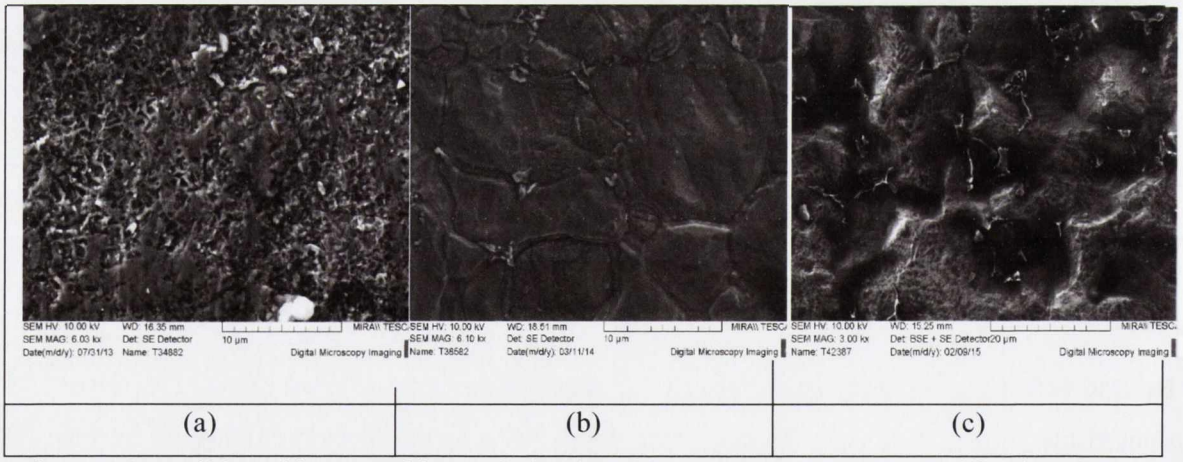

Figure 4.37: Mild steel immersed in capric:lauric acid on (a) Day 1 6000x magnification (b) Day 200 6000x magnification (c) Day 540 3000x magnification

4.6.3.4 Salt Hydrate SP22

SP22 has been shown to result in severe corrosion on aluminium in the gravimetric analysis and minor corrosion on the remainder of the samples. It is interesting to note that corrosion may not be evident in the gravimetric analysis but the initial stages of corrosion can be seen using SEM

imaging. An example of this is copper immersed in SP22 as pitting can be seen in Figure 4.38(c) and had a mass loss of 0.02 g by Day 540. This is due to the large magnification of the SEM images which showed the initial stages of corrosion which were not large enough to be determined by the scale.

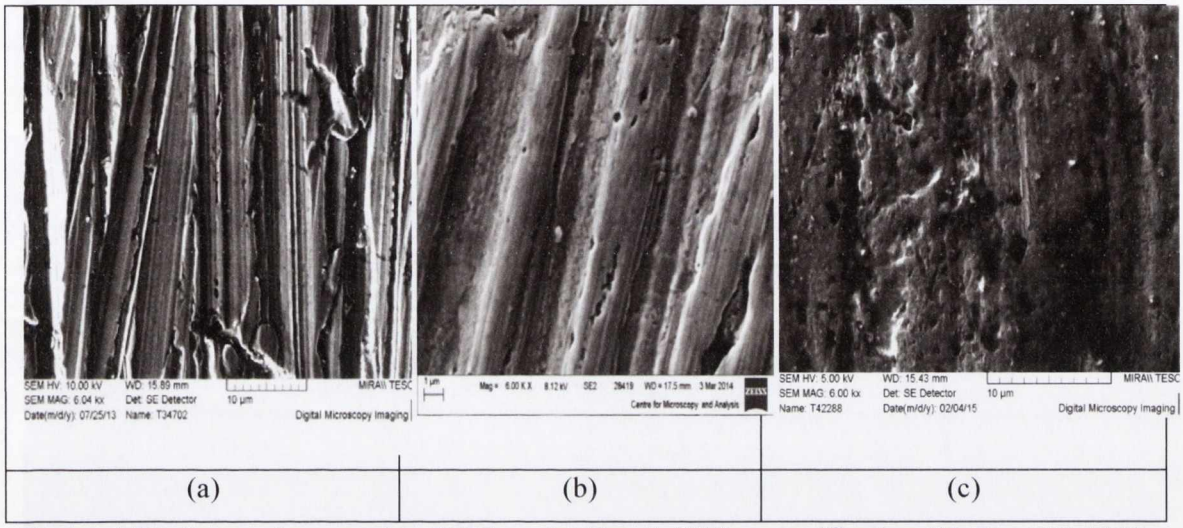

Figure 4.38: Copper immersed in SP22 on (a) Day 1 6000x magnification (b) Day 200 6000x magnification (c) Day 540 6000x magnification

Images of aluminium which has been immersed in SP22 are presented in Figure 4.39. The aggressive corrosion is evident as pitting can be seen in (b) after only 25 days.

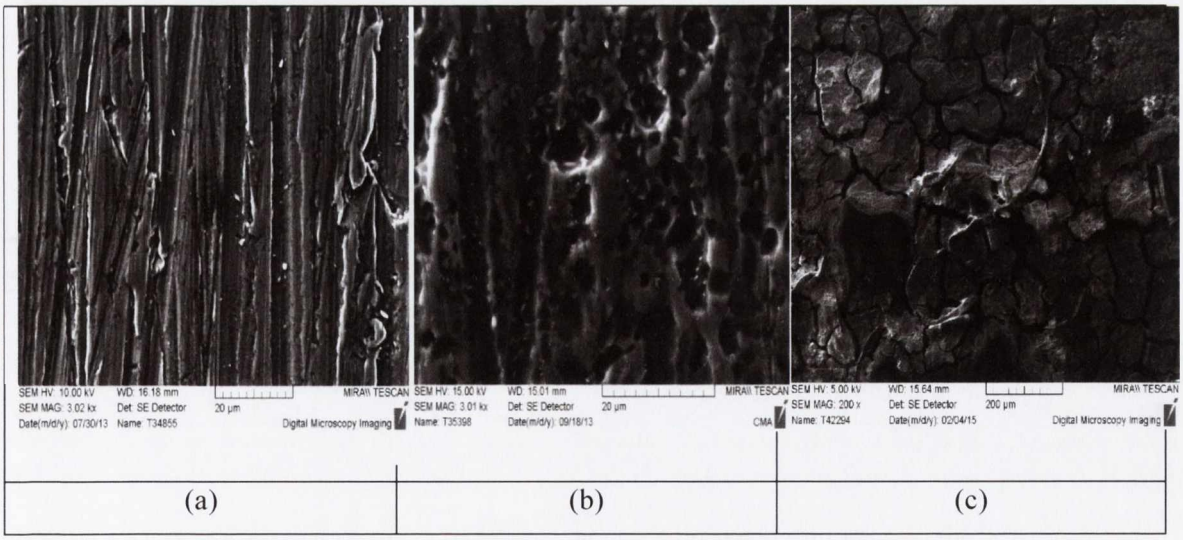

Figure 4.39: Aluminium immersed in SP22 on (a) Day 1 3000x magnification (b) Day 25 3000x magnification (c) Day 540 200x magnification

The grain boundaries can be seen to be depleted in (c) which has been taken on Day 540 when mass loss of 0.01 g was reported. The delay in mass can be explained by the initial low mass of the material sample, 3.14 g. Such extensive corrosion can compromise the mechanical properties of materials.

4.6.3.5 Micronal®

Although, copper and brass immersed in Micronal® did not show signs of corrosion in the gravimetric analysis, early stage corrosion can be seen in Figure 4.40 and Figure 4.41 for these materials. Small pockets of pitting in the images taken on Day 540 suggest given time the material will further corrode which is also shown by the progressive mass loss of 0.01 g on Day 200 and 0.04 g on Day 540 experienced by both materials.

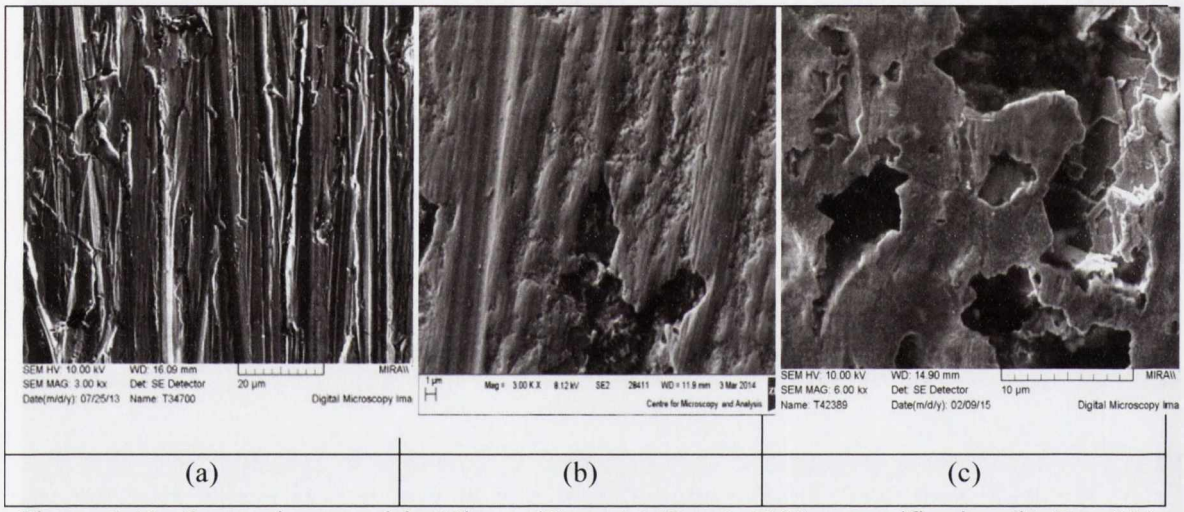

Figure 4.40: Copper immersed in Micronal® on (a) Day 1 3000x magnification (b) Day 200 3000x magnification (c) Day 540 6000x magnification

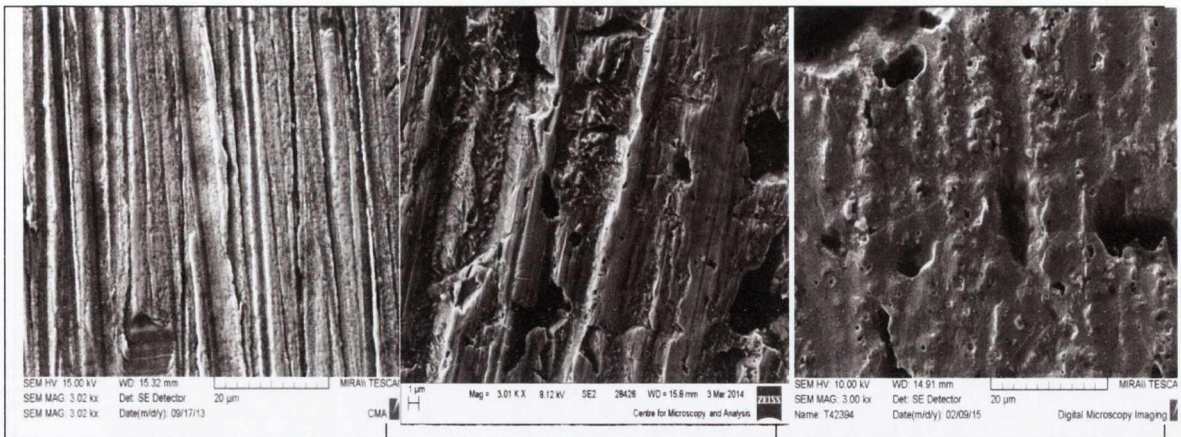

Figure 4.41: Brass immersed in Micronal® on (a) Day 25 3000x magnification (b) Day 200 3000x magnification (c) Day 540 3000x magnification

Aluminium was extensively corroded from exposure to Micronal®. Numerous small areas of pitting can be seen in Figure 4.42(b) which increase and grow in size by Day 540 this reflects the reported mass loss of 0.01 g (Figure 4.42c). It is worth noting this image is taken at a magnification of 200X to emphasis the aggressive nature of Micronal® on aluminium.

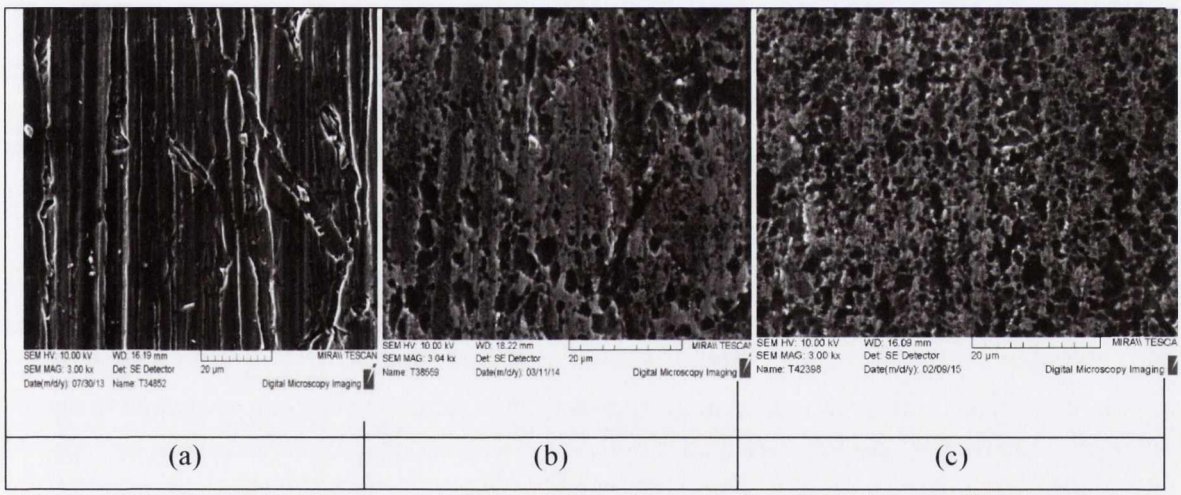

Figure 4.42: Aluminium immersed in Micronal® acid on (a) Day 1 3000x magnification (b) Day 200 3000x magnification (c) Day 540 3000x magnification

4.6.4 Evaluation and Recommendation

The final results of the mass loss and corrosion rate of each material immersed in PCM after 722 days are summarised in Table 4.4.

Table 4.4: Corrosion results obtained by gravimetric analysis after 722 days

	Capric acid		Capric: palmitic acid		Capric: lauric acid		SP22		Micronal®	
Metal sample	Mass loss (g)	Corrosion rate (mg/cm^2 yr)	Mass loss (g)	Corrosion rate (mg/cm^2yr)	Mass loss (g)	Corrosion rate (mg/cm^2yr)	Mass loss (g)	Corrosion rate (mg/cm^2yr)	Mass loss (g)	Corrosion rate (mg/cm^2yr)
Copper	0.65	22.15	0.48	16.39	0.5	17.4	0.02	0.68	0.05	1.67
Brass	0.39	13.57	0.27	9.31	0.32	10.9	0.02	0.7	0.03	1.02
Aluminium	0.2	7.08	0.34	12.04	0.12	4.25	1.17	41.45	0.01	0.33
Stainless steel	0.01	0.37	0	0	0	0	0	0.0	0	0
Mild steel	0.93	31.07	1.09	37.58	0.88	30.34	0.08	2.75	0.4	14.72
Perspex	0	0	0	0	0	0	0.02	0.63	0	0

Figure 4.43 and Figure 4.44 show the summarised values presented in Table 4.4 for mass loss and corrosion rate, respectively. Overall, it can be seen that mild steel is an unlikely candidate for encapsulation of PCM particularly fatty acids and Micronal® which was shown to have the highest mass loss of 0.88 g to 1.09 g and 0.4 g for fatty acids and Micronal®, respectively. Aluminium showed the highest mass loss of all materials immersed in SP22 of 1.17 g; the salt hydrate was shown to aggressively attack the passivation layer it produces for self-protection causing further corrosion of the material. Brass and copper are seen to be corroded by the fatty acids more than the other PCM with corrosion rates of up to 22.15 mg/cm^2year compared to the corrosion rate of 1.67 mg/cm^2year of copper in Micronal®. Aluminium is affected by fatty acids which have shown corrosion rates of up to 12.04 mg/cm^2year although this is less than the corrosion rate of copper, brass and mild steel which have shown corrosion rates of up to 37.58 mg/cm^2year in fatty acids. The material loss of stainless steel and Perspex is negligible and it can be assumed these materials are compatible for use with PCM.

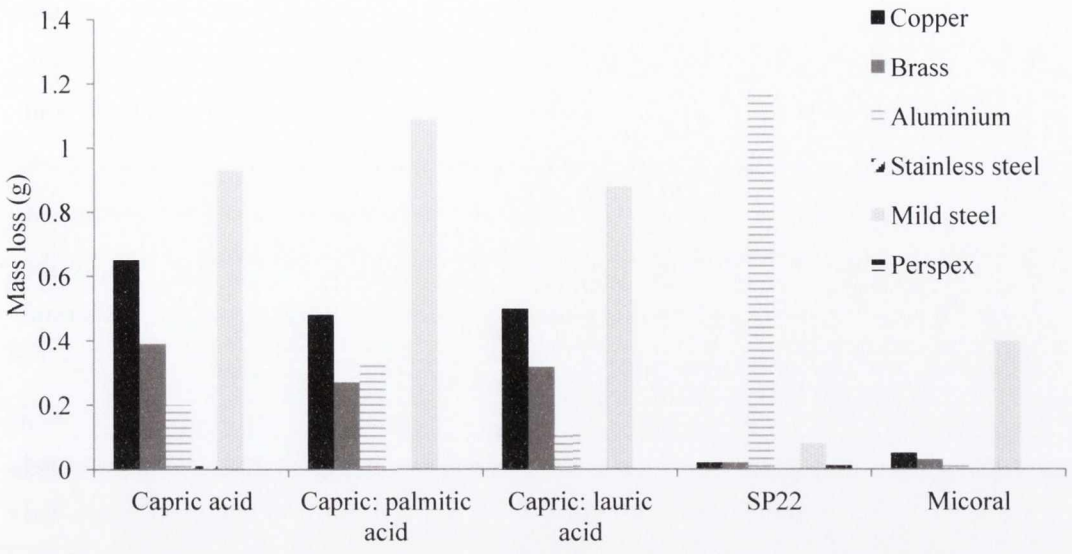

Figure 4.43: Summary of mass loss experienced by each material due to PCM

The corrosion rate was measured in g/cm^{2}year which has been changed to mg/ cm^{2}year to be used in combination with the corrosion weight loss standard guide. The document is used in industry to define the degree of corrosion considered excessive and gives an indication of the period of recommended use. The results of the suitability of tested encasement material - PCM pairs are presented in Table 4.5. The metallographic investigation is also taken into account when making the decision.

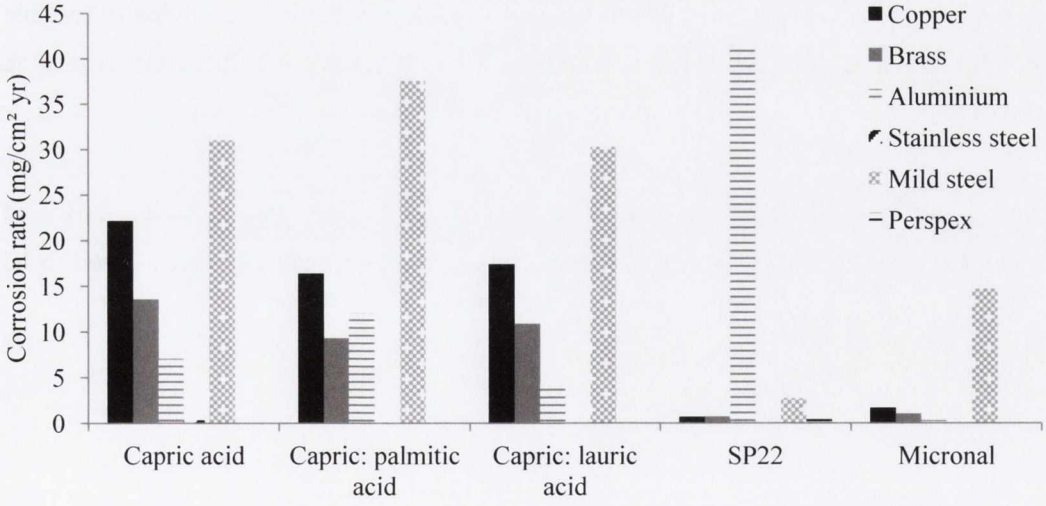

Figure 4.44: Summary of corrosion rates experienced by each material due to PCM

Samples have been categorised into recommended, not recommended and caution. Recommended suggests the material-PCM pair is compatible for long term service as the corrosion rate was less than 0.3 mg/cm^{2}yr. A 'Recommended' result improves the overall economic feasibility of the system when considering the suitability of a PCM - encasement material pair as it as suggests the container will not have to be replaced during the lifetime of the system. Ideally, a material with a recommended relationship with a PCM would be the primary choice for integration into a PV/T/PCM system. However, other factors such as thermal conductivity and implications of manufacture should be also considered.

Caution is advised (as shown in Table 4.5) when using material-PCM pairs with a recorded corrosion weight loss of 10 mg/cm^{2}yr – 49 mg/cm^{2}yr. Extra care must be taken to assess the specific application and the potential for corrosion under these conditions. It would be recommended to carry out an initial investigation such as building a prototype to determine the full extent of potential corrosion. In a PV/T/PCM system, it would not be recommended to use an encasement material – PCM pair which advises caution as the container may not last the lifetime of the system.

Container material – PCM pairs with corrosion rates great than 50 are not recommended for service. However if applications necessitate the use of certain materials then depending on the level of corrosion, encasement material – PCM pairs can be used for periods of less than one year (corrosion rate 50 mg/cm^{2}yr – 99 mg/cm^{2}yr) or less than one month (corrosion rate 100 mg/cm^{2}yr – 999 mg/cm^{2}yr). This is application specific as it may not be economically feasible to replace parts of a system following a month or year in service which is the case in a PV/T/PCM system.

Stainless steel and Perspex are the most resistant to corrosion or deformation by the fatty acid PCM as they have shown to be the only two materials of the five materials investigated to be recommended for use with all PCM.

Table 4.5: Suitability of material – PCM pairs studied

	Capric acid	Capric: palmitic acid	Capric: lauric acid	SP22	Micronal®
Metal					
Copper	Caution	Caution	Caution	Recommended	Recommended
Brass	Caution	Caution	Caution	Recommended	Recommended
Aluminium	Caution	Caution	Caution	Not recommended	Recommended
Stainless steel	Recommended	Recommended	Recommended	Recommended	Recommended
Mild steel	Caution	Caution	Caution	Recommended	Caution
Perspex	Recommended	Recommended	Recommended	Recommended	Recommended

This was the first investigation into the behaviour of fatty acids and metals and it has been found to show caution when using copper, brass, aluminium and mild steel with capric acid and fatty acid eutectics, capric:palmitic and capric:lauric. The corrosion rate for these metal- PCM pairs remained within 4.5 mg/cm^2/year and 37 mg/cm^2/year.

Aluminium is not recommended for use with SP22 as has been shown with other salt hydrates PCM which has been reported in previous studies (Cabeza et al., 2005). Despite this, it has been recommended for use with all other material samples.

The corrosive behaviour of Micornal® has not been investigated previous to this study and it has shown that it is compatible with all materials tested except mild steel where caution is recommended.

4.6.5 Preventative Measures

One of the main prevention measures is to remove contact between the PCM and the metal using macro-encapsulation methods. The most cost effective methods in use are polyethylene and polypropylene plastic bottles. Plastic plates and pouches containing PCM are also commercially available which are most commonly used as cooling packs (PCM products, 2015). However the plastic packaging hinders heat transfer to and from the PCM. Thin plated metal and mild steel cans have also been used for this application although ingress of moisture can drastically impact their performance (Regin et al., 2008).

It has been reported that plating surfaces can prevent corrosion once the plating does not break down. One example of this is copper heat pipe exchangers encased in aluminium, on to which aluminium fins are attached thereby plating the copper surface with aluminium. However, if minor cracks form in such casings the copper will become cathodic to the aluminium and the PCM will act as an electrolyte resulting in galvanic corrosion (Farrell et al., 2006). It was suggested in the same study to immerse a sacrificial anode such as zinc into the system in order to reverse the corrosive effects of the aluminium.

Pendyala (2012) investigated the potential to encapsulate PCM with a metal oxide to produce a coated PCM pellet using electrochemical coating. Other potential concepts explored in the study included the application of a coating of silicates and sand encapsulation. However, difficulties including leakages and sustainability of the coatings were reported.

It has been shown that the adhesives tested break down when in contact with PCM. Containment of PCM must be void of any joints or sealing during manufacture. It is recommended metals be fused together using metal joining techniques such as welding and materials which cannot be welded, such as that of Perspex be cast to avoid possible leaks.

Perspex and stainless steel have shown corrosion rates of less than 0.63 mg/cm^{2}year as a result both materials can withstand the corrosive effect of the PCM as a result no measures are necessary to reinforce the corrosive resistance of Perspex and stainless steel.

Aluminium, copper and brass have shown higher corrosion rates than that of Perspex and stainless steel in fatty acid PCM. The corrosion rate varies from 425 mg/cm^{2}year to 22 mg/cm^{2}year depending on the encasement material – PCM pair. Aluminium can experience galvanic corrosion whereby tin plating can reduce the effect and an oxide inhibiting compound can also be used on the surface to avoid the ingress of moisture on the contact surface. Tin and nickel plating is also an option to consider reducing the effects of corrosion on copper. There are different grades of brasses available which are designed for harsh environments and these could also be considered for encapsulation of PCM.

Mild steel is highly susceptible to corrosion based on the corrosion results presented in Section 4.6.4 which show corrosion rates of mild steel reach 47 mg/cm^{2}year in capric:palmitic acid. As a result it is recommended that mild steel undergoes a plating or surface treatment to prevent them from corroding. Zinc plating involves providing a sacrificial corrosion protection to seal

the outer surface. If the possibility of corrosion is low, covering the container with an anti-corrosion paint would be an effective option.

4.7 Conclusion

This chapter presented the characterisation of five PCM using DSC and THM methods. The melting range, melting temperature, solidification range, and heat of fusion were found based on the variation of heat flow versus temperature graph (found using the DSC). The specific heat capacities and solidification point was found using the cooling process of the THM method. The temperature ranges of all the materials varied from 15 °C to 30 °C as this was the temperature range required for use in a PV/T/PCM system in an Irish climate. The results give an indication of materials which have potential to be used for PV regulation and heat storage applications in PV.

Based on the characterisation tests, it was concluded that the PCMs SP22 and Micronal would be unsuitable for integration into a PV/T/PCM system due to the risk of segregation and leakage, respectively. The chemical stability, a required property of a TES material, was found to be unstable in these materials as shown by the double peaks in the DSC results. Fatty acids were found to have the most potential for integration into a PV/T/PCM system. They have high heats of fusion, are chemically stable and do not undergo segregation.

The material chosen for integration with a PV/T/PCM system was capric:palmitic acid. It was found to have a melting range of 16 °C - 25 °C, which was suitable for the Irish climate as it was higher than the ambient temperature in summer. The heat of fusion was found to be 209 kJ/kg, which was higher than any other PCM investigated in the study. Capric:palmitic acid was recommended for use in a PV/T/PCM system in Ireland due to the high heat of fusion and the applicable melting temperature.

Initial investigation into the use of sealants as a method of fabricating a container PV/T/PCM system found all sealants used have been shown to react with PCM, making them unsuitable adhesives for PCM containment. As a result of the effect of the PCM on adhesives, there has been no investigation of the corrosive effect of the particular fatty acids studied. As a result investigation into the corrosive properties of the PCM was carried out by immersing them in six commonly used materials to assess the materials which would be compatible for PCM

containment. The experiment involved immersing the material samples in liquid PCM for up to 722 days.

Stainless steel was seen to be unaffected by all PCM over the 722 day period except capric acid where a 0.37 mg/cm^{2}year corrosion rate was calculated. This is not a cause for concern as the material is still recommended for use with capric acid based on industry guidelines. Perspex also showed minimal corrosion when immersed in PCM, the maximum of which was 0.63 mg/cm^{2}year when immersed in SP22. However, all other Perspex samples were shown to have no mass loss and therefore 0 mg/cm^{2}year corrosion rate. Aluminium is not recommended for use with SP22 as shown with a corrosion rate of 42 mg/cm^{2}year. However, fatty acids are compatible with aluminium if caution is exerted as the maximum corrosion rate of all fatty acids was found to be 12.4m g/cm^{2}year. Mild steel has been recommended for use with SP22 as the corrosion rate is 2.75 mg/cm^{2}year. However, caution is advised when integrating the material with fatty acid or Micronal® which have shown corrosion rates of 37.6 g/cm^{2}year and 14.72 g/cm^{2}year, respectively. Copper and brass showed common results when considering the suitability of encasement material – PCM pairs, both were recommended for integration with SP22 and Micronal® however caution is advised when encapsulating fatty acids. The corrosion rate of copper when immersed in SP22, Micronal® and capric acid was found to be 0.68 g/cm^{2}year, 1.67 g/cm^{2}year and 22.15 g/cm^{2}year, respectively. Brass was found to have a lower corrosion rate of 13.6 g/cm^{2}year than copper when immersed in capric acid. SP22 and Micronal were found to have corrosion rates of 0.68 g/cm^{2}year and 1.67 g/cm^{2}year, respectively.

Throughout the corrosion tests images were taken using a SEM to assess the level of corrosion on the surface of the material. These images along with the results of the corrosion tests helped to draw conclusions on the most appropriate PCM-encasement material pairs for use in the PV/T/PCM system.

Chapter 5

Performance Evaluation of a Photovoltaic/ Thermal/ Phase Change Material Systems

Chapter 5. Performance Evaluation of a Photovoltaic/Thermal/ Phase Change Material System

5.1 Introduction

The PV/T/PCM system was characterised in outdoor conditions in Dublin, Ireland over a period of 18 months to determine the performance. The design and installation of a photovoltaic/thermal system integrated with phase change material (PV/T/PCM) was presented in Chapter 3, Section 3.3. The electrical data has been presented however, the main focus of this chapter remains with the thermal performance of the system and the efficiency of the PCM to charge and discharge. The thermal of the system has been studied in detail and the results analysed. In order to assess the thermal performance of the PV/T/PCM system under higher temperature climatic conditions a forced heat supply was used at the system surface was conducted and the results presented. The chapter is sub-divided into three sections:

1. Heat retention of a PV/T/PCM system
2. Electrical analysis of a PV/T/PCM system
3. Performance of a PV/T/PCM system under simulated climatic conditions

The aim of this chapter is to determine a method to assess the thermal performance of a PV/T/PCM system. In addition to this to investigate the performance of the PV/T/PCM system in Ireland and under simulated climatic conditions.

5.2 Overview of Experimental Systems

To give an overview of the experimental systems involved in the study, the three reference systems and the PV/T/PCM system as presented in detail in Chapter 3 are briefly described below:

- System 1 PV only
- System 2 PV with heat sink (container)
- System 3 PV with thermal collector (container, pipe network and tank)
- System 4 PV with thermal collector and thermal energy storage (container, pipe network, tank and PCM)

On considering the performance of the PV/T/PCM system in comparison with the PV/T system, it must be noted that the investigation is focused on the thermal performance of the systems and the ability of the PCM to charge and discharge over the course of a day. The thermal assessment does not take into account the usage of hot water and therefore, the temperature of the water being circulated around the thermosyphon and into the tank.

5.3 Thermal Analysis Methodology of PV/T/PCM System

A comparison of the thermal performance of System 2 (PV/T with container), System 3 (PV/T) and System 4 (PV/T/PCM) is presented in this Chapter. System 1 (PV) was removed from this investigation as it does not generate thermal energy. The approach taken to investigate the thermal performance of the systems relative to each other was divided into two investigations,

(i) The quantity of thermal energy absorbed by the system

(ii) The level of useful energy

The analysis of the thermal performance of PV/T systems generally involves using an equation derived from the relationship for measuring collector energy gain and is widely known as the Hottel–Whillier–Bliss equation (Equation 5.1) (Duffie and Beckman, 1992):

$$Q_u = F_R A_{PV}[G_{Tot}(\tau\alpha) - U_L(T_i - T_a)] \tag{5.1}$$

Where,

Q_u = Useful energy gain (W)

A_{PV} = Surface area of PV (m^2)

G_{Tot} = Intensity of solar irradiance ($W.m^2$)

α = Absorptivity of plate

τ = Transmissivity of glazing

T_i = Inlet Temperature (°C)

T_a = Ambient Temperature (°C)

F_R = Collector heat removal factor

The collector heat removal factor, F_R, relates the actual useful energy of a collector to the useful gain if the whole collector surface were at the inlet fluid temperature and can be calculated using the following expression:

$$F_R = \frac{m_w\, C_p(T_o - T_i)}{A_{PV}[G_{Tot}(\tau\alpha) - U_L(T_i - T_a)]} \tag{5.2}$$

Where,

m_w = Mass flow rate of fluid (kg/sec)

U_L = Overall heat loss coefficient (W/m^2)

C_p = Specific heat capacity of fluid (kJ/kg.K)

T_o = Temperature at the outlet of the collector (°C)

After using these equations to calculate an efficiency of the PV/T/PCM system, it was found they were unsuitable as they do not consider the heat stored in the PCM. It was also necessary to consider the efficiency on a daily basis rather than an instantaneous efficiency as the pre-heated water was available at night when the denominator, solar irradiance, was zero thereby reducing the value of useful energy to 0.

It was decided a more accurate measure of the PV/T/PCM performance is the collector efficiency (η_{TH}). This is defined as the ratio of the useful energy gain (Q_u) (by both the amount of heat carried away in the fluid and the quantity of storage by the PCM (Q_s)) to the incident solar energy in addition to the time for which the availability of heat has been extended (t_{ext}) over a particular period:

$$\eta_{TH} = \frac{\left(\frac{Q_u}{A_{PV} * \alpha\tau * G_{Tot}} + \frac{Q_s}{A_{PV} * \alpha\tau * G_{Tot}} + \left(\left(\frac{t_{ext}}{24}\right) * 100\right)\right)}{2} \tag{5.3}$$

Where,

Q_s = Heat stored by thermal collector (kJ)

t_{ext} = Time period for which water can be heated outside of sunrise and sun set (hrs)

The value of η_{TH} indicates how efficient the system is at removing and using the heat that was made available to the system by the solar irradiance. The three terms in the thermal efficiency equation represent the methods through which the heat energy is distributed throughout the PV/T/PCM system:

(i) Useful heat in the water flow as shown (Equation 5.4)

(ii) Stored heat in the container (Equation 5.5)

(iii) Period for which the heat in the container is available to the water flow (Equation 5.6)

$$Q_u = m_w C_{p,w}(T_o - T_i) \tag{5.4}$$

$$Q_s = mC_{p,IC}(T_{IC} - T_i) \tag{5.5}$$

Where, T_{IC} is the temperature inside the container and $C_{p,IC}$ is the specific heat capacity of the material in the container.

The term t_{ext} (Equation 5.6) was used to represent the time for which the heat was available in a PV/T/PCM system compared to a PV/T system. This equation is applied only to the hours outside of sunrise and sunset in order to assess the advantage of the integration of the PCM and its ability to store energy when the energy input, the sun, has gone down.

$$t_{ext} = t_{T_{IC}>T_i} \qquad \text{When, } t < t_{sunrise} \text{ or } t > t_{sunset} \tag{5.6}$$

The equation representing the stored heat (Equation 5.5) was based on the energy balance equation of a PV/PCM system for a unit surface area as presented by Huang et al. (2006c). The energy balance is the incoming solar irradiation is equal to electrical energy generated based on PV efficiency, the system losses and the heat stored in the PCM.

$$\alpha\tau * I * \Delta t = \eta_{PV} * I * \Delta t + U_L(T_{PV} - T_{amb})\Delta t + Q_s \tag{5.7}$$

Where:

η_{PV} is the cell efficiency of the PV

The energy in the entire PV/PCM system, including the PV, was found using Equation (5.7). In this current study the aim was to find the energy stored by the PCM which could potentially be transferred to the water. As a result, the temperature differential used to find the stored energy in the PCM was the difference between T_{pcm} and T_i rather than the value between T_{pv} and T_{amb}, as used in Equation (5.7) when calculating Q_s. The following equations were used to find the energy stored in the PCM in a PV/T/PCM system:

$$Q_s = mC_p(T_{PCM} - T_i) \qquad T_{inlet} < T_{PCM} < T_m \qquad (5.8)$$

$$Q_s = mC_p(T_{PCM} - T_i) + C_L \qquad T_m \leq T_{PCM} < T_m + \Delta T \qquad (5.9)$$

$$Q_s = mC_p(T_{PCM} - T_i) + C_L + mC_p(T_{PCM} - T_m) \qquad T_{PCM} \geq T_m \qquad (5.10)$$

Where;

T_m is the melting temperature

T_i is inlet water temperature

T_{PCM} is the PCM temperature

ΔT is the range of phase change

The temperature difference between T_{pcm} and T_{inlet} was considered as the PCM has the potential energy storage to heat the inlet to the PCM temperature. It is clear that the above Equations 5.8 - 5.10 are specific to the PV/T/PCM system and are the generic equivalent to Equation 5.5. In the case of a PV/T/PCM system which assumes the specific heat of PCM in liquid and solid states is negligible, as is the case here and that the initial temperature is T_{inlet}, Equations 5.8 - 5.10 are used to find the energy stored by the PCM in the system.

All terms may not be applicable in each system; however, Table 5.1 indicates which thermal energy terms are applicable to each of the systems. If the thermal energy equation does not apply to a system then the term is assigned '0' by default. The heat storage potential term is divided by 24 to get a value which represents the fraction of the day for which heat is available to the water. System 1 (PV) has no thermal collector and as a result the thermal efficiency will automatically be assigned the value '0'. System 2 (PV with container) has a no stored energy in the container and no t_{ext} due to the absence of PCM. The thermal collector in System 3 (PV/T) gains heat energy which provides a useful heat gain. As System 4 (PV/T/PCM) has a thermal collector and PCM, it will provide a value for all thermal energy terms.

Table 5.1: Table indicating the form of thermal energy in each system

	System 1 (PV)	System 2 (PV with container)	System 3 (PV/T)	System 4 (PV/T/PCM)
Q_u	X	X	✓	✓
Q_s	X	X	X	✓
t_{ext}	X	X	✓	✓

Absorptivity of PV (α) and transmisivity of PV glass (τ) indicate the fraction of solar irradiance absorbed by the PV and was used in Equation 5.3. The absorptivity of PV cells is 0.9 as reported by Santbergen and van Zolingen (2008). The transmisivity was found using Equation 5.11:

$$\tau = \tau_r * \tau_a \tag{5.11}$$

Where,

τ_r = Transmissivity due to reflection

τ_a = Transmissivity due to absorption

Transmittance due to reflection, τ_r, and absorption, τ_a, were calculated using Equation 5.12 and (13), respectively.

$$\tau_r = \frac{(1-\rho)}{1+(2C-1)\rho)} \tag{5.12}$$

$$\tau_a = e^{-KL} \tag{5.13}$$

Where,

ρ = Monochromatic hemispherical reflectance

C = Number of covers

K = Extinction coefficient cm^{-1}

L = Thickness of the glass cover

The thickness of the glass, *L*, was 3mm as detailed in the specification data of the PV panels. The coefficient of extinction, *K*, was 0.94 cm^{-1} as reported by Rubin (1985). The

monochromatic hemispherical reflection was calculated using Equation 5.14, where n_1 is the refractive index which was assigned a value of 1.47 as reported by Junghänel et al. (2010) for solar glass. Air has a refractive index, n_2, of unity.

$$\rho = \left(\frac{n_1 - n_2}{n_1 + n_2}\right)^2 \tag{5.14}$$

Strictly speaking, n and K are functions of the wavelength of radiation, but for most solar energy applications they can be assumed to be independent of the wavelength (Duffie and Beckman, 1992).The transmittance-absorptance product was calculated as 0.63 for the PV system presented.

5.4 Heat Retention of a Photovoltaic/Thermal Collector with Phase Change Material

Investigation of the performance of the novel PV/T/PCM system in real outdoor operating conditions was carried out in Dublin, Ireland to quantify the performance of the system in comparison to three other reference systems (presented in Chapter 3, Section 3.3 and in the overview in Section 5.2). The systems were assessed over a period of 18 months. Data is presented from the 4th to 6th of July 2013 for the assessment of heat retention of the PV/T/PCM system, with the three days assigned 'Day 1', 'Day 2', and 'Day 3', respectively. The design and installation of the system along with the installation and experimental procedure have been presented in Chapter 3.

5.4.1 Environmental Conditions

The weather conditions for these days are presented in Figure 5.1. The solar irradiance was above 800 W/m^2 for over three hours with low wind speeds of less than 5 m/s. The peak solar irradiance recorded was 1177 W/m^2 which occurred at 13:25 hours on Day 1, although solar irradiance was variable due to cloudy conditions as indicated by the level of noise in the graph. The high solar irradiance reading was an instantaneous value which did not exist for a prolonged period of time. The average solar irradiance over the period 11:00 hours to 13:00 hours was less than 1000 W/m^2.Of the three days analysed the peak temperature was 24.46 °C at 19:20 hours on Day 2 and the ambient temperature also remained above 20 °C for

approximately 5 hours from 16:30 hours to 21:30 hours on this day. The solar irradiance remained above 880 W/m^2 for approximately 3.5 hours on Day 3.

A temperature of 25 °C (as discussed in Section 3.2.1) must be reached in order for the PCM to fully charge. Overcast conditions give lower PV surface temperatures meaning full charging of the PCM may not have occurred. Optimum weather conditions for PV/T/PCM systems are days with high solar irradiance and low wind speeds. This helps to ensure that the PV temperature rises above the PCM melting point.

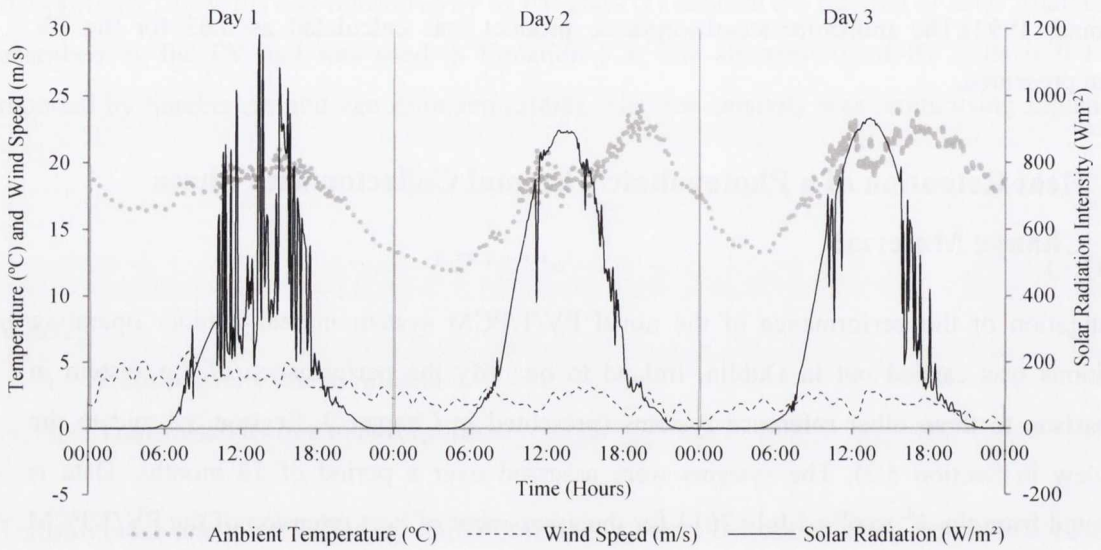

Figure 5.1: Ambient temperature, wind speed and solar irradiance measured in Dublin (53.33 N, 6.25 W) on the 4th - 6th of July 2013

5.4.2 Results and Discussion

The process of heat transfer through the systems was reflected in the presentation of the results with the temperature at the back of the PV panel being initially analysed. This was followed by the temperature inside the container (if applicable) and the charging and discharging of the PCM. Lastly, the temperature of the back of the stainless steel container (if applicable) along with the water temperatures were presented.

The recorded temperature of the back of the PV panel in each system is shown in Figure 5.2. The graph shows the elevated temperatures of each system compared with the reference (System 1). In System 2 an empty stainless steel container insulates the back of the PV panel so

the temperature was higher than that of the reference system (PV). System 2 (PV/container) had an increase of more than 10 °C during Day 2 and Day 3 which was caused by the empty container attached to the rear of the PV panel reducing natural convective cooling by the wind. The addition of the thermal and PCM systems caused an increase in the temperature of the back of the panel, as in Systems 3 and 4.

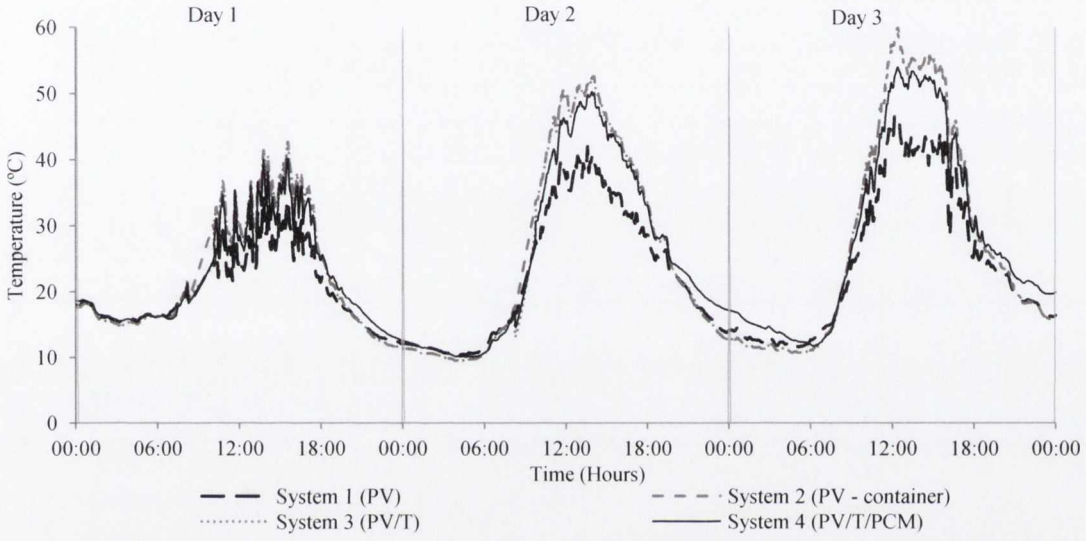

Figure 5.2: Temperature on the back of the PV panel in System 1 (PV), System 2 (PV/container), System 3 (PV /T), and System 4 (PV/T/PCM)

The differential of the temperatures of the back of the containers of System 1 and System 2 is presented in Figure 5.3(a) which have been influenced by the solar radiation. This difference represents the heating effect of the container on the back panel temperature of the PV. It can be seen that it is having the effect of increasing the temperature of the back of the PV.

The difference between System 2 and System 3, as illustrated in Figure 5.3(b), shows that the water flowing through the thermosyphon inside the container has a negligible effect on the temperature of the back of the panel. There is insufficient heat transfer from the container to the water to affect the temperature of the back of the panel. The temperatures of Systems 2 and 3 are very similar for the duration of the experiment as shown in Figure 5.3(b).

The difference between System 3 and System 4 represents the effect of the addition of PCM to the system. As presented in Figure 5.3(c), it can be seen that the PCM slows down the rate of temperature decrease of the back of the panel in the evening and through the night as it is

storing the heat energy for release later. Clearly, not all heat is released to the water and the increase in the temperature of the back of the panel during the night implies losses to the environment from the container.

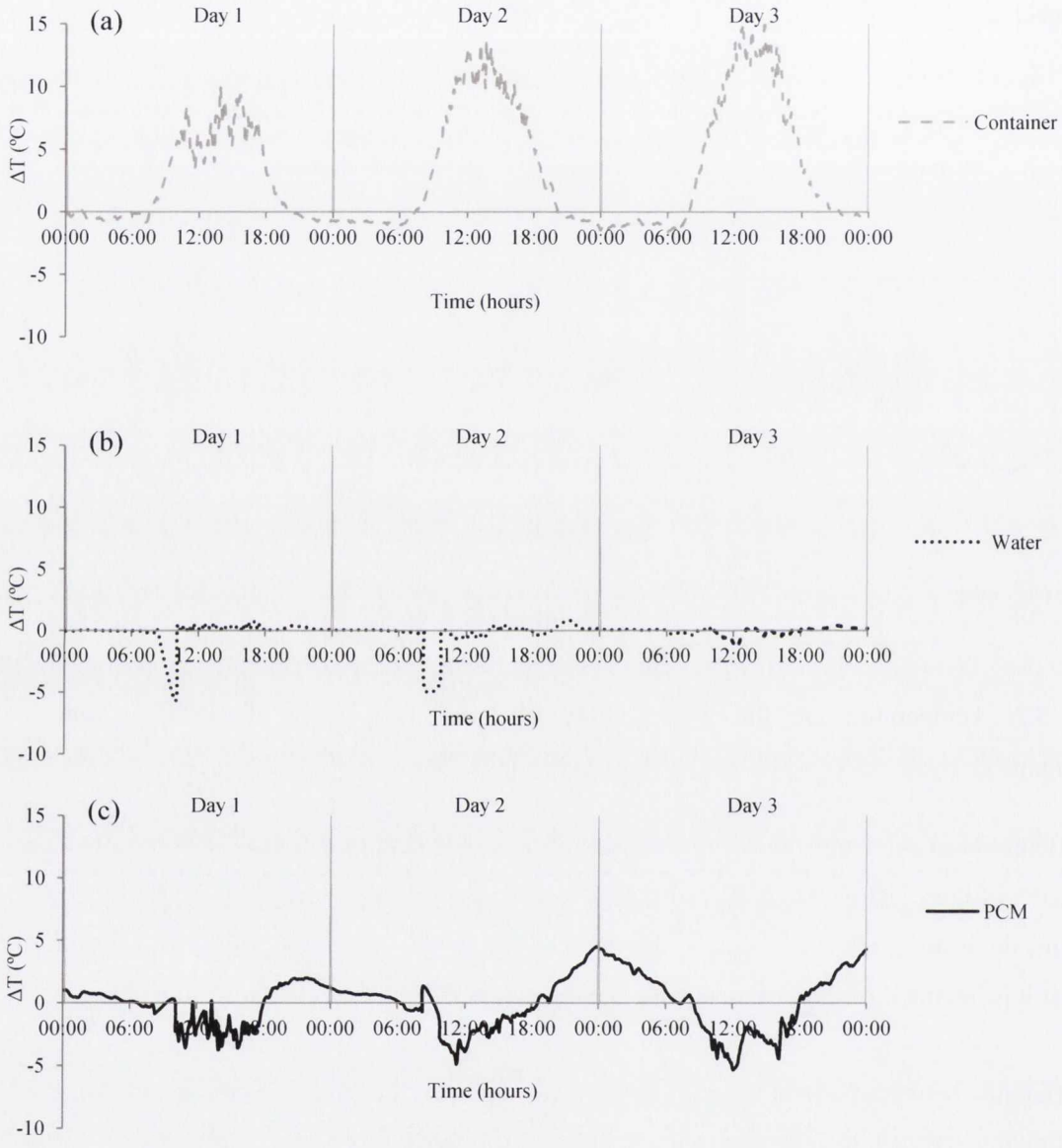

Figure 5.3: Effect of the addition of (a) container (b) water (c) PCM on the temperature of the back of the PV panel

During daylight hours the thermal energy generated by the PV in System 1 (PV), System 2 (PV with container) and System 3 (PV/T) was instantly available. In these systems pre-heated water should be used immediately (or stored elsewhere) otherwise the heat would be lost to the environment as there is no storage of heat in these systems.

The container heats the back of the panel as discussed previously and shown in Figure 5.3(a). However, during the hours of approximately 9:00 and 17:30 hours on all days, the back panel temperature is regulated by the PCM as shown in Figure 5.3(c) where the temperatures are lower than the reference (i.e. below 0). Considering that the power temperature coefficient of the panels used in the experiment is -0.675 W/ °C a daily power saving of 11.6 Wh, 13.2 Wh, and 17.7 Wh was made on Day 1, Day 2, and Day 3, respectively, as a result of the addition of PCM to the system and its ability to regulate the temperature of the PV through the absorption of latent heat, as shown in Figure 5.4.

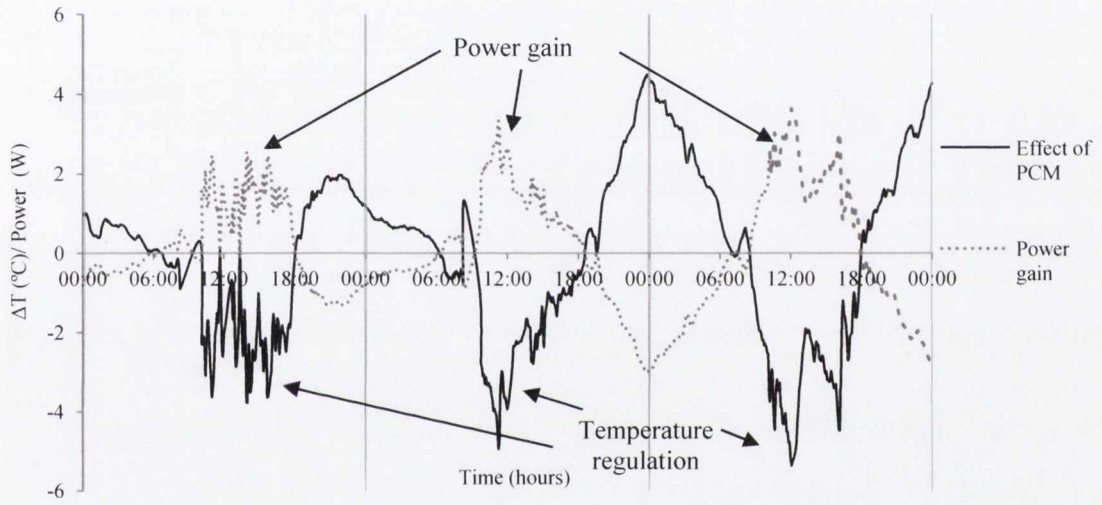

Figure 5.4: Temperature regulation of PV due to addition of PCM and the power gained due to the temperature regulation

The drivers of the systems, ambient temperature and solar irradiance, are shown in Figure 5.5(a), ensures that the heat and solar energy are most readily available during daylight hours. Figure 5.5 shows the inside container temperature difference between the different systems across the 3 days. The locations of the thermocouples inside the container have been presented in Section 3.3.6.

The recorded temperature inside the container of System 4 (PV/T/PCM), presented in Figure 5.5(d), is the lowest of all the temperatures inside the different system containers due to the PCM absorbing a proportion of the thermal energy made available by the PV. Figure 5.5(b) and (c) show temperatures inside the containers of System 2 (PV with container) and 3 (PV/T). The temperature inside System 3 is lower than that of System 2 due to the heat transfer from the inside of the container to the water.

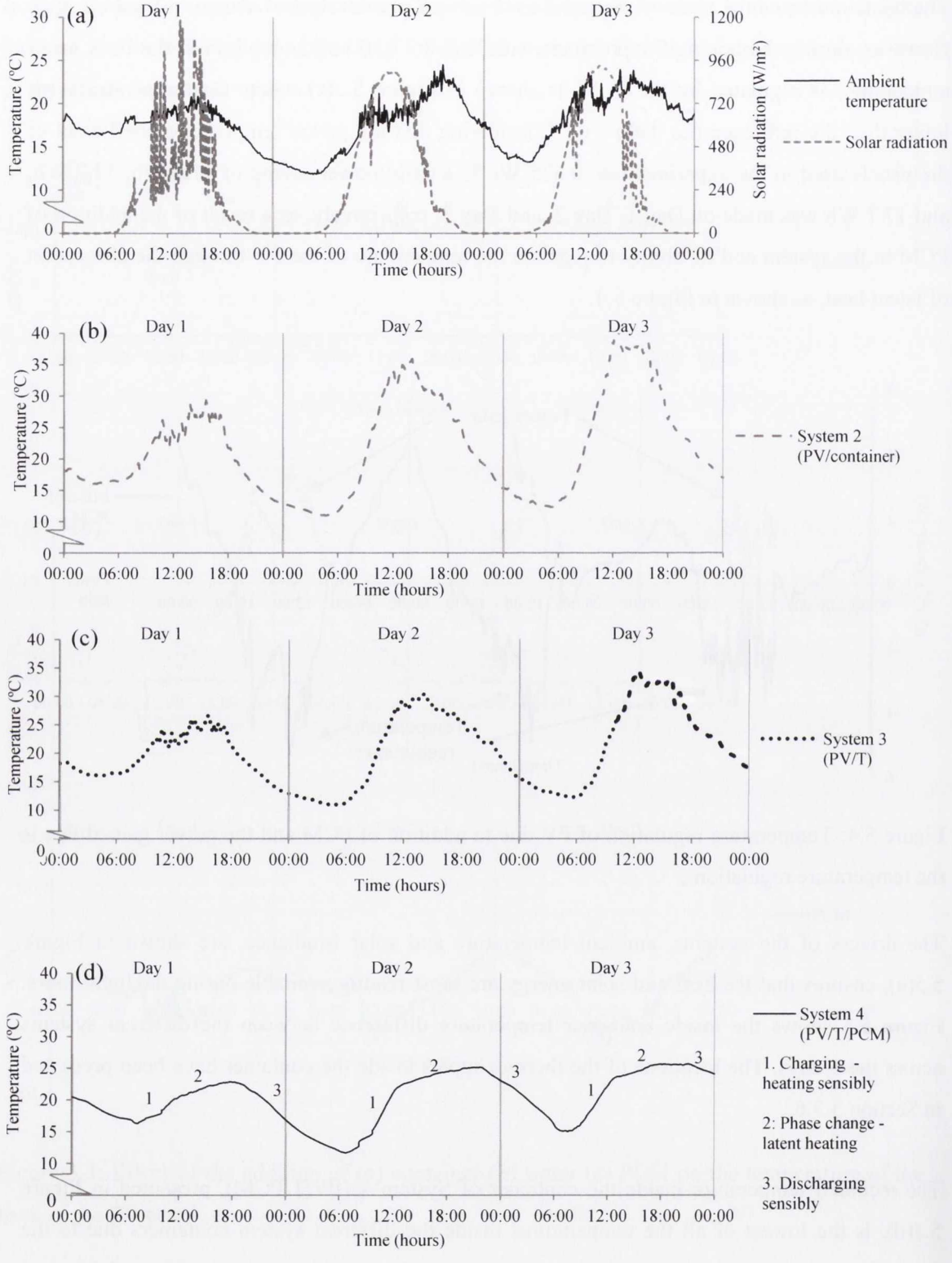

Figure 5.5: Internal container temperature in (a) System drivers – solar irradiance and ambient temperature, (b) System 2 (PV with container) and (c) System 3 (PV/T) and (d) System 4 (PV/T/PCM)

The difference of the temperature inside the containers of System 2 and System 3, shown in Figure 5.6(a), shows how the water absorbs heat from the container almost instantly from approximately 8:00 hours to 18:00 hours on each day.

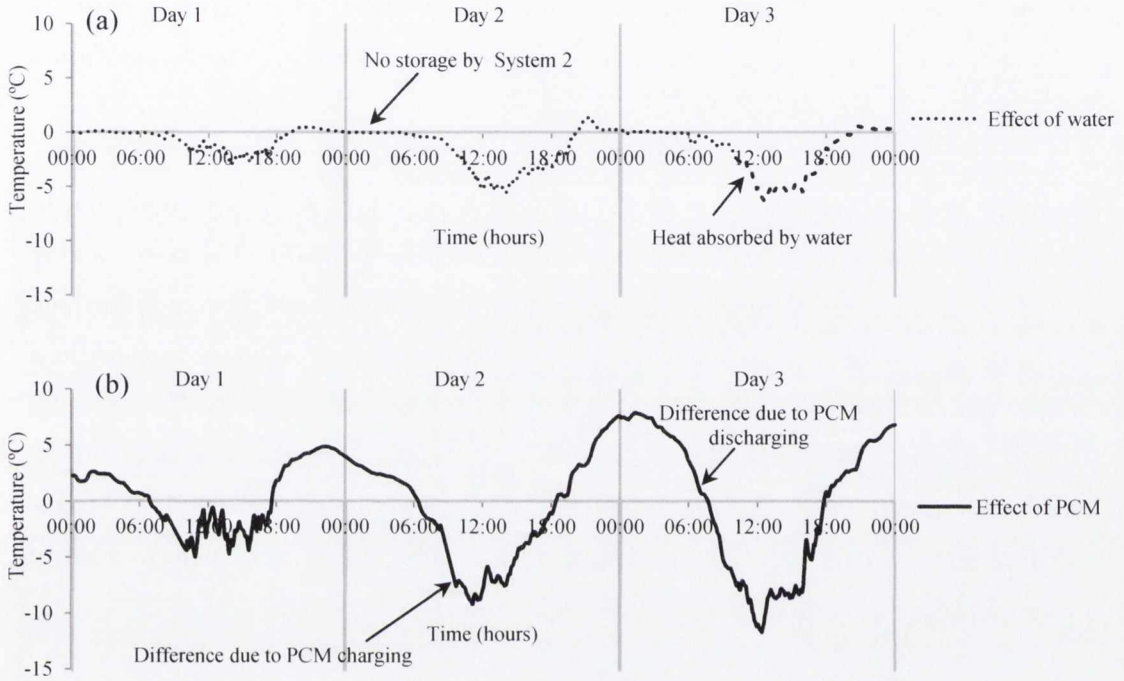

Figure 5.6: The effect of (a) the water and (b) the PCM on the internal container temperature

System 4 (PV/T/PCM) stores heat for an extended period of time which then can be used for space and water heating applications at a later time. The PCM was thermally charged during the day and discharged between the hours of 18:00 and 06:00 hours when the heat was transferred to the water. As a result, the temperature inside the container in the PV/T/PCM system is lower than the other two systems between 06:00 and 18:00 hours as it is absorbing thermal energy. Although the PV in System 4 remains at a higher temperature at night (due to the PCM storing heat) compared to the PV in the other systems, it has no effect on the PV performance as it would not be generating power during the night.

Whereas the temperature is higher between 18:00 and 06:00 hours as heat is being discharged. Figure 5.6(b) shows how PCM extends the time for which the heat is available for use by

allowing for a shift in the peak load from daytime, approximately 08:00 to 18:00 hours to 18:00 to 06:00 hours.

The melting and charging process of the PCM in System 4 demonstrates how the material was heating latently (as shown in Figure 5.5(d)). The material initially heats sensibly (System 4) on the morning of each day, indicated by a gentle linear increase. At point 2, the material is charging as the slope of the heating curve is increasing at a much slower rate and finally during the evening the discharging of the PCM is taking place as the curve descending.

Ambient temperature has been shown to affect the ability of PCM to store thermal energy due to the heat transfer from the atmosphere through the container to PCM. Therefore, during discharging the PCM can reach temperatures only as low as the ambient temperature at the time. If the PCM does not reach temperatures below its solidification temperature it remains in a liquid state, with no capacity to latently store thermal energy the following day. This effect is seen on Day 3 in Figure 5.5(d) as the temperature of the PCM has reached just below 15 °C compared to Day 2 where the temperature of the PCM reaches approximately 11.5 °C. Hence, the system presented would be more suited to a climate with clear skies at night to avail of solidification by radiative cooling to night skies with minimal cloud cover.

The temperature variation on the rear of the stainless steel container gives an indication of the thermal losses from the container to the environment. The losses from System 4 are higher due to the increased temperature difference between the back of the panel and the environment compared to System 3, as in Figure 5.7. The smoothing of the temperature on the back of the container is evident in the temperature of the PCM in System 4 as shown in Figure 5.7(d) due to the charging of the PCM which minimises the sudden temperature variation.

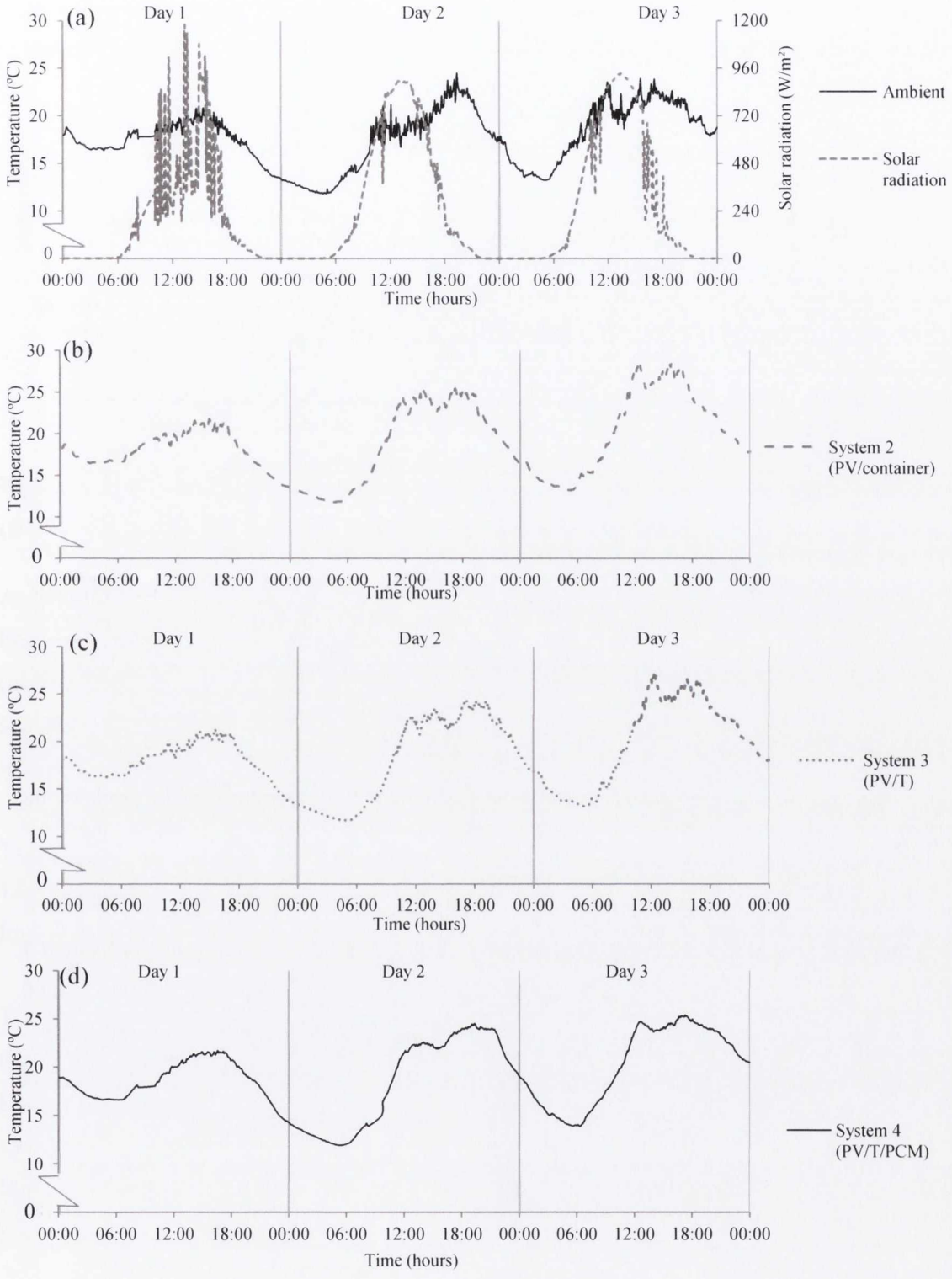

Figure 5.7: Temperature of the back of container in (a) System drivers (b) System 2 (PV/container), (c) System 3 (PV/T) and (d) System 4 (PV/T/PCM)

The water and PCM cool the back of the container during the day due to the absorption of heat as shown in Figure 5.8. At night, the container temperature of the PV/T/PCM system is higher due to the stored heat being discharged from the PCM.

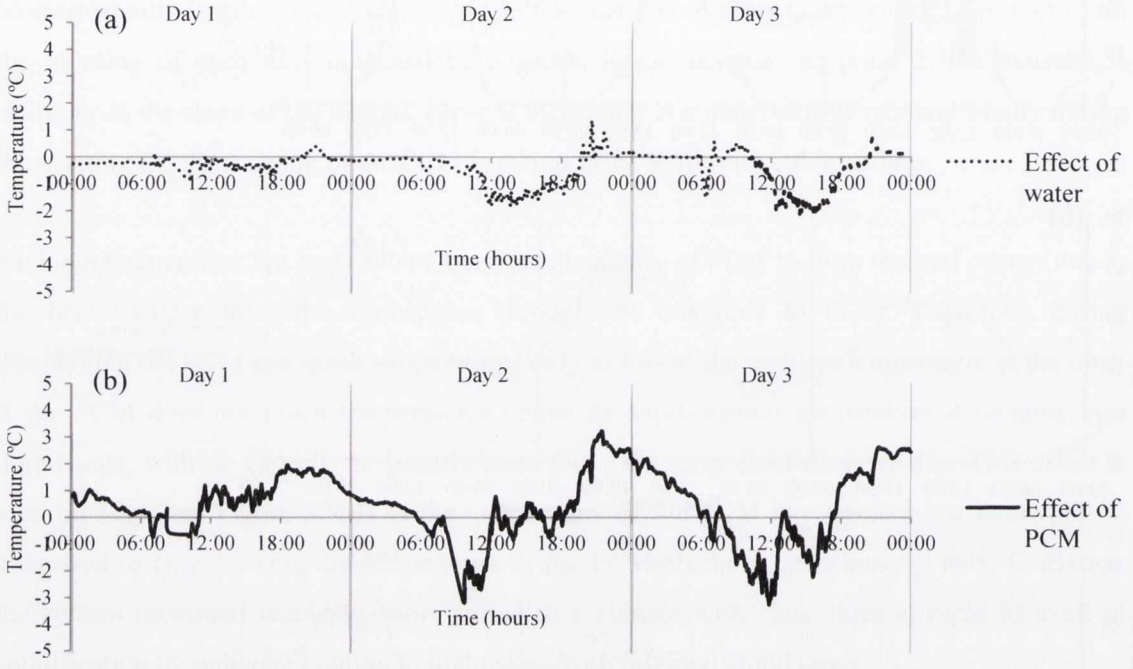

Figure 5.8: The effect of (a) water and (b) the PCM on the temperature of the back of the container

The temperature of the water at the inlet and outlet pipes in System 3 (PV/T) and System 4 (PV/T/PCM) is shown in Figure 5.9. The daily temperature variation of the water in System 4 shows the storage of heat by the PCM during daylight hours (approximately 12:00 – 20:00 hours) as the change between the inlet and outlet of the thermosyphon is an average of 0.8 °C.

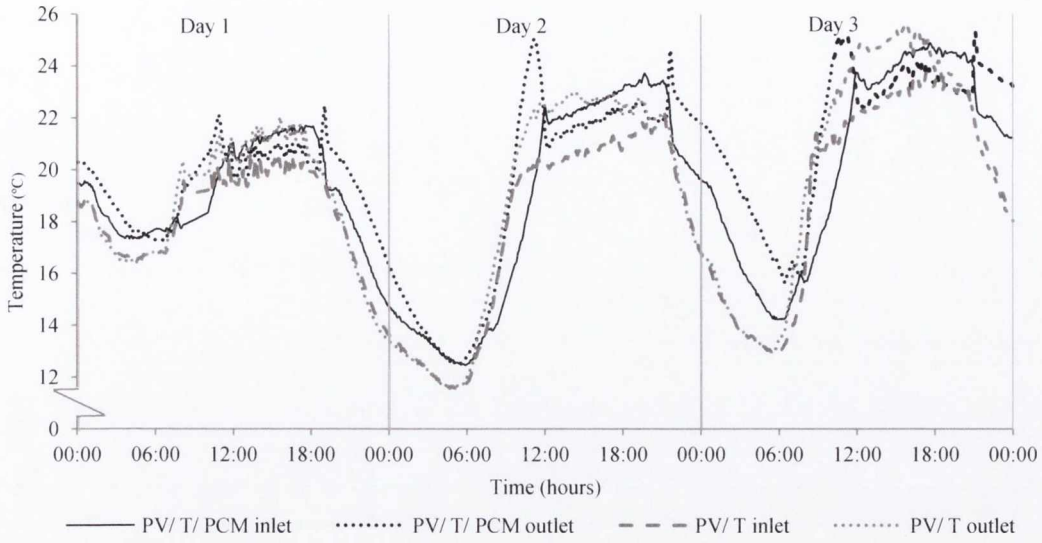

Figure 5.9: Temperature at the inlet and outlet pipes in System 4 (PV/T/PCM) and System 3 (PV/T)

As the ambient temperature decreases at sunset, the PCM begins to discharge, transferring the heat to the water as illustrated in Figure 5.10(c) whereby the temperature of the water increases (between 21:00 – 10:00 hours approximately). Prior to the onset of heat storage, the PCM heats sensibly with the temperature of the water reaching an initial peak at approximately 10:00 hours where the water is being heated before the PCM begins to store the heat.

The temperature of the water in System 3 (PV/T) increases during the day (between 09:00 – 18:00 hours approximately) as the heat generated by the PV is absorbed by the water as highlighted in Figure 5.10(b).

The temperature difference between the two systems (as illustrated in Figure 5.10) shows that the water is 5.5 °C higher in System 4 (PV/T/PCM) at 06:00 hours than that in System 3 (PV/T). For many domestic dwellings, unoccupied during working hours, 06:00 hours would be a better suited time for pre-heated water supply, rather than midday when the water temperature in System 3 (PV/T) is at its highest. The water in System 3 (PV/T) is preheated by up to 2.5 °C, which is less than half of the maximum temperature increase seen in the PV/T/PCM system.

The outlet temperature of both collectors did not reach sufficient values to have an effect on the temperature of the water in the tank. As a result it was not necessary to take account of the usage of hot water.

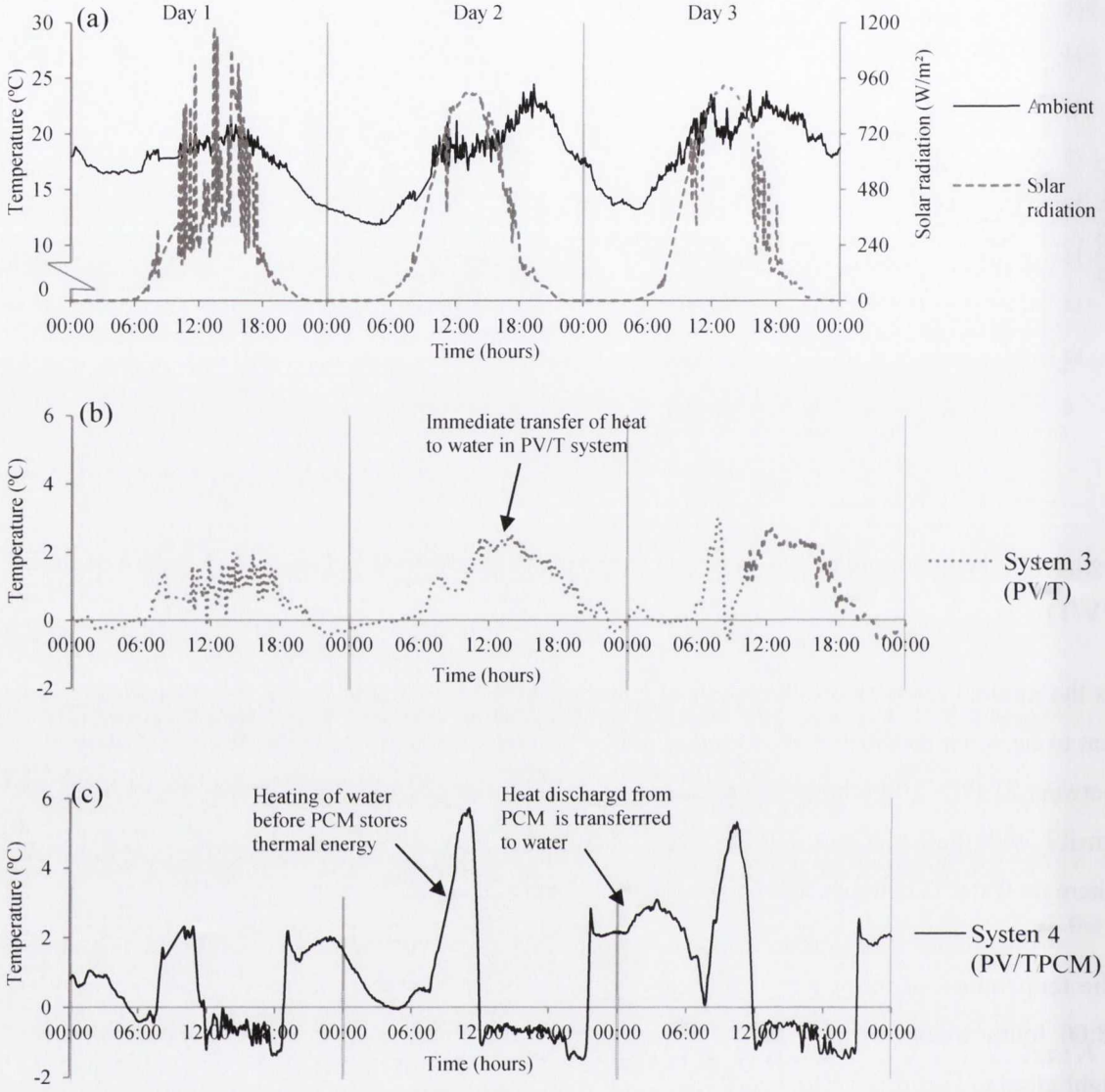

Figure 5.10: (a) Solar irradiance and ambient temperature. Temperature differential of water at the inlet and outlet of (b) System 3 (PV/ T) and (c) System 4 (PV/T/PCM)

The advantage of the integration of PCM can be seen in Figure 5.11 where the period of time for which there was potential for heat transfer energy from the container to the water. This occurred when the temperature inside the container was greater than the inlet water temperature. The period of time for which that has occurred can be determined using Equation 5.15. On Day 1, Day 2, and Day 3, System 4 extended the amount of time for which the heat was available by 5.8 hours, 2.4 hours and 6.4 hours, respectively relative to System 2. This was due to the heat storage capability of PCM in System 4.

$$t_{pp} = t_{T_{IC}>T_i} \tag{5.15}$$

Where, t_{pp} is the period of potential pre-heating and $t_{Tic>Ti}$ is the period of time when the temperature inside the container is greater than the inlet water temperature.

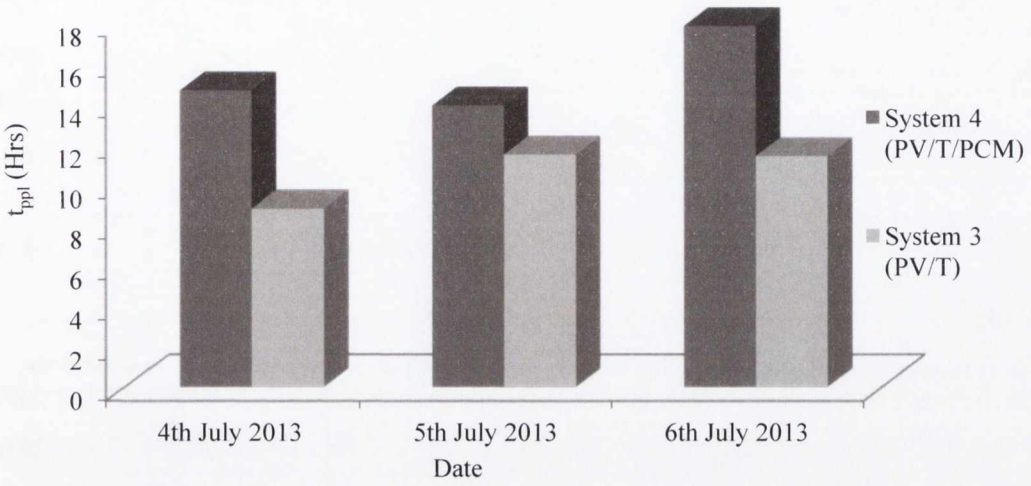

Figure 5.11: Time for which heat can be transferred from PCM to water on each day

However, the temperature within the container must decrease to 10 °C in order for the PCM to completely solidify which creates a heat sink for the PV panel the following day. If the PCM was semi-melted due to ambient temperature conditions, it loses potential to store heat from the PV. Figure 5.12 shows that the lowest temperature reached on the back of the reference PV was approximately 12 °C, for a very short period of time, suggesting that the PCM was storing the maximum amount of heat energy on a daily basis.

These results are broadly expected given that the solidification temperature of the PCM capric:palmitic acid was ranges between 12 °C and 17 °C (as detailed in Chapter 3). As a result the ambient temperature at night needs to be below 12 °C in order for the PCM to solidify. During the days examined the ambient temperature reached lows of just above 10°C which would not be sufficient to fully solidify the PCM in order to provide its full storage capacity during the following day.

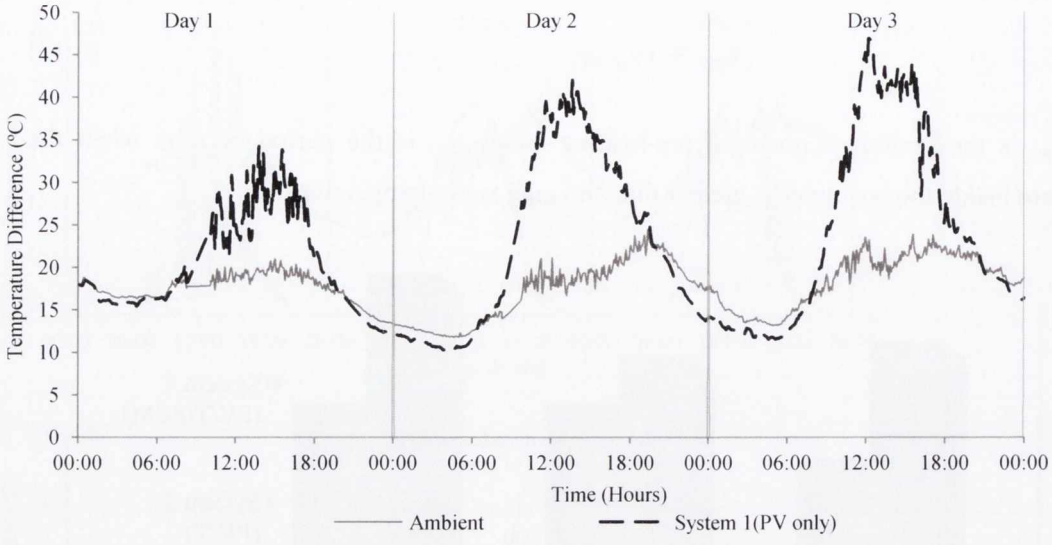

Figure 5.12: Temperature comparison of the back of panel in System 4 and ambient temperature

The water flow in the pipe network was low for the most part of the day (as shown in Figure 5.13) and if increased it would likely improve heat transfer in the systems. One possible solution would be to increase the height difference between the absorbers and the water tank to increase flow and thus the heat transfer. However, this would also increase fluid flow resistance.

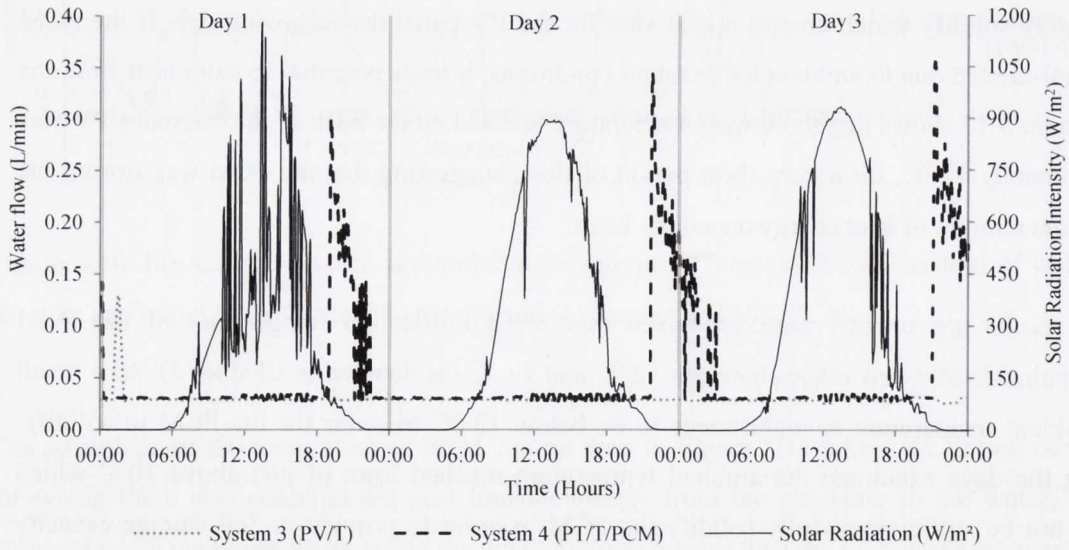

Figure 5.13: Flow of the water in the pipe network and solar irradiance for the experimental period

A pump can be used though this would require a power input (that would come from the PV), incurs an additional initial cost, requires associated sensors, control circuits, and periodic maintenance for this system size deemed infeasible.

The results show that the primary issue with the system is that heat transfer from the PV to the PCM is gradual. Improving this process would enhance the performance of the systems, thus improving the economic feasibility. One method of achieving this would be to increase the thermal conductivity of the PCM with carbon additives (Choi et al., 2014). Daily gains of PV/T can be stored in a separate store in an active (not thermosyphon) system.

5.5 Analysis of the Performance of Electrical and Thermal Efficiency in a Photovoltaic/Thermal/Phase Change Material System

The electrical and thermal efficiency of the systems are discussed in this section. The thermal investigation compares the absorption of energy by each system and quantifies the amount of useful heat gain, heat stored, and the level of potential each system has to heat water if material conductivities were improved.

The effect of the addition of a container, a thermal collector, and PCM on the PV temperature and thus the efficiency of the PV panels within the system is presented. It was found that the addition of the container negatively affects the electrical efficiency of the PV.

5.5.1 Thermal Performance of the Systems

The calculation of the thermal performance of the systems was based on the methodology presented in Section 5.3.

5.5.1.1 Environmental Conditions

The experiment was conducted for a period of 18 months in total. However, the thermal performance comparison will be assessed on the same three days as the study which investigates the heat retention of a PV/T/PCM system in Section 5.4. The detailed study and discussion of the heat retention will assist in an improved understanding of the thermal performance of the systems.

The weather conditions for the Day 1, Day 2 and Day 3 (4th – 6thJuly 2013) are presented in Figure 5.1. The ambient temperature was above 18 °C for approximately five hours each day with solar irradiance reaching values above 800W/m^2 for approximately four hours each day. The wind speed remained below 5 m/s for the duration of the three days. The ambient temperature and solar irradiance on the days presented would be considered to be well above average for the Irish summer climate.

5.5.1.2 Results and Discussion

The efficiency terms which make up the thermal efficiency equation (Equation 5.3) of a PV/T/PCM system are presented separately before being used to present a total efficiency of each system.

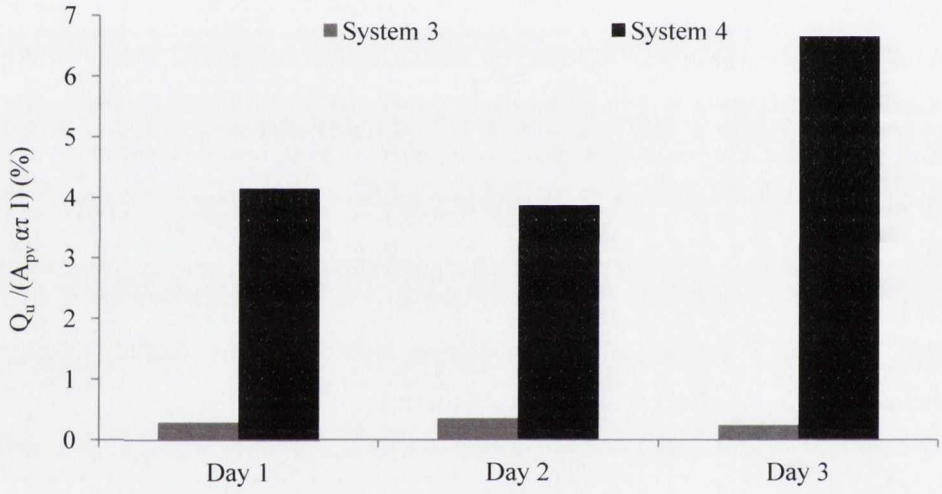

Figure 5.14: Useful heat efficiency, Q_u, of each system on Day 1, Day 2 and Day 3

The useful heat (Q_u), which is the heat transferred to the water can only be compared between System 3 (PV/T) and System 4 (PV/T/PCM) as these systems contain a pipe network and tank. As a result, System 1 (PV) and System 2 (PV with container) have been removed from the graph as thermal efficiency is 0 %. As illustrated in Figure 5.14, System 3 (PV/T) can be seen to have a much lower efficiency of useful heat than that of System 4 (PV/T/PCM). The loss from the thermal collector is much larger in the PV/T system due to the absence of PCM. The PCM in System 4 can slowly release the heat to the water compared to System 3 where the heat is immediately available to the water which, if not transferred to the water, is lost to surrounding environment.

The stored heat efficiency, Q_s, is the amount of heat energy stored by the system compared to the amount of energy made available by the solar flux on a daily basis. System 4 (PV/T/PCM) was the only system to store the energy made available as shown in Figure 5.15, where the efficiency of System 4 (PV/T/PCM) reached values of up to 6.6 % (average 4.85 %).

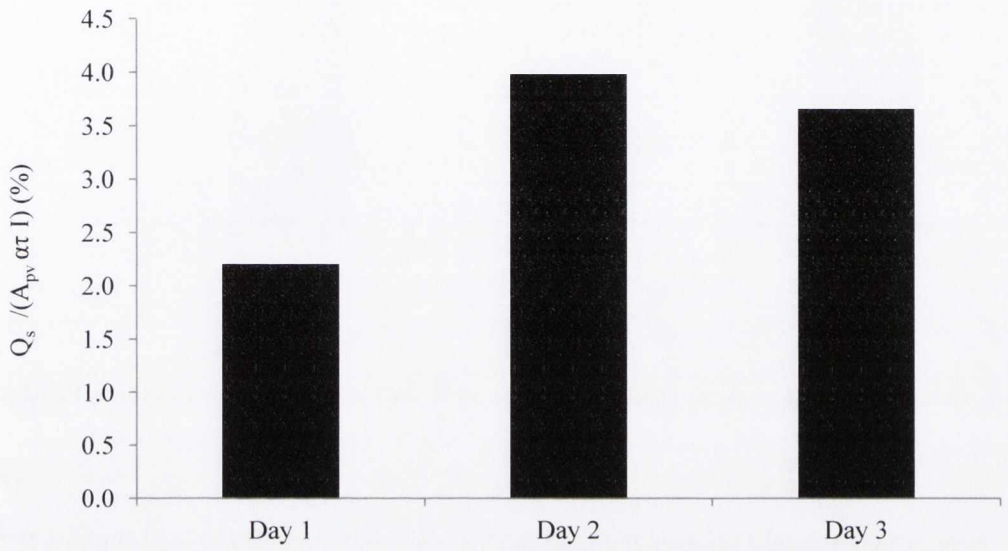

Figure 5.15: Stored heat efficiency of System 4 on Day 1, Day 2 and Day 3

The PCM can be seen to be more efficient at storing the energy compared to other systems in the experiment. However, one issue is that a large quantity of the heat stored in the PCM is failing to reach the water. Methods to increase the heat transfer from the PCM to the water might include the installation of fins (metal conductors) around the pipe to increase the surface area for greater heat transfer and improve thermal conduction.

The extended time of heat availability (t_{ext}) efficiency is the amount of time for which there is an opportunity to transfer heat from the inside of the container to the water, over a daily period. The added advantage of storage in System 4 (PV/T/PCM) is evident (from Figure 5.16) as the system can potentially transfer heat for 28 % longer than that of the PV/T system.

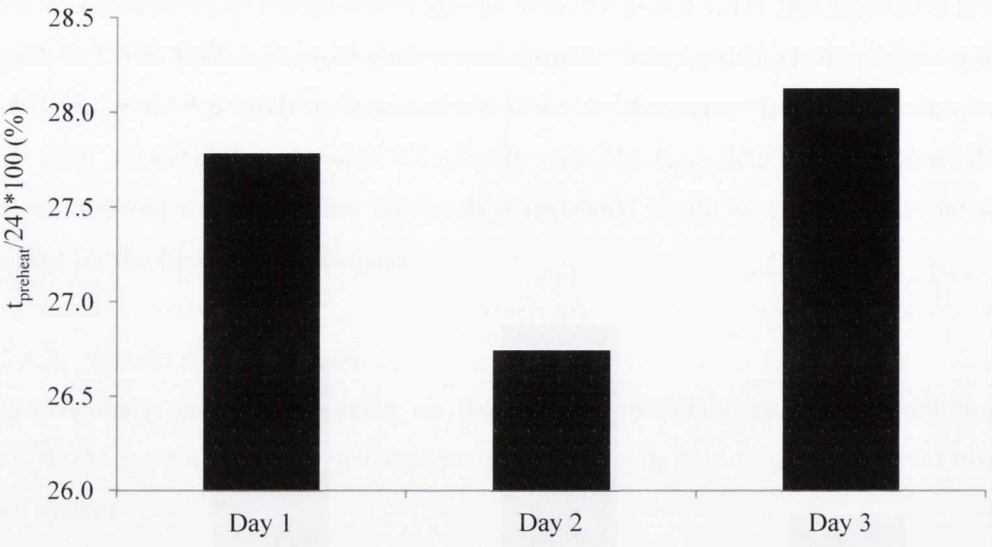

Figure 5.16: Efficiency of System 4 on Day 1, Day 2 and Day 3 of the time for which the PCM extended heat availability

Summing all terms of the thermal efficiency equation gave the results presented in Figure 5.17. System 3 (PV/T) is has a cumulative thermal efficiency of less than 1 % as the system is unable to store heat but can transfer the heat to water when it was immediately available. The system can only contain heat for as long as ambient conditions allow which was not sufficient for the system to be on a comparable scale with regard to thermal efficiency of System 4 (PV/T/PCM). System 4 (PV/T/PCM) has an increased efficiency of up to 19 %. This is due to the added thermal store of PCM and fluid (water) in the collector in the system.

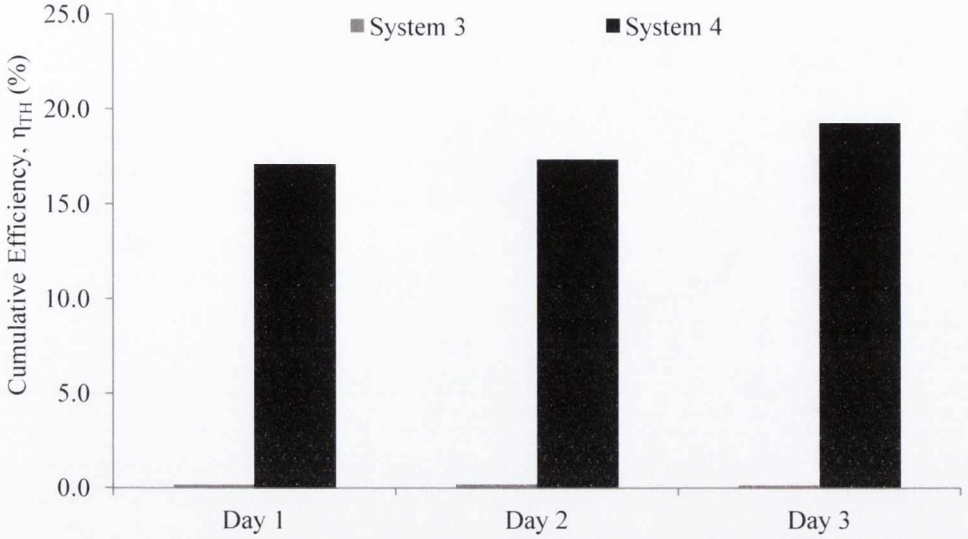

Figure 5.17: Total thermal efficiency of each system

An equation to assess the efficiency of a PV/T/PCM system by summing the useful heat gain by the water, the stored energy and the period of time for which the heat is stored was presented. Applying Equation 5.3 to the systems presented, it was found that the PV/T/PCM system was the most efficient due to the added PCM heat store. However, it became evident that the storage of heat in the PCM was not fully transferred to the water and the system was incurring losses.

The average daily outlet temperature of System 4 (PV/T/PCM) is illustrated in Figure 5.18. The temperature variation throughout the year can be seen to range from approximately 6 °C in Winter to 25 °C in the Summer months. The low temperatures indicated that a PV/T/PCM system could be used as pre-heat system in conjunction with a domestic heating system.

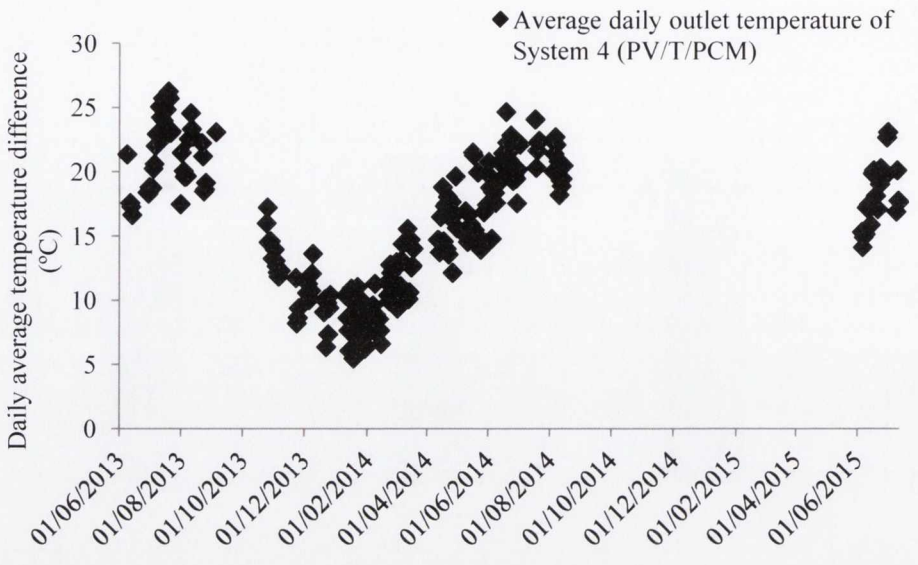

(a)

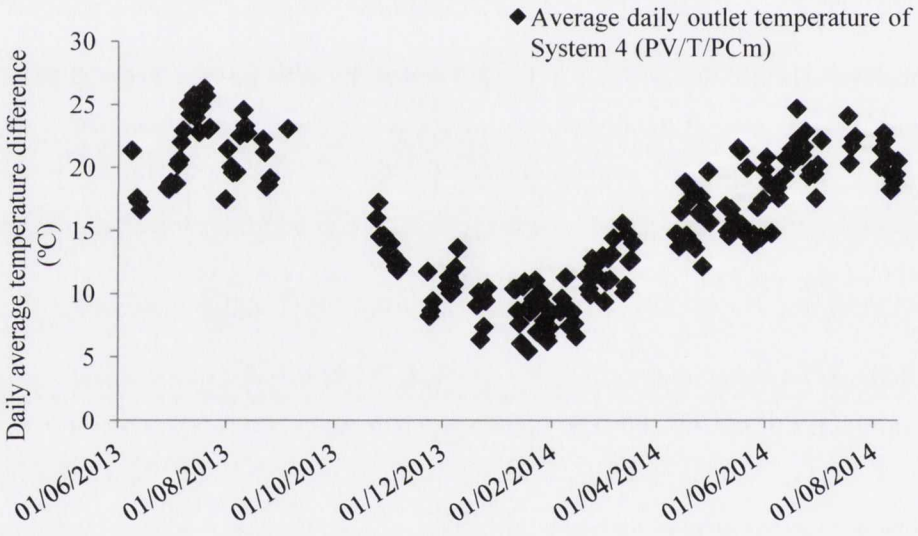

(b)

Figure 5.18: Daily average value of outlet water temperature of System 4 (PV/T/PCM) over (a) entire experimental period (b) October 2013 – September 2014

5.5.2 Electrical Efficiency

The electrical experimental analysis will assess the performance of the PV in each of the four systems. The power produced by each system will be compared to investigate the effect of the addition of a container, a thermal collector and a thermal collector with PCM, respectively. The voltage and current of each PV was recorded using a series of resistors and shunts as detailed in Chapter 2.

5.5.2.1 *Characterising PV Panels*

Prior to installation of the experiment, the PV panels were characterised using an ISM 490 Solar Module analyser (Iso-Tech, 2009). The analyser output was PV power and voltage value based on a user programmed current range scanned, solar radiation on the PV panel and panel area. Following numerous characterisation tests, all panels were found to have a measured efficiency deviation of within ± 0.25% of each other.

5.5.2.2 *Environmental Conditions*

The analysis of the electrical performance of each system was carried out on the field trial data recorded on the 30th June 2014. This day was chosen as the meteorological conditions were optimum for assessing the electrical behaviour of PV systems with cloudless skies and low wind speeds. Clear sky conditions (Figure 5.19) allowed for accurate comparisons to be made between the PV/T/PCM system and the reference systems as there were no sudden dips due to passing clouds. The solar irradiance peaked at approximately 960 W/m^2, the wind speed remained below 5 m/s and ambient temperature exceeded 18 °C for 12 hours during the day.

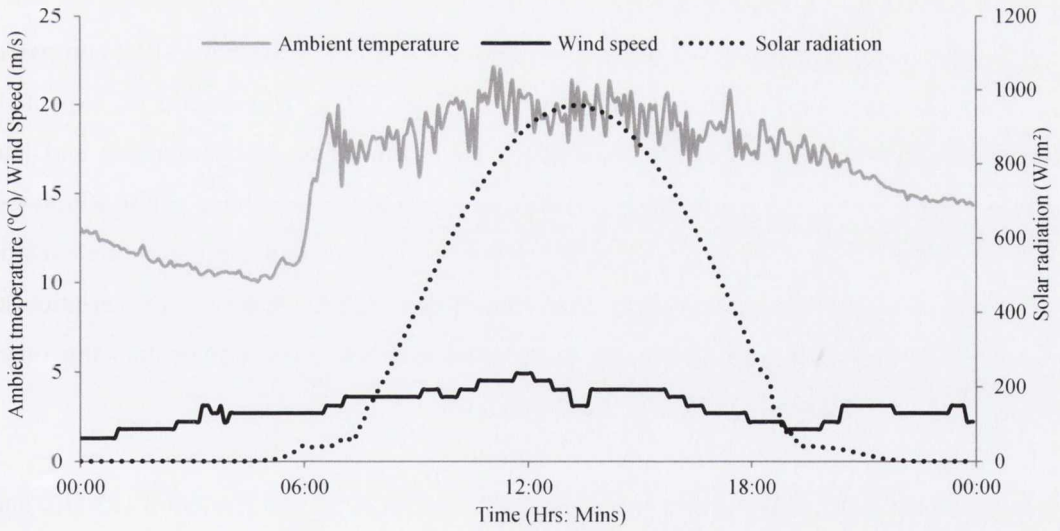

Figure 5.19: Meteorological conditions on the 30th of June 2014

5.5.2.3 *Results and Discussion*

The power generated by the PV panel in each system has been presented in Figure 5.20. System 2 (PV with container), System 3 (PV/T), and System 4 (PV/T/PCM) produce similar levels of

power over the period of the day. However, System 1 (PV) can be seen to produce approximately 9 % more power than any of the other three systems.

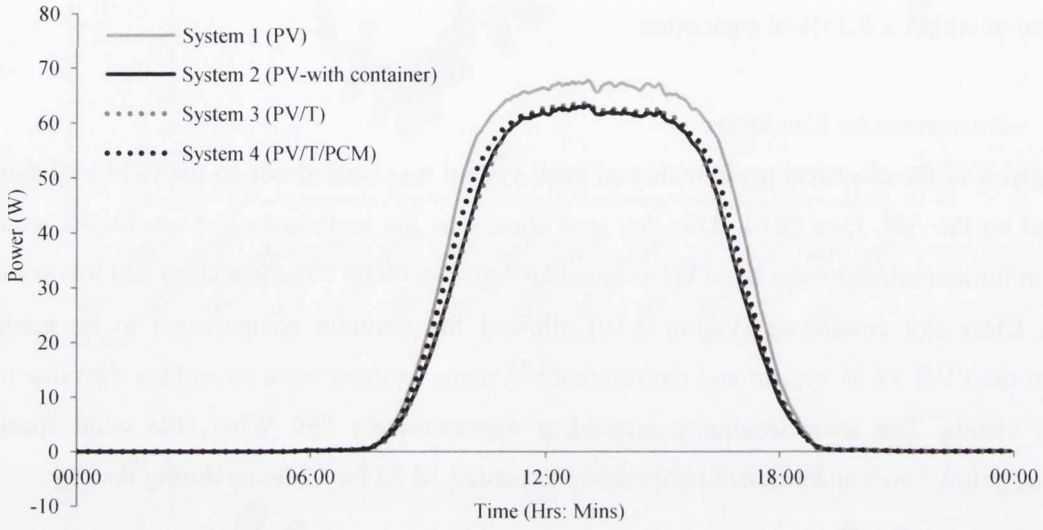

Figure 5.20: Power generated by PV in each system

This can be attributed to the decreased temperature of the PV panel in System 1 (PV) compared to the PV in the other three systems (as shown in Figure 5.21). This would be expected, considering that the temperature of the back of the panel during the early morning and late afternoon is below ~ 25 °C, which is the standard test conditions temperature below which the PV power in all the PV is not adversely affected. However, once the temperature on the back of the PV in System 1 begins to deviate away from that of the other three systems, a variation in power is evident. System 1 is producing at peak conditions 6W more power than the other systems, this is due to the heating effect of the container.

The difference in PV efficiency between System 2 (PV with container), System 3 (PV/T), and System 4 (PV/T/PCM) has been shown to be statistically insignificant as determined by a single factor analysis of variance (ANOVA) test. The statistical analysis investigated the variation in power output between the systems which resulted in a P-value of 0.99, much greater than the confidence interval cut-off point. This result suggests that the primary effect on the temperature of the PV panel is the installation of a stainless steel container. The PCM and pipe network are

not seen to have a significant effect on the power output of the panel as shown by the results and the ANOVA test.

The temperature of the PV is dependent on the water temperature in PV/T system however in PV/T/PCM systems the integration of PCM changes this. Replacing the stainless steel container with a material of higher thermal conductivity could potentially improve the transfer of heat away from the back of the panel and to the PCM or to the container.

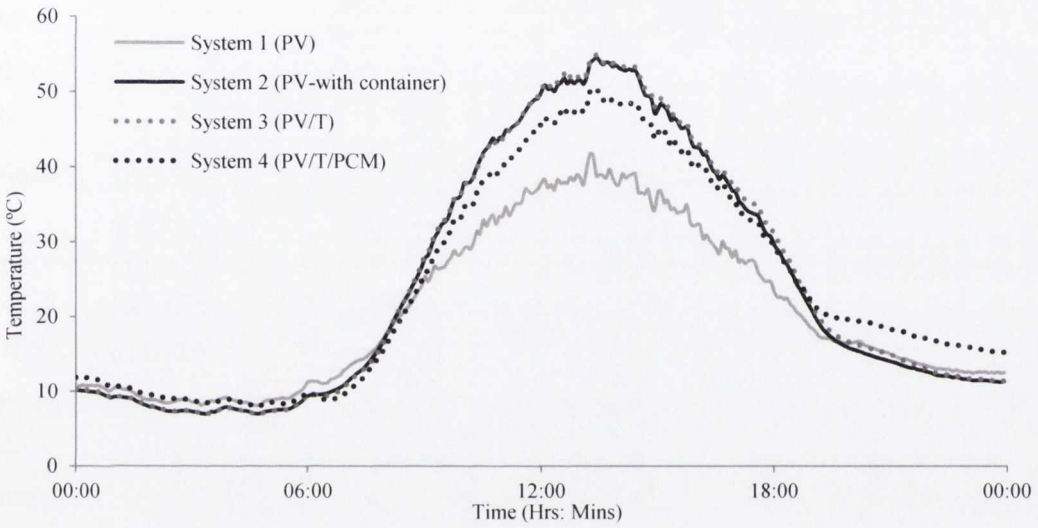

Figure 5.21: Temperature of the back of the PV panel in each system

The daily energy generation by each system was calculated for the duration of the experiment as shown in Figure 5.22(a) with (b) showing a reduced period of time, October 3013 to September 2014. The graphs indicate that the summer months produce the highest daily energy yield, reaching a maximum of approximately 20 Wh/day per panel.

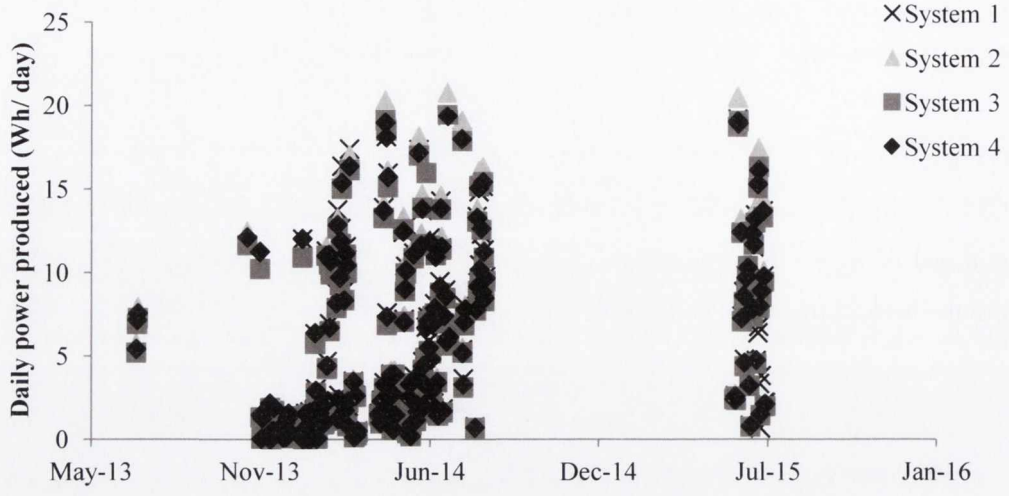

(a)

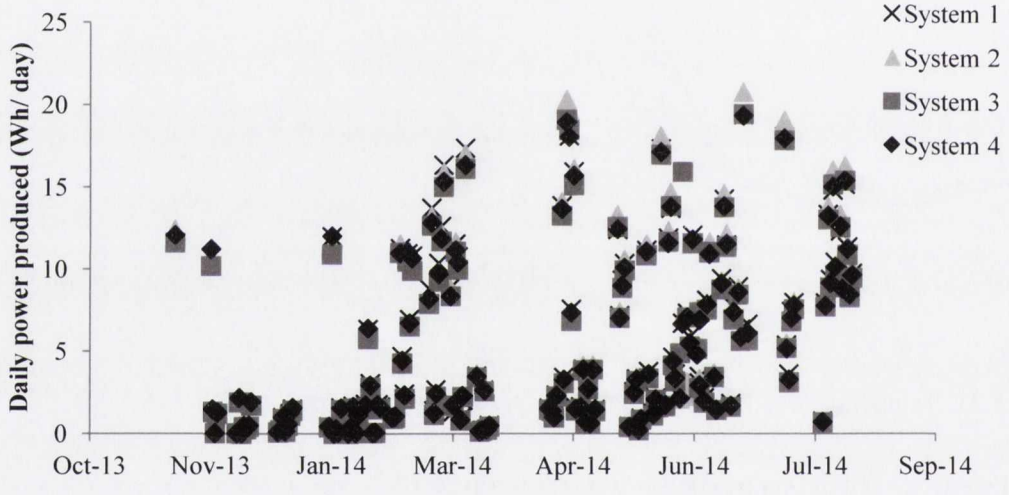

(b)

Figure 5.22: Power generated over (a) entire experimental period (b) October 2013 – Septembe 2014

As with many PV/T systems, there is a design conflict arising from the difference between th electrical and thermal performance. In this system there is a trade off between PV efficiency an thermal output as there is a minor loss of PV efficiency due to the addition of a stainless stee container. It is widely accepted that a distinctive characteristic of a PV/T system is th generation of both electrical and thermal energy in such a way that the individual system yield are generally lower than two separate systems of a conventional PV and solar thermal systen

side by side. A PV/T system generates both in a single unit at less roof space, thereby a saving is being made on both roof space and the cost of two systems.

5.6 Evaluation of Photovoltaic/Thermal/Phase Change Material System Under Increased Simulated Temperatures

The results of the experimental characterisation of the PV/T/PCM system gave a good indication of the performance of the system in a temperate maritime climate. However, in order to give a better overall assessment of the potential performance of a PV/T/PCM system it was decided to investigate the system under increased simulated temperatures. This would give an indication as to its suitability in locations with higher ambient temperatures and increased solar radiation exposure.

5.6.1 Methodology of Forced Heating Conditions on a PV/T/PCM System

The experiments were conducted with the experimental setup described in Chapter 3 using two of the four PV systems: System 3 (PV/T), and System 4 (PV/T/PCM). The experiment was designed as a comparative study. For the first three days (9^{th} – 11^{th} of September 2014) a heat mat was applied to the surface of the systems and for the final three days (12^{th} – 14^{th} of September 2014) the forced heat was removed.

The forced heat was generated using a wire wound silicon rubber heat mat as shown in Figure 5.23 with the temperature controller. The PV panel was removed and replaced by the heat mat which was positioned on the container in order to imitate the temperature on the back of the PV panel. As a result there was no calculation of PV power and the experiment is solely used to assess the thermal performance and energy storage and dissipation of heat by the systems under increased temperatures. The temperature of the heat mat was based on temperatures of the back of a PV panel located in Dhahran, Saudi Arabia in the month of July (Rehman and El-Amin, 2012) and (National Meteorology & Environment Center, 2015).

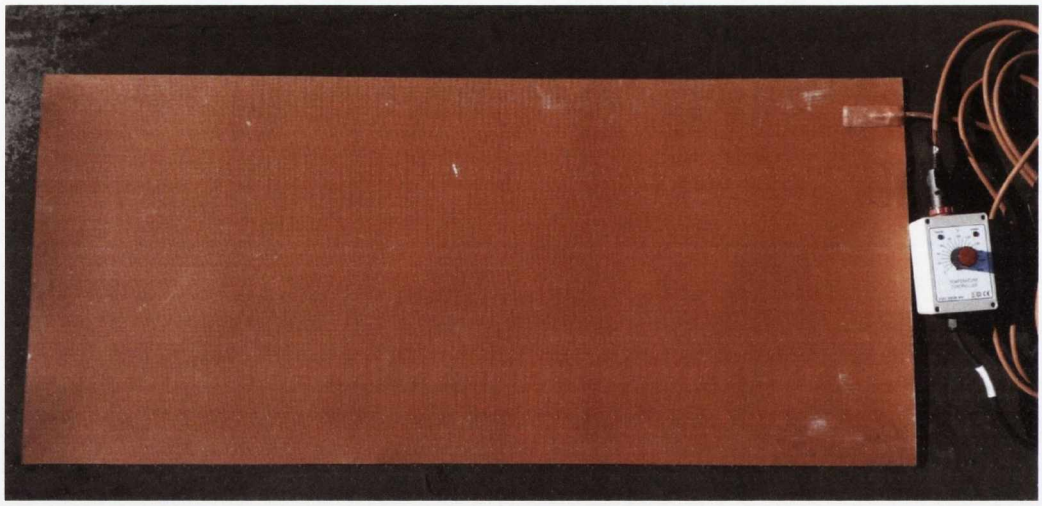

Figure 5.23: Heat mat with temperature controls used to generate forced heat

5.6.2 Environmental Conditions

The ambient temperatures and wind speed during the period of 9th- 14th September which are typical meteorological conditions of Dublin's climate are presented in Figure 5.24. The ambient temperature reached a high of 19 °C and solar irradiance exceeded 800 W/m^2 on the days tested. The first three days are simulating the solar irradiance conditions of Saudi Arabia and the temperature effect on the PV however, the ambient temperature remains to be of that in Dublin as the experiment was carried out in Dublin, Ireland. The last three days are data collected under Irish climatic conditions.

During the period 9th – 11th September the effect of the solar irradiance in Saudi Arabia (as shown in Figure 5.24) on the temperature of a PV panel was simulated using a heat mat. The solar irradiance during 12th-14th of September was the environmental conditions of Ireland. The six day experiment allowed for comparisons to be drawn between system performances under high (Saudi Arabia) and low (Ireland) solar irradiance conditions as these parameters were the primary drivers of the system.

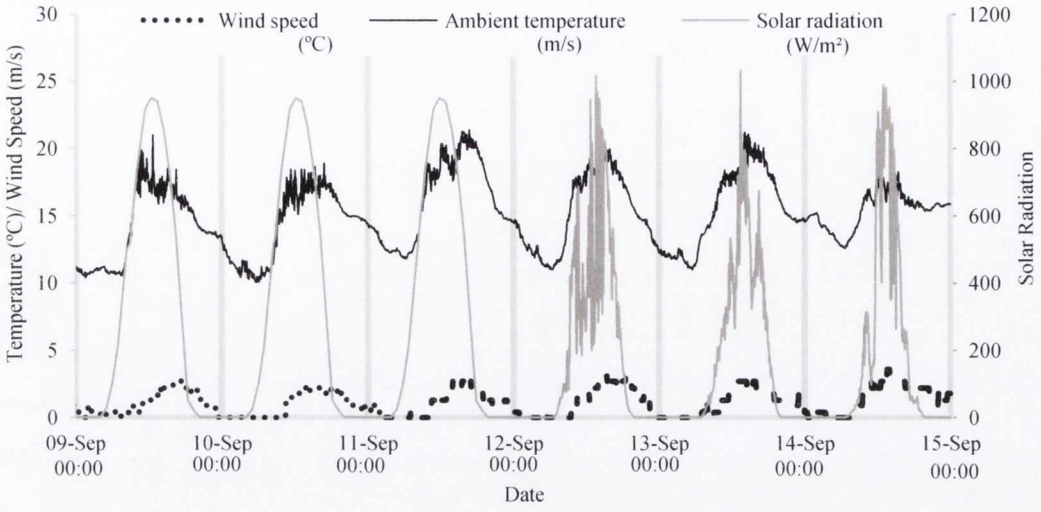

Figure 5.24: Environmental conditions for duration of experiment

The temperature of the back of the panel in System 3 and System 4 from the 9th to 14th September 2014 is presented in Figure 5.25. The heat mat was used to generate a forced heat over the first three days however, it must be noted the ambient temperature was lower than that in Saudi Arabia.

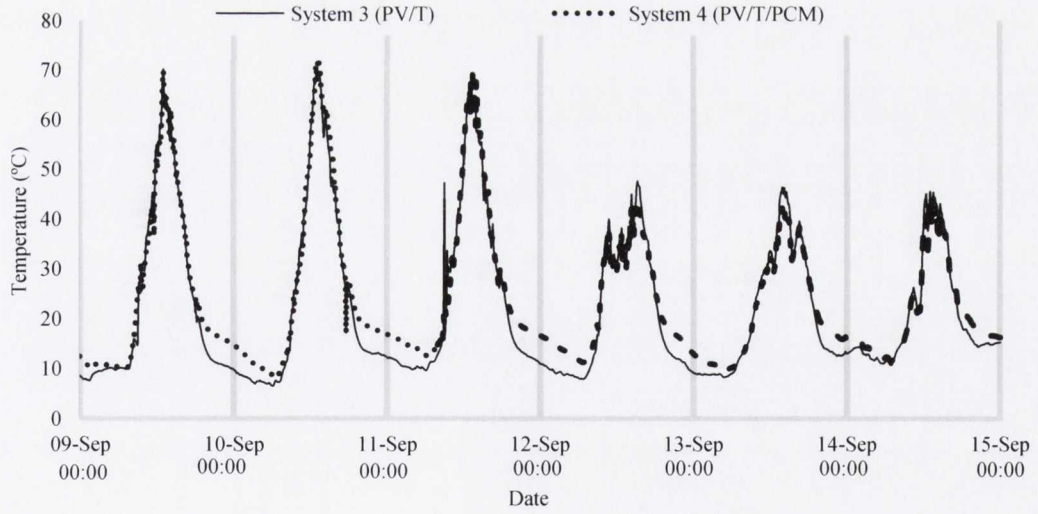

Figure 5.25: Temperature at the back of the panel

The initial temperature of the heat mat was approximately 20 °C at 09:00 hours. This was increased incrementally to approximately 66 °C at 13:00 hours and again the temperature was

reduced in small steps to approximately 25 °C at 17:30 hours which replicated the temperature of the rear of a PV panel in a desert climate (Rehman and El-Amin, 2012).

5.6.3 Results and Discussion

5.6.3.1 Charging and Discharging Phase Change Material

The inlet and outlet temperatures of both the PV/T and PV/T/PCM system are presented in Figure 5.26.

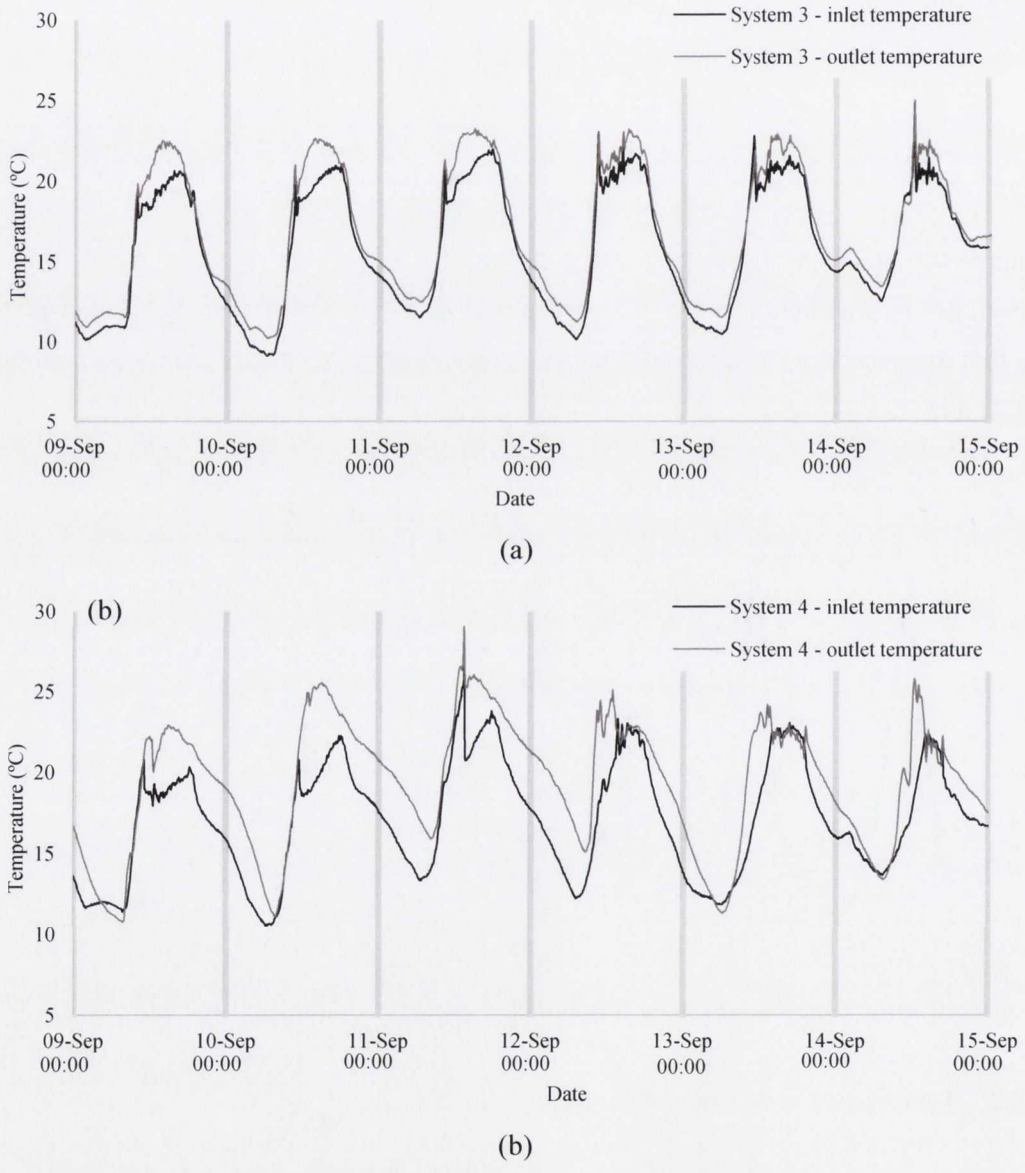

Figure 5.26: Inlet and outlet water temperatures of (a) System 3 (b) System 4

It can be seen that the outlet temperature of System 4 (average 3.03°C) is higher than System 3 (average) when simulating Saudi Arabian conditions. This is due to the PCM storing the heat during the day and releasing it to the water at night and during the early morning.

The temperature inside the container of the PV/T/PCM system is lower than that of the PV/T system due to the storage of heat by the PCM. There is a lag in the temperature increase of the inside of the container in the PV/T/PCM system compared to that of the PV/T system as the PCM is initially storing the heat. This is seen in when the temperature of the inside of the container of PV/T/PCM system is slower to increase than the temperature of the PV/T system and water.

The temperature difference between the inside of the container and the outlet water temperature is shown in Figure 5.27. In the case of System 3, the difference was between the air in the container and the outlet temperature and System 4 presented the difference between the PCM temperature and the outlet water temperature. The delay in the temperature rise in the container in System 4 compared to that of System 3 showed the PCM is initially storing heat prior to increasing in temperature.

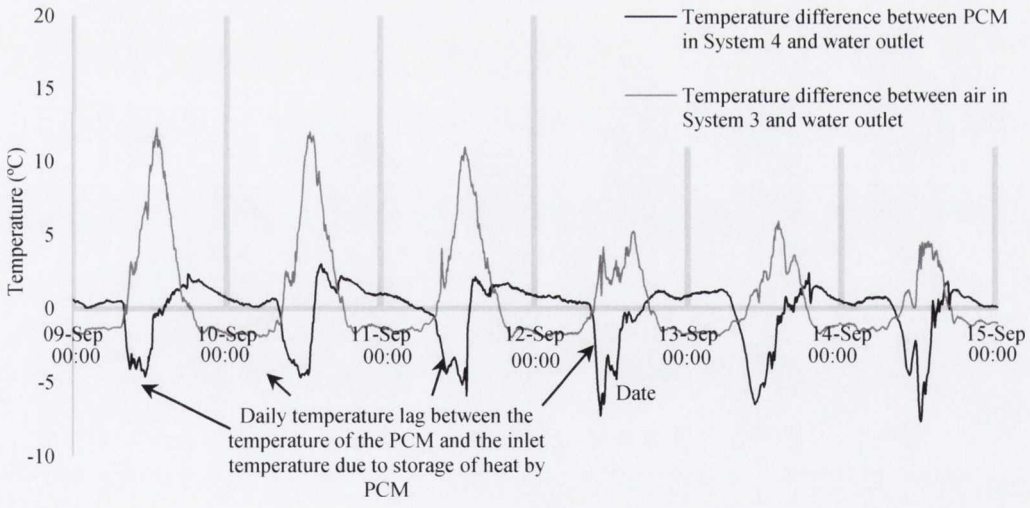

Figure 5.27: Temperature difference between inside of container and outlet temperature in PV/T/PCM and PV/T systems

PCM in the PV/T/PCM system extends the time for which the heat is available as it absorbs latent heat and charges during the day. The PV/T system only allows for immediate availability

of the heat gained by the system with the peak at approximately midday when the simulated temperatures are at their highest. The PCM shifts the time for which the heat is used as the heat gain is stored until discharging of the PCM occurs.

5.6.3.2 Available Heat Stored

The available heat stored (AHS), calculated using Equation 5.16, calculates the amount of time for which there was a potential for heat transfer to the water at the inlet from the inside of the container and the units of which is hour. Under simulated conditions, AHS in the PV/T/PCM system can be seen to be up to 50% larger than the AHS of the PV/T system, as illustrated in Figure 5.28. This is due to the latent heat capacity of the PCM and its ability to charge and discharge under certain temperatures. Although the values of AHS are not as high under Irish climatic conditions the amount of energy stored by the PV/T/PCM system is still approximately 33% larger than that for the PV/T system.

$$AHS = t_{T_{IC}>T_i} \tag{5.16}$$

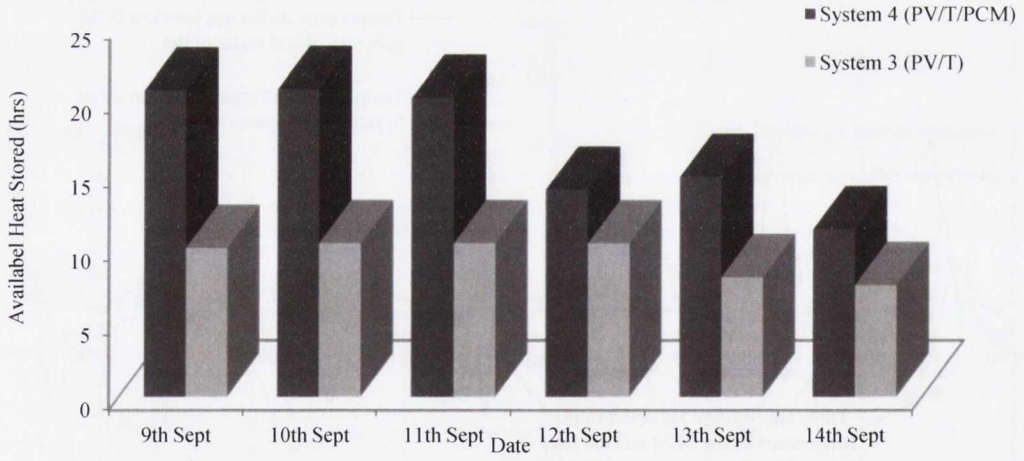

Figure 5.28: Available heat stored (y-axis) and preheat water potential with and without heating mats

For the first three days of the experiment when higher ambient temperatures were simulated (as shown in Figure 5.28), PCM increases the *AHS* by almost 100% (up to 20 hours; compared to the PV/T system which has a heat availability period of just over 10 hours). During the latter

three day period under Irish environmental conditions the period of available heat is reduced in both systems due primarily to the reduction in the heat input. However the PVT//PCM system still resulted in an extended period of available heat of up to 14 hours compared to the 8 hours from a system with no PCM (75% increase).

5.6.3.3 Water Temperature

The temperature difference of the water in the PV/T compared to the PV/T/PCM system as illustrated in Figure 5.29 is a result of the charging and discharging of the PCM. The daily temperature variation of the water in the PV/T-PCM system shows that the heat generated by the PV is being stored by the PCM during the day (approximately 11:00-18:00 hours), as there is a low temperature difference between the incoming and outgoing water. As ambient temperature decreases the PCM discharges heat gained to the water. This process is seen most clearly when the temperature of the water increases (approximately between 18:00-07:00 hours).

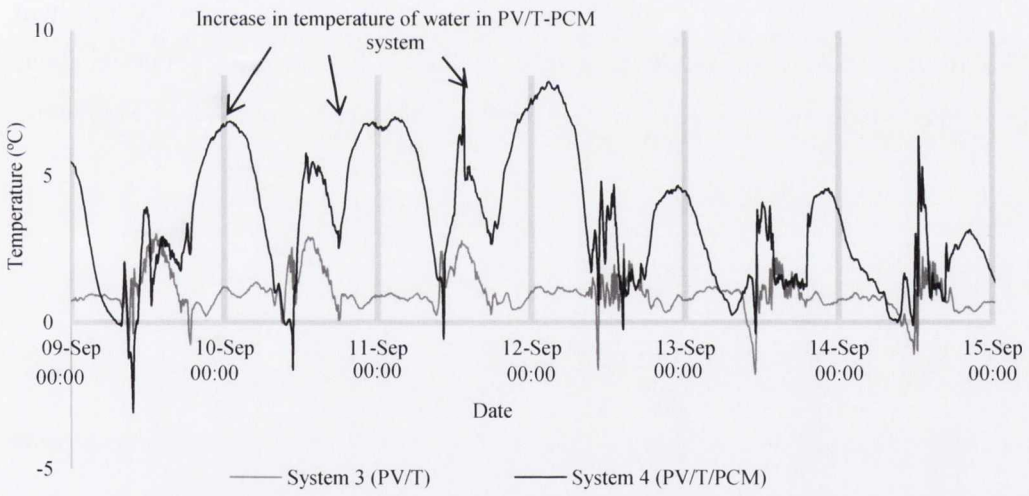

Figure 5.29: Temperature differential of the water inlet and outlet in PV/T-PCM and PV/T

The immediate availability of heat in the PV/T system can be seen as the temperature of the water peaks at approximately midday, allowing for no storage or extended time of availability. This heat is then stored in the hot water tank of the PV/T system.

The improvement in the potential of the PV/T/PCM system under simulated conditions is evident during the first three days of the experiment as the temperature difference between the

inlet and outlet is reaching highs of approximately 8 °C (mean 3.5 °C) compared to that of temperate conditions reaching highs of approximately 4 °C (mean 0.95 °C). PCM relocate the point of storage of heat from the hot water tank in a PV/T system to the PCM in a PV/T/PCM system. This could reduce the required size of the tank in a PV/T/PCM system compared to a PV/T system as the PCM can store an increased quantity of heat than water due to its heat of fusion of 210 kJ/kg.

5.6.3.4 Thermal Efficiency

An analysis of the daily thermal efficiency of the systems was undertaken using the equations presented in Section 5.3. The useful heat and storage gain experienced by the PV/T and PV/T/PCM systems are presented in Figure 5.30 and Figure 5.31, respectively. The useful heat gain (Equation 5.4) attained by the PV/T/PCM system was larger than that of the PV/T system over the first three days, when the simulated heat was applied to the systems. Once the PCM was fully charged the influx of heat is transferred to the water in the pipes. Following the removal of the heat mats the heat stored in the PCM was discharged to the water causing an increased value of useful energy gain by the PV/T/PCM system. Interestingly, the PV/T system is more efficient with regard to the useful energy gain on the last two days. This is definitely as a result of the higher rate of water flow in the PV/T system compared to the PV/T/PCM system.

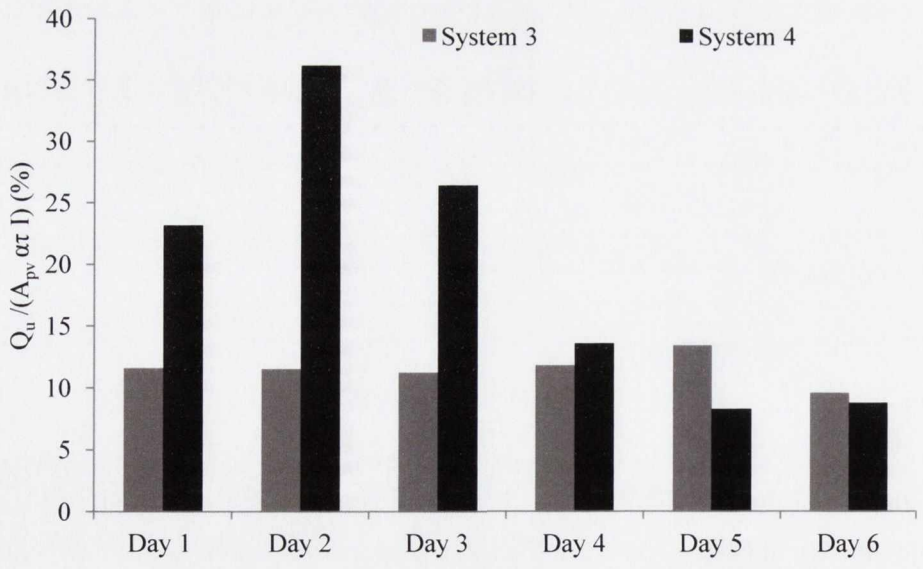

Figure 5.30: Useful heat gain, Q_u, by each system

During the day the temperature of the water in the PV/T system reaches higher temperatures than that of the water in the PV/T/PCM system and as a result the flow of water in the PV/T system is higher. The PCM slowly discharges the heat to the water over a longer period of time. The results show that the level of solar irradiance on Day 5 and Day 6 is not sufficient enough to charge the PCM fully and generate useful heat gain.

The storage efficiency of System 4 is shown in Figure 5.31. As there is no PCM in System 3, the storage efficiency is zero. During the increased solar conditions the PCM stored more heat than that of the final three days under the conditions of an Irish climate in autumn. The phase change temperature is important when choosing a PCM for an application. This is emphasised in Figure 5.31 as the phase change temperature is not reached on the last three days and as a result the PCM is reaching lower storage efficiencies.

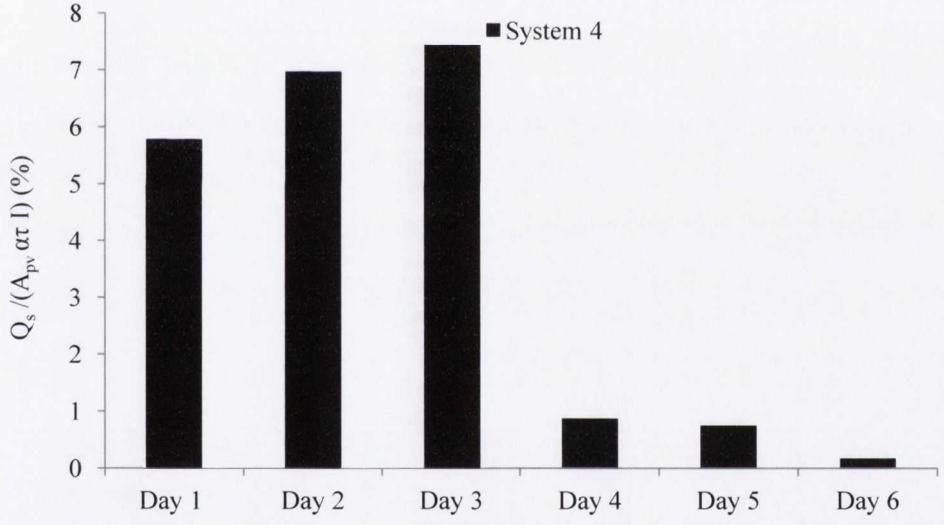

Figure 5.31: Heat stored, Q_s, by System 4

The extended time for which heat is stored (as shown in Figure 5.32) shows the values to remain at approximately 42% ± 3%, except on Day 1 where the early morning storage was missed as the forced heat was applied only during that day. As a result the early morning of Day 2 benefitted from the applied heat on Day 1. The remainder of the storage efficiencies can be seen to be at approximately the same value as the ambient temperature which causes the inlet to remain at a lower temperature than that of the PCM allowing for potential heat transfer for the majority of the time before sunrise and after sunset.

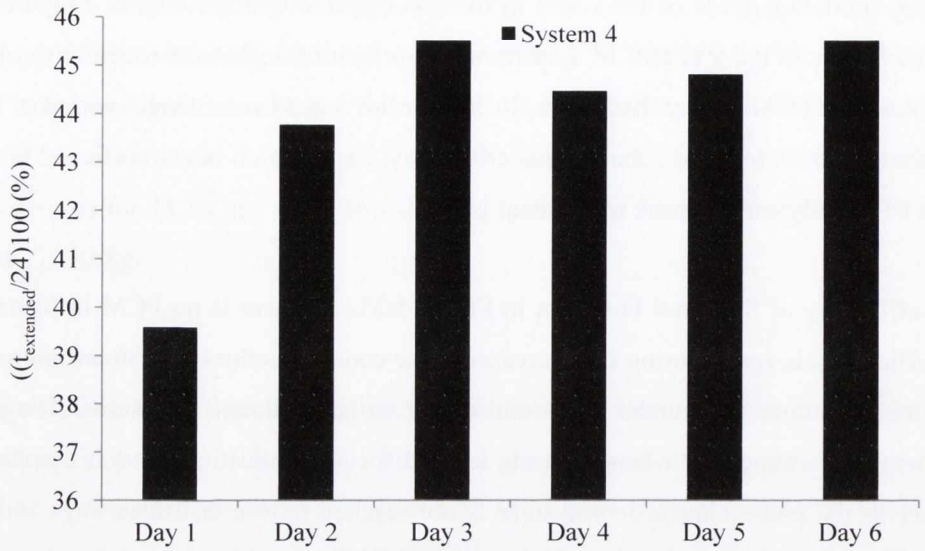

Figure 5.32: Heat storage potential of each system

The cumulative thermal efficiency of PV/T system (as shown in Figure 5.33) of the PV/T system was approximately 5% ± 1% over the course of the six days. The efficiency of the PV/T system is not affected by the increase in solar irradiance as the useful heat gain increases with respect to an increase in solar irradiance.

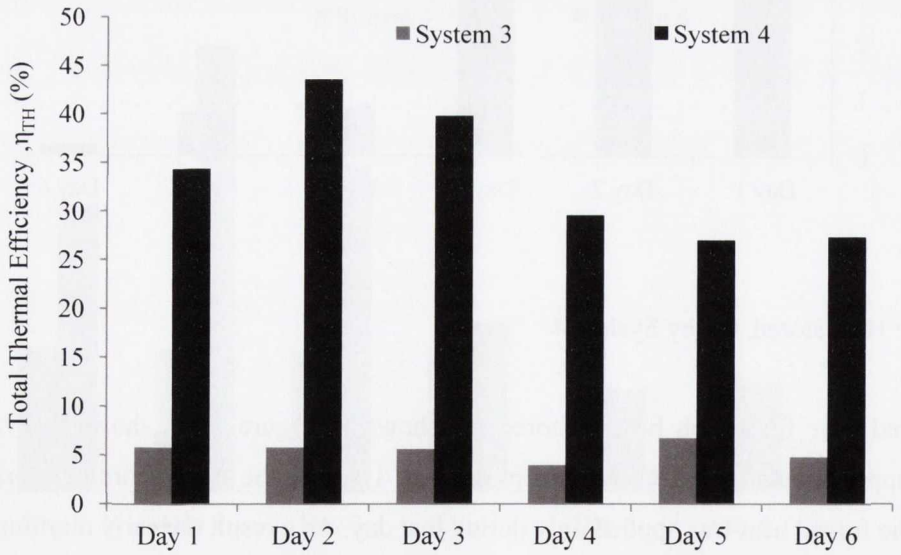

Figure 5.33: Total efficiency of the PV/T/PCM systems

The PV/T/PCM system shows an improved cumulative thermal efficiency during the days when a heat mat was applied. This increase is attributed to the increase in stored energy as the PCM was heated to a higher temperature. The results show that the increase in solar irradiance results in a greater improvement in PV/T/PCM compared to a PV/T system.

In conclusion it can be seen that the total efficiency of a PV/T/PCM system can be seen to dramatically improve under forced conditions compared to a temperate climate like that of Ireland. The gain in useful heat, the amount which is transferred to the water, was found to increase by approximately 50 % compared to a system without PCM, thereby increasing the energy gain by the system.

5.7 Conclusion

Following the analysis of the PV/T/PCM system, the daily process of the system can be explained using the stage process diagram in Figure 5.34.

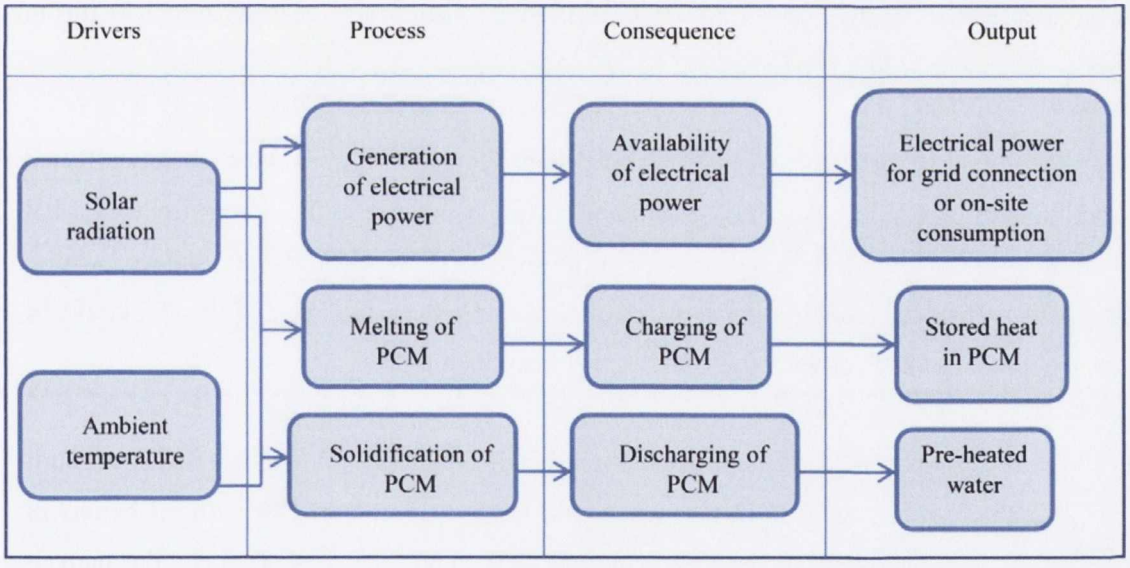

Figure 5.34: Stage process diagram of a PV/T/PCM system

The drivers of the passive system are solar radiation and ambient temperature which generate an electric current in the PV and melt the PCM, respectively. As a result of melting, the PCM stores thermal energy and remains in the charged state until it is discharged by the flow of water absorbing the heat from the PCM and a reduction in solar radiation and ambient temperature.

A novel PV/T/PCM system was characterised in Dublin, Ireland and its performance compared with three reference systems. The system was monitored for 220 days and 3 days were analysed. The advantages of the integration of the PCM, capric: palmitic acid has shown that the thermal performance of the system can be enhanced as water is heated to a higher temperature for a prolonged period of time compared to a system without PCM. The maximum temperature difference of the water in the system with and without PCM was 5.5 °C and occurred at approximately 6 am. The availability of heat was extended by up to 6.4 hours compared to a system without PCM.

An Equation 5.3 was developed and presented in order to analyse the thermal efficiency of a PV/T/PCM system. The equation took three terms into account: the gain in useful energy by the working fluid (water in this case), the heat stored by the system, and the time for which the heat is available to the working fluid. The thermal efficiency and the electrical efficiency were summed to give the cumulative efficiency of a system. The thermal efficiency of the novel PV/T/PCM system presented was found to range between 20 % - 25 %. However, it was noted that the release of heat from the PCM to the water needs to be improved by the increasing the thermal conductivity of the PCM or adding heat transfer enhancement techniques such as fins to the pipe network or within the container.

The power output of the PV in the PV/T/PCM system has been shown to be adversely affected by the addition of the thermal collector container when compared to the performance of a PV system. If the stainless steel container used in the installation presented was replaced with a material of higher conductivity, the transfer of heat away from the back of the PV could be improved and thus the electrical efficiency of the system maintained.

The PV/T/PCM system presented a method of pre-heating water by using a heat influx which is freely available and a system of this nature would be used in conjunction with oil boilers or domestic immersion heaters. The process behind the system has been described and the analysis of the heat transfer through the system has been presented.

Chapter 6

Modelling a Photovoltaic/Thermal/Phase Change Material System

Chapter 6. Modelling a Photovoltaic/ Thermal/ Phase Change Material System

6.1 Introduction

This chapter presents a numerical model of the performance of a Photovoltaic/Thermal/Phase Change Material (PV/T/PCM) system using two commercially available software packages, with particular focus on the level of electrical energy generated by the PV panel and the level of thermal energy stored within the system.

The specific objectives of this chapter are to:

- Develop models for the PV/T/PCM system described in Chapter 3 using TRNSYS and COMSOL
- Describe the model developed
- Presentation of the model results
- Model validation using data collected on-site

The validated model will then be used as a tool to predict system performance under varying environmental and operating conditions. It will also be used to carry out a parametric study for system optimisation.

6.2 Model Structure

Transient System Simulation Tool (TRNSYS) was used in conjunction with COMSOL Multiphysics modelling software to build a virtual PV/T/PCM system and accurately predict its performance. TRNSYS is used to simulate the electrical performance of the PV panel in the systems as well as the thermal performance. Limitations within TRNSYS made simulating the charging and discharging of PCM unreliable as the software specialises in system simulation. There was a component which modelled PCM available, however the absence of any mathematical reference made it ineffective. It was considered a CFD tool would be more reliable as it could consider heat transfer through the PCM. As a result, COMSOL was used to model the thermal energy storage component (PCM) which was designed to simulate physical processes therefore allowing the simulation of PCM.

The process of modelling the PV/T/PCM model involved simulating the basic PV system first and building upon this to simulate a PV/T/PCM system as described in Section 3.3. There was no reason to model System 2 as the effect of the container has been recognised in the experimental results. The process involved the following systems:

- PV system model (System 1-TRNSYS)
- PV/T system model (System 3- TRNSYS)
- PV/T system model (System 3 - TRNSYS and COMSOL)
- PV/T/PCM system model (System 4 - TRNSYS and COMSOL)

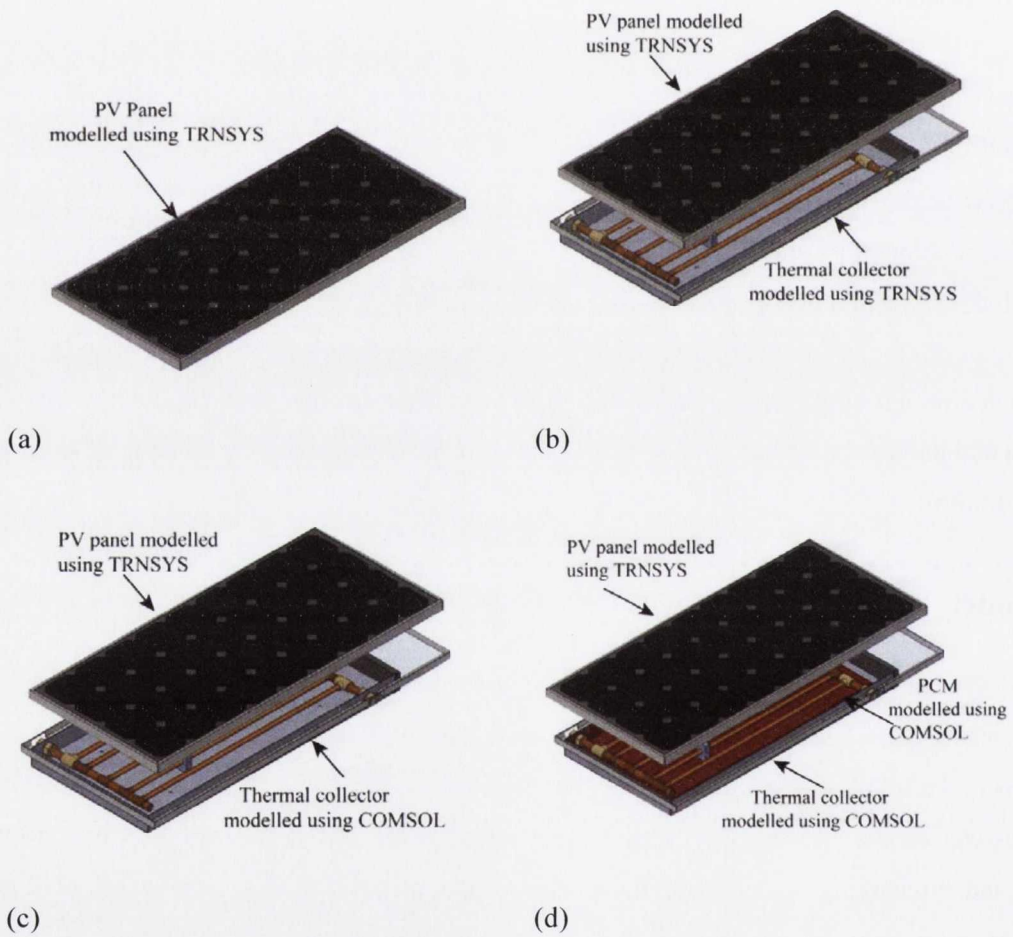

Figure 6.1: Schematic indicating the software used for various components of (a) System 1 (PV panel) (b) System 3 (PV/T) (c) System 3 (PV/T) (d) System 4 (PV/T/PCM)

The four systems were modelled to enable the presentation of the development process of the numerical simulation of a PV/T/PCM system. Beginning with the most basic, the performance

of a PV panel to a PV/T collector and finally to a PV/T/PCM system. This showed a clear path of building the model.

Similar to the experimental setup, the model will model solely the performance of the collectors over a 24 hour period. As shown in the experimental study the low outlet temperatures had no effect on the water tank temperature and as a result the water usage from the tank was not taken into account.

The software (as described in Section 2.5.3.1 and Section 3.4.2) used to model the components within each system is shown in Figure 6.1. TRNSYS was the main platform on which all system components are called and connected in order to build a simulation to model the system performance. TRNSYS models the electrical generation of the PV panel and the system configuration (such as pipes and tanks). There are two options to model the thermal collector depending on whether a phase change material is integrated into the system. If this is not the case, the thermal collector is simulated using TRNSYS. If the thermal collector has an integrated heat store, PCM, COMSOL is called to model the PCM, pipe network and container (see Figure 6.1) and the results of which are then exported to TRNSYS.

6.2.1 TRNSYS

As detailed in Chapter 3, TRNSYS is a visual based software used to model and simulate the behaviour of transient energy systems for applications such as solar systems, heating ventilation and air conditioning (HVAC) systems with advanced design features, and for assessing the energy performance of buildings. TRNSYS enables system components to be selected in order to construct a model for the system. The mathematical models for the system components are represented in the form of ordinary differential or algebraic equations. Components are referred to as 'Types' within TRNSYS and are assigned an identification number. The entire problem of a system simulation reduces to a problem of identifying all the components or Types that comprise the particular system and formulating a general mathematical description of each individual component (Kalogirou, 2001). In this study TRNSYS has been used to model both the PV panel and the PV/T system, which are presented in the subsequent sections.

6.2.1.1 Photovoltaic (PV) System Model (System 1)

The photovoltaic system, System 1, is modelled by connecting selected components in TRNSYS. The information flow diagram for the model is shown in Figure 6.2(a), along with the

schematic graphic presented via the graphical user interface of the software (Figure 6.2b). The green and blue arrows signify model inputs and model outputs, respectively. Black arrows are used to show minor calculations such as a change of unit. Red arrows will be used in later schematics to show the system process.

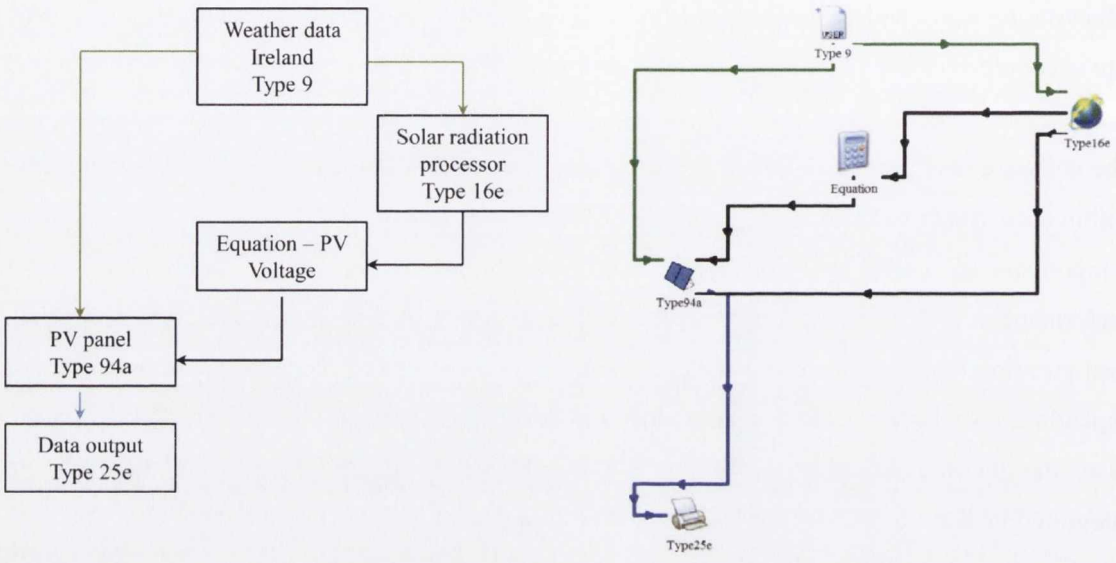

(a) (b)

Figure 6.2: Model of PV system (a) information flow diagram (b) TRNSYS schematic

The main components of the model are the PV panel (Type94a), standard data reader used to import weather data (Type 9), solar radiation processor (Type 16e) and the data output printer (Type 25e). Enclosed in the brackets are the components identification numbers which are used in the graphical user interface.

Type 94a uses a four parameter model developed by Townsend (1989) and detailed by Duffie and Beckman (1992) to model the electrical performance of a crystalline photovoltaic panel or array. It employs equations for an empirical circuit model to predict the current-voltage (IV) characteristics of a single module. The strength of the current source is dependent on the solar radiation and the IV characteristics of the diode are temperature-dependent (TRNSYS Manual, 2014). The PV model employs these environmental conditions along with the four module constants to generate an IV curve at each time step;

- $I_{L,\,ref}$ (module photocurrent at reference conditions);

- $I_{o,\,ref}$ (diode reverse saturation current at reference conditions),
- γ (empirical PV curve fitting parameter)
- R_s (module series resistance)

The current-voltage equation of the circuit is shown in Equation 6.1, where R_s and γ are constants.

$$I = I_L - I_0 \left[\exp\left(\frac{q}{\gamma k_B T_c}(V + IR_s)\right) - 1\right] \tag{6.1}$$

Where, q is the electron charge constant, k is Boltzmann constant and T_c is the cell temperature. The photocurrent, I_L, is determined from incident irradiance (Equation 6.2), where the solar irradiance at reference conditions (G_{ref}) is given as a parameter. The diode reverse saturation current, I_o, is a temperature dependent quantity determined from Equation 6.3.

$$I_L = I_{L,ref}\frac{G_T}{G_{T,ref}} \tag{6.2}$$

$$\frac{I_0}{I_{0,ref}} = \left(\frac{T_c}{T_{c,ref}}\right)^3 \tag{6.3}$$

Equation (6.1) gives the current implicitly as a function of voltage. Newton's method is applied to calculate the PV current once I_0 and I_L are found using Equations 6.2 and 6.3 (TRNSYS Manual, 2014). Experimental input parameters of the PV which were inputs to the model are presented in Table 6.1.

Type 9 serves the purpose of reading numerical data at regular time intervals from an excel data file, converting it to a desired system of units and making it easily available to other TRNSYS components as time varying forcing functions. The data was collected on-site at the location of the PV/T/PCM system using a pyranometer and weather station. Forcing functions have a behaviour characterised by a repeated pattern. The pattern of forcing functions is established by a set of discrete points indicating the value of the function at various times throughout one cycle. Linear interpolation is provided in order to generate a continuous forcing function from

the discrete data. The environmental data in the model presented is read from a excel file and imported into the model.

Table 6.1: Experimental input parameters of photovoltaic panel

Parameter	**Value**	**Unit**
Module short-circuit current at reference conditions	5.04	amperes
Module open-circuit voltage at reference conditions	21.6	V
Reference temperature	298	K
Reference insolation	1000	W/m^2
Module voltage at max power point and reference conditions	17.5	V
Module current at max power point and reference conditions	4.8	amperes
Temperature coefficient of Isc at (ref. cond)	0.003	-
Temperature coefficient of Voc (ref. cond.)	-0.13	-
Number of cells wired in series	36	-
Number of modules in series	1	-
Number of modules in parallel	1	-
Module temperature at NOCT	313	K
Ambient temperature at NOCT	293	K
Insolation at NOCT	1000	W/m^2
Module area	0.648	m^2
tau-alpha product for normal incidence	0.90	-
Semiconductor bandgap	1.12	-
Slope of IV curve at Isc	0	-
Module series resistance	-1	-
Module short-circuit current at reference conditions	5.04	amperes

A solar radiation processor accurately calculated the solar irradiance intensities related to the position of the sun. The beam and diffuse solar radiation, which were collected on-site at the location of the PV/T/PCM system and were used to estimate the insolation on a number of surfaces of fixed orientation as this was required as component inputs (TRNSYS Manual, 2014).

6.2.1.2 Photovoltaic/ Thermal (PV/T) System Model (System 3)

The information flow diagram (Figure 6.3a) details the layout of the model and the connections between components.

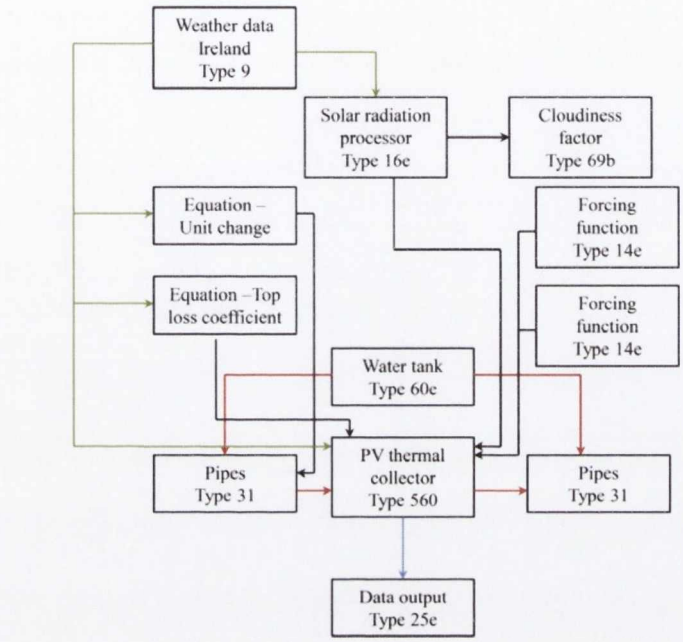

(a)

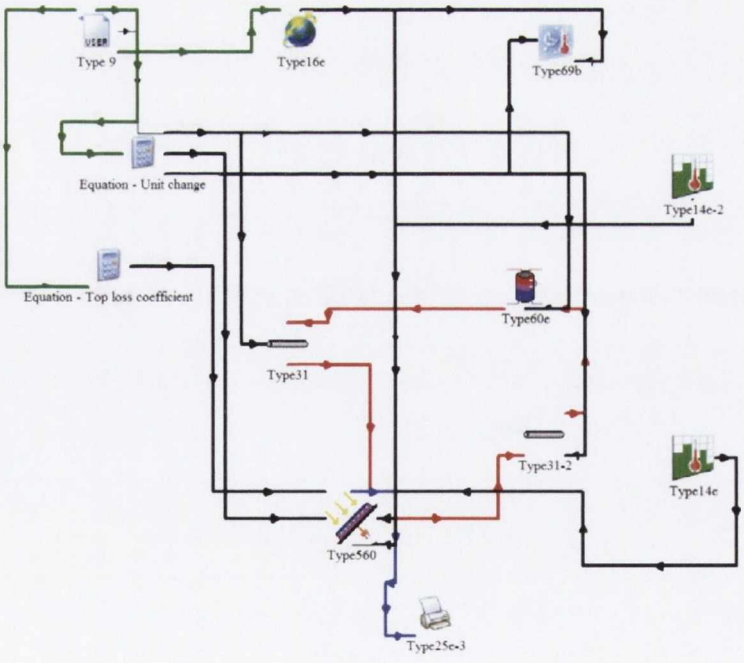

(b)

Figure 6.3: Model of PV/T system (a) information flow diagram (b) TRNSYS schematic

The graphical user interface of the model simulating the photovoltaic/thermal system as shown in Figure 6.3(b); the model which was built on the previous TRNSYS model replaces a PV with a PV/T system.

As in the PV system model described in the previous section, weather data was imported and was processed to determine the solar radiation intensities. The effective sky temperature (T_{sky}) , the temperature of a black body for which the measured radiative flux is the same as for the sky (Curtis, 2013), was required as an input for the PV/T system component and was calculated (Type 69b) which was shown to peak at 22 °C in the early evening. In order to calculate the effective sky temperature Equation 6.4 was used where the ambient temperature (T_{amb}), air humidity (peaked at 80%), cloudiness factor of the sky (C_c), emittance of a clear sky (ε_0) and the local air pressure (P_{atm}) are required as inputs. The cloudiness factor, C_c, refers to the fraction of sky obscured by clouds at a particular location which was shown to peak at 1 and reduce to 0.31 and was calculated using Equation (6.5). The emittance of a clear sky, ε_0, is the measure of the efficiency in which the sky emits thermal energy and is calculated using Equation 6.4.

$$T_{sky} = T_{amb}(\varepsilon_0 + 0.8(1 - \varepsilon_0)C_C)^{0.25} \tag{6.4}$$

Equation 6.5 calculates the cloudiness factor as a function of the horizontal diffuse solar irradiance ($G_{dif,\,h}$) and the horizontal global irradiance (G_{gh}) (TRNSYS Manual, 2014).

$$C_C = \left(1.4286\,\frac{G_{dif,h}}{G_{g\,h}} - 0.3\right)^{0.5} \tag{6.5}$$

Equations (6.6) and (6.7) were used to calculate the P_{atm} and T_{amb}, respectively.

$$P_{atm} = P_0 e^{\frac{g\rho_0 h}{P_0}} \tag{6.6}$$

$$\varepsilon_0 = 0.711 + 0.005T_{sat} + 7.3x10^{-5}T_{sat}^2 + 0.013cos\left[2\pi\frac{time}{24}\right] + 12x10^{-5}(P_{atm} - P_0) \tag{6.7}$$

Where;

- P_0 = pressure at height 0 m (Pa)

- g = gravitational acceleration (m/s^2)
- h = elevation above sea level (m)
- ρ_0 = density of air at height 0 m (kg/m^3)
- T_{sat} = dew point temperature at ambient temperature (°C)

The main component of the model is the photovoltaic thermal collector which is modelled using Type 560. Type 560 is a combined PV/T solar collector which simulates an unglazed solar collector which has the dual purpose of creating power from embedded PV cells and providing heat to a fluid stream passing through tubes bonded to an absorber plate located beneath the PV cells, as shown in Figure 6.4.

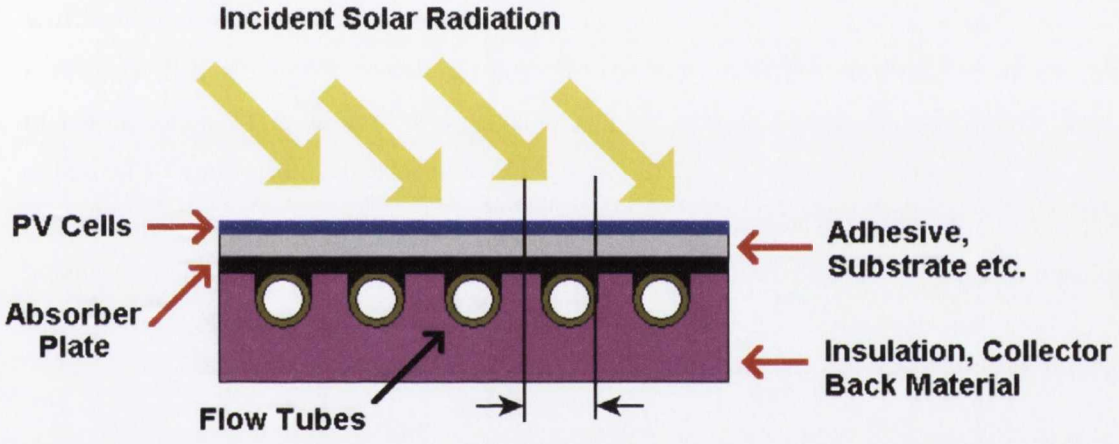

Figure 6.4: PV/T system as modelled in TRNSYS (Type 560) (TRNSYS Manual, 2014)

The model relies on linear factors relating the efficiency of the PV cells to the cell temperature and the solar radiation. The cells are assumed to be operating at maximum power point conditions which require the implementation of a device which maximises the power output of a PV such as a maximum power point tracker (MPPT). A MPP charge controller calculates the maximum voltage of the module (V_{mp}) and operates the modules to extract this value regardless of the battery voltage. Once the voltage has been drawn from the module by the charge controller, it is converted by the charge controller to the battery voltage at the output. In order to equate power drawn from the PV to power directed to the battery, the charge current is increased to make up for the reduction in the voltage, thus, maximising power drawn from the PV.

An overview of the equations used to model a PV/T system as described in Section 3.3.1.2 and illustrated in Figure 6.1(b) are presented in the following paragraphs. An energy balance at any point along the collector surface (neglecting conduction along the surface) shows the relationship:

$$S - h_{outer}(T_{PV} - T_{amb}) - h_{rad}(T_{PV} - T_{sky}) - \frac{T_{PV} - T_{abs}}{R_T} = 0 \tag{6.8}$$

Where; S is the net absorbed solar irradiance and accounts for the absorbed solar irradiance minus the PV power produced, h_{outer} is the heat transfer coefficient from the top of the collector (PV surface) to the ambient air, T_{abs} is the absorber plate temperature and R_T is the resistance of heat transfer provided by the material between the PV cells and the absorber. To account for off-normal solar irradiance effects the incidence angle modifier (IAM) for both sky and diffuse irradiance are determined within the component. The efficiency of the PV cells (η_{PV}) is a function of the cell temperature (X_{ct}) and the incident solar irradiance (X_{rad}) as shown in Equation 6.9. The multiplier for the cell efficiency as function of cell temperature, X_{ct}, is used to recalculate the PV efficiency taking into account the cell temperature. The multiplier for the cell efficiency as function of solar irradiance, X_{rad}, is used to recalculate the PV efficiency taking into account the current value of the solar irradiance. The nominal efficiency, η_{nom}, is the efficiency at standard test conditions.

$$\eta_{PV} = (\eta_{nom})(X_{ct})(X_{rad}) \tag{6.9}$$

Where,

$$X_{ct} = 1 + Eff_T(T_{PV} - T_{ref}) \tag{6.10}$$

$$X_{rad} = 1 + Eff_G(G_{Tot} - G_{ref}) \tag{6.11}$$

T_{PV} and T_{ref} are the temperatures of the PV and the reference temperature at STC. G_{Tot} and G_{ref} are the solar irradiance values incident on the solar collector surface and reference conditions at STC, respectively. Eff_T and Eff_G are the modifiers for PV efficiency as a function of cell temperature and solar irradiance, respectively. The cell temperature modifier was the value by which the efficiency was effected per degree Celsius increase in cell temperature, in this case the value was 0.675 W/°C as found in the PV datasheet (Solar Technology International, 2013). The solar irradiance was not considered to have an effect of the cell efficiency and so was '0'.

An energy balance was taken for a generic sample along the absorber plate; from the midpoint of the two adjacent tubes to the end of a tube as indicated in Figure 6.4. From the energy balance equation the temperature distribution is known along the tube and the base area of the absorber plate. The useful energy gain to the fluid can then be determined as a function of the base temperature using Equation 6.12. The heat transfer to the fluid per unit length of the collector was q'_f. The temperature of the base area of the absorber plate and the fluid are T_b and T_f. The internal fluid heat transfer coefficient was h_f which in this case the fluid was water. The tube diameter was D_t and was assigned a value of 0.02 m and C_B is the conductance between the absorber plate and the bond tube.

$$q'_f = \left(\frac{T_b - T_f}{\frac{1}{h_f \pi D_t} + \frac{1}{C_B}} \right) \tag{6.12}$$

The top loss coefficient of the PV/T collector, U_T, was determined using Equation 6.13 (Duffie and Beckman, 1992) which was calculated using a function within TRNSYS. The heat transfer coefficient of the wind, h_w, is calculates as a function of the wind velocity, V_w, as shown in Equation 6.14. The heat transfer coefficient between the plate and the cover plate of the absorber, $h_{p\text{-}c}$, was calculated as a function of the temperature of the plate, T_{plate}, and the cover plate, $T_{p\text{-}c}$ and i is the plate spacing.

$$U_T = h_w + h_{p-c} \tag{6.13}$$

Where,

$$h_w = 5.7 + V_w * 3.8 \tag{6.14}$$

$$h_{p-c} = \left(1 - 0.0018\left(\left(\frac{T_p + T_{cp}}{2}\right) - 10\right)\right)\left(1.14\left(\frac{(T_p - T_{cp})^{0.31}}{i^{0.07}}\right)\right) \tag{6.15}$$

The input parameters of the PV/T solar collector and the water storage tank are listed in Table 6.2 and Table 6.3, respectively.

Table 6.2: List of experimental parameters of the PV/T collector

Parameter	**Value**	**Unit**
Collector length	1.196	m
Collector width	0.542	m
Absorber plate thickness	0.02	m
Thermal conductivity of the absorber	0.9252	kJ/hr.m.K
Number of tubes	5	-
Tube diameter	0.02	m
Bond width	0.02	m
Bond thickness	0.001	m
Bond thermal conductivity	1443.599962	kJ/hr.m.K
Resistance of substrate material	0.000087	h.m2.K/kJ
Resistance of back material	0.216111	h.m2.K/kJ
Fluid specific heat	4.190	kJ/kg.K
Reflectance	0.15	Fraction
Emissivity	0.9	Fraction
1st order IAM	0	-
PV cell reference temperature	25.0	°C
PV cell reference radiation	3600	kJ/hr.m^2
PV efficiency at reference condition	0.124	Fraction
Efficiency modifier - temperature	-0.675	1/°C
Efficiency modifier - radiation	0	h.m2/kJ

Table 6.3: List of experimental parameters of the water tank

Parameters	Value	Units
User-specified inlet positions	2	-
Tank volume	0.144	m^3
Tank height	1.05	m
Tank perimeter	-1	m
Height of flow inlet 1	0.2	m
Height of flow outlet 1	0.1	m
Fluid specific heat	4.190	kJ/kg.K
Fluid density	1000.0	kg/m^3
Tank loss coefficient	2.55	kJ/hr.m^2.K
Fluid thermal conductivity	1.40	kJ/hr.m.K
Boiling temperature	100.0	C

As the programmed component within TRNSYS is not a replicate of the PV/T system that was tested, assumptions were made with respect to Type 560 (shown in Figure 6.5).

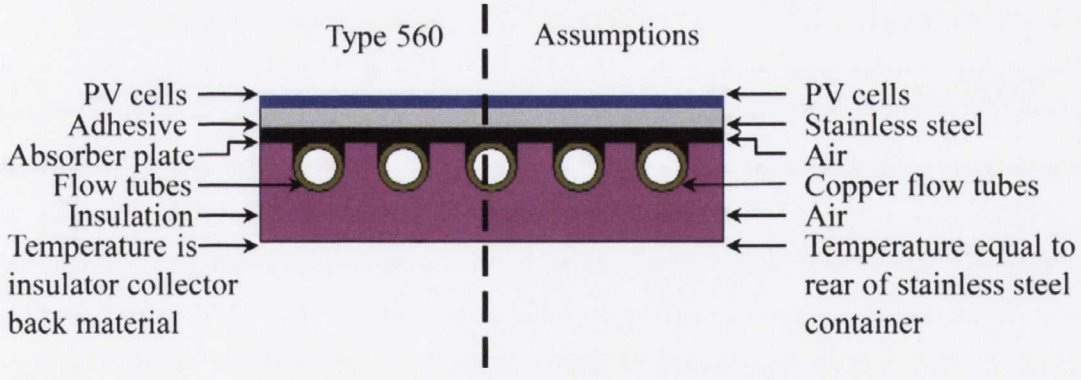

Figure 6.5: Assumptions based on Type 560

The model assumptions were implemented by varying the input values of the material properties to match the experiment as shown in Figure 6.1(b). The left of Figure 6.5 shows the design of the model and the intended components of the system. However, this was not a direct reflection of the PV/T system designed in this research so the material properties were varied to match the

experimental component. The components on the left were replaced with the properties of the corresponding component on the right, for example, the adhesive was assigned material properties of stainless steel as shown in Figure 6.5. It was also assumed that the PV panel was functioning at maximum power for the duration of the simulation.

Additional components were implemented in the model to include the pipe ducts, hot water cylinder which were assigned the experimental parameters of the respective components.

6.2.2 COMSOL

As detailed in Chapter 3, COMSOL is a finite element analysis, solver and simulation software package. It allows the integration of various discipline-specific modules (including stress/strain analysis, heat transfer analysis, fluid flow analysis and electromagnetic analysis) on a single graphical user interface. The software allows the geometry of a system to be constructed followed by the allocation of material properties and boundary conditions. The process of obtaining an appropriate mesh can be done using an automatic mesh generation procedure. Meshing generation is the name given to the practice of subdividing the physical domain into sub domains called finite elements. The application of meshing is used in finite element software packages such as that of COMSOL to generate a polygonal or polyhedral mesh and approximate physical quantities such as temperature of each domain. COMSOL also provides a platform for results visualisation.

COMSOL has been used in this thesis to model the thermal collector component of the system both with and without PCM as it was found to have a superior approach to modelling phase change material compared to TRNSYS which allowed the temperature variation of the PCM at different locations within the container to be assessed. This is due to COMSOL's capacity to integrate physical processes in a single model, such a pipe flow and heat transfer as is required when modelling the thermal collector. The results are exported to TRNSYS and are used to assess the performance of the system as a whole including the thermal and electrical energy generation.

6.2.2.1 Thermal Collector Model

The thermal collector system model was built in COMSOL based on the experimental setup presented in Chapter 3. The system geometry of the container and pipe network is presented in Figure 6.6.

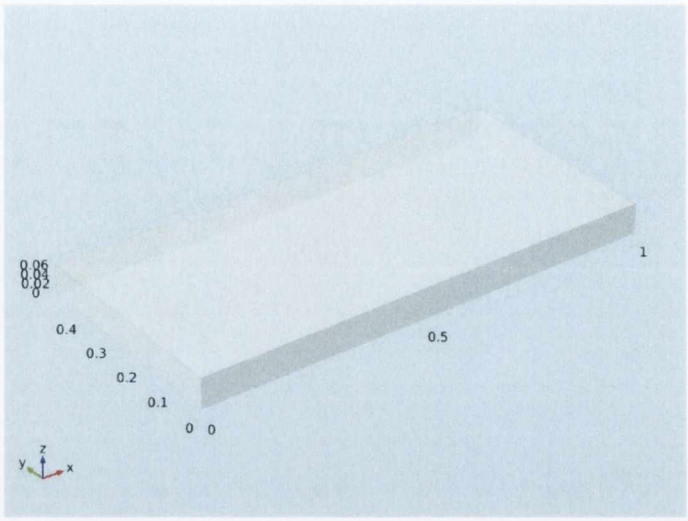

(a)

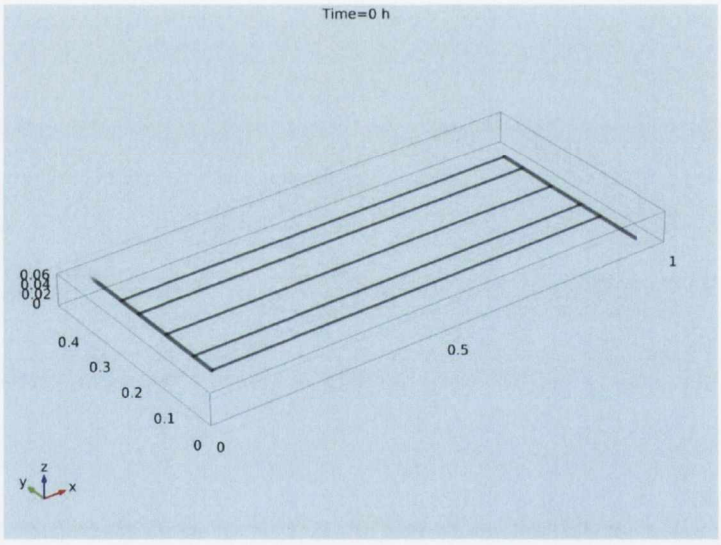

(b)

Figure 6.6: Geometry of the thermal collector built using COMSOL (a) container (b) pipe network

Built-in material properties of air, stainless steel, copper and water were allocated to the relevant geometries. The application of assigning physical processes to the system required choosing a fluid (non-isothermal pipe flow) and a mechanical (heat transfer in solids) operation module which allowed water movement throughout the pipe network as well as the transfer of heat through the system to be simulated.

Non-isothermal pipe flow interface approximates the pipe flow by making 1D assumption in curved segments or lines. These lines are drawn in 3D and represent simplifications of hollow tubes in order to calculate the temperature, velocity, and pressure fields in the pipes. The '*Fluid*' node was linked to the relevant material properties (i.e. water). The momentum and continuity equations for flow in a pipe, as shown in Equations 6.16 and 6.17, are given by Barnard et al. (1966):

$$\rho \frac{\partial \mathbf{u}}{\partial t} = -\nabla p - f_D \frac{\rho}{2d_h} \mathbf{u}|\mathbf{u}| + \mathbf{F} \tag{6.16}$$

$$\frac{\partial A\rho}{\partial t} + \nabla.(A\rho\mathbf{u}) = 0 \tag{6.17}$$

Where, the second term on the right hand side of Equation 6.16 represents the pressure drop due to viscous shear and;

- **u** is the cross section averaged velocity,
- ρ the density,
- p is the pressure,
- f_D the Darcy friction factor
- **F** is a volume force term

The hydraulic diameter (d_h) is given by Equation 6.18, where A is the cross section area and Z is the wetted perimeter (COMSOL 5.0, 2014).

$$d_h = \frac{4A}{Z} \tag{6.18}$$

The energy equation for incompressible fluid flowing in a pipe is (Lurie, 2008):

$$\rho A C_p \frac{\partial T}{\partial t} + \rho A C_p \mathbf{u} \cdot \nabla \mathrm{T} = \nabla \cdot \mathrm{Ak}\nabla \mathrm{T} + \mathrm{f_D} \frac{\rho \mathrm{A}}{2\mathrm{d_h}} |\boldsymbol{u}|^3 + Q + Q_{wall} \tag{6.19}$$

Where;

- ρ is the fluid density
- A is the pipe cross section area available for flow
- C_p is the heat capacity at constant pressure

- T is the temperature
- **u** is a velocity field
- k is the thermal conductivity

The second term on the right hand side corresponds to friction heat dissipated due to viscous shear. Q represents the general heat source and Q_{wall} represents external heat exchange through pipe wall.

The radial heat transfer from the surroundings into the pipe is given by:

$$Q_{wall} = (hZ)_{eff}(T_{ext} - T) \tag{6.20}$$

Where;

$(hZ)_{eff}$ is an effective value of the heat transfer coefficient, h, times the wall perimeter Z and T_{ext} is the external temperature outside of the pipe (COMSOL 5.0, 2014).

The pipe shape and flow resistance are defined using the equations presented in Equations 6.21 - 6.24 below. The constants C_x and C_y are calculated as functions of the Reynolds number, Re, surface roughness, e and hydraulic diameter, d_h. The Reynolds number is calculated using the fluid density, ρ, kinematic viscosity, u, and the dynamic viscosity, μ. The flow resistance (f_D) is defined as:

$$f_D = 8\left[\left(\frac{8}{Re}\right)^{12} + (c_x + C_y)^{-1.5}\right]^{\frac{1}{12}} \tag{6.21}$$

Where;

$$Re = \frac{\rho u d_h}{\mu} \tag{6.22}$$

$$C_x = \left[-2.457ln\left(\left(\frac{7}{Re}\right)^{0.9} + 0.27\left(\frac{e}{d_h}\right)\right)\right]^{16} \tag{6.23}$$

$$C_y = \left(\frac{37530}{Re}\right)^{16} \tag{6.24}$$

The velocity conditions at the inlet were matched to experimental conditions. The heat transfer across the pipe wall was determined using Equation 6.25 where the equation for the effective heat transfer coefficient, $(hZ)_{eff}$ of round pipes is:

$$(hZ)_{eff} = \frac{2\pi}{\frac{1}{r_0 h_{int}} + \frac{1}{r_n h_{ext}} + \sum_{n=1}^{N}\left(\frac{ln\left(\frac{r_n}{r_{n-1}}\right)}{k_n}\right)} \tag{6.25}$$

Where;

- h_{int} is the heat transfer coefficient on the inside of the pipe
- h_{ext} is the heat transfer coefficient on the outside of the pipe
- k_n is the thermal conductivity of the wall
- r_0 is the outer radii
- r_n is the and inner radii

Friction coefficients for each junction were specified and are used to calculate the pressure drop introduced by the bend or T-junction, depending on the pipe connection.

The following assumptions were applied by the model with regard to calculations involving non-isothermal pipe flow:

- The velocity profile is fully developed and does not change within a section. As a result the equations only solve for an average velocity and the pipe is represented by a line in the geometry
- The cross section area is allowed to change between pipe segments
- Empirical functions describe viscous losses
- Shocks are neglected, although in this case fluid would not be moving at such a speed to warrant shocks

The simulation of the heat transfer in the air by convection and radiation in a solid was calculated using Equation 6.26 (COMSOL 5.0, 2014).

$$\rho C_p \frac{\partial T}{\partial t} + \rho C_p \mathbf{u} \cdot \nabla T + \nabla \cdot (-k\nabla T) = Q \tag{6.26}$$

The density (ρ), heat capacity (C_p) and thermal conductivity (k) of air are used to calculate the heat transfer (Q). It also includes the velocity of fluid flow, **u**.

In order to simulate the effect of ambient temperature on the surface of the container, a radiative and convective heat flux was applied to the boundary surface of the stainless steel container using Equations 6.27 and 6.28 (COMSOL 5.0, 2014).

$$-\mathbf{n} \cdot (-k\nabla T) = \varepsilon\sigma\left({T_{amb}}^4 - T^4\right) \tag{6.27}$$

$$-\mathbf{n} \cdot (-k\nabla T) = h \cdot (T_{amb} - T) \tag{6.28}$$

The thermal properties and thickness of the stainless steel container were defined and located on the boundary of the PCM. A transient temperature was applied to the stainless steel container surface in order to imitate the temperature of the back of the PV panel. The temperature of the back of the PV panel was generated in TRNSYS and was exported to COMSOL.

As tetrahedral shapes are recommended for 3D volumes (COMSOL 5.0, 2014) it was used in the mesh of the PV/T system in Figure 6.7 which consisted of elements varying in size from 0.004 m – 0.055 m. The mesh size can vary depending on the parameters specified in the model. Smaller meshes are more detailed and require increased computational calculations as more detail is needed than that of larger mesh sizes. As a result, there is a compromise between detail of the model and the computational power and time available.

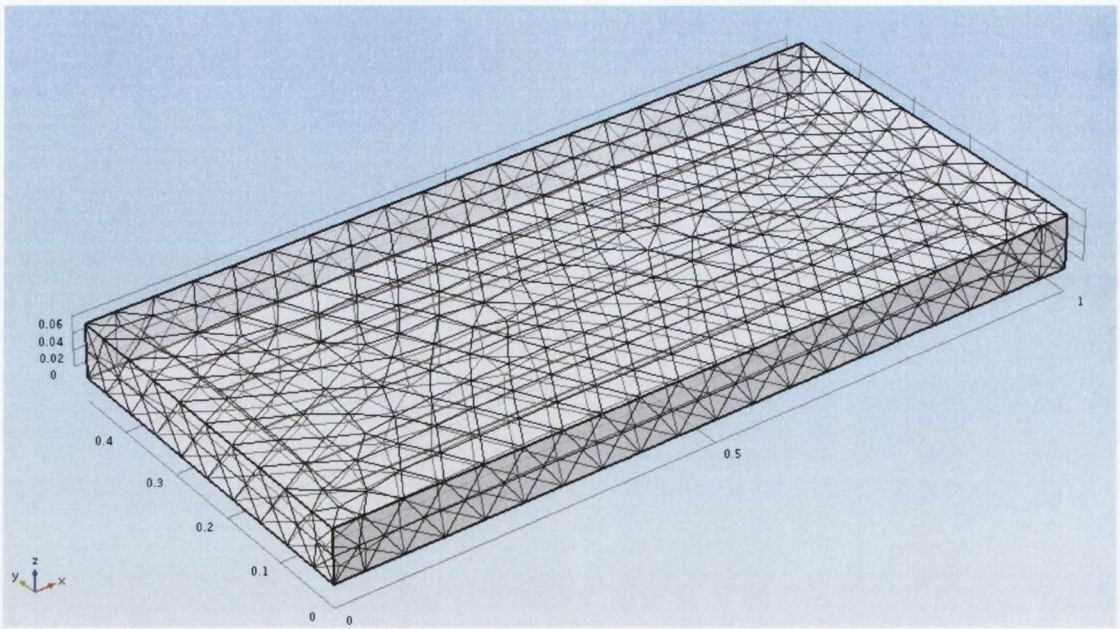

Figure 6.7: Mesh of PV/T system generated in COMSOL

The time-dependent study used a time step of 12 minutes as a further reduction in time step increased the computational power and time required to simulate the system however, did not decrease the model error sufficiently (±0.2%) as shown in Figure 6.8.

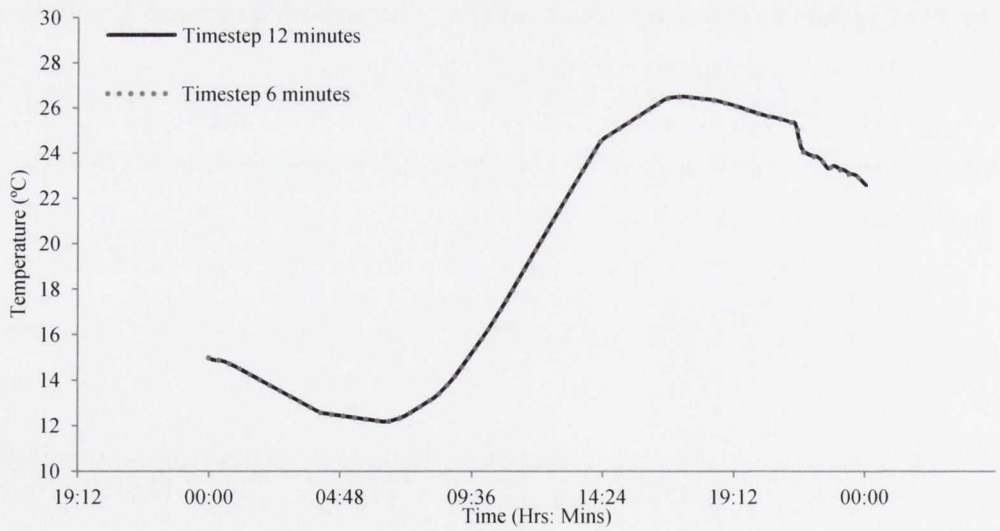

Figure 6.8: Variation in outlet temperature at 12 and 6 minute time steps

6.2.2.2 Thermal Collector with Phase Change Material Model

The thermal collector with phase change material was based on the thermal collector presented earlier in Sections 3.3.2 and 5.2. The air was substituted with PCM in the thermal collector (as shown in Figure 6.9) by implementing the material properties of capric:palmitic acid.

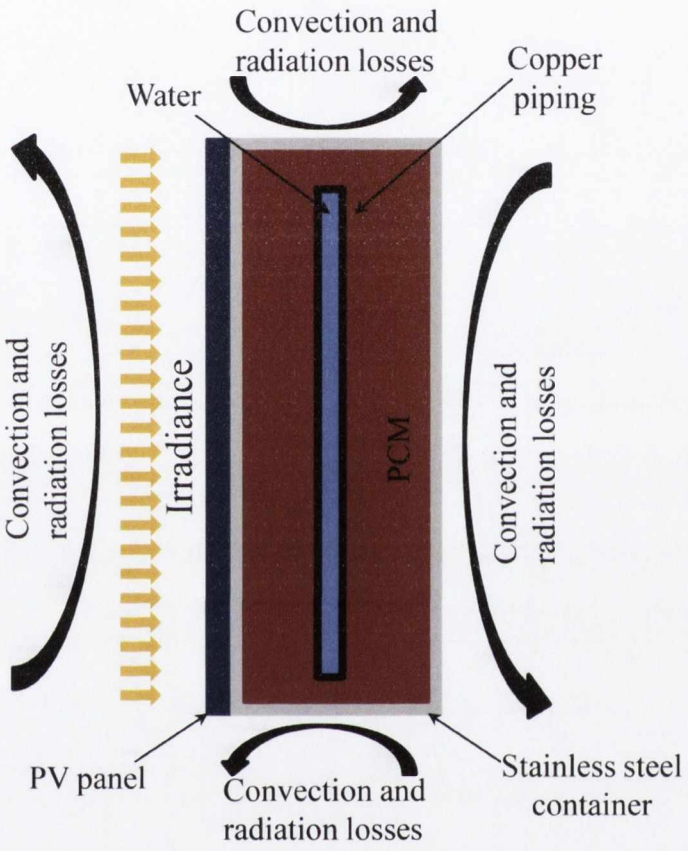

Figure 6.9: Schematic illustration of heat transfer mechanism in PVTPCM system as modelled in COMSOL

The PCM was integrated into the model by defining the material properties of capric:palmitic acid in the solid and liquid phases. The properties are defined as shown in Table 6.4 which is based on the results of the material characterisation reported in Chapter 3.

Table 6.4: Material and phase change properties as defined in model

Property	Value	Units
Capric:palmitic - Solid		
Thermal conductivity	2.5	W/m K
Density	870	kg/m^3
Heat capacity	2300	J/kg K
Capric:palmitic –Liquid		
Thermal conductivity	0.139	W/m K
Density	790	kg/m^3
Heat capacity	2300	J/kg K
Phase Change		
Phase change temperature	20	°C
Transition interval	9.5	°C
Latent heat	210	J/kg K

After specifying the properties of the phase change material according to the heat capacity formulation the heat Equation 6.26 was solved. It was assumed the phase transition occurred over a temperature interval:

$$T_{pc} - \Delta T_{sol-\frac{liq}{2}} \; to \; T_{pc} + \Delta T_{sol-\frac{liq}{2}} \tag{6.29}$$

Where;

- T_{pc} is the phase change temperature

In this interval, the material phase is modelled by a smoothed function, θ, representing the fraction of phase transition or the fraction of material that is solid. This value is equal to 1 when at solid state ($T_{pc} - (\Delta T_{sol\text{-}liq}/2)$) and 0 at liquid state ($T_{pc} + (\Delta T_{sol\text{-}liq}/2)$), where $\Delta T_{sol\text{-}liq}$ is the transition interval between solid and liquid. The density, ρ, and the specific enthalpy, h, are expressed by:

$$\rho = \theta\rho_{sol} + (1 - 0)\rho_{liq} \tag{6.30}$$

$$\rho h = \theta\rho_{sol}h_{sol} + (1 - 0)\rho_{liq}h_{liq} \tag{6.31}$$

Where, *sol* and *liq* indicate the material properties in solid and liquid phase, respectively. Differentiating with respect to temperature and following a series of formal transformations, the following formula for the specific heat capacity was used in the heat equation:

$$C_p = \frac{1}{\rho}\left(\theta_{sol}\rho_{sol}C_{p,sol} + \theta_{liq}\rho_{liq}C_{p,liq}\right) + C_L \tag{6.32}$$

Where;

- $\theta_{sol} = \theta$
- θ_{liq} 1-θ
- C_L is latent heat capacity

The effective thermal conductivity and density during phase change are then reduced to Equation 6.33 and 6.34.

$$k = \theta_{sol}k_{sol} + \theta_{liq}k_{liq} \tag{6.33}$$

$$\rho = \theta_{sol}\rho_{sol} + \theta_{liq}\rho_{liq} \tag{6.34}$$

The equations presented in this chapter were used to model the heat transfer through the PCM in COMSOL.

6.2.3 Combining TRNSYS and COMSOL

As a combination of TRNSYS and COMSOL was used the integration of the two programs was carried out using a TRNSYS platform. The outputs of the COMSOL model were called into TRNSYS.

6.3 Validation of Model – Results and Discussion

Following the development of the models in section 6.2 the results were compared with experimental data collected over the course of the experimental work presented in Chapter 5. Mean absolute percentage error (MAPE) was used to assess the ability of the model to match the experimental result. It is a measure of prediction accuracy of the model compared to the experimental dataset and is useful in expressing the accuracy of the model based on experimental results however problems can occur when calculating the MAPE value with a series of small denominators as this can create very large errors.

6.3.1 Weather data

It was decided to model the system using typical Irish Summer weather data; the days were 30th of June 2014 and 5th of June 2013. The majority of weather conditions were used as inputs to the TRNSYS model, i.e. ambient temperature, wind speed and humidity. However, as solar irradiance data is recorded for the majority of locations as horizontal radiation, a solar radiation processor was used to calculate the experimental tilt radiation on the PV surface (installed at a 52° slope) based on the horizontal beam and diffuse radiation. The assumed reflection albedo was 0.2, an approximate value for ground reflectance. Figure 6.10 shows the experimental tilt solar irradiance compared to the simulated tilt solar irradiance generated in TRNSYS for the 30th of June 2014.

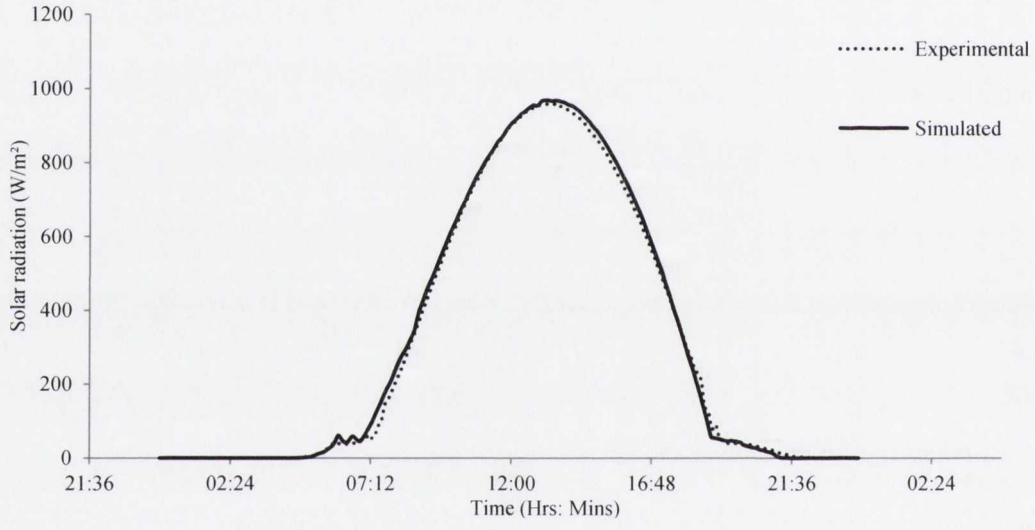

Figure 6.10: Solar irradiance experimental with simulated results

The graph shows that the model can predict accurately the global tilted solar irradiance given the beam and diffuse irradiance of a location. The maximum and minimum mean absolute percentage error (MAPE) was calculated to be 17% and 0%, respectively between 08:00 hours to 20:00 hours. However, 82 % of the results had MAPE values of less than 5 %. The maximum MAPE occurred during the early hours of the morning and later in the evening when the solar irradiance values were low (<200) which can cause issues as series of small denominators can create very large errors.

6.3.2 Photovoltaic (PV) System Model (System 1) – TRNSYS

The experimental results of System 1 (PV panel) were used to validate the results of the model. However, in order to get to the validation stage a series of steps had to be undertaken due to the design of the experimental set up.

A solar charge controller regulated the voltage and/or the current to keep the batteries from overcharging, some of which function as maximum power point (MPP) charge controllers which ensure the PV is functioning at full capacity at all times. However, given that this PV circuit did not include a charge controller device it was not programmed to extract a set load voltage from the PV. This caused a varying voltage to be drawn from the PV depending on the level of solar irradiance.

The results of the characterisation of the PV in System 1 were used to determine a load voltage equation (Equation 6.35) dependent on solar irradiance, as presented in Figure 6.11. Prior to PV installation, all PV panels were characterised using an ISM 490 Solar Module Analyser (Iso-Tech, 2009).

$$V_{Load} = -0.00002(G_{Tilt})^2 + 0.0388(G_{Tilt}) - 1.7564 \quad (6.35)$$

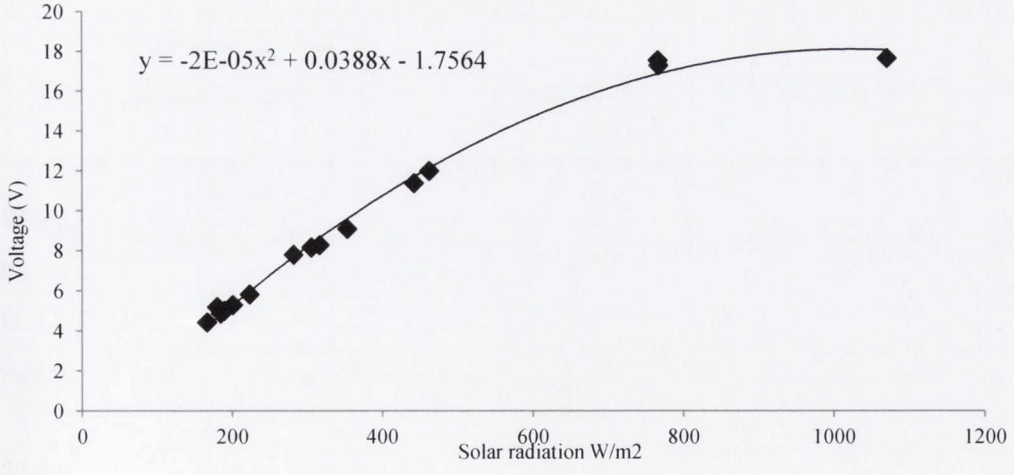

Figure 6.11: Characterisation of System 1 at a resistance of 5 ohms

The experimental and simulated results for the PV voltage, current and power on the 30th of June 2014 are presented in Figure 6.12.

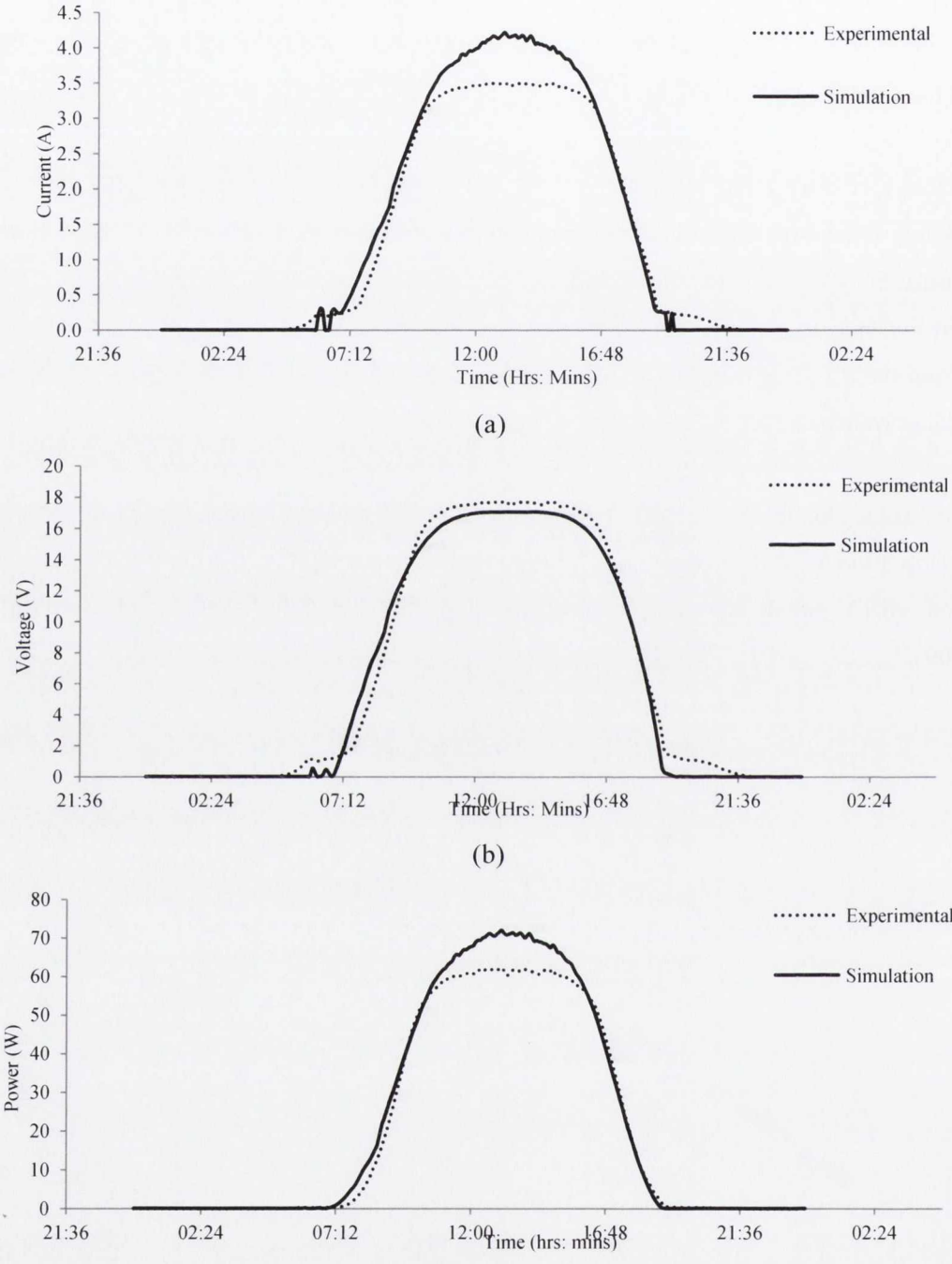

Figure 6.12: Experimental and simulated results of PV (a) current (b) voltage and (c) power simulated for 30th of June 2014

The experimental results show plateauing at approximately 62 W which is due to the current constrained to remain at approximately 3.5 A during peak solar radiation. This issue arose due to the design of the PV circuit in the experiment. The resistance of the circuit of the PV in System 1 is 5 Ω which was determined by dividing the experimental voltage by the current. As a result, the maximum current through the circuit is 3.5 A.

Despite the plateauing between 10:40 hrs – 16:50 hrs at the peak of the graph, the simulated current and voltage has been shown to predict the measured current and voltage with an average MAPE of less than 5 % over the remainder of the day. Although, the current and voltage were underestimated at the earlier and later stages of the day, this can be ignored as the values are less than 0.3 A and 1.1 V. As the low values of power generated during this period were not greater than 1 W which had a negligible impact on the overall performance of the PV panel as presented in Figure 6.12(c), where modelled and measured values follow the same trend at these times of the day.

Prior to the installation of the PV panels in the experiment, an electrical characterisation of the PV panels was performed. The efficiency of each panel was determined and the efficiency of the PV installed in System 1 was found to be 12.4 %. This method of correction was used as it is a reasonable representation of the power generated by the PV under the environmental conditions. The power was corrected for the time period between 10:40 hrs – 16:50 hrs to remove the flat lining error using Equation 6.36.

$$P_m = \frac{\eta_{PV}}{G \; x \; A_{PV}} \tag{6.36}$$

Where;

P_m = Maximum power of the PV (W)

G = Solar irradiance (W/m^2)

A_{PV} = Area of the panel (m^2)

The PV current was recalculated based on the experimental voltage and the corrected PV power value. Figure 6.13(a) shows the corrected experimental values and simulated current. The model overestimates the corrected experimental current by approximately 0.01 A. It can be seen in Figure 6.13(b) the model underestimates the experimental voltage by 0.6 V.

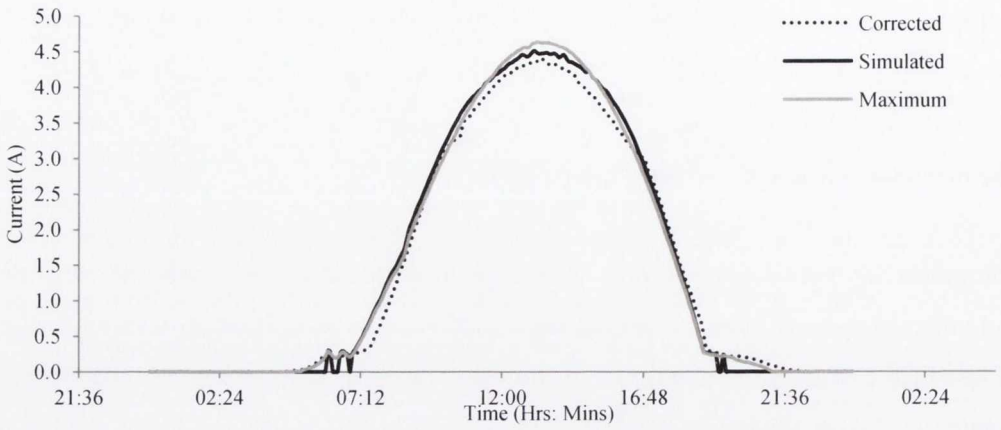

(a)

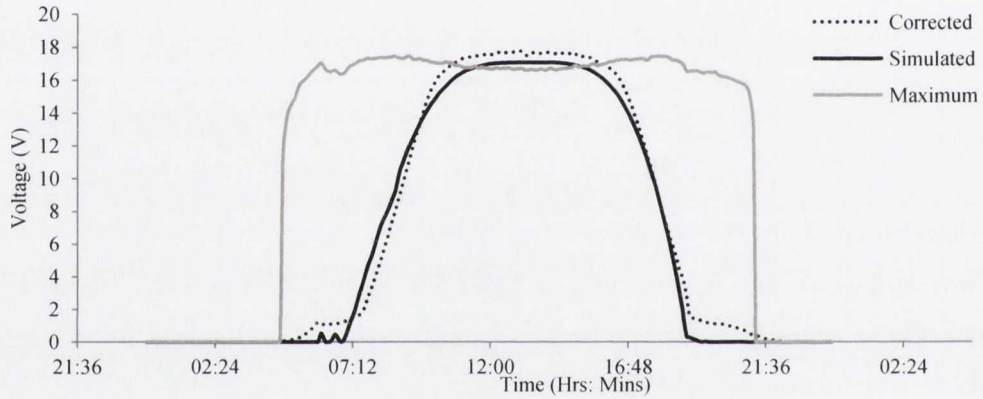

(b)

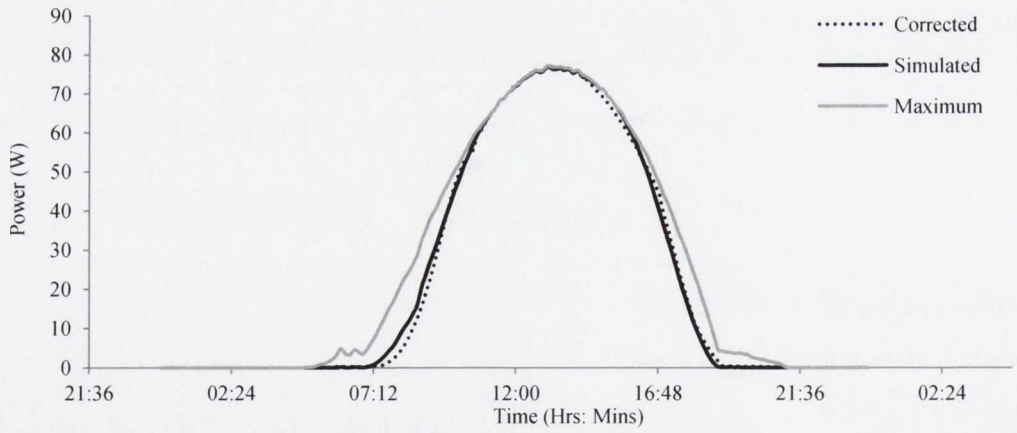

(c)

Figure 6.13: Corrected experimental and simulated values of PV (a) current (b) voltage (c) power

The power generated by the PV, as shown Figure 6.13(c), shows the model is in good agreement with the experimental results. The corrected experimental power values are in good

agreement with the simulated results with a maximum MAPE of 20%, which occurred for 2.7 % of the dataset and 77 % of the results showed an MAPE of <5%.

The 'Maximum' plotted line in each graph in Figure 6.13 shows the simulated results of the PV current, voltage and power, respectively. The graphs represented the modelled results of the PV system if the circuit incorporated a maximum power point (MPP) charge controller. The graphs indicate that the behaviour of the measured power from the PV panel is a good indication of the behaviour of the system despite the absence of a charge controller.

The TRNSY model of a PV panel has been shown to accurately predict the current, voltage and power values of the corrected experimental PV system. The model has been shown to predict the power although there is a small error in the prediction of the current which has been overestimated and voltage which has been under estimated at the peak of the graphs by approximately 8 % and 5 % which equates to a power variation of 4 W and occurred during the early hours of the morning when the output power was low. It should be noted that in both cases the modelled values follow the same trend as the measured values. The maximum power values of each, the voltage, current and power have been presented to show the performance of the system if a charge controller was installed. The charge controller has no effect on the current however, it was seen to maintain the voltage of the PV at its maximum, 17 V, as would be anticipated for such a device.

6.3.3 Photovoltaic/Thermal (PV/T) System Model (System 3) – TRNSYS

The validation of the model was completed in two parts:

(i) Electrical energy generated by the PV and
(ii) Heat energy generated by the thermal collector.

The electrical results of the PV/T model were validated using experimental data recorded on the 30th of June 2013.

Figure 6.14 shows the power generated in the experimental PV/T system against the simulated power generated which is the maximum power simulated in TRNSYS. The variation between the experimental and simulated results is due to the absence of an MPP charge controller in the experimental circuit as the voltage is not being maximised.

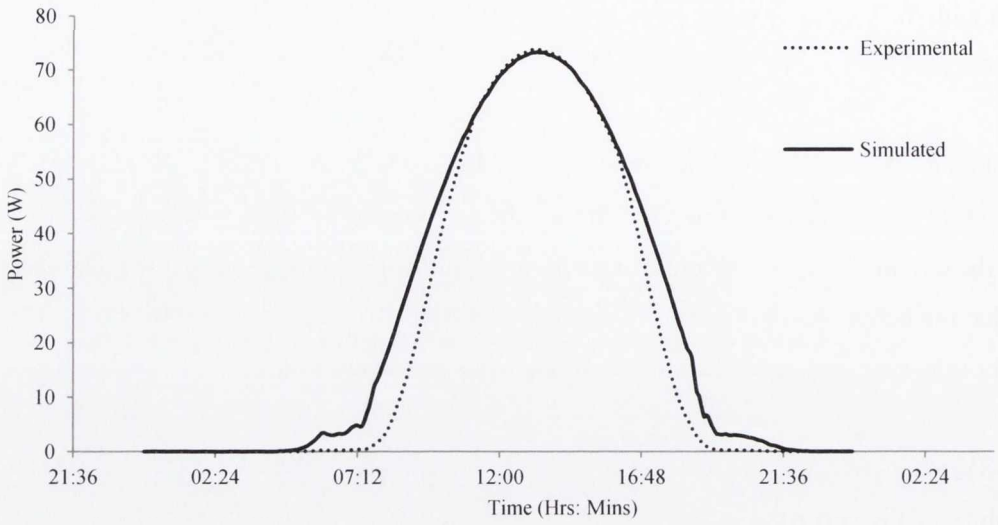

Figure 6.14: Experimental and simulated PV/T power generated

If an MPP charge controller was installed in the system, the experimental PV voltage would stabilise at approximately 17 V as shown in previous section (maximum voltage of the PV panel) and circled in Figure 6.15. The voltage would be maintained at the maximum allowable voltage of the PV due to the control of the MPPT which would generate the maximum power at any time. Figure 6.16 shows the experimental power generated if a MPP charge controller was installed in the experimental circuit. This was calculated by assuming that the voltage was 17 V and the current remained as was recorded on the 30th June. The MAPE has been calculated to be approximately 4%, when considering power values above 20 W, suggesting the model can accurately predict the performance of the PV. It has been shown that the model presented can be used to accurately predict the maximum power output of the PV panel in a PV/T system.

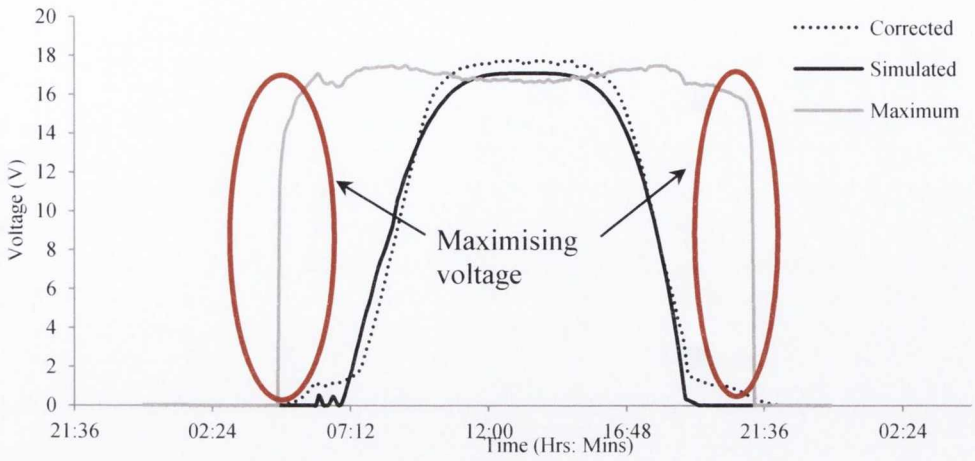

Figure 6.15: Maximised voltage when using a MPPT

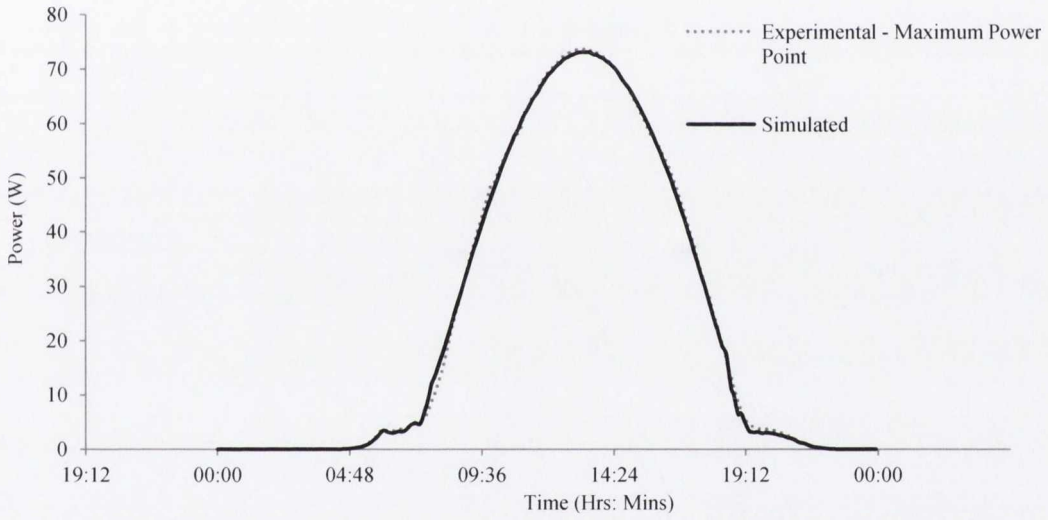

Figure 6.16: Experimental and simulated maximum power generated In PV/T simulated in TRNSYS

The thermal energy generated in the PV/T system was simulated, a PV/T component which was detailed in Section 6.2.1.2. This section concentrates on the representation of the thermal behaviour of the thermal collector device on the 5th of July 2013. Figure 6.17 and Figure 6.18 show the experimental and simulated temperatures for the inlet and outlet of the PV/T system, respectively.

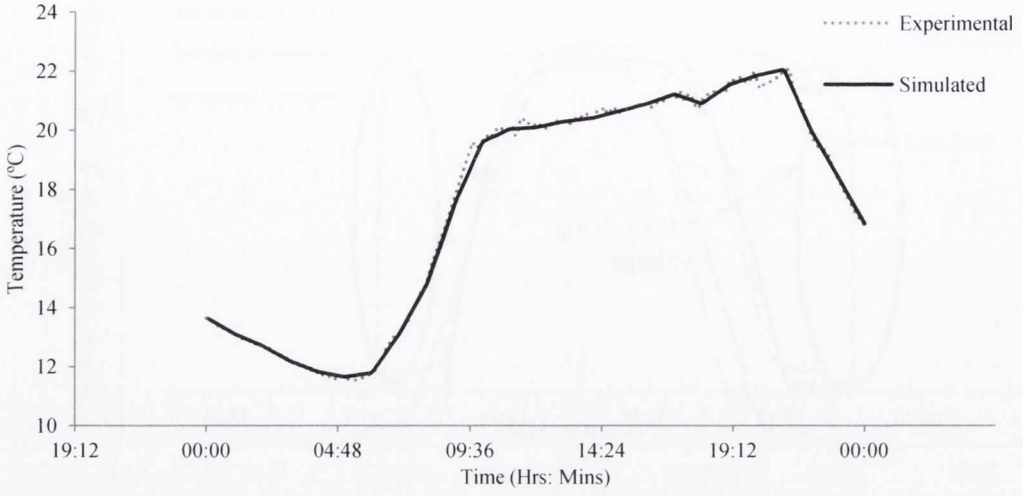

Figure 6.17: Experimental and simulated temperature at the inlet of the PV/T system

It can be seen that the model predictions for the inlet follow closely the same trend as the measured temperatures with a MAPE of 1%.

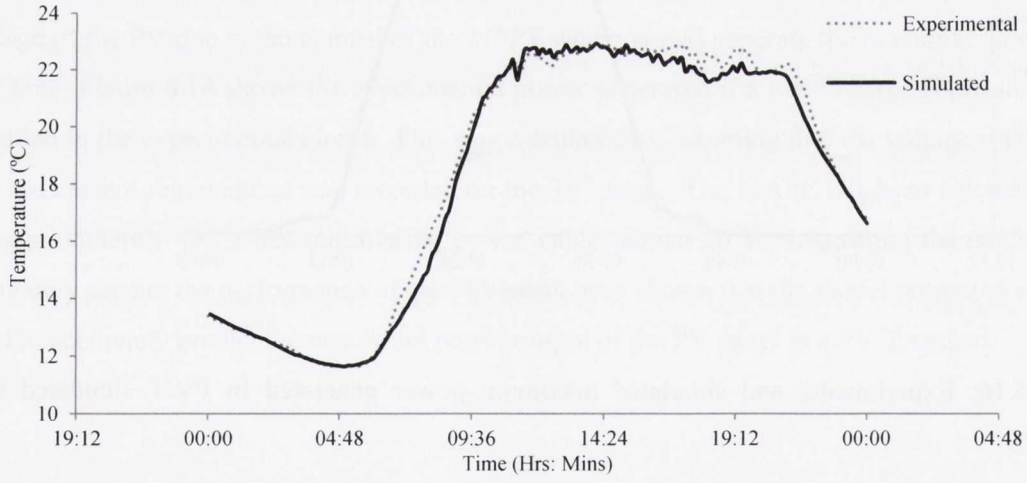

Figure 6.18: Experimental and simulated temperature at the outlet of the PV/T system in TRNSYS

However, the measured outlet temperature showed MAPE of 6% between 07:00 hours to 09:00 hours and 4% between 17:00 hours to 19:00 hours. However outside these two hour periods the MAPE was less than 2%. The errors are relatively small however the differences can be attributed to the assumptions made with regard to the design of the thermal collector, which was discussed in section 6.2.1.2.

The results of the PV/T system model represent the behaviour in the field trial data at the inlet and outlet water temperatures despite the assumptions that were made between the design presented and the design of the PV/T component as explained in section 6.2.1.2.

6.3.4 Photovoltaic/Thermal (PV/T) System Model (System 3) – TRNSYS and COMSOL

Given that a number of assumptions had to be made when using TRNSYS, it was decided to use a combination of TRNSYS and COMSOL in order to model the PV/T system as shown in Figure 6.1(c). In addition to this, the PV/T simulation in TRNSYS did not allow for the assessment of the heat transfer through the collector and the temperatures inside the collector. However COMSOL allowed for increased access to the heat transfer process inside the thermal collector which was required when assessing the melting and solidification of PCM.

The experimental and simulated electricity of a PV/T system is presented in Figure 6.16 which was simulated in TRNSYS to generate the power generated by the PV/T system. The model simulated the performance of the PV in the system and the results could be used in conjunction with COMSOL to achieve the water outlet temperature.

The simulation results of the thermal collector in COMSOL described in section 6.2.2.1 was based on field trial data collected on the 5th July and are presented below. Figure 6.19 shows measured and modelled collector input temperature for the PV/T system. It was seen that the modelled values follow the same trend as the measured values and the calculated maximum MAPE was 2% which can be attributed to the interpolation function rounding off the inlet temperature.

The advantage of using COMSOL arises from its ability to assess the transfer of heat inside the container. The modelled and measured temperature from inside the container of air is shown in Figure 6.20. It was seen that model predictions closely follow the same trend as the measured temperature from inside the container with a calculated maximum MAPE value of 6% which occurred between 10:00 hours and 10:30 hours and the MAPE was found to be approximately 4% between 17:15 hours and 18:15 hours. These differences can be attributed to the model heating air in the container faster than the experiment in the morning and cooling down faster in the evening. The model does not take into account the potential for the existence of an air gap between the PV and the container. Outside of these time frames the MAPE was found to be less than 2%.

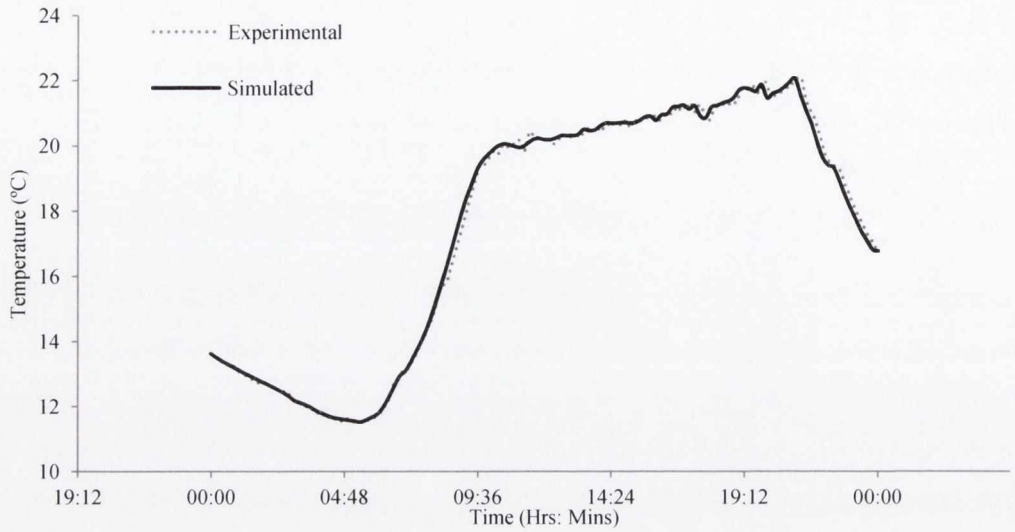

Figure 6.19: Experimental and simulated temperature at the inlet of the PV/T system in COMSOL

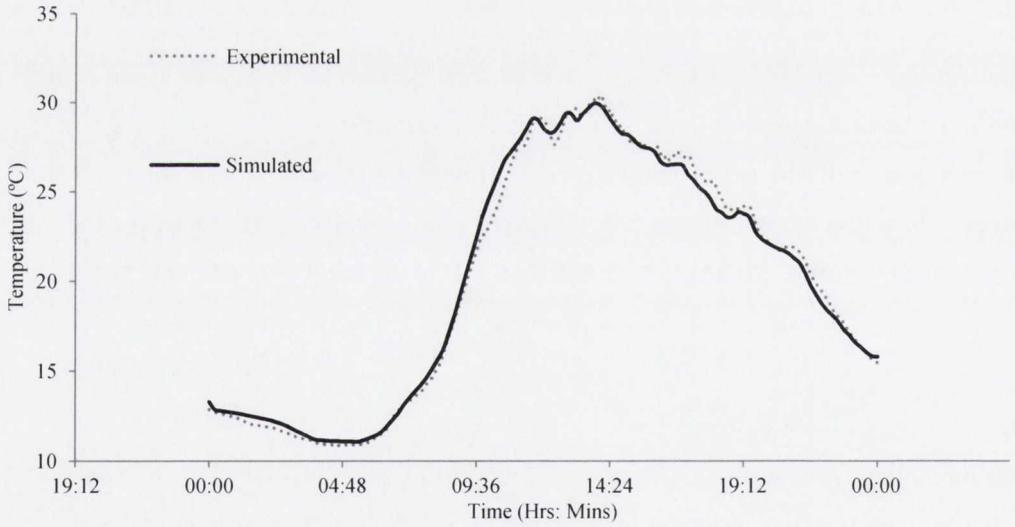

Figure 6.20: Experimental and simulated temperature of the air inside the container of PV/T system in COMSOL

The experimental and simulated outlet temperature of the thermal collector in the PV/T system (Figure 6.21) shows both sets of data following a similar trend. Initially, the model overestimated the temperature of the water at the outlet by a maximum value of 0.8 °C in the early hours of the morning (00:00 hours to 03:00 hours) and then underestimated it during the

time period between 06:45 hours to 10:45 hours by approximately 2 °C. The delay in the temperature increase of the outlet water in the model can be attributed to an additional solar gain by the pipe in the experiment during the morning when the sun rises. Considering the time period after 12:00 hours, the MAPE is less than 1 % which was an acceptable level of error.

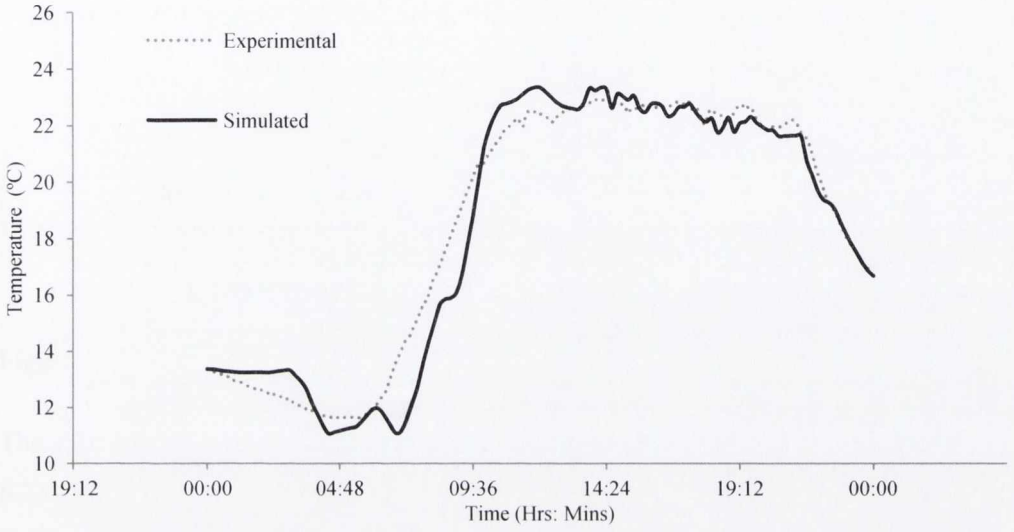

Figure 6.21: Experimental and simulated temperature at the outlet of the PV/T system in COMSOL

The combination of TRNSYS and COMSOL to model a PV/T system has been shown to provide more information on the heat transfer through the PV/T system compared to the PV/T system modelled solely in TRNSYS. The temperature of the inside of the thermal collector can be accurately assessed using COMSOL. This allowed for a greater insight into the performance of the system as the rate of heat transfer through the system can be investigated.

6.3.5 Photovoltaic/Thermal/Phase Change Material (PV/T/PCM) System Model (System 4) – TRNSYS and COMSOL

The PV/T/PCM system was modelled using a combination of TRNSYS and COMSOL, similar to the PV/T system in the previous section. As detailed previously, the combination of both gives an improved capability of predicting the results of both the electricity generation and the temperature at the outlet, inlet, and inside of the thermal collector compared to TRNSYS alone.

Figure 6.22 presents the measured and modelled power generated by the PV in a PV/T/PCM system. The trend of the simulated results follows that of the measured experimental values and based on this it can be concluded that the simulation can be used to forecast the power under varying environmental conditions. The model has a maximum MAPE of less than 2 % when considering the time frame outside of 16:00 hours to 18:10 hours, during this period the experimental and simulated values have a power difference of up to 6 W (average 4 W), this can be attributed to estimation of the experimental power when correcting the data.

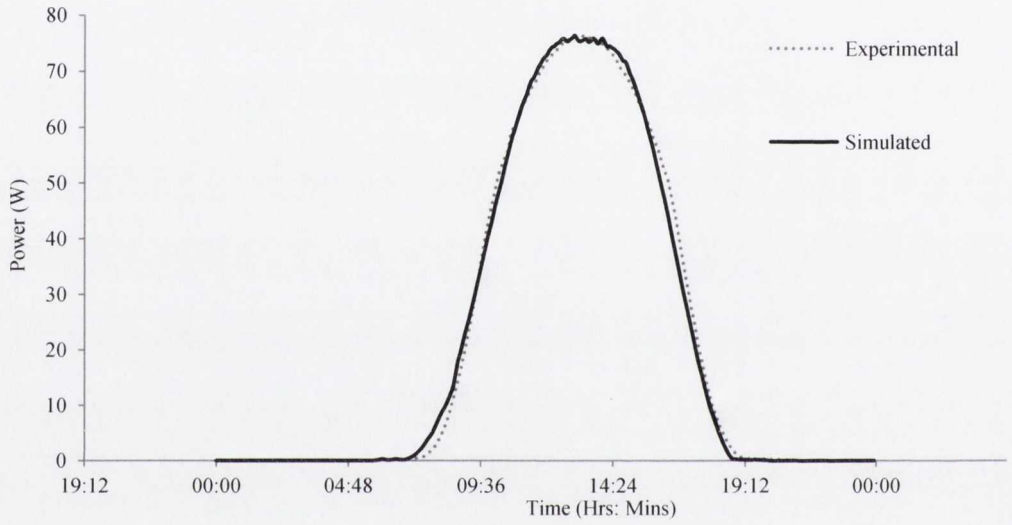

Figure 6.22: Experimental and simulated power generated in a PV/T/PCM system simulated in TRNSYS

The thermal collector containing the PCM in the PV/T/PCM system was simulated using the COMSOL model described in section 6.2.2.2. Two days with varying solar irradiance values were simulated. The 5th July and 23rd December 2013 (Figure 6.23) represent the higher and lower end of the spectrum of solar irradiance values that would be expected in an Irish climate.

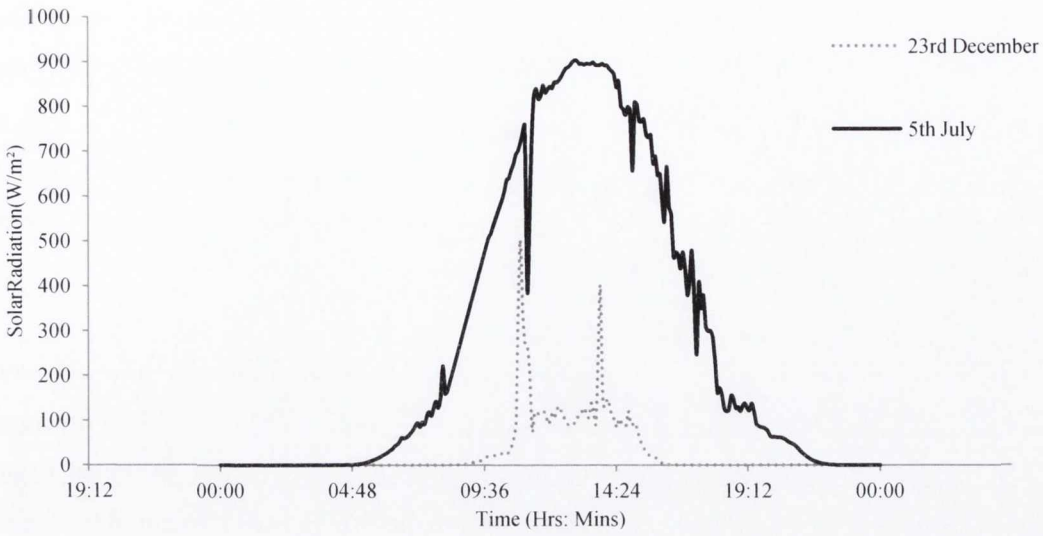

Figure 6.23: Solar irradiance on the 23rd of December and 5th of July 2013

The first simulation analysed is based on the field trial data of the 23rd December 2013. Figure 6.24 shows the experimental and simulated temperature at the inlet of the thermal collector. Between the hours of 06:30 and 08:15 hours the MAPE varies between 3 % - 6 % which equates to a temperature difference of between 0.2 °C - 0.4 °C which can be attributed to the calculation of the inlet water temperature at a certain time step. The maximum MAPE was less than 0.6 % for the remainder of the data.

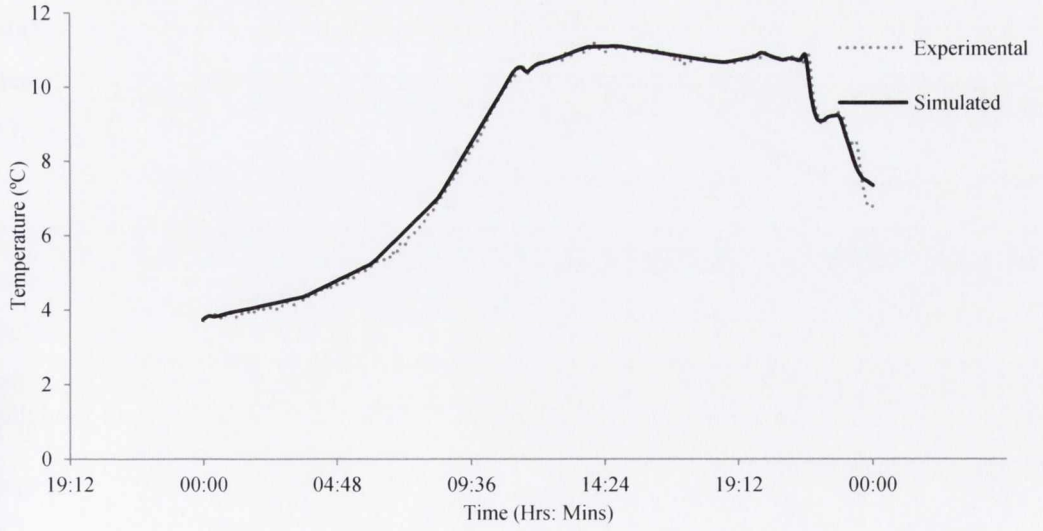

Figure 6.24: Experimental and simulated inlet water temperature in a PV/T/PCM system simulated in COMSOL (23rd December 2013)

Figure 6.25 presents the experimental and the simulated results of the temperature inside the PCM container for the PV/T/PCM system. As this experiment was undertaken in December, the PCM did not melt due to the low solar radiation and ambient temperatures. A PCM with a melting range of between 16 °C - 25 °C is not a functional material for TES under winter conditions in Ireland. As a result it would be recommended to replace the material with a lower temperature PCM to make full use of the latent heat storage.

In Figure 6.25, the simulated and experimental can be seen to deviate from each other between approximately 05:30 hours and 08:05 hours and showed a maximum MAPE of 11 % (average 7%) which equated to a difference of 0.5 °C (average 0.3 °C). This can be attributed to an increased heat flux into the PCM in the model compared to the experiment. This could be due to an underestimation of losses to the environment. Outside of this time period the maximum MAPE was less than 3 % which is within the simulation error. It can be seen from the graph that the simulated results follow the trend of the experimental data, showing that the model can be used for the qualitative projection of the behaviour of the PCM in a PV/T/PCM system under varying environmental conditions.

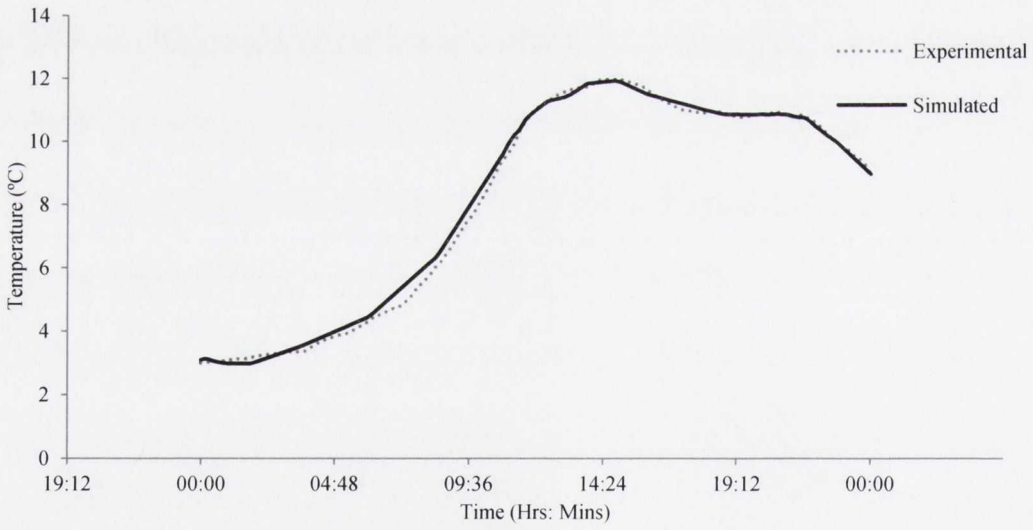

Figure 6.25: Experimental and simulated temperature of PCM in a PV/T/PCM system modelled in COMSOL (23rd December 2013)

The simulated temperature at the outlet of the thermal collector (Figure 6.26) can be seen to follow the same trend as the experimental temperature at the outlet. The average, maximum and minimum MAPE are 2.5 %, 16 % and 0.02 % which equate to a temperature variation of 0.3 °C, 1.6 °C and 0.02 °C, respectively. The model overestimates the PCM temperature during melting

this can be attributed to the underestimation of losses during the transfer of heat from the PV to the PCM which causes the model to have increased the temperatures.

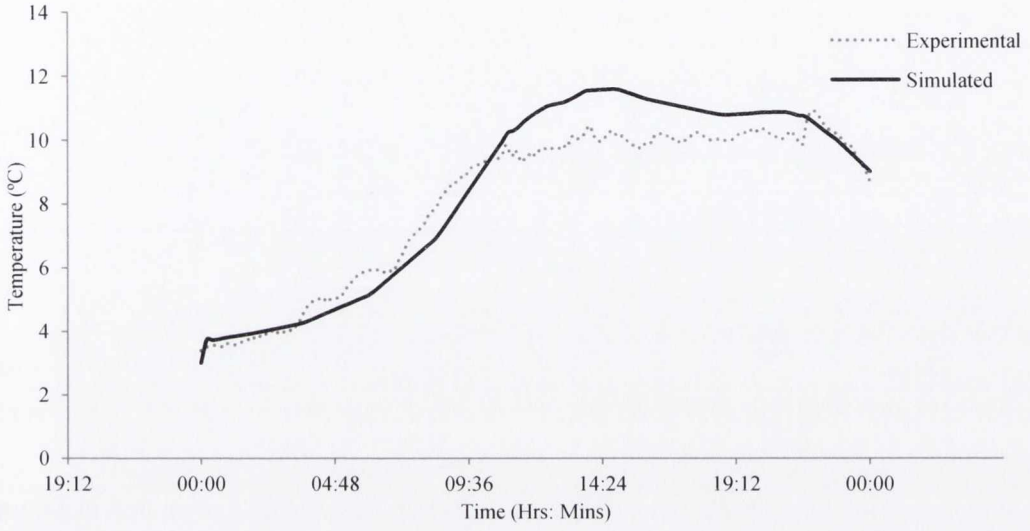

Figure 6.26: Experimental and simulated outlet water temperature in a PV/T/PCM system simulated in COMSOL (23rd December 2013)

The system simulation at lower solar radiation conditions shows that the model can accurately predict the temperatures of the water at the inlet and outlet and of the PCM in a PV/T/PCM system. The next three graphs were simulated based on the weather conditions on the 5th July 2013, with the higher of the two solar irradiance datasets presented in Figure 6.23.

The experimental and simulated water temperature for the collector inlet temperature is presented in Figure 6.27. It can be seen that the model predictions for the inlet temperature closely follow the measured inlet temperature. There are deviations from the experimental results from 04:45 hours to 05.45 hours and 12:00 hours to 12:30 hours of approximately 0.3 °C and 0.25 °C which can be attributed to the rounding off of the inlet temperatures by the interpolation function in COMSOL. The maximum MAPE was 1% which suggested the model can be used as a method to predict the system performance under varying environmental conditions.

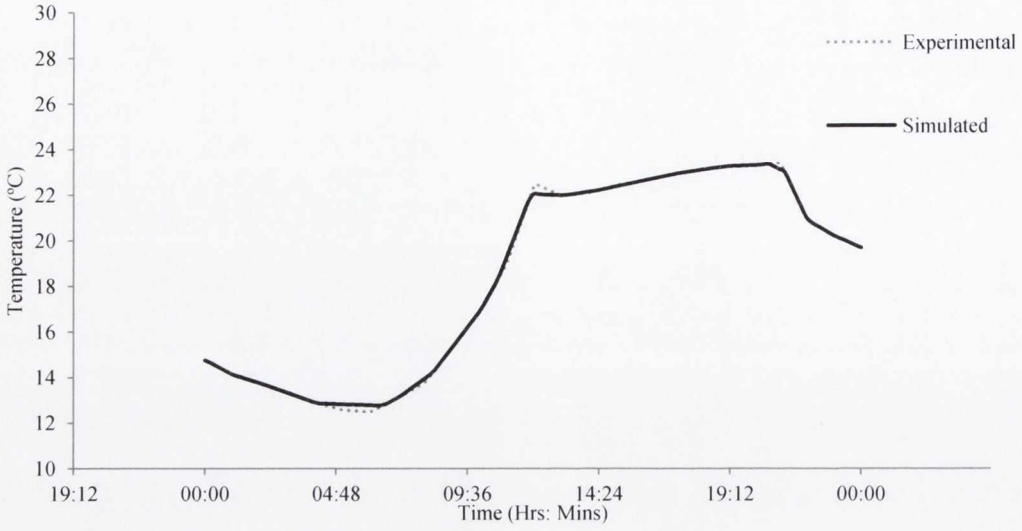

Figure 6.27: Experimental and simulated inlet water temperature in a PV/T/PCM system simulated in COMSOL (5th July 2013)

The measured and simulated PCM temperature in a PV/T/PCM system is presented in Figure 6.28. It can be seen that the modelled values follow the same trend as the measured values. The model slightly overestimates the temperature of the PCM during the afternoon. The discrepancy can be traced back to the underestimation of the losses incurred by the system when ambient temperature is at its maximum with the maximum MAPE calculated as 9% which equates to a temperature difference of 2.1 °C. In the simulation it is assumed that a large percentage of heat is transferred to the PCM when in fact the experimental results would suggest it was lost to ambient.

The simulation is in close agreement with the experimental results which have increased and decreased at similar times. This suggests the thermal conductivity and rate of heat loss/gain have been simulated to represent the experimental PV/T/PCM system.

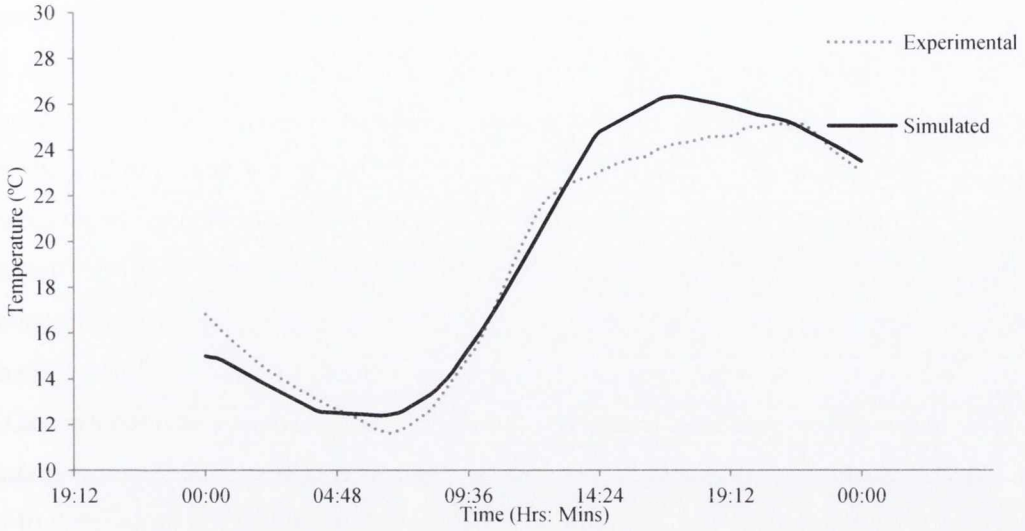

Figure 6.28: Experimental and simulated temperature of PCM in a PV/T/PCM system modelled in COMSOL (5th of July 2013)

The measured and simulated outlet temperature of the PV/T/PCM system is presented in Figure 6.29. It can be seen that the general trend of the experimental data is matched by the simulated model results. However, evidently there is some discrepancy where the initial experimental temperature is underestimated and then overestimated in the afternoon.

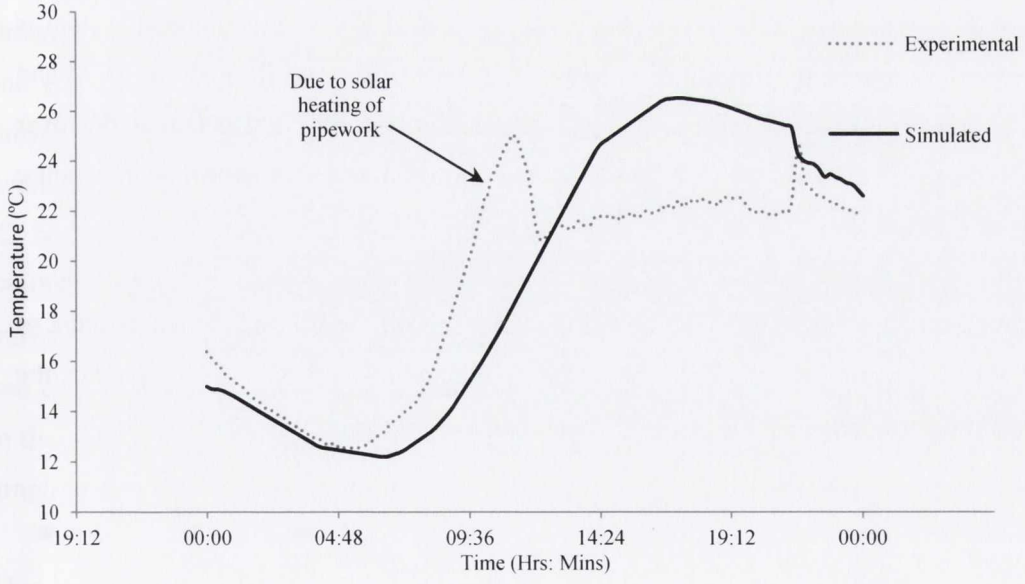

Figure 6.29: Experimental and simulated outlet water temperature in a PV/T/PCM system simulated in COMSOL (5th of July 2013)

It has been found that the peak in the experimental result was attributed to the system positioning. The peak is due to the water in the outlet pipe being heated by an external source i.e. solar irradiance and is not entirely due to the heating effect from the PCM. Due to the positioning of the system, the sun rises and heats the outlet pipe in the morning, consequently heating the water contained in the pipe. Following this, the flow of water in the pipe begins to increase as the PCM melts, causing cooler water to replace the heated water at the outlet thus creating the peak at approximately 11:30 hours. Further evidence to reinforce this interpretation is the absence of a peak in the morning under low solar irradiance conditions (Figure 6.26) suggesting it is the angle of incidence is causing the direct solar irradiance to increase the temperature during the morning. Taking this theory into account when considering the measured and simulated outlet temperature as presented in Figure 6.29 and disregarding the initial peak of the experimental results the maximum MAPE was found to be 17 % which equates to a temperature difference of approximately 4 °C. However, this has been attributed to the underestimation of losses during the transfer of heat from the PV to the PCM. The model has been shown to follow the general trend of the experimental results.

To avoid the direct heating of the pipes which connect the tank to the PV a lower incident angle would be recommended. This would also maximise the solar flux reaching the PV.

During the afternoon, when ambient temperature is at its maximum, the simulation diverges away from the experimental dataset. The heat loss experienced by the experimental system is higher than the heat loss in the simulation showing that the heat transfer through the PCM and the pipes to the water is more efficient in the model. This can be attributed to the over estimation of the temperature of the PCM as in Figure 6.28 which in turn affects the temperature of the water at the outlet.

The model presented has been shown to predict the behaviour of the PV and the temperature of the PCM and, inlet and outlet water which shows the model can be used to predict the performance of the system under varying environmental conditions.

6.4 Conclusion

This chapter presented the approach taken to modelling a PV/T/PCM system. TRNSYS models were developed for a PV system and a PV/T system. The models were validated using field trial data for systems installed in Dublin, Ireland. Results obtained showed the PV model predicted

the power and the maximum MAPE was found to be 8 % which equated to a power output of 4 W. The PV/T system modelled in TRNSYS used an integrated PV and thermal collector components. The results showed the model adequately matched the system behaviour with a MAPE of 4 %. However, one problem with this method was that a number of assumptions were made when applying TRNSYS components to the model. It was not practically feasible to assess the temperature inside the thermal collector; therefore the model was unable to give satisfactory indication of the transfer of heat throughout the system. In order to overcome this challenge, COMSOL was used in combination with TRNSYS to model the PV/T system. COMSOL modelled the thermal collector component of the PV/T system. The analysis showed the maximum MAPE of 2 % when simulating the inlet water temperature, this can be attributed to the interpolation function rounding off of numbers when calculating the inlet temperature. The outlet temperature showed maximum MAPE of 6 % and 4 % during the hours of 10:00 hours to 10:30 hours and 17:15 hours to 18:15 hours, respectively. This was due to the model overestimating the temperature inside the container in the morning and underestimating it in the afternoon while it is cooling down. The can be attributed to the contact surface between the PV and the container as the model is assuming full contact however, some areas of the back of the PV may not be in full contact with the container which can reduce the heat transfer across the PV to the container and thus the rate of heat transfer. The outlet temperature was underestimated by 2.0 °C in the morning; this can be attributed to an error in the model in calculating the transfer of heat to the water within the container. The remainder of the model showed a MAPE of less than 1 % which is an acceptable level of error when comparing a model and experimental results. To develop the PV/T TRNSYS and COMSOL combination model further, PCM was added in order to simulate a PV/T/PCM system. The PCM temperature was overestimated in the model resulting in a maximum temperature difference of approximately 4 °C between the experimental and simulated results during high solar irradiance conditions (>1000W/m^2), which was due to the model underestimating the heat loss behaviour of the transfer of heat in the model. The modelled outlet temperature was overestimated; however this can be attributed to the increased heat availability in the simulated PCM which was transferred to the water. Overall, the experimental rates of heating and cooling as seen by the slopes of the graphs were matched by the simulation values in the PV/T/PCM system.

This is the first model of a PV/T/PCM system of this design which has been validated using a full-scale experimental setup. The results of the PV/T/PCM simulation represent the system behaviour and as a result the model can be used to:

- Optimise the PV/T/PCM system to maximise heat output
- Simulate system performances under varying weather and operating conditions
- Predict longer term performances of the electrical and thermal energy generation capabilities of a PV/T/PCM system

Chapter 7

Optimisation and Up-scale of a Photovoltaic/Thermal/Phase Change Material System

Chapter 7. Optimisation and Up-scale of a Photovoltaic/Thermal/Phase Change Material System

7.1 Introduction

Optimisation is maximising or minimising a function by systematically choosing input values from within an allowed set and computing the value of the output function (Farshchimonfared et al., 2015). The idea behind optimising the PV/T/PCM system presented in the current research is to control system inputs to maximise the output of water temperature, stored heat and the time for which heat is stored. This chapter presents the comprehensive optimisation of a PV/T/PCM system based on a transient numerical simulation presented in Chapter 6 based on the weather conditions of July 5th 2013 as shown in Figure 6.23 . The system optimisation of each input parameter will be assessed by calculating the improvement of the thermal efficiency compared to the validated model. The input values which provide the largest improvement in system performance will be numerically applied to the system which will be implemented in an up-scaled domestically sized 1.12 kW system. The optimised system will be up-scaled to mimic a realistic thermal collector surface area of a domestic dwelling and will be investigated under climatic conditions of Ireland and Saudi Arabia. The chapter presents a discussion on potential system applications and associated advantages.

7.2 Optimisation

From the analysis and simulation of the PV/T/PCM system performance, a series of parameters were identified which if varied could potentially improve system efficiency. The material properties identified as possible optimisation parameters are presented in Table 7.1.

Table 7.1: Material parameters of the experimental system (used in the validated model)

Name	Notation	Values
Phase Change Material Thermal Conductivity	k_{PCM}	0.139 W/m.K
Heat of Fusion	H	210 kJ/kg
Mass Flow Rate	m_w	~0.0005 kg/sec
Thermal conductivity of Container	k_{con}	19 W/m.K

The optimisation investigation involved individually assessing a range of values for each parameter listed. The input range was determined by values of other available PCM. The results

of this parametric study could then be used to implement changes to the system to improve system performance. For the most part, the study concentrates on the optimisation of the thermal collector and PCM properties. The results are presented with those of the validated model to allow for a visual comparison.

7.2.1 Phase Change Material Thermal Conductivity

The thermal conductivity of PCM is the rate at which heat passes through the material and is expressed as the amount of heat that flows per unit time through a unit area with a temperature gradient of one degree per unit distance (W/m.K) (Incropera and Dewitt, 1985). The thermal conductivity determines the rate of heat transfer through the PCM thereby influencing the amount of heat energy stored by the PCM, lost to the environment and transferred to the water. The thermal conductivity of the container was varied to assess the effect of different PCM containment materials on the transfer of heat through the systems (collector). Fatty acids are known to have low thermal conductivities which can decrease heat storing and releasing rates during melting and solidification however methods are being introduced to improve this value (Rozanna et al., 2005) such as graphite, carbon naontubes and other carbon additives (Choi et al., 2014) .

The thermal conductivity of capric:palmitic acid, the PCM in the PV/T/PCM system, is 0.139 W/m.K. Considering the PCM available and the thermal conductivity values associated with these (Zalba et al., 2003; Cabeza et al., 2011), it was decided to investigate from 0.2 W/m.K to 1.4 W/m.K, in increments of 0.2 W/m.K. The lower values (0.2 W/m.K – 0.4 W/m.K) investigated are the thermal conductivity values of paraffin waxes, fatty acids and eutectics as well as salt hydrates. However values above this, from 0.4 W/m.K to 1.0 W/m.K, are thermal conductivities of salt hydrates only. Thermal conductivities above 1 W/ m.K are not available in a PCM's current form although infusing the material with expanded graphite and carbon fibres, thermal conductivities of this level can be achieved (Frusteri et al., 2005; Karaipekli et al., 2007).

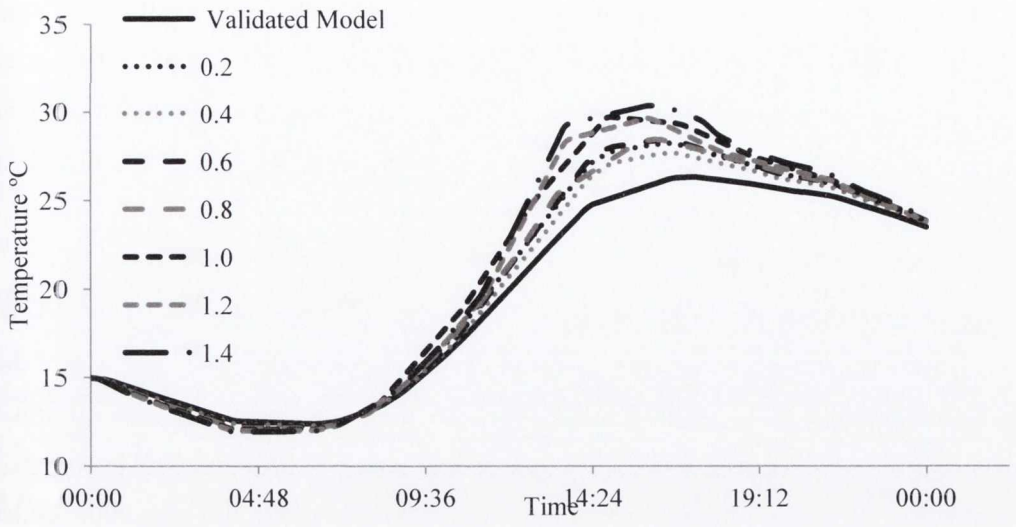

(a)

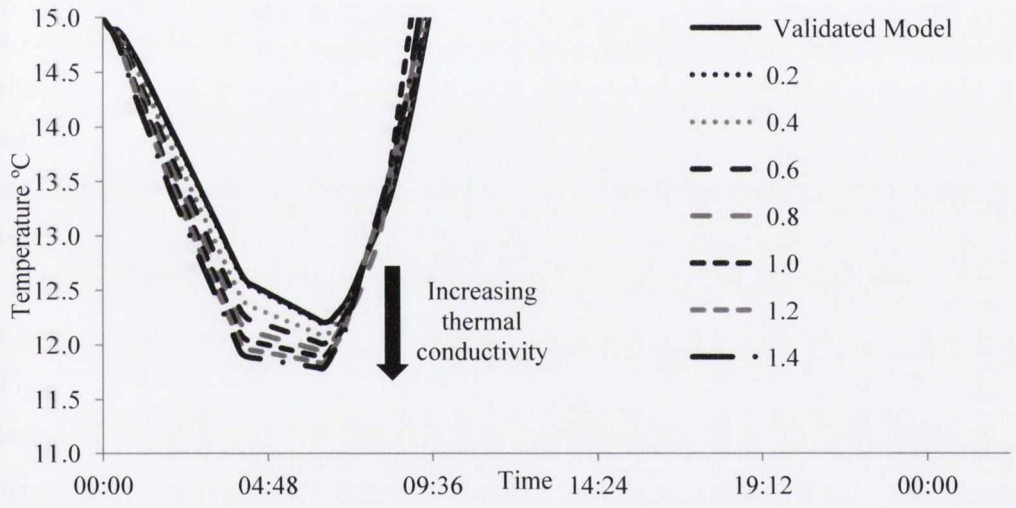

(b)

Figure 7.1: Effect of varying the PCM thermal conductivity (W/m.K) on the PCM temperature over the course of (a) one day (b) three hours

The rate of heat transfer was seen to increase through the PCM with an increase in thermal conductivity as was shown by the temperature increase of the PCM in Figure 7.1(a) compared to the validated model. Considering the early morning from 00:00 hours to 09:00 hour approximately, there is an increased heat loss from the PCM with an increase in thermal conductivity as shown in Figure 7.1(b) where the temperature of the PCM is lower with higher thermal conductivities. However, this loss can be offset by the increase in temperature during the afternoon and evening between the hours of 01:00 and 6:30 (as shown in Figure 7.1(a)). It can be seen that the temperature of the PCM increases with increasing thermal conductivity as

the maximum temperature reached by thermal conductivities of 0.139 W/m.K and 1.4 W/m.K was 26.5 °C and 29.6 °C, respectively. This was due to an increase in the rate of heat transfer through the PCM thereby increasing the temperature. The investigation of thermal efficiency in the next section considers whether or not the heat gained by the PCM during the afternoon outweighs the increased rate of heat loss in the morning.

Similarly, the temperature of the water at the outlet (Figure 7.2) reflects that of the PCM. During the morning the lowest outlet temperature of the validated model was 12.3 °C and the corresponding temperature of 1.4 W/m.K was 11.8 °C. This is due to the increased thermal conductivity of the PCM allowing a higher heat transfer from the water into the PCM compared to the validated model. During the afternoon, the adverse occurs where the maximum outlet temperature of the water in the system with a thermal conductivity of 1.4 W/m.K is higher than the validated model by approximately 4.3 °C. Similarly the increased thermal conductivity of the PCM allows for a higher heat transfer from the PCM to the water.

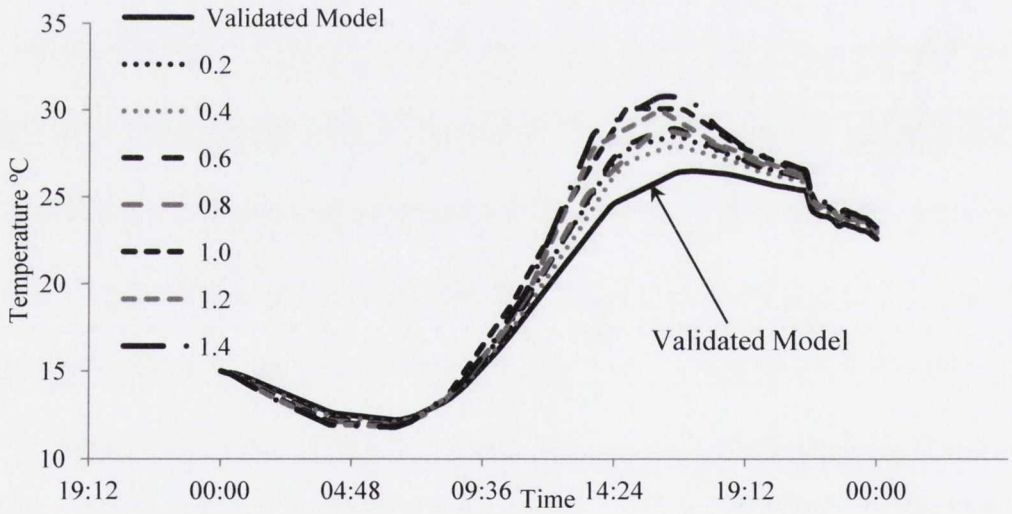

Figure 7.2: Effect of varying the PCM's thermal conductivity (W/m.K) on the outlet water temperature

It was decided to consider the simulation outputs of the model with a PCM thermal conductivity of 1.4 W/m.K for a further investigation as the outlet water reached the highest temperature.

7.2.2 Phase Change Material Heat of Fusion

The temperature at which this occurs is the phase change range. PCM have a high heat of fusion which are capable of storing and releasing large amounts of energy during melting and solidification in a PV/T/PCM system. During solidification of PCM the idea is to transfer the energy to the working fluid, water. If the heat of fusion was decreased, phase change would occur faster as the required energy to melt the PCM was reduced. However, this would also reduce the amount of energy available to be transferred to the water during discharge resulting in the water not gaining as much energy and thus not being heated to the same extent. However, if the heat of fusion was increased, the PCM would require more energy to change from a solid to a liquid. Although, sufficient energy must be provided to the PCM to ensure that it changes phase to store the latent heat.

The heat of fusion of capric:palmitic acid is 210 kJ/kg and is presented as the simulated 'Validated Model' in the following graphs. The heat of fusion range assessed depended on the value associated with available PCM with melting temperatures of approximately 23 °C. It was found the heat of fusion of PCM varied from 100 kJ/ kg to 300 kJ/ kg (Zalba et al., 2003; Cabeza et al., 2011). This range included a variation of organic, inorganic and eutectic PCM.

The heat of fusion from 100 kJ/kg to 240 kJ/kg presented similar PCM temperatures as shown in Figure 7.3. The results of the values 100 kJ/ kg and 240 kJ/ kg suggest that the PCM is absorbing the maximum heat energy available as there is negligible increase in PCM temperature. The heat of fusion of 300 kJ/kg shows a temperature decrease of 0.8 °C compared to that of the other simulated PCM temperatures. The increase in the heat of fusion caused a reduction in the PCM temperature due to the higher energy requirement to change phase.

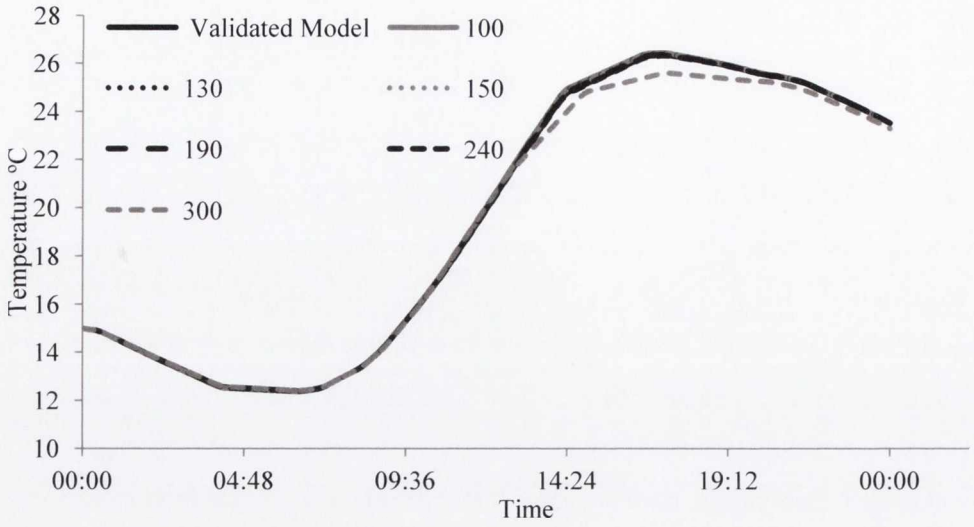

Figure 7.3: Effect of varying the PCM's heat of fusion (kJ/ kg) on the PCM

Similarly, all values between 100 kJ/ kg and 240 kJ/ kg present similar outlet temperatures, within 0.15 °C of each other as shown in Figure 7.4. The outlet temperature of the model with a heat of fusion of 300 kJ/ kg deviated from the other simulations at approximately 14:30 hours. This was due to the reduced temperature of the PCM as an increased energy was required to change phase which in turn reduced the water outlet temperature.

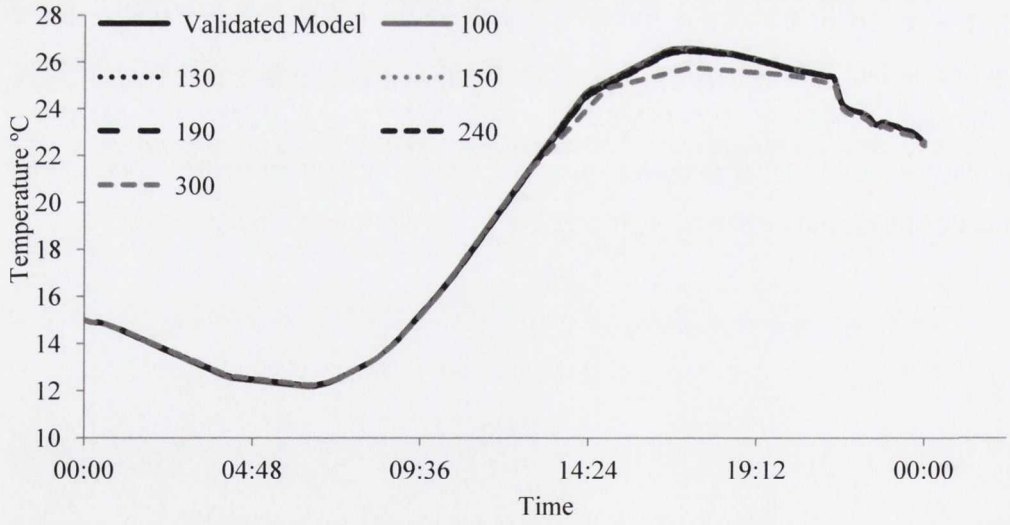

Figure 7.4: Effect of varying the PCM's heat of fusion (kJ/ kg) on the water outlet temperature

The difference between the validated model and the model with a heat of fusion of 300 kJ/kg presented the largest difference; this model will be used to assess the thermal efficiency

compared to other optimisation modifications. The compromise between the useful heat gain by the water and the increase of heat energy stored by the PCM is assessed. In addition to this the value of 240 kJ/kg will also be assessed with respect to its thermal efficiency as the results presented have shown that the temperature of the outlet did not decrease but a gain in energy was achieved.

7.2.3 Phase Change Material Heat Capacity

A large heat capacity requires more energy to heat the material than that of a lower heat capacity and as a result a material can take longer to heat but will have stored a higher amount of energy. As the heat capacity of the PCM currently used in the system is 2300 kJ/kg.K, it was decided to assess the effect of approximately halving and doubling this value. This was a reasonable assumption to make considering the heat capacity of available PCM such as commercial PCM from Rubitherm and savEnrg PCM (Rubiterm, 2015; SavEnrg, 2015).

The heat of fusion has little effect on the temperature of the PCM as shown in Figure 7.5.

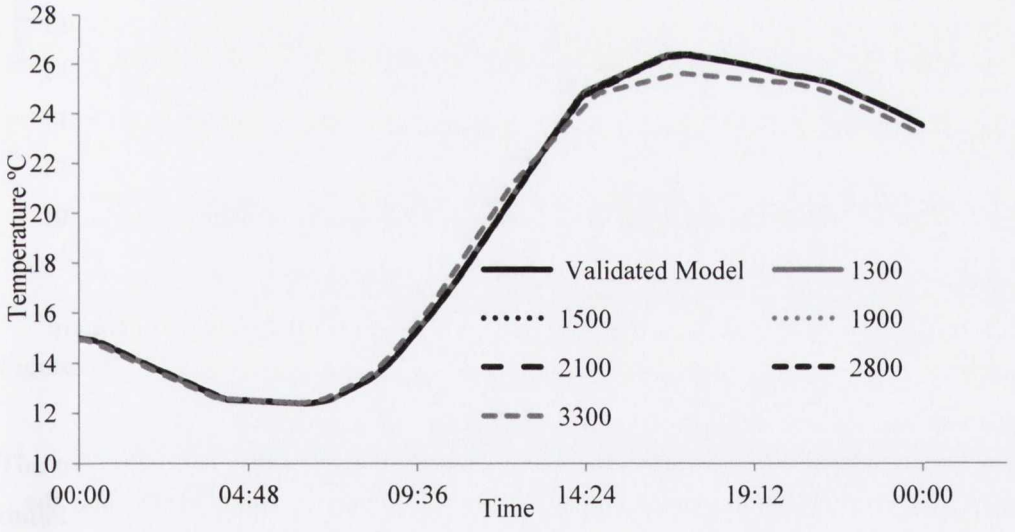

Figure 7.5: Effect of varying the PCM heat capacity (kJ/kgK) on the (a) PCM (b) water outlet temperature

The heat of fusion value of 3300 kJ/ kgK deviates away from the validated model during the evening and afternoon to a temperature approximately 0.6 °C lower. As expected, an increase in heat capacity would cause a decrease in PCM temperature as more energy is required to heat the material to the same temperature (Zalba et al., 2003; Cabeza et al., 2011).

The variation between the validated model and the model with a heat capacity of 3300 kJ/kgK is also reflected in the outlet temperature of the water which is approximately 0.7 °C lower than the validated model as shown in Figure 7.6.

It was clear that by changing the heat capacity of the PCM results in a minor effect on the temperature of the PCM and the outlet temperature. As a result it was decided to further investigate the thermal efficiency of the results of the model based on a heat capacity value of 3300 kJ/kg K due to the temperature variation at the outlet compared to the validated model. In addition to this, the thermal efficiency of 2800 kJ/kg.K is also assessed as energy was gained with a negligible loss in outlet water temperature.

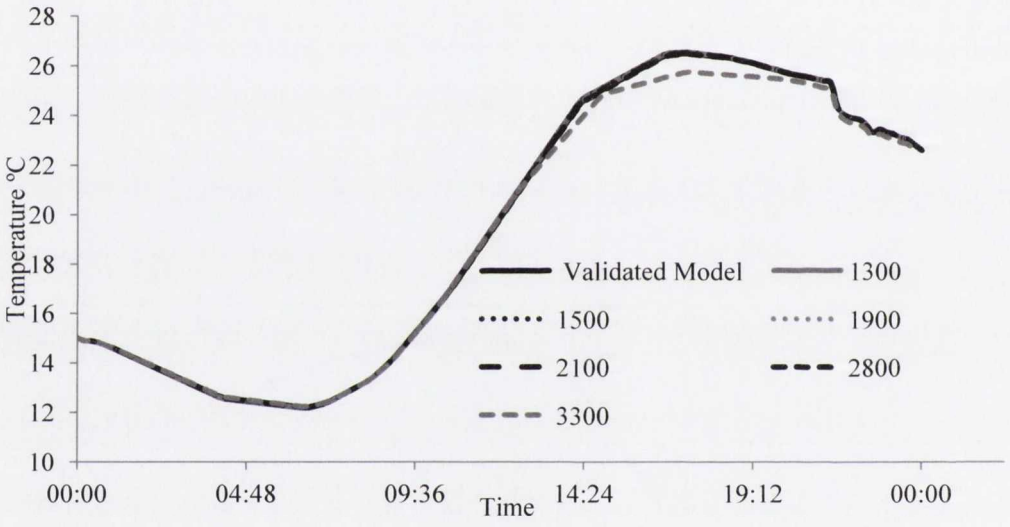

Figure 7.6: Effect of varying the PCM heat capacity (kJ/ kg K) on the outlet water temperature

7.2.4 Mass Flow Rate

For all thermal collectors, there is a compromise between the mass of water heated and the temperature differential of the inlet and outlet water temperature. If the mass flow rate is low, a smaller volume of water would be pre-heated to a higher temperature. However, a lower temperature differential would result if the mass flow rate was increased as a larger volume of water would be pre-heated to a lower temperature. The aim was to find the optimum mass flow rate value which would extract the largest amount of energy from the PCM and allow sufficient time for the water to absorb it.

The range of mass flow rates were chosen based on the minimum and maximum viable levels of flow. The minimum level was dictated by the natural flow of water in the system. In the system presented the lowest flow was 0.0005 kg/sec which was taken as the minimum flow rate. The maximum fluid flow was chosen based on the value which showed a zero temperature difference between the inlet and outlet.

The result for the mass flow rate parametric study on the variation in temperature of the PCM is presented in Figure 7.7. The temperature of the PCM was affected by the variation in mass flow rate from approximately 16:00 hours onwards. This is due to the water extracting the heat from the PCM during discharge. As expected, the lower the mass flow rate, the higher the temperature of the PCM as the heat is being discharged from the PCM at a reduced rate.

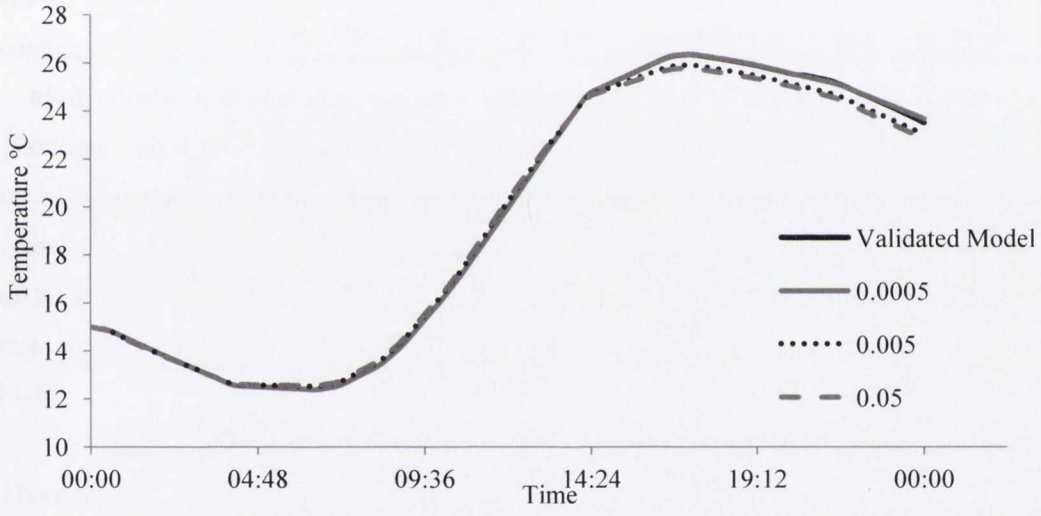

Figure 7.7: Effect of varying the PV/T/PCM system mass flow rate (kg/ sec) on the PCM

The temperature of the water at the outlet is presented in Figure 7.8. The temperature of the outlet of the lowest mass flow rate investigated, 0.0005 kg/sec, is similar to that of the validated model as the mass flow rate varied between 0.0005 kg/sec and 0.003 kg/sec but remained at approximately 0.0005 kg/sec for 90 % of the day. The water outlet temperature reached the highest value, 26.5 °C, at this mass flow rate level at 0.0005 kg/sec due to the water passing through the system at the lowest rate, thereby allowing for more time for it to absorb heat from the PCM.

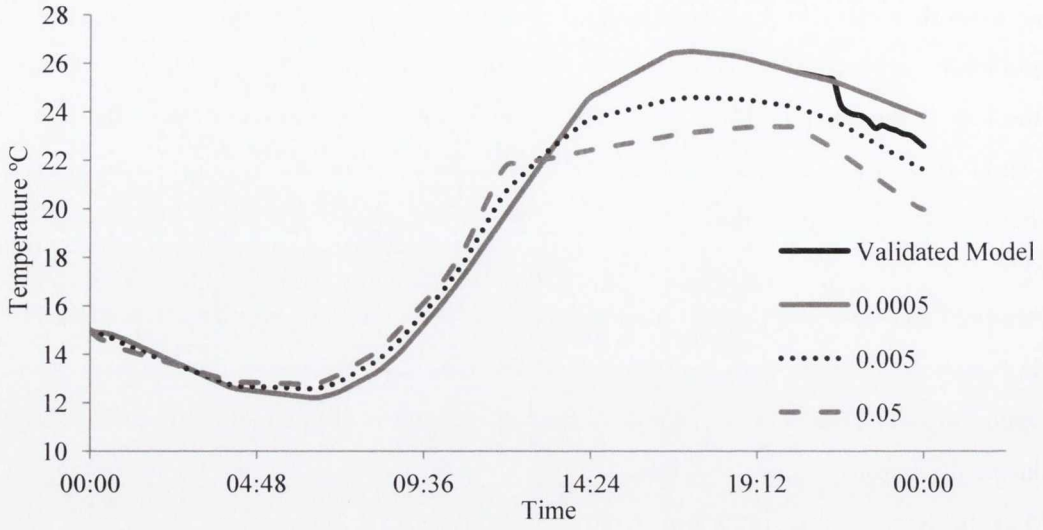

Figure 7.8: Effect of varying the PV/T/PCM system mass flow rate on the outlet water temperature

A mass flow rate of greater than 0.05 kg/ sec was too high to allow adequate heat transfer from the PCM to the water. This is shown in Figure 7.9, as the temperature of the inlet is the same as that of the outlet up until 21:30 hours, after which there is an increase of approximately 0.7 °C.

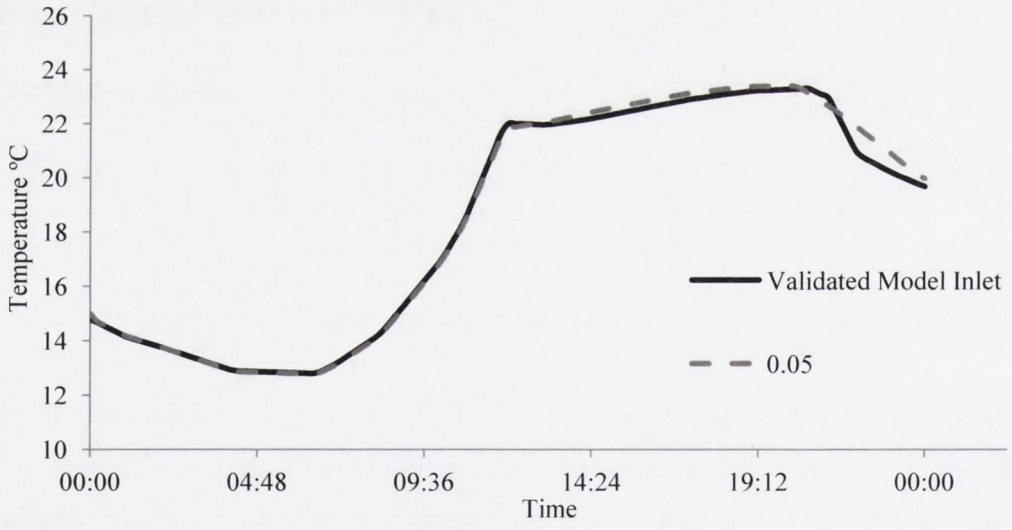

Figure 7.9: Temperature of inlet and outlet flow at 0.05 kg/ sec

As a result the mass flow rate of 0.05 kg/ sec can be disregarded for the purpose of further analysis as it does not allow sufficient time for heat transfer from the PCM to water.

The maximum outlet temperature reached at a flow rate of 0.0005 kg/sec is 8 % higher than the maximum temperature of 24.5 °C reached by the flow rate of 0.005 kg/sec. This is as a result of the compromise between flow rate and the temperature difference gained between the inlet and outlet. The larger rate of mass flow results in an increased mass of water being pre-heated.

Based on the results of the parametric study a mass flow rate of 0.005kg/sec will be further assessed in Section 7.2.6 which will look at increasing thermal efficiency.

7.2.5 Thermal Conductivity of Container

The container thermal conductivity determines the rate of energy transfer into and out of the thermal collector thus affecting the charging and discharging of the PCM and the transfer of energy to the working fluid. The value used in the validated model was 19 W/m.K, the thermal conductivity of stainless steel.

The thermal conductivity of the container housing the pipe network and PCM in the experiment is manufactured from Grade 316 stainless steel. The container has been shown to be a contributing factor in the insulation of the PV panel as seen in Chapter 5 and as a result the rate of heat transfer from the PV panel to the PCM is reduced. One option to increase the heat transfer from the PV panel to PCM is to replace the PCM encasement material with one of a higher thermal conductivity.

Thermal conductivities of commonly used materials, as presented in Table 7.2, were employed in the model to investigate the optimum material thermal conductivity. (Immersion corrosion tests were also carried out on these materials and the results were presented in Chapter 3.)

Table 7.2: Range of thermal conductivities modelled in a PV/T/PCM system

Material	**Thermal Conductivity (W/ m K)**
Aluminium	205
Brass	109
Copper	401
Mild Steel	54
Perspex	0.2
Stainless Steel (Validated Model)	19

The results of the parametric study investigating the effect of different values of thermal conductivity on PCM and outlet water temperature in Figure 7.10 and Figure 7.11, respectively. The transfer of heat through the PV/T/PCM system increases with an increase in thermal conductivity as expected, which can be seen as the PCM and outlet water temperature increase simultaneously.

For the most part of the day, the temperature of the PCM for the respective thermal conductivities matched the result of the validated model. The temperatures began to deviate away from the validated model when the solar radiation and ambient temperatures peak.

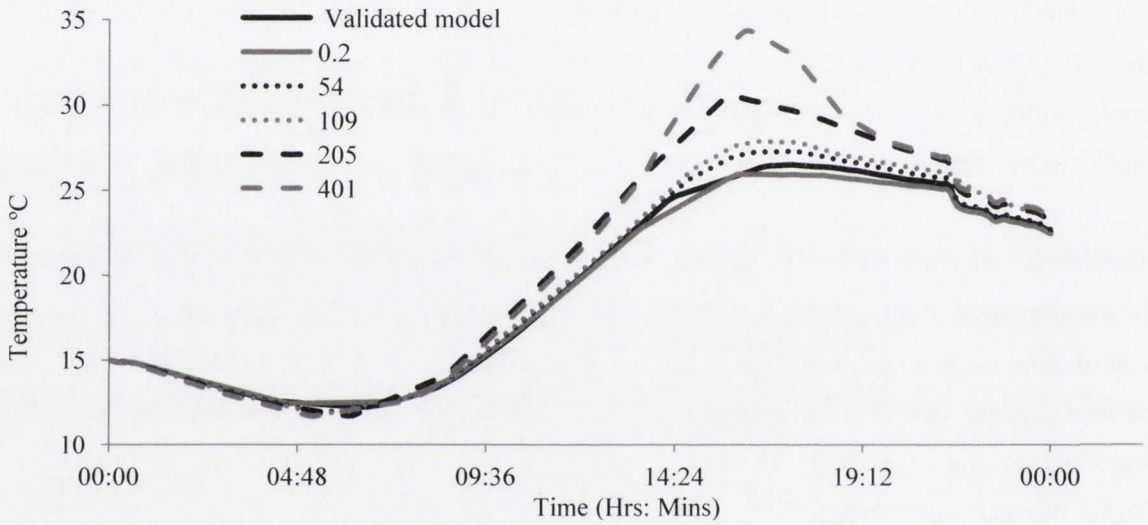

Figure 7.10: Effect of varying the thermal conductivity of the PCM encasement material (W/mK) on the PCM temperature

The highest thermal conductivity for the container, considered was that for copper, 401 W/ mK. This showed the largest gain in temperature of the PCM, reaching maximum value of 32.9 °C. However, given that copper is a relatively expensive; it would have to be taken into account in the economic analysis (presented in Chapter 8). It was also found that copper is susceptible to corrosion by most PCM and caution is advised when using copper and PCM in a system.

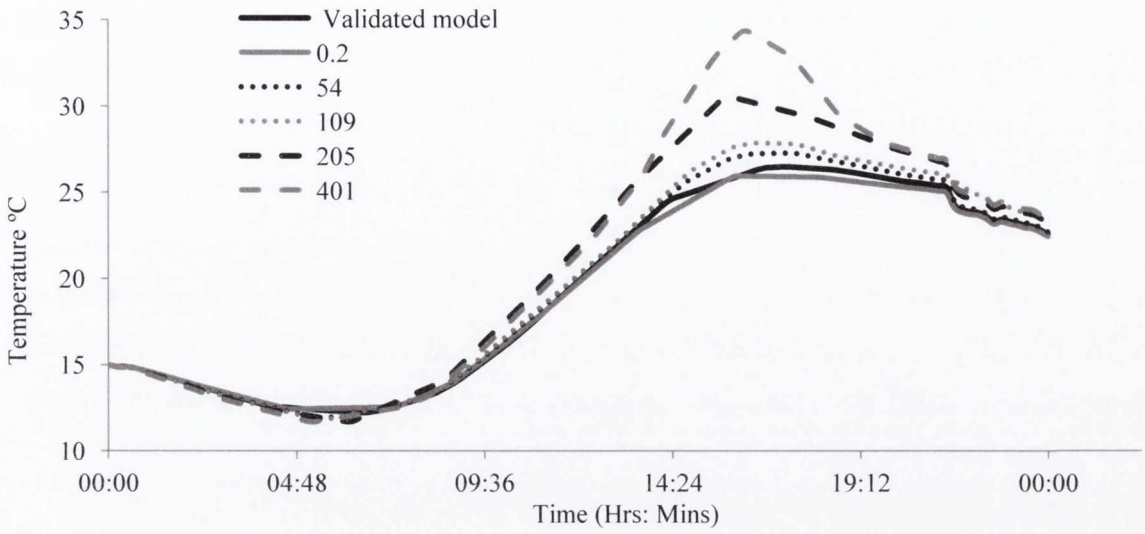

Figure 7.11: Effect of varying the thermal conductivity (W/mK) of the water outlet temperature

Aluminium with a thermal conductivity of 205 W/mK showed the second highest gain in heat energy by the PCM and the water outlet compared to the validated model reaching approximately 30 °C, respectively. This is due to the increase in the container thermal conductivity from 19 W/mK in the validated model to 205 W/mK. The deviation between the validated model and the parametric analysis results occurred from approximately 09:30 hours and lasted approximately 12 hours. During the early hours of the morning the loss of heat from the container to the environment was minimal in all systems as the temperature of the PCM had reached steady state with ambient.

The maximum temperature difference at the water outlet between the validated model (19 W/mK) and the parametrically tested materials with thermal conductivities of 109 W/mK and 54 W/mK (brass and mild steel) was 1.52 °C and 0.92 °C respectively, which occurred at approximately 16:30 hours. As these improvements were not greater than that of the improvements by aluminium, the two materials can be neglected in the thermal assessment in Section 7.2.6. Perspex resulted in a decreased temperature of the PCM at the water outlet compared to that of the validated model as expected given that the thermal conductivity of Perspex is 0.2 W/mK. This material insulates the system and minimises heat transfer from the PV to the PCM and as a result it was not considered an option in optimisation.

The thermal conductivity of aluminium resulted in one of the higher temperature gains as shown in Figure 7.11. It would be an economically viable material to use in a PV/T/PCM system

because it is a relatively cheap material and widely available, as a result it has been used in the thermal efficiency study for further analysis.

7.2.6 Discussion of Thermal Efficiency of the Parametric Models

As discussed in the previous section, specific values from each parameter list were selected based on the results of the PCM and water temperature outputs for a thermal efficiency comparison with the validated model. The thermal efficiency of the selected model simulation results was calculated using the equations presented in Chapter 5 which quantify the system performance based on the:

- Useful energy gained by the water
- Stored energy in the PCM
- Extended time for which preheating water can occur

The validated model is used as a comparison to assess the results of the parametric study which are shown in Table 7.3. To assess the results, the energy gain or loss of each system is presented as a percentage of the energy gained in the validated model as shown in Figure 7.12. Included in Table 7.3 are the electrical and thermal efficiencies of a PV/T system designed and installed by Pei et al. (2010) which is a representation of conventional PV/T system in order to compare with a PV/T/PCM system. The PV/T design includes an enclosed pipe network with attached tanks similar to the PV/T/PCM system design.

Increasing the thermal conductivity of the PCM from 0.139 W/m.K to 1.4 W/m.K improves the useful energy gained by the PV/T/PCM system by 4.6% which equates to 78.9 % of the energy gained by the validated model. However, the stored heat and extended time of heat availability has been reduced by 13.3 % (0.6 %) and 33.3% (6.7 %) that of the validated model. The improvement in useful heat gain is due to the increased rate of heat transfer through the PCM and therefore, reaching the water. This indirectly affected the capacity of stored heat as the increased thermal conductivity increased the losses from the PCM to the environment. As there was a reduction in the amount of stored heat and the time for which the heat was available was also reduced as there was less heat stored compared to the validated model. Realistically a value such as 1.4 W/m.K would only be achieved through the influence of thermal conductivity enhancements such as carbon fibre and expanded graphite. Consideration would have to be

given to the extra cost incurred to the system if such thermal conductivity additives replace PCM and the reduction in the latent heat storage capacity.

Table 7.3: The results of the thermal analysis of the parametric study

Model	Parameter		$\frac{Q_u}{A_{PV} * \tau\alpha * I}$ (%)	$\frac{Q_s}{A_{PV} * \tau\alpha * I}$ (%)	$\left(\frac{t_{ext}}{24}\right)$ (%)	Cumulative Thermal Efficiency (%)
-	Thermal (FPC) (Ayompe and Duffy, 2013b)		0	0	0	38
-	PV (Ayompe et al., 2011)		0	0	0	0
-	PV/T system (Pei et al., 2010)		23.8	0	0	23.8
1	Validated Model		5.8	4.5	20	15.2
2	Thermal Conductivity 1.4 W/m.K		10.4	3.9	13.3	13.8
3	Heat of Fusion	240 kJ/kg	5.7	4.9	20	15.4
4		300 kJ/kg	5.2	5.3	19.2	14.8
5	Heat Capacity	2800 kJ/kg.K	5.8	5.1	20	15.4
6		3300 kJ/kg.K	5.2	5.3	17.5	14.0
7	Mass Flow Rate 0.005 kg/ sec		10.2	4.1	17.5	15.9
8	Thermal Conductivity of Container 205 W/m.K		10.1	5.4	16.7	16.1

Two values of heat of fusion, 240 kJ/kg and 300 kJ/kg, were investigated to assess the change in thermal efficiency compared to the validated model. A heat of fusion value of 240 kJ/kg had a higher cumulative efficiency of 15.4 % compared to the validated model (15.2 %) however the value of 300 kJ/kg decreased the thermal efficiency by 0.4 %. This was due to the increased latent heat requirement to change phase and as a result the PCM with the higher heat of fusion

did not reach as high temperatures as that of the PCM with a 240 kJ/kg heat of fusion. The PCM did not get an opportunity to heat up further as once it had fully charged solar radiation and ambient temperature were decreasing as the sun was setting. A knock-on effect caused by the reduction in PCM temperature was the reduced temperature of the outlet water which resulted in a 0.1 % decrease of useful energy, 11 % of the energy gained by the validated model, as shown in Figure 7.12. As the overall cumulative thermal efficiency of 240 kJ/kg showed a positive increase on the validated model this will be implemented in the optimised model.

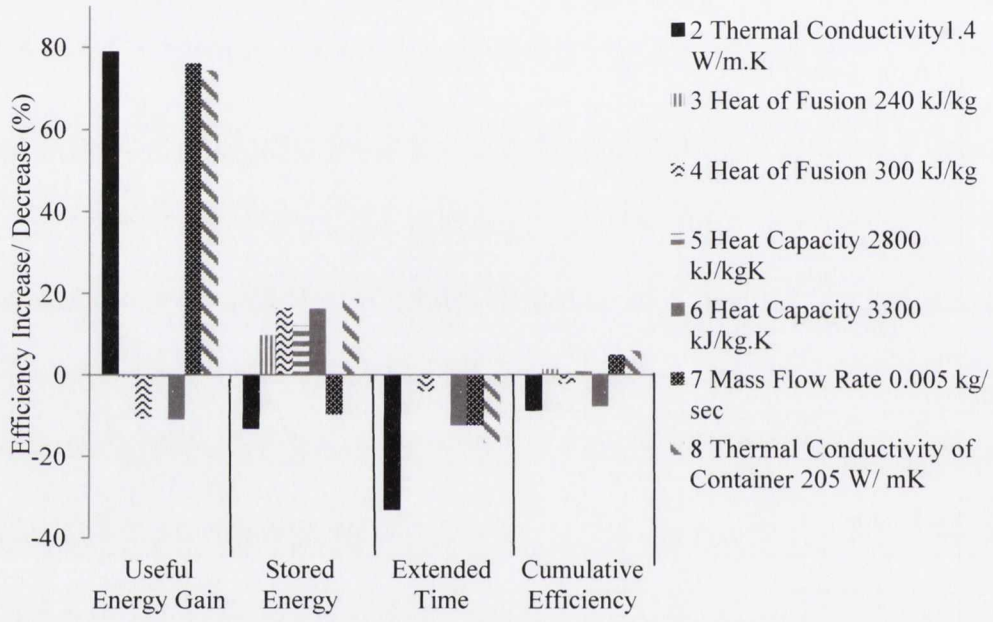

Figure 7.12: Change in thermal energy utilisation for different models as presented in Table 7.3

The heat capacity values considered in the thermal efficiency discussion are 2800 kJ/kg.K and 3300 kJ/kg.K. It was found the results based on the heat capacity value of 2800 kJ/kg.K had a minor effect (0.2 % increase) on the cumulative efficiency compared to that of the validated model. A loss of 0.6 % was made on the stored energy, compared to the validated model. Although the heat capacity of 3300 kJ/kg.K showed a larger increase in stored energy than either the validated model or the model of 2800 kJ/kg.K, the useful energy gain and extended time of heat storage were adversely affected with a loss of 0.6 % and 2.5 %, respectively. That equates to a loss of 11 % and 12.5 % of the energy gained by the validated model. As the model results based on a heat capacity value of 3300 kJ/kg.K were shown to reduce the cumulative

thermal efficiency compared to the validated model, a value of 2800kJ/kg.K will be used in the optimised model.

The mass flow rate was shown to have the most useful energy gain of all the systems by increasing the useful energy gain output by 74 % of that of the validated model. However, the stored energy and time extended for preheating were reduced by 9.8 % and 12.5 % of the energy gained by the validated model as shown in Figure 7.12 and Table 7.4. The increase in the useful energy gain by increasing the mass flow rate is evidence of the compromise between the temperature of the water and the mass of water heated. As shown in Figure 7.9 the temperature of the water outlet did not reach that of the validated model. However, as the mass flow rate was increased a larger volume of water was heated to a lower temperature. This shows the compromise between temperature differential and the volume of water in a PV/T/PCM system. The mass flow rate in the validated model, which matches that of the experimental data, is approximately 0.0005 kg/sec which is due to the gravitational force as measured in experimental Systems 3 and 4 in Chapter 5, Section 5.4. If this value is to be increased to the optimised mass flow rate of 0.005 kg/sec the system would require a pump which would incur an additional cost to the system in addition to an energy input.

Container thermal conductivity of 205 W/m.K (an improvement of 186 W/m.K on the value used in the validated model) improved the useful heat gained and the heat stored by 74 % and 18.6 %, respectively, of the validated model. The extended time for which the heat was available decreased by 16.7 % of the validated model as the thermal conductivity of the container allowed for an increased heat transfer to the environment. Despite this, the optimisation of the container thermal conductivity has increased the heat transfer into the PCM and away from the PV. It has been shown that by using this configuration the temperature of the PV can be regulated (Hasan et al., 2014a; Sarwar et al., 2014). An economic benefit of the system is that aluminium is less expensive than that of stainless steel (London Metal Exchange, 2015) thereby decreasing the cost of the overall system and thus, the payback period. Ideally, the adoption of aluminium in a PV/T/PCM system to encase the PCM would work in a climate with low precipitation due to the risk of corrosion as outlined in Chapter 4, Section 4.6.2. In climates of lower temperatures, lower container thermal conductivity would increase system efficiency as it would reduce heat losses to the environment.

7.3 Optimised PV/T/PCM System Performance

The summary of the optimised study in Figure 7.12 and Table 7.3 shows the parameters investigated to increase the system performance. Based on these summaries, the following optimisation techniques were used in the numerical simulation:

- PCM thermal conductivity of 1.4 W/m.K
- Heat of fusion of 240 kJ/kg
- Heat capacity of 2800 kJ/kg.K
- Mass flow rate of 0.005 kg/sec
- Thermal conductivity of container of 205W/m.K

The performance of the optimised model will be analysed under conditions in Ireland and Saudi Arabia with regard to thermal and electrical efficiency.

7.3.1 Optimised PV/T/PCM System in Ireland

The optimised model was numerically investigated under the environmental conditions of Ireland on the 5th of July 2013. These are the conditions under which the model was developed and validated and the parametric study was undertaken.

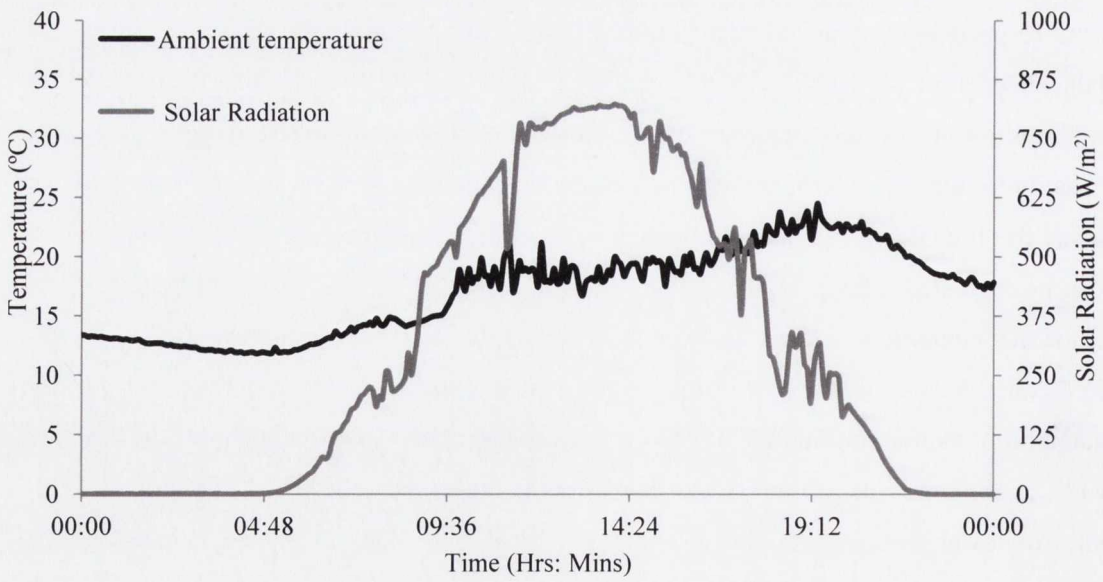

Figure 7.13: Ambient temperature and solar irradiance of Ireland

The temperature of the PCM has decreased to a minimum of 12 °C between the hours of 00:00 and 06:30 to a temperature 0.5 °C lower than that of the validated model as shown in Figure 7.14.

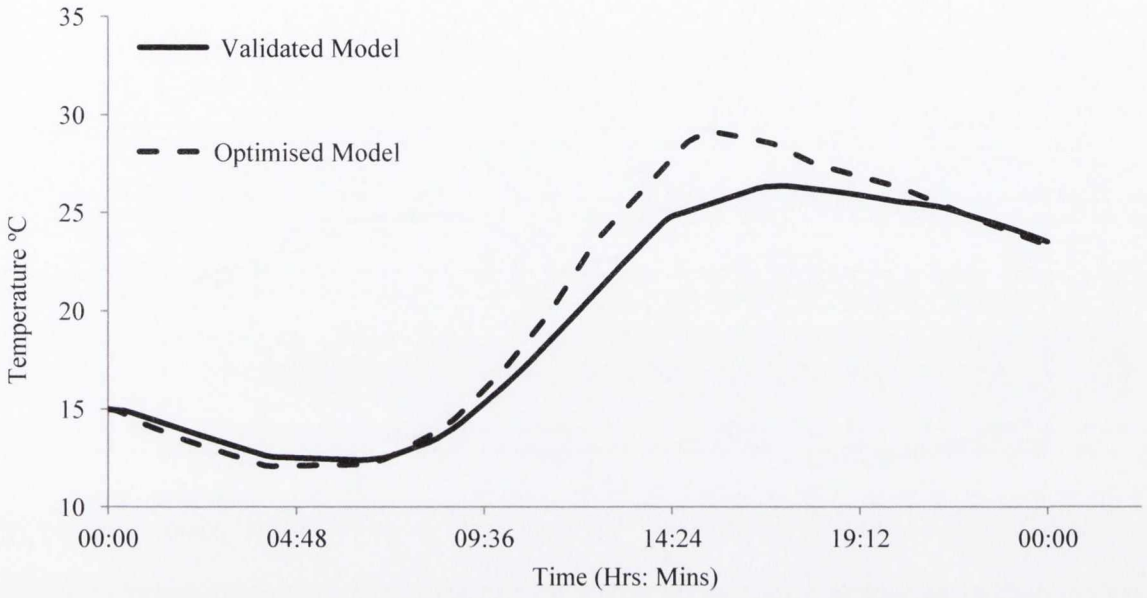

Figure 7.14: PCM temperature of the optimised and validated models

This was due to the increased thermal conductivity of the PCM and as a result the heat transfer through the material was increased during the hours of the early morning which shows this can be a disadvantage as the heat was transferred to ambient. To counteract this, a series of fins could be positioned at the pipes to increase the heat transfer surface area from the PCM to the water, the preferred route than to the environment where it was lost. However, an increase in thermal conductivity was shown to be advantageous to the system between the hours of 09:00 to 12:30, when the PCM reached an increased temperature than that of the validated model. As the stored energy in the PCM was increased as the temperature of the PCM was increased, this allowed for larger energy storage and increased potential to heat the water.

During the early morning from approximately 00:00 hours to 7:00 hours, the validated model was on average 0.27 °C higher than the optimised model (Figure 7.15). The increased thermal conductivity and mass flow rate contribute to the reduced temperature in the optimised model. During the afternoon and evening, 07:00 hours to 21:00 hours the outlet water temperature was approximately 0.93 °C, with a maximum of 2.2 °C, higher than the validated model. The increased thermal conductivity and energy storage allowed for an accelerated energy transfer to

the water. Towards the end of the evening, from 21:00 hours onwards, the outlet temperature of the optimised model is approximately 0.6 °C less than the validated model. The increased mass flow rate is shown to be heating the water to a value just under the validated model but heated a much larger capacity, approximately ten times the validated model.

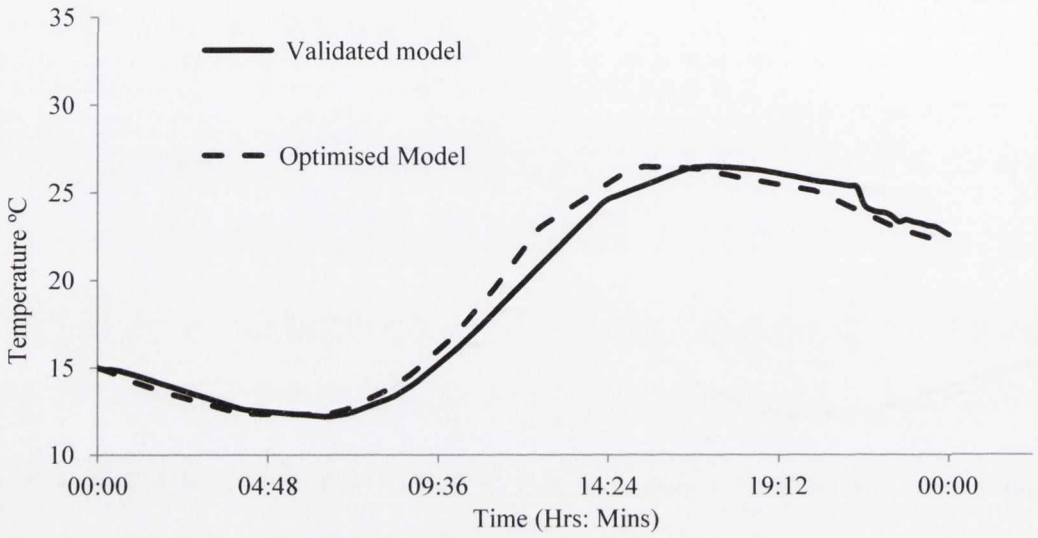

Figure 7.15: Outlet water temperature of the optimised and validated models

The temperature variation of the PCM in the PV/T/PCM system over the course of the day is presented in Figure 7.16(a-d), starting from 06:00 hours to 24:00 hours. The short range of variation of the PCM temperature at 06:00 hours is due to the lack of solar radiation as a result the temperature variation of the PCM remains with 1 °C. However, this changed at 12:00 hours as the temperature of the PCM on the surface closest to the PV has increased in temperature to approximately 40 °C. It can be seen at this point of the day a large proportion of the PCM has fully melted as the temperature is approximately 23 °C. By 18:00 hours the PCM has started to discharge to the water however, the PCM shows that the temperature achieved at the underside of the PCM (opposite side of the PV surface) was at approximately 24 °C which is approximately 6 °C less than the surface in contact with the PV, which shows the low heat transfer through the PCM. The PCM is cooling at the point of contact between the container and the PV surface and at the area which the pipe network was located, this showed there was a loss of heat from the PCM at the PV surface however there was also heat transfer to the water in the pipes. Further research could assess methods to increase the heat transfer from the edge of the PCM toward the pipe network.

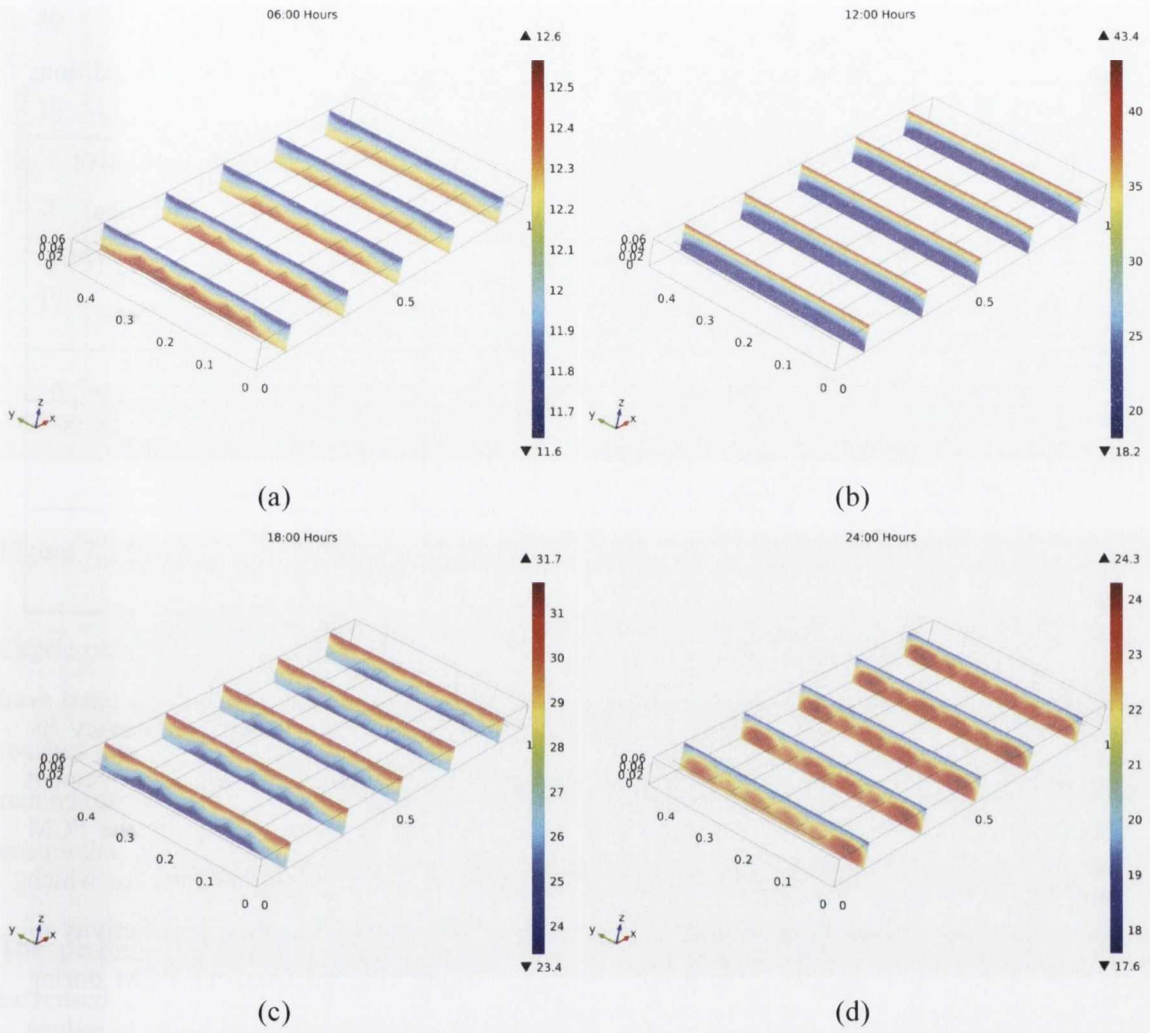

Figure 7.16: Images of the temperature of the PCM at (a) 06:00 hours (b) 12:00 hours (c) 18:00hours (d) 00:00 hours

The optimised model showed an increase in the useful heat gain and the stored energy efficiencies compared to the validated model presenting efficiencies of 16.2 % and 3.3 % (as shown in Table 7.4), respectively, which equates to a 342 % and 14 % increase on the useful heat gain on the validated model. However, the time of availability of the energy stored has decreased from 20 % in the validated model to 12.5 % in the optimised model. This is not due to the reduction in the energy stored but to the thermal conductivity of the PCM and the rate of removal of heat from the PCM as thermal conductivity increased. The energy transfer to the water or ambient increased the rate of charging and discharging. The energy removal from the

PCM occurred at an increased rate as the increased mass flow rate discharged the PCM faster than the validated model.

Table 7.4: Efficiencies of the optimised PV/T/PCM system under Irish environmental conditions

Parameter	$\frac{Q_u}{A_{PV} * \tau\alpha * I}$ (%)	$\frac{Q_s}{A_{PV} * \tau\alpha * I}$ (%)	$\left(\frac{t_{ext}}{24}\right)$ (%)	Cumulative Thermal Efficiency (%)	Cumulative Electrical Efficiency (PV) (%)
PV/T system	23.8	0	0	23.8	9.5
PV/T/PCM Validated Model	5.8	4.5	20.0	15.2	12
PV/T/PCM Optimised Model	25.0	5.1	12.5	21.3	12

The optimisation of a PV/T/PCM system has shown to improve the thermal efficiency by approximately 6.1 % compared to the PV/T/PCM system investigated. The main improvement was in the useful energy gain by the water and the increase in the energy stored by the PCM which improved by 19.2 % and 0.6 %, respectively. However, the extension of time for which the heat was stored was reduced. This was as a result of the increased thermal conductivity of the PCM and the container which allowed for increased heat transfer from the PCM during discharge although insulating the container to minimise losses to the environment could reduce this.

7.3.2 Optimised PV/T/PCM System in Saudi Arabia

The PV/T/PCM system was modelled under the environmental conditions of Dhahran, Saudi Arabia as shown in Figure 7.17. The data was sourced from the Ministry of Defence, Aviation Saudi Arabia which manage the National Meteorology and Environment Centre see Appendix 3 (National Meteorology & Environment Center, 2015). The data was recorded on the 5th of July 2010 which coincides with the heat simulation experiment carried out in Chapter 5. As the solar irradiance graph does not show any dips or peaks it was assumed that clear sky conditions existed. The ambient temperature remained above 30 °C for up to 15 hours.

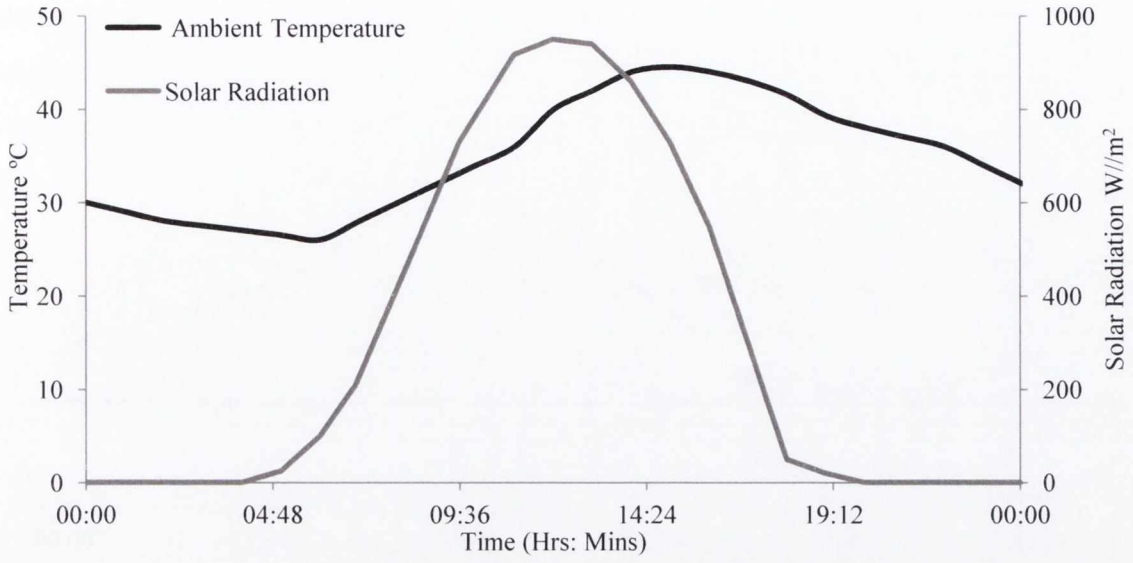

Figure 7.17: Ambient temperature and solar radiation of Saudi Arabia

Capric:palmitic acid has a phase change range from 16.5 °C to 25 °C. The latent heat would not have been discharged in an environment such as Saudi Arabia as the ambient temperature never reaches temperatures as low as 25 °C making the latent heat inaccessible to the system and thus redundant. As a result the PCM phase change range of between 30 °C to 35 °C was modelled to ensure that the PCM had an opportunity to charge during the day and discharge at night.

The performance of the optimised PV/T/PCM system has been shown to improve under increased solar irradiance and ambient temperature conditions compared to Irish weather conditions as presented in Figure 7.18. The increase in ambient temperature and solar irradiance has shown to increase all thermal aspects of the efficiency of the PV/T/PCM system as the temperature of the PV charging the PCM has increased (as shown in Table 7.5). The useful heat gain has increased from 25 % in Ireland to 98.1 % under Saudi Arabian conditions. The high thermal conductivity of PCM and increased solar irradiance allowed for an increase in heat transfer to the water, thereby increasing the temperature difference between the inlet and outlet water. It can be seen that the water was heated throughout the night and into the early morning, showing the PCM extended the time for which the heat was available and therefore, shifting the time at which the water was preheated.

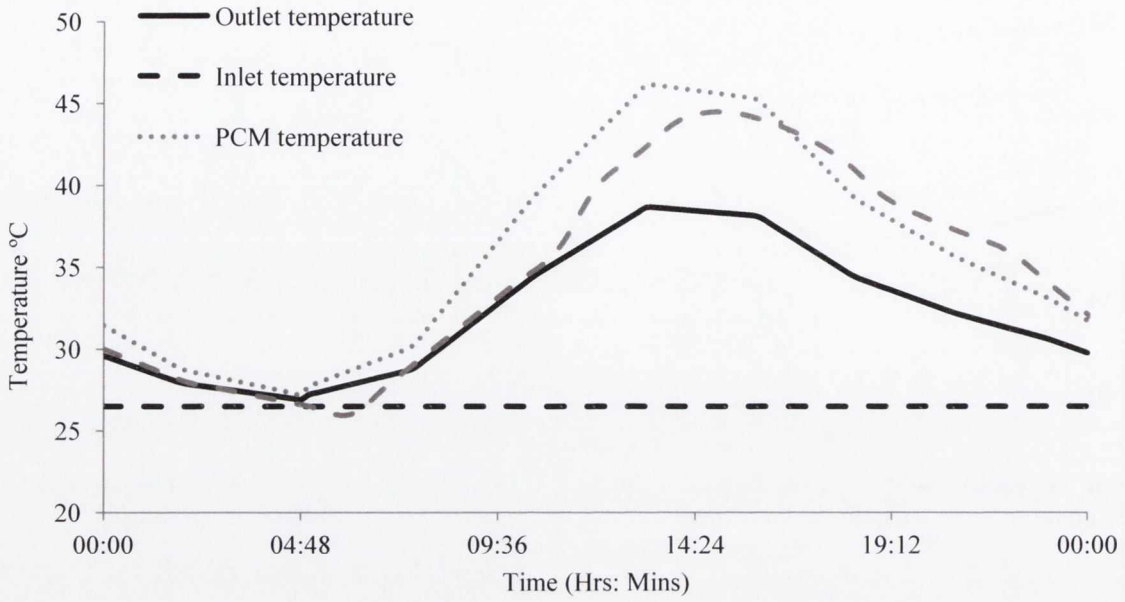

Figure 7.18: Results of the optimised model under environmental conditions of Saudi Arabia

Similarly, the PCM has been charged during the day at an increased rate due to the increase in solar irradiance and ambient temperature. The PCM discharged the heat after 15:00 hours when the values of solar irradiance and ambient temperature begin to decline. The increased thermal conductivity resulted in the PCM discharging heat at a faster rate than the validated model. This could potentially be controlled by insulating the PCM at night to minimise the thermal losses from the system. In addition to this, the mass flow rate could be controlled indirectly curbing the immediate discharge from the PCM. By increasing the mass flow rate the heat from the PCM was removed faster and by decreasing it, the opposite effect can occur as can be seen in the parametric study in Figure 7.7. Through controlling the removal of heat from the PCM and to the water the time for which the thermal energy is available is shifted. However, a compromise must be gained between the time of discharge and ambient temperature as the PCM can lose heat energy to the environment which needs to be avoided.

The PCM was seen to reach temperatures lower than that of ambient in the afternoon, approximately 16:00 hours. This was due to the thermocouples positioned in the middle of the PCM which are located at the same depth as the pipe network and as such the PCM were continuing to discharge heat to the water. The inside of the PCM cools at a faster rate than that of the outside as the water removes the heat from the PCM. The can be seen in the images taken at six hour intervals which showed the heat transfer into and out of the PCM over the course of

the day as presented in Figure 7.19(a-e), temperature of each figure varies over a different range as described by the legend.

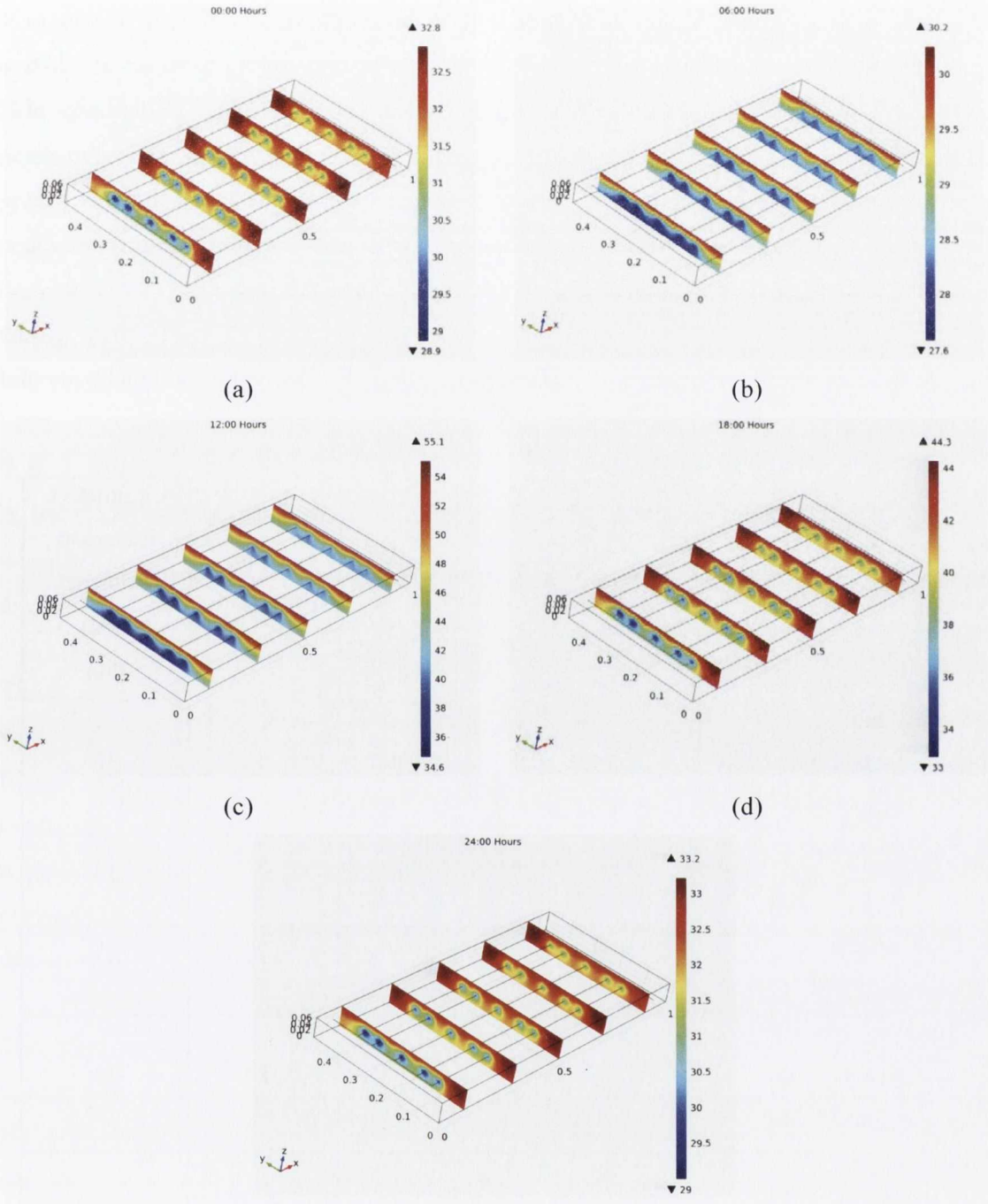

Figure 7.19: Images of the temperature of the PCM at (a) 00:00 hours (b) 06:00 hours (c) 12:00 hours (d) 18:00hours (e) 24:00 hours

The PCM can be seen to be cooling down in Figure 7.19(a), particularly around the pipe network where the PCM is discharging heat to the water. The edge of the PCM can be seen to maintain the highest temperature which implies that a percentage of this is being lost to the environment. At 06:00 hours (b) the surface of the PCM in contact with the PV can be seen to be heating at a faster rate than the rest of the PCM. The PCM temperature increases at 12:00 hours as shown in (c) at which stage the PCM is fully melted. The initial stages of discharge of heat from the PCM to the water can be seen (d) where the PCM temperature in the area of the pipe network is lower than the PCM edge. It can be assumed that the PCM has a higher heat loss around the edge than in the centre of the container. Fins would be an option to increase the heat transfer from the edges into the centre of the PCM to minimise heat loss.

Table 7.5: Efficiencies of the optimised PV/T/PCM system under environmental conditions of Saudi Arabia

Parameter	$\frac{Q_u}{A_{PV} * \tau\alpha * I}$ (%)	$\frac{Q_s}{A_{PV} * \tau\alpha * I}$ (%)	$\left(\frac{t_{ext}}{24}\right)$ (%)	Cumulative Thermal Efficiency (%)	Cumulative Electrical Efficiency (PV) (%)
Thermal (FPC) (Ayompe and Duffy, 2013b)	0	0	0	0	38
PV (Ayompe et al., 2011)	0	0	0	0	15
PV/T system (Pei et al., 2010)	23.8	0	0	23.8	9.5
PV/T/PCM Optimised Model Ireland	25.0	5.1	12.5	21.3	12
PV/T/PCM Optimised Model Saudi Arabia	98.1	4.4	33.3	68.4	9.2

PV/T/PCM system efficiencies have been improved by varying the environmental conditions in particular higher solar irradiance and ambient temperatures. The useful energy gain, the stored energy and the time for which the heat is available to the water had efficiencies of 98.1 %, 4.4 % and 33.3 %, respectively. It has been shown that the PV/T/PCM system functions better under higher ambient temperatures and solar irradiance values than that of an Irish climate. However, it also must be noted that the higher efficiencies are as a result of a positive influence of the environment and this is included in the energy gain of the system. As with all PV/T systems the reduced electrical energy generated compared to a conventional PV system is compromised by the production of thermal and electrical energy in a single unit. Due to the increase in PV temperature the electrical efficiency has been decreased from 12 % to 9.2 %, taking into account the temperature coefficient of the panel (-0.675 W/K (Solar Technology International, 2013))

7.4 Up-scaling Optimised Domestic Scale PV/T/PCM System

A PV/T/PCM system was designed in Ireland and Saudi Arabia for domestic application, whereby the electrical energy generated is stored or sold on the grid. It is envisaged the thermal energy would be used on-site for water or space heating.

The system has been numerically up-scaled using the optimised model presented in Section 7.3 which has improved PCM and container thermal conductivity and PCM properties; heat of fusion and heat capacity. The up-scaled model involves connecting 14 PV panels for a combined power output of 1.12 kWp and four of the panels will have an attached container with a pipe network and integrated phase change material. To upscale with any further PCM containers had shown no change in the outlet temperature when simulated. An example of the design of such a system can be seen in Figure 7.20.

The up-scaled PV/T/PCM system is a realistic setup as it represents an installed domestic system with 1.12 kW covering an area of 7 m^2 and four times the amount of storage of a single PV/T/PCM system. In the analysis of the results, the PCM temperatures are considered based on the fourth and final container in the array. As with previous numerical investigations into a PV/T/PCM system presented in Chapter 6, the water load required will not be taken into account. The main focus of this research is the temperature variation of the PCM material and water temperatures at the thermosyphon inlet and outlet.

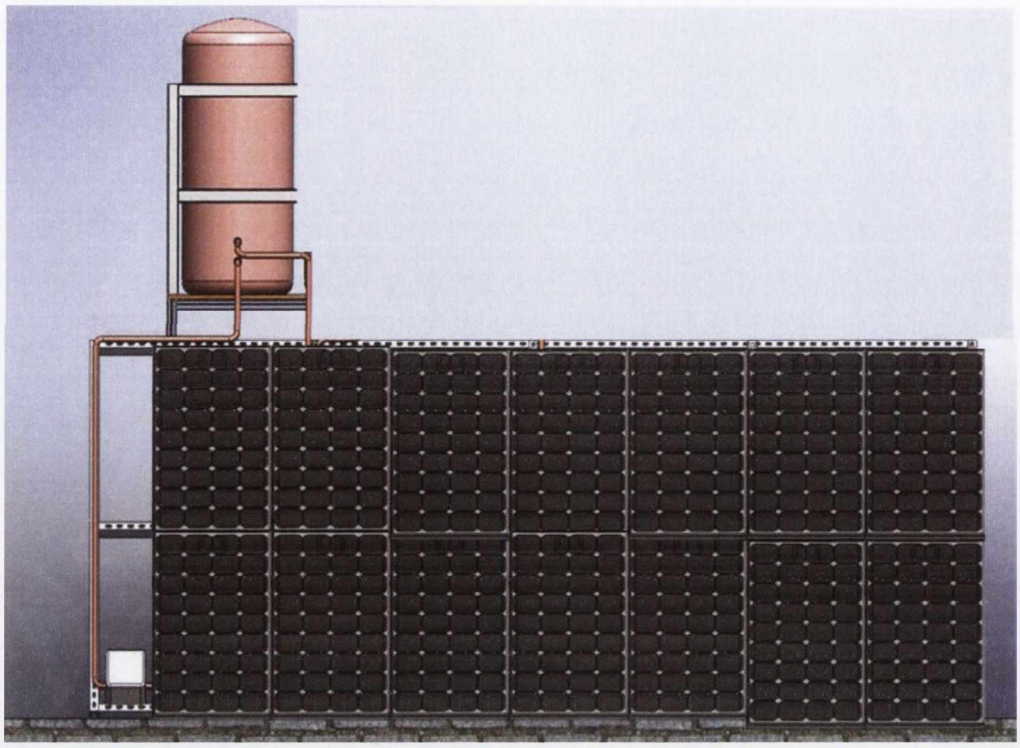

Figure 7.20: The design of an up-scaled PV/T/PCM system

7.4.1 Up-scaled Optimised System in Ireland

Performance of an optimised PV/T/PCM system was modelled under Irish environmental conditions as shown in Figure 7.13 on 5th July 2013. PCM temperature of the optimised up-scaled model is presented with the optimised model results in Figure 7.21. In the early hours of the morning, 00:00 hours to 05:00 hours, the temperatures of the PCM in both models are within ±0.2 °C of each other. The difference is mainly to do with the increased thermal conductivity of the PCM in the optimised and up-scaled model compared to the validated model. However, after approximately 09:30 hours, the temperature of the PCM in the up-scaled optimised model increased at a faster rate than that of the optimised model. The maximum temperature reached by the outlet of the up-scaled optimised model was 30.8 °C, 2.3 °C higher than the individual optimised system. This is the fourth and final panel in the array by the time the inlet water reaches this panel it will have been pre-heated as it had flowed through three previous panels. As a result there is a lower ΔT between the PCM and inlet temperature in the fourth panel compared to the individual system which would cause reduced heat transfer from the PCM and thus it remained at a higher temperature than that of the other system.

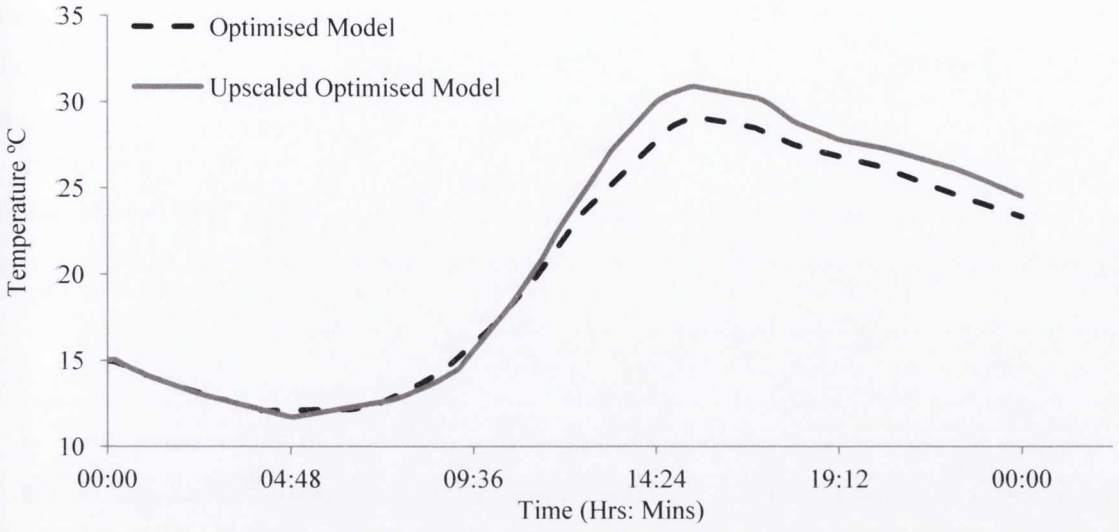

Figure 7.21: PCM temperature of an up-scaled optimised model of a PV/T/PCM system under Irish weather conditions

The ΔT of the water outlet in the up-scaled optimised and optimised models was ±0.3 °C up until 21:50 hours as shown in Figure 7.22.

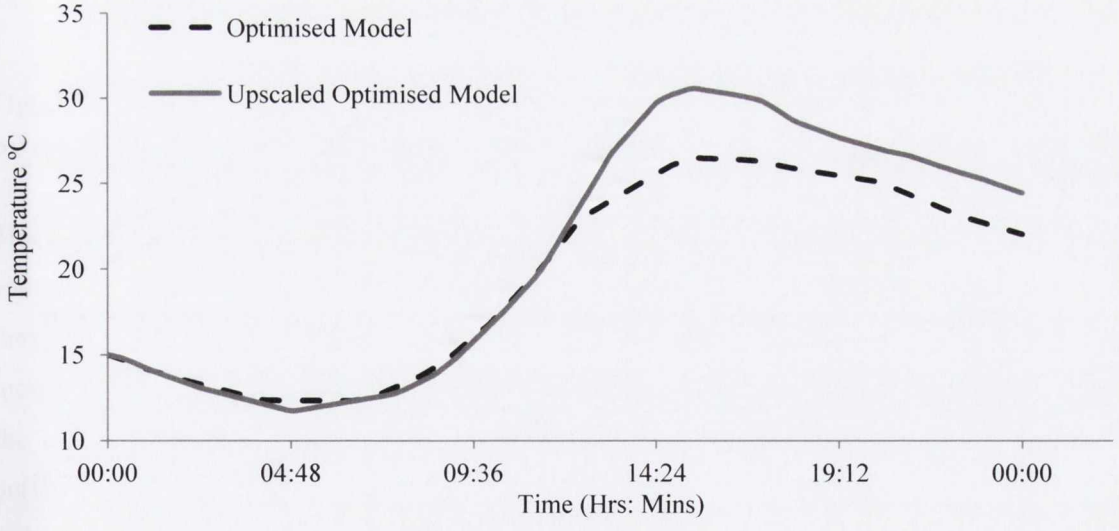

Figure 7.22: Outlet temperature of an up-scaled optimised model of a PV/T/PCM system under Irish weather conditions

The outlet temperature of the up-scaled and optimised system reached a maximum temperature of 30.5 °C, 4.2 °C (average 2.7 °C) higher than that of the optimised model. As the up-scaled optimised model has four PCM thermal collectors to flow through, the water has more time to

absorb the heat from the PCM and an increased energy store is available to it due to the increased mass of PCM.

Up-scaling the PV/T/PCM system in an Irish climate can be seen to increase the temperature of both the PCM and the outlet temperature of the water. The efficiency values of the system are presented in Table 7.6 and will be discussed in the following section.

7.4.2 Up-scaled Optimised System in Saudi Arabia

The performance of the up-scaled PV/T/PCM system was modelled under Saudi Arabian environmental conditions as this system showed the most improved performance based on the validated model. As with the optimised model, the PCM had a phase change range of 30 °C to 35°C.

Similar to Irish conditions, the PCM temperature of the up-scaled optimised model was found to increase above the optimised model as shown in Figure 7.23.

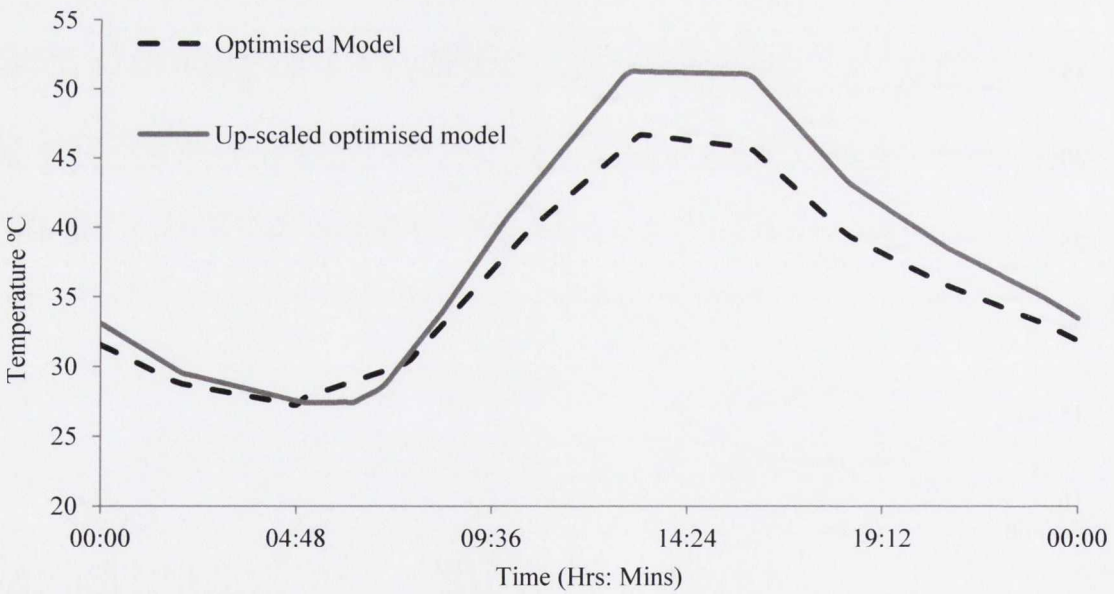

Figure 7.23: PCM temperature of the up-scaled optimised and optimised model of a PV/T/PCM system under Saudi Arabian weather conditions

The PCM temperature of the fourth panel in the array of the up-scaled system reaches a maximum of 51.8 °C, 5.7 °C (averaging 3.6 °C from 7:30 hours) higher than the optimised

model. As the water was being pre-heated by the previous three panels before reaching the fourth, the energy required to heat the water was reduced, therefore allowing the PCM to remain at an increased temperature than that of the optimised system.

The outlet temperature of the up-scaled optimised model has increased by up to 11.6 °C compared to the optimised model as shown in Figure 7.24.

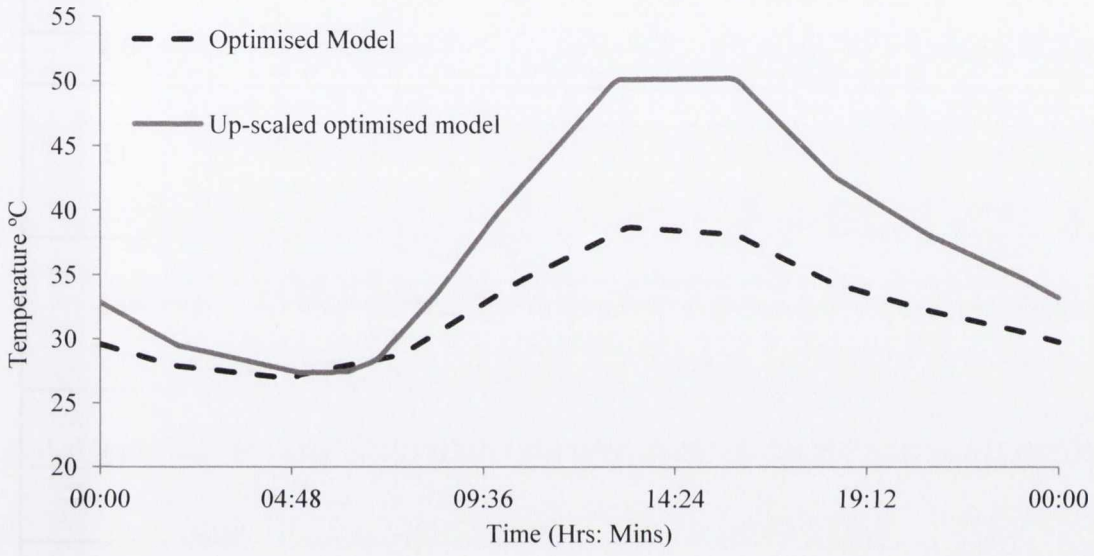

Figure 7.24: Water outlet temperature of the up-scaled optimised and optimised model of a PV/T/PCM system under Saudi Arabian weather conditions

The advantage of four thermal collectors with integrated PCM in series allowed more time and energy to the water allowing it to pre-heat to a higher temperature than that of the single PCM thermal collector. This is ideal if the role of the system is to heat the water, however the increased temperatures would negatively affect the PV performance which is a compromise in the up scaled device. The addition of extra thermal collectors could potentially increase the outlet temperature of the water however; this would have to be considered further in full as the maximum temperature the PCM can reach is dictated by rate of heat transfer from the PV.

The efficiencies of the numerical analysis of the up-scaled and optimised PV/T/PCM systems in Ireland and Saudi Arabia are presented in Table 7.6 along with the efficiencies of a conventional PV/T system and an individual optimised PV/T/PCM system.

Table 7.6: Efficiencies of the up-scaled optimised systems in Ireland and Saudi Arabia compared to a conventional PV/T system

Parameter	$\frac{Q_u}{A_{PV} * \tau\alpha * I}$ (%)	$\frac{Q_s}{A_{PV} * \tau\alpha * I}$ (%)	$\left(\frac{t_{ext}}{24}\right)$ (%)	Cumulative Thermal Efficiency (%)	Cumulative Electrical Efficiency (PV) (%)
PV/T system	23.8	0	0	23.8	9.5
PV/T/PCM Optimised Model Ireland	25.0	5.1	12.5	21.3	12
PV/T/PCM Optimised Model Saudi Arabia	98.1	4.4	33.3	68.4	9.2
PV/T/PCM system Up-scaled Optimised Ireland	13.2	6.7	13.3	15.8	12
PV/T/PCM system Up-scaled Optimised Saudi Arabia	52.7	6.4	33.3	46.2	9.2

The up-scaled optimised models under both Irish and Saudi Arabian conditions were shown to increase the energy storage by 1.6 % and 2 %, respectively, compared to a single PV/T/PCM system. The temperature of the PCM increased in the up-scaled models and thus increasing the energy stored in each system. The time extension for which heat was available increased in the Irish up-scaled system, however, it remained the same under Saudi Arabian conditions. However, the useful heat gain efficiency was reduced in both up-scaled optimised systems compared to the optimised systems 11.8 % and 45.4% in Ireland and Saudi Arabia, respectively. The reduced efficiency was caused as the increase in water temperature did not match the relative increase in thermal collector surface area. However, it must be noted that the water temperature in each up-scaled optimised system reached higher temperatures than the optimised system which would reduce the energy required in auxiliary heating.

The cumulative efficiency was 15.8 % and 46.2 % for the up-scaled optimised systems in Ireland and Saudi Arabia, respectively. These are less than that of a single optimised PV/T/PCM system in each respective location however, it must be noted that the heat stored is increased by four times that of an individual system.

7.5 Applications

A PV/T/PCM system combines a series of operations into one system as shown in Figure 7.25.

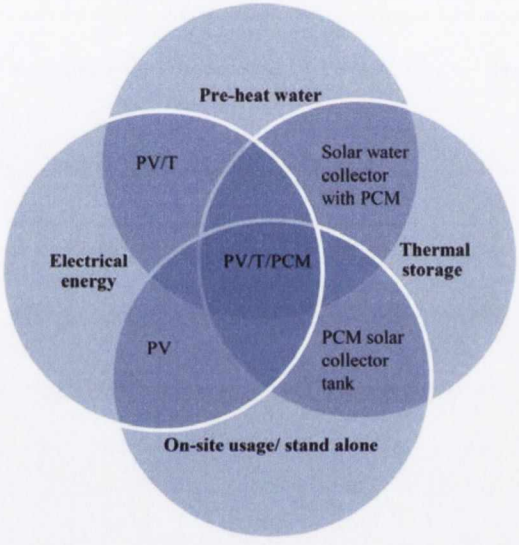

Figure 7.25: Venn diagram of the advantages of a PV/T/PCM system

The intended application for such a system was in a domestic dwelling with grid connection and a regular heated water load. The Venn diagram indicates the overlapping of each system and the advantages of a PV/T/PCM system.

The design of the PV/T/PCM system allows it to function as a standalone system with battery storage which can be used on-site, generating electrical energy, acting as a thermal store and pre-heating water. Such systems are more suited to remote developing areas where systems have a relatively long service time and with nearly no maintenance.

A further application of a PV/T/PVCM system involves the storage of thermal energy in the case of a small water tank. The PCM can be used to shift the location of storage from the water to the PCM, with the added advantage of gaining energy during latent heating and reducing the water tank storage size requirements. This would increase the ease with which a retrofit PV/T/PCM system could be installed than that of a solar thermal collector system which necessitates a larger tank for heat storage requirements.

7.6 Pathogenic Bacteria

Congenial temperatures that exist in the water tanks of systems, such as the one presented in this paper, have to adhere to regulations to minimise the proliferation of pathogenic bacteria, such as Legionella. It is worth noting the PV/T/PCM system is a pre-heat system only which would be a part of a larger system and an auxiliary heater would be used to boost water temperature if required in a climate like Ireland. However, the performance of the system in climates such as that of Saudi Arabia a PV/T/PCM system has potential to act as solar disinfection system during the day and as a source of stored energy in the evening which can be discharged for space or water heating.

7.7 Conclusion

This validated model of a novel PV/T/PCM system is a robust method of analysing the performance of the system under varying system configurations. A parametric study was completed based on a range of values for each material property. An increase in PCM thermal conductivity reduced heat storage efficiency of 2.6 % which was attributed to increased losses from the system as the heat transfer to the water and the environment increased, this could be minimised by insulating the rear of the container. This was outweighed by a gain of 6.7 % in useful energy to preheat the water. Heat capacity and heat of fusion were shown to increase the energy stored in the system by approximately 0.4 % -0.5 % compared to the validated model but had a minor impact on heating the water and extending the time for which heat was available. The increase in mass flow rate was shown to increase the useful heat gain to 6.6 %, an improvement of 2.8 % on the validated mode. However, as the heat was being removed at a faster rate from the PCM, the storage energy was also reduced. It was considered that if the mass flow rate was controlled so too could the discharge of heat from the PCM. However, this would have to be considered in connection with the ambient temperature to avoid the discharge of heat from the PCM to the environment. The cost of installing a pump would also have to be taken into account. The increase in the thermal conductivity of the container showed an increase

in the useful heat gain and stored energy to 6.5 % and 3.5 %, respectively, compared to the validated model. However, the reduced heat storage extended time was reduced as the heat transferred through the container at an increased rate than the validated model.

The PV/T/PCM system design was optimised based on the results of the parametric study which maximised the performance of the system. The optimised system was numerically considered under the environmental conditions of Ireland and Saudi Arabia. The electrical efficiency was negatively affected due to the increased PV temperature under Saudi Arabian conditions compared to that in Ireland. However, it was shown that the cumulative thermal efficiency of the system in Saudi Arabia increased to over three times that of the system simulated in Irish conditions.

The PV/T/PCM system was up-scaled to assess the performance on a larger and more realistic scale and numerically investigated under the environmental conditions of Dublin, Ireland and Dhahran, Saudi Arabia as the efficiency of heat stored and time extended for which heat available was increased. There was also four times the amount of energy stored in the up-scaled system compared to a single PV/T/PCM system. Although the useful energy gain efficiency decreased when the system was up-scaled, the temperature to which the outlet reached was increased thus reducing the energy required from an auxiliary heater.

The applications of a PV/T/PCM system have been presented. Although the system is recommended for domestic use, it can also work as a standalone system. Particularly, in developing rural areas where connecting to a grid is still an issue a standalone system can use battery storage. The advantage of installing a PV/T/PCM system is the added thermal storage to the system which can be used at a later time. PCM shifts the location of the stored heat. In a PV/T system the heat is stored in the domestic hot water tanks which require the installation of larger tanks than that of typical domestic tanks. However with a PV/T/PCM system the heat is stored in the PCM which would not require a tank reducing the need to upsize the water tank. Under high solar irradiance and increased ambient conditions the performance of the system improved compared to that of Ireland.

In conclusion, a PV/T/PCM system is a more viable option for a country with high daily solar irradiance (~1000 W/m^2) and low ambient temperatures at night to maximise the discharging of the PCM than that of Ireland where the thermal efficiency of Saudi Arabia conditions showed an increase of 73.1 % compared to the environmental conditions in Ireland. Optimisation

techniques investigated improved the thermal performance of the system by 19.2 %, increasing the economic feasibility.

Chapter 8

Economic Assessment of a Photovoltaic/Thermal/Phase Change Material System

Chapter 8. Economic Assessment of a Photovoltaic/Thermal/Phase Change Material System

The aim of this chapter is to evaluate the economic feasibility of a novel PV/T/PCM system. The cost analysis is an important aspect of this system particularly because the study involves a new technology. Specific objectives of this chapter are to:

- Investigate the current cost and market position of PV and PCM
- Calculate the cost of a PV/T/PCM system
- Calculate the simple payback period of a PV/T/PCM system

8.1 Cost Analysis of a PV/T/PCM System

The cost analysis of a PV/T/PCM system involves calculating the total cost of the system installed and the cost of one system if manufactured on a mass produced scale. The cost of the system was calculated for Ireland and Saudi Arabia and was used to determine the feasibility of the investment.

The illustrative range of PV and PCM (as shown in Figure 8.1) shows the evolution of a PV/T/PCM system. In low-insolation climates, high PV temperatures are infrequent so cooling by natural convection from the front and near surfaces is employed. In climates with higher insolation, thermal management interventions using PCM offer more effectively maintained lower PV temperatures but incur additional capital cost. However, this cost can be offset by the extraction of heat from the PCM using a system design such as that of a PV/T/PCM system. In very high insolation climates, the heat extracted can be a very valuable resource for night time space cooling and, in some instances, dehumidification. The idea is to increase the useful heat output in order to reduce the payback period of the system capital cost. The illustration shows the higher the insolation the increased availability of energy which if captured and used or stored can increase the economic feasibility of the system.

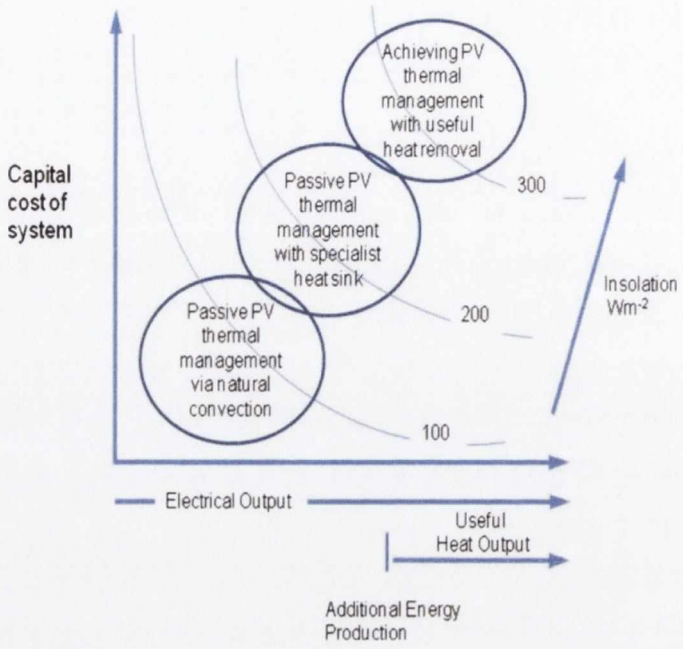

Figure 8.1: Illustrative ranges for thermal management and heat removal in a PV system (Browne et al., 2015b)

8.1.1 Cost of Photovoltaic Panels

The PV system pricing has shown a downward trend as presented in Figure 8.2 (Feldman, 2014) which shows the cost per watt of PV installation (PV module, components and installation) in recent years. This has been primarily due to the pricing competitive positioning amongst manufacturers becoming more pronounced, principally the low cost Chinese suppliers pushing PV prices down. The graph gives an indication of the prices of residential, commercial and utility prices in U.S. as well as predicted costs for the years 2014 to 2016. The figure is in line with the downward projected predictions for the market pricing of PV globally.

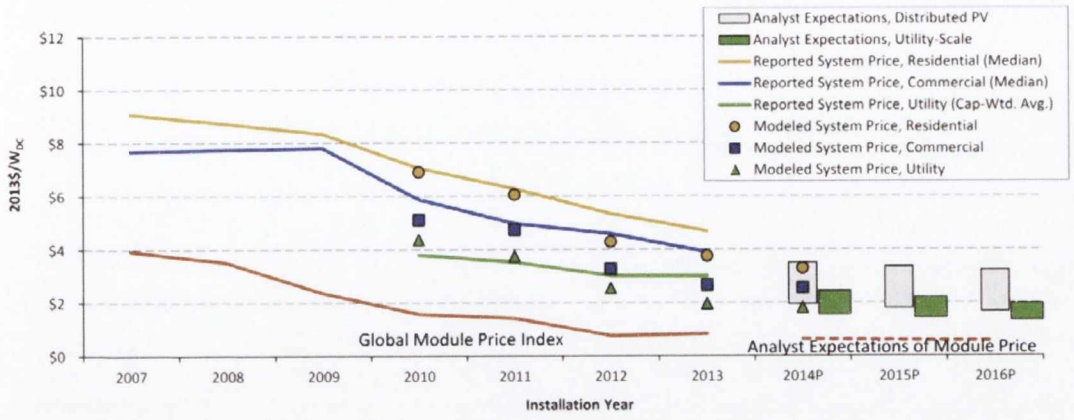

Figure 8.2: Average U.S PV installation prices over time (Feldman, 2014)

In a report on the European status of PV energy, the EC reported that the worldwide average price of a residential system was given as 1.70 EUR/Wp (Jäger-Waldau, 2013). This was the price applied to the PV modules in the cost analysis of the PV/T/PCM system.

The cost reduction trend of PV modules in recent years is a promising sign for the solar energy industry in general, increasing the cost competitiveness of a newly developed technology such as that of a PV/T/PCM system.

8.1.2 Cost and Commercial Availability of Phase Change Material

Material cost depends on both the demand and classification of a material. If the material has increased demand the cost advantage of economies of scale will cause a decrease in the price however, if the material is not widely available but in high demand this could cause the price increase. Some PCM are relatively inexpensive due to their abundant supply such as paraffin ($1.88–$2.00 /kg) and calcium chloride ($0.13–$0.20 /kg) (Kośny et al., 2013). There is a need for further cost reductions in order to make a PV/T/PCM system a viable option; this will only occur if the demand for the material increases and production costs reduce. With growing interest in the areas of PCM integration for cooling and thermal storage a reduction in product cost should occur in the future.

PV/T/ PCM systems are not yet sold as one unit although companies mentioned in Table 8.1 do offer sheets of PCM which can be easily integrated with PV. However, the aim of the sheets is to maintain lower PV temperatures. There is potential that the sheets could be used to integrate with a pipe network removing the requirement of a container.

Table 8.1: Commercial PCM manufacturers (Agyenim et al., 2010)

Manufacturer	Temp Range (°C)	Types of PCM available	Types of product	Class
RUBITHERM	-3°C 100 °C	29	Inorganic, organic	Bulk, macro-encapsulated
Cristopia	-33°C to 27 °C	12	Inorganic	Micro-encapsulated
TEAP	-50°C to 78 °C	22	Inorganic	Bulk, macro-encapsulated
Mitsubishi Chemical	9.5°C to 118 °C	6	Inorganic	Bulk
Climator	-18°C to 70 °C	9	Inorganic	Bulk
EPS Ltd/PCM Products	-114°C to 164 °C	61	Inorganic, organic, eutectic	Bulk, macro-/ micro-encapsulated
BASF	21°C to 26 °C	6	Organic	Micro-encapsulated
Phase Change Energy Solutions	23°C to 27 °C	3	Not available	Macro-encapsulated
Entropy Solutions Inc/ PureTemp PCM	-37°C to 151 °C	36	Organic	Bulk, macro-/ micro-encapsulated
Phase Change Products Pty Ltd (PCP)	-21°C to 58 °C	10	Inorganic	Bulk

Commercial PCM for PVs are now available for the intention of thermal management, although PCM sheets have the potential to store heat allowing for extraction later (Pause, 2010 2011, Henkel, 2011; Henkel Corporation, 2011). Currently on the market is a compact storage module which is a panel containing PCM that could be integrated with PV and a pipe network to produce a PV/T/PCM system (Rubiterm, 2015). Other available products are BioPCmat

designed to be placed in solar collectors, drop ceilings, roofing or insulation to reduce heating, ventilation and air conditioning loads (Energy Solutions, 2014) and ENERGAIN®, a thermal mass panel with integrated PCM which is used as a construction material to assist in passive cooling during summer and passive heating during winter (DuPont, 2014). Building on an updated a list of commercial PCM manufacturers (Agyenim et al., 2010) the temperature ranges and number of PCMs available is presented in Table 8.1.

Interest in the area of PCM and integration with building materials, including PV, to improve the energy generation and decrease the energy consumed by buildings has increased suggesting the cost of the material will decrease with an increase in PCM usage through economies of scale.

8.1.3 Economics of Incorporating PCM with PV

The economics of a PV/T/PCM system is highly dependent on the location; increased energy generation means higher PV temperatures and an increased potential PCM heat storage. A numerical study maps the global geographic distribution of PV energy potential with and without PCM considering temperature effects (Kawajiri and Oozeki, 2011). Considering this, areas of Africa and Australia which are seen to be most affected by PV temperature increase would particularly benefit from PCM application making PCM a more financially viable option. Hasan et al. (2014a) carried out an economic assessment of a PV/PCM system. It was found that a mass-produced system, depending on PCM applied, would be valued at just under €100, or €50 - €60 in Pakistan. The financial benefit of the systems was estimated to be approximately €4.81 /kW. The financial benefit of the system was found to be less in Ireland than that of Pakistan due to the higher cost incurred during production and lower performance benefit and the increased efficiency due to a higher solar resource.

8.1.4 Cost of a PV/T/PCM System

The additional costs incurred by installing an up-scaled optimised PV/T/PCM system were considered which consisted of a 1.12 kWp PV array with four PCM thermal collectors as outlined in Section 7.3 and are presented in Table 8.2. The cost of manufacturing an individual PV/T/PCM system is considerably more expensive than the mass manufacture of such a system and would not be economically feasible to install. As a result, two system costs were presented, manufacturing and material costs of a single unit and a system in mass production. As the optimised up-scaled system performance was assessed in Ireland and Saudi Arabia, the mass

manufacturing costs of each country are presented. The 'Single system fabrication' costs are of materials and construction of the PV/T/PCM system installed in Dublin, Ireland.

The cost of the PV panel was based on the average global price of a residential PV system of 1.7 EUR/Wp (Jäger-Waldau, 2013) for a 1.12 kW PV array which includes balance of systems. However, if PV modules were bought in large quantities directly from a producer the cost would reduce to €1.07 per Wp (Galen et al., 2014).

The cost of PCM has been discussed as one of barriers to the application of PCM. The PCM was purchased from Sigma Aldrich (Sigma-Aldrich, 2015) at a cost of €11.72 /kg. This is an impractical material cost when considering the economic feasibility of a PV/T/PCM system. However, a method has been described to reduce the cost of methyl-branched fatty acids which could potentially be applied to fatty acids such as capric and palmitic to reduce productions costs (Ngo et al., 2014). The process predicts the best case scenario production cost of $2.37 per kg (€2.13 per kg). This value was used for the mass produced cost analysis of the system as although it may not be an immediate option, there is clearly scope for PCM price reduction.

The cost of the specifically manufactured container for the experimental work of this thesis according to our specifications was €296. The cost of the item can be drastically reduced if the containers were ordered in large quantities. The current bulk cost of aluminium in Ireland and Saudi Arabia is €2239/tonne and €1567/tonne, respectively (European Commission, 2013). The cost of four containers in Ireland and Saudi Arabia are €57 and €40, respectively. Components such as copper piping were considered to have the same relative price difference between both locations as that of aluminium. The cost of copper when bought in bulk was €4735 /tonne (London Metal Exchange, 2015) and based on this the component cost of pipes was €23 and €18 for Ireland and Saudi Arabia, respectively.

The assembly of the PV/T/PCM system has been considered as the 'Production' cost in the cost analysis. It has been reported that by mass producing thermal collectors on an industrial scale from 10^3 m^2 to 10^4 m^2 could reduce the thermal collector production costs by 30% (Jäger, 2013). This resulted in a cost reduction of €30 from the €100 of the individual system production. The cost of production in Saudi Arabia was found to be €30 which was based on the relative difference between the national annual minimum wage of Ireland and Saudi Arabia.

Table 8.2: Summary of manufacturing and material costs of a PV/T/PCM system

		Ireland (€)		Saudi Arabia (€)
		Single system fabrication	Mass manufacture	Mass manufacture
Cost	PV System (1.12 kW)	1905	1198	1198
	PCM	1125	204	204
	Container	1185	57	40
	Components (pipes)	50	23	18
	Production	100	70	30
	Net Cost	4365	1545	1490

The cost analysis presented breaks down the costs incurred by implementing a PV/T/PCM system to generate both electrical and thermal energy as well as acting as a heat storage mechanism. The system is clearly not feasible when constructed as a bespoke item. A major reduction can be seen when assessing the cost incurred by the PCM, container and pipe network. In Ireland mass production has reduced the cost of the system by approximately 29 %. This was further reduced when mass produced in Saudi Arabia which saw a decreased of 46% in the cost of the thermal collector with integrated PCM.

8.2 Economic Assessment of a PV/T/PCM System

The economic assessment required the calculation of the annual energy output by the PV/T/PCM system; this included the sum of electrical energy generated by the PV and the thermal energy stored in the PCM and in pre-heating the water.

8.2.1 Thermal and Electrical Energy Analysis of a PV/T/PCM System

The daily thermal energy generation was calculated based on the peak sunshine hours, h_p, which refers to the solar irradiance a particular location received if the sun were shining at its maximum for a specified number of hours which was calculated using Equation 8.1.

$$h_p = \frac{\int G\, dt}{G_{stc}} \tag{8.1}$$

Where, G is the daily solar irradiance in units of kWh/m^2 and G_{stc} is the solar radiance during standard test conditions in this research it is 1 kW/m^2.

The daily energy generated by the PV/T/PCM system was calculated based on the electrical energy generated by the PV, the stored energy in the PCM, Q_s, and the useful energy gain of the water, Q_u. The energy yield per peak sunshine hour was calculated using Equation 8.2.

$$Q_y = \frac{Q_u + Q_s}{h_p} \tag{8.2}$$

The annual sunshine peak hours were assumed to be 1700 hours for Ireland based on meteorological data from Ireland (Met Eireann, 2015a) and 3394 hours for Saudi Arabia (Sabbagh et al., 1986).

The annual electricity generated was calculated based on the solar resource and photovoltaic electricity potential maps which were generated by the SolarGIS (Huld et al., 2012) as shown in Appendix 1 and 2. The map of Europe, Africa and the Middle East were used to specify the yearly sum of solar electricity generated by 1 kW_p system. It is assumed the panels are optimally inclined and equator orientated with PV system performance ratios of 0.75, a typical value for polycrystalline silicon (Šúri et al., 2006) as shown in Appendix 1 and Appendix 2 (Huld et al., 2012; SolarGIS, 2013). The yearly sum generated by a 1.12 kW_p system in one year in Ireland and Saudi Arabia was 1008 kWh and 1932 kWh, respectively. The total annual energy yields by a PV/T/PCM system in each location are presented in Table 8.3 which has been calculated using the methodology in Section 5.3.

Table 8.3: Total energy yield of a PV/T/PCM system in Ireland and Saudi Arabia

	Ireland (kWh/year)	Saudi Arabia (kWh/year)
Electrical energy	1008	1932
Stored energy (PCM)	170	320
Useful energy gain	6	44
Total	1184	2296

8.2.2 Simple Payback Period

SPP is the minimum amount of time (years) required for the positive cash flows to surpass the initial investment. The drawbacks are that the timing of cash flows is ignored and cash flows beyond the payback period are not accounted for (Kaplan, 1983). The payback period is the ratio of the extra first cost C_0 (or capital cost) to the annual savings, S and is given as (Masters, 2013):

$$SPP = \frac{C_0}{S} \tag{8.3}$$

The savings, S, are calculated based the energy yield of the PV/T/PCM system and the equivalent energy saving based on the current cost of electricity, oil and gas in each respective location. The payback period will be assessed over three scenarios, all of which assumed the thermal energy generated is used on-site in addition to:

- All electrical energy (100 %) generated is used on-site
- 50 % electrical energy is used on-site and 50 % is sold on the grid
- 0 % electrical energy is used on-site and 100 % is sold on the grid

It is assumed the remainder of the power required will be generated by one method electricity, oil or gas. It must also be must also be noted that the economic assessment has not taken into account the cost of the balance of systems (battery, wiring, mounting systems, solar inverters). As discussed in Chapter 7, the performance calculations are based on optimum days and do not include the effect of the whole system in relation to hot water usage or storage. The payback period was calculated in Ireland and Saudi Arabia as these were the two locations which were investigated experimentally and numerically in Chapter 5 and Chapter 7, respectively.

A feed-in tariff is a policy mechanism which is designed to accelerate investment in renewable technologies and requires the utility or electricity supplier to pay the person or company for generating renewable electricity which they have exported to the grid. A generation tariff is the price per unit of electricity paid by a government to a person or company for generating energy using renewable methods for their own consumption (Ayompe, 2011). The government of Ireland supports alternative energy generation through a micro-generation project however the tariffs received are not available to systems which generate over 11kW (Electric Ireland, 2015). Saudi Arabia have not yet incentivised the generation of renewable energy through the implementation of generation and feed-in tariffs (FIT). In the absence of generation and feed-in

tariffs the payback period of a renewable energy system is increased. In order to consider the impact of such incentives on the payback period of a PV/T/PCM system the economic assessment also included two other locations where incentives are implemented. UK and Spain were chosen due to the similar solar resource of Ireland and Saudi Arabia, but where financial incentives are available (Feed-in Tariff UK, 2015; Tarifasgasluz, 2015).

The energy generated by the PV/T/PCM system was assumed to be the same in Ireland and the UK (as shown in Table 8.4) due to the similar climatic conditions. In Ireland, there are no legislated tariffs available from the government however, one electricity supplier, 'Electric Ireland', runs a micro-generation scheme. Micro-generation covers small scale generators where domestic customers produce their own electricity and export the surplus on to the grid for a payment rate of 9 c/kWh (Electric Ireland, 2015). The annual average household energy consumption was assumed to be 20000 kWh/year (SEAI, 2013) with the cost of electricity, gas and oil in Ireland being reported as 25.4 c/kWh, 7.45 c/kWh and 5.7 c/kWh, respectively (Eurostat, 2015). In the UK, the government endorses both an energy generation and feed-in tariff which are currently priced at 8 c/kWh and 7 c/kWh (Feed-in Tariff UK, 2015).

Table 8.4: PV/T/PCM energy generation, annual household energy consumption and energy cost in Ireland and the UK

	Ireland	UK
PV/T/PCM Annual Energy Generated	1184 kW/h/year	1184 kW/h/year
Feed –in Tariff	9 c/kWh	8 c/kWh
Generation tariff	0 c/kWh	7 c/kWh
Annual Household Energy Consumption	20000 kW/h/year	20000 kW/h/year
Cost of Electricity	25.4 c/kWh	20.1 c/kWh
Cost of Gas	7.45 c/kWh	6.2 c/kWh
Cost of Oil	5.7 c/kWh	5.6 c/kWh

The annual household energy consumption was reported to be 20000 kWh/year (Ofgem, 2015b). The electricity, gas and oil prices were reported to be 20.1 c/kWh, 6.2 c/kWh and 5.6 c/kWh, respectively.

The annual energy generated in Saudi Arabia using a PV/T/PCM system was 2296 kW/h/year as calculated in Section 8.2.1 and shown in Table 8.5. The thermal energy yield per peak sunshine hour in Saudi Arabia was used to calculate the annual thermal energy yield in Spain based on annual peak sunshine hours (Gil et al., 2015). The annual electrical energy generated was calculated based on the yearly sum of solar electricity generated by 1 kW_p system as shown in Appendix 1 and 2 (Huld et al., 2012; SolarGIS, 2013). The cumulative thermal and electrical energy generated using a PV/T/PCM system in Spain was 2070 kW/h/year. Currently, Saudi Arabia does not implement feed-in tariffs however, it aims to obtain one third of its power from renewable sources by 2032 which suggests feed-in tariffs may be introduced (Renewable Energy Focus, 2012). Spain currently offers 12 c/kWh exported to the grid (Tarifasgasluz, 2015). Saudi Arabia has one of the world's highest energy consumption per capita and this is reflected in the annual household energy consumption of 25000 kW/h/year (Taleb and Sharples, 2011). Annual household energy consumption in Spain is 11000 kW/h/year, compared to its European counterparts, Ireland and UK, this is just over half. However, a large proportion of energy consumption is used for space heating which is not as relevant in Spain as it is in Ireland and the UK due to colder climates (Pastorello, 2010). As a country with large quantities of non-renewable energy reserves, Saudi Arabia has some of the world's lowest prices in electricity, gas and oil of 6 c/kWh, 0.23 c/kWh and 4.1 c/kWh, respectively (Matar et al., 2015). The cost of electricity, gas and oil are 23.7 c/kWh, 9.6 c/kWh and 5.9 c/kWh in Spain (Eurostat, 2015).

Table 8.5: PV/T/PCM energy generation, annual household energy consumption and energy cost in Saudi Arabia and Spain

	Saudi Arabia	Spain
PV/T/PCM Annual Energy Generated	2296 kW/h/year	2070 kW/h/year
Feed –in Tariff	0 c/kWh	12 c/kWh
Annual Household Energy Consumption	25000 kW/h/year	11000 kW/h/year
Cost of Electricity	6 c/kWh	23.7 c/kWh
Cost of Gas	0.23 c/kWh	9.6 c/kWh
Cost of Oil	4.1 c/kWh	5.9 c/kWh

The results of the study are presented based on the type of energy resource used to generate the remainder of the domestic energy consumption after the energy yield of the PV/T/PCM system was taken into account.

If the main source of power to a household was electricity, the SPP of each location under the scenarios explained is presented in Figure 8.3. The most efficient payback period occurs when all of the energy generated by the PV/T/PCM system is used within the household compared to exporting all or 50 % of energy generated to the grid this as all locations lowest SPP is in the '100% used on-site' category. This can be attributed to the reduced cost of electricity due to the savings made on the power generated by the PV/T/PCM system. However, in the '100 % exported' case, all the power generated by the PV/T/PCM system is exported to the grid where the feed-in tariff is lower than the cost of electricity or in the case of Saudi Arabia is zero. The best case scenario is 100% usage on-site. However, it is not always possible to match production with demand and the results of '50 % exported and 50 % used on-site' to the grid reflect this scenario where half is used on-site and the rest is exported to the grid. Following 100 % usage on-site, this is the next best approach to reducing the SPP.

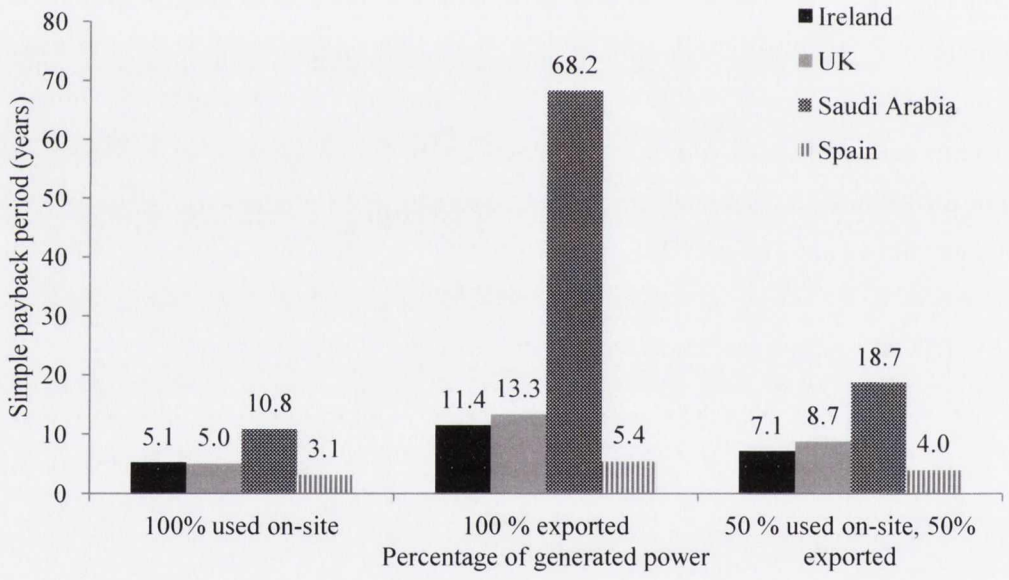

Figure 8.3: SPP of a PV/T/PCM system of a household depending solely on electricity

Considering the locations in the scenario '100 % used on-site' of Figure 8.3, Spain has shown the best SPP period of 3.1 years, followed by the UK and Ireland with SPP of 5.0 years and 5.1 years, respectively. This is due to the increased electricity costs in the European Union compared to Saudi Arabia where the SPP is 10.8 years and so the annual savings are reduced drastically when the electricity price is low.

The SPP of a PV/T/PCM system in a household dependent on natural gas in each location is presented in Figure 8.4. Considering the cost of natural gas in Ireland, the most efficient approach to reducing the SPP is to export all the power generated by the PV/T/PCM system as the price of gas is cheaper than the feed-in tariff, as shown with a SPP of 14.9 hours. The savings made is the difference between the feed-in tariff and the cost of purchasing the required natural gas. This is similar to Spain where the shortest SPP is 6.4 years. However as there was a generation tariff in UK, it is more efficient to export all power generated and the system can be paid back within 10.7 years. Saudi Arabia has shown unrealistic SPP due to the low price of gas.

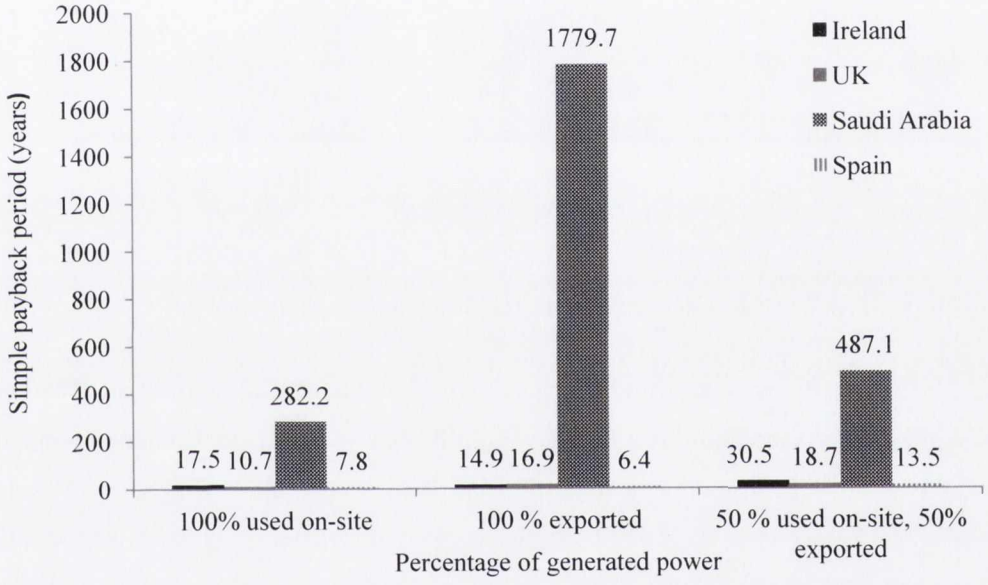

Figure 8.4: SPP of a PV/T/PCM system of a household depending solely on gas

A household dependent solely on oil and a PV/T/PCM system would have SPPs as shown in Figure 8.5. The most efficient method of making a return on the initial investment in Ireland was to export 100 % of the energy generated as the feed-in tariff was greater than the price of oil. This resulted in a SPP of 15.3 years. This is not the case with the UK due to the generation tariff which, along with the saving made on the cost of oil, allows a lower SPP of 11.3 years when 100 % of the energy generated is used on-site. The lack of generation tariff in Spain has also shown that exporting 100 % of the energy generated reduces the SPP to 6.7 years (the lowest of all scenarios) compared to other usage patterns. As with the other resources of energy

the shortest SPP in Saudi Arabia is 15.8 years when 100 % is used on-site as there are no incentives to export to the grid.

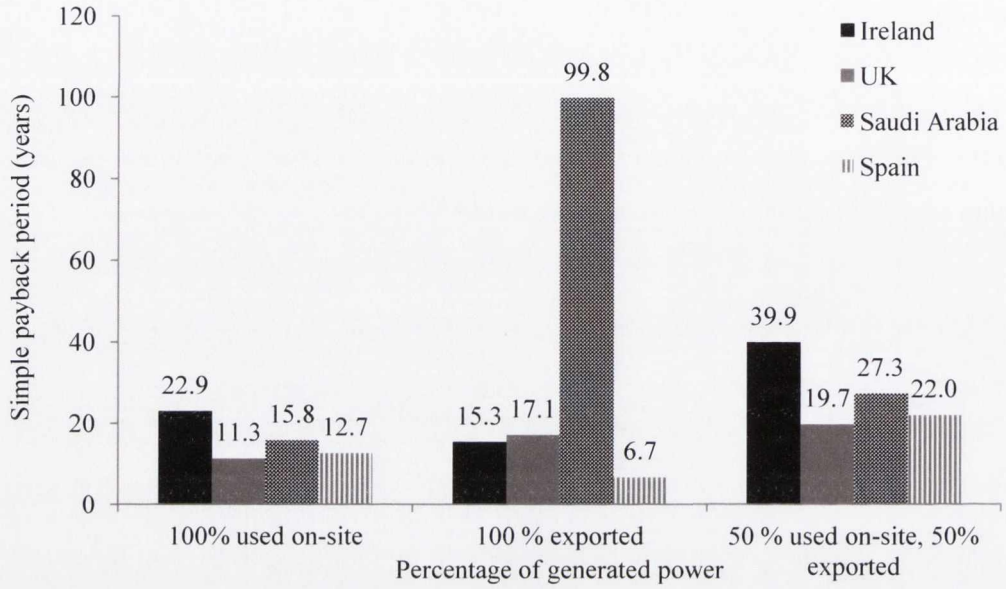

Figure 8.5: SPP of a PV/T/PCM system of a household depending solely on oil

Considering the length of payback periods of a PV/T/PCM system in four different locations under two similar solar resources, it has been shown that governmental interventions of financial incentives are one of the main determinants of the economic viability of PV solar energy systems (McCormack and Norton, 2013). Ireland and the UK have similar levels of solar irradiance however, it can be seen that under certain conditions the payback in UK is shorter mainly due to the government policy of generation tariffs. Spain has a high solar resource which is evident in the SPP as in most cases they are shorter than Ireland and the UK. This is not the case in Saudi Arabia as the cost of a kWh of electricity is a quarter of the price in Spain. As a result of this, it is not economical to purchase renewable energy technologies in Saudi Arabia as energy prices are so low the SPP was shown to be up to hundreds of years. In countries such as this, it is the government's responsibility to promote the use of green energy to minimise climate change and promote local economic development.

The sizing of a PV/T/PCM system is dependent on the incentives offered for green energy generation and the cost of the source of energy used in each location. In Ireland, it would be recommended to size the system based on the baseload of the domestic unit as the cost of electricity is 25.4 c/kWh and the micro-generation tariff received is much less than this at 9

c/kWh. However, if the main provider of domestic energy was gas or oil it would be recommended to oversize the PV/T/PCM system as there would be a financial gain based on the green energy generation incentives which are higher per kWh than the cost of oil or gas at 7.45 c/kWh and 5.7 c/kWh, respectively. UK and Spain presented similar size dependencies to that of Ireland due to the similar cost of energy and available incentives. However, UK showed an extra financial gain when a household is dependent solely on electricity to provide power as the generation incentive of 7 c/kWh along with the saving of electricity cost but as with Ireland it is only necessary to size the system for the baseload. The cost of energy in Saudi Arabia is low and there are no financial incentives as a result there is little point in exporting to the grid. However, it would be recommended to size a system for the domestic baseload if the household was solely dependent on electricity due to the lack of financial incentives. A PV/T/PCM system would not be recommended for households where gas and oil provide energy as these fuels are so low-cost it does not make economic sense to invest in such a system.

Other benefits which are available but have not been taken into account as a PV/T/PCM system would have to undergo tests and procedures to be approved for such programmes. However, if the system was validated there are thermal incentives for the generation of heat from renewable sources such as biomass, solar thermal and geothermal heat pumps that could be considered. The generation of energy using solar thermal collectors offer a tariff of 19.51 p/kWh (26 c/kWh) in the UK for domestic customers which can be extended for non-domestic buildings (Ofgem, 2015a). However, in Ireland and Spain such a scheme has been proposed but tariffs have yet to be announced and the programme to be implemented (Bechberger, 2011; SEAI, 2015). Saudi Arabia has yet to implement any incentives for renewable energies.

8.3 Conclusion

The production and manufacturing cost in Ireland of an individual 1.12 kW_p PV/T/PCM system with four thermal collectors integrated with PCM was found to be €4365 (as shown in Table 8.2) which is not economically feasible when considering payback period of the installation. However, if the system was mass produced the cost per system would reduce to €2261 (as shown in Table 8.2) in Ireland and €2197 (as shown in Table 8.2) in Saudi Arabia. A lower cost system reduces the SPP and therefore, make it a more attractive green energy source.

The SPP back period of a 1.12 kW_p PV/T/PCM system with four thermal collectors integrated with PCM based on the mass produced system was calculated. SPPs were presented for Ireland,

UK, Saudi Arabia and Spain based on the energy consumption of an average household in each location. It was found that the UK had shorter SPPs than that of Ireland, mainly due to the generation and feed-in tariff incentives compared to Ireland where only a micro-generation payment rate is endorsed by the Sustainable Energy Authority of Ireland. SPP of a PV/T/PCM system of a household depending solely on electricity in Ireland 5.1 years in Ireland and 5.0 years in the UK. Spain also showed shorter SPPs of 3.1 years compared to Saudi Arabia, 10.8 years; this was due to financial incentives for the generation of green energy in Spain and the low non-renewable energy cost in Saudi Arabia. In this instance it can be seen that the low costs electricity, oil and gas in Saudi Arabia are much lower than the initial investment of the green energy technology causing the system to be uneconomical. It is in locations such as here that the government implement policy options to encourage the adoption of PV and green technologies to reduce the global impact on climate change.

Chapter 9

Conclusions

Chapter 9. Conclusions

9.1 Contributions to Knowledge

The primary aim of this research was to design and install a PV/T/PCM system. However, this involved various investigations into PCM characterisation and containment prior to system design. Differential Scanning Calorimetry and Temperature History Method were used to characterise capric acid, capric:palmitic acid, capric:lauric acid, SP22 and Micronal phase change materials. It was found capric:palmitic acid had the highest heat of fusion of 209 kJ/kg and a melting temperature of 16.5 °C - 25.4°C, ensuring it would not melt in ambient temperatures. Capric:palmitic acid was found to be the most suitable PCM investigated for integration in a PV/T/PCM system due to the melting temperature and the high latent heat of fusion.

It was found that all sealants used in the container manufacture were not suitable for use with PCM as they lost their adhesive strength once immersed in PCM for over 5 days and became detached from the container material which resulted in leaks. To avoid joints and sealing it is recommended that all containers be welded or cast to ensure full sealed containment.

The corrosive properties of PCM were investigated in long term immersion corrosion tests which involved immersing six commonly used materials in liquid PCM for up to 722 days. Images of the samples were taken Day 1, 25, 200 and 540 using a scanning electron microscope which showed the physical effect of the PCM on each sample material over the course of the investigation. Stainless steel was shown to be a compatible material with all PCM as was Perspex. Caution is recommended when using copper, brass and aluminium with the PCM. It is recommended to consider the environment in which the container will endure as moisture would also affect the rate of corrosion. As a result of the investigation, it was found stainless steel was the most compatible with capric:palmitic acid taking into account the wet climate of Ireland.

The PV/T/PCM system was developed to generate electrical and thermal energy simultaneously but also allow for the storage of thermal energy for later applications. The transfer of heat through the system, the power generated and the level of thermal energy stored and transferred to the water were experimentally investigated under Irish climatic conditions and compared to three reference systems. It was found that the maximum temperature difference of the water

with and without PCM was 5.5 °C and occurred at approximately 6 am, extending the availability of heat by up to 6.4 hours compared to a system without PCM.

An equation was developed to assess the performance of a PV/T/PCM system, taking into account the gain in useful energy by the working fluid (water in this case), the heat stored by the system, and the time for which the heat is available to the working fluid. The cumulative thermal efficiency of a PV/T/PCM system was found to range between 17% -18 % compared to a PV/T system of 0.2 % under the climatic conditions of Ireland. The efficiency was shown to increase under an increased solar resource. Simulated climatic conditions of Saudi Arabia were shown to generate efficiencies of 25 % -35 % compared to PV/T efficiencies of 11 %.

A transient numerical model simulation was developed and validated based on field trial data for systems installed in Dublin, Ireland. TRNSYS was used in conjunction with COMSOL Multiphysics to simulate a PV/T/PCM system. The model overestimated the PCM temperature, based on a maximum percentage error of 10%, however this only occurs during high levels of solar irradiance (>1000 W/m^2), which was attributed to the underestimation of the heat loss behaviour such as losses from the transfer of heat from the PV to the container and PCM. Nevertheless, the model has shown to predict the temperature of the outlet temperature and the PCM and can be used to predict the system performance under varying environmental conditions being the first numerical model to predict the transfer of heat through a PV/T/PCM system.

A parametric study was undertaken based on the validated numerical model and the results of which were used to optimise the PV/T/PCM system. The effect of PCM thermal conductivity, heat of fusion, and specific heat capacity, mass flow rate of working fluid and thermal conductivity of container on the PCM and outlet water temperature were assessed. The results of the parametric analysis were used to maximise the outputs of the model thereby optimising the PV/T/PCM simulation. The optimised PV/T/PCM system resulted in a 6.1 % increase in thermal efficiency compared to the validated PV/T/PCM system, increasing to 21.3 %. By increasing the solar resource and ambient temperature, the efficiency of the system increased as was shown when simulated under Saudi Arabian conditions where a thermal efficiency of 68.4 % was calculated.

As domestic systems are much larger than 80 W, the system was numerically up-scaled to 1.12 kW with four thermal collectors containing PCM and a pipe network. Although the useful

energy gain decreased in the up-scaled system in both Ireland and Saudi Arabia, the temperature achieved by the outlet water increased thus reducing the energy required from an auxiliary heater. There is also four times more storage due to the increased mass of PCM in the up-scaled systems. The cumulative thermal efficiencies in Ireland and Saudi Arabia were found to be 15.8 % and 46.2 %, respectively.

The cost of manufacturing a PV/T/PCM system as a customised product in Ireland was €4365 as shown in Table 8.2, this is not economically feasible when considering the payback period. However, if the system was mass produced the cost per system would reduce to €2261 in Ireland and €2197 in Saudi Arabia. A household investing in a PV/T/PCM system which depends solely on electricity as their power supply would have a SPP of 7.5 years in Ireland and 15.9 years in Saudi Arabia. However, it was noted that as these countries do not implement financial incentives for green energy the payback period is longer than that of a country which avails of such policies. UK and Spain endorse the production of green energy and incentivise the use of renewable technologies. This was shown in the shorter SPP of 7.3 years and 4.6 years in UK and Spain, respectively.

9.1.1 Summary of the Contributions to Knowledge

A brief summary of the contributions to knowledge of this thesis are:

- Long term immersion corrosion tests between the commonly available materials; copper, brass, stainless steel, mild steel and Perspex and fatty acids capric:palmitic and capric:lauric acid eutectics
- Presentation of guidelines of suitable encapsulation material for PCM
- Design and installation of a novel photovoltaic/thermal/phase change material system in Dublin with the ability to generate electricity, heat water and store thermal energy for later use.
- Outdoor experimental investigation of a PV/T/PCM system and performance comparison with three reference systems
- Experimental PV/T/PCM system performance assessment under simulated climatic conditions
- Development of a validated heat transfer PV/T/PCM system model to predict the quantity of power generated, and the temperature of water and PCM

- Parametric study considering the effect of PCM thermal conductivity, specific heat capacity and latent heat capacity of PCM, mass flow rate of water and container thermal conductivity on the performance of a PV/T/PCM system
- Optimisation of a PV/T/PCM system and performance assessment of the optimised design under a low and high solar resource
- Up-scaled design for an optimised PV/T/PCM system and an investigation into system performance under a low and high solar resource
- Economic assessment of the payback period of a PV/T/PCM system based on the annual performance in a country with a low and high solar resource, with and without financial incentives

9.2 Recommendations for Further Research

- Further research should be conducted into methods to improve the thermal conductivity of PCM in a PV/T/PCM system. Currently, efforts have been made through the use of dispersing thermal-conductive nano-particles within PCM, inserting metallic matrix and compositing PCMs with expanded graphite which could be applied to a PV/T/PCM system.
- It has been shown that some metals have a tendency to corrode when immersed in PCM. Certain metals such as aluminium or mild steel are less expensive than stainless steel however they have shown to be more susceptible to corrosion by PCM. If the cheaper metals could be applied with a surface treatment or plating it could reduce the effect of corrosion thereby increasing the lifetime of the system. An investigation into the metal and plating finishing and the compatibility with PCM could provide a method to reduce system costs and the initial investment.
- It has been shown that the extraction of heat from the PCM was slow. Improvement of the heat extraction from the PCM and the transfer of heat to the water will reduce system losses and increase the economic viability of the system. The application of fins in the PCM to increase the heat transfer from the PCM to the water and to minimise the heat lost to the environment. Fins are surfaces that extend from an object to increase the rate of heat transfer to or from the environment by increasing convection. It would be possible to apply fins to the pipe network to increase the heat transfer from the water to the PCM. Further investigation would involve the assessment of the change in hydraulic flow of the PCM as a result of the addition of fins.

- The water temperature in the up-scaled optimised system reached higher temperatures than the optimised system which would reduce the energy required in auxiliary heating. In addition to this the storage capacity of the PCM has increased in the up-scaled system. Another method to quantify the available energy in a system would be useful to assess the energy yield of a system.
- Up-scaling the PV/T/PCM system showed a large increase in the temperature of the water. This was as a result of the increased temperature of the PCM. The inlet and outlet temperature difference could be increased further if the melting temperature of the PCM varied in each container. A further study could investigate the effect of the phase change melt temperature increasing incrementally in each container. This would allow the water to pre-heat to a higher temperature in each container but also allow the PCM to store latent heat at different temperature allowing the slow discharge to the water to minimise losses to the environment.
- Due to the large increase in the outlet water temperature of an up-scaled system and the effect on the water tank, a more detailed simulation could incorporate the effect of the daily hot water usage on the overall thermal performance of the PV/T/PCM system.
- During days of increased ambient temperature and solar radiation, the PCM charges at a faster rate and once it is fully charged can act as an insulator. To minimise the insulating effect and maximise heat storage, it would be possible to use PCM layers in the container. If the first layer had a melting point of 25 °C for example, and then the next layer of PCM had a melting point of 35 °C, this would allow for constant charging of PCM throughout the day and avoid the insulation effect of the PCM as shown in Figure 9.1. It would also allow the storage of latent heat at various temperatures which would allow for a constant discharge of PCM to the water and minimise losses.
- The charging and discharging cycles in a PV/T/PCM system could be assessed using a cold water flow through the collector. This would allow the investigation of the effect of water temperature, the application of a pump and passive flow.
- Using high performance computing to carry out the PV/T/PCM system simulations would enable much finer grids to be set around the areas of higher heat transfer such as the pipes as well as further investigation into the effect of timestep and other modelling parameters.
- Further investigation into the annual performance of a PV/T/PCM collector would show the envelope of performance for a range of conditions throughout the year in both Ireland and locations with a hotter climate such as Saudi Arabia.

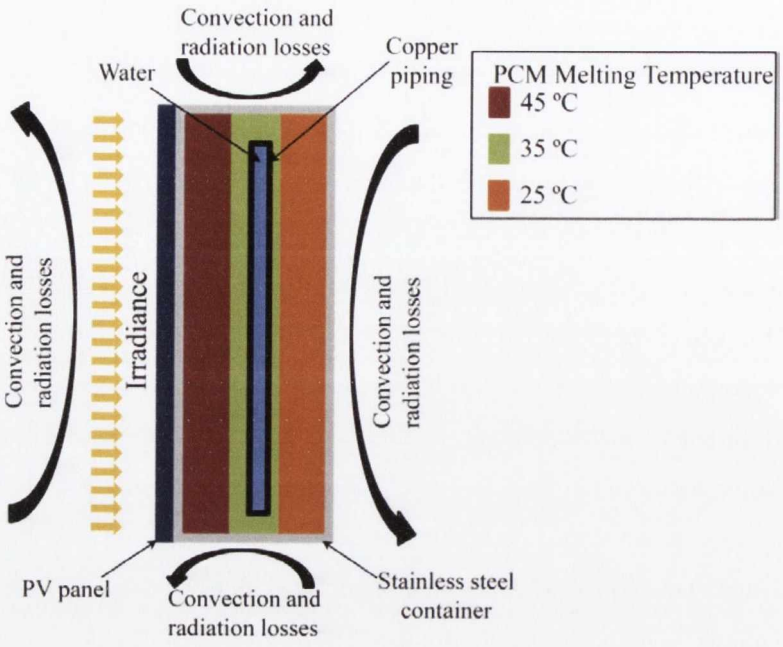

Figure 9.1: Schematic of PV/T/PCM system with varying PCM melting temperatures

- Investigation into suitable melting temperatures for various locations would allow systems to be adjusted depending on the environmental conditions of a specific area offering an adaptable building solution in a global context.
- Investigation into optimum storage options for an up-scaled PV/T/PCM system would involve assessing the number of PCM storage tanks and the size requirement of a water tank to optimise the financial feasibility and efficiency of the PV/T/PCM system.
- Investigate the addition of insulation in the container or at the rear for stronger climatic conditions.
- Experimentally investigate the performance of a PV/T/PCM system in a hotter climate assessing the radiative cooling at night, length of time of heat storage and the level of insulation of the PCM if required.
- Investigate the effect of the thermal conductivity of PCM containment materials in a PV/T/PCM collector under low ambient temperature conditions. A low thermal conductivity material such as Perspex would insulate the back of the collector minimising heat loss while a higher thermal conductivity material such as aluminium or copper would be used to increase the transfer of heat from the PV to the PCM.

- Compare the PV/T/PCM system performance with the individual of a PV array and a storage collector. Following the assessment of each system performance an investigation into system costs would be undertaken.

References

Abdolzadeh, M. & Ameri, M., 2009. Improving the effectiveness of a photovoltaic water pumping system by spraying water over the front of photovoltaic cells. *Renewable Energy,* 34, 91-96.

Aelenei, L., Pereira, R. & Goçalves, H., BIPV/T versus BIPV/T-PCM: A numerical investigation of advanced system integrated into Solar XXI building façade. *2nd International Conference on Sustainable Energy Storage*, 2013 Trinity College, Dublin, Ireland.

Aelenei, L., Pereira, R., Goçalves, H. & Athienitis, A., 2014. Thermal Performance of a Hybrid BIPV-PCM: Modeling, Design and Experimental Investigation. *Energy Procedia,* 48, 474-483.

Agarwal, R. K. & Garg, H. P., 1994. Study of a photovoltaic-thermal system—Thermosyphonic solar water heater combined with solar cells. *Energy Conversion and Management,* 35, 605-620.

Agyenim, F., Hewitt, N., Eames, P. & Smyth, M., 2010. A review of materials, heat transfer and phase change problem formulation for latent heat thermal energy storage systems (LHTESS). *Renewable and Sustainable Energy Reviews,* 14, 615-628.

Akhmad, K., Kitamura, A., Yamamoto, F., Okamoto, H., Takakura, H. & Hamakawa, Y., 1997. Outdoor performance of amorphous silicon and polycrystalline silicon PV modules. *Solar Energy Materials and Solar Cells,* 46, 209-218.

Al-Hallaj, S. & Selman, J. R., 2005. Thermal management of battery systems. United States of America patent application.

Al-Saadi, S. N. & Zhai, Z., 2013. Modeling phase change materials embedded in building enclosure: A review. *Renewable and Sustainable Energy Reviews,* 21, 659-673.

Alam, T. E., Dhau, J. S., Goswami, D. Y. & Stefanakos, E., 2015. Macroencapsulation and characterization of phase change materials for latent heat thermal energy storage systems. *Applied Energy,* 154, 92-101.

Aldoss, T. K. & Rahman, M. M., 2014. Comparison between the single-PCM and multi-PCM thermal energy storage design. *Energy Conversion and Management,* 83, 79-87.

Ames, W. D., 1983. Photovoltaic devices for producing electrical and heat energy. United States of America patent application.

Arcol. 2011. http://www.arcolresistors.com/resistors/hs100/ [Online]. [Accessed 22/04 2015].

Asadi, E., Da Silva, M. G., Antunes, C. H. & Dias, L., 2012. A multi-objective optimization model for building retrofit strategies using TRNSYS simulations, GenOpt and MATLAB. *Building and Environment,* 56, 370-378.

Aste, N., Del Pero, C. & Leonforte, F., 2012a. Optimization of Solar Thermal Fraction in PVT Systems. *Energy Procedia,* 30, 8-18.

Aste, N., Del Pero, C. & Leonforte, F., 2012b. Optimization of Solar Thermal Fraction in PVT Systems. *Energy Procedia,* 30, 8-18.

ASTM,1994. Standard Practice for Preparing, Cleaning and Evaluating Corrosion Test Specimen. *Annual book of ASTM standards, Section 3, metal test methods and analytical procedures.* American Society for Testing and Materials (ASTM), West Conshohocken, PA, US.

Axaopoulos, P. J. & Fylladitakis, E. D., 2013. Performance and economic evaluation of a hybrid photovoltaic/thermal solar system for residential applications. *Energy and Buildings,* 65, 488-496.

Ayompe, L., 2011. Performance and Policy Evaluation of Solar Energy Technologies for Domestic Application in Ireland. *Dublin Institute of Technology.*

Ayompe, L. & Duffy, A., 2013a. Thermal performance analysis of a solar water heating system with heat pipe evacuated tube collector using data from a field trial. *Solar Energy,* 90, 17-28.

Ayompe, L. M. & Duffy, A., 2013b. Analysis of the thermal performance of a solar water heating system with flat plate collectors in a temperate climate. *Applied Thermal Engineering,* 58, 447-454.

Ayompe, L. M., Duffy, A., McCormack, S. J. & Conlon, M., 2011. Measured performance of a 1.72 kW rooftop grid connected photovoltaic system in Ireland. *Energy Conversion and Management,* 52, 816-825.

Azad, E., 2012. Assessment of three types of heat pipe solar collectors. *Renewable and Sustainable Energy Reviews,* 16, 2833-2838.

Bagienski, W. & Gupta, M. C., 2011. Temperature dependence of polymer/fullerene organic solar cells. *Solar Energy Materials and Solar Cells,* 95, 933-941.

Bajare, D., Kazjonovs, J. & Korjakins, A., 2011. The thermal characteristics of gypsum boards with phase change materials (PCM). *Environ Technol Resour.*

Bansal, N. & Buddhi, D., 1992. An analytical study of a latent heat storage system in a cylinder. *Energy conversion and management,* 33, 235-242.

Barnard, A., Hunt, W., Timlake, W. & Varley, E., 1966. A theory of fluid flow in compliant tubes. *Biophysical Journal,* 6, 717.

Barreneche, C., Solé, A., Miró, L., Martorell, I., Fernández, A. I. & Cabeza, L. F., 2013. Study on differential scanning calorimetry analysis with two operation modes and organic and inorganic phase change material (PCM). *Thermochimica Acta,* 553, 23-26.

Basf, 2012. Micronal PCM - Intelligent Temeperature Management for Buildings.

Beard, J. T., 1978. Engineering analysis and testing of water-trickle solar collector, *Mechanical and Aerospace Engineering Department, Virginia State University and Polytechnic.*

Bechberger, M., 2011. Renewable Energy in Spain –from a strategic approach to a purely cost focused policy, Austria.

Biwole, P. H., Eclache, P. & Kuznik, F., 2013. Phase-change materials to improve solar panel's performance. *Energy and Buildings,* 62, 59-67.

Boden, T. A., Marland, G. & Andres, R. J., 2010. Global, Regional, and National Fossil-Fuel CO2 Emissions, Carbon Dioxide Information Analysis Center, Oak Ridge National Laboratory, U.S. Department of Energy, Oak Ridge, Tenn., U.S.A.

Bony, J. & Citherlet, S., 2007. Numerical model and experimental validation of heat storage with phase change materials. *Energy and Buildings,* 39, 1065-1072.

Borderon, J., Virgone, J. & Cantin, R., 2015. Modeling and simulation of a phase change material system for improving summer comfort in domestic residence. *Applied Energy,* 140, 288-296.

Bouadila, S., Fteïti, M., Oueslati, M. M., Guizani, A. & Farhat, A., 2014. Enhancement of latent heat storage in a rectangular cavity: Solar water heater case study. *Energy Conversion and Management,* 78, 904-912.

Browne, M., Norton, B. & McCormack, S., 2015a. Phase change materials for photovoltaic thermal management. *In Review Renewable and sustainable energy reviews.*

Browne, M. C., Norton, B. & McCormack, S. J., 2015b. Phase change materials for photovoltaic thermal management. *Renewable and Sustainable Energy Reviews,* 47, 762-782.

Bruton, T. M., 2002. General trends about photovoltaics based on crystalline silicon. *Solar Energy Materials and Solar Cells,* 72, 3-10.

Cabeza, L. F., Barreneche, C., Martorell, I., Miró, L., Sari-Bey, S., Fois, M., Paksoy, H. O., Sahan, N., Weber, R. & Constantinescu, M., 2015. Unconventional experimental technologies available for phase change materials (PCM) characterization. Part 1. Thermophysical properties. *Renewable and Sustainable Energy Reviews,* 43, 1399-1414.

Cabeza, L. F., Castell, A., Barreneche, C., De Gracia, A. & Fernández, A. I., 2011. Materials used as PCM in thermal energy storage in buildings: A review. *Renewable and Sustainable Energy Reviews,* 15, 1675-1695.

Cabeza, L. F., Castellón, C., Nogués, M., Medrano, M., Leppers, R. & Zubillaga, O., 2007. Use of microencapsulated PCM in concrete walls for energy savings. *Energy and Buildings,* 39, 113-119.

Cabeza, L. F., Illa, J., Roca, J., Badia, F., Mehling, H., Hiebler, S. & Ziegler, F., 2001a. Immersion corrosion tests on metal-salt hydrate pairs used for latent heat storage in the 32 to 36°C temperature range. *Materials and Corrosion,* 52, 140-146.

Cabeza, L. F., Illa, J., Roca, J., Badia, F., Mehling, H., Hiebler, S. & Ziegler, F., 2001b. Middle term immersion corrosion tests on metal-salt hydrate pairs used for latent heat storage in the 32 to 36°C temperature range. *Materials and Corrosion,* 52, 748-754.

Cabeza, L. F., Roca, J., Nogueés, M., Mehling, H. & Hiebler, S., 2005. Long term immersion corrosion tests on metal-PCM pairs used for latent heat storage in the 24 to 29°C temperature range. *Materials and Corrosion,* 56, 33-39.

Çakmak, G. & Yıldız, C., 2011. The drying kinetics of seeded grape in solar dryer with PCM-based solar integrated collector. *Food and Bioproducts Processing,* 89, 103-108.

Caliskan, H., Dincer, I. & Hepbasli, A., 2012. Thermodynamic analyses and assessments of various thermal energy storage systems for buildings. *Energy Conversion and Management,* 62, 109-122.

Castellón, C., Günther, E., Mehling, H., Hiebler, S. & Cabeza, L. F., 2008. Determination of the enthalpy of PCM as a function of temperature using a heat-flux DSC—A study of different measurement procedures and their accuracy. *International Journal of Energy Research,* 32, 1258-1265.

Cellura, M. C., Branco, G. L., Marvaglia, V. & Orioli, A., A photovoltaic panel coupled with a phase changing material heat storage system in hot climates. *25th Conference on Passive and Low Energy Architecture*, 2008 Dublin.

Chaabane, M., Mhiri, H. & Bournot, P., 2014. Thermal performance of an integrated collector storage solar water heater (ICSSWH) with phase change materials (PCM). *Energy Conversion and Management,* 78, 897-903.

Charalambous, P. G., Maidment, G. G., Kalogirou, S. A. & Yiakoumetti, K., 2007. Photovoltaic thermal (PV/T) collectors: A review. *Applied Thermal Engineering,* 27, 275-286.

Chargui, R., Sammouda, H. & Farhat, A., 2013. Numerical simulation of a cooling tower coupled with heat pump system associated with single house using TRNSYS. *Energy Conversion and Management,* 75, 105-117.

Cheng, J., Wang, C., Wang, W., Du, X., Liu, Y., Xue, Y., Wang, T. & Chen, B., 2013. Improvement of thermal stability in the solar selective absorbing Mo–Al2O3 coating. *Solar Energy Materials and Solar Cells,* 109, 204-208.

Choi, D. H., Lee, J., Hong, H. & Kang, Y. T., 2014. Thermal conductivity and heat transfer performance enhancement of phase change materials (PCM) containing carbon additives for heat storage application. *International Journal of Refrigeration,* 42, 112-120.

Chou, H.-M., Chen, C.-R. & Nguyen, V.-L., 2013. A new design of metal-sheet cool roof using PCM. *Energy and Buildings,* 57, 42-50.

Chow, T. T., 2010. A review on photovoltaic/thermal hybrid solar technology. *Applied Energy,* 87, 365-379.

Chow, T. T., Hand, J. W. & Strachan, P. A., 2003. Building-integrated photovoltaic and thermal applications in a subtropical hotel building. *Applied Thermal Engineering,* 23, 2035-2049.

Chow, T. T., Tiwari, G. N. & Menezo, C., 2012. Hybrid Solar: A Review on Photovoltaic and Thermal Power Integration. *International Journal of Photoenergy,* 2012, 17.

Christ, N., Kettlitz, S. W., Valouch, S., Mescher, J., Nintz, M. & Lemmer, U., 2013. Intensity dependent but temperature independent charge carrier generation in organic photodiodes and solar cells. *Organic Electronics,* 14, 973-978.

Chwieduk, D., 2014. Solar Energy in Buildings: Thermal Balance for Efficient Heating and Cooling, *Elsevier.*

Chwieduk, D. A., 2013. Dynamics of external wall structures with a PCM (phase change materials) in high latitude countries. *Energy,* 59, 301-313.

Ciobanu, D., Eftimie, E. & Jaliu, C., 2014. The Influence of Measured/simulated Weather Data on Evaluating the Energy Need in Buildings. *Energy Procedia,* 48, 796-805.

Ciulla, G., Lo Brano, V., Di Dio, V. & Cipriani, G., 2014. A comparison of different one-diode models for the representation of I–V characteristic of a PV cell. *Renewable and Sustainable Energy Reviews,* 32, 684-696.

Comsol 5.0, 2014. User's guide.

Cost Action Tu0802, 2013. Deliverable 1.5b: Characterisation DSC Round Robin Tests.

Cox, C. H. & Raghuraman, P., 1985. Design considerations for flat-plate-photovoltaic/thermal collectors. *Solar Energy,* 35, 227-241.

Curtis, F. A., 2013. Energy Developments: New Forms, Renewables, Conservation: Proceedings of ENERGEX'84, The Global Energy Forum, Regina, Saskatchewan, Canada, May 14-19, 1984, *Elsevier.*

Czichos, H., Saito, T. & Smith, L. E., 2006. Materials measurement methods, *Springer.*

Dickinson, E. J. F., Ekström, H. & Fontes, E., 2014. COMSOL Multiphysics®: Finite element software for electrochemical analysis. A mini-review. *Electrochemistry Communications,* 40, 71-74.

Duffie, J. & Beckman, W., 1992. Solar Engineering of Thermal Processes, Newe York, USA, *John Wiley and Sons.*

Dupeyrat, P., Ménézo, C. & Fortuin, S., 2014. Study of the thermal and electrical performances of PVT solar hot water system. *Energy and Buildings,* 68, Part C, 751-755.

Dupont,2014. www.energain.co.uk/Energain/en_GB/index.html. Last access 10/03/2014.

Ehrmann, N. & Reineke-Koch, R., 2012. Selectively coated high efficiency glazing for solar-thermal flat-plate collectors. *Thin Solid Films,* 520, 4214-4218.

Ehrmann, N., Reineke-Koch, R., Föste, S. & Giovannetti, F., 2013. The influence of process parameters and coating properties of double glazing coated with transparent conducting oxides on the efficiency of solar-thermal flat-plate collectors. *Thin Solid Films,* 532, 132-140.

El Omari, K., Kousksou, T. & Le Guer, Y., 2011. Impact of shape of container on natural convection and melting inside enclosures used for passive cooling of electronic devices. *Applied Thermal Engineering,* 31, 3022-3035.

Electric Ireland. 2015. Electric Ireland Micro-Generation Pilot Scheme [Online]. [Accessed 24 September 2015].

Energy Solutions, P. C.,2014. http://www.phasechange.com/. Last accessed 07/02/2014.

EU Directive 2009/28/Ec,2009. Directive 2009/28/EC on the promotion of the use of energy from renewable sources and amending and subsequently repealing Directives 2001/77/EC and 2003/30/EC. *In:* 2009, E. P. A. O. T. C. O. A. (ed.).

European Commission, 2013. The State of Aluminium Prduction in Europe.

Eurostat. 2014. Energy prduction and imports . Online statistical databases of the European Commission's Directorate General for Statistics (EUROSTAT). http://ec.europa.eu/eurostat/ [Online].

Eurostat, 2015. Energy Price Statistics, Publications Office of the European Union.

Evola, G., Papa, N., Sicurella, F., Wurtz, E.,. Simulation of the behaviour of phase change materials for the improvement of thermal comfort in lightweight buildings. *Building Simulation* 2011 Sydney, Australia.

Farid, M. M., Khudhair, A. M., Razack, S. a. K. & Al-Hallaj, S., 2004. A review on phase change energy storage: materials and applications. *Energy Conversion and Management,* 45, 1597-1615.

Farrell, A. J., Norton, B. & Kennedy, D. M., 2006. Corrosive effects of salt hydrate phase change materials used with aluminium and copper. *Journal of Materials Processing Technology,* 175, 198-205.

Farshchimonfared, M., Bilbao, J. I. & Sproul, A. B., 2015. Channel depth, air mass flow rate and air distribution duct diameter optimization of photovoltaic thermal (PV/T) air collectors linked to residential buildings. *Renewable Energy,* 76, 27-35.

Fazilati, M. A. & Alemrajabi, A. A., 2013. Phase change material for enhancing solar water heater, an experimental approach. *Energy Conversion and Management,* 71, 138-145.

Feed-in Tariff Uk. 2015. http://www.fitariffs.co.uk/FITs/ [Online].

Feldman, D., 2014. Photovoltaic (PV) pricing trends: historical, recent, and near-term projections.

Feldman, D., Shapiro, M. M., Banu, D. & Fuks, C. J., 1989. Fatty acids and their mixtures as phase-change materials for thermal energy storage. *Solar Energy Materials,* 18, 201-216.

Fernández, E. F., Siefer, G., Almonacid, F., Loureiro, A. J. G. & Pérez-Higueras, P., 2013. A two subcell equivalent solar cell model for III-V triple junction solar cells under spectrum and temperature variations. *Solar Energy,* 92, 221-229.

Ferrer, G., Solé, A., Barreneche, C., Martorell, I. & Cabeza, L. F., 2015. Corrosion of metal containers for use in PCM energy storage. *Renewable Energy,* 76, 465-469.

Florschuetz, L. W., 1979. Extension of the Hottel-Whillier model to the analysis of combined photovoltaic/thermal flat plate collectors. *Solar Energy,* 22, 361-366.

Fraisse, G., Ménézo, C. & Johannes, K., 2007. Energy performance of water hybrid PV/T collectors applied to combisystems of Direct Solar Floor type. *Solar Energy,* 81, 1426-1438.

Fraunhofer Institute, 2013. Fraunhofer Institute for Solar Energy Systems ISE, Freiburg, *Fraunhofer.*

Frusteri, F., Leonardi, V., Vasta, S. & Restuccia, G., 2005. Thermal conductivity measurement of a PCM based storage system containing carbon fibers. *Applied Thermal Engineering,* 25, 1623-1633.

Galen, L. B., Samantha, W. & Darghouth, N. R., 2014. Tracking the Sun VII: An Historical Summary of the Installed Price of Photovoltaics in the United States from 1998-2013.

Gallo, A., Molina, B. T., Prodanovic, M., Aguilar, J. G. & Romero, M., 2014. Analysis of Net Zero-energy Building in Spain. Integration of PV, Solar Domestic Hot Water and Air-conditioning Systems. *Energy Procedia,* 48, 828-836.

Gao, F., Wang, Y., Zhang, J., Shi, D., Wang, M., Humphry-Baker, R., Wang, P., Zakeeruddin, S. M. & Grätzel, M., 2008. A new heteroleptic ruthenium sensitizer enhances the absorptivity of mesoporous titania film for a high efficiency dye-sensitized solar cellw. *Chem Comm,* 44, 2635-2637.

García-Romero, A., Delgado, A., Urresti, A., Martín, K. & Sala, J. M., 2009. Corrosion behaviour of several aluminium alloys in contact with a thermal storage phase change material based on Glaubers salt. *Corrosion Science,* 51, 1263-1272.

Garg, H. P., Agarwal, R. K. & Bhargava, A. K., 1990. Experimental and theoretical studies on a photovoltaic/ thermal hybrid solar collector water heater. *In:* FUJII, T. H. K. T. N. (ed.) *Clean and Safe Energy Forever.* Oxford: Pergamon.

Ghoneim, A. A., 1989. Comparison of theoretical models of phase-change and sensible heat storage for air and water-based solar heating systems. *Solar Energy,* 42, 209-220.

Gil, A., Barreneche, C., Moreno, P., Solé, C., Inés Fernández, A. & Cabeza, L. F., 2013. Thermal behaviour of d-mannitol when used as PCM: Comparison of results obtained by DSC and in a thermal energy storage unit at pilot plant scale. *Applied Energy,* 111, 1107-1113.

Gil, V., Gaertner, M. A., Sanchez, E., Gallardo, C., Hagel, E., Tejeda, C. & De Castro, M., 2015. Analysis of interannual variability of sunshine hours and precipitation over Peninsular Spain. *Renewable Energy,* 83, 680-689.

Gin, B., Farid, M. M. & Bansal, P. K., 2010. Effect of door opening and defrost cycle on a freezer with phase change panels. *Energy Conversion and Management,* 51, 2698-2706.

Gong, D., Liu, H., Luo, G., Zhang, P., Cheng, X., Yang, B., Wang, Y., Min, J., Wang, W., Chen, S., Cui, Z., Kewei, L. & Lifang, H., 2015. Thermal aging test of AlCrNO-based solar selective absorbing coatings prepared by cathodic arc plating. *Solar Energy Materials and Solar Cells,* 136, 167-171.

Gowreesunker, B. L., Tassou, S. A. & Kolokotroni, M., 2013. Coupled TRNSYS-CFD simulations evaluating the performance of PCM plate heat exchangers in an airport terminal building displacement conditioning system. *Building and Environment,* 65, 132-145.

Groll, M., Brost, O. & Heine, D., 1990. Corrosion of steels in contact with salt eutectics as latent heat storage materials: Influence of water and other impurities. *Heat Recovery Systems and CHP,* 10, 567-572.

Guha, S., Yang, J. & Yan, B., 2013. High efficiency multi-junction thin film silicon cells incorporating nanocrystalline silicon. *Solar Energy Materials and Solar Cells,* 119, 1-11.

Günther, E., Hiebler, S., Mehling, H. & Redlich, R., 2009. Enthalpy of Phase Change Materials as a Function of Temperature: Required Accuracy and Suitable Measurement Methods. *International Journal of Thermophysics,* 30, 1257-1269.

Gustafsson, S., 2011. Corrosion properties of aluminium alloys and surface treated alloys in tap water.

Gutiérrez, E., Álvarez, M. S., Deive, F. J., Sanromán, M. A. & Rodríguez, A., 2014. Phase segregation in aqueous solutions of non-ionic surfactants using ammonium, magnesium and iron salts. *The Journal of Chemical Thermodynamics,* 70, 147-153.

Hadj Arab, A., Chenlo, F. & Benghanem, M., 2004. Loss-of-load probability of photovoltaic water pumping systems. *Solar Energy,* 76, 713-723.

Haillot, D., Franquet, E., Gibout, S. & Bédécarrats, J.-P., 2013. Optimization of solar DHW system including PCM media. *Applied Energy,* 109, 470-475.

Hamdy, M. A., Luttmann, F. & Osborn, D., 1988. Model of a spectrally selective decoupled photovoltaic/thermal concentrating system. *Applied Energy,* 30, 209-225.

Hammad, M. A., 1994. Experimental study of the performance of a solar thermal-photovoltaic integrated system. *Renewable Energy,* 4, 897-905.

Hasan, A., 2010a. Phase Change Materials for Thermal Regulation of Building Integrated Photovoltaics. PhD Thesis, *Dublin Institute of Technology.*

Hasan, A., McCormack, S., Huang, M. & Norton, B., 2014a. Energy and Cost Saving of a Photovoltaic-Phase Change Materials (PV-PCM) System through Temperature Regulation and Performance Enhancement of Photovoltaics. *Energies,* 7, 1318-1331.

Hasan, A., McCormack, S. J., Huang, M. J. & Norton, B., 2014b. Characterization of phase change materials for thermal control of photovoltaics using Differential Scanning Calorimetry and Temperature History Method. *Energy Conversion and Management,* 81, 322-329.

Hasan, A., McCormack, S. J., Huang, M. J., Norton, B., 2010b. Evaluation of phase change materials for thermal regulation enhancement of building integrated photovoltaics. *Solar Energy,* 84, 1601-1612.

Hasan, A. & Sayigh, A. A., 1994. Some fatty acids as phase-change thermal energy storage materials. *Renewable Energy,* 4, 69-76.

Hawes, D. W., Feldman, D. & Banu, D., 1993. Latent heat storage in building materials. *Energy and Buildings,* 20, 77-86.

Hayakashi, B., Mizusaki, K., Satoh, T. & Hatanaka, T., 1990. Research and development of photovoltaic/ thermal hybrid solar power genereration system. *In:* HORIGOMEK, T., KIMURAT, K., TAKAKURAT, T., NISHINOI, T. & FUJII, I. (eds.) *Clean and Safe Energy Forever.* Oxford: Pergamon.

He, H., Yue, Q., Gao, B., Zhang, X., Li, Q. & Wang, Y., 2013. The effects of compounding conditions on the properties of fatty acids eutectic mixtures as phase change materials. *Energy Conversion and Management,* 69, 116-121.

Heim, D., Two solution methods of heat transfer with phase change within whole building dynamic simulation. *9th International IBPSA Conference, Montréal, Canada,* 2005.

Helmers, H., Schachtner, M. & Bett, A. W., 2013. Influence of temperature and irradiance on triple-junction solar subcells. *Solar Energy Materials and Solar Cells,* 116, 144-152.

Henkel Corporation, 2011. Thermal Management Phase-Change Materials for Concentrator Photovoltaics, Irvine, California, United States of America.

Ho, C. J., Chou, W.-L. & Lai, C.-M., 2015. Thermal and electrical performance of a water-surface floating PV integrated with a water-saturated MEPCM layer. *Energy Conversion and Management,* 89, 862-872.

Ho, C. J., Jou, B.-T., Lai, C.-M. & Huang, C.-Y., 2013. Performance assessment of a BIPV integrated with a layer of water-saturated MEPCM. *Energy and Buildings,* 67, 322-333.

Ho, C. J., Tanuwijava, A. O. & Lai, C.-M., 2012. Thermal and electrical performance of a BIPV integrated with a microencapsulated phase change material layer. *Energy and Buildings,* 50, 331-338.

Hoffmann, W. & Pellkofer, T., 2012. Thin films in photovoltaics: Technologies and perspectives. *Thin Solid Films,* 520, 4094-4100.

Höhne, G., Hemminger, W. & Hammersheim, H. J., 2003. Differential Scanning Calorimetry, 2nd Edition, New York, *Springer Verlag Heidelberg.*

Hong, H., Kim, S. K. & Kim, Y.-S., 2004. Accuracy improvement of T-history method for measuring heat of fusion of various materials. *International Journal of Refrigeration,* 27, 360-366.

Horne, W. E., 1993. Solar energy system.

Hou, Y., Wang, D., Yang, X. H., Fang, W. Q., Zhang, B., Wang, H. F., Lu, G. Z., Hu, P., Zhao, H. J. & Yang, H. G., 2013. Rational screening low-cost counter electrodes for dye-sensitized solar cells. *Nat Commun,* 4, 1583.

Huang, C.-Y. & Huang, C.-J., 2013. A study of photovoltaic thermal (PV/T) hybrid system with computer modeling. *International Journal of Smart Grid and Clean Energy,* Vol. 3, 75-79.

Huang, M. J., Eames, P. C. & Hewitt, N. J., 2006a. The application of a validated numerical model to predict the energy conservation potential of using phase change materials in the fabric of a building. *Solar Energy Materials and Solar Cells,* 90, 1951-1960.

Huang, M. J., Eames, P. C. & Norton, B., 2000. Chapter 454 - The Application of Computational Fluid Dynamics to Predict the Performance of Phase Change Materials for Control of Photovoltaic Cell Temperature in Buildings. *World Renewable Energy Congress VI.* Oxford: Pergamon.

Huang, M. J., Eames, P. C. & Norton, B., 2004. Thermal regulation of building-integrated photovoltaics using phase change materials. *International Journal of Heat and Mass Transfer,* 47, 2715-2733.

Huang, M. J., Eames, P. C. & Norton, B., 2006b. Comparison of a small-scale 3D PCM thermal control model with a validated 2D PCM thermal control model. *Solar Energy Materials and Solar Cells,* 90, 1961-1972.

Huang, M. J., Eames, P. C. & Norton, B., 2006c. Phase change materials for limiting temperature rise in building integrated photovoltaics. *Solar Energy,* 80, 1121-1130.

Huang, M. J., Eames, P. C., Norton, B. & Hewitt, N. J., 2011. Natural convection in an internally finned phase change material heat sink for the thermal management of photovoltaics. *Solar Energy Materials and Solar Cells,* 95, 1598-1603.

Huang, M. J., Eames, P.C. And Norton, B. , 2007. Comparison of Predictions Made Using a New 3D Phase Change Material Thermal Control Model with Experimental Measurements and Predictions Made Using a Validated 2D Model. *Heat Transfer Engineering,* 28, 1.

Huld, T., Müller, R. & Gambardella, A., 2012. A new solar radiation database for estimating PV performance in Europe and Africa. *Solar Energy,* 86, 1803-1815.

Ibáñez, M., Cabeza, L. F., Solé, C., Roca, J. & Nogués, M., 2006. Modelization of a water tank including a PCM module. *Applied Thermal Engineering,* 26, 1328-1333.

Ibáñez, M., Lázaro, A., Zalba, B. & Cabeza, L. F., 2005. An approach to the simulation of PCMs in building applications using TRNSYS. *Applied Thermal Engineering,* 25, 1796-1807.

IEA, 2013. International Energy Outlook 2013, Washington D.C.

Incropera, F. P. & Dewitt, D. P., 1985. Introduction to Heat Transfer, Unites States of America, *John Wiley and Sons.*

IPCC, 2014. Summary for policymakers.

IRENA, 2014. REmap 2030:A Renewable Energy Roadmap, Abu Dhabi.

Iso-Tech, 2009. ISM 490 Solar Module Analyser.

Jäger-Waldau, A., 2013. PV status report. *JRC/European Commission.*

Jäger, F., 2013. Solar energy applications in houses: performance and economics in Europe, *Elsevier.*

Jamekhorshid, A., Sadrameli, S. M. & Farid, M., 2014. A review of microencapsulation methods of phase change materials (PCMs) as a thermal energy storage (TES) medium. *Renewable and Sustainable Energy Reviews,* 31, 531-542.

Jankowski, N. R. & Mccluskey, F. P., 2014. A review of phase change materials for vehicle component thermal buffering. *Applied Energy,* 113, 1525-1561.

Japs, E., Sonnenrein, G., Steube, J., Vrabec, J., Kenig, E. & Krauter, S., Technical Investigation of a Photovoltaic Module with Integrated Improved Phase Change Material. *28th European Photovoltaic Solar Energy Conference and Exhibition*, 2013 Paris, France.

Jaworski, M., 2012. Thermal performance of heat spreader for electronics cooling with incorporated phase change material. *Applied Thermal Engineering,* 35, 212-219.

Jay, A., Clerc, S., Boillot, B., Bontemps, A. & Jay, F., Use of Phase Change Material in order to maintain the temperature of integrated PV modules at a reasonable level. *25th European Photovoltaic Solare Energy Conference and Exhibition and 5th World Conference on Photovoltaic Energy Conversion*, 2010 Valencia, Spain,.

Jin, X., Xu, X., Zhang, X. & Yin, Y., 2014. Determination of the PCM melting temperature range using DSC. *Thermochimica Acta,* 595, 17-21.

Junghänel, M., Schädel, M., Stolze, L. & Peters, S., Black multicrystalline solar modules using novel multilayer antireflection stacks. *Proc. 25th Eur. Photovoltaic Solar Energy Conf,* 2010.

Kalogirou, S., Tripanagnostopoulos, Y. & Souliotis, M., 2005. Performance of solar systems employing collectors with colored absorber. *Energy and Buildings,* 37, 824-835.

Kalogirou, S. A., 2001. Use of TRNSYS for modelling and simulation of a hybrid pv-thermal solar system for Cyprus. *Renewable Energy,* 23, 247-260.

Kalogirou, S. A., 2004. Solar thermal collectors and applications. *Progress in Energy and Combustion Science,* 30, 231-295.

Kamel, R. S. & Fung, A. S., 2014. Modeling, simulation and feasibility analysis of residential BIPV/T+ASHP system in cold climate—Canada. *Energy and Buildings,* 82, 758-770.

Kandasamy, R., Wang, X.-Q. & Mujumdar, A. S., 2007. Application of phase change materials in thermal management of electronics. *Applied Thermal Engineering,* 27, 2822-2832.

Kandasamy, R., Wang, X.-Q. & Mujumdar, A. S., 2008. Transient cooling of electronics using phase change material (PCM)-based heat sinks. *Applied Thermal Engineering,* 28, 1047-1057.

Kaplan, S., 1983. Energy economics: quantitative methods for energy and environmental decisions, *McGraw-Hill College.*

Karaipekli, A., Sarı, A. & Kaygusuz, K., 2007. Thermal conductivity improvement of stearic acid using expanded graphite and carbon fiber for energy storage applications. *Renewable Energy,* 32, 2201-2210.

Katz, E. A., Faiman, D., Tuladhar, S. M., Kroon, J. M., Wienk, M. M., Fromherz, T., Padinger, F., Brabec, C. J. & Sariciftci, N. S., 2001. Temperature dependence for the photovoltaic device parameters of polymer-fullerene solar cells under operating conditions. *Journal of Applied Physics,* 90, 5343-5350.

Kawajiri, K. & Oozeki, T., 2011. Effect of Temperature on PV Potential in the World. *Environmental Science and Technology,* 45 (20), pp 9030–9035.

Kenisarin, M. & Mahkamov, K., 2007. Solar energy storage using phase change materials. *Renewable and Sustainable Energy Reviews,* 11, 1913-1965.

Kern, E. C. & Russell, M. C., 1978. Combined photovoltaic and thermal hybrid collecotr systems. *Conference Record of the IEEE Photovoltaic Specialists Conference,* 1153-1115.

Klančnik, G., Medved, J. & Mrvar, P., 2010. Differential thermal analysis (DTA) and differential scanning calorimetry (DSC) as a method of material investigation Diferenčna termična analiza (DTA) in diferenčna vrstična kalorimetrija (DSC) kot metoda za raziskavo materialov. *RMZ–Materials and Geoenvironment,* 57, 127-142.

Klein, S. A., Duffie, J. A., Et Al.,1976. TRNSYS - A Transient Simulation Program. Solar Energy Laboratory, University of Wisconsin, Madison (WI).

Koca, A., Oztop, H. F., Koyun, T. & Varol, Y., 2008. Energy and exergy analysis of a latent heat storage system with phase change material for a solar collector. *Renewable Energy,* 33, 567-574.

Kordzadeh, A., 2010. The effects of nominal power of array and system head on the operation of photovoltaic water pumping set with array surface covered by a film of water. *Renewable Energy,* 35, 1098-1102.

Kośny, J., Biswas, K., Miller, W. & Kriner, S., 2012. Field thermal performance of naturally ventilated solar roof with PCM heat sink. *Solar Energy,* 86, 2504-2514.

Kośny, J., Nitin, S. & Fallahi, A., 2013. Cost Analysis of Simple Phase Change Material-Enhanced Building Envelopes in Southern U.S. Climates, *U.S Department of Energy.*

Kousksou, T., Bruel, P., Jamil, A., El Rhafiki, T. & Zeraouli, Y., 2014. Energy storage: Applications and challenges. *Solar Energy Materials and Solar Cells,* 120, Part A, 59-80.

Krauter, S., 2004. Increased electrical yield via water flow over the front of photovoltaic panels. *Solar Energy Materials and Solar Cells,* 82, 131-137.

Krauter, S., Araújo, R. G., Schroer, S., Hanitsch, R., Salhi, M. J., Triebel, C. & Lemoine, R., 1999. Combined photovoltaic and solar thermal systems for facade integration and building insulation. *Solar Energy,* 67, 239-248.

Kumar, A., Baredar, P. & Qureshi, U., 2015. Historical and recent development of photovoltaic thermal (PVT) technologies. *Renewable and Sustainable Energy Reviews,* 42, 1428-1436.

Kurtz, S., 2006. High-efficiency, multijunction solar cells for large-scale solar electricity generation. *American Physical Society March 2006Meeting.*

Kuznik, F. & Virgone, J., 2009. Experimental investigation of wallboard containing phase change material: Data for validation of numerical modeling. *Energy and Buildings,* 41, 561-570.

Kuznik, F., Virgone, J. & Johannes, K., 2010. Development and validation of a new TRNSYS type for the simulation of external building walls containing PCM. *Energy and Buildings,* 42, 1004-1009.

Lai, C.-M. & Hokoi, S., 2014. Thermal performance of an aluminum honeycomb wallboard incorporating microencapsulated PCM. *Energy and Buildings,* 73, 37-47.

Lalović, B., Kiss, Z. & Weakliem, H., 1986. A hybrid amorphous silicon photovoltaic and thermal solar collector. *Solar Cells,* 19, 131-138.

Lázaro, A., Zalba, B., Bobi, M., Castellón, C. & Cabeza, L. F., 2006. Experimental study on phase change materials and plastics compatibility. *AIChE journal,* 52, 804-808.

Li, Y., Witharana, S., Cao, H., Lasfargues, M., Huang, Y. & Ding, Y., 2013. Wide spectrum solar energy harvesting through an integrated photovoltaic and thermoelectric system. *Particuology,* 15, 39-44.

Li, Z. & Zhao, J., 2013. Aqueous solution-chemical derived NiAl2O3 solar selective absorbing coatings. 2. Wetting agents and spreading of aqueous solutions on aluminum substrate. *Applied Surface Science,* 268, 231-236.

Lillo-Bravo, I., Silva-Perez, M. & Larraneta Gomez-Caminero, M., Use of Phase Change Materials in Photovoltaic Modules with Solar Concentration of up to 2x *26th European*

Photovoltaic Solar Energy Conference and Exhibition, September 2011 Hamburg, Germany. 634-639.

Lin, W., Ma, Z., Sohel, M. I. & Cooper, P., 2014. Development and evaluation of a ceiling ventilation system enhanced by solar photovoltaic thermal collectors and phase change materials. *Energy Conversion and Management,* **88,** 218-230.

Ling, Z., Zhang, Z., Shi, G., Fang, X., Wang, L., Gao, X., Fang, Y., Xu, T., Wang, S. & Liu, X., 2014. Review on thermal management systems using phase change materials for electronic components, Li-ion batteries and photovoltaic modules. *Renewable and Sustainable Energy Reviews,* 31, 427-438.

Liu, M., Saman, W. & Bruno, F., 2011. Validation of a mathematical model for encapsulated phase change material flat slabs for cooling applications. *Applied Thermal Engineering,* 31, 2340-2347.

Liu, M., Saman, W. & Bruno, F., 2012. Review on storage materials and thermal performance enhancement techniques for high temperature phase change thermal storage systems. *Renewable and Sustainable Energy Reviews,* 16, 2118-2132.

Liu, M., Saman, W. & Bruno, F., 2014. Computer simulation with TRNSYS for a mobile refrigeration system incorporating a phase change thermal storage unit. *Applied Energy,* 132, 226-235.

Lo Brano, V., Ciulla, G., Piacentino, A. & Cardona, F., 2013. On the Efficacy of PCM to Shave Peak Temperature of Crystalline Photovoltaic Panels: An FDM Model and Field Validation. *Energies,* 6, 6188-6210.

Lo Brano, V., Ciulla, G., Piacentino, A. & Cardona, F., 2014. Finite difference thermal model of a latent heat storage system coupled with a photovoltaic device: Description and experimental validation. *Renewable Energy,* 68, 181-193.

Lo Brano, V., Orioli, A. & Ciulla, G., 2012. On the experimental validation of an improved five-parameter model for silicon photovoltaic modules. *Solar Energy Materials and Solar Cells,* 105, 27-39.

Lo Brano, V., Orioli, A., Ciulla, G. & Di Gangi, A., 2010. An improved five-parameter model for photovoltaic modules. *Solar Energy Materials and Solar Cells,* 94, 1358-1370.

London Metal Exchange. 2015. www.lme.com [Online]. [Accessed 10 September 2015].

Lu, K., 2014. Materials in Energy Conversion, Harvesting, and Storage, *John Wiley & Sons*.

Lu, S., Liu, S., Huang, J. & Kong, X., 2014. Establishment and experimental verification of PCM room's TRNSYS heat transfer model based on latent heat utilization ratio. *Energy and Buildings,* 84, 287-298.

Lurie, M. V., 2008. Modeling of Oil Product and Gas Pipeline Transportation, KGaA, Weinheim, Germany, *Wiley-VCH Verlag GmbH & Co.*

Ma, T., Yang, H., Zhang, Y., Lu, L. & Wang, X., 2015. Using phase change materials in photovoltaic systems for thermal regulation and electrical efficiency improvement: A review and outlook. *Renewable and Sustainable Energy Reviews,* 43, 1273-1284.

Maiti, S., Banerjee, S., Vyas, K., Patel, P. & Ghosh, P. K., 2011. Self regulation of photovoltaic module temperature in V-trough using a metal-wax composite phase change matrix. *Solar Energy,* 85, 1805-1816.

Malvi, C. S., Dixon-Hardy, D. W. & Crook, R., 2011. Energy balance model of combined photovoltaic solar-thermal system incorporating phase change material. *Solar Energy,* 85, 1440-1446.

Marchi, S., Pagliolico, S. & Sassi, G., 2013. Characterization of panels containing micro-encapsulated Phase Change Materials. *Energy Conversion and Management,* 74, 261-268.

Marín, J. M., Zalba, B., Cabeza, L. F. & Mehling, H., 2003. Determination of enthalpy–temperature curves of phase change materials with the temperature-history method: improvement to temperature dependent properties. *Measurement science and technology,* 14, 184.

Massaguer, E., Massaguer, A., Montoro, L. & Gonzalez, J. R., 2014. Development and validation of a new TRNSYS type for the simulation of thermoelectric generators. *Applied Energy,* 134, 65-74.

Masters, G. M., 2013. Renewable and efficient electric power systems, *John Wiley & Sons.*

Matar, W., Murphy, F., Pierru, A. & Rioux, B., 2015. Lowering Saudi Arabia's fuel consumption and energy system costs without increasing end consumer prices. *Energy Economics,* 49, 558-569.

Maturi, L., Belluardo, G., Moser, D. & Del Buono, M., 2014. BiPV System Performance and Efficiency Drops: Overview on PV Module Temperature Conditions of Different Module Types. *Energy Procedia,* 48, 1311-1319.

McCormack, S. J. & Norton, B., 2013. The shadows cast by inadequate energy governance: why more sun does not necessarily mean more photovoltaic electricity.

Met Eireann, 2015a. Sunshine in Ireland.

Met Eireann. 2015b. Temperature in Ireland [Online]. Available: http://www.met.ie/climate/temperature.asp.

Mettawee, E.-B. S. & Assassa, G. M. R., 2006. Experimental study of a compact PCM solar collector. *Energy,* 31, 2958-2968.

Moreno, P., Miró, L., Solé, A., Barreneche, C., Solé, C., Martorell, I. & Cabeza, L. F., 2014. Corrosion of metal and metal alloy containers in contact with phase change materials (PCM) for potential heating and cooling applications. *Applied Energy,* 125, 238-245.

Moriarty, P. & Honnery, D., 2012. What is the global potential for renewable energy? *Renewable and Sustainable Energy Reviews,* 16, 244-252.

Murali, G. & Mayilsamy, K., 2015. An overview of PCM usage to enhance solar water heating system. *International Journal of ChemTech Research,* Vol. 7, 1802-1807.

Najafi, H., 2012. Evaluaion of alternaive cooling techniques for photovoltaic panels. Master of Science Masters of Science, *The University of Alabama.*

Nallusamy, N., Sampath, S. & Velraj, R., 2007. Experimental investigation on a combined sensible and latent heat storage system integrated with constant/varying (solar) heat sources. *Renewable Energy,* 32, 1206-1227.

National Meteorology & Environment Center. 2015. *R*E: Surface Monthly Climatological Report. Type to COMMUNICATION, P.

National Renewable Energy Laboratory. 2012. NREL, UCLA Certify World Record for Polymer Solar Cell Efficiency. Available: http://www.nrel.gov/news/press/2012/1801.html.

Ngo, H. L., Yee, W. C., Mcaloon, A. J. & Haas, M. J., 2014. Techno-economic analysis of an improved process for producing saturated branched-chain fatty acids. *Journal of Agricultural Science,* 6, p158.

Nkwetta, D. N. & Haghighat, F., 2014. Thermal energy storage with phase change material A state-of-the art review. *Sustainable Cities and Society,* 10, 87-100.

Nkwetta, D. N. & Smyth, M., 2012. Performance analysis and comparison of concentrated evacuated tube heat pipe solar collectors. *Applied Energy,* 98, 22-32.

Nkwetta, D. N., Smyth, M., Zacharopoulos, A. & Hyde, T., 2012a. In-door experimental analysis of concentrated and non-concentrated evacuated tube heat pipe collectors for medium temperature applications. *Energy and Buildings,* 47, 674-681.

Nkwetta, D. N., Smyth, M., Zacharopoulos, A. & Hyde, T., 2012b. Optical evaluation and analysis of an internal low-concentrated evacuated tube heat pipe solar collector for powering solar air-conditioning systems. *Renewable Energy,* Volume 39, 65-70.

NREL, 2015. Best Research-Cell Efficiencies.

Ofgem. 2015a. Tariffs and payments for the domestic renewable heat incentive [Online]. [Accessed 9 October 2015].

Ofgem. 2015b. www.ofgem.gov.uk [Online]. Available: https://www.ofgem.gov.uk/gas/retail-market/monitoring-data-and-statistics/typical-domestic-consumption-values.

Oliver, A., 2012. Thermal characterization of gypsum boards with PCM included: Thermal energy storage in buildings through latent heat. *Energy and Buildings,* 48, 1-7.

Ölz, S., Pflüger, A. & Tulej, P., 2007. Contribution of renewables to energy security, IEA information paper.

Oró, E., Barreneche, C., Farid, M. M. & Cabeza, L. F., 2013. Experimental study on the selection of phase change materials for low temperature applications. *Renewable Energy,* 57, 130-136.

Oró, E., De Gracia, A., Castell, A., Farid, M. M. & Cabeza, L. F., 2012a. Review on phase change materials (PCMs) for cold thermal energy storage applications. *Applied Energy,* 99, 513-533.

Oró, E., Miró, L., Farid, M. M. & Cabeza, L. F., 2012b. Improving thermal performance of freezers using phase change materials. *International Journal of Refrigeration,* 35, 984-991.

Osterman, E., Tyagi, V. V., Butala, V., Rahim, N. A. & Stritih, U., 2012. Review of PCM based cooling technologies for buildings. *Energy and Buildings,* 49, 37-49.

Padovan, R. & Manzan, M., 2014. Genetic optimization of a PCM enhanced storage tank for Solar Domestic Hot Water Systems. *Solar Energy,* 103, 563-573.

Pastorello, C., 2010. Energy efficiency and energy consumption in the household sector.

Pasupathy, A., Velraj, R. & Seeniraj, R. V., 2008. Phase change material-based building architecture for thermal management in residential and commercial establishments. *Renewable and Sustainable Energy Reviews,* 12, 39-64.

Pattabi, M., Krishnan, S., Ganesh & Mathew, X., 2007. Effect of temperature and electron irradiation on the I-V characteristics of Au/CdTe Schottky diodes. *Solar Energy,* 81, 111-116.

Pause, B. H., New Textile-based hybrid photovoltaic (PVIT) system. *WREC XI,* September 2010 Abu Dhabi, UAE.

Pcm Products. 2015. http://www.pcmproducts.net/ [Online]. [Accessed 13/07/2015.

Peach, M., 2013. Heliatek achieves 12% organic solar cell efficiency. Optics.org.

Peck, J. H., Kim, J.-J., Kang, C. & Hong, H., 2006. A study of accurate latent heat measurement for a PCM with a low melting temperature using T-history method. *International Journal of Refrigeration,* 29, 1225-1232.

Pedersen, C. O., Advanced zone simulation in EnergyPlus: incorporation of variable properties and phase change material (PCM) capability. *Building Simulation,* 2007 Beijing, China.

Pei, G., Zhang, T., Yu, Z., Fu, H., Wang, J. & Ji, J., Comparative Study of a Heat Pipe PV/T and a Water-Thermosiphon PV/TComparative Study of a Heat Pipe PV/T and a Water-Thermosiphon PV/T. *Power and Energy Engineering Conference (APPEEC), 2010 Asia-Pacific,* 28-31 March 2010 2010. 1-4.

Pendyala, S., 2012. Macroencapsulation of phase change materials for thermal energy storage.

Philibert, C., 2011. Solar Energy Perspectives - International Energy Acency Publication.

Porciúncula, C., Marcilio, N., Tessaro, I. & Gerchmann, M., 2012. Production of hydrogen in the reaction between aluminum and water in the presence of NaOH and KOH. *Brazilian Journal of Chemical Engineering,* 29, 337-348.

Porisini, F. C., 1988. Salt hydrates used for latent heat storage: Corrosion of metals and reliability of thermal performance. *Solar Energy,* 41, 193-197.

Prakash, J., 1994. Transient analysis of a photovoltaic-thermal solar collector for co-generation of electricity and hot air/water. *Energy Conversion and Management,* 35, 967-972.

Prakash, J., Garg, H. P. & Datta, G., 1985. A solar water heater with a built-in latent heat storage. *Energy Conversion and Management,* 25, 51-56.

Rabin, Y., Bar-Niv, I., Korin, E. & Mikic, B., 1995. Integrated solar collector storage system based on a salt-hydrate phase-change material. *Solar Energy,* 55, 435-444.

Radziemska, E., 2003. The effect of temperature on the power drop in crystalline silicon solar cells. *Renewable Energy,* 28, 1-12.

Raga, S. R. & Fabregat-Santiago, F., 2012. Temperature effects in dye-sensitized solar cells. *Physical Chemistry Chemical Physics,* 15, 2328-2336.

Redpath, D. A., 2012. Thermosyphon heat-pipe evacuated tube solar water heaters for northern maritime climates. *Solar energy,* 86, 705-715.

Regin, A. F., Solanki, S. C. & Saini, J. S., 2008. Heat transfer characteristics of thermal energy storage system using PCM capsules: A review. *Renewable and Sustainable Energy Reviews,* 12, 2438-2458.

Rehman, S. & El-Amin, I., 2012. Performance evaluation of an off-grid photovoltaic system in Saudi Arabia. *Energy,* 46, 451-458.

Renewable Energy Focus, 2012. Saudi Arabia aims for 41GW of solar. *Renewable Energy Focus,* 13, 8.

Riffat, S., Zhao, X. & Doherty, P., 2005. Developing a theoretical model to investigate thermal performance of a thin membrane heat-pipe solar collector. *Applied thermal engineering,* 25, 899-915.

Rodriguez-Ubinas, E., Ruiz-Valero, L., Vega, S. & Neila, J., 2012. Applications of Phase Change Material in highly energy-efficient houses. *Energy and Buildings,* 50, 49-62.

Royon, L., Karim, L. & Bontemps, A., 2013. Thermal energy storage and release of a new component with PCM for integration in floors for thermal management of buildings. *Energy and Buildings,* 63, 29-35.

Rozanna, D., Chuah, T., Salmiah, A., Choong, T. S. & Sa'ari, M., 2005. Fatty acids as phase change materials (PCMs) for thermal energy storage: a review. *International Journal of Green Energy,* 1, 495-513.

Rubin, M., 1985. Optical properties of soda lime silica glasses. *Solar energy materials,* 12, 275-288.

Rubiterm. 2015. www.rubitherm.de/english/ [Online]. [Accessed 2015 31/05].

Sabbagh, J. A., Sayigh, A. a. M. & El-Salam, E. M. A., 1986. Correlation of solar radiation and sunshine duration in Riyadh. *Pakistan Journal of Scientific and Industrial Research,* 16, 16.

Safa, A. A., Fung, A. S. & Kumar, R., 2015. Heating and cooling performance characterisation of ground source heat pump system by testing and TRNSYS simulation. *Renewable Energy,* 83, 565-575.

Salvi, D., Boldor, D., Aita, G. M. & Sabliov, C. M., 2011. COMSOL Multiphysics model for continuous flow microwave heating of liquids. *Journal of Food Engineering,* 104, 422-429.

Santbergen, R. & Van Zolingen, R. J. C., 2008. The absorption factor of crystalline silicon PV cells: A numerical and experimental study. *Solar Energy Materials and Solar Cells,* 92, 432-444.

Sarı, A., 2006. Eutectic mixtures of some fatty acids for latent heat storage: Thermal properties and thermal reliability with respect to thermal cycling. *Energy Conversion and Management,* 47, 1207-1221.

Sarı, A. & Karaipekli, A., 2008. Preparation and thermal properties of capric acid/palmitic acid eutectic mixture as a phase change energy storage material. *Materials Letters,* 62, 903-906.

Sarı, A. & Kaygusuz, K., 2003. Some fatty acids used for latent heat storage: thermal stability and corrosion of metals with respect to thermal cycling. *Renewable Energy,* 28, 939-948.

Sari, A., Sari, H. & Önal, A., 2004. Thermal properties and thermal reliability of eutectic mixtures of some fatty acids as latent heat storage materials. *Energy Conversion and Management,* 45, 365-376.

Sarwar, J., 2012. Experimental and Numerical Investigation of Thermal Regulation of Photovoltaic and Concentrated Photovoltaic using Phase Change Materials, PhD Thesis. *Dublin Institute of Technology.*

Sarwar, J., 2013. Experimental and Numerical Investigation of Thermal Regulation of Photovoltaic and Concentrated Photovoltaic using Phase Change Materials. *Dublin Institute of Technology.*

Sarwar, J., McCormack, S. J., Huang, M. J. & Norton, B., 2014. Numerical investigation and experimental validation of thermal behaviour of organic phase change materials for temperature regulation enhancement of photovoltaics. *International Journal of Heat and Mass Transfer,* In review.

Sasmito, A. P., Shamim, T. & Mujumdar, A. S., 2013. Passive thermal management for PEM fuel cell stack under cold weather condition using phase change materials (PCM). *Applied Thermal Engineering,* 58, 615-625.

Savenrg. 2015. http://www.rgees.com/products.php [Online]. Available: http://www.rgees.com/products.php [Accessed 1st October 2015].

Schossig, P., Henning, H. M., Gschwander, S. & Haussmann, T., 2005. Micro-encapsulated phase-change materials integrated into construction materials. *Solar Energy Materials and Solar Cells,* 89, 297-306.

Schranzhofer, H., Puschnig, P., Heinz, A., Streicher, W., . Validation of a TRNSYS simulation model for PCM energy storages and PCM wall construction elements. *Ecostock 2006 - Tenth International Conference on Thermal Energy Storage*, May 31 – June 2 2006 USA.

SEAI, 2013. Energy in the Residential Sector.

SEAI, 2015. Achieving Ireland's 2020 Renewable Heat Target.

Shafiee, S. & Topal, E., 2009. When will fossil fuel reserves be diminished? *Energy Policy,* 37, 181-189.

Sharma, A., Tyagi, V. V., Chen, C. R. & Buddhi, D., 2009. Review on thermal energy storage with phase change materials and applications. *Renewable and Sustainable Energy Reviews,* 13, 318-345.

Sharma, A., Won, L. D., Buddhi, D. & Park, J. U., 2005. Numerical heat transfer studies of the fatty acids for different heat exchanger materials on the performance of a latent heat storage system. *Renewable Energy,* 30, 2179-2187.

Sigma-Aldrich. 2015. www.sigmaaldrich.com/ [Online]. [Accessed 31/05 2015].

Solangi, K. H., Islam, M. R., Saidur, R., Rahim, N. A. & Fayaz, H., 2011. A review on global solar energy policy. *Renewable and Sustainable Energy Reviews,* 15, 2149-2163.

Solar Technology International,2013. 80W Solar Panel Kit STP080.

Solargis,2013. GeoModel Solar (www.solargis.info).

Solé, A., Miró, L., Barreneche, C., Martorell, I. & Cabeza, L. F., 2013. Review of the T-history method to determine thermophysical properties of phase change materials (PCM). *Renewable and Sustainable Energy Reviews,* 26, 425-436.

Solé, A., Miró, L., Barreneche, C., Martorell, I. & Cabeza, L. F., 2015. Corrosion of metals and salt hydrates used for thermochemical energy storage. *Renewable Energy,* 75, 519-523.

Solomon, G. R., Karthikeyan, S. & Velraj, R., 2013. Sub cooling of PCM due to various effects during solidification in a vertical concentric tube thermal storage unit. *Applied Thermal Engineering,* 52, 505-511.

Sriprapha, K., Piromjit, C., Limmanee, A. & Sritharathikhun, J., 2011. Development of thin film amorphous silicon oxide/microcrystalline silicon double-junction solar cells and their temperature dependence. *Solar Energy Materials and Solar Cells,* 95, 115-118.

Stanković, S. B. & Kyriacou, P. A., 2013. Improved measurement technique for the characterization of organic and inorganic phase change materials using the T-history method. *Applied Energy,* 109, 433-440.

Stritih, U. & Butala, V., 2010. Experimental investigation of energy saving in buildings with PCM cold storage. *International Journal of Refrigeration,* 33, 1676-1683.

Stritih, U. & Novak, P., 1996. Solar heat storage wall for building ventilation. *Renewable Energy,* 8, 268-271.

Stultz, J. W. & Wren, L. C., 1978. Thermal performance testing and analysis of photovoltaic modules in natural sunlight, Pasadena, California, *Jet propulsion laboratory.*

Subiantoro, A. & Ooi, K. T., 2013. Analytical models for the computation and optimization of single and double glazing flat plate solar collectors with normal and small air gap spacing. *Applied Energy,* 104, 392-399.

Summers, E. K., Antar, M. A. & Lienhard V, J. H., 2012. Design and optimization of an air heating solar collector with integrated phase change material energy storage for use in humidification-dehumidification desalination. *Solar Energy,* 86, 3417-3429.

Šúri, M., Huld, T. A., Dunlop, E. D., M., M. A. & Wald, L., Online data and tools for estimation of solar electricity in Africa: the PVGIS approach. *Proceedings from 21st European Photovoltaic Solar Energy Conference and Exhibition,* 4-8 October 2006 Dresden, Germany.

Sustainable Energy Ireland, 2011. Energy security in Ireland: A statistical overview.

Swanson, R. M., 2000. The promise of concentrators. *Progress in Photovoltaics Research and Applications,* 8, 93-111.

Taleb, H. M. & Sharples, S., 2011. Developing sustainable residential buildings in Saudi Arabia: A case study. *Applied Energy,* 88, 383-391.

Tanuwijava, A., Ho, C., Lai, C.-M. & Huang, C.-Y., 2013. Numerical Investigation of the Thermal Management Performance of MEPCM Modules for PV Applications. *Energies,* 6, 3922-3936.

Tarifasgasluz. 2015. http://tarifasgasluz.com/faq/precio-kwh-2015#1 [Online]. Available: http://tarifasgasluz.com/faq/precio-kwh-2015#1 [Accessed 24 September 2015].

Toivola, M., Peltokorpi, L., Halme, J. & Lund, P., 2007. Regenerative effects by temperature variations in dye-sensitized solar cells. *Solar Energy Materials and Solar Cells,* 91, 1733-1742.

Tonui, J. K. & Tripanagnostopoulos, Y., 2007. Improved PV/T solar collectors with heat extraction by forced or natural air circulation. *Renewable Energy,* 32, 623-637.

Toppi, T. & Mazzarella, L., 2013. Gypsum based composite materials with micro-encapsulated PCM: Experimental correlations for thermal properties estimation on the basis of the composition. *Energy and Buildings,* 57, 227-236.

Townsend, T. U., 1989. A method for estimating the long-term performance of direct-coupled photovoltaic systems. *University of Wisconsin-Madison.*

Tripanagnostopoulos, Y., Nousia, T., Souliotis, M. & Yianoulis, P., 2002. Hybrid photovoltaic/thermal solar systems. *Solar Energy,* 72, 217-234.

Tripanagnostopoulos, Y., Souliotis, M. & Nousia, T., 2000. Solar collectors with colored absorbers. *Solar Energy,* 68, 343-356.

Trnsys Manual,2014. TRNSYS 17 - Documentation.

Troviano, M. & Taretto, K., 2011. Temperature-dependent quantum efficiency analysis of graded-gap Cu(In,Ga)Se2 solar cells. *Solar Energy Materials and Solar Cells,* 95, 3081-3086.

Tyagi, V. V., Panwar, N. L., Rahim, N. A. & Kothari, R., 2012. Review on solar air heating system with and without thermal energy storage system. *Renewable and Sustainable Energy Reviews,* 16, 2289-2303.

Ullah, K. R., Saidur, R., Ping, H. W., Akikur, R. K. & Shuvo, N. H., 2013. A review of solar thermal refrigeration and cooling methods. *Renewable and Sustainable Energy Reviews,* 24, 499-513.

Ulleberg, Ø. & Mørner, S. O., 1997. TRNSYS simulation models for solar-hydrogen systems. *Solar Energy,* 59, 271-279.

Usami, A., Seki, S., Mita, Y., Kobayashi, H., Miyashiro, H. & Terada, N., 2009. Temperature dependence of open-circuit voltage in dye-sensitized solar cells. *Solar Energy Materials and Solar Cells,* 93, 840-842.

Villalva, M. G., Gazoli, J. R. & Filho, E. R., 2009. Comprehensive Approach to Modeling and Simulation of Photovoltaic Arrays. *Power Electronics, IEEE Transactions on,* 24, 1198-1208.

Walsh, B. P., Murray, S. N. & O'sullivan, D. T. J., 2013. Free-cooling thermal energy storage using phase change materials in an evaporative cooling system. *Applied Thermal Engineering,* 59, 618-626.

Wasim, S. M., Rincón, C., Marín, G., Bocaranda, P., Hernández, E., Bonalde, I. & Medina, E., 2001. Effect of structural disorder on the Urbach energy in Cu ternaries. *Physical Review B,* 64, 195101.

Wazwaz, A., Salmi, J., Hallak, H. & Bes, R., 2002. Solar thermal performance of a nickel-pigmented aluminium oxide selective absorber. *Renewable Energy,* 27, 277-292.

Wolf, M., 1976. Performance analyses of combined heating and photovoltaic power systems for residences. *Energy Conversion,* 16, 79-90.

Wu, S.-Y., Zhang, Q.-L., Xiao, L. & Guo, F.-H., 2011. A heat pipe photovoltaic/thermal (PV/T) hybrid system and its performance evaluation. *Energy and Buildings,* 43, 3558-3567.

Wu, Y., 2009. Thermal management of concentrator photovoltaics, PhD Thesis. *University of Warwick, UK.*

Wu, Y. & Eames, P., Experimental Characterisation of an Asymmetric Compound Parabolic PV Concentrator Complied with a Phase Change Material. *7th Photovoltaic Science, Applications and Technology Conference*, 2011 Heriot-Watt University, Edinburgh, Scotland.

Wu, Y. & Wang, T., 2015. Hydrated salts/expanded graphite composite with high thermal conductivity as a shape-stabilized phase change material for thermal energy storage. *Energy Conversion and Management,* 101, 164-171.

Yang, Y.-T. & Wang, Y.-H., 2012. Numerical simulation of three-dimensional transient cooling application on a portable electronic device using phase change material. *International Journal of Thermal Sciences,* 51, 155-162.

Yin, H. M., Yang, D. J., Kelly, G. & Garant, J., 2013. Design and performance of a novel building integrated PV/thermal system for energy efficiency of buildings. *Solar Energy,* 87, 184-195.

Yinping, Z., Yi, J. & Yi, J., 1999. A simple method, the-history method, of determining the heat of fusion, specific heat and thermal conductivity of phase-change materials. *Measurement Science and Technology,* 10, 201.

Yoon, S.-J., Song, M.-S., Park, I.-W., Lee, D.-W., Park, G.-C. & Kim, E.-S., 2013. Assessment of COMSOL capability to analyze thermal-hydraulic characteristics of Korean helium cooled test blanket. *Fusion Engineering and Design,* 88, 2240-2243.

Yuan, Y., Zhang, N., Tao, W., Cao, X. & He, Y., 2014a. Fatty acids as phase change materials: A review. *Renewable and Sustainable Energy Reviews,* 29, 482-498.

Yuan, Y., Zhang, N., Tao, W., Cao, X. & He, Y., 2014b. Fatty acids as phase change materials: A review. *Renewable and Sustainable Energy Reviews,* 29, 482-498.

Yuasa. 2015. http://www.yuasabatteries.com/ [Online]. [Accessed 14 October 2015].

Zalba, B., Marín, J. M., Cabeza, L. F. & Mehling, H., 2003. Review on thermal energy storage with phase change: materials, heat transfer analysis and applications. *Applied Thermal Engineering,* 23, 251-283.

Zhang, H., Xu, Q., Zhao, Z., Zhang, J., Sun, Y., Sun, L., Xu, F. & Sawada, Y., 2012a. Preparation and thermal performance of gypsum boards incorporated with microencapsulated phase change materials for thermal regulation. *Solar Energy Materials and Solar Cells,* 102, 93-102.

Zhang, X., Zhao, X., Smith, S., Xu, J. & Yu, X., 2012b. Review of R&D progress and practical application of the solar photovoltaic/thermal (PV/T) technologies. *Renewable and Sustainable Energy Reviews,* 16, 599-617.

Zondag, H. A., 2008. Flat-plate PV-Thermal collectors and systems: A review. *Renewable and Sustainable Energy Reviews,* 12, 891-959.

Zondag, H. A., De Vries, D. W., Van Helden, W. G. J., Van Zolingen, R. J. C. & Van Steenhoven, A. A., 2002. The thermal and electrical yield of a PV-thermal collector. *Solar Energy,* 72, 113-128.

Zondag, H. A., De Vries, D. W., Van Helden, W. G. J., Van Zolingen, R. J. C. & Van Steenhoven, A. A., 2003. The yield of different combined PV-thermal collector designs. *Solar Energy*, 74, 253-269.

Publications

Journals

- Browne, M.C., Lawlor, K., Kelly, A., Norton, B., and McCormack, S.J., 2015, Indoor Characterisation of a Photovoltaic/Thermal Phase Change Material System, *Energy Procedia*,70, Pages 163-171 (*Section 5.5 of thesis*)

- Browne, M.C., Norton, B., McCormack, S.J., 2015, Phase Change Materials for Photovoltaic Thermal Management, *Renewable and Sustainable Energy Reviews*, 47, Pages 762-782 (*Section 2.2 – 2.6 of thesis*)

- Browne, M.C., Norton, B., McCormack, S.J., 2015, Heat Retention of a Photovoltaic/Thermal Collector with PCM, *Solar Energy*, Under Review (*Section 5.2 and 5.6 of thesis*)

- Navarro, L., de Gracia, A., Niall, D., Castell, A., Browne, M.C., McCormack, S.J., Griffiths, P., Cabeza L.F., 2015, Thermal Energy Storage in Building Integrated Thermal Systems: A Review. Part 2 Integration as Passive System, *Renewable Energy*, In Press, Corrected Proof

- Navarro, L., de Gracia, A., Colclough, S., Browne, M.C., McCormack, S.J., Griffiths, P., Cabeza L.F., 2015, Thermal Energy Storage in Building Integrated Thermal Systems: A Review. Part 1 Integration as an Active System, *Renewable Energy*, Under Review

Conferences

- Browne, M.C., Barbesino, A. and S McCormack, . J., Short Term Corrosion Testing of Metals and Plastics in a PCM Environment for Use in Latent Heat Storage, *2nd International Conference on Sustainable Energy Storage*, June 19th -21st 2013, Trinity College Dublin, Ireland

- Browne, M.C., Severino, I., Patil, P., O'Farrell, K., Candenando, L., McCormack, S. J. and Norton, B., Initial System Design and Experimental Set-up for a Photovoltaic/Phase Change Material System, *2nd International Conference on Sustainable Energy Storage,* June 19th -21st 2013, Trinity College Dublin, Ireland

- Browne, M.C., McCormack, S. J., O'Farrell, K., Candenando, L. and Norton, B., Preliminary Results of a Photovoltaic/Phase Change Material Thermal System, *28th European Photovoltaic Solar Energy Conference and Exhibition*, 30th September – 4th October 2013, Parc de Expositions Paris Nord Villepinte, France

- Browne, M.C., Norton, B. and McCormack, S. J., 2014, Indoor Characterisation of a Photovoltaic/Thermal Phase Change Material System, *World renewable Energy Congress XIII,* 3rd -8th August 2014, Kingston University, London, U.K.

- Browne, M.C., Quigley, D., Hard, H.R., Gilligan, S., Cardoso Campos Ribeiro, N., Almeida, N. and McCormack, S. J.,2015, Application of Phase Change Material in Photovoltaic/Thermal System, *Solar Heating and Cooling Conference,* 2nd - 4th December 2015, Istanbul, Turkey.

Appendix 1

Photovoltaic Solar Electricity Potential in European Countries (Huld et al., 2012; SolarGIS, 2013)

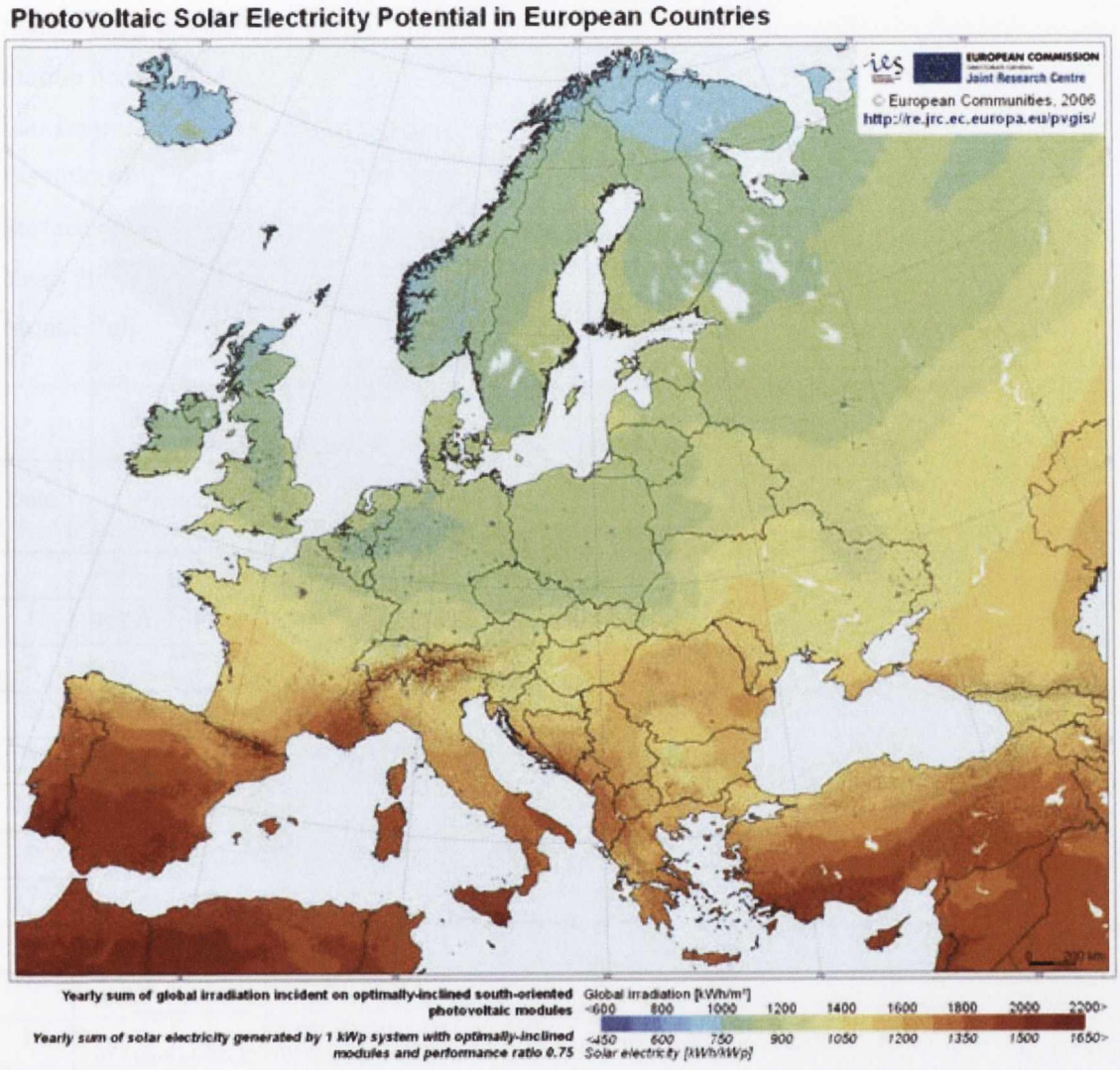

Appendix 2

Photovoltaic Solar Electricity Potential in African and Middle Eastern Countries (Huld et al., 2012; SolarGIS, 2013)

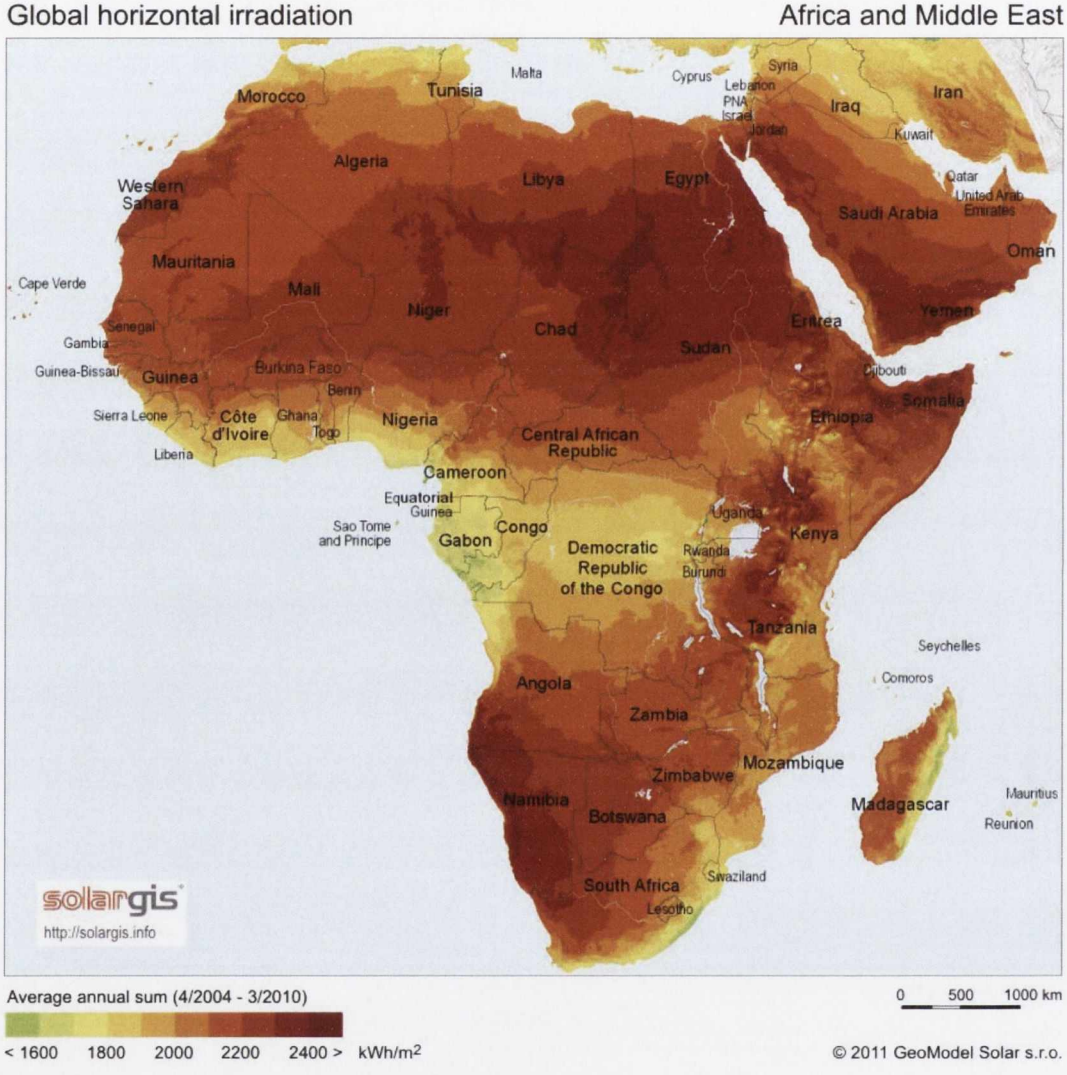

Appendix 3

Kingdom of Saudi Arabia, Ministry of Defence and Aviation, National and Environment Centre (National Meteorology & Environment Center, 2015)

Station number: 40416

Station name: Dhahran

Lat/ Long: 26 15 34N, 50 08 39E

Elevation 16.77 m

Surface Monthly Climatology Report

Year: 2000

Month: July

Date	Pressure (hPa)			Wind Velocity (m/s)		Ambient temperature (°C)			Relative Humidity (%)		
	Max	Min	Ave	Direction	Ave	Max	Min	Ave	Max	Min	Ave
1	997.0	993.7	995.2	NW	11	46.0	28.0	37.6	33	10	19
2	995.7	993.4	994.5	WNW	11	46.0	31.0	39.1	21	13	16
3	996.3	993.9	995.4	N	12	43.0	30.0	36.9	34	13	21
4	997.1	994.7	995.6	NE	7	43.0	28.0	34.5	83	15	33
5	996.7	994.5	995.3	WNW	6	45.0	26.0	35.8	100	12	4Surf
6	995.5	992.5	994.0	NNW	13	47.0	30.0	39.1	31	7	17
7	995.6	993.1	994.4	N	12	46.0	31.0	37.0	32	12	24
8	998.0	995.7	996.8	N	6	45.0	28.0	35.7	89	13	48
9	997.8	994.9	996.3	SE	8	43.0	27.0	35.1	93	22	64
10	997.7	995.5	996.5	E	8	47.0	31.0	37.1	74	26	51
11	998.7	995.5	996.9	E	7	42.0	31.0	36.0	69	20	50
12	997.2	992.5	994.8	E	6	46.0	31.0	37.6	83	22	52
13	993.2	990.8	991.9	NE	7	48.0	32.0	39.3	78	10	45
14	993.7	990.8	992.4	NE	6	49.0	31.0	38.0	8	12	43
15	995.7	993.6	994.7	W	8	46.0	29.0	36.5	71	13	44
16	997.0	993.2	994.9	E	5	47.0	28.0	37.5	73	13	37
17	994.3	992.3	993.3	N	13	46.0	31.0	39.4	52	14	23
18	996.1	993.1	994.3	N	14	43.0	35.0	38.6	30	16	24

19	995.3	991.9	993.5	N	14	43.0	35.0	39.0	41	16	23
20	992.5	989.6	991.0	NW	12	44.0	34.0	38.5	19	13	17
21	991.8	989.1	990.8	N	9	42.0	31.0	36.5	77	17	34
22	992.8	990.8	991.9	WNW	6	46.0	28.0	36.4	80	13	42
23	993.9	991.6	992.7	N	10	45.0	32.0	37.7	39	13	24
24	993.7	991.2	992.4	N	8	47.0	28.0	37.5	62	13	22
25	992.9	989.6	991.4	W	8	48.0	29.0	37.4	69	9	28
26	994.3	991.7	993.1	N	12	46.0	31.0	37.9	49	12	24
27	994.4	991.5	993.0	N	11	44.0	31.0	36.9	32	16	23
28	992.7	990.1	991.4	WNW	9	47.0	31.0	37.7	56	13	25
29	993.4	990.8	992.3	E	5	42.0	31.0	36.7	60	20	35
30	995.0	992.5	993.5	ENE	7	44.0	31.0	36.5	83	17	52
31	995.7	993.4	994.5	ENE	7	43.0	30.0	36.0	89	22	59

Station number: 40416

Station name: Dhahran

Lat/ Long: 26 15 34N, 50 08 39E

Elevation 16.77 m

Year: 2000

Month: July

Day 5th

Time	Temperature (°C)	Solar Irradiance (W/m^2)
0	29.9	0
1	29.0	0
2	28.1	0
3	27.5	0
4	27.1	0
5	26.4	22
6	26.0	93
7	28.0	226
8	30.2	419
9	32.3	613

10	33.8	774
11	36.1	917
12	40.3	947
13	42.6	933
14	43.9	867
15	44.5	733
16	44.1	548
17	42.8	322
18	41.6	47
19	39.2	18
20	37.9	0
21	37	0
22	35.8	0
23	34.1	0
24	32.1	0